Transactions of the ASME, Journal of Fluids Engineering (ISSN 0098-2202) is published bimonthly (Jan., Mar., May, July, Sept., Nov.) by The American Society of Mechanical Engineers, Three Park Avenue, New York, NY 10016. Periodicals postage paid at New York, NY and additional mailing offices.
POSTMASTER: Send address changes to Transactions of the ASME, Journal of Fluids Engineering, c/o THE AMERICAN SOCIETY OF MECHANICAL ENGINEERS, 22 Law Drive, Box 2300, Fairfield, NJ 07007-2300.
CHANGES OF ADDRESS must be received at Society headquarters seven weeks before they are to be effective. Please send old label and new address.
STATEMENT from By-Laws. The Society shall not be responsible for statements or opinions advanced in papers or ... printed in its publications (B7.1, Par. 3).

INDEXED by Applied Mechanics Reviews and Engineering Information, Inc. Canadian Goods & Services Tax Registration #126148048.

Journal of Fluids Engineering

Published Bimonthly by ASME

VOLUME 126 • NUMBER 3 • MAY 2004

TECHNICAL PAPERS

(Contents continued on inside back cover)

This journal is printed on acid-free paper, which exceeds the ANSI Z39.48-1992 specification for permanence of paper and library materials. ♾™
♲ 85% recycled content, including 10% post-consumer fibers.

Journal of Fluids Engineering Volume 126, Number 3 MAY 2004

TECHNICAL BRIEFS

DISCUSSION

The ASME Journal of Fluids Engineering is abstracted and indexed in the following:

Applied Science & Technology Index, AMR Abstracts Database, Chemical Abstracts, Chemical Engineering and Biotechnology Abstracts (Electronic equivalent of Process and Chemical Engineering), Civil Engineering Abstracts, Computer & Information Systems Abstracts, Corrosion Abstracts, Current Contents, Ei EncompassLit, Electronics & Communications Abstracts, Engineered Materials Abstracts, Engineering Index, Environmental Engineering Abstracts, Environmental Science and Pollution Management, Excerpta Medica, Fluidex, Index to Scientific Reviews, INSPEC, International Building Services Abstracts, Mechanical & Transportation Engineering Abstracts, Mechanical Engineering Abstracts, METADEX (The electronic equivalent of Metals Abstracts and Alloys Index), Petroleum Abstracts, Process and Chemical Engineering, Referativnyi Zhurnal, Science Citation Index, SciSearch (The electronic equivalent of Science Citation Index), Shock and Vibration Digest, Solid State and Superconductivity Abstracts, Theoretical Chemical Engineering

Separation Criterion for Turbulent Boundary Layers Via Similarity Analysis

Luciano Castillo

Xia Wang

Rensselacr Polytechnic Institute,
Department of Mechanical, Aerospace and
Nuclear Engineering,
Troy, NY 12180

William K. George
Chalmers University of Technology,
Department of Thermo and Fluid Dynamics,
SE-412 96 Göteborg,
Sweden

By using the RANS boundary layer equations, it will be shown that the outer part of an adverse pressure gradient turbulent boundary layer tends to remain in equilibrium similarity, even near and past separation. Such boundary layers are characterized by a single and constant pressure gradient parameter, Λ, and its value appears to be the same for all adverse pressure gradient flows, including those with eventual separation. Also it appears from the experimental data that the pressure gradient parameter, Λ_θ, is also approximately constant and given by $\Lambda_\theta = 0.21 \pm 0.01$. Using this and the integral momentum boundary layer equation, it is possible to show that the shape factor at separation also has to within the experimental uncertainty a single value: $H_{sep} \cong 2.76 \pm 0.23$. Furthermore, the conditions for equilibrium similarity and the value of H_{sep} are shown to be in reasonable agreement with a variety of experimental estimates, as well as the predictions from some other investigators. [DOI: 10.1115/1.1758262]

1 Introduction

Turbulent boundary layer separation is a very important area of research, particularly in the design of airfoils, diffusers and so on. The strongest possible adverse pressure gradient is maintained so that airfoils can achieve maximum lift or a diffusers can obtain maximum pressure recovery. If separation occurs, however, it causes many new complications. For example, separation reduces the lift of an airfoil, and it will also increase the required size of a diffuser. Separation in a turbulent boundary layer is very complex, and it happens as a process instead of a single event as in the laminar case, Simpson et al. [1,2] and Kline et al. [3] etc. In the 1980s the extensive work of Simpson [2,4] led to new insight and definitions for separation in the turbulent boundary layer. Some of the most relevant definitions are:

- Incipient Detachment (ID): the reverse flow occurs occasionally about 1% of the time.
- Intermittent Transitory Detachment (ITD): the reverse flow occurs about 20% of the time.
- Transitory Detachment (TD): the instantaneous back flow occurs 50% of the time.
- Detachment (D): it occurs when the time averaged wall shear stress is zero.

Recent experimental data [2,5,6] suggests that the location where the instantaneous back flow coefficient is about 50% corresponds to the position where the average skin friction is zero.

Many researchers have tried to investigate this process, to characterize separation, and to predict the detachment position. The classic log-law for the velocity profile does not work for the separation flow since the velocity scaling, u_τ, is zero at the separation position, Driver [7] and Schofield [8]. In the 1950s, Stratford [9] introduced an empirical criterion based on the pressure coefficient to predict the point of separation. He further argued that the inner (or near wall) velocity profiles should be scaled using:

$$U_{sep} = \frac{\nu}{\rho} \frac{dP_\infty}{dx} \tag{1}$$

and the inner length scaled using

$$\eta_{sep} = \frac{1}{\rho \nu} \frac{dP_\infty}{dx} \tag{2}$$

instead of the usual Prantdl variables, u_* and ν/u_*. These scalings are known as the ''Stratford variables,'' and clearly are necessary because of the vanishing of the shear stress at separation (cf., Tennekes and Lumley 1972 [10] or from more recent perspectives, George and Castillo 1993 [11], Skote and Henningson [12].) These near wall results are not of interest in this paper which focuses on the outer boundary layer and its implications for separation.

In the 1960s and 1970s Kline and his co-investigators established correlation parameters for separation in terms of the shape factor, H, and the ratio of displacement thickness to the boundary layer thickness, δ_* / δ. In particular, Sandborn and Kline [13] suggested that the shape factor at separation was given by,

$$H = 1 + \frac{1}{1 - \delta_* / \delta}, \tag{3}$$

where δ_* / δ must be determined at the point of separation. They further showed that the shape factor is 2.7 at the Intermittent Transitory Detachment (ITD) position. In subsequent work, Kline, Bardina and Strawn [3] developed a one parameter model and concluded that the shape factor was given by $H = 2.7$ at the ITD position and $H = 4.0$ at the separation position.

There are a number of other empirical separation criteria which have been proposed. Sajben and Liao [14] assumed that detachment occurs where the normalized specific momentum defect reaches a maximum as a function of the shape factor; they found a value of the shape factor of 2.7 for ITD turbulent boundary layer. Cebeci and Bradshaw [15] have reported that separation takes place when the values of H fall in the range of $1.8 \leqslant H_{sep} \leqslant 2.4$. By contrast, Senoo and Nishi [16] proposed that:

$$H_{sep} = 1.8 + 7.5 \left. \frac{\delta_*}{W} \right|_{sep} \tag{4}$$

for flow in diffusers, where W is the passage width at the point of separation, and δ_* is determined at the point of separation as well. A similar empirical form, which shows a linear relationship between H and χ_w, can be found in the experiment carried out by Dengel and Fernholz [5] (and more recently by Gustavsson [17]) as:

Contributed by the Fluids Engineering Division for publication in the JOURNAL OF FLUIDS ENGINEERING. Manuscript received by the Fluids Engineering Division October 4, 2001; revised manuscript received November 8, 2003. Associate Editor: T. B. Gatski.

$$H \approx 2.2 + 1.4\chi_w, \tag{5}$$

where χ_w is the back flow coefficient and its value is between 0.20 and 0.70 for this experiment. Meanwhile, Dengel and Fernholz [5] showed that the shape factor H is $2.85 \pm 0.1\%$ at $\chi_w = 50\%$ where the boundary layer is presumed to separate when $\overline{\tau_w} = 0$ (detachment).

Schofield [8] proposed a separation criterion based on the Schofield-Perry analysis [18], and found a shape factor of 3.3 at the separation position. His results, however, were partially based on the measurements by Simpson and his collaborators [1,2] which misidentified the location of transitory detachment, at least according to Dengel and Fernholz [5]. Alving and Fernholz [6] made similar measurements as Dengel and Fernholz [5] for the asymmetric boundary layer with separation. Their results are consistent with each other, yielding shape factors of 2.85 ± 0.1 and 2.76 for Dengel and Fernholz [5] and Alving and Fernholz [6], respectively.

The entire question of where separation occurs experimentally is considerably complicated by the fact that the skin friction is very hard to determine within the boundary layer, and even worse when the shear stress is near zero. The hot-wire anemometer has been the classical tool to measure the velocity profile, but its directional insensitivity limits its application in separating flows for it cannot measure the back-flow velocity accurately. In the past two decades, the advent of new and more precise measuring techniques allowed many investigators to obtain a new understanding of the problem in a physical way. Simpson [1,2] used the directionally sensitive laser anemometer to measure the instantaneous flow direction near the separation region. Dengel and Fernholz [5] and Alving and Fernholz [6] presented pulsed-wire measurements for the separated region and downstream of reattachment region. The PIV has also begun to be applied to separation studies (e.g., Angele and Muhamad-Klingman [19]). Even so, there are still many questions (especially theoretical) that remain to be answered.

The primary goal of this paper is to describe how some recent theoretical advancements in the understanding of turbulent boundary layers lead to a simple separation criterion which is in reasonable agreement with measurements, as well as the results from some other investigators. The detached separation of the steady flow is the main focus in this investigation (cf. Simpson's definitions [2,4,20]). Attention will be given to only the 2-D steady turbulent boundary layer in which the flow is not affected by the turbulence intensity of the free stream. Surface curvature or roughness are also presumed not present in the problem. In brief, the separation is presumed to be caused by the strong adverse pressure gradient alone.

The equilibrium similarity analysis of Castillo and George [21] for the pressure gradient boundary layers will be applied to the *outer* part of adverse pressure gradient boundary layers upstream of and up to separation. These results will then be combined with the integral momentum boundary layer equation to obtain a separation criterion. This separation criterion surprisingly appears to be both quite simple and universal.

2 Review of the Castillo/George Analysis

Castillo and George [21] have set forth in detail the case for considering the outer part of most turbulent boundary layers to be *equilibrium similarity* boundary layers.[1] Surprisingly, the experimental data suggest that only three values of the pressure gradient similarity parameter, Λ (defined below), appear to describe all of the flows considered—one each for zero pressure gradient (ZPG), adverse pressure gradient (APG) and favorable pressure gradient (FPG). In this paper only the adverse pressure gradient results will be considered.

For a 2-D, incompressible boundary layer that is statistically steady in the mean the boundary layer equation for the *outer* flow (valid for $y/\delta > 0.1$ typically) reduces to:

$$U\frac{\partial U}{\partial x} + V\frac{\partial U}{\partial y} = -\frac{1}{\rho}\frac{dP_\infty}{dx} + \frac{\partial}{\partial y}[-\langle uv\rangle] + \frac{\partial}{\partial x}[\langle v^2\rangle - \langle u^2\rangle], \tag{6}$$

where $U \to U_\infty$, $\langle uv\rangle \to 0$ as $y \to \infty$, $\langle u^2\rangle$ and $\langle v^2\rangle \to 0$ as $y \to \infty$ as well. This equation, together with the continuity equation, describes the flow exactly in the limit of infinite Reynolds number as long as $y > 100\nu/u_*$ or $y^+ > 100$ typically. It is important to note that after flow separates, the boundary layer thickness may grow drastically, and the boundary layer simplifications are not accurate any longer. Note that the normal stresses components $\langle u^2\rangle, \langle v^2\rangle$ have been retained because in APG flows, particularly those approaching separation, their contributions are about 30% (Simpson et al. [4], Dengel and Ferholz [5], Alving and Fernholz [6], Elsberry et al. [22]). The component Reynolds stress equations must also be included in the analysis, but have not been written here since they are the same as for the zero-pressure gradient boundary layer and have been considered in detail elsewhere (cf. George and Castillo 1997 [23]).

The outer scales of the turbulent boundary layer equations must be determined from an equilibrium similarity analysis of the governing equations and boundary conditions, and can not be chosen a priori. George and Castillo [23] applied this concept to the outer boundary layer equations for the ZPG flow, and determined that the mean velocity and Reynolds shear stress scale with U_∞ and $U_\infty^2 d\delta/dx$, respectively. Unlike the Reynolds shear stresses, the Reynolds normal stresses scale with U_∞^2. Castillo and George [21] extended this similarity analysis to include pressure gradient boundary layers. Their approach and results can be summarized as follows:

Similarity Solution Profiles. The basic assumption is that it is possible to express any dependent variable, in this case the outer deficit velocity, $U - U_\infty$, the outer Reynolds shear stress, $\langle uv\rangle$, and the outer Reynolds normal stresses, $\langle u^2\rangle$, $\langle v^2\rangle$ as a product of two functions; i.e.,

$$U - U_\infty = U_{so}(x) f_{op}(\overline{y}, \delta^+; \Lambda; *); \tag{7}$$

$$-\langle uv\rangle = R_{so}(x) r_{op}(\overline{y}, \delta^+; \Lambda; *); \tag{8}$$

$$\langle v^2\rangle - \langle u^2\rangle = R_{no}(x) r_{opn}(\overline{y}, \delta^+; \Lambda; *); \tag{9}$$

where U_{so}, R_{so}, R_{no} are the outer velocity scale, the outer Reynolds shear stress scale, and the Reynolds normal stress difference, all of which depend only on x. Note that all of these *must* be determined from the boundary layer and Reynolds stress equations together with the appropriate boundary conditions. The arguments inside the similarity functions (f_{op}, r_{op}, and r_{opn}) represent the outer similarity coordinate, $\overline{y} = y/\delta_{99}$, the local Reynolds number dependence, $\delta^+ = \delta u_*/\nu$, the pressure gradient parameter, Λ, and any possible dependence on the upstream conditions, *, respectively.

Asymptotic Invariance Principle: AIP. This principle can be simply stated as follows: since in the limit as the $\mathrm{Re} \to \infty$ the outer boundary layer equations become independent of the local Reynolds number, therefore any solution to them must also become asymptotically independent of δ^+. Thus, in this limit, Eq. (7)–Eq. (9) must become independent of local Reynolds number; i.e.,

$$f_{op}(\overline{y}, \delta^+; \Lambda; *) \to f_{op\infty}(\overline{y}, \Lambda, *); \tag{10}$$

$$r_{op}(\overline{y}, \delta^+; \Lambda; *) \to r_{op\infty}(\overline{y}, \Lambda, *); \tag{11}$$

[1]The term '*equilibrium similarity*' should not be confused with the 'equilibrium' boundary layer of Clauser. The Clauser analysis has much more restrictive criteria and is based on approximate equations truncated at first order in u_τ/U_∞, whereas the Castillo/George analysis is valid to third order.

$$r_{opn}(\overline{y},\delta^+;\Lambda;*)\rightarrow r_{opn\infty}(\overline{y},\Lambda,*); \tag{12}$$

as $\delta^+\rightarrow\infty$. The subscript ∞ is used to distinguish these infinite Reynolds number solutions from the finite Reynolds number profiles used in Eq. (7)–Eq. (9).

The Transformed Equations. Substituting Eq. (10)–Eq. (12) into Eq. (6) and clearing terms yields:

$$\left[\frac{\delta}{U_{so}}\frac{dU_\infty}{dx}+\left(\frac{U_\infty}{U_{so}}\right)\frac{\delta}{U_{so}}\frac{dU_{so}}{dx}\right]f_{op\infty}+\left[\frac{\delta}{U_{so}}\frac{dU_{so}}{dx}\right]f_{op\infty}^2-\left[\frac{U_\infty}{U_{so}}\frac{d\delta}{dx}+\frac{\delta}{U_{so}}\frac{dU_\infty}{dx}\right]\overline{y}f'_{op\infty}-\left[\frac{d\delta}{dx}+\frac{\delta}{U_{so}}\frac{dU_{so}}{dx}\right]f'_{op\infty}\int_0^{\overline{y}}f_{op\infty}(\tilde{y})d\tilde{y}$$
$$=\left[\frac{R_{so}}{U_{so}^2}\right]r'_{op\infty}+\left[\frac{\delta}{U_{so}^2}\frac{dR_{no}}{dx}\right]r_{opn\infty}-\left[\frac{R_{no}}{U_{so}^2}\frac{d\delta}{dx}\right]\overline{y}r'_{opn\infty} \tag{13}$$

where the term involving $-dP_\infty/dx$ has been cancelled by the $\rho U_\infty dU_\infty/dx$ term from Euler's equation for the external flow.

The Equilibrium Similarity Conditions. For the particular type of ''equilibrium'' similarity solutions suggested in George [24], all the terms in the governing equations must maintain the same relative balance as the flow develops. These *equilibrium similarity* solutions exist only if all the square bracketed terms have the same x-dependence and are independent of the similarity coordinate, $\overline{y}$. Thus, the bracketed terms must remain proportional to each other as the flow develops; i.e.,

$$\frac{\delta}{U_{so}}\frac{dU_{so}}{dx}\sim\frac{\delta}{U_{so}}\frac{dU_\infty}{dx}\sim\left(\frac{U_\infty}{U_{so}}\right)\frac{\delta}{U_{so}}\frac{dU_{so}}{dx}\sim\frac{d\delta}{dx}\sim\left(\frac{U_\infty}{U_{so}}\right)\frac{d\delta}{dx}$$
$$\sim\frac{R_{so}}{U_{so}^2}\sim\frac{R_{no}}{U_{so}^2}\frac{d\delta}{dx}\sim\frac{\delta}{U_{so}^2}\frac{dR_{no}}{dx} \tag{14}$$

where '$\sim$' means 'has the same x-dependence as'.

It is clear that (just as for the zero pressure gradient boundary layer), full similarity (of the ''equilibrium-type'') is possible only if

$$U_{so}\sim U_\infty, \tag{15}$$

$$R_{so}\sim U_{so}^2\frac{d\delta}{dx}\sim U_\infty^2\frac{d\delta}{dx} \tag{16}$$

and

$$R_{no}\sim U_\infty^2. \tag{17}$$

Note that both the Reynolds shear and normal stress scalings can be shown to be consistent with the Reynolds stress equations themselves (cf. George and Castillo [23]).

Thus, the outer equations do admit to full similarity solutions in the limit of infinite Reynolds number, *and these solutions determine the outer scales*. No other choice of scales can produce profiles (of the assumed form) which are asymptotically independent of the local Reynolds number, at least unless they reduce to these scales in the limit.

The Pressure Gradient Parameter for Equilibrium Flows. Besides the similarity conditions for the mean velocity and Reynolds stresses, there exist other constraints. In particular,

$$\frac{d\delta}{dx}\sim\frac{\delta}{U_\infty}\frac{dU_\infty}{dx}\sim\frac{\delta}{\rho U_\infty^2}\frac{dP_\infty}{dx}. \tag{18}$$

It follows from Eq. (18) that $\Lambda=$ const is a necessary condition for equilibrium similarity to exist, where the pressure gradient parameter Λ is defined as:

$$\Lambda\equiv\frac{\delta}{\rho U_\infty^2 d\delta/dx}\frac{dP_\infty}{dx}=constant, \tag{19}$$

or equivalently,

$$\Lambda\equiv-\frac{\delta}{U_\infty d\delta/dx}\frac{dU_\infty}{dx}=constant. \tag{20}$$

A consequence of this is that for $\Lambda\neq0$, the imposed pressure gradient, dP_∞/dx, controls the growth rate of an equilibrium similarity boundary layer. Eq. 20 can be integrated directly to obtain:

$$\delta\sim U_\infty^{-1/\Lambda}, \tag{21}$$

so there must be a power law relation between the free stream velocity and the boundary layer thickness. Therefore, an equilibrium similarity boundary layer exists only if the experimental data in log-log plot show a linear relation between the boundary layer thickness (e.g., $\delta_{0.99}$ or $\delta_{0.95}$) and the free-stream velocity (U_∞ or more typically U_{edge}). There are virtually no measurements for which this is not easily tested [25].

From the perspective of the Castilo/George analysis outlined above, an ''equilibrium'' boundary layer is one where $\Lambda=$constant and $\delta\sim U_\infty^{-1/\Lambda}$. Since it is the free stream velocity, U_∞ (or dP_∞/dx), which is usually imposed on the boundary layer by external means, this is a restrictive constraint on δ. As a consequence it provides a powerful experimental test of the theory, and is most easily demonstrated by the linear relationship between $\log(U_\infty)$ and $\log(\delta)$. Figure 1, taken from Castillo and George [21], shows examples for both favorable (FPG) and adverse (APG) pressure gradient boundary layers. All of the existing experimental data show similar behavior. Thus, by the Castillo/George criterion, it appears that most pressure gradient boundary layer are in equilibrium. In the following section the same test will be applied to boundary layers with eventual separation and reattachment.

3 Boundary Layers With Eventual Separation

Figure 2 shows the equilibrium condition of $\log(U_\infty)$ versus $\log(\theta,\delta_*,\delta)$ for the experimental measurements of Schubauer and Klebanoff [26], Newman [27], Ludweig and Tillmann [28], Simpson et al. [1,2], Alving and Fernholz [6], all of which were made in boundary layers which separated. The linear fit for these measurements continues to and sometimes even after the separation point. Note the close correspondence between the slopes of the plots using δ and θ, and a correspondence that does not hold for δ_* for these separating flows.

Unfortunately there is no explicit relation between θ and δ, although an implicit one can be derived using the momentum integral equation and additional assumptions about the velocity profiles (cf. George and Castillo [23]). For all the adverse pressure gradient boundary layers considered (and as will be shown later), $\Lambda\approx\Lambda_\theta$, to within the experimental error, where

$$\Lambda_\theta\equiv\frac{\theta}{\rho U_\infty^2 d\theta/dx}\frac{dP_\infty}{dx}=-\frac{\theta}{U_\infty d\theta/dx}\frac{dU_\infty}{dx}, \tag{22}$$

and the θ is the momentum thickness. Most importantly, for all the boundary layers considered, Λ_θ also appears to be a single constant. Thus, at least for these boundary layers, the additional semi-empirical relation,

$$\theta\sim U_\infty^{-1/\Lambda_\theta}, \tag{23}$$

is at least approximately valid. Clearly this is satisfied for the APG data of Fig. 2.

Table 1 lists all the linear fit results of Fig. 2. It is clear that there is a good linear relationship between the $\log(U_\infty)$ and both $\log(\theta)$ and $\log(\delta)$, exactly like the APG boundary layers which did not separate. Thus, even though the boundary layer approaches separation, the outer flow apparently tends to remain in equilibrium similarity, and its state can be characterized by either Λ or Λ_θ, at least until the boundary layer equations themselves break down. This is important, since the *theory* depends only on δ, and θ can only be inferred from the momentum integral (cf. George and Castillo [23]). Note that the average value $\Lambda=0.23$ is slightly

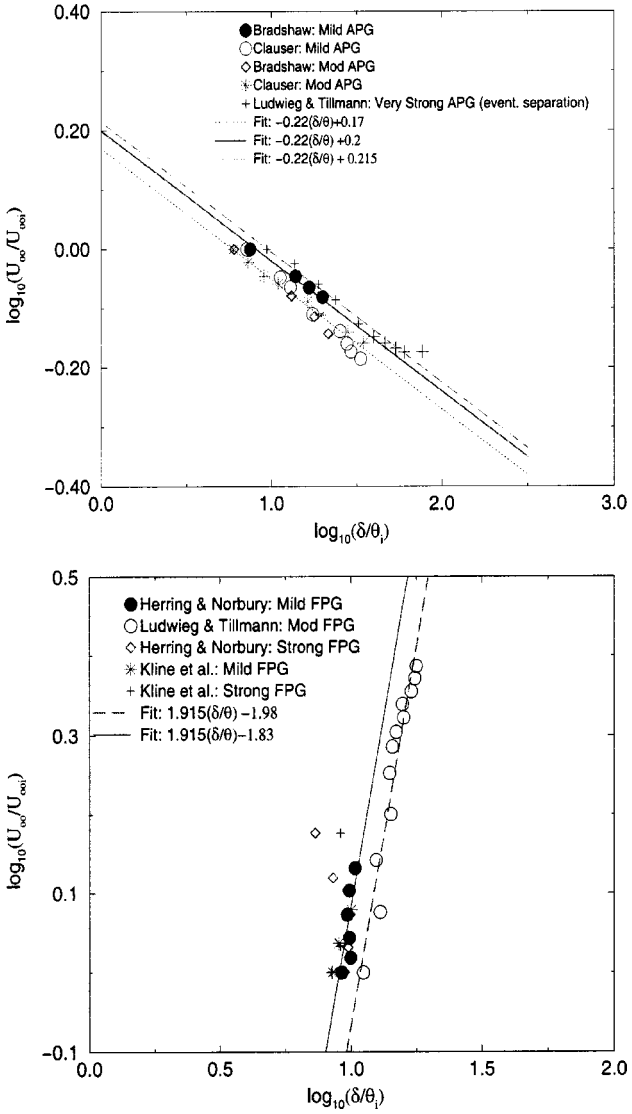

Fig. 1 ***Top*: Plots of U_∞ versus δ_{99} for APG data. *Bottom*: Plots of U_∞ versus δ_{99} for FPG data. Both plots are normalized with $U_{\infty i}$ and θ_i for first measured location. The data have been normalized by the free stream velocity and the momentum thickness at the most upstream position.**

higher than the value of 0.22 for equilibrium adverse pressure gradient boundary layer suggested by Castillo and George [21], and slightly higher than the average of the Λ_θ values.

Figure 3, shows the same experimental data of Fig. 2. but now characterized with the single average value of $\Lambda_\theta = 0.21$. Clearly, all the measurements with eventual separation can also be characterized by a single value. If the constancy of this value was not a surprise before, its applicability to these boundary layers certainly is.

4 The Integral Momentum Equation and the Separation Criterion

The integral boundary layer equation can be written as

$$\frac{C_f}{2} = \frac{d\theta}{dx} - (2+H)\frac{\theta}{\rho U_\infty^2}\frac{dP_\infty}{dx}. \tag{24}$$

This can be rewritten using the definition for the pressure parameter Λ_θ as:

$$\frac{C_f}{2} = \frac{d\theta}{dx}[1-(2+H)\Lambda_\theta]. \tag{25}$$

Using the definition for separation by Simpson [2], the mean shear stress $C_f = 0$ but $d\theta/dx \neq 0$ at the same point. Then the above integral boundary layer equation *at separation* reduces to,

$$H_{sep} = \frac{1}{\Lambda_\theta} - 2. \tag{26}$$

This form of the integral equation would be of little use if it was not for the fact that the log-log plots show that the equilibrium similarity theory appears to describe the outer boundary layer almost and perhaps beyond separation with a constant value, $\Lambda_\theta \cong 0.21 \pm 0.01$. It follows immediately that the value of the shape factor at separation is given by $H_{sep} \cong 2.76 \pm 0.23$. This is an amazingly simple result, and is determined entirely by the equilibrium similarity of the *outer* boundary layer, with no assumptions at all about the inner part.

Table 2 shows the shape factor at separation from various experiments cited previously, along with the present similarity analysis results for shape factor. The experimental values are those provided by the original authors even though the methods of determination varied. Notice that the experimental data studied here include the classical experimental data of Schubauer and Klebanoff [26], Newman [27], and Ludweig and Tillmann [28], in which they use hot-wire as a measurement tool. Because of directional insensitivity of hot-wire, they could not give an exact description of separation location in the flow. Therefore, only the last measured position is shown here, which could be regarded as the intermittent separation point. Simpson [2,1] used an LDA measured the velocity profile in the separation region, and the intermittent detachment region was interpolated from the experimental data. Alving and Fernholz [6] used an asymmetric boundary layer flow with eventual separation and reattachment region, and a pulse-wire to measure the back flow.

Comparing the experimental result with the current result, the new result is remarkably successful, especially given the uncertainty of the data, both for Λ_θ and the value of H at separation. In addition, notice that we are seeking the shape factor at the separation position. However, this result seems to describe the ITD position for the some of classical experiments. For the relatively new experiments, this value proves very successful.

It should be noted that the value of $\Lambda_\theta = 0.21$ is a composite value obtained by regression fits to many data sets as shown in Table 2 and Fig. 3. The success of this value is illustrated by figures in this paper. The individual estimates, however, varied by as much as ± 0.01 from the composite value. Thus, the individual estimates of H_{sep} could also vary as $2.5 < H_{sep} < 3.0$. This is a large range indeed, and certainly spans the range of the experimental values in the table. Clearly, there is a demand for new experiments to determine whether the values of Λ_θ and H_{sep} are universal, or whether the differences are real.

The proposed theoretical value is very close to some of the previous empirical results discussed earlier.

• First, the proposed shape factor is consistent with the result by Sandborn and Kline [13], Eq. 3, which shows that the incipient separation occurs when $\delta_* / \delta_{sep} = 0.43$ and $H_{sep} = 2.7$. Working backwards, the uncertainty range of H from the present theory using the data cited above suggests that δ^*/δ at separation should be in the range of $0.33 \leqslant \delta^*/\delta \leqslant 0.5$. The relation between the present theory and the Sandborn/Kline correlation can best seen by plotting H versus δ^*/δ as shown in Fig. 4. The vertical lines show the range of the Sandborn/Kline values, the horizontal lines the uncertainty range of H from the present theory. The top plot in Fig. 4. shows all the equilibrium turbulent boundary layers with very strong adverse pressure gradient, [26,29,30,31,32], but without separation. It is obvious that all of these measurements are below the separation zone. The bottom plot in Fig. 4. shows all the

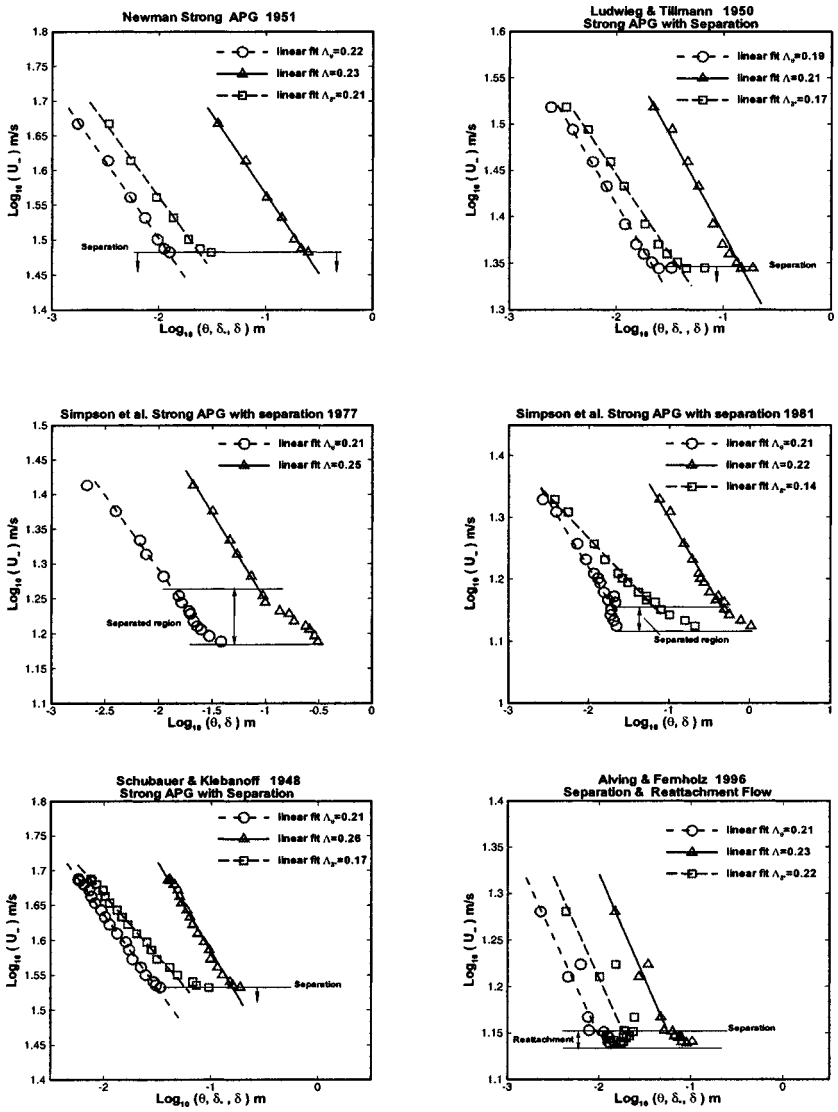

Fig. 2 Equilibrium boundary layers with eventual separation: log-log plots of U_∞ versus θ, δ_* and δ.

experiments with separation. The separated or intermittent separation positions have been circled. It is clear that most of these points fall into the separation region, which is remarkable considering the difficulty of the actual measurement. Therefore, Fig. 4. provides a useful picture to describe the separation zone, and emphasizes that separation in the turbulent boundary layer is perhaps a process instead of a single event (as indicated by Simpson [2]).

• Second, this result agrees with Kline et al. [3] one-parameter correlation prediction. The shape factor at the intermittent detachment is shown to be 2.7. Notice that the intermittent detachment here refers to $\gamma_w = 5\% - 20\%$ instead of $\gamma_w = 20\%$ by Simpson et al. [2].

• Third, this investigations is also in agreement with the recent study by Sajben and Liao [14]. They assumed that the normalized specific momentum defect reaches a maximum value at detachment position, which experimentally corresponds to ITD with $H = 2.7$.

• Forth, this result is consistent with the latest experimental data for separation by Alving and Fernholz [6]. Using a pulse-wire as the measurement tool, a shape factor of 2.78 is found at the separation position. Also this result is within the range of 2.85 ± 0.1 reported by the Dengel and Fernholz [5].

Table 1 The pressure parameter for turbulent boundary layers with separation

Experiments (separation)	Λ_θ	Λ	Λ_{δ_+}
Newman [27]	0.223	0.228	0.212
Ludweig & Tillmann [28]	0.194	0.213*	0.171
Alving & Fernholz [6]	0.212	0.226	0.219
Simpson et al. [2]	0.214	0.222	0.137
Simpson et al. [1]	0.212	0.251	—
Schubauer & Klebanoff [26]	0.213	0.257*	0.174
R.M.S.	0.21 ± 0.01	0.23 ± 0.02	0.19 ± 0.03

*δ_{95} is used instead of δ_{99}

Finally, in addition to the experimental evidence cited above, there are a number of indirect inferences which can be made from industrial practice and from laboratory experiments in which the boundary layers did not separate. For example, one common design criterion for industrial turbine designers to avoid separation on compressor blades is to *not* allow the shape factor to exceed 2.5 (Håll [29]. Another example is the recent experiment of Els-

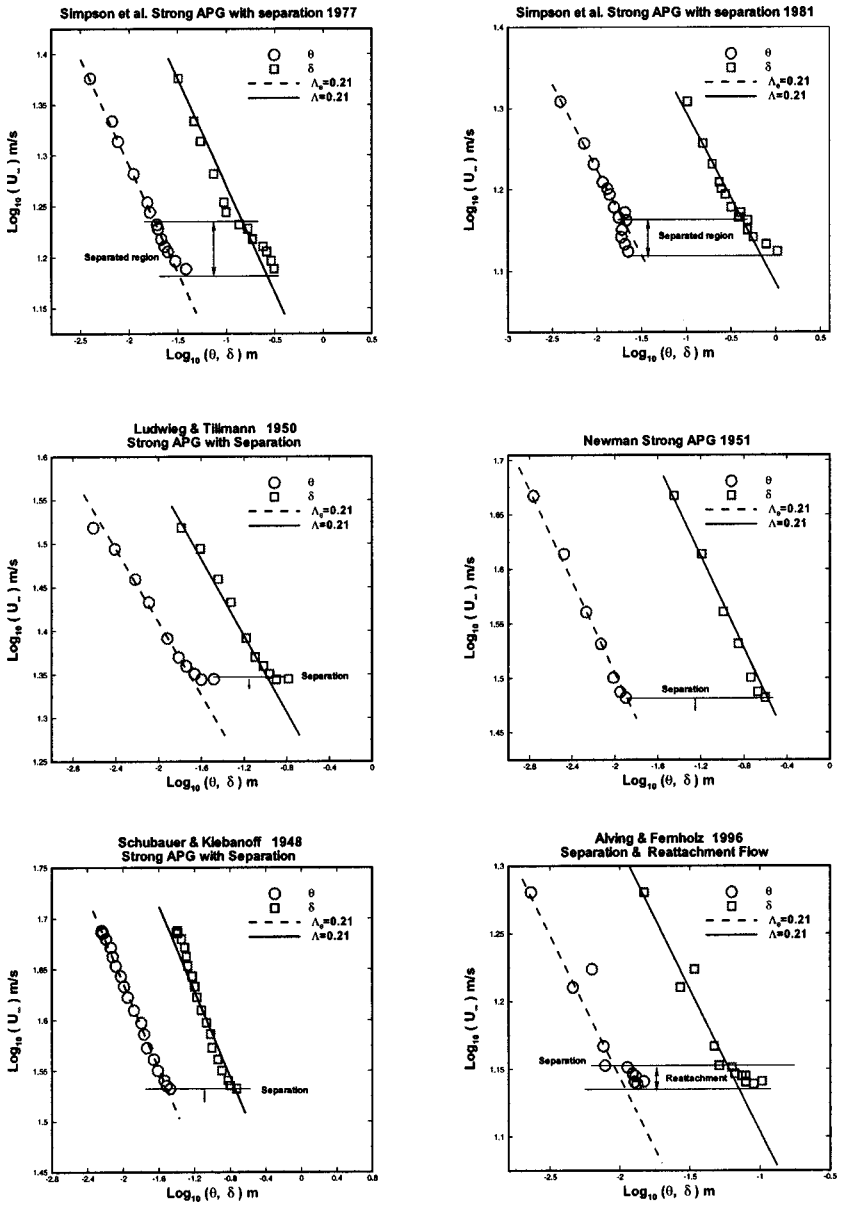

Fig. 3 Equilibrium boundary layers with eventual separation: log-log plots of U_∞ versus δ and θ.

berry et al. [22] that created an equilibrium boundary layer on the verge of separation, but found it necessary to keep the shape factor below 2.6.

5 Summary and Conclusions

Using the RANS equations and similarity analysis, it was shown that:

- The outer part of separating boundary layers are also equilibrium similarity boundary layers characterized by a constant pressure parameters.
- The pressure parameter Λ_θ is nearly same for all the APG flows with eventual separation; in particular, $\Lambda_\theta = 0.21 \pm 0.01$.
- It is possible to characterize boundary layers at separation by $H_{sep} = 2.76 \pm 0.23$. This value of shape factor is in close agree-

Table 2 The values for the shape factor *H*

Experiment	Λ_θ	H_{sep}	$H = \frac{1}{\Lambda_\theta} - 2$	Position	Boundary layer description
Schubauer & Klebanoff [13]	0.21	2.84	2.76	the last point	airfoil type flow-hot-wire
Newman [27]	0.22	2.46	2.55	the last point	airfoil type flow-hot-wire
Ludwieg & Tillmann [28]	0.19	2.04	3.26	the last point	diverging channel flow-hot-wire
Simpson et al. [1]	0.21	2.62	2.76	ITD	airfoil type flow-LDA
Simpson et al. [2]	0.21	2.97	2.76	ITD	airfoil type flow-LDA
Alving & Fernholz [6]	0.21	2.78	2.76	Detachment	asymmetric flow-Pulse-wire

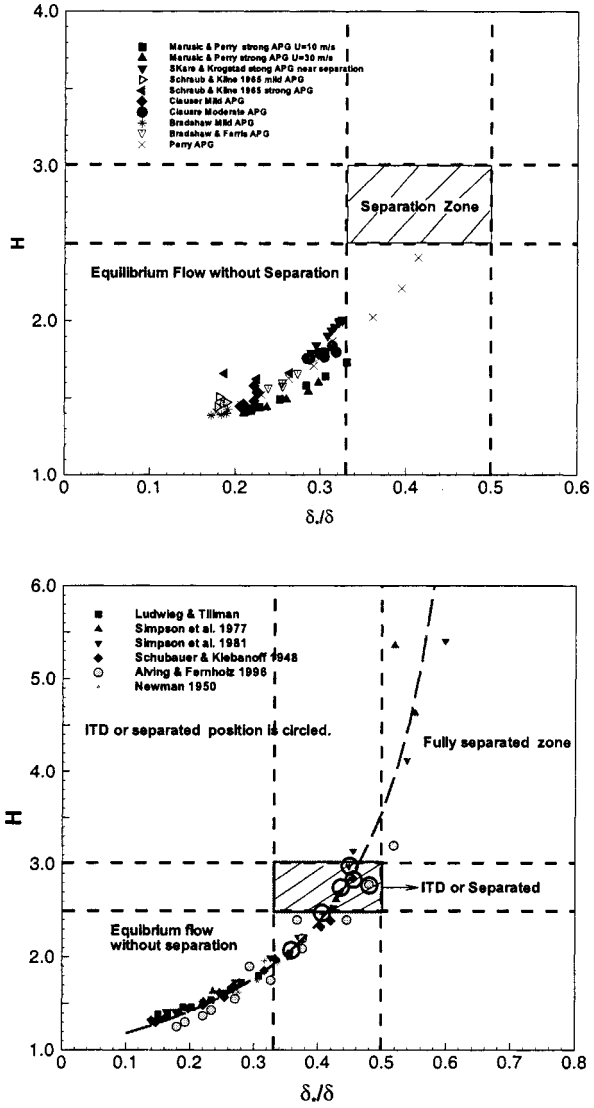

Fig. 4 ***Top*: H and δ_*/δ correlation for equilibrium APG flows. *bottom*: H and δ_*/δ correlation for strong APG flows with separation.**

ment with the ITD position for the experimental data studied here. This result also agrees with other investigations for the ITD position.

In conclusion, it appears that even separating boundary layers have a tendency to remain in an equilibrium similarity state, at least the outer part of the boundary layer. These equilibrium boundary layers are characterized by a constant pressure parameter $\Lambda_\theta = 0.21$. Nonetheless, although a correlation for separation has been established *if it occurs*, the important task of explaining *why* it happens and *how* it can be predicted remains. Perhaps equilibrium similarity considerations will ultimately provide this insight as well.

Acknowledgment

The authors are very thankful to Professor Wygnanski from Arizona State University and Professor Marusic from University of Minnesota for providing their original data, and to the reviewers for their insightful comments.

Nomenclature

H = shape factor
H_{sep} = shape factor at separation
R_{so} = outer Reynolds stress scale
U_{sep} = velocity at separation
U_{so} = unknown outer velocity scale
U_∞ = free stream velocity
$U_\infty - U$ = velocity deficit
u_* = friction velocity, $u_*^2 = \tau_w/\rho$
Λ = pressure parameter, $(\delta/\rho U_\infty^2 d\delta/dx)(dP_\infty/dx)$
δ = boundary layer thickness, δ_{99}
θ = momentum thickness, $\int_0^\infty (U/U_\infty)(1-U/U_\infty)dy$
Λ_{δ_*} = pressure parameter, $(\delta_*/\rho U_\infty^2 d\delta_*/dx)(dP_\infty/dx)$
Λ_θ = pressure parameter, $(\theta/\rho U_\infty^2 d\theta/dx)(dP_\infty/dx)$
δ_* = displacement thickness, $\int_0^\infty (1-U/U_\infty)dy$
θ_i = momentum thickness at first measured position
$*$ = (unknown) dependence on upstream conditions

References

[1] Simpson, R. L., and Strickland, J. H., 1977, "Features of a separating turbulent boundary layer in the vicinity of separation," J. Fluid Mech., **79**, pp. 553–594.
[2] Simpson, R. L., and Chew, Y. T., 1981, "The structure of a separating turbulent boundary layer. Part 1. Mean flow and Reynolds stresses," J. Fluid Mech., **113**, pp. 23–51.
[3] Kline, S. J., Bardina, J. G., and Strawn, R. C., 1983, "Correlation of the detachment of two-dimensional turbulent boundary layers," AIAA J., **21**, pp. 68–73.
[4] Simpson, R. L., and Chew, Y. T., 1981, "The structure of a separating turbulent boundary layer. Part 2. Higher-order turbulence results," J. Fluid Mech., **113**, pp. 53–73.
[5] Dengel, P., and Fernholz, H. H., 1990, "An experimental investigation of an incompressible turbulent boundary layer in the vicinity of separation," J. Fluid Mech., **212**, pp. 615–636.
[6] Alving, A. E., and Fernholz, H. H., 1995, "Turbulence measurements around a mild separation bubble and down-stream of reattachment," J. Fluid Mech., **322**, pp. 279–328.
[7] Driver, D. M., 1991, "Reynolds Shear stress measurements in a separated boundary layer flow," AIAA-91-1787, 22nd Fluid Dynamics, Plasma Dynamics, and Lasers Conference.
[8] Schofield, W. H., 1986, "Two-dimensional Separating Turbulent Boundary layers," AIAA J., **24**, No. 10, pp. 1611–1620.
[9] Stratford, B. S., 1959, "The prediction of separation of the turbulent boundary layer," J. Fluid Mech., **5**, pp. 1–16.
[10] Tennekes, H., and Lumley, J. L., 1972, A First Course in Turbulence, MIT Press, Cambridge, MA.
[11] George, W. K., and Castillo, L., 1993, "Boundary Layers with Pressure Gradient: Another look at the equilibrium boundary layer," Near Wall Turbulence (So, R. et al. eds.), pp. 901–910, Elsevier, NY.
[12] Skote, M., and Henningson, D. S., 2002, "Direct numerical simulation of a separated turbulent boundary layer," J. Fluid Mech., **471**, pp. 107–136.
[13] Sandborn, V. A., and Kline, S. J., 1961, "Flow models in boundary-layer stall inception," J. Basic Eng., **83**, pp. 317–327.
[14] Sajben, M., and Liao, Y., 1995, "Criterion for the detachment of laminar and turbulent boundary layers," AIAA J., **33**, No. 11, pp. 2114–2119.
[15] Cebeci, T., and Bradshaw, P., 1977, *Momentum Transfer in Boundary Layers*, McGraw Hill Book Co., New York, pp. 194.
[16] Senoo, Y., and Nishi, M., 1975, "Prediction of flow separation in a diffuser by a boundary layer calculation," ASME J. Fluids Eng., **99**, pp. 379–389.
[17] Gustavsson, J., 1998, "Experiments on turbulent flow separation," Master's thesis, Royal Institute of Technology, Sweden.
[18] Perry, A. E., and Schofield, W. H., 1973, "Mean velocity and shear stress distributions in turbulent boundary layers," Phys. Fluids, **16**, 12, pp. 2068–2074.
[19] Angele, K., and Muhammad-Klingman, B. 2003 "Self-similarity velocity scalings," in Ph.D. dissertation of K. Angele, 'Experimental studies of turbulent boundary layer separation and control,' Dept. of Mechanics, KTH, Stockholm, Sweden, 81–105.
[20] Simpson, R. L., 1989, "Turbulent boundary-layer separation," Annu. Rev. Fluid Mech., **21**, pp. 205–234.
[21] Castillo, L., and George, W. K., 2001, "Similarity analysis for turbulent boundary layer with pressure gradient: outer flow," AIAA J., **39**, No. 1, pp. 41–47.
[22] Elsberry, K., Loeffler, J., Zhou, M. D., and Wygnanski, I., 2000, "An experimental study of a boundary layer that is maintained on the verge of separation," J. Fluid Mech., **423**, pp. 227–262.
[23] George, W. K., and Castillo, L., 1997, "Zero-pressure-gradient turbulent boundary layer," Appl. Mech. Rev., **50**, pp. 689–729.
[24] George, W. K., 1995, "Some new ideas for similarity of turbulent shear flows," *Turbulence, Heat and Mass Transfer*, ed. by K. Hanjalic and J. C. F. Pereira, Begell House, NY.
[25] Castillo, L., 1997, "Similarity Analysis of turbulent boundary layers," Ph.D.

Dissertation, Department of Mechanical and Aerospace Engineering, SUNY/Buffalo, Buffalo, NY.
[26] Schubauer, G. B., and Klebanoff, P. S., 1951, ''Investigation of separation of the turbulent boundary layer,'' NACA Report 1030, NACA Technical Note 2133.
[27] Newman, B. G., 1951, ''Some Contributions to the Study of the Turbulent Boundary Near Separation,'' *Austr. Dept. Supply Rep.* ACA-53.
[28] Ludweig, H., and Tillmann, W., 1950, ''Investigations of the wall shearing stress in turbulent boundary layers,'' NACA TM 1285.
[29] Håll, U., 2003 private communication to WKG by U. Håll, Professor of Turbomachinery at Chalmers Univ. of Technology, Gothenburg, Sweden.
[30] Skåre, P. E., and Krogstad, P., 1994, ''A turbulent equilibrium boundary layer near separation,'' J. Fluid Mech., **272**, pp. 319–348.
[31] Coles, D. E., and Hirst, E. A., 1968, Computational of Turbulent Boundary Layers-1968 AFOSR-IFP-stanford conference, Vol. II.
[32] Marusic, I., and Perry, A. E., 1995, ''A wall-wake model for the turbulence structure of boundary layers. Part 2. Further experimental support,'' J. Fluid Mech., **298**, pp. 389–407.

Assessment of Reynolds-Averaged Turbulence Models for Prediction of the Flow and Heat Transfer in an Inlet Vane-Endwall Passage

Hugo D. Pasinato[1]
Kyle D. Squires
Ramendra P. Roy

Mechanical and Aerospace Engineering Department,
Arizona State University,
Box 876106,
Tempe, AZ 85287-6106

Predictions of the flow and thermal fields in an inlet vane passage are obtained via solution of the incompressible Reynolds-averaged Navier-Stokes (RANS) equations. RANS predictions of the steady-state solutions are obtained using two scalar eddy viscosity models and full Reynolds stress transport to close the turbulent stress in the momentum equations. The turbulent heat flux is modeled using a constant turbulent Prandtl number. In the geometric configuration of the inlet vane passage, the hub endwall is flat. Calculations are performed for a baseline configuration and an additional configuration in which secondary air is injected through three small, angled slots positioned upstream of the vane leading edge. Solutions are obtained on unstructured grids with the densest mesh comprised of 1.9×10^6 elements. The simulations are assessed via an inter-comparison of predictions obtained using the different models, as well as through evaluation against experimental measurements of the Stanton number and cooling effectiveness on the hub endwall. The flow develops from a turbulent boundary layer at momentum thickness Reynolds number 955 prescribed at the inlet to the computational domain, 1.3 axial chord lengths upstream of the vane leading edge. The mean velocity at the inlet is prescribed to match an experimentally-measured profile with low freestream turbulence. For the case with secondary air injection, the blowing ratio was 1.3. Solid surfaces are isothermal at temperatures below that of the mainstream gas. Simulation results show that the vortical structures resolved by the models in the vicinity of the vane leading edge for the baseline case are relatively insensitive to the particular turbulence closure. The elevation in heat flux levels due to entrainment of higher temperature mainstream gas towards the endwall by the horseshoe vortex is captured, Stanton number distributions exhibit adequate agreement with measured values. While there are similarities in the coherent structures resolved by the models, details of their evolution through the passage lead to differences in heat transfer distribution along the endwall. Secondary air injection strongly distorts the flow structure in the vicinity of the leading edge, the vortical structures that develop in the calculations with air injection evolve primarily from the interaction of the fluid issuing from the slots and the mainstream flow. Elevated levels of cooling effectiveness predicted by the models correspond to larger areas of the endwall than measured, peak Stanton numbers are higher than the experimental values. [DOI: 10.1115/1.1760535]

1 Introduction and Overview

The flow within vane passages in gas turbine engines is complex, characterized by interactions between coherent vortical motions that affect endwall and vane surface heat transfer and contribute significantly to aerodynamic losses. From a thermal standpoint, the environment of the first-stage vane and endwalls (hub, tip) is particularly harsh. Consequently, strategies for component cooling have been under investigation for many years (e.g., see the recent review by Dunn [1] and references therein). As is also discussed by Dunn [1], in order to improve the knowledge base for understanding, and eventually controlling, the heat transfer, an understanding of the underlying flow structure is needed. Numerical simulation and modeling provide a valuable tool for studying flow and heat transfer in complex flows; as computer capacity continues to increase the efficiency of simulations, modeling will evolve as a more integral component in analysis and design.

All aspects of computational strategies for predicting the velocity and temperature fields in vane passages are challenging, from the design and construction of the grid on which the Navier-Stokes equations are discretized, to solution, and subsequent post-processing and interpretation. A hierarchy of simulation techniques are possible, from the most fundamental—Direct Numerical Simulation (DNS) in which no explicit turbulence model is used—to techniques that introduce more empiricism, e.g., Large Eddy Simulation (LES) which models the effect of the small, unresolved scales of motion, and Reynolds-averaged Navier-Stokes (RANS) approaches which model the entire spectrum of turbulent motions. The computational cost of time-dependent, eddy-resolving techniques such as DNS and LES is not insignificant, even more so for geometries with finer-scale features, e.g., cooling passages, discrete slots, and/or film cooling holes. While these methods are valuable research tools and will continue to be applied to complex flows, the bulk of current modeling is based on application of RANS methods.

[1]Current address: Universidad Nacional de la Patagonia San Juan Bosco, Facultad de Ingenicria, Departmento de Mecanica, Comodoro Rivadavia, Argentina.

Contributed by the Fluids Engineering Division for publication in the JOURNAL OF FLUIDS ENGINEERING. Manuscript received by the Fluids Engineering Division April 25, 2003; revised manuscript received November 20, 2003. Associate Editor: T. Gatski.

In RANS modeling, the governing equations are averaged over time or ensembles, the averaging process yielding the turbulent Reynolds stress and turbulent heat flux in the momentum and energy equations, respectively. Many of the more widely used closure models link the Reynolds stress to the mean strain rate via scalar eddy viscosity, more complex approaches solve for the Reynolds stresses from their (modeled) transport equations. Irrespective of the details of the particular closure model, substantial empiricism is required. For flows with heat transfer, additional modeling is required to close the turbulent heat flux, often by assuming it can be modeled using a gradient-transport approach and then introducing the turbulent Prandtl number. In gas turbine applications, the velocity field in inlet vane passages is characterized by influences that are difficult to capture, e.g., strong pressure gradients, mean-flow skewing, and streamline curvature. Thus, given the level of empiricism in RANS models, prediction of configurations that combine many of the complicating influences encountered in practice provides a useful avenue for evaluating current capabilities. The overall objective of this contribution is application and assessment of RANS models in predicting the flow and thermal fields in an inlet vane passage. The simulations are evaluated via an inter-comparison of the solutions obtained using different models and compared to experimental measurements of endwall distributions of the Stanton number and cooling effectiveness.

Related works include the investigation reported by Hildebrandt and Fottner [2] on the influences of the turbulence closure and grid resolution, the calculations were evaluated using experimental measurements of the compressible flow through a linear turbine cascade. Three two-equations models were used in the study, one high- and two low-Reynolds number k-ε closures, along with two levels of mesh refinement (up to 1.14×10^6 hexahedral cells). For the high-Reynolds number model, the distance to the first cell center from the wall was $z_1^+>30$ and with $z_1^+<2$ for the low-Reynolds number closures. The investigators concluded that the main effect on the quality of the computations was grid resolution and that additional calculations were needed in order to develop grid-independent solutions, illustrating the challenge faced in developing completely grid-independent predictions of three-dimensional turbulent flows through complex geometries.

Kalitzin and Iaccarino [3] modeled the flow and thermal fields in the endwall and airfoil boundary layers of a linear cascade, also focusing on the roles of the turbulence models and grids in determining solution quality. Computations were performed using Fluent [4] and CFL3D. One focus of the study was the influence of the turbulence models on heat transfer predictions, using for comparison experimental measurements obtained in the NASA-Glenn Transonic Turbine Blade Cascade Facility. The Spalart-Allmaras [5] and $\overline{v^2}-f$ [6] RANS models were used in the computations. Five critical regions at the endwall were identified in the heat transfer solution—at the vane-endwall junction near the stagnation point, in the region of minimum pressure near the vane suction surface, across the entire mid-downstream region of the passage, a localized region near the trailing edge in the wake, and a thin strip near the end of the vane suction side. Both RANS models performed adequately without clear differences between the predictions. The need for high-quality meshes, required to capture the vortical flows dominating the region around the leading edge and in the passage, was highlighted by the investigators.

Heidmann et al. [7] used Reynolds-averaged approaches to predict the three-dimensional flow and heat transfer in a film-cooled turbine vane, the geometry corresponding to that chosen for an experimental investigation. A low-Reynolds number k-ε model was used, the flow was resolved using a grid size of 1.2×10^6 hexahedral cells. A focus of the investigation was on the flow physics and details of the solution in the vicinity of the cooling holes. Simulation results showed that the holes exhibited the expected jetting behavior as reported in Leylek and Zerkle [8], the peak mass flux was influenced by both external static pressure variation and the hole orientation. Shaped holes, for example, were effective in producing a low-velocity, uniform film layer.

For brevity and because this paper mainly reports computational work, a separate review of earlier experimental works relevant to the present study is not presented. However, in a recent review, Dunn [1] presented an extensive overview of the existing literature related to both measurement and prediction of heat transfer in turbomachinery applications.

1.1 Objectives. One of the principal motivations for the present effort is mitigation of high heat flux levels in the vicinity of the vane leading edge and along the endwall. As is well known, increases in heat transfer rate near the leading edge of the vane is brought about via the rollup of the upstream boundary layer into a horseshoe vortex, which in turn provides a mechanism for transport of hot mainstream gas to the endwall (e.g., see [9,10] and references therein). Cooling strategies, e.g., the use of film cooling, have long been employed to reduce vane and endwall temperatures with a substantial body of research focusing on vane-passage aerodynamics to interpret and understand heat transfer characteristics brought about by film cooling (e.g., see [11,1]). In this study, the approach employed to alleviate high heat transfer in the vicinity of the vane leading edge is the introduction of secondary air through three discrete slots in the endwall, upstream of the vane leading edge. The slots are angled with respect to the hub endwall and provide a means to increase cooling effectiveness in the critical region at the vane-endwall junction.

As shown below, the secondary air injection strongly alters the vortical structure in the flow, both in the vicinity of the vane leading edge as well as within the passage. Insight into the changes are investigated via identification of coherent structures in the flow using the scheme proposed by Jeong and Hussain [12]. Coherent structures are identified based on an eigenvalue analysis of the symmetric tensor $S_{ik}S_{kj}+\Omega_{ik}\Omega_{kj}$ where S_{ij} and Ω_{ij} are the strain- and rotation-rate tensors, respectively. Using this approach, it is possible to identify in the baseline configuration (without introduction of secondary air) the dominant vortical structures and to contrast the view of the structural elements in the solutions under the influence of air injection.

In the following, the velocity and temperature fields are solved within a single passage. The role of the turbulence model is examined in a series of computations of a baseline configuration and a subsequent geometry in which cooler secondary air is introduced through three discrete slots angled at 20 deg to the endwall and positioned upstream of the vane leading edge. The influence of the vortical motions in the flow on endwall transfer is investigated. As shown later, the coherent structures predicted by the models, while possessing globally similar features (e.g., rollup of a horseshoe vortex), do not describe identical evolutions of the vortical flow upstream of and through the passage. These structural differences resolved by the models are relevant in that it is also shown that surface heat transfer characteristics can be interpreted via the coherent structures resolved by a given model. The calculations are assessed via inter-comparison of results obtained using the various models along with evaluation against experimental measurements of the endwall Stanton number and cooling effectiveness.

2 Approach

2.1 Configuration and Primary Diagnostics. A plan view of the geometry near the leading edge of the vane is shown in Fig. 1. The vane configuration in the computations follows the midspan shape of the three-dimensional vanes used in the companion set of experiments. The calculations were of the flow around a single vane, with periodicity applied in the pitchwise (y) direction. Also shown in Fig. 1 are surface grids on the endwall and the leading-edge region of the vane. The plan view in Fig. 1*a* shows the three small slots, inclined at 20 deg to the endwall (Fig. 1*b*),

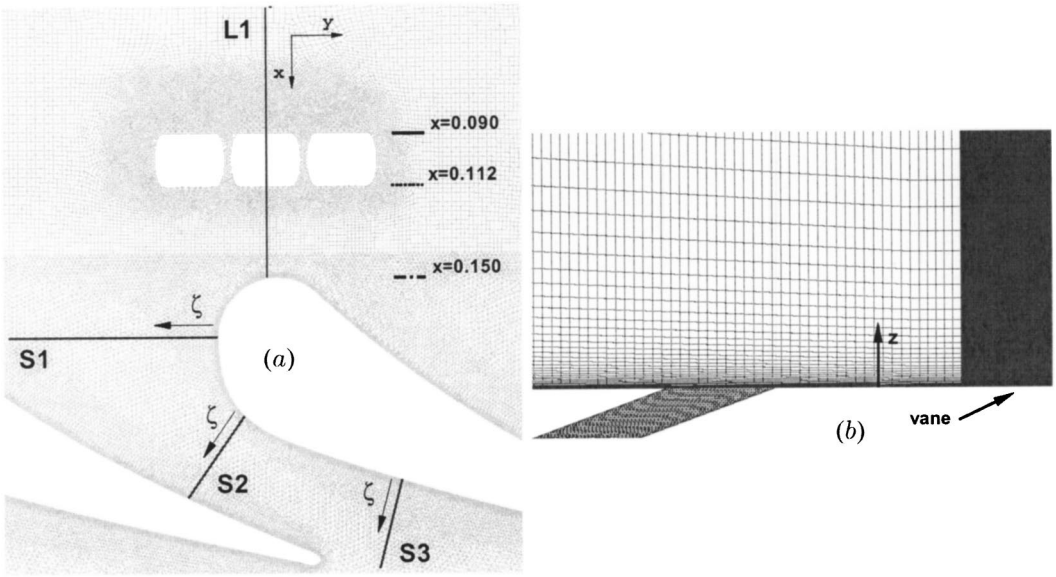

Fig. 1 View of the hub endwall in the vicinity of the vane leading edge and slots for secondary air injection. (*a*) plan view; (*b*) side view showing plane L1. The four planes for which solutions are analyzed in more detail shown in the plan view. Streamwise (*x*), distances in meters.

positioned upstream of the vane and used for injection of secondary air. The four planes indicated in Fig. 1*a* define the plane labeled L1 and the planes labeled S1, S2, and S3 which are normal to the vane suction surface at the locations along the passage shown in the figure. As discussed in greater detail in the next section, properties of the solutions in these planes are investigated in interpretation of the simulation results. The inlet boundary to the domain was 1.3 axial chord lengths upstream of the vane leading edge. In the experiments, a turbulent boundary layer was created by tripping the flow upstream of this position. The momentum thickness Reynolds number of the boundary layer 1.3 axial chord lengths upstream of the vane was $\mathrm{Re}_\theta = 955$, a turbulent profile at the same Re_θ was then introduced at the inlet to the computational domain. Other geometric and flow parameters are summarized in Table 1.

For computations in which secondary air was introduced, the slots were included in the computational domain, a view in plane L1 that includes the center slot is shown in Fig. 1*b*. This allowed non-uniformities in the exiting flow to be partially accounted for by the computational model, though without a complete inclusion of the supply plenum the present approach remains approximate. For the incompressible flow considered in this work, the blowing ratio, *BR*, reduces to the ratio of the uniform inlet velocity at the entrance to the slot normalized by the freestream velocity at the inlet to the computational domain. The blowing ratio was set equal to $BR = 1.3$ for calculations with secondary air injection (the same value as in the experiments with blowing).

Comparison against experimental measurements is achieved using the endwall distributions of the Stanton number, *St*, and cooling effectiveness, η. These quantities are defined as,

Table 1 Inlet boundary layer properties and vane characteristics.

Parameter	Value
Momentum thickness Reynolds number, Re_θ	955
Boundary layer thickness, δ_{99}	14 mm
Boundary layer shape factor	1.41
δ_{99}/R (R = vane leading edge radius)	0.62
vane inlet angle, exit angle	0, 75 deg
vane pitch/true chord length	0.75

$$St = \frac{q''_w}{\rho U_\infty c_p (T_r - T_w)}, \quad \eta = \frac{T_\infty - T_r}{T_\infty - T_s}, \tag{1}$$

where ρ and c_p represent the fluid density and specific heat at standard atmospheric conditions, respectively. The free-stream velocity and freestream temperature are denoted U_∞ and T_∞ in (1), respectively, T_r is the reference fluid temperature at the wall (i.e., the adiabatic wall temperature), q''_w is the heat flux into the wall, and T_s is the temperature of the secondary air injected through the slots. The wall temperature is denoted T_w in (1). Note that the reference fluid temperature T_r $(= \eta T_s + (1-\eta) T_\infty)$ represents the temperature of the mixed main air and secondary (cooling) air, the difference $(T_r - T_w)$ drives the heat transfer from the (hotter) mixed air to the wall.

To obtain *St* and η for the solution with secondary air injection, two computations using different secondary air temperatures were performed. The first with ''hot'' secondary air, i.e., at a temperature above the mainstream fluid and a second calculation with ''cold'' secondary air at a temperature below that of the mainstream gas. By assuming that the Stanton number and cooling effectiveness are the same for the two computations, (1) can be solved for *St*, η, and T_r. This approach is identical to the procedure employed in the companion experiments to calculate these quantities. In the simulations, the consistency of these procedures was checked by performing an additional computation with insulated walls (zero heat flux), which yielded the adiabatic wall temperature T_r directly, the distribution found identical to that obtained using the two computations with hot and cold secondary air.

The specific values of the temperatures of the mainstream fluid at the inlet to the computational domain and of the secondary air introduced into the slots were the same as in the experiments. The mainstream fluid temperature was 316.8 K, the ''hot'' and ''cold'' secondary air temperatures for the computations with blowing were 322.1 K and 313.1 K, respectively. The walls were isothermal with a temperature boundary condition of 309.15 K, identical to the transition (to color green) temperature of the thermochromic liquid crystal (TLC) used for the heat transfer measurements. The simulations reported in this contribution were performed with low freestream turbulence, corresponding to the ≈1% freestream turbulence intensity in the companion experiments.

In the experiments, the heat transfer distribution on the hub

endwall was measured by convective the transient TLC technique. The uncertainty in the measured heat transfer coefficient is estimated to be $\pm 10\%$ over most of the endwall. That in the cooling effectiveness is about the same. However, since a one-dimensional, semi-infinite medium formulation of transient heat conduction was used for the hub endwall in the TLC method, higher uncertainty (up to $\pm 12\%$) in the measurements is expected near the vane-endwall junction.

2.2 Solution Procedure and Turbulence Models. The Reynolds-averaged equations governing conservation of mass and momentum for an incompressible fluid and assuming constant fluid properties were solved using Fluent [4]. The thermal field within the vane passage was predicted via solution of the Reynolds-averaged thermal energy equation. The numerical method is based on a finite-volume approach and is second-order accurate, the SIMPLEC method [13] is used for the pressure-velocity coupling. The resulting system of algebraic equations were solved using a segregated iterative approach.

Computations were performed on a series of unstructured grids comprised of hexahedra and prisms that were generated using Gambit [4]. Each grid was comprised of two blocks, one that contains the inlet boundary layer and the second block containing the domain around the vane, propagated into the wake region downstream of the vane. In the first block, hexahedral cells were employed, using quadrangular elements at the endwall and at the lateral faces of the domain, and then projecting the (two-dimensional) endwall mesh through the spanwise direction. In the second block, a two-dimensional O-mesh with quadrangular elements was created around the vane using a boundary-layer grid-type in Gambit. The stretching ratio between consecutive cells from the vane wall was 1.17, the same as for the stretching from the hub endwall. For the finest grids, and for both configurations (i.e., with and without secondary air injection) grid cells were clustered near solid surfaces. Based on the friction velocity at the inlet, the first cell center was within 0.7 viscous units of the endwall. The mesh within the slots for air injection was created using hexahedral elements, including resolution of the boundary layer along the slot walls. Initially, a two-dimensional grid was created across the slot (i.e., a plane parallel to the endwall), that for the finest grid was comprised of 28×28 elements. The planar grid was then projected through the slot, 32 nodes were used to resolve the solution along the streamwise axis of the slot. For the configuration with secondary air injection, additional refinement of the mesh in the vicinity of the slots above the endwall was also employed.

A series of calculations were used to investigate grid convergence, with the coarsest grid comprised of 2.5×10^5 to the finest grid of 1.9×10^6 cells. Convergence in the skin friction with the grid is demonstrated in plane L1 and plane S3 in Fig. 2. Figure 2*a* shows that in plane L1 the skin friction upstream of the vane is relatively insensitive to the grid, though the figure also shows that for x larger than about 0.14 m, deviations are apparent with the skin friction predicted using the coarsest grid below that using the finer meshes. For the two finest grids, Fig. 2*a* shows little difference in C_f. In plane S3, a similar influence of the grid on skin friction predictions is observed. On the coarsest mesh, C_f levels are substantially below those on the finer grids. Results presented below were obtained on the finest mesh of 1.9×10^6 cells.

The computations presented in the next section were of the steady-state solution, convergence was monitored using the local mass residual, i.e., the maximum imbalance of the mass flux in any control volume at a given iteration. Residuals from the other transport equations (momentum, thermal energy, and turbulence transport equations) were typically smaller than those from conservation of mass. Thus, basing convergence on satisfaction of mass conservation represented the most stringent criterion. In the present simulations, a numerical solution was considered converged when the maximum mass imbalance for any control volume within the domain was less than 10^{-8}, rather than the usual standardized residual. Using this criterion, approximately 4000 iterations were required for convergence.

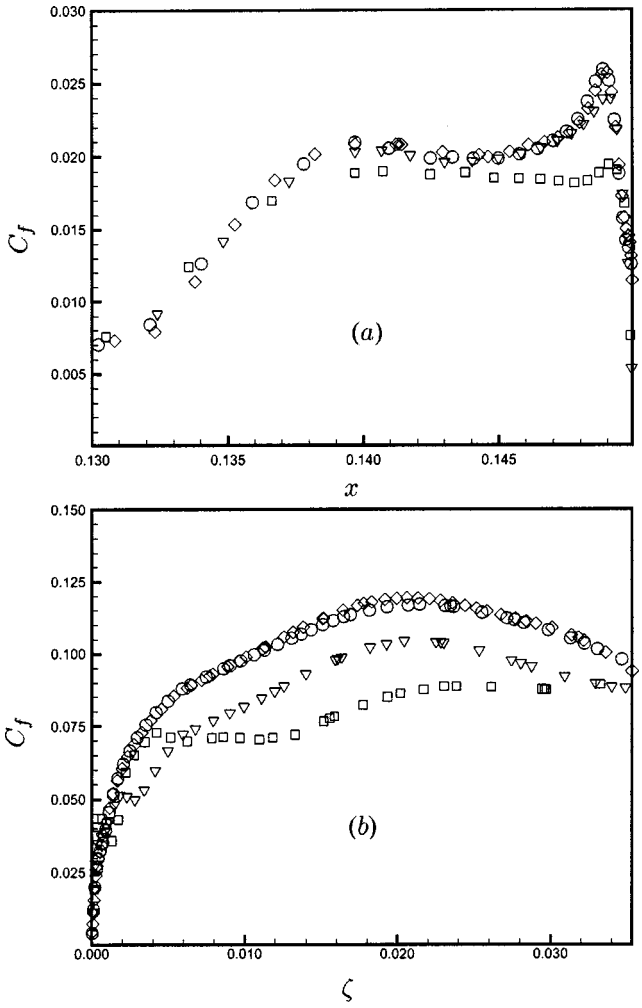

Fig. 2 Variation in the skin friction coefficient with grid resolution, baseline configuration. (*a*) plane L1, the vane leading edge coincides with the right vertical boundary in the figure; (*b*) plane S3, the view is into the passage from upstream with the suction side of the vane coinciding with the left vertical boundary of the frame, the coordinate ζ is defined in the plane (c.f., Fig. 1). Horizontal axis dimensions in meters. □ 2.5×10^5 cells; ▽ 4.75×10^5 cells; ○ 9×10^5 cells; ◇ 1.9×10^6 cells.

The inlet velocity profile was obtained from an auxiliary calculation in which boundary layer parameters matched the measured values (c.f., Table 1). The outlet boundary condition was applied along a plane $x=cnst$, one axial chord length downstream of the trailing edge. At the outlet, a constant pressure condition for the momentum equations was prescribed along with zero surface-normal gradient for the temperature and turbulence variables. Computations with fixed mass-flux conditions at the outlet yielded essentially the same predictions of the flow within the passage. No-slip and constant temperature conditions were prescribed along the vane and hub endwall. For computations that included secondary air injection, a uniform velocity was prescribed at the slot inlet, no-slip conditions were applied to the surface within the slots. In the present computations, which resolved the vane and endwall boundary layers, taking into account the entire range of geometrical complexity, e.g., inclusion of the secondary air ple-

num, was not possible. A zero stress condition was applied to the upper (tip) endwall, periodic conditions were applied along the pitchwise direction.

Results from computations performed using three RANS models are presented in the next section: the Spalart-Allmaras [5] (referred to as S-A throughout) one-equation model, RNG k-ε [14], and a Reynolds stress transport model [15] (referred to as RSM throughout). S-A and RNG k-ε relate the turbulent Reynolds stress to the mean strain rate using a scalar eddy viscosity. In S-A, a single transport equation is solved for a working variable, $\tilde{\nu}$, which is related to the turbulent eddy viscosity, ν_T, the advantage of the working variable is its linear behavior near the wall and that damping functions are not required. The model includes a wall destruction term that reduces the turbulent viscosity in the log layer and laminar sublayer, and trip terms that provides a smooth transition from laminar to turbulent flow. Note that in the present investigation, because the boundary layer in the experiments was fully turbulent (having been tripped upstream), the trip terms were not used in the computations.

RNG k-ε computes the eddy viscosity using solutions of the transport equations governing the turbulence kinetic energy and dissipation rate. An approach based on Renormalization Group Theory is developed in Yakhot et al. [14] for derivation of model constants different from the standard k-ε model, in addition to new terms and functions in the transport equations for both variables. An important difference between RNG k-ε and the standard k-ε model appears in the dissipation equation through an additional term that has the effect of raising ε, consequently lowering k and also the turbulent eddy viscosity, in regions of high strain rate. This feature should, in principle, be an advantage in application to the current vane-passage.

The Reynolds stress transport model was used in the present computations in order to improve context in interpretation of the results obtained using the other closures. In Reynolds stress transport, the turbulent Reynolds stress is computed directly from its transport equation, solution of the ε equation provides the remaining turbulence scale. In flows with complicating effects such as those encountered in vane passages—strong pressure gradients, mean-flow skewing, and streamline curvature—RSM models would appear to offer an advantage over scalar eddy viscosity approaches in that the transport equations possess several exact terms and, therefore, a closer connection to the exact equations. The production of turbulent Reynolds stress via normal-stress anisotropy is an example of an improvement that can be captured by RSM models and not the scalar eddy viscosity approaches (employing a Boussinesq constitutive relation). In addition, Reynolds stress transport modeling also formally accounts for the effects of streamline curvature, and rapid changes in strain rate more rigorously than one- and two-equation models. While possessing more exact terms, the computational cost of the calculation is substantially greater—the approach requires solutions of seven transport equations for the model—and the models are not without empiricism (e.g., in the pressure and dissipation terms). In the present computations, for example, a linear model is used for pressure-strain [16,15] and with the turbulent diffusion terms closed using a scalar (rather than tensor) diffusivity [17].

All the closures are integrated to solid surfaces, i.e., the near-wall flow is resolved rather than modeled using wall functions. The boundary condition on the modified viscosity in the S-A model is straightforward, $\tilde{\nu}=0$. For the RNG k-ε and RSM closures the two-layer approach of Chen and Patel [18] is employed in which the eddy viscosity in the viscous region is computed using the kinetic energy obtained from its transport equation and an algebraic mixing length. The dissipation rate computed from an algebraic relation is used to smoothly bridge the near-wall distribution of ε to the values obtained from the transport equation in the fully turbulent region. For the RSM predictions, the pressure-strain closure is modified as outlined by Launder and Shima [19] in which the model coefficients are modified in terms of the Reynolds stress invariants and turbulence Reynolds number, $\mathrm{Re}_t = k^2/\nu\varepsilon$ where ν is the kinematic viscosity of the fluid.

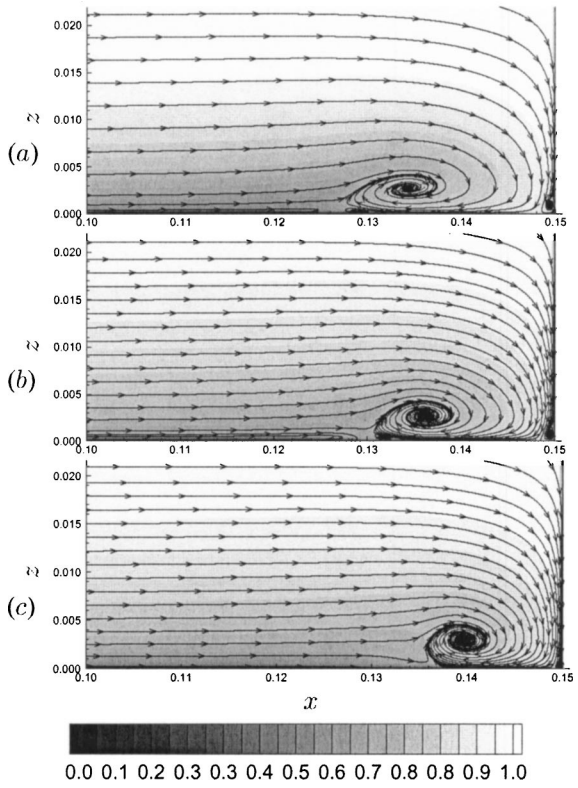

Fig. 3 Streamlines and contours of the dimensionless temperature $\theta=(T-T_w)/(T_\infty-T_w)$ in plane L1, baseline flow. The vane leading edge coincides with the right vertical boundary of each frame, axis dimensions are in meters. (*a*) S-A; (*b*) RNG k-ε; (*c*) RSM.

For all of the computations, the turbulent heat flux appearing in the Reynolds-averaged thermal energy equation was closed using a constant turbulent Prandtl number, $Pr_t=0.9$. Note that for the RSM calculations, the turbulent Prandtl number is used to calculate the turbulent eddy thermal diffusivity after forming the eddy viscosity ν_T using the same formula as in the RNG k-ε model. The sensitivity of thermal field predictions was examined by performing additional simulations using the S-A model with the turbulent Prandtl number lowered from 0.9 to 0.8 and then with Pr_t increased to 1.0.

3 Results

3.1 Baseline Configuration. Shown in Fig. 3 are temperature contours and streamlines predicted by each of the RANS models for the baseline configuration in plane L1. All of the models show the development of the horseshoe vortex as evidenced by the rollup of the streamlines, the figure showing variation in the vortex location and size predicted by each model. Temperature contours in Fig. 3 exhibit the distortion of the thermal field in the leading edge plane due to the presence of the vane and rollup of boundary layer fluid. The figure shows a slight thickening of the temperature boundary layer upstream of the horseshoe vortex and evidence of the transport of hotter mainstream fluid to the endwall in the vicinity of the vane-endwall junction. In addition to the primary horseshoe vortex, Fig. 3 also shows that in each of the calculations a secondary, corner vortex is resolved (shown in the lower right region of each frame). Compared to the S-A result in Fig. 3*a*, the RNG k-ε prediction of the rollup of the horseshoe vortex is nearer the vane leading edge. The S-A result also predicts a horseshoe vortex with a more elliptic cross-section and,

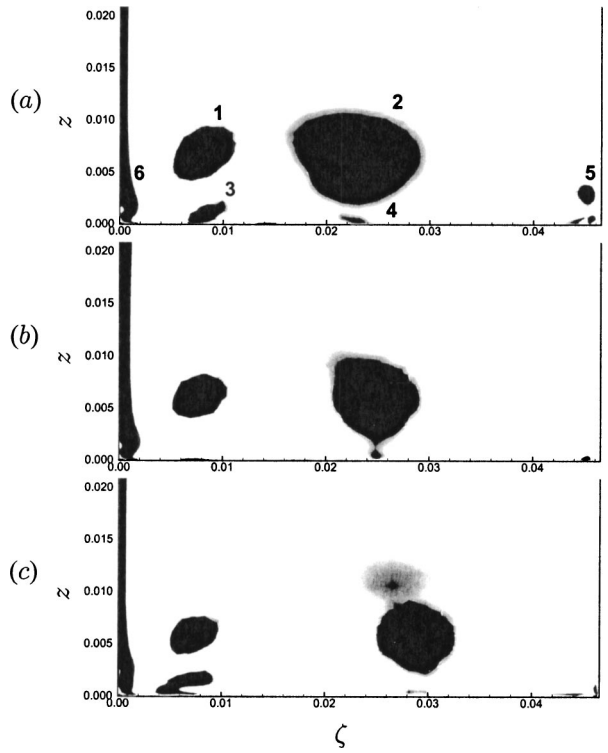

Fig. 4 Coherent structures in plane S2, baseline flow. View is into the passage from upstream (suction surface on the left vertical boundary, pressure surface of adjacent vane on the right vertical boundary of the frame), axis dimensions in meters. (*a*) S-A; (*b*) RNG *k*-ε; (*c*) RSM. Structures identified in the S-A prediction, 1: suction-side leg of the horseshoe vortex; 2: pressure-side leg of the horseshoe vortex from the adjacent vane; 3: counter-rotating structure induced beneath the suction-side leg; 4: counter-rotating structure induced beneath the pressure-side leg; 5: corner vortex adjacent to the pressure surface of the adjacent vane; 6: vortical structure induced along the vane suction surface.

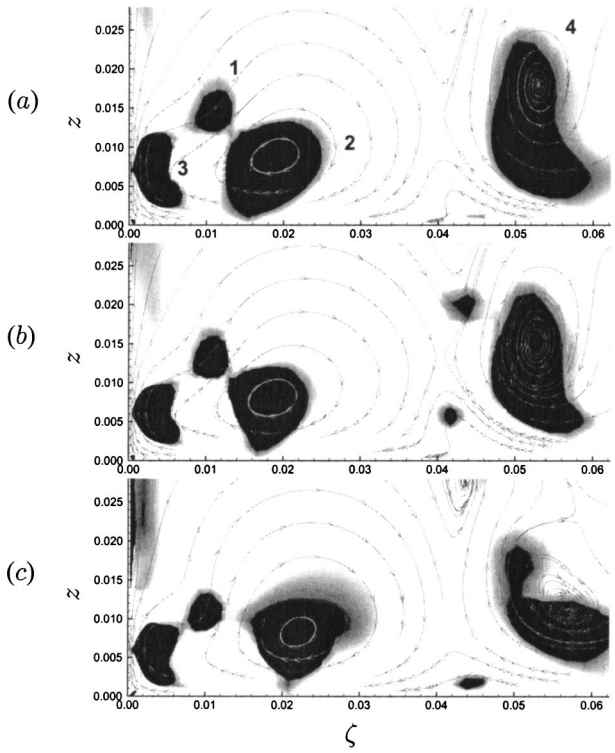

Fig. 5 Coherent structures in plane S3, baseline flow. View is into the passage from upstream (suction surface on the left vertical boundary of the frame), axis dimensions in meters. (*a*) Spalart-Allmaras; (*b*) RNG *k*-ε; (*c*) RSM. Structures identified in the S-A prediction, 1: suction-side leg of the horseshoe vortex; 2: pressure-side leg of the horseshoe vortex from the adjacent vane; 3: evolution of the counter-rotating structure induced beneath the suction-side leg shown in plane S2; 4: coherent structure from the neighboring passage.

though not obvious from Fig. 3, a small recirculating region is induced slightly upstream of the horseshoe vortex (roughly in the region $0.12<x<0.13$). The RSM prediction in Fig. 3*c* yields different flow features to those resolved using scalar eddy viscosity models, the horseshoe vortex is more compact and nearer the vane-endwall junction. Thus, the figure shows that the details of the solutions obtained using the RANS closures differ though the overall thickness of the recirculating region is comparable, consistent with similar descriptions of the boundary layer upstream of the vane.

Shown in Fig. 4 are contours of the coherent structures in plane S2. The prediction in Fig. 4*a* was obtained using the S-A model and the suction- and pressure-side legs of two (this vane and the adjacent vane, respectively) horseshoe vortices are identified (using ''1'' and ''2,'' respectively, in the figure). Streamlines are not drawn in plane S2 because of problems associated with post-processing, i.e., obscuring the contours of the coherent structures. Overall, RANS predictions of the size and relative positions of the legs of the horseshoe vortex using the three models are similar. The pressure-side leg of the horseshoe vortex from the adjacent vane (''2'' in Fig. 4) predicted in the S-A result is larger and closer to the suction side of the vane than predicted by the other models. The suction-side leg of the horseshoe vortex predicted using S-A is also slightly larger than that obtained in the predictions using RNG *k*-ε and RSM. The S-A and RSM results show that there is a secondary structure (''3'' in Fig. 4*a*) that is induced by the suction-side leg, possessing the same sign of vorticity as the pressure-side leg of the horseshoe vortex from the adjacent vane. An analogous secondary structure is resolved beneath the pressure-side leg (''4'' in Fig. 4*a*) for all the models. Finally, the S-A prediction shows at the right border of the frame, corresponding to the pressure side of the adjacent vane, a corner vortex (''5'' in Fig. 4*a*). In addition, all of the models show that along the vane suction surface (left vertical border of the figure) a coherent structure is identified (''6'' in Fig. 4*a*).

Figure 5 shows coherent structures further into the passage, in plane S3. Also shown in the figure are streamlines of the in-plane velocities. Note that in plane S3, the structures in the left-half portion of each frame are within the passage, while the structures in the right-half portion of each frame are from the neighboring passage and have evolved further along the mainstream direction. In Fig. 5*a*, the suction-side leg of the horseshoe vortex (''1'') is identified, along with the pressure-side leg (''2'') from the adjacent vane. A kidney-shaped coherent structure (''3'') is identified and represents the vortical structure that has developed from that induced beneath the suction side leg shown in Fig. 4 (''3'' in Fig. 4), along with structures developed near the vane-endwall junction. In the right-half portion of the frame, the larger kidney-shaped structure (''4'' in Fig. 5*a*) represents the downstream evolution from those shown on the left-half sides of the frame. The larger structure now represents the amalgamation of the pressure-side leg and kidney-shaped structure shown in the left-half of the frame. In the RNG *k*-ε prediction, the suction-side leg from the neighboring passage remains distinct while in the S-A prediction the suction-side leg is no longer identified in the right-hand side of the frame, having been diffused by the turbulence model and numerics. Overall, and similar to the observation concerning the flow structure shown in plane S2 (c.f., Fig. 4), RANS predictions

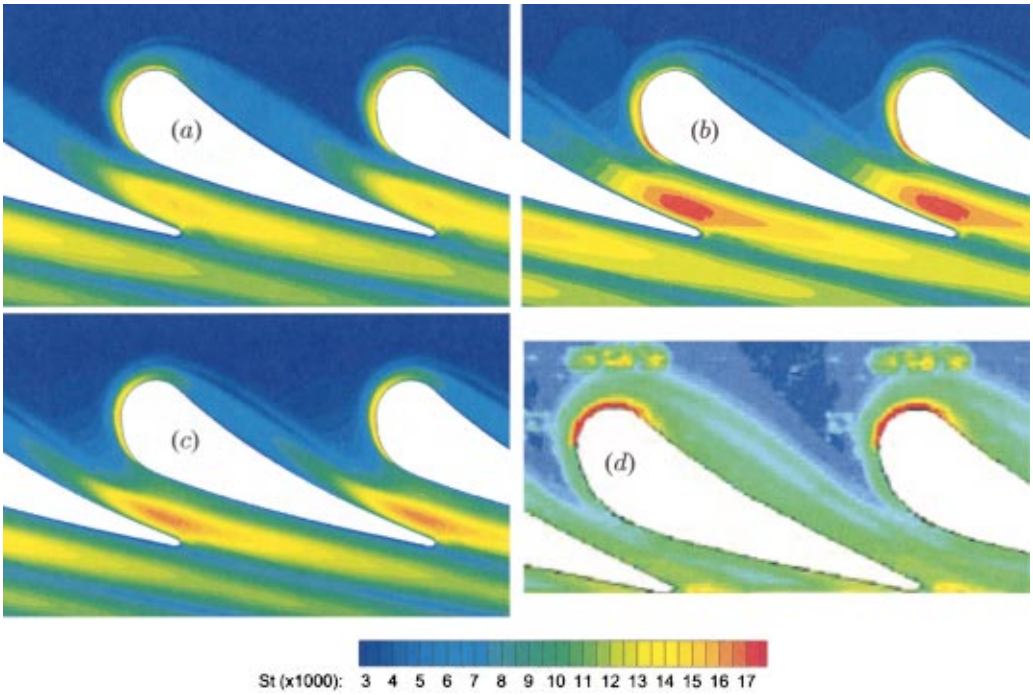

Fig. 6 Hub-endwall Stanton number distribution, baseline configuration. (*a*) Spalart-Allmaras; (*b*) RNG k-ε; (*c*) RSM; (*d*) measured.

of the vortical structure are not markedly different from one another in plane S3. The in-plane streamlines exhibit comparable features, showing the clockwise (when viewed from upstream as in Fig. 5) rotation of the fluid due to the turning of the flow through the passage. Figure 5 shows that the vortical motions identified in the plane 'modulate' this overall clockwise rotation, an important effect since endwall *St* distributions are directly influenced by these motions as shown next.

Distributions of the hub-endwall Stanton number, *St*, for the baseline configuration are shown in Fig. 6. Shown are the RANS predictions obtained using all of the models, in addition to the experimentally measured distribution. The experimental measurement in Fig. 6*d* shows that the maximum Stanton number is achieved in the leading edge region and is nearly 0.016, substantially higher than the values in the upstream flow. Through the passage and towards the pressure side of the vane, measured *St* levels remain relatively high, in the range $St \approx 0.012-0.013$. In general, the measured *St* distribution exhibits similar features as reported in the work by Radomsky and Thole [10], e.g., the similarly elevated heat transfer rates in the leading edge region.

The features in the endwall *St* distributions predicted by the RANS models are consistent with the flow visualizations of the coherent structures described above. Rollup of the upstream boundary layer around the leading edge of the vane and formation of the horseshoe and corner vortices leads to high values of *St* at the vane-endwall junction with predictions of the *St* distribution correlated to the flow structure resolved using the various closures. Maxima in the Stanton number, for example, are not predicted at the same locations along the endwall for each of the models, the particular ranges and distributions being dependent upon the relative proximity of the vortical structures to the vane and endwall, as well as their size and intensity (e.g., as measured by the peak vorticity within the structure). RNG k-ε predictions of the peak *St* in the leading edge region are the highest, $St \approx 0.0167$, compared to S-A, $St \approx 0.0160$. In general, in the leading edge region *St* levels predicted using the Reynolds-stress transport model are slightly lower than that obtained from the scalar eddy viscosity models, e.g., the peak value is $St = 0.0152$ for RSM. Comparison of the measured *St* to that predicted shows that the region corresponding to high *St* levels directly adjacent to the vane leading edge covers an area of somewhat greater extent than predicted, though the maximum measured value, $St \approx 0.016$ is predicted by the computations. Into the passage, near the suction side, all the models predict higher *St* maxima than measured. The RNG k-ε predictions of the Stanton number are the largest downstream of the leading edge along the thin strip that follows the contour of the vane suction side. In general, the elevated levels of *St* in this location arise from the interaction of the horseshoe and corner vortices, which promote transport of hotter mainstream fluid to the endwall. As the flow evolves further through the passage close to the suction side, *St* levels decrease to a range of roughly $0.009-0.011$. Figure 6 shows that differences in RANS predictions of the endwall *St* are most apparent within the passage, downstream of the minimum-area section. All of the models predict increases in the Stanton number, with the most significant elevations obtained in the RNG k-ε result (maximum $St = 0.0165$ in the passage), followed by RSM (maximum $St = 0.0159$), and then S-A (maximum $St = 0.0147$). These regions of elevated *St* are again strongly correlated to the local flow structure, e.g., the overall transport of the flow from the pressure side to the suction side within the passage, an effect that transports hotter mainstream fluid to the endwall (c.f., Fig. 5). Closer to the suction side, the overall upward motion of the flow results in comparatively lower *St*. These effects are less apparent in the experimental measurements, though there is some reduction in *St* observed across the passage, from the pressure to the suction sides.

For the RNG k-ε predictions the core of the vortical structures are characterized by eddy viscosity levels lower by about a factor of two compared to the S-A predictions and higher peak-vorticity (almost two times the levels resolved in the vortex cores using S-A). RNG k-ε predictions yield correspondingly smaller and relatively more intense vortical structures than resolved in the S-A predictions. Though not shown here, for the RNG k-ε and RSM models, elevated levels of turbulent kinetic energy are strongly correlated to the coherent structures in the vicinity of the vane leading edge, exhibiting less correlation with continued downstream evolution. As a result of these differences, in the middle of the passage the pressure-side leg of the horseshoe vortex in the RNG k-ε predictions has the highest peak vorticity, an aspect that

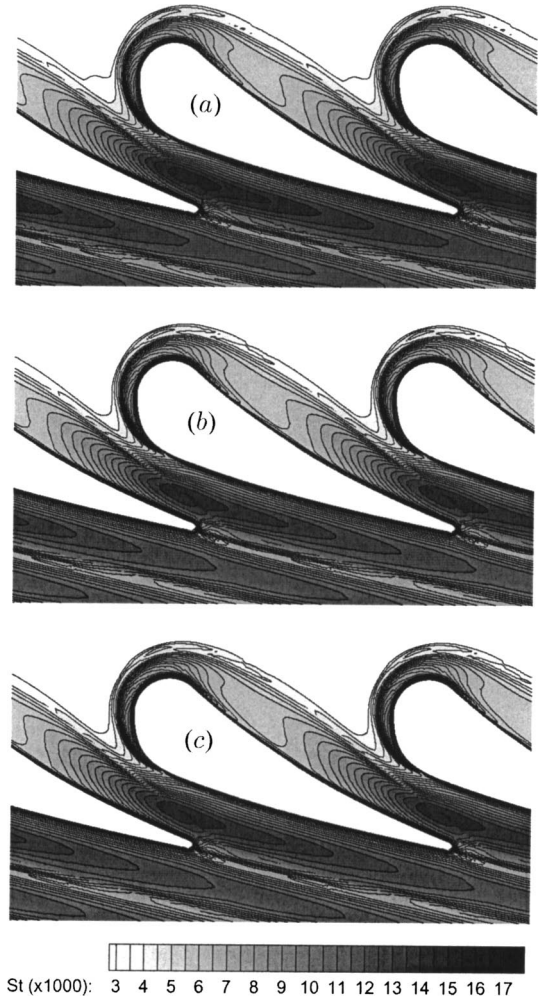

Fig. 7 Influence of Pr_t on the hub-endwall Stanton number distribution, baseline configuration. Predictions obtained using the S-A model. (*a*) $Pr_t=0.8$; (*b*) $Pr_t=0.9$; (*c*) $Pr_t=1$.

promotes more efficient entrainment towards the endwall and, consequently, higher Stanton numbers. In the RSM predictions, the peak vorticity in the pressure-side leg is lower than in the RNG k-ε predictions, and about 40% higher than obtained using S-A. Thus, in the RSM predictions, as in the RNG k-ε, the vortical structure of the pressure-side leg of the horseshoe vortex is more intense, as indicated by the peak vorticity levels, than that obtained in the S-A results. This implies that smaller and more intense vortical structures characterize the coherent structures in the RSM predictions, which results in higher endwall heat transfer rates than S-A, though lower than RNG k-ε.

As described in the previous section, while the underlying closure models for the momentum equations differ in various respects, the turbulent heat flux is modeled by introducing a constant turbulent Prandtl number, $Pr_t=0.9$. Shown in Fig. 7 is the influence of Pr_t on the endwall Stanton number distribution from predictions obtained using the S-A model. In addition to the calculation performed using $Pr_t=0.9$, endwall *St* distributions are also shown from calculations with $Pr_t=0.8$ and 1.0. In the vicinity of the leading edge where the Stanton number is high via the entrainment of hot mainstream gas by the horseshoe and corner vortices, the maxima in *St* from the three calculations are essentially the same, i.e., $St_{\max}\approx 0.0160$. Further downstream, within the passage and past the minimum-area section, the figure shows more sensitivity to Pr_t, with the highest levels in *St* obtained for the smallest turbulent Prandtl number of 0.8. The maxima in *St* within the passage are 0.0157, 0.0147, and 0.0147 for $Pr_t=0.8$, 0.9, and 1.0, respectively. Thus, while the variations are not substantial, the results seem generally consistent with the fact that reductions in Pr_t correspond to increases in the thermal eddy diffusivity compared to the value governing turbulent momentum transport, the increases in maximum Stanton number levels with reductions in Pr_t indicative of greater mixing of the thermal field leading to an increase in the temperature gradient at the wall and associated higher heat flux.

3.2 Effect of Secondary Air Injection. Predictions of the flow and thermal fields used to investigate the influence of secondary air injection were obtained using the S-A and RNG k-ε models. Because of the limitations of available computational resources, it was not possible to obtain solutions on the finest meshes needed for grid independent solutions using the Reynolds stress closure.

The effect of secondary air injection on flow structure in plane L1 is shown in Fig. 8. The temperature contours shown in Fig. 8*a* are from the solutions using cold secondary air, i.e., with the secondary air temperature below that of the mainstream flow. Comparison of the temperature contours to the corresponding baseline case in Fig. 3*a* shows a significant alteration of the solution in plane L1 due to injection. The vane-endwall junction is now effectively shielded by the secondary air, with most of the fluid near the junction close to the temperature of the injected fluid. Though not as pronounced as in the baseline configuration, very near the vane-endwall junction, boundary layer fluid rolls up and forms a small horseshoe vortex. The coherent structures educed in the leading edge plane are shown in Fig. 8*b*, the horseshoe vortex identified as "1" in the figure. Above the small horseshoe vortex a second larger coherent structure is identified ("2" in the figure), which is the structure that develops around the vane due to the

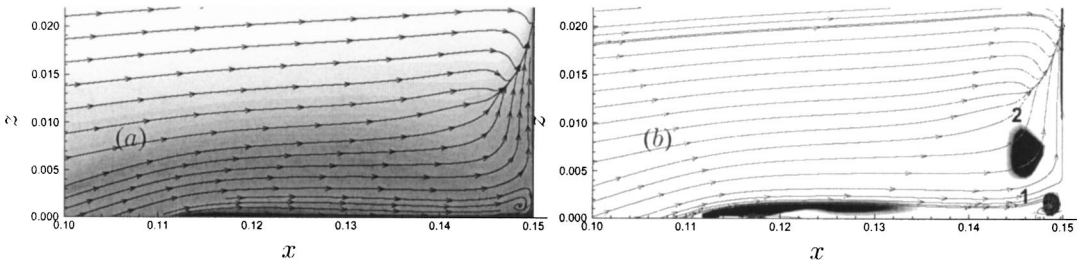

Fig. 8 Streamlines and contours of the dimensionless temperature $\theta=(T-T_w)/(T_\infty-T_w)$ (in *a*), and contours of the coherent structures (in *b*) in plane L1, $BR=1.3$. Predictions obtained using S-A model. The vane leading edge coincides with the right vertical boundary of each frame, axis dimensions are in meters.

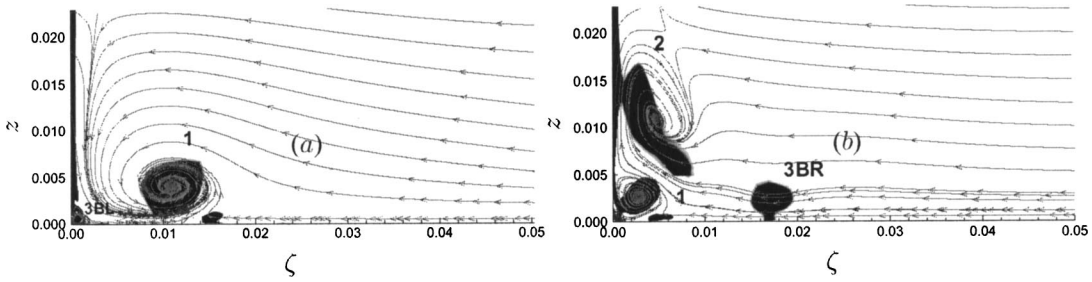

Fig. 9 Streamlines and contours of the coherent structures in plane S1. View is into the passage from upstream (suction surface on the left vertical boundary of the frame), axis dimensions in meters. Predictions obtained using the S-A model. (*a*) baseline; (*b*) *BR*=1.3.

interaction of the secondary air with the vane. Also shown in Fig. 8*b* is an identifiable structure that evolves slightly downstream of the central slot location.

Streamlines, coherent structures, and temperature contours are contrasted for the baseline configuration and secondary air injection case in Figs. 9 and 10. Shown in Fig. 9 are streamlines and coherent structure contours in plane S1. Coherent structures shown for the baseline configuration in Fig. 9*a* show the suction-side leg of the horseshoe vortex (''1'' in the figure), a secondary structure induced by the horseshoe, and the corner vortex that is initially formed near the vane leading edge (''3BL'' in the figure). Entrainment of hotter mainstream gas towards the endwall in the baseline configuration, as shown in Fig. 10*a*, is the mechanism responsible for elevated heat transfer levels in the vicinity of the suction surface-endwall junction. Under the influence of secondary air injection, the vortical structure around the vane and near the endwall is strongly distorted as shown in Fig. 9*b*. The small horseshoe vortex identified in the leading edge plane in Fig. 8*b* corresponds to the structure identified ''1'' in Fig. 9*b*. Similar to that shown in Fig. 9*a*, the suction-side leg of the horseshoe vortex in the flow with secondary air injection also induces a smaller structure as observed in Fig. 9*b*. The jet fluid that interacts with the vane above the endwall corresponds to the structure identified ''2'' in Fig. 9*b*, the remaining structure identified in Plane S1 (''3BR'' in the figure) corresponds to a vortical structure that has developed at the periphery of the suction-side slot.

Streamlines are again drawn in Fig. 10 along with temperature contours from the calculation with secondary air injected at a temperature below that of the freestream value. The result in Fig. 10*a* is the prediction of the flow and temperature field in plane S1 from the baseline configuration, using the S-A model. Between the suction side of the vane and suction-side leg of the horseshoe vortex, the figure shows the entrainment of hotter mainstream gas to the wall, an effect that results in elevated *St* (c.f., Fig. 6). For the solution with secondary air injection the temperature field in Plane S1 shown in Fig. 10*b* is strongly distorted compared to that obtained in the baseline configuration. Because of the injection of cooler secondary air, fluid in the region near the suction side of the vane and along the endwall is at a lower temperature than observed in the baseline configuration. As shown below, this is synonomous with a reasonably broad coverage of the endwall with high cooling effectiveness.

The Stanton number and cooling effectiveness distribution on the hub endwall from calculations performed using the S-A and RNG k-ε models and the experimental measurements are shown in Fig. 11. Note that the images in Figs. 11*e*, *f* are actual laboratory images (CCD camera) of the vanes, endwall, and injection slots. Any apparent mismatch in dimensions between these two frames and Figures 11*a-d* results form the scaling of the laboratory images. In general, the *St* distributions upstream of the vane leading edge exhibit structure consistent with the interactions between the vortical flow resulting from the interaction with fluid injected from the slots and the endwall. Both the S-A and RNG k-ε predictions show, for example, local increases in *St* downstream of the narrow gap between the slots. Measured values of *St* shown in Fig. 11*e* exhibit a similar effect though the measured values are higher than predicted. The measured increase in *St* just downstream of the slots is an effect apparent in the RNG k-ε results, while the S-A predictions do not yield similar increases. Analogous to the baseline configuration, the S-A prediction shows a thin region near the vane leading edge and slightly into the suction side in which *St* levels are high, the maximum value is around 0.020 compared to a maximum of 0.016 in the baseline configuration (c.f., Fig. 6*a*). While the S-A predictions of *St* are high in the leading edge region, Fig. 11*b* shows that the cooling effectiveness in the vicinity of the vane leading edge is substantial. The S-A and RNG k-ε predictions of η exhibit similar features, reasonable coverage of elevated cooling effectiveness near the leading edge and with roughly half the of the endwall area within the passage, near the pressure side, also corresponding to

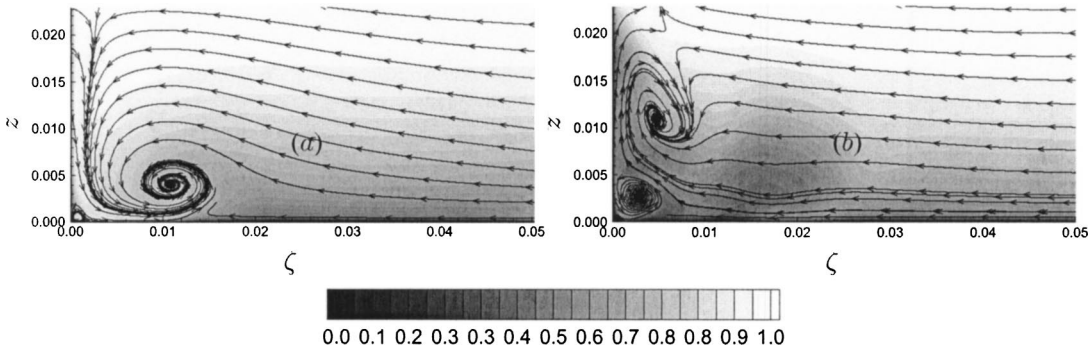

Fig. 10 Streamlines and contours of the dimensionless temperature $\theta=(T-T_w)/(T_\infty-T_w)$ in plane S1. View is into the passage from upstream (suction surface on the left vertical boundary of the frame), axis dimensions in meters. Predictions obtained using the S-A model. (*a*) baseline; (*b*) *BR*=1.3.

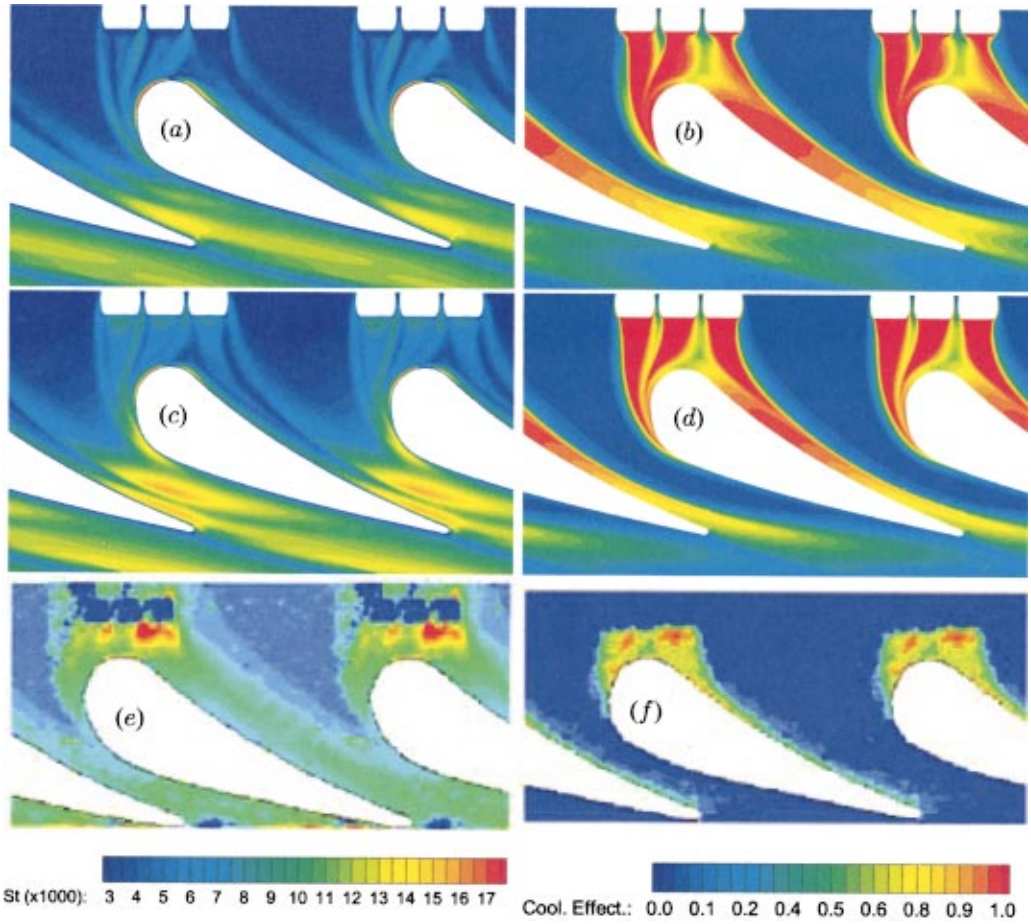

Fig. 11 Hub-endwall Stanton number and cooling effectiveness, $BR=1.3$. (*a*)-(*b*) Spalart-Allmaras; (*c*)-(*d*) RNG k-ε; (*e*)-(*f*) measured.

high η. Measured values of η are high downstream of the slots close to the leading edge of the vane, values around 0.5 are measured along the strip adjacent to the vane pressure side. Both the RNG k-ε and S-A models predict a larger area of elevated η near the pressure side of the vane.

4 Summary

RANS predictions of the flow and thermal fields in an inlet vane passage were obtained using scalar eddy viscosity approaches based on one- and two-equation transport models, in addition to (for the baseline case) predictions from a Reynolds stress transport model. The calculations were evaluated via an inter-comparison of the different model results and against experimental measurements of the Stanton number and cooling effectiveness on the hub endwall. For all of the models, the turbulent heat flux was closed using a constant turbulent Prandtl number of 0.9. Computations were also performed using the S-A model and turbulent Prandtl numbers of 0.8 and 1.0 in order to gauge sensitivity of endwall heat transfer predictions to the choice of Pr_t.

Vortical structures in the solutions were educed using the technique developed by Jeong and Hussain [12]. In the baseline case, a well-defined horseshoe vortex develops in the leading edge region of the vane, with a small corner vortex also resolved in the calculations. The evolution of the vortical flow through the passage exhibits similar features for each model, though differences in structural features are strongly correlated to the differences in the endwall surface transfer characteristics.

The flow field predictions were generally similar, especially in the leading edge region. The particular Reynolds stress transport model employed in this investigation did not offer strong advantages in the leading edge region since simpler models are well calibrated, able to accurately describe boundary layer growth upstream of the vane, in turn describing somewhat similar vortical structures in the leading edge region. Within the passage, differences are observed in the structural/vortical features resolved by the models, and it might be anticipated that other Reynolds stress models that are more sensitive, for example, to streamline curvature could show larger variations. Relevant in this regard is the quadratic pressure-strain model of Speziale et al. [20]. More comprehensive investigations that should include experimental measurements of the passage flow field would be valuable in shedding light on these issues.

Computations with secondary air injection through slots upstream of the vane showed a very strong distortion of the vortical structure in the vicinity of the leading edge region. Development of vortical structures due to the interactions of the fluid issuing from the slots with the mainstream flow resulted in significant structural differences in the vicinity of the vane leading edge, resulting in endwall signatures of St and η that were substantially altered compared to the baseline case.

In the vicinity of the leading edge, the region of substantial cooling effectiveness was relatively large, similar to that observed in the experimental measurements. Computed endwall Stanton numbers very close to the vane leading edge were higher than in the baseline configuration, unlike the change in the measured values caused by the introduction of secondary air. Flow visualizations from the computations show that in the regions with relatively high cooling effectiveness, fluid temperatures are near that of the secondary air. A marked difference compared to the experi-

mental measurements of η was the larger extent of the cooled endwall surface within the passage in the calculations.

Acknowledgments

The authors gratefully acknowledge the support of the National Science Foundation, Thermal Transport and Thermal Processing Program, Division of Chemical and Thermal Systems, under grant number CTS-9904172 as well as Honeywell Engines and Systems, Phoenix, Arizona.

References

[1] Dunn, M. G., 2001, ''Convective Heat Transfer and Aerodynamics in Axial Flow Turbines,'' ASME J. Turbomach., **123**, pp. 637–686.
[2] Hildebrandt, T., and Fottner, L., 1999, ''A Numerical Study of the Influence of Grid Refinement and the Turbulence Modeling on the Flow Field Inside a Highly Loaded Turbine Cascade,'' ASME J. Turbomach., **121**, pp. 709–716.
[3] Kalitzin, S., and G. Iaccarino, 1999, ''Computation of the Heat Transfer in a Linear Cascade,'' *Annual Research Briefs—Center for Turbulence Research*, pp. 277–288.
[4] Fluent 6.0 User's Guide, 2000, Fluent, Inc.
[5] Spalart, P. R., and Allmaras, S. R., 1994, ''A One-Equation Turbulence Model for Aerodynamic Flows,'' La Recherche Aerospatiale, **1**, pp. 5–21.
[6] Durbin, P. A., 1991, ''Near-Wall Turbulence Closure Without Damping Functions,'' Theoretical and Computational Fluid Dynamics, **3**(1), pp. 1–13.
[7] Heidmann, J. D., Rigby, D. L., and Ameri, A. A., 2000, ''A Three-Dimensional Coupled Internal/External Simulation of a Film-Cooled Turbine Vane,'' ASME J. Turbomach., **122**, pp. 348–359.
[8] Leylek, J. H., and Zerkle, R. D., 1994, ''Discrete-Jet Film Cooling: A Comparison of Computational Results with Experiments,'' ASME J. Turbomach., **116**, pp. 358–368.
[9] Langston, L. S., Nice, M. L., and Hooper, R. M., 1977, ''Three-Dimensional Flow Within a Turbine Cascade Passage,'' ASME J. Eng. Power, **99**, pp. 21–28.
[10] Radomsky, R. W., and Thole, K. A., 2000, ''Flowfield measurements for a highly turbulent flow in a stator vane passage,'' ASME J. Turbomach., **122**, pp. 255–262.
[11] Friedrichs, S., H. P. Hodson, and W. N. Dawes, 1998, ''The Design of an Improved Endwall Film-Cooling Configuration,'' Paper 98-GT-483.
[12] Jeong, G., and Hussain, F., 1995, ''On the Identification of a Vortex,'' J. Fluid Mech., **285**, pp. 69–94.
[13] van Doormal, J. P., and Raithby, G. D., 1984, ''Enhancements of the SIMPLE Method for Predicting Incompressible Fluid Flow,'' Numer. Heat Transfer, **7**, pp. 147–163.
[14] Yakhot, V., Orszag, S. A., Tangham, S., Gatski, T. B., and Speziale, C. G., 1992, ''Development of Turbulence Models for Shear Flows by a Double Expansion Technique,'' Phys. Fluids, **7**, pp. 1510–1520.
[15] Launder, B. E., 1989, ''Second-moment closure and its use in modeling turbulent industrial flows,'' Int. J. Numer. Methods Fluids, **9**, pp. 963–985.
[16] Gibson, M. M., and Launder, B. E., 1978, ''Ground effects on pressure fluctuations in the atmospheric boundary layer,'' J. Fluid Mech., **86**, pp. 491–511.
[17] Lien, F. S., and Leschziner, M. A., 1994, ''Assessment of turbulent transport models including non-linear RNG eddy-viscosity formulation and second-moment closure,'' Comput. Fluids, **23**(8), pp. 983–1004.
[18] Chen, H. C., and Patel, V. C., 1988, ''Near-wall turbulence models for complex flows including separation,'' AIAA J., **26**(6), pp. 641–648.
[19] Launder, B. E., and Shima, N., 1989, ''Second-moment closure for the near-wall sublayer: development and application,'' AIAA J., **27**(10), pp. 1319–1325.
[20] Speziale, C. G., Sarkar, S., and Gatski, T. B., 1991, ''Modeling the pressure-strain correlation of turbulence: an invariant dynamical systems approach,'' J. Fluid Mech., **227**, pp. 245–272.

Marko Hočevar*
e-mail: marko.hocevar@fs.uni-lj.si
Phone: +386 1 4771 774
Fax: +386 1 2518 567

Brane Širok
e-mail: brane.sirok@fs.uni-lj.si
Phone: +386 1 4771 410
Fax: +386 1 2518 567

Faculty of Mechanical Engineering,
Hydraulic Machines Laboratory,
University of Ljubljana,
Aškerčeva 6, P.O. Box 394,
SI-1000 Ljubljana, Slovenia

Igor Grabec
e-mail: igor.grabec@fs.uni-lj.si
Faculty of Mechanical Engineering,
Laboratory of Technical Physics,
University of Ljubljana,
Aškerčeva 6, P.O. Box 394,
SI-1000 Ljubljana, Slovenia
Phone: +386 1 4771 605
Fax: +386 1 2518 567

Experimental Turbulent Field Modeling by Visualization and Neural Networks

Turbulent flow field was modeled based on experimental flow visualization and radial-basis neural networks. Turbulent fluctuations were modeled based on the recorded concentration at various locations in the Karman vortex street, which were used as inputs and outputs of the neural network. From the measured and the modeled concentration the power spectra and spatial correlation functions were calculated. The measured and the modeled concentration power spectra correspond well to the −5/3 turbulence decay law, and exhibit the basic spectral peak of fluctuation power at the same frequency. The predicted and measured correlation functions of concentration exhibit similar behavior.
[DOI: 10.1115/1.1760534]

1 Introduction

Our purpose was to model the concentration in a Karman vortex street using an experimental modeling technique. The experimental method was based on measurements of concentration by a visualization technique, and modeling using a radial-basis neural network (RBNN).

Recently, some attempts have been made to apply artificial neural networks (ANNs) to problems in fluid dynamics. Faller et al. [1,2] utilized an ANN to predict separation pressure on an aircraft foil after training it with existing unsteady airfoil data obtained at different pitch rates. Jacobson and Reynolds [3] used two different ANN controllers to alter the shear stress on the wall of a modeled boundary layer, and deduced a skin friction reduction of 8%. ANNs are also increasingly being applied in pattern recognition problems, and their application has been extended to particle image velocimetry and similar techniques (Jambunathan et al. [4], Grant and Pan [5], Kimura et al. [6]). Dibike et al. [7] applied ANNs in generation of wave equations from hydraulic data. Blackwelder [8] and Ferre-Gine et al. [9] used ANNs for turbulent eddy classification and detection of eddy patterns. A velocity field flow prediction was attempted by Delgado et al. [10], Zhang et al. [11], and Giralt et al. [12]. Neural networks were applied towards the formulation of accurate and wide-range calibration methods for such flow-diagnostics instruments as multi-hole and cross-wire probes [13,14].

For flow control applications, ANNs offer a possibility of adaptive controllers that are simpler and potentially less sensitive to parameter variations as compared to conventional controllers (Gad-el-Hak [15], Lee et al. [16]). The controller does not necessarily require velocity field information, but also accepts other quantities, which characterize the structure of the flow field, for example flow visualization pictures (Gillies, 1998 [17]). We considered a turbulent flow of the Karman vortex street. Its properties were characterized by the power spectra and correlation functions of an added passive tracer concentration.

Experimental conditions were selected such that a common example of turbulent field was obtained. In this case, the effect of the molecular diffusivity and the kinematic viscosity could be neglected. These occur at wavenumbers of fluctuating flow that are much smaller than the dissipation cut-off k_d and the diffusion cut-off k_c ($k \ll k_c; k \ll k_d$). The scalar variance spectrum was then described by the well known power law (McComb [18])

$$F(k) = \beta \chi \varepsilon^{-1/3} k^{-5/3}. \tag{1}$$

Here β is the Obukhov-Corrsin constant, χ is variance of scalar concentration field, and ε is turbulent kinetic energy dissipation rate. It was pointed out by Batchelor [19], that the proposed diffusion cut-off k_c is only valid for viscosities smaller than the diffusion coefficient $v \ll D$. In the following we show that our experimental arrangement provided for the generation of a turbulent field with this power spectrum, and demonstrate that the modeled field exhibited the same property.

It is convenient to describe the statistical properties of the turbulent field based upon the correlation between two concentrations. The simultaneous measurements of concentration at two locations in the image permit to obtain directly the space autocorrelation coefficient Q, from which the Taylor length scale λ_c for concentration is deduced. The autocorrelation coefficient for concentration can be approximated by a parabolic function in a similar way as shown by Hinze [20] for velocity

$$Q(r) = 1 - \frac{r^2}{\lambda_c^2} + O(r^3) \tag{2}$$

for very small values of separation r.

Our goal was to solve the following problem: *Provided that the flow in some region is given, how can the flow in the surrounding region be forecast*? We used a method that is similar to the recognition of patterns by intelligent beings and is based on statistical modeling. This method was based on the information provided by past observations of the same phenomenon in equivalent environ-

*Corresponding author.

Contributed by the Fluids Engineering Division for publication in the JOURNAL OF FLUIDS ENGINEERING. Manuscript received by the Fluids Engineering Division March 20, 2003; revised manuscript received January 5, 2004. Associate Editor: M. V. Ötügen.

ment. The information was presented by joint data about the flow in the given region and its surroundings. The recorded and stored data served as basic parameters of the statistical model. It turned out that such a model exhibited the structure of an ANN (Grabec [21]), which operates in two different modes named learning and prediction. During learning the ANN obtains experimental data from intervals that can be spatially or temporary separated. These joint data are stored in the memory of the ANN and form the parameters of the model. During application, the ANN obtains only partial data from one interval and predicts the data in another interval. We demonstrated the applicability of this method on the Karman vortex street. In our case the concentration of an injected passive tracer in one region of the vortex street was modeled using the measured concentration in the other region.

In the following parts of the article we will explain some basic properties of the experimental modeling and experimental arrangement. The performance of the method will then be estimated by comparing the properties of the predicted and the corresponding recorded data.

2 Experimental Modeling

A natural law is usually described by the relationship between dependent and independent variables $y=f(\mathbf{x})$. In our case, $\mathbf{x}$ represented the data vector describing the field in the given interval, while y described the field in the surrounding interval. A fundamental problem was then to formulate a method by which a function f could be modeled based on the given experimental data. A parametric or non-parametric approach can be applied for this purpose. In the parametric approach, the form of the function f must be known a-priori, which was not the case in our treatment. Therefore we proceeded with the non-parametric modeling—which learns from the provided measured samples-to model the function f (Grabec [21]). From among several available methods we used RBNN. One of the primary contributors to the popularity of RBNN was probably their fast learning time as compared to other methods (Simon [22]). The Radial Basis function Neural Networks are also convenient for high dimensional surface fitting problems (Kim and Lee [23]).

The schematic of an RBNN is shown in Fig. 1. RBNN is an information processing system comprised of K memory cells called neurons with a localized receptive field. This field is described by a radially symmetric basis function $g(\mathbf{x})$ of the input vector $\mathbf{x}$. We employed the Gaussian function $g_k(\mathbf{x})$

$$g_k(\mathbf{x})=\exp\left(-\frac{\|\mathbf{x}-\mathbf{q}_k\|^2}{2\sigma_k^2}\right), \tag{3}$$

in which the parameters $\mathbf{q}_k$ and σ_k denote the center and the width of the receptive field of the k-th neuron, respectively. All neurons obtained the same input $\mathbf{x}$. The output $y(\mathbf{x})$ from the network was described by a linear superposition of individual outputs

$$y(\mathbf{x})=\sum_k^K m_k g_k(\mathbf{x}). \tag{4}$$

This superposition represented the model of function f, which was specified by the set of parameters m_k, q_k and σ_k. They were statistically estimated from a given set of experimental samples $(\mathbf{x}_n, y_n)$, $n=1 \ldots N$, such that the mean square error between the network output $y(\mathbf{x}_n)$ and the experimental datum y_n was minimal

$$E\lfloor (y(\mathbf{x}_n)-y_n)^2 \rfloor \Rightarrow \min(m_k,\sigma_k,q_k). \tag{5}$$

Various algorithms for minimizing this criterion function are available; from among them we used the algorithm derived by Orr [24].

In our modeling, the concentration of a passive tracer in a selected input region was used as the input $\mathbf{x}$. The output y denoted the corresponding concentration at some point of the output region in the surrounding. However, the field in the complete output region could be modeled using several equivalent networks which were adapted for each point separately.

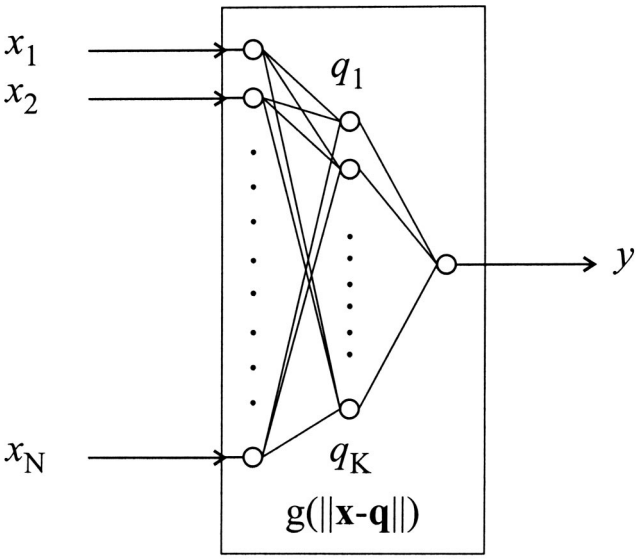

Fig. 1 Schematic of an ANN.

3 The Experiment

Measurements of passive tracer concentration are based on recording the light scattered on a passive tracer in a wind tunnel by assuming that the intensity of the scattered light is proportional to the passive tracer concentration (Gerdes and Olivari [25], Simoens and Ayrault [26], Aider and Westfried [27], Grisch and Bresson [28], Chatzipanagiotidis and Olivari [29], Law and Wang [30], Balu et al. [31]). Local concentration was recorded as the instantaneous gray level of each pixel of the acquired image. However, no calibration method was applied to measure concentration as a physical quantity.

We examined the Karman vortex street by the experimental configuration shown in Fig. 2. Visualization measurements were performed in a low-speed wind tunnel with a test section of 1 m

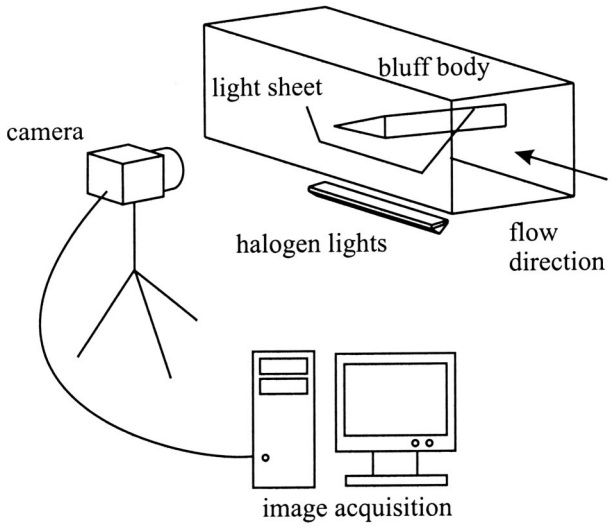

Fig. 2 Experimental configuration.

$\times 0.3$ m$\times 0.3$ m. In the present experiment, the Reynolds number, based on the bluff body's height, was $Re_b = 5{,}100$. A triangular bluff body with the height $b = 43$ mm was bound by its ends to the wind tunnel walls. The length of the bluff body was 48 mm and the span was 300 mm. The triangular shape was chosen because of the well-defined point of flow separation.

The vortex street was illuminated by a light sheet from below. A slit with characteristic dimension of 1 mm was placed between two halogen lamps and the vortex street. Paraffin oil smoke was used as a passive tracer. Paraffin oil was dripped on the heater inside the generator. To ensure a steady passive tracer ejection, the paraffin was dosed using a dripping tube. The passive tracer was injected through two 1 mm openings close to the flow separation point on the bluff body.

A typical flow pattern is shown in Fig. 3. When a bluff body is placed in a uniform moving fluid, two wakes of counter rotating vortices are formed. The average size $L = 40$ mm of the vortices was estimated from a series of images (Fig. 3) and used to normalize the coordinates in the vortex street.

The images were recorded by a digital progressive scan area B/W camera at a frame rate of 50/s. The resolution of the camera was 256×256 pixels and the image depth was 256 levels. The camera was placed in the bluff body's axis. The images were stored in the computer for further analysis.

The most favorable property of the visualization method is its spatial resolution. In this experiment the spatial resolution was around 0.9 mm. Each active CCD element acts as a concentration sensor. Spatial resolution is better than in using other state-of-the-art devices; however, the visualization method also has several drawbacks.

The estimated uncertainty of concentration measurement was below $\pm 5\%$. This included the wind tunnel turbulence level, the unsteady passive tracer generation, the light sheet nonuniformity and the camera acquisition uncertainty. For the assessment of the experimental uncertainty measurements of the passive tracer concentration with the bluff body removed from the wind tunnel were performed. The uncertainty of concentration measurement was estimated from deviations of the measured concentration of the injected passive tracer from the average value in both time and space. The uncertainty of the frequency measurement was below ± 0.05 Hz, and was established by the total time of measurements.

4 The Results

4.1 Inputs and Outputs of RBNN. The performance of the RBNN was demonstrated using 2,300 images. The initial 2000 images were used as a training subset, and the subsequent 300 were used for testing. Records of concentrations in a rectangular input region of the size $0.525\,L$ by $0.375\,L$ or 21×15 pixels, were the inputs to the RBNN, as shown in Fig. 4. A sequence of six successive images was concatenated to form the input $\mathbf{x}$ of the length $21 \times 15 \times 6 = 1890$. The output vector $\mathbf{y}$ of the size of 60 components describes the concentration on a line downstream of the input region. Five vertical positions h of outputs and inputs were used. The series of concentrations are presented in Fig. 5. At $d = 0.025\,L$ the square mean difference between the measured and the modeled concentrations divided by the mean value of fluctuations was 1 to 3%; at $d = 0.5\,L$ it was 6 to 9%; and at $d = 1\,L$ it was 6 to 13%. Here d is the downstream distance from the input window. The distance d and its orientation in the vortex street are shown in Fig. 4.

From such signals the power spectra and correlation functions were calculated.

4.2 Power Spectra. In order to provide for statistical estimation of modeling performance we determined the power spectra. For this purpose the signals from two characteristic distances $d = 0.025\,L$ and $d = 1\,L$ between the input and the output were chosen. The FFT algorithm was used with Hanning window. The power spectra of the measured and the modeled concentration are presented in Fig. 6 using a log/log scale for several vertical positions $h = 0\,L$, $0.5\,L$, $1\,L$, $1.5\,L$ and $2\,L$.

4.2.1 Spectral Characteristics of Measured Concentration. In the measured power spectra, the basic peak of the vortex street takes place at the frequency of 4.98 Hz. Besides this, the second and third harmonic peaks are also well expressed. Based on Eq. (1), a turbulent flow can be expected in its inertial diffusive range with a characteristic $-5/3$ slope of the spectral distribution. The corresponding dependence is indicated by a line in Fig. 6. Due to the low acquisition frequency of the experimental setup only a very limited frequency range up to the maximum resolvable frequency, which is 25 Hz, can be observed.

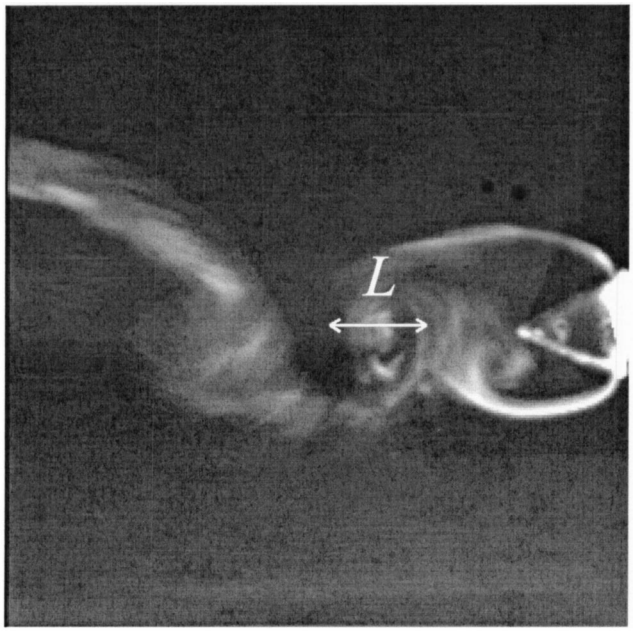

Fig. 3 Karman vortex street. Flow direction is from right to left. $L = 40$ mm is the estimated average vortices size.

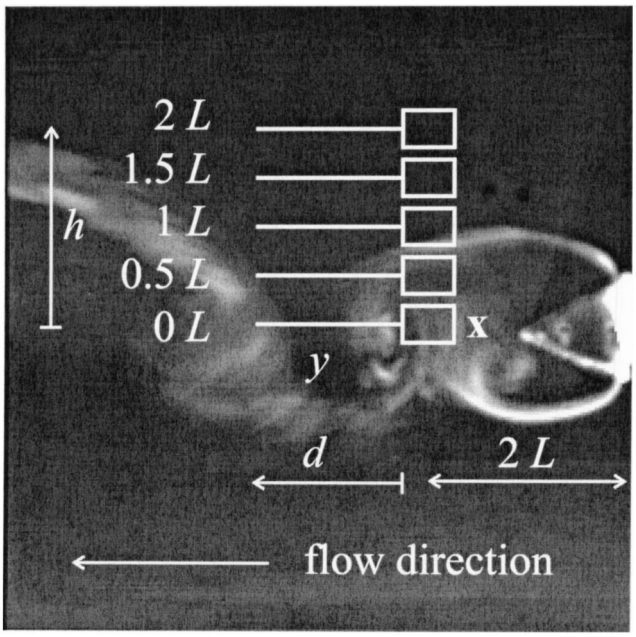

Fig. 4 Position of input and output regions. Time series of concentration $x(i)$ and $y(d)$ were used as inputs to and the required outputs from the RBNN, respectively.

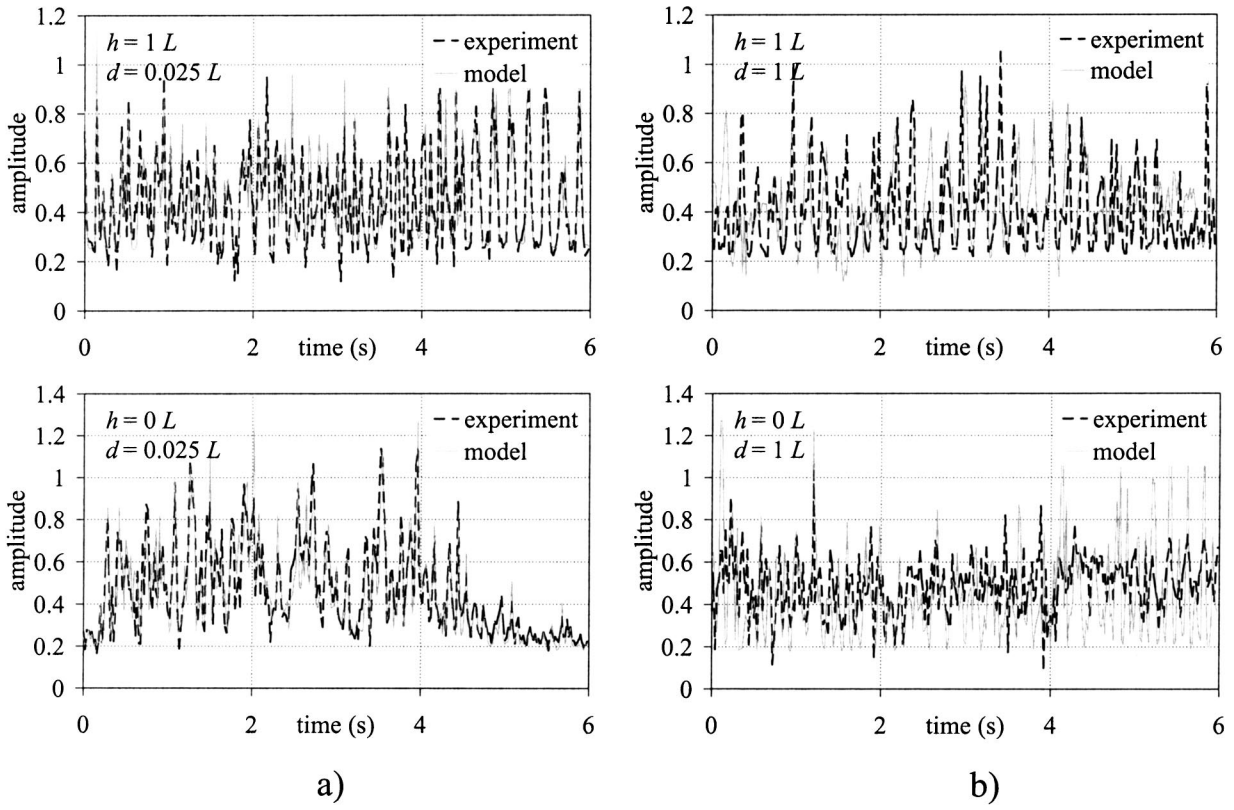

Fig. 5 Time series of measured and modeled concentrations: *a*) small distance $d=0.025\,L$ between the input and the output region, *b*) large distance $d=1\,L$ between the input and the output region. The records were acquired in two characteristic regions corresponding to $h=1\,L$ (above) and $h=0\,L$ (below).

The records in Fig. 6 indicate two different types of concentration power spectra in the vortex street. The left and right column in Fig. 6 reveal that the power spectra of measured concentration at different distances d from the input region do not differ essentially.

In the region outside the vortex street, e.g. at the vertical position $y_n=2\,L$, large coherent structures are not present, which is the effect of the shape of the wake. The signal/noise ratio is very low because of the low passive tracer concentration in the input region. Consequently, the power spectra do not exhibit agreement with the $-5/3$ law. In the regions of other vertical positions the concentration can be well resolved. There we observe a fairly good agreement of power spectra with the $-5/3$ decay law of the turbulence in the frequency region between the basic peak frequency and the maximum resolvable frequency of our experimental setup. The vertical position $y_n=0\,L$ lies in a recirculation region. Here the second harmonic peak is more pronounced. The reason lies in that in this region, vortices are shed from the lower and upper part of the bluff body that doubles the frequency of fluctuations. A similar observation was reported by Urner [32] and Anagnostopoulos [33].

4.2.2 Spectral Characteristics of Modeled Concentration. The power spectra of modeled concentration at downstream location $d=0.025\,L$ from the input region are shown in the column a) of Fig. 6. Due to the proximity between the input region and the output, agreement between the measured and the modeled power spectra is on average very good. The agreement is especially outstanding in the frequency region below the basic spectral peak. This agreement confirms that the frequency and amplitude of basic harmonic and higher harmonic peaks can be well predicted by the utilized modeling method. Besides this, the power spectra of the modeled concentration also agree well with the $-5/3$ turbulence decay law in the frequency region between the basic peak frequency and the maximum resolvable frequency of the experimental setup. However, due to the low signal/noise ratio, the power spectrum at the vertical position $h=2\,L$ is again an exception. The average uncertainty of basic frequency peaks amplitude detection at $d=0.025\,L$ is 17%, while the frequency of the peaks was determined with a typical uncertainty of 0.1 Hz.

The power spectra of the modeled concentrations at larger downstream distances $d=0.5\,L$ and $d=1\,L$ are shown in columns b) and c) of Fig. 6. Agreement between the measured and the modeled power spectra is worse than at the smaller distance $d=0.025\,L$. The details in the spectral distribution below the basic peak cannot be well predicted by our method, although the mean value of fluctuations is still correctly resolved. The frequency and amplitude of the modeled power spectral peaks agree fairly with the measured ones. The average uncertainty of basic frequency peaks amplitude detection at $d=0.5\,L$ is 26%, while the average uncertainty at $d=1\,L$ is 32%. The frequency of the peaks was determined with a typical uncertainty of 0.1 Hz.

The power spectra of the modeled concentrations also approximately follow the $-5/3$ turbulence decay law in the frequency region between the basic peak frequency and the maximum resolvable frequency of the experimental setup.

4.2.3 Spatial Correlation Functions. The performance of the modeling method can also be estimated by comparing the spatial correlation functions of the modeled and measured concentrations. The correlation function was determined as a temporal average of the output signals at two positions

$$Q(d)=\overline{y(0)y(d)}. \tag{6}$$

Here d denotes the distance between the points of concentration observation. The measured and modeled cases are denoted by indexes e and m, respectively. The corresponding correlation func-

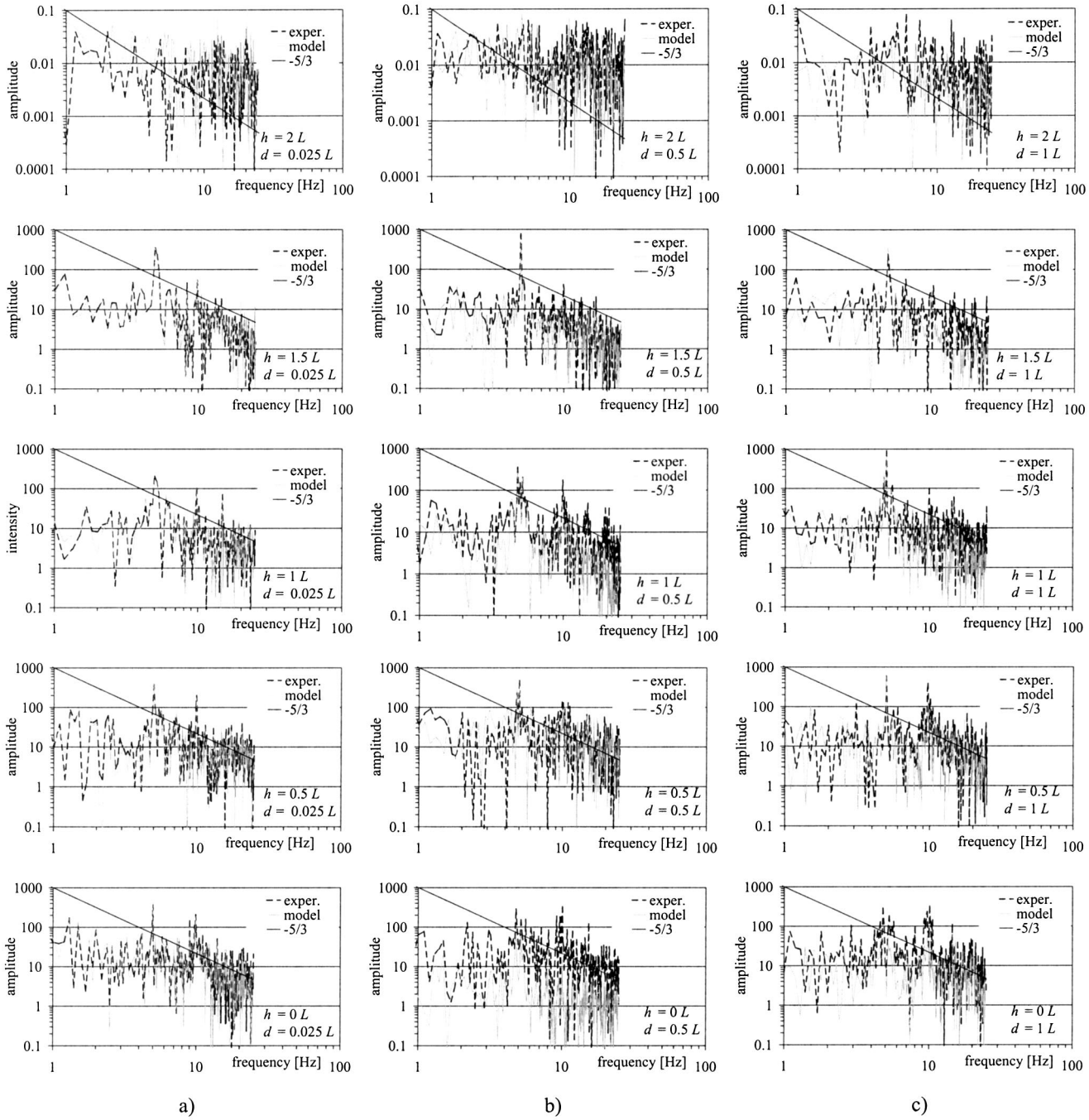

Fig. 6 Spectra of measured and modeled tracer concentrations compared to the −5/3 decay law of turbulence: *a*) the distance between the input and the output region $d=0.025\,L$, *b*) the distance between the input and the output region $d=0.5\,L$ and *c*) the distance between the input and the output region $d=1\,L$. *h* denotes the vertical position of the input/output region.

tions Q_e and Q_m are shown in Fig. 7. Beside them, two curves fitted to the initial portion of correlation functions are drawn. From these curves the Taylor microscale λ is determined at the intersection with the *x* axis.

The most outstanding feature is the similar course of both correlation functions. The correlation function of the modeled concentration Q_m is less smooth than the experimental one, Q_e. Fluctuations of Q_m are more expressed, presumably as the consequence of RBNN training on a finite number of experimental samples. Discrepancy between both correlation functions can be estimated to be of the order of standard deviation of the fluctuations introduced by statistical modeling. The next outstanding feature is that the correlation function at a higher vertical position *h* exhibits a longer correlation length. This indicates that turbulence is governed by larger vortices in an upper region than in the wake behind the bluff body. However, even here the agreement between Q_e and Q_m in the region at $h=2\,L$ is low, presumably due to the low signal/noise ratio.

From these observations we have concluded that the position of the input region influences the characteristic parameters of the correlation functions.

The Taylor scale λ_c was determined by fitting a parabola over

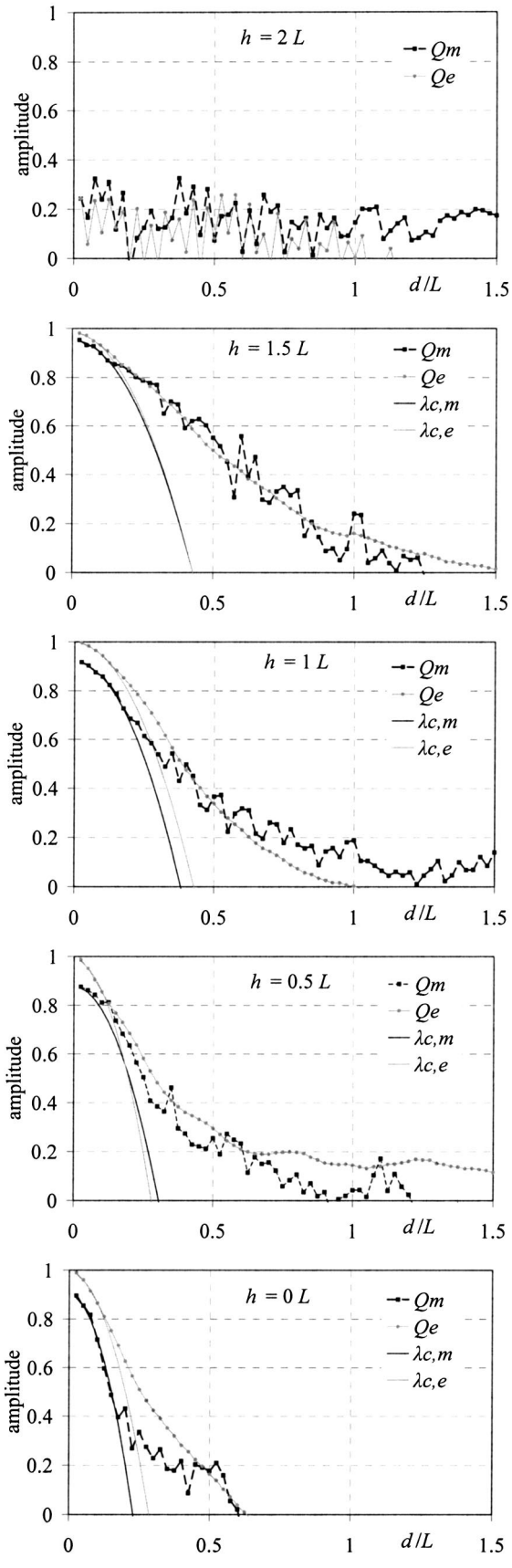

Fig. 7 Comparison of measured and modeled concentration correlation functions Q_e and Q_m, Taylor scales $\lambda_{c,m}$ and $\lambda_{c,e}$ at five off-axis distances from $h=0$ L to $h=2$ L.

several points of correlation functions around $d=0$ by minimizing the mean square error. The scale determined from both correlation functions matches fairly well.

5 Discussion

The presented results have confirmed that the visualization method is suitable for the characterization of turbulent fields. The most favorable feature of visualization is an outstanding spatial resolution. A disadvantage of this method is low acquisition rate, which—in our case—was limited to 25 Hz. According to the cascade theory, the inert turbulence region extends to several kHz (Landau and Lifshitz [34]), and therefore, a rather small region of the inert-convective portion of concentration power spectra can be observed by the visualization method. Consequently, the performance of our method has not been tested in a broad spectral region. Since the resolution of the visualization method with respect to characteristic periods in space and time is not comparable, a reasonable comparison of the time and space correlation functions could not be drawn.

By showing that both the experimental and modeled curve correspond to $-5/3$ turbulence decay law we have confirmed that the presented model can be used for modeling of turbulent phenomena.

The correlation function of passive tracer concentration decreases with the increasing distance between the input and output windows. The correlation function is at its largest 2 L above the vortex street centerline, where the flow velocity vector's changes are relatively small in comparison with the other regions. In the recirculation region, the correlation function at small distance is large, but decreases significantly as the distance increases. This is the consequence of fluctuating flow direction in the recirculation region. The height and shape of the correlation function thus depends on flow characteristics at certain position in the flow field, which indicates nonhomogeneous turbulence. Hence, a spatially invariant modeling is not possible in this case.

The RBNN was utilized for prediction of passive tracer concentrations in the turbulent state based on experimental records of the same variable. Our results reveal fairly good agreement between the characteristics of the predicted and the corresponding actually measured concentration fluctuations in a turbulent state.

In the present experiments the input region included 21×15 points. Additional tests have shown that the doubling of this size does not significantly improve prediction performance. The reason is presumably in that an increased number of input points should be accompanied by an increased number of learning samples, which has not been the case in our treatment, since this would increase the complexity of modeling. It is a well-known fact that the size of the learning set has to be adapted to the dimensionality of the learning vector. The learning set should normally be much larger than the input window dimensionality. Larger input windows will also reduce the learning rate.

By reducing the input vector's dimensionality, a shorter calculation time required for prediction could be achieved; this could also make on-line prediction of the flow properties possible. Similar conclusions are reported by Gad-el-Hak [15], Gillies [17], Delgado [10] and Keles [35].

The influence of Reynolds numbers has not been studied in this work. A large increase in Reynolds numbers would have exceeded the capabilities of the visualization method, which has a limited frequency resolution. Beside this, time-dependent turbulence modeling methods are limited to modest Reynolds numbers (Spalart, [36]).

6 Conclusions

A novel method of turbulent field modeling is presented. It is based on flow visualization and a radial-basis neural network. In the experiment a passive tracer concentration in the Karman vortex street was characterized using flow visualization. The perfor-

mance of the modeling was estimated based on the comparison of the measured and the modeled power spectra and correlation functions.

The power spectra of the modeled concentration at small distance between the input and the output region agree well with the measured power spectra. The frequency and the amplitude of spectral peaks as well as the $-5/3$ law of turbulence decay can be accurately reproduced by modeling on small scales. At increasing the scales of the characteristic vortex size L, only the position of the basic spectral peak and the $-5/3$ law of turbulence decay can be reproduced. Spatial correlation functions of the measured and the modeled concentration exhibit similar agreement as the power spectra.

Improvements of the presented method could be achieved by optimizing the number of samples used in modeling. For this purpose, the resolution of experimental set-up and the redundancy of experimental information have to be properly considered (Grabec [37]).

Nomenclature

b = characteristic dimension of bluff body, (m)
d = distance from input region, (m)
D = diffusivity due to molecular motion, ($m^2 s^{-1}$)
$f(\mathbf{x})$ = RBNN modeling function, $(-)$
$F(k)$ = scalar variance spectrum, (m^{-1})
$g(\mathbf{x})$ = Gaussian radial-basis function
h = vertical position, (m)
K = number of neurons, $(-)$
k = wavenumber, (m^{-1})
k_c = diffusion cut-off in the energy spectrum, (m^{-1})
k_d = Kolmogorov dissipation wavenumber, (m^{-1})
L = estimated vortices size, (m)
m_k = weight of k^{th} neuron, $(-)$
N = number of experimental samples, $(-)$
q_k = center of k^{th} neuron, $(-)$
Q = spatial correlation function, $(-)$
Q_e = experimental spatial correlation function, $(-)$
Q_m = modeled spatial correlation function, $(-)$
q = centers of neurons, $(-)$
Re = Reynolds number, $(-)$
Re_b = Reynolds number, based on characteristic dimension of bluff body $(-)$
r = separation, (m)
$\mathbf{x}$ = input to neural network, $(-)$
$\mathbf{x}_n$ = n^{th} input to neural network, $(-)$
y = output from neural network, $(-)$
β = Obukhov-Corrsin constant, (m^{-3})
ε = turbulent kinetic energy dissipation rate, ($m^2 s^{-3}$)
χ = variance of scalar concentration field, (s^{-1})
λ_c = Taylor length scale for concentration, (m)
$\lambda_{c,e}$ = Taylor length scale for concentration, experimental (m)
$\lambda_{c,m}$ = Taylor length scale for concentration, modeled (m)
ν = kinematic viscosity, ($m^2 s^{-1}$)
σ = width of neurons, (m)
ANN = artificial neural network
FFT = fast Fourier transformation
CCD = charge coupled device camera
RBNN = radial basis neural network

References

[1] Faller, W. E., and Schreck, S. J., 1995, "Real Time Prediction of Unsteady Aerodynamics, Application for Aircraft Control and Maneuverability Enhancement," IEEE Trans. Neural Netw., **6**(6), pp. 1461–1468.
[2] Faller, W. E., and Schreck, S. J., 1996, "Neural Networks: Applications and Opportunities in Aeronautics," Prog. Aerosp. Sci., **32**(5), pp. 433–456.
[3] Jacobson, S. A., and Reynolds, W. C., 1998, "Active Control of Streamwise Vortices and Streaks in Boundary Layers," J. Fluid Mech., **360**, pp. 179–211.
[4] Jambunathan, K., Fontama, V. N., Hartle, S. L., and Ashford-Frost, S., 1997, "Using ART2 Networks to Deduce Flow Velocities," Artif. Intell. Eng., **11**, pp. 135–141.
[5] Grant, I., and Pan, X., 1997, "The Use of Neural Techniques in PIV and PTV," Meas. Sci. Technol., **8**, pp. 1399–1405.
[6] Kimura, I., Hattori, A., Kuroe, Y., and Kaga, A., 1998, "Estimation of Flow Velocity Vector Fields Using Neural Networks," 8th International Symposium on Flow Visualization, Sorrento, pp. 151.1–151.7.
[7] Dibike, Y. B., Minns, A. W., and Abbot, M. B., 1999, "Applications of Artificial Neural Networks to the Generation of Wave Equations from Hydraulic Data," J. Hydraul. Res., **37**(1), pp. 81–97.
[8] Blackwelder R., 1995, "A Preliminary Attempt to Use Neural Networks for Turbulent Eddy Classification," Anual Research Briefs, Center for turbulence research, Stanford University.
[9] Ferre-Gine, J., Rallo, R., Arenas, A., and Giralt, F., 1997, "Extraction of Structures from Turbulent Signals," Artif. Intell. Eng., **11**(4), pp. 413–419.
[10] Delgado, A., Benning, R., and Becker, T., 1998, "On the Use of ANN in the Prediction of the Flow Fields," EUFIT 98, pp. 7–10.
[11] Zhang, L., Akiyama, M., Sugiyama, H., and Ninomiya, N., 1997, "Application of Structured Artificial Neural Networks to Computational Fluid Dynamical Problems," Japanese Journal of Fuzzy Theory and Systems, **9**, pp. 511–520.
[12] Giralt, F., Arenas, A., Ferre-Gine, J., Rallo, R., and Kopp, G. A., 2000, "The Simulation and Interpretation of Free Turbulence with a Cognitive Neural System," Phys. Fluids, **12**(7), pp. 1862–1869.
[13] Rediniotis, O. K., and Chrisanthakopoulos, G., 1998, "A Wide-Range, High-Accuracy Neural/Fuzzy Calibration Technique for Flow-Diagnostics Instrumentation," ASME J. Fluids Eng., **120, 1**, pp. 95–101.
[14] Fan, H. Y., Lu, W. Z., Xi, G., and Wang, S. J., 2003, "A New Neural-Network-Based Calibration Method for Aerodynamic Pressure Probes," ASME J. Fluids Eng., **125, 1**, pp. 113–120.
[15] Gad-el-Hak, M., 1996, "Modern Developments in Flow Control," Appl. Mech. Rev., **49**, pp. 365–379.
[16] Lee, C., Kim, J., Babcock, D., and Goodman, R., 1997, "Application of Neural Networks to Turbulence Control for Drag Reduction," Phys. Fluids, **9**(6), pp. 1740–1747.
[17] Gillies, E. A., 1998, "Low Dimensional Control of the Circular Cylinder Wake," J. Fluid Mech., **371**, pp. 157–180.
[18] McComb, W. D., 1996, The Physics of Fluid Turbulence, Clarendon Press, Oxford, UK.
[19] Batchelor, G. K., 1971, The Theory of Homogeneous Turbulence, Cambridge University Press, Cambridge, UK.
[20] Hinze, J. O., 1975, Turbulence: An introduction to its mechanism and theory, second edition, McGraw-Hill book company, New York, USA.
[21] Grabec, I., and Sachse, W., 1997, Synergetics of Measurement, Prediction and Control, Springer, Berlin, Germany.
[22] Simon, D., 2002, "Training Radial Basis Neural Networks with the Extended Kalman Filter," Neurocomputing, **48**, pp. 455–475.
[23] Kim, H. S., and Lee, J. Y., 2002, "Image Coding by Fitting RBF-Surfaces to Subimages," Pattern Recogn. Lett., **23**, pp. 1239–1251.
[24] Orr, M., 1999, "Matlab Functions for Radial Basis Function Networks," http://www.anc.ed.ac.uk/~mjo/software/rbf2.zip
[25] Gerdes, F., and Olivari, D., 1999, "Analysis of Pollutant Dispersion in an Urban Street Canyon," Eng. Educ., **81**(1), pp. 105–124.
[26] Simoens, S., and Ayrault, M., 1994, "Concentration Flux Measurements of a Scalar Quantity in Turbulent Flows," Exp. Fluids, **16**, pp. 273–28.
[27] Aider, J. L., Westfried, and J. E., 1995, "Visualization and PDF of the Fluctuations of a Passive Scalar in a Turbulent Görtler Flow," FED, Experimental and numerical flow visualization, ASME 218, pp. 123–130.
[28] Grisch, F., and Bresson, A., 2001, "Radical Imaging and Temperature Mapping in Turbulent Gaseous Flowfields," C. R. Acad. Sci., Ser IV: Phys., Astrophys., **2**(7), pp. 1037–1047.
[29] Chatzipanagiotidis, A., and Olivari, D., 1996, "Pollutant Dispersal Downstream of a Hill in Different Wind Conditions," J. Wind. Eng. Ind. Aerodyn., **64**(2-3), pp. 233–248.
[30] Law, A. W. K., and Wang, H., 2000, "Measurement of Mixing Processes with Combined Digital Particle Image Velocimetry and Planar Laser Induced Fluorescence," Exp. Therm. Fluid Sci., **22**, pp. 213–229.
[31] Balu, M., Balachandar, R., and Wood, H., 2001, "Concentration Estimation in Two-Dimensional Bluff Body Wakes Using Image Processing and Neural Networks," J. Fluids Struct., **8**(2-3), pp. 121–140.
[32] Urner, P., 1980, Beitrag zum Einfluß der Strömung auf das Meßsignal bei der Wirbelfrequenz-Durchflußmessung, Ph.D. Thesis, TU Dresden, Fakultät für Maschinenwesen.
[33] Anagnostopoulos, P., 1997, "Computer Aided Flow Visualization and Vorticity Balance in the Laminar Wake of a Circular Cylinder," J. Fluids Struct., **11**, pp. 33–72.
[34] Landau, L. D., and Lifshitz, E. M., 1987, Fluid Mechanics, Pergamon, Oxford, UK.
[35] Keles, R. S., 2000, "Active Control of Transition to Turbulence in the Wake of a Cylinder," J. Aircr., **3**, pp. 1–15.
[36] Spalart, P. R., 2000, "Strategies for Turbulence Modelling and Simulations," Int. J. Heat Fluid Flow, **21**, pp. 252–263.
[37] Grabec, I., 2001, "Experimental Modeling of Physical Laws," Eur. Phys. J. B, **22**, pp. 129–135.

Phase-Average Mean Flow and Turbulence Structure in a Staggered Cylinder Array Subjected to Pulsating Cross-Flow

E. Konstantinidis
S. Balabani
M. Yianneskis[1]

Experimental and Computational Laboratory for the Analysis of Turbulence, Department of Mechanical Engineering, King's College, London, Strand, WC2R 2LS, London, U.K.

The unsteady turbulent flow field in a staggered array of cylinders with streamwise and transverse spacing to diameter ratios of 2.1 and 3.6, respectively, was studied experimentally by means of laser-Doppler anemometry for a Reynolds number of 2300. Flow pulsations in the streamwise direction were employed to control the frequency of vortex shedding in the array as has been previously demonstrated in Konstantinidis et al. [1]. Under these conditions, it was possible to obtain velocity measurements and for each velocity sample assign the phase-angle with respect to the pulsation cycle. This methodology allowed reconstruction of the unsteady (periodic) mean flow and random turbulence fields over an average vortex shedding cycle. The experimental data obtained are analyzed and the results offer a unique insight into the flow processes that take place inside the cylinder array. [DOI: 10.1115/1.1760538]

1 Introduction

When a fluid flows past an array of cylinders, eddying motions are observed in the cylinder wakes [2]. This phenomenon has great practical implications in the design of tube-bundle heat exchangers and other similar engineering structures. The eddies periodically separate from the cylinders and the resulting unsteady flow field produces oscillatory forces acting on the cylinders that can excite structural vibrations. If large-amplitude vibrations can be sustained then failure may occur [3]. Therefore, understanding of the pertinent fluid mechanics is important in order to improve the design of such engineering structures.

A number of visualization studies have dealt with vortex shedding phenomena in cylinder arrays with geometric configurations typical of heat exchangers [4–11]. These studies have clearly shown that periodic vortex shedding occurs in the cylinder wakes at characteristic frequencies resulting in a constant Strouhal number phenomenon, often referred to as Strouhal periodicity in the literature. The detailed vortex shedding patterns are complicated by the flow interference of the unsteady cylinder wakes and the corresponding Strouhal numbers depend on the array configuration, spacing between cylinders, location in the array (i.e. there might be multiple Strouhal numbers) and even on the Reynolds number.

Periodic vortex shedding in the wakes induces oscillatory fluid forces acting on the surface of the cylinders. When the wake oscillation (Strouhal) frequency is close to a structural natural frequency, the hydrodynamic force can be large enough so as to excite the cylinders to self-sustained vibrations [12]. In gas flows, the aerodynamic force is generally small in order to cause any vibration but 'acoustic resonance' may occur between the wake frequency and transverse acoustic standing waves in the container of the array [13]. Then the wake oscillations correlate with the acoustic particle velocities and intense noise may be produced. In either case, resonance occurs and there is a corresponding lock-on effect where the vortex shedding frequency is captured by the vibration or acoustic frequency over a range of flow velocities.

The vortices shed in the wakes of cylinders in the front rows dissipate into small-scale three-dimensional turbulence, which acts as a random source of excitation for the downstream cylinders (turbulence buffeting). Even though buffeting forces can result in small amplitude vibrations, they pose a concern over the life span of heat exchangers [13].

In an effort to better describe the flow past cylinder arrays, laser-Doppler anemometry (LDA) has been employed for measurements of the velocity field by some investigators [14–17]. The LDA technique is particularly suited for such measurements owing to the prevailing flow conditions, which exhibit regions of pronounced reversed flow and high turbulence levels. Nonetheless, the measurements are usually limited to time-averaged velocity statistics, i.e., the mean velocity and turbulence intensity (or Reynolds stresses) and many of the intrinsically unsteady flow features remain concealed. Balabani and Yianneskis [18] carried out time-resolved LDA measurements and showed that the true turbulence levels were considerably overestimated by the ensemble-averaged root-mean-square (rms) velocity due to the periodic fluctuations associated with mean flow instabilities, i.e., vortex shedding.

The continuous advances in computer power and numerical techniques allowed sophisticated simulations of the unsteady velocity and temperature fields to be obtained in recent years. Significant progress in this direction has been achieved by novel problem formulation, e.g., simulations of unsteady laminar flow [19] and the advent of Large Eddy Simulation (LES), e.g., simulations of unsteady turbulent flow [20–22]. However, owing to the complexity of the geometry and flow, these simulations often have limitations and further refinement and verification is often necessary. Furthermore, comparison with experimental data is limited and usually based on the time-averaged velocity statistics and the unsteady flow features are not taken into account owing to the lack of experimental data. Improvements in turbulent flow modeling for complex geometries where periodic vortex shedding occurs, require phase-resolved turbulence quantities, as for example in single cylinder wakes [23]. To the knowledge of the authors, no such data have been published for cylinder arrays.

[1]Corresponding author. E-mail: michael.yianneskis@kcl.ac.uk

Contributed by the Fluids Engineering Division for publication in the JOURNAL OF FLUIDS ENGINEERING. Manuscript received by the Fluids Engineering Division April 25, 2003; revised manuscript received November 20, 2003. Associate Editor: M. V. Ötügen.

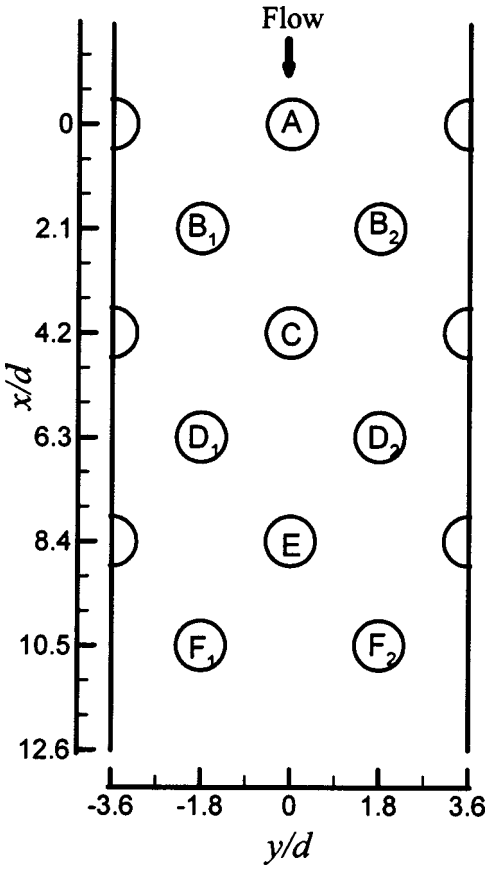

Fig. 1 The configuration of the cylinder array studied

We have previously investigated the response of a staggered array of cylinders to streamwise flow pulsations of the approaching flow [1]. A lock-on region was found for a range of pulsation frequencies in which vortex shedding from all the cylinders was forced at half the imposed frequency. These resonance conditions offered a convenient case to study the process of turbulent vortex shedding inside cylinder arrays and provide a unique insight of the phenomena. By taking velocity measurements at constant phase with reference to the pulsation cycle, it is possible to separate the periodic fluctuations associated with vortex shedding from the random fluctuations due to turbulence in the flow. In this paper, we present the results from such a fundamental experimental study.

2 Experimental Details

2.1 Flow Configuration. The experiments were conducted in the same water tunnel facility used by Konstantinidis et al. [1]. It comprised a closed-loop pipework installation equipped with appropriate arrangements of hexagonal honeycomb and screens to condition the flow entering a 72×72 mm square test section. The latter was made of transparent plastic (Plexiglas) to allow optical access for LDA measurements and flow visualization. Flow pulsations of controllable frequency and amplitude were introduced upstream of the array via the action of a rotating valve.

The cylinder array used in the experiments is shown in Fig. 1. It consisted of a staggered array of cylinders with six rows and either three (one full and two half) or two (full) cylinders per row. The longitudinal distance between rows was 21 mm and the transverse distance between cylinders in each row was 36 mm. The cylinders had a circular cross-section, 10 mm in diameter, d, and spanned the entire width of the test section. The cylinders were rigidly mounted by pressing them tightly in precision-bore holes on the end walls in order to eliminate the possibility of vibrations which would interfere with the flow under investigation. Half cylinders were mounted on the test section walls to simulate an infinite array and minimize wall effects. The present array configuration allowed sufficient space for LDA measurements of the interstitial flow between the cylinders but has the disadvantage that only few cylinders could be fitted across the test section width. The number of cylinders per row and the proximity of the test section walls have an effect on the vortex patterns, especially in unforced flow, as has been addressed in previous work [1]. However, for the conditions of the present experiment, i.e. under vortex shedding lock-on, generality of the results can be justified because the vortex patterns are forced by the flow pulsation, i.e., vortex shedding from all cylinders is synchronized and in-phase as explained in detail in [1] and demonstrated later in the paper.

Table 1 Principal characteristics of the LDA system

Helium-Neon laser	
Wavelength, λ	632.8 nm
Power	10 mW
Beam diameter, b_0	0.83 mm
Diffraction grating	
Number of lines, n_l	4000
Rotational speed, N_G	200 Hz
Frequency shift, f_S	1.6 MHz
Measurement volume	
Length, b_z	466 μm
Diameter, b_x	48.8 μm
Waist, b_y	48.5 μm
Angle of beam intersection in air, θ	5.98 deg
Number of stationary fringes	16
Fringe spacing, λ^*	3.04 μm

2.2 Measurement Technique. A single-component dual-beam laser-Doppler anemometer was employed for the present measurements. The principal characteristics of the anemometer are shown in Table 1. The anemometer operates with a 10 mW Helium-Neon (632.8 nm) and a rotating diffraction grating disk for splitting and shifting the frequency of the resulting beam pair. At the intersection of the beams, a measuring control volume of 49 μm in diameter and 466 μm, based on the e^{-2} light intensity cut-off point, was produced. The light scattered from particles crossing the measurement volume was collected in the forward direction by the receiving optics and directed onto a photo-multiplier tube. The signal from the photo-multiplier was band-pass filtered before being processed with a TSI frequency counter, model 1990B, which was interfaced to a personal computer with appropriate hardware and software for data acquisition. The band-pass filter settings were selected at 1–5 MHz in order to remove high-frequency noise and low-frequency pedestal of the signal, with all Doppler frequencies being well inside this range for the frequency shift employed. The counter processor was operated in the ''single measurement per burst'' mode and 16 cycles per burst. The Doppler signal was monitored on an oscilloscope to check the signal-to-noise ratio and to ensure that background noise did not exceed or even approach the counter processor threshold level of 50 mV. Monitoring the bursts on the oscilloscope also indicated that there was typically one particle in the measurement volume per Doppler burst. The impurities of London tap water circulating in the flow loop scattered the laser light and produced good quality Doppler bursts and therefore no seeding particles were added to the flow. The number of Doppler bursts per unit time, i.e., the data rate, depends on the measurement location within the cylinder array and is generally proportional to the local velocity magnitude. Typical data rates for the present experiments ranged between 300–1000 samples/s.

To permit detailed flow investigations, the transmitting and receiving optics were mounted on a metallic frame which in turn was mounted on manually-driven three-dimensional traversing unit. This enabled positioning the measuring control volume at any point in the test section and simplified the alignment procedure of the optics that was carried out once before each set of measurements as the optics moved in unison. The accuracy of the traversing unit was 0.05 mm in the two directions perpendicular to the flow whereas a linear encoder was used to measure the position in the flow direction with an accuracy of 0.01 mm. The error associated with the zero location of the measuring control volume at some reference points, i.e., at the test section walls, is of the order of half the size of the measurement volume in the corresponding direction. Careful alignment and measurement procedure significantly minimized positioning errors, as confirmed by repeatability tests.

The flow was visualized using a light sheet from an Argon-Ion laser positioned at right angles to the axes of the cylinders and midway along the span, and by seeding the flow with 15 μm hollow glass particles. The interstitial flow could be illuminated only with light passing between the cylinders and thus lighting was not homogeneous, producing light and dark patches. Video recordings of the flow were obtained using a CCD camera equipped with a zoom lens. Individual frames of the video were obtained by digitizing the video frames with a grabber on a personal computer.

2.3 Data Processing. The data acquisition and analysis procedure used in the present study in order to resolve the unsteady mean flow and turbulence fields is briefly described below. A detailed description of the procedure can be found in [24]. The velocity data at any measurement location in the flow contain fluctuations due to *i*) unsteadiness of mean flow associated with periodic vortex shedding, *ii*) random turbulence in the flow and *iii*) external flow pulsations. Under resonance conditions, i.e., when the vortex shedding frequency locks on to half the pulsation frequency, the velocity fluctuations can be divided to *a*) periodic due to vortex shedding and flow pulsations and *b*) random due to turbulence. In this case, the periodic fluctuations can be resolved by averaging the velocity data at constant phase of vortex shedding over two consecutive pulsation cycles or one vortex shedding cycle. An optical encoder attached to the valve shaft was used to determine the angular position of the pulsation-generating rotating valve, in order to assign the vortex shedding (or pulsation) phase. This provided the relative pulsation (or vortex shedding) phase-angle with respect to an arbitrary reference zero-phase. Resetting the phase every two consecutive pulsation cycles was readily accomplished by using the index pulse of the encoder once per revolution, since each revolution corresponds to two pulsation cycles as the periodic blockage of the valve repeated itself twice in each revolution.

Given the phase-angle of each velocity sample, a mean velocity at constant phase $\langle u \rangle$ that describes the periodic flow patterns can be estimated from:

$$\langle u \rangle_i = \frac{1}{N_i} \sum_{j=1}^{N_i} u_{ij} \tag{1}$$

where i denotes a particular phase-angle interval and N_i is the number of velocity samples u_i that fall within this interval. The random turbulent fluctuations superimposed on the unsteady mean flow can be characterized by the root mean square (rms) velocity at constant phase,

$$u_i' = \left[\frac{1}{N_i} \sum_{j=1}^{N_i} (u_{ij} - \langle u \rangle_i) \right]^{1/2} \tag{2}$$

In the following the index i is dropped for brevity.

The total number of samples in each phase-angle interval and the window size affect the measured quantities, particularly the turbulent part. In the present study, a minimum number of five hundred samples in each phase-angle interval was required to ensure accurate estimates. In order to determine the turbulent fluctuations accurately, the window size has to be made as small as possible, especially if the unsteady mean flow exhibits large temporal gradients [25]. On the other hand, the use of a very small window size requires extremely large number of data to be acquired. A method proposed by Sonnenberger et al. [26] that improves the accuracy of the estimates and produces smooth data was adopted in the present analysis. In this method, a Fourier series is fitted to the estimates of all 1 deg phase-angle intervals up to a cut off-frequency as shown in Fig. 2. The cut-off frequency is selected large enough to consider all frequencies of physical relevance whereas higher frequencies resulting from statistical uncertainty are filtered out. Thus, a cut-off frequency of ten times the pulsation frequency was employed in the present study.

Implementation of the data analysis procedure was not straightforward in practice because the phase of vortex shedding could change by ± 180 deg during the course of the experimental measurements. In order to remove this phase ambiguity the data analysis was carried out on-line; by monitoring the results on the computer display it could be readily verified that the data obtained corresponded to the same phase. More details about the procedure can be found in [24].

LDA inherently yields individual velocity data randomly distributed in time as particles suspended in the fluid pass through the measurement volume. The probability of high velocity particles crossing the measurement volume is greater than that of low velocity particles. This results in the so-called 'velocity bias' and normally some correction may be required to account for that effect especially in unsteady flows. An investigation of bias effects showed that these were insignificant and therefore no correction was applied to the time-averaged data [24].

2.4 Statistical Uncertainty. A statement for the statistical uncertainty of the reported mean and rms velocity values (phase average) needs to be made. This uncertainty arises entirely from the finite sample length and is independent of the measurement error of the LDA system. Uncertainty estimates for 95% confidence levels can be calculated using the following equations:

$$e_{mean} = \pm 1.96 \sqrt{\frac{\sigma^2}{N}} \tag{3}$$

for the mean velocity, and

$$e_{rms} = \pm 1.96 \sqrt{\frac{\sigma^2}{2N}} \tag{4}$$

for the rms velocity. N is the number of samples and σ is the standard deviation $(=u',v')$ for each phase-angle interval. These equations were derived from Benedict and Gould [27] on the assumption of normal distribution. Obviously, the statistical uncertainty depends on phase-angle and measurement location. Therefore, both the average and the maximum statistical uncertainties calculated are shown in Table 2. It should be noted that the uncertainty of mean and rms velocities after Fourier filtering is expected to be lower than the values reported in Table 2 [26].

3 Results and Discussion

The measurements were obtained for a bulk flow velocity $U_b = 0.17\ \mathrm{m\,s^{-1}}$ which corresponds to a Reynolds number $\mathrm{Re} = 2300$ based on cylinder diameter and gap velocity, which from continuity is equal to $1.385U_b$. The upstream flow was pulsed at a frequency of 10.0 Hz with an average peak-to-peak amplitude $0.056\ \mathrm{m\,s^{-1}}$ (Fig. 3). Under these conditions, vortex shedding resonance prevails in the entire array and the shedding frequency occurs at exactly half the pulsation frequency [1]. The measurements were obtained at mid-span of the cylinders within a unit cell between the third and fourth rows so as to include the influ-

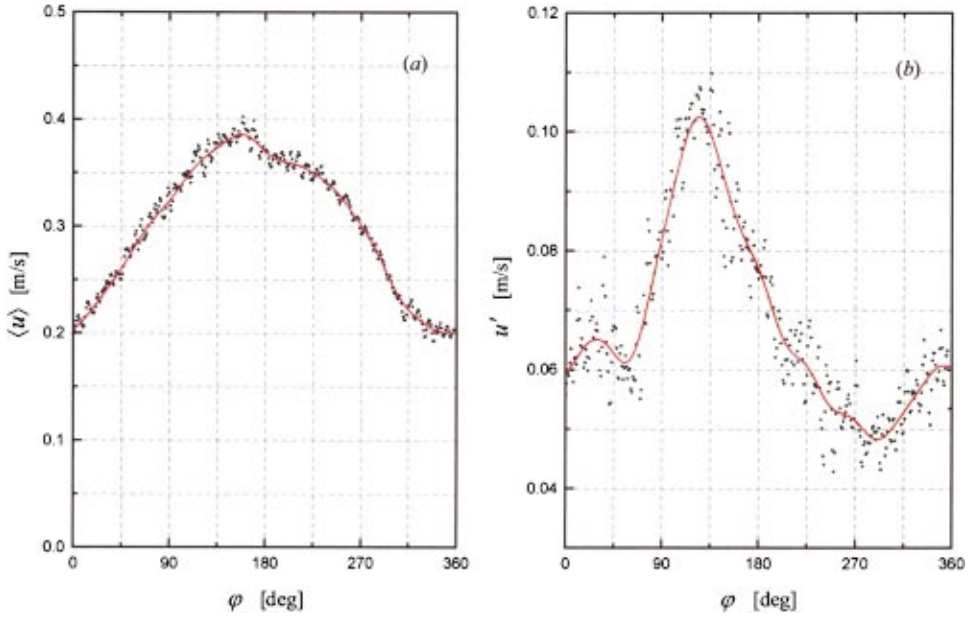

Fig. 2 Phase-average mean (*a*) and rms (*b*) velocities for a measurement location. The data before filtering (dots) exhibit statistical fluctuations which are removed with a low-pass filter. The filtered result yields improved estimation of the measured quantities and smooth curves. Cut-off frequency=100 Hz.

ence of vortices shed from upstream rows. It should be noted that the flow in this region is affected by entrance phenomena and it is not representative of a fully-developed flow inside the array.

3.1 Unsteady Mean Velocity Vectors. A sequence of the mean velocity vectors at eight phase-angles over half a shedding cycle, i.e., one pulsation cycle, that illustrates the unsteady (periodic) flow patterns in the wake of the third row of the array, is shown in Fig. 4. In order to produce a coherent picture of the distributions over a domain extending to both the positive and negative *y*-directions from measurements that were obtained only in the positive *y*-direction (see Fig. 1 for coordinate system), data for different phase-angles 180 deg apart were combined. On the positive *y*-direction data are presented for phase-angles 0–180 deg whereas on the negative *y*-direction data for phase-angles $\phi = 180-360$ deg are presented after reflection in the line of symmetry (*y*-axis) and reversing the sign of the v-component. This transformation assumes that the periodic flow pattern is antisymmetric with respect to the wake centerline, an assumption readily verified from the visualization study. A counter-clockwise vortex is shown behind cylinder C at $\phi = 0$ deg. The presence of another vortex with opposite sense of rotation on the right hand side and very close to the base of cylinder C can be inferred by extrapolation of the vector field all the way back to the cylinder. The shear layer separating from the right side is drawn across the wake and restricts the supply of vorticity to the counter-clockwise vortex from the favorable shear layer on the left side. The counter-clockwise vortex is thus shed and convected downstream during the next three phases shown ($\phi = 0-72$ deg). While convected, the vortex is deformed and its presence becomes obscure in the vector field. At $\phi = 96$ deg, the clockwise vortex emerges in the measurement region with its center lying on the wake centerline. During the next three phases shown ($\phi = 96-168$ deg) this vortex grows in size and becomes elongated in the presence of the favorable shear layer on the right side of cylinder C. This concludes half a vortex shedding cycle and the vector field is almost the mirror image of that at $\phi = 0$ deg. The same process is then repeated but mirrored during the next half of a shedding cycle ($\phi = 180-360$ deg), not shown for brevity. Some features of the periodic flow field related to vortices shed from upstream cylinders are not evident in the vector plots of the unsteady mean flow field but become clear in the section where the mean vorticity field is presented.

3.2 Sectional Streamlines of Unsteady Mean Flow. Figure 5 shows the sectional streamlines of the unsteady mean flow at eight phase-angles over half a vortex shedding cycle. The streamlines were calculated by integration in a series of small steps in the direction of the local mean velocity vector (Fig. 4) from various starting points in the flow field. The streamlines show the existence of a focus and a saddle which are clearly associated with

Table 2 Statistical uncertainty ($\pm$m s^{-1}).

	$\langle u \rangle$	u'	$\langle v \rangle$	v'
Average	0.006	0.004	0.006	0.004
Max	0.012	0.009	0.015	0.010

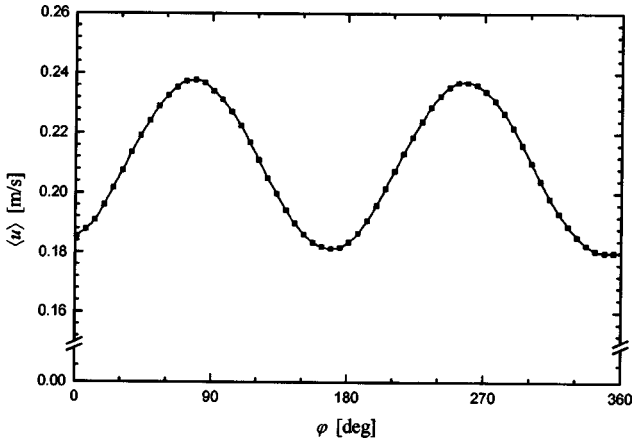

Fig. 3 The pulsation waveform upstream of the cylinder array. Two pulsation cycles correspond to 360 deg (one vortex shedding cycle)

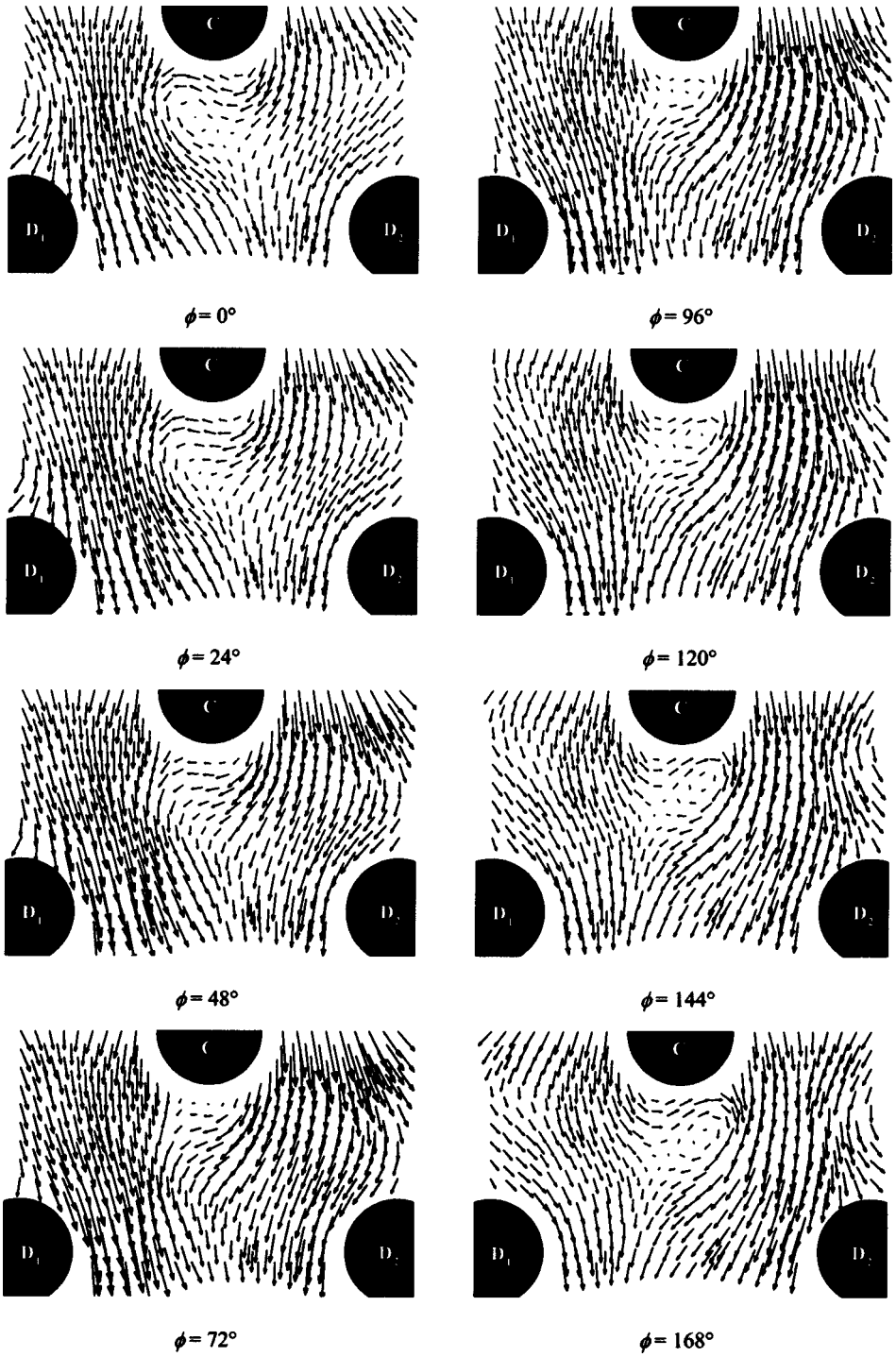

Fig. 4 Mean velocity vectors

the stages of vortex evolution in the wake of cylinder C. A focus exists near the vortex center indicating an inward spiraling motion. Fluid around the spiral is directed towards its focus, compatible with the entrainment of fluid from the main flow path into the vortex. The inward spiral might be an indicator of spanwise three-dimensionality; the vortex undergoes stretching along its axis in the spanwise direction [28]. It should be noted, however, that the size of the focus depends primarily on the direction of a small number of vectors in a region where measurement of the vector direction might be less reliable due to low velocities and high turbulence levels; as a result, the sectional streamline patterns should be interpreted with caution, particularly in relation to the existence of a spanwise component. Given the fact that vortex shedding lock-on improves the spanwise coherence of the flow, one would expect any three dimensional effects to be averaged out over many cycles. Thus, the existence of a focus may be disputed unless three-dimensional instabilities are phase-locked with the mean flow pulsations and repeat from cycle to cycle, a hypothesis that requires further investigation to be substantiated. Another interesting feature of the streamline patterns is the formation of a cross-over (saddle) point in the wake. Cantwell and Coles [23] suggested that there is a relationship between the initial appearance of the saddle point and the location where the vortex is fully grown. The initial appearance of a saddle point cannot be deter-

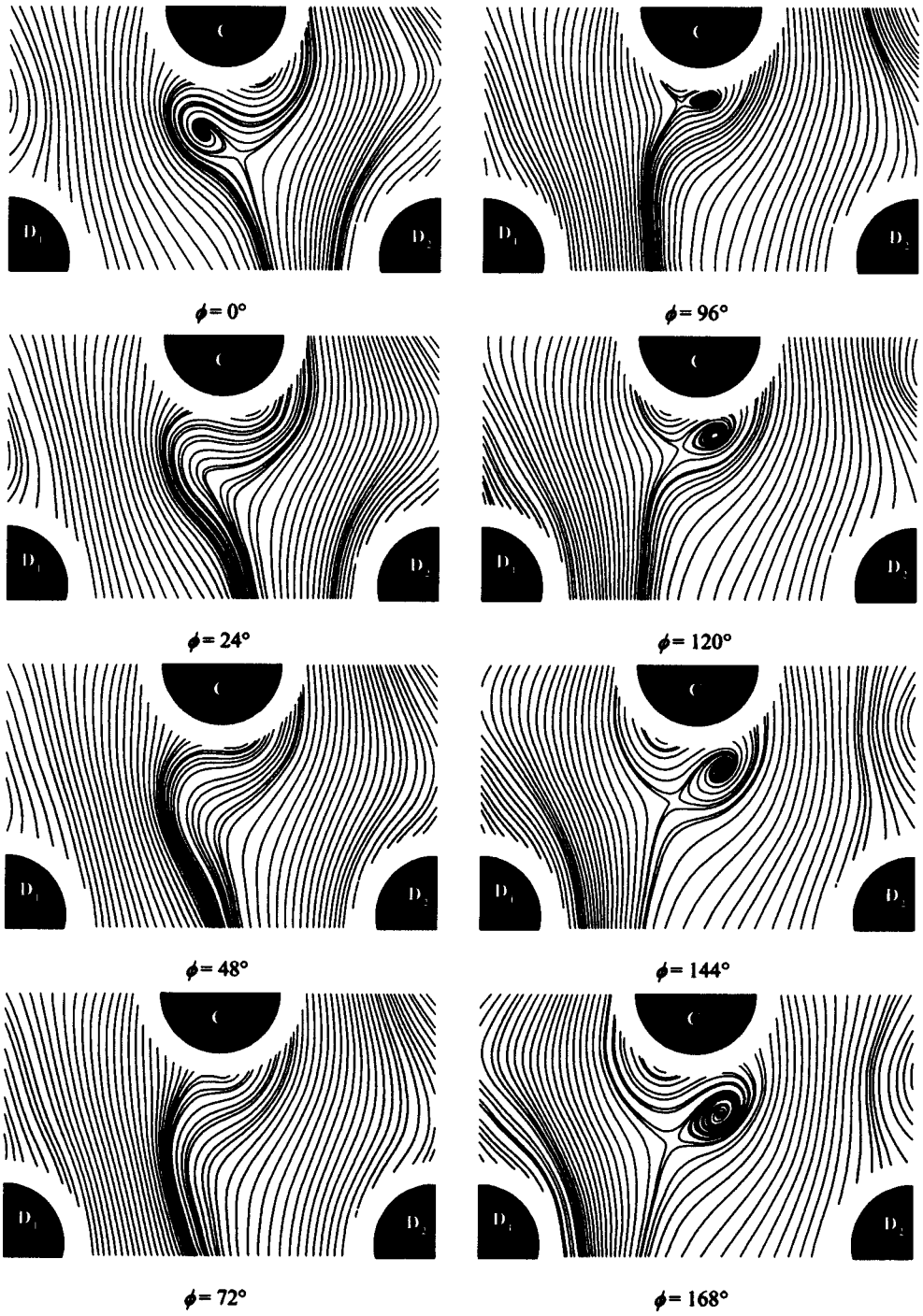

Fig. 5 Sectional streamlines of the unsteady mean flow

mined exactly from the present data due to the limited measurements close to the cylinder but a saddle point is seen as close as $0.8d$ below the center of cylinder C, i.e., remarkably close, which implies a very short vortex formation region. This is about the same as in the wake of a single cylinder at a much higher Re (140,000) seen in [23]. The shedding of vortices of opposite angular momentum alternately on the rear side of the cylinder C results in a sinuous motion of the streamlines in its wake.

3.3 Vorticity Field. The processes of vortex formation and shedding can be shown more clearly in the mean vorticity field at constant phase, defined by

$$\langle \zeta \rangle = \frac{\partial \langle v \rangle}{\partial x} - \frac{\partial \langle u \rangle}{\partial y} \tag{5}$$

Figure 6 shows the corresponding normalized iso-vorticity contours $\langle \zeta \rangle d/U_b$ at eight different phase-angles. The gradients were calculated using a first-order central finite-difference scheme of the interpolated mean velocity values. Since the interpolation results near the cylinders, where fewer measurements were obtained, may be spurious, the vorticity values in these regions can be erroneous and, therefore, should be treated cautiously. Contour

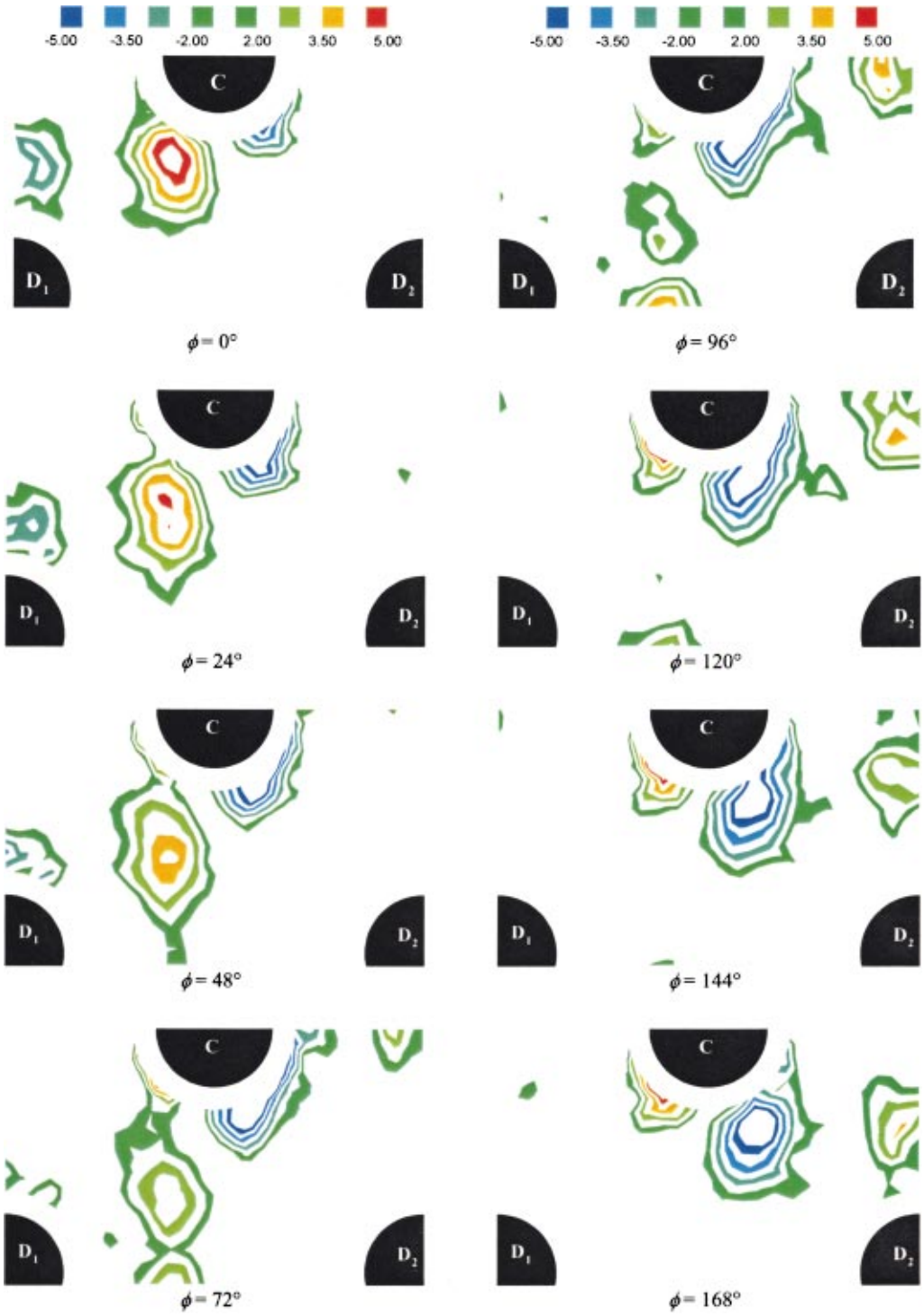

Fig. 6 Mean vorticity contours

levels between normalized values of -1 and 1 were removed in order to produce a clearer picture of the vorticity field.

The formation and shedding of vorticity of opposite signs alternately from the two sides of cylinder C is clearly depicted in Fig. 6. Positive vorticity values represent a counter-clockwise vortex and vice-versa. Furthermore, vorticity shed from upstream cylinders, i.e., from the first and second rows, appears in the measurement region. For example, a clockwise vortex is shown above cylinder D_1 at $\phi=0$ deg. This vortex was shed from cylinder B_1 a quarter of a shedding period earlier. During the next three phases shown, the vortex impacts on cylinder D_1 and is destroyed. Similarly, a counter-clockwise vortex shed at $\phi=0$ deg from cylinder B_2 appears in the measurement region a quarter of a shedding period later ($\phi=96$ deg), heading towards cylinder D_2. Gaydon and Rockwell [29] studied the interaction of incident vortices upon an oscillating cylinder and found a drastic decrease in the formation length and a five-fold increase in the lift coefficient compared to the absence of incident vortices. Here too, an extremely short formation length is observed and thus it may be reasonable to expect increased loading for cylinders subjected to incident vortices.

A small amount of the vorticity shed from the first row (cylin-

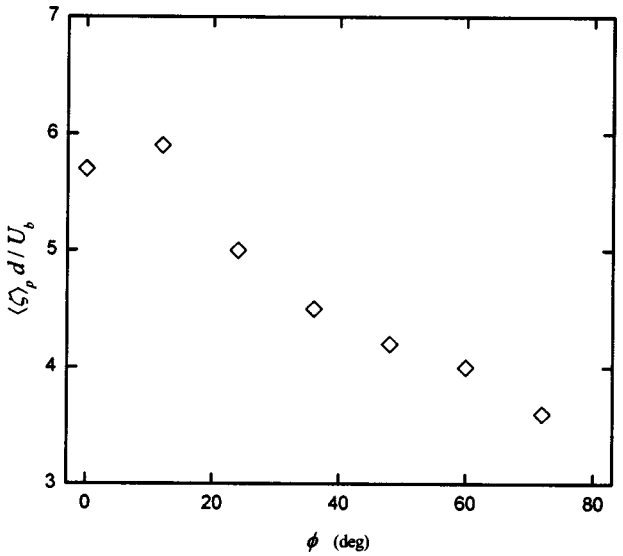

Fig. 7 Peak vorticity as a function of phase-angle

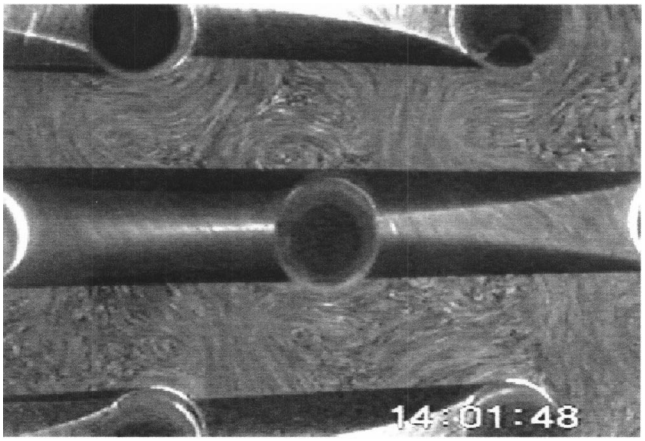

Fig. 8 The global flow pattern around the third row in the cylinder array. Flow direction is from top to bottom.

der A) survives the impact with cylinder C and appears as a small patch of positive vorticity attached to the side of the growing clockwise vortex at $\phi = 96$ deg. Part of this vorticity merges with the growing clockwise vortex in the wake and part of it is destroyed in the high shear region between the growing vortex and the flow lane. This observation might explain how the periodic fluctuations that occur at a high frequency in the first row for unforced flow, could be detected even behind the third row where vortex-shedding occurs at a frequency lower than that in the first row [1].

The peak vorticity near the center of the vortices is a useful parameter to understand the motion of the vortices and provides a relative measure of their strength. Figure 7 shows the variation of the normalized peak vorticity as a function of phase-angle in the wake of cylinder C. The peak vorticity reaches a maximum value at the location where the vortex is fully-grown and shed ($\phi = 12$ deg). Subsequently, the peak vorticity decays as the vortex is convected downstream. Although the absolute values of peak vorticity may be susceptible to inaccuracies involved in the estimation of spatial derivatives from interpolated mean velocity values, it is instructive to compare the present results with those of Cantwell and Coles [23] obtained in the wake of a single cylinder for Re $= 140{,}000$. Table 3 shows the location of peak vorticity (x_p, y_p) with respect to the center of the cylinder and the corresponding value $\langle\zeta\rangle_p$ from two phases of [23] (phase 4 and 8, their Table 3) in comparison to our data (phase 0 and 72 deg). The peak vorticity in the present case is considerably higher than that in the wake of a single cylinder. This might be partly attributed to the fact that there is less space for the vortices to develop in the array, which in turn leads to higher vorticity in the center of the vortex so that the circulation around the vortices is comparable in the two cases. It is also known that both vortex strength and maximum peak vorticity increase at lock-on [30]. This is another factor contributing to the high values of peak vorticity observed in the present case. A comparison of the decay of peak vorticity for the single cylinder and the cylinder array shows that the decay is much faster in the array; the peak vorticity decreases by nearly 40% at a location $0.6d$ downstream of the location of its maximum value in the array compared to a decrease of 25% at the corresponding locations behind the single cylinder. This might be partly expected due to the deformation of the vortices in the array under the action of substantial shear as the vortices are squeezed in the narrow gap between the cylinders of the subsequent row. The fast decay of vorticity together with the spiraling motion of the fluid in the vortex center indicates a strong three-dimensionality of the flow and might suggest a three-dimensional mechanism for the dissipation of vorticity. This might explain why two-dimensional simulations in the context of LES cannot capture essential features of the flow, which are essentially 3-D [31].

It can be seen in Table 3 that although the longitudinal distance of the location of the peak vorticity is approximately the same for the single cylinder and the cylinder array (non-withstanding the difference in Reynolds number), the transverse distance from the wake centerline is nearly twice in the latter case. This substantial difference initially led a re-evaluation of the present results. However, the published literature suggests that lock-on is accompanied by a strong modification of the wake structure; by changing the frequency and amplitude of the pulsations one can conceivably control the formation length of the vortices as well as the arrangement of the wake vortex street [29,32].

3.4 Flow Visualization. A visualization study was undertaken in order to supplement the LDA measurements. The global flow pattern in the cylinder array is illustrated in Fig. 8. It is seen that vortex shedding from all cylinders is synchronized and in-phase. The general features of the flow pattern depicted in the picture, including the formation of vortices in the wake, the sinuous motion of the wake, the impact of vortices shed from upstream on downstream cylinders and the timing of the events, agree well with those described in the previous sections. This provides confidence that the methodology employed for averaging at constant phase has yielded a reliable set of experimental data.

Figure 9 shows two close-up pictures of the instantaneous flow field around cylinder C. The pictures are characteristic of the vortex formation process and are very repeatable from cycle-to-cycle.

Table 3 Decay of peak vorticity in cylinder wakes

Single cylinder (Cantwell and Coles [23])				Cylinder array (present study)			
Phase	x_p/d	y_p/d	$\langle\zeta\rangle_p d/U_b$	Phase	x_p/D	y_p/d	$\langle\zeta\rangle_p d/U_b$
4	1.04	0.23	3.63	0 deg	0.94	0.44	5.7
8	1.71	0.17	2.68	72 deg	1.58	0.43	3.5

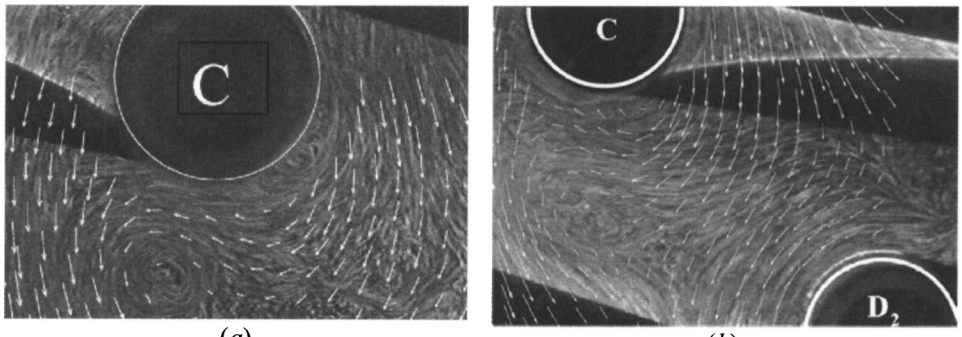

Fig. 9 The instantaneous flow structure in the measurement region with superimposed phase-average mean velocity vectors: (*a*) $\phi=0$ deg; (*b*) $\phi=12$ deg

The mean velocity vectors for the corresponding phase-angles in the cycle are overlaid on the picture. The direction of the vectors compares well with the direction of the particle streak-lines in most locations. The measurements appear to underestimate the transverse velocity component in some locations. However, it should be emphasized that the vectors are averages over many shedding cycles in contrast to the picture that depicts the instantaneous flow field. Fig. 9(*a*) clearly depicts the formation of a clockwise vortex very close, practically on, the right rear side of cylinder C, the existence of which was previously assumed when discussing Fig. 4. Furthermore, the anti-symmetry of the flow pattern with respect to the wake centerline is readily verified from the visualization pictures in Figs. 8 and 9. Indeed, there is strong flow across the wake centerline inducing intense mixing in the wake in spite of the symmetric flow perturbation imposed by the pulsations.

3.5 Turbulence Field. The random fluctuations of the velocity superimposed on the periodic mean flow are treated as the turbulence content of the flow. Therefore, a turbulence field corresponds to each phase-angle which can be described by the distributions of the streamwise and transverse components u'/U_b and v'/U_b respectively. Instead of showing these distributions separately, it was deemed more appropriate to define a turbulent kinetic energy $q=1/2(u'^2+v'^2)/U_b^2$ for describing the turbulence field. The turbulent kinetic energy q is shown at eight phase-angles over half a vortex shedding cycle in Fig. 10. Superimposed on the colored contours of kinetic energy, are contour lines of the mean vorticity field in order to elucidate the correlation between vortex formation/shedding and turbulence in the flow.

The distributions show clearly that regions of high vorticity correspond to islands of high turbulent kinetic energy. During the initial stages of vortex formation in the wake of the third row cylinder, e.g., see the clockwise forming vortex during $\phi=96-168$ deg, both the contours of vorticity and turbulent kinetic energy increase in size and peak values increase in magnitude. The high turbulence levels must be associated with the production of turbulence due to the strain field imposed by the forming vortex in analogy to the wake of an isolated cylinder [23]. Subsequently, as the shed vortex is convected downstream it is squeezed in the flow passage between the cylinders in the fourth row and it would appear reasonable to assume that high turbulence levels are caused by the disintegration of the coherent vortices into 3-D turbulent flow. This is also evident by looking at the islands of high q that enter the measurement region from above associated with the disintegration of the vortices shed from the cylinders in the second row, e.g., see region above cylinder D_2 during $\phi=96-168$ deg. However, it is difficult to explain the existence of a small distinct peak in q just left to cylinder D_2 for $\phi=24-72$ deg. It should be noted that variations in the strength and path of the vortices from cycle to cycle (phase jitter) may contribute towards higher turbulence levels. Although this is a common problem in phase-averaging, it is expected that the effect of phase jitter is not pronounced in the present study because under lock-on conditions vortex shedding is controlled by the imposed pulsations; thus, vortex strength and path do not vary from cycle to cycle as randomly as for unforced flow.

The turbulence field observed in the wake of a cylinder array studied here exhibits strong similarities to that observed in the wake of an isolated cylinder [23]. Therefore, it might be argued that the mechanism of turbulence production is the same. However, the turbulence field in the array is far more complex because it involves both the production of turbulence associated with vortex shedding in the wake and also the dissipation of turbulence produced by the disintegration of vortices shed from upstream cylinders.

3.6 Periodic and Random Reynolds Stresses. In the analysis of the wake characteristics, it is instructive to separate the contributions from the periodic and the random fluctuations to the Reynolds stresses. The periodic Reynolds stresses arise from fluctuations of the unsteady mean flow over the time-averaged or steady mean flow. A periodic velocity component $\tilde{u}$ may thus be defined following the notation used in Cantwell and Coles [23],

$$\tilde{u}=\langle u\rangle-\overline{u} \tag{6}$$

where $\overline{u}$ is the time-averaged mean velocity and $\langle u\rangle$ is the mean velocity at constant phase. The corresponding normal Reynolds stress at constant phase is $\tilde{u}\tilde{u}/U_b^2$ (normalized). The random fluctuations over the unsteady mean flow also contribute to the total Reynolds stress and the corresponding term is $u'u'/U_b^2$ (normalized). The total Reynolds stress at constant phase is the sum of the periodic and random contributions.

Figure 11 shows the distributions of the periodic and random Reynolds stresses at a particular phase-angle ($\phi=0$ deg). The distributions at other phase-angles are not shown for economy of presentation. At the particular phase-angle shown, the streamwise periodic Reynolds stress $\tilde{u}\tilde{u}$ displays high values in the flow region between the cylinders, particularly on the right-hand side (Fig. 11*a*). At this instant, which corresponds to the minimum pulsation velocity upstream of the array (Fig. 3), the counter-clockwise vortex formed behind cylinder C has its maximum size (Fig. 6). The formed vortex on one side of the cylinder results in asymmetric distribution of the normal stress. Note that, although the external pulsations impose a symmetric perturbation with respect to the wake axis, the resulting flow field displays strongly anti-symmetric features due to the fluid motions associated with vortex shedding.

The distribution of the transverse periodic Reynolds stress $\tilde{v}\tilde{v}$ exhibits peaks above and below vortex centers associated with rotation of fluid elements (Fig. 11*b*). At the particular phase-angle

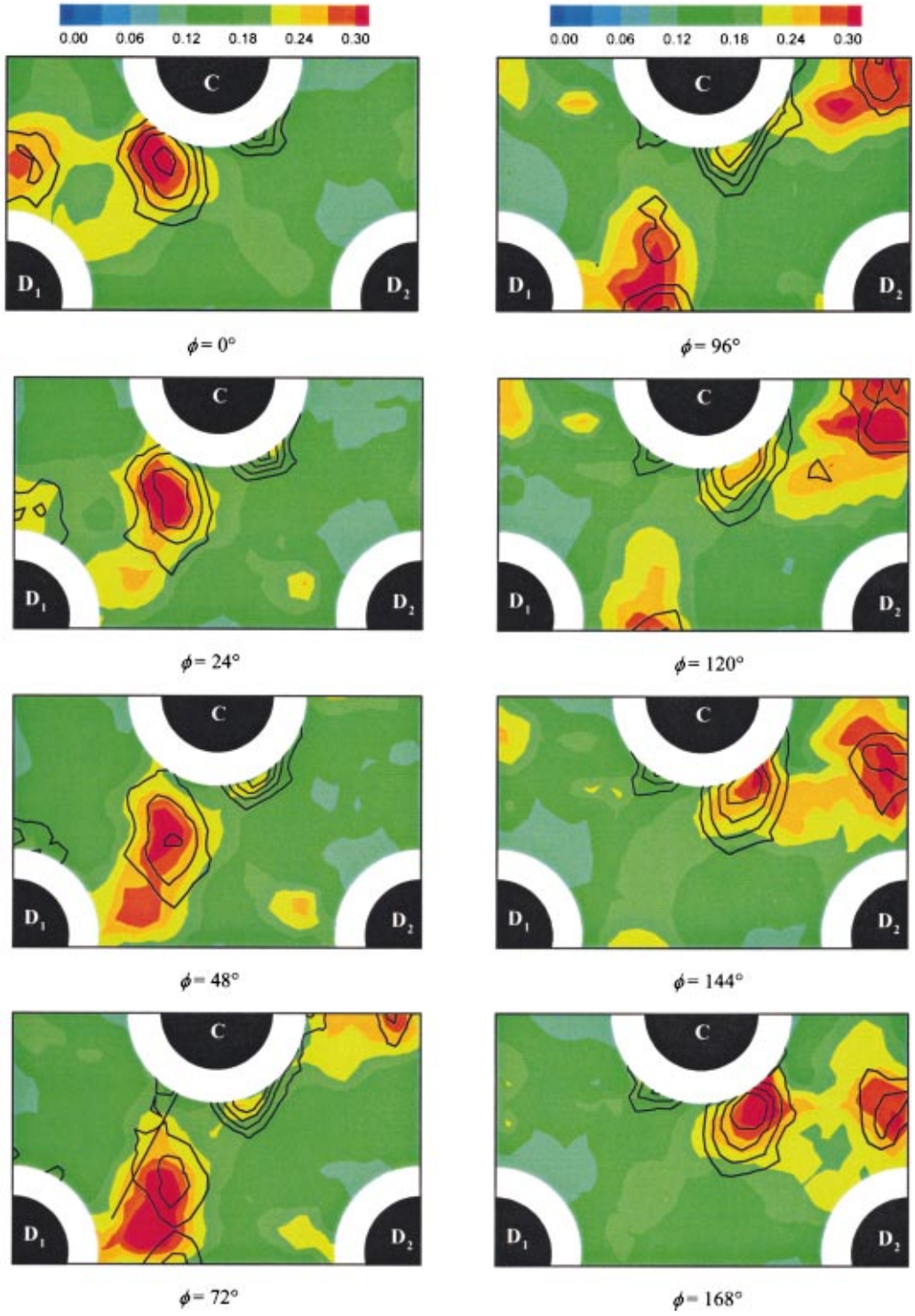

Fig. 10 The turbulence kinetic energy field

shown, the counter-clockwise vortex directs the fluid above its center towards the left hand side and that below on the opposite direction (cf. Fig. 4). The presence of three vortices can be inferred from the distribution at the particular phase-angle shown consistent with the vorticity field shown in Fig. 6.

The random Reynolds stresses at $\phi = 0$ deg are shown in Fig. 11*c* and 11*d* for the streamwise and transverse components respectively. Note that the average of the two distributions is the turbulence kinetic energy q shown in Fig. 10 ($\phi = 0$ deg). Both distributions indicate the correlation between large-scale vortex formation and small-scale random turbulence, i.e., the random Reynolds stresses are high near the vortex centers (both in the wake of cylinder C and upstream of cylinders D_1 and D_2). The influence of disintegrating vortices shed from upstream cylinders results in complicated distributions and overall the random Reynolds stresses are quite homogeneous compared to the periodic stresses.

Figure 11*e* shows the variation of the mean velocity at constant phase $\langle u \rangle$ and the corresponding Reynolds stress $\tilde{u}\tilde{u}$ resulting from this variation as a function of phase-angle at a particular

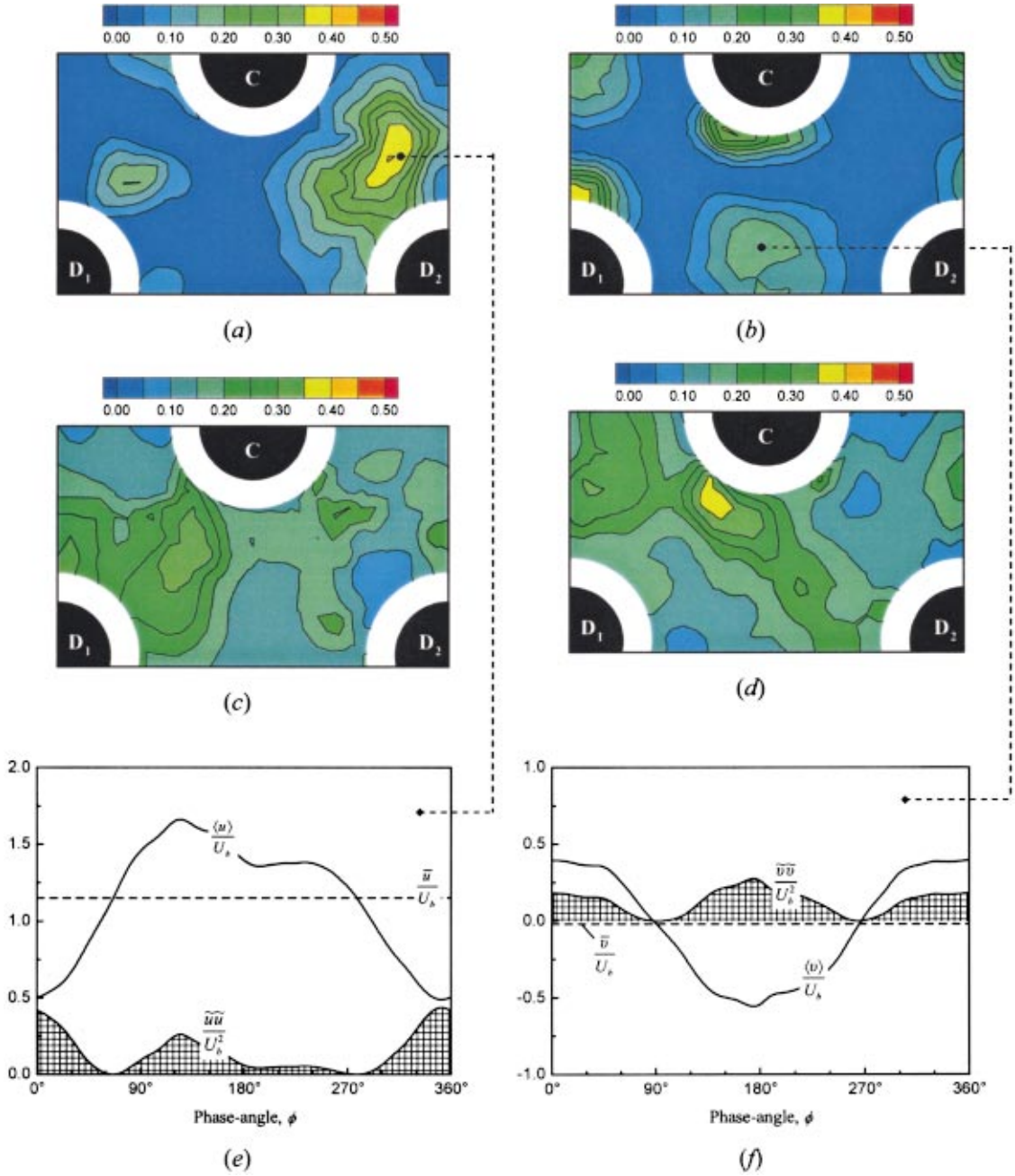

Fig. 11 The periodic and random Reynolds stress for $\phi=0$ deg; (*a*) $\tilde{u}\tilde{u}/U_b^2$, (*b*) $\tilde{v}\tilde{v}/U_b^2$, (*c*) $u'u'/U_b^2$, (*d*) $v'v'/U_b^2$. Periodic mean velocity and the corresponding Reynolds stress as a function of phase-angle; (*e*) streamwise and (*f*) transverse component.

point. The variation shown indicates the strong pulsating of the flow in the streamwise direction. Note that the oscillations of the streamwise velocity due to the imposed pulsations constitute only a small fraction of the total variation. The variation of the transverse component $\langle v \rangle$ and the corresponding Reynolds stress $\tilde{v}\tilde{v}$ illustrate the strong oscillations of the flow across the wake axis (Fig. 11*f*).

By averaging the periodic and random Reynolds stresses over all phases the conventional (time-averaged) Reynolds stresses are obtained. Following the notation used in Cantwell and Coles [23] and extended further in Govardhan and Williamson [33], the total Reynolds stresses are introduced below:

$$\text{Total} = \text{Periodic} + \text{Random}$$

$$\overline{\hat{u}\hat{u}} = \overline{\tilde{u}\tilde{u}} + \overline{u'u'}$$

$$\overline{\hat{v}\hat{v}} = \overline{\tilde{v}\tilde{v}} + \overline{v'v'} \tag{7}$$

Figure 12 shows the distributions of the time-averaged periodic and total Reynolds stresses for both the streamwise and transverse components.

The periodic part of the streamwise Reynolds stress $\overline{\tilde{u}\tilde{u}}$ has high values in the main flow paths in-between the cylinders, particularly at the shoulder of the cylinders where the maximum blockage to the flow occurs and low values along the wake axis

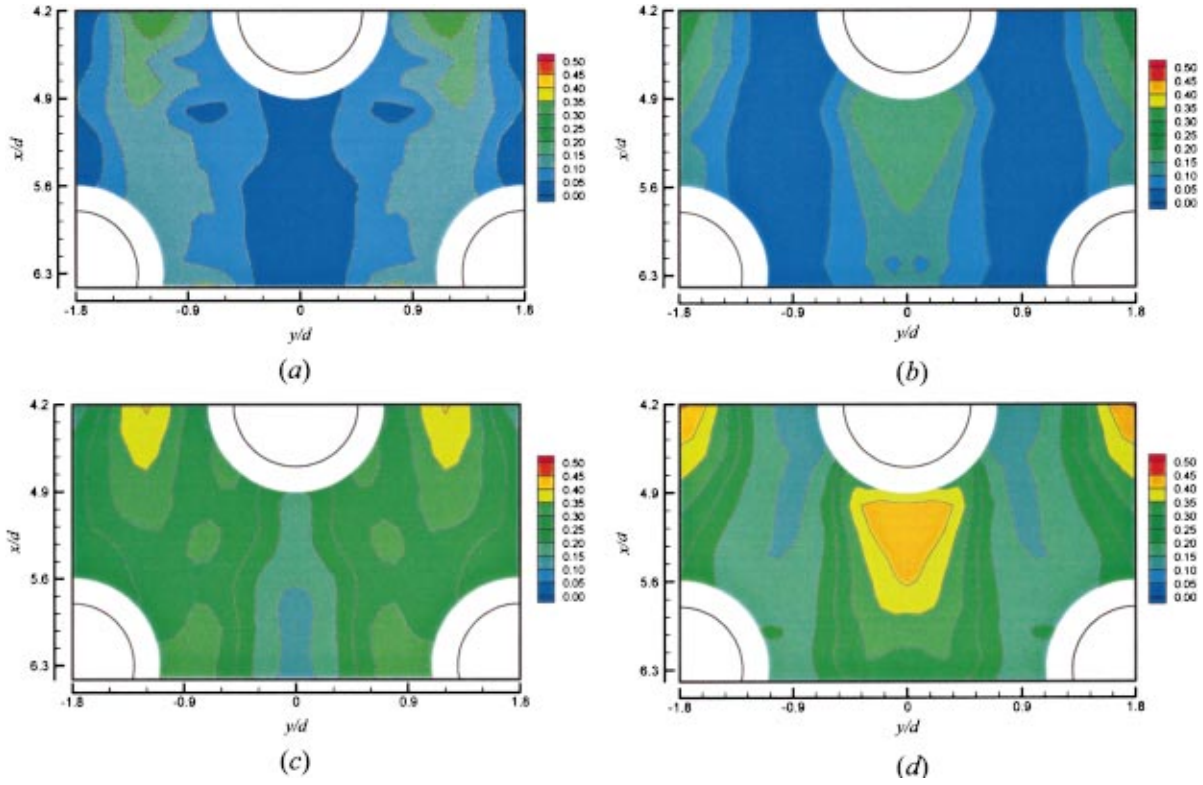

Fig. 12 Distributions of the periodic and total Reynolds stresses; (*a*) $\overline{\tilde{u}\tilde{u}}/U_b^2$, (*b*) $\overline{\tilde{v}\tilde{v}}/U_b^2$, (*c*) $\overline{\hat{u}\hat{u}}/U_b^2$ and (*d*) $\overline{\hat{v}\hat{v}}/U_b^2$.

(Fig. 12*a*). It is known that the fluctuations due to vortex shedding are comparatively low along the wake axis [23,34]. The $\overline{\tilde{u}\tilde{u}}$ stress is dominated by the streamwise pulsation of the flow in the array associated with periodic vortex shedding (as has already been noted the imposed external pulsations contribute only a small fraction). The distribution of $\overline{\tilde{u}\tilde{u}}$ indicates that periodic fluctuations have higher amplitude in the second row than in the third row; a consequence of stronger vortices shed from the second row [1]. A remarkable feature of the distribution is a spot of low values around $(x/d,y/d)=(5,0.8)$. It is suggested that at this region the propagated fluctuations of the velocity induced by vortex shedding from the second and third row collide and cancel out.

The periodic part of the transverse Reynolds stress $\overline{\tilde{v}\tilde{v}}$ exhibits the opposite distribution to that of the streamwise component with high values in the wake axis and low values in the flow lanes (Fig. 12*b*). The $\overline{\tilde{v}\tilde{v}}$ stress is dominated by the oscillations of the flow across the wake axis associated with the entrainment of fluid from the main flow paths into the shed vortices. Again, it is evident that the periodic fluctuations associated with vortex shedding from the second row have higher amplitude than those from the third row, e.g., $\overline{\tilde{v}\tilde{v}}=0.30$ at $(x/d,y/d)=(4.2,1.8)$ compared to 0.15 at (6.3, 0).

The distributions of the total Reynolds stresses $\overline{\hat{u}\hat{u}}$ and $\overline{\hat{v}\hat{v}}$ (Fig. 12*c* and 12*d*) are qualitatively similar to those of their periodic counterparts in Fig. 12*a* and 12*b* but the absolute values are significantly higher. It can be seen that the peak values of the total Reynolds stresses in the actual wake of the cylinder are approximately equal to 0.35 and 0.45 for the streamwise and transverse components respectively. However, although the streamwise value is much higher than those reported for the wake of a stationary cylinder by both Cantwell & Coles [23] and Govardhan and Williamson [33] the transverse one compares well with that reported in [23].

The peak values of the periodic part of the Reynolds stresses $\overline{\tilde{u}\tilde{u}}$ and $\overline{\tilde{v}\tilde{v}}$ (Fig. 12*a* and 12*b*) are 0.10 and 0.20 respectively. These compare well with 0.08 and 0.23 reported for a single cylinder despite the much larger Reynolds number in the latter case [23]. In the present study the contribution of the periodic part of the transverse component to the total stress is higher (45%) than that of the streamwise component (29%). This trend is in agreement with observations in the wake of a stationary cylinder but the actual percentage contributions reported for a single cylinder are significantly higher [23,33]. It should be noted, however, that if the whole flow cell under investigation is considered, i.e., if we also take into account the higher stress values associated with vortex shedding from the second row, then the periodic parts of both the streamwise and transverse components contribute about the same (nearly 67%) to the corresponding total Reynolds stresses despite the distinctly different distributions observed in connection with periodic vortex shedding. On the contrary, the random parts of the Reynolds stresses (not shown here for brevity) exhibit homogeneity in connection with the small-scale turbulence in the flow.

3.7 Comparison to Unforced Flow. The velocity measurements reported in this paper were obtained under the condition of vortex shedding resonance or lock-on imposed by external streamwise pulsations of the flow approaching the cylinder array. Without controlling the frequency of vortex shedding in the array via the pulsations it would not be possible to separate the periodic velocity fluctuations of the unsteady mean flow that describe the vortex shedding process from the random turbulent fluctuations. Under no control, there exist multiple vortex shedding frequencies in the array that are dispersed over wide ranges [1]. Undoubtedly, the imposed pulsations can modify the velocity characteristics but it is believed that qualitatively the flow patterns remain relatively unchanged. A comparison between forced and unforced conditions of the time-averaged velocity characteristics, for which the comparison is possible, is shown in Fig. 13. The comparison is made in terms of profiles of the time-averaged mean velocity and the total root mean square (rms) fluctuation.

The profiles of the streamwise mean velocity $\overline{u}$ are more flat

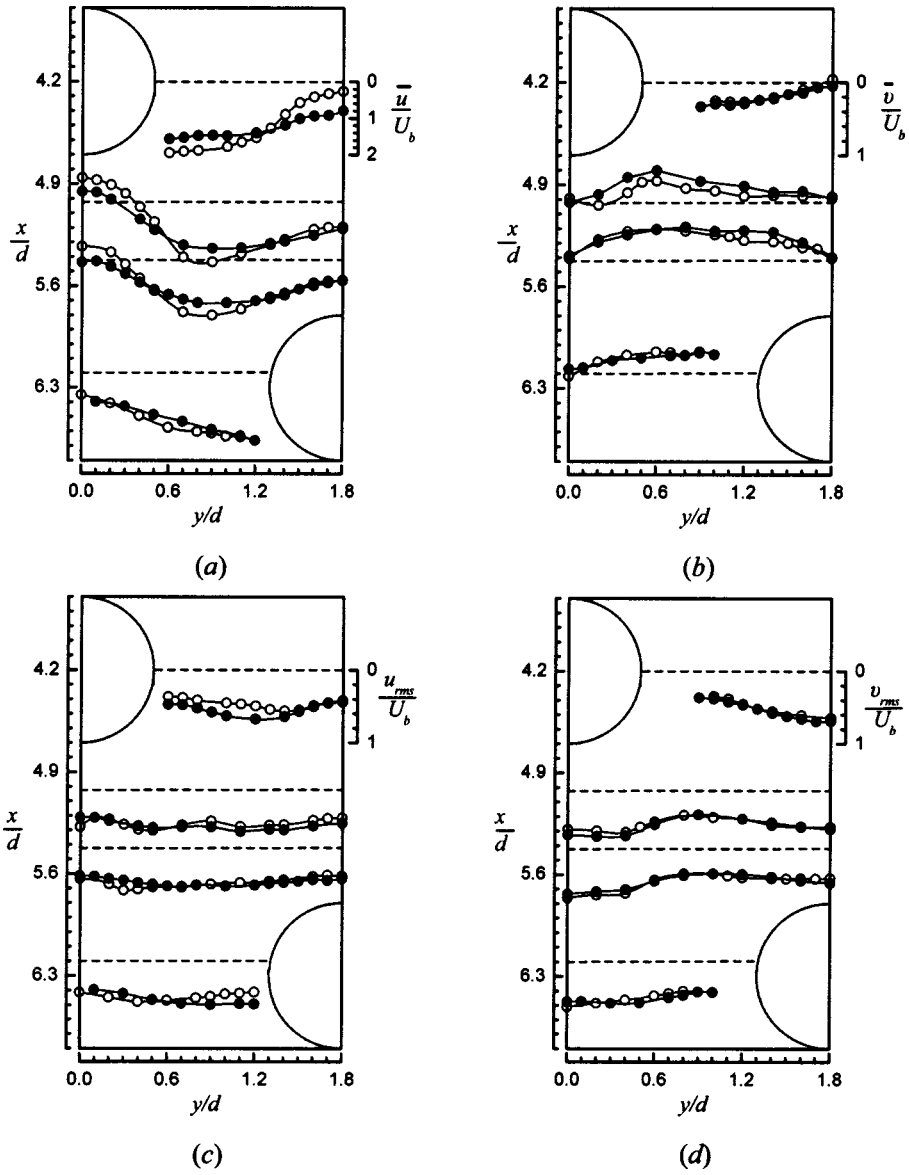

Fig. 13 Comparison between unforced (open symbols) and forced flow (solid symbols) in terms of the time-averaged velocity statistics (*a*) streamwise mean velocity, (*b*) transverse mean velocity, (*c*) streamwise total rms velocity, and (*d*) transverse total rms velocity.

and the deficit is less in forced flow (solid symbols) than in unforced (open symbols). The degree of flatness of the profiles is an indication of the development of the flow in the array [35]. Hence, under forced conditions the flow develops faster, i.e., in fewer rows. The differences in the profiles indicate a strong modification of the time-averaged mean flow field. On the other hand, the profiles of the transverse mean velocity $\bar{v}$ are quite similar in forced and unforced flow, except for the profiles at $x/d=5$. These profiles display more negative values for forced flow than for unforced which indicates a stronger deflection of the fluid and might be associated with the entrainment of fluid from the flow lanes in the wake; a process which is intensified under resonance.

The total rms fluctuation remains relatively unchanged between forced and unforced flow. Given that the periodic fluctuations associated with variations of the mean flow increase under lock-on conditions [1], it may be argued that the true turbulence levels are a little reduced. This suggests that comparisons based on the total rms fluctuation can be misleading and that more elaborate data may be needed. The superposition of large amplitude perturbations might be expected to give rise to a systematic difference between forced and unforced rms data of the streamwise velocity component. However, the vortex shedding lock-on phenomenon is associated with a more complex modification of the wake structure and is not simply a linear superposition of the perturbations on the unsteady mean flow, particularly in a cylinder array. This is supported by the fact that the results in Fig. 13 do not show a systematic trend, even though it can be seen that u_{rms} values are higher at some locations in forced flow than in unforced.

4 Conclusions

Velocity measurements were carried out in a staggered array of cylinders under conditions of vortex shedding lock-on using laser-Doppler anemometry. Lock-on was imposed by external flow pulsations in the streamwise direction. The velocity fluctuations were split into periodic and random components by averaging at constant phase with respect to the pulsation phase. Due to the phase-locking between vortex shedding and imposed pulsations, the

measurements allowed the reconstruction of the unsteady mean flow and turbulence fields over an average cycle of vortex shedding that takes place in the third-row wake of the array.

The results obtained include data for the unsteady mean velocity (vectors), streamlines, mean vorticity and turbulence fields at constant phase, which have not been available previously. The Reynolds stresses that arise from periodic and random fluctuations were further analyzed. It is found that periodic fluid motions are associated with a strong pulsation of the fluid in the flow direction and entrainment of fluid from the flow lanes across the wake, as a result of the formation and shedding of coherent vortices in the cylinder wake. Random flow fluctuations are associated with turbulence production due to vortex shedding in the cylinder wake as in the case of a single cylinder, and disintegration of coherent vorticity into small-scale three-dimensional turbulence as the vortices are squeezed in the narrow passage between the cylinders of the downstream row.

This fundamental study should enhance understanding of the complex cross-flow phenomena in cylinder arrays and provide a reliable and analytical set of experimental data for testing and verification of computational models. A further comment deserves mention here. In the computations of the cross-flow in cylinder arrays made by Beale and Spalding [19], the periodic behavior is established by applying an initial disturbance of frequency f_0 in an upstream module of the array and, assuming the flow is 'doubly periodic,' the outflow from a downstream module is used as the disturbance for the upstream module to establish a feedback loop. If, for studying the array configuration here, the initial disturbance frequency f_0 is matched with the excitation frequency f_e of pulsation employed here to control the vortex shedding frequency and maintained constant, then direct comparisons can be made between computations and the present experimental data.

Acknowledgments

The authors gratefully acknowledge the financial support of the Engineering and Physical Sciences Research Council (EPSRC, Grant GR/L60937) during the course of this investigation.

References

[1] Konstantinidis, E., Balabani, S., and Yianneskis, M., 2002, ''A study of vortex shedding in a staggered tube array for steady and pulsating cross-flow,'' ASME J. Fluids Eng., **124**, pp. 737–746.
[2] Wallis, R. P., 1939, ''Photographic study of fluid flow between banks of tubes,'' Proc. Inst. Mech. Eng., **142**, pp. 379–387.
[3] Païdoussis, M. P., 1983, ''A review of flow-induced vibrations in reactors and reactor components,'' Nucl. Eng. Des., **74**, pp. 31–60.
[4] Abd-Rabbo, A., and Weaver, D. S., 1986, ''A flow visualization study of flow development in a staggered tube array,'' J. Sound Vib., **106**, pp. 241–256.
[5] Weaver, D. S., and Abd-Rabbo, A., 1985, ''A flow visualization study of a square array of tubes in water cross-flow,'' ASME J. Fluids Eng., **107**, pp. 354–363.
[6] Ziada, S., and Oengören, A., 1993, ''Vortex shedding in an in-line tube bundle with large tube spacings,'' J. Fluids Struct., **7**, pp. 661–687.
[7] Weaver, D. S., Lian, H. Y., and Huang, X. Y., 1993, ''A study of vortex shedding in rotated square arrays,'' J. Fluids Struct., **7**, pp. 107–121.
[8] Price, S. J., Païdoussis, M. P., and Mark, B., 1995, ''Flow visualization of the interstitial cross-flow through parallel triangular and rotated square arrays of cylinders,'' J. Sound Vib., **181**, pp. 85–98.
[9] Polak, D. R., and Weaver, D. S., 1995, ''Vortex shedding in normal triangular tube arrays,'' J. Fluids Struct., **9**, pp. 1–17.
[10] Oengören, A., and Ziada, S., 1998, ''An in-depth study of vortex shedding, acoustic resonance and turbulent forces in normal triangle tube arrays,'' J. Fluids Struct., **12**, pp. 717–758.
[11] Ziada, S., and Oengören, A., 2000, ''Flow periodicity and acoustic resonance in parallel triangle tube bundles,'' J. Fluids Struct., **14**, pp. 197–219.
[12] Moretti, P. M., 1993, ''Flow-induced vibrations in arrays of cylinders,'' Annu. Rev. Fluid Mech., **25**, pp. 99–114.
[13] Weaver, D. S., and Fitzpatrick, J. A., 1988, ''A review of cross-flow induced vibrations in heat exchanger tube arrays,'' J. Fluids Struct., **2**, pp. 73–93.
[14] Halim, M. S., and Turner, J. T., 1986, ''Measurements of cross flow development in a staggered tube bundle,'' 3rd Int. Symp. Appl. Laser Tech. Fluid Mech., Lisbon, paper 21.7.
[15] Simonin, O., and Barcouda, M., 1986, ''Measurements of fully developed turbulent flow across tube bundle,'' 3rd Int. Symp. Appl. Laser Tech. Fluid Mech., Lisbon, paper 21.5.
[16] Meyer, K. E., and Larsen, P. S., 1994, ''LDA study of turbulent flow in a staggered tube bundle,'' 7th Int. Symp. Appl. Laser Tech. Fluid Mech., Lisbon, paper 39.4.
[17] Balabani, S., and Yianneskis, M., 1996, ''An experimental study of the mean flow and turbulence structure of cross-flow over tube bundles,'' Proc. Inst. Mech. Eng., Part C: J. Mech. Eng. Sci., **210**, pp. 317–331.
[18] Balabani, S., and Yianneskis, M., 1997, ''Vortex shedding and turbulence scales in staggered tube bundle flows,'' Can. J. Chem. Eng., **75**, pp. 823–831.
[19] Beale, S. B., and Spalding, D. B., 1999, ''A numerical study of unsteady fluid flow in in-line and staggered tube banks,'' J. Fluids Struct., **13**, pp. 723–754.
[20] Barsamian, H. R., and Hassan, Y. A., 1997, ''Large eddy simulation of turbulent cross-flow in tube bundles,'' Nucl. Eng. Des., **109**, pp. 103–122.
[21] Rollet-Miet, P., Laurence, D., and Ferziger, J., 1999, ''LES and RANS of turbulent flow in tube bundles,'' Int. J. Heat Fluid Flow, **20**, pp. 241–254.
[22] Castiglia, D., Balabani, S., Papadakis, G., and Yianneskis, M., 2001, ''An experimental and numerical study of the flow past elliptic cylinder arrays,'' Proc. Inst. Mech. Eng., Part C: J. Mech. Eng. Sci., **215**, pp. 1287–1301.
[23] Cantwell, B., and Coles, D., 1983, ''An experimental-study of entrainment and transport in the turbulent near wake of a circular-cylinder,'' J. Fluid Mech., **136**, pp. 321–374.
[24] Konstantinidis, E., 2001, ''Pulsating flow in cylinder arrays,'' Ph.D. Thesis, King's College London, University of London.
[25] Zhang, Z., Eisele, K., and Hirt, F., 1997, ''The influence of phase-averaging window size on the determination of turbulence quantities in unsteady turbulent flows,'' Exp. Fluids, **23**, pp. 263–267.
[26] Sonnenberger, R., Graichen, K., and Erk, P., 2000, ''Fourier averaging: a phase averaging method for periodic flow,'' Exp. Fluids, **28**, pp. 217–224.
[27] Benedict, L. H., and Gould, R. D., 1996, ''Towards better uncertainty estimates for turbulence statistics,'' Exp. Fluids, **22**, pp. 129–136.
[28] Lin, J. C., Towfighi, J., and Rockwell, D., 1995, ''Instantaneous structure of the near-wake of a circular-cylinder-on the effect of Reynolds-number,'' J. Fluids Struct., **9**, pp. 409–418.
[29] Gaydon, M., and Rockwell, D., 1999, ''Vortices incident upon an oscillating cylinder: flow structure and loading,'' J. Fluids Struct., **13**, pp. 709–722.
[30] Armstrong, B. J., Barnes, F. H., and Grant, I., 1987, ''A comparison of the structure of the wake behind a circular-cylinder in steady flow with that in a perturbed flow,'' Phys. Fluids, **30**, pp. 19–26.
[31] Konstantinidis, E., Castiglia, D., Papadakis, G., Balabani, S., and Bergeles, G., 2000, ''Vortex lock-on phenomena due to pulsating flow in tube arrays,'' 10th Int. Symp. Appl. Laser Tech. Fluid Mech., Lisbon, Portugal.
[32] Griffin, O. M., and Ramberg, S. E., 1976, ''Vortex shedding from a cylinder vibrating in line with an incident uniform flow,'' J. Fluid Mech., **75**, pp. 526–537.
[33] Govardhan, R., and Williamson, C. H. K., 2001, ''Mean and fluctuating velocity fields in the wake of a freely-vibrating cylinder,'' J. Fluids Struct., **15**, pp. 489–501.
[34] Bloor, M. S., and Gerrard, J. H., 1966, ''Measurements of turbulent vortices in a cylinder wake,'' Proc. R. Soc. London, **A294**, pp. 319–342.
[35] Aiba, S., Tsuchida, H., and Ota, T., 1982, ''Heat-transfer around tubes in staggered tube banks,'' Bull. JSME, **25**, pp. 927–933.

Towards Practical Flow Sensing and Control via POD and LSE Based Low-Dimensional Tools

J. A. Taylor
e-mail: taylorja@clarkson.edu
Mechanical and Aeronautical Engineering,
Clarkson University,
Potsdam, New York 13699-5725

M. N. Glauser
e-mail: mglauser@syr.edu
Mechanical, Aerospace and Manufacturing Engineering,
Syracuse University,
Syracuse, New York 13244-1240

Low-dimensional methods including the Proper Orthogonal Decomposition (POD) and Linear Stochastic Estimation (LSE) have been applied to the flow between a backward facing ramp and an adjustable flap. A range of flap angles provide a flow which is incipiently separated and can be used to flesh out ideas for active feedback separation control strategies. The current study couples Particle Image Velocimetry (PIV) and multi-point wall pressure measurements using POD and LSE to estimate the full velocity field from the wall pressure alone. This technique yields a sufficiently accurate estimate of the velocity field that the incipient condition can be detected. The ability to estimate the state of the flow without inserting probes into the flow is important for the development of practical active feedback flow control strategies. [DOI: 10.1115/1.1760540]

1 Introduction

We present two important advances for the future implementation of active feedback control in incipiently separated flows. The first, suggests that the POD modes can be used for active feedback control as long as the ensemble from which the POD basis is extracted has knowledge of the controlled state included. The second addresses the practical implementation of closed-loop control in situations where it is often undesirable or impossible to monitor the flow using probes positioned within the field. For these cases a technique to estimate the flow field from some point external to the flow such as at the wall is demonstrated (see Taylor [1], Taylor [2], and Taylor and Glauser [3]). The Proper Orthogonal Decomposition, POD, was originally developed by Lumley [4] as a tool for identifying the most energetic coherent structures, or eddies, contained within a turbulent flow field. Berkooz et al. [5] provide a comprehensive review of the early applications of the POD to a variety of flows. In 1997, Jorgensen [6] presented the POD modes for a separated flow behind a fence that had been perturbed using a large upstream oscillating disturbance. The POD modes were shown for the base flow, the perturbed flow, and phase aligned with the disturbance. The author used this information to argue that phase aligned data provided the optimal basis set for decomposing a perturbed flow in a particular state. However, the question facing the turbulence and flow control communities at this point is how well a basis set constructed using information from the base flow will function in the presence of a perturbation, i.e. an excitation of the flow through the use of an actuator.

Chapman [7] and Chapman et al. [8] showed that as the flow over a swept airfoil passed through a laminar to turbulent transition region, there was a shift in the dominance of the POD modes. Prior to transition, the first POD mode dominated. As the flow transitioned to a turbulent flow, the energy associated with the first POD decayed while the second POD mode grew. A balance between the two modes was reached at the center of the transition region. For a comprehensive review of low dimensional modeling in transitioning flows see Rempfer [9]. Similarly, Eaton [10] found that as the flow within the axisymmetric sudden expansion passed its mean reattachment point, the energy contribution was initially dominated by the first azimuthal Fourier mode but shifted to a dominant ring mode. This is significant, because it shows clearly that the POD based low-dimensional descriptions are sensitive to relatively subtle changes in the structure of the flow. These studies provide reason to believe that a low-dimensional description constructed using information extracted from the full range of flow states will describe the entire separation process. Such a description will contain a single mode, or combination of a few modes, which will characterize the large scale features of the flow, i.e. the emergence of an inflectionary profile and formation of a recirculating region for the flow studied here. Recent results in an engine cylinder flow (Fogleman et al. [11], Boree et al. [12]) clearly show the utility of such an approach. In these studies, the POD is computed for fixed crank-angle over a number of cycles. They then average over the crank-angles to obtain phase invariant POD modes. These crank angle invariant POD modes show desirable properties for forming a suitable basis for future low-dimensional models.

Given a basis set that spans the range of all possible flow states and an indicator of the instantaneous flow state, the challenge for implementing feedback control systems includes the daunting task of developing nonintrusive techniques for sensing the time-dependent indicator. In 1977, Adrian [13] proposed the use of stochastic estimation as a potential replacement for conditional sampling approaches in the study of coherent structures in turbulent flows. Cole et al. [14] showed that a coarse grid of hot-wire anemometers could be coupled with two-point statistics acquired on a grid with sufficient fidelity to avoid spatial aliasing could be used to obtain an estimate of the velocity field in the axisymmetric jet shear layer. Ukeiley et al. [15] and Bonnet et al. [16] built upon the work of Adrian [13] and Cole et al. [14] by combining the LSE with the POD to form a tool for obtaining the time dependent low-dimensional description of a turbulent flow field. The swept wing transition research of Chapman [7] used a correlation between the shear stress from an array of surface mounted hot-film anemometers and x-wire measurements of the velocity field to estimate a low-dimensional description of the time-dependent flow from information at the surface of the airfoil. Similarly, Delville et al. [17] has shown that it is possible to use linear stochastic estimation techniques to estimate the instantaneous velocity field in an axisymmetric jet using an array of microphones placed in a streamwise array outside the jet shear layer, and appropriate statistics from the velocity field. Boree [18] has recently proposed a technique very similar to the method presented in this paper, that he refers to as the extended POD. This technique is claimed to provide an objective means to extract correlated structures occurring in the velocity and pressure, particle motion, or concentration fields.

The current study will show that the correlation between surface pressure and the POD expansion coefficients describing the flow field can be used in conjunction with the surface pressure to estimate the full (mean and fluctuating) velocity field in an incipiently separating flow.

Contributed by the Fluids Engineering Division for publication in the JOURNAL OF FLUIDS ENGINEERING. Manuscript received by the Fluids Engineering Division June 12, 2003; revised manuscript received December 10, 2003. Associate Editor: H. Johari.

2 Proper Orthogonal Decomposition (POD)

In 1967, Lumley [4] proposed the Proper Orthogonal Decomposition (POD) as an unbiased technique for studying coherent structures in turbulent flows. For more information regarding the details of the proper orthogonal decomposition, the reader is referred to, Lumley [4,19], Glauser et al. [20], George [21], Moin and Moser [22], Glauser and George [23] and Berkooz et al. [5].

The POD is a mathematical approach based on the Karhunen-Loeve expansion, which is used to decompose the fluctuating velocity field into a finite number of empirical functions. These functions, ϕ, are linearly independent and form a basis set chosen to maximize the mean square projection, α, on the fluctuating field, $\vec{u}$.

$$\frac{\overline{|\vec{u}\cdot\vec{\phi}|^2}}{|\vec{\phi}\cdot\vec{\phi}^*|}=\overline{|\alpha^2|} \tag{1}$$

The * denotes the complex conjugate, and the inner product is defined as $(f,g)=\int_D f(x)g^*(x)dx$, where D defines a finite domain. The inner product of the candidate structure, ϕ, with its complex conjugate normalizes Eq. (1) and allows us to study the degree of the projection rather than its magnitude. Lumley [24] showed that this maximization can be performed using calculus of variations, and Berkooz [25] presented a method of solving the maximization by defining a Hermitian operator. Both of these techniques lead to an integral eigenvalue problem of the form:

$$\int\int R_{ij}(\vec{x},\vec{x}')\phi_j(\vec{x}')d\vec{x}'=\lambda\phi_i(\vec{x}), \tag{2}$$

where the kernel of Eq. (2) is the ensemble averaged two-point correlation tensor, $R_{ij}(\vec{x},\vec{x}')$,

$$R_{ij}(\vec{x},\vec{x}')=\langle u_i(\vec{x})u_j(\vec{x}')\rangle. \tag{3}$$

By construction the kernel, R_{ij}, will always be hermitian. If the random field occurs over a finite domain (D), such that the integral in Eq. (2) is also over a finite domain, the solutions to Equation (2) follow the Hilbert-Schmidt theory (Lumley [4]).

According to the Hilbert-Schmidt theory there are a discrete set of solutions to Eq. (2) which may be selected such that $\phi^{(n)}$ are orthonormal,

$$\int_D \phi_i^{(p)}(\vec{x})\phi_i^{(q)}(\vec{x})d\vec{x}=\delta_{pq}, \tag{4}$$

and given a hermitian kernel, the eigenvalues are uncorrelated.

$$\langle a_n(t)a_m(t)\rangle=\lambda^{(n)}\delta_{nm}. \tag{5}$$

Additionally, the projection of the random quantity on the eigenfunctions will yield a set of uncorrelated coefficients,

$$a_n(t)=\int_D u_i(\vec{x},t)\phi_i^{(n)*}(\vec{x})d\vec{x}, \tag{6}$$

which can be combined with the eigenfunctions to reconstruct the original field,

$$u_i(\vec{x},t)=\sum_{n=1}^{\infty} a_n(t)\phi_i^{(n)}(\vec{x}). \tag{7}$$

There are two possible methods of applying the POD to flows that span multiple states (i.e., separated and attached boundary layers, or favorable and adverse pressure gradients). It is possible to solve the POD for each flow state separately. The kernel of the integral eigenvalue problem for this ''conditional'' approach is computed for each flow state, which is dictated by the flap angle, β, as:

$$R_{ij}(\vec{x},\vec{x}',\beta)=\langle u_i(\vec{x},\beta)u_j(\vec{x}',\beta)\rangle. \tag{8}$$

An alternate approach to this problem would be to disregard the individual flow states and average the kernel over the entire range of states, or flap angles. Dubbed the ''composite'' approach, this method uses a kernel for the integral eigenvalue problem that has been averaged over all flap angles,

$$R_{ij}(\vec{x},\vec{x}')=\langle u_i(\vec{x})u_j(\vec{x}')\rangle. \tag{9}$$

Substituting the ''conditional'' or ''composite'' kernels into Eq. (2), and accounting for the temporal and spatial limitations of the single 2-D PIV system used in the current study, yields two eigenvalue problems. Both approaches have clear advantages and disadvantages. The ''conditional'' approach provides an optimal basis set for the decomposition of a particular flow state, but must be interpolated or scaled between the measured states. The ''composite'' approach on the other hand, represents a compromise between optimality and robustness. By averaging the ''composite'' kernel over all the possible flow states, more eigenmodes are needed to capture the structure of the flow, but the eigenfunctions need not be scaled or manipulated so long as the flow state to be described falls within the range of states included in the ensemble that forms the basis for the kernel.

3 Linear Stochastic Estimation (LSE)

In the previous section we discussed the POD and how it could be employed to describe quantities spanning a range of flow states. The ''conditional'' and ''composite'' POD approaches are different ways of analyzing flows that tend to change their character. In this section, we will explain how the POD, in either of the forms discussed above, can be combined with surface pressure information and stochastic estimation techniques to estimate the velocity field and thus tackle another problem facing flow control system scientists: remote sensing of the velocity field.

A large number of investigations have been performed, in a variety of flows, using conditional averaging techniques to capture a particular feature within the flow field. Adrian [13] recognized that the statistical information contained within the two-point correlation tensor, $R_{ij}(\vec{x},\vec{x}')$, could be combined with instantaneous, or conditional, information to form a technique for estimating the flow field given. Cole et al. [14] then proposed that rather than defining an arbitrary indicator such as Adrian's ''conditional eddy,'' the instantaneous velocity field could be used. The adoption of the velocity field yielded an estimation technique capable of minimizing the complexity of difficult experiments. This reduction in complexity is accomplished by combining the statistical information, acquired on a fine spatial grid, with instantaneous velocity measurements, acquired on a coarse spatial grid, to estimate the full instantaneous flow field.

To effectively apply closed-loop control in practical applications it is generally undesirable or impossible to monitor the in situ flow using probes positioned within the field as proposed by Cole et al. [14]. In these cases a technique is needed to estimate the flow field from some point external to the flow. By combining the LSE technique with the POD, an estimate of the random POD coefficients can be obtained from the instantaneous surface pressure.

In the modified stochastic estimation, the conditional structure is defined by the random POD coefficients, a_n, from Eq. (6). The surface pressure was selected as an indicator of the presence of the chosen conditional structure as a result of its integrated nature, which corresponds to the random POD coefficients. The equivalent conditional approach can be written as:

$$\vartheta_n=\langle a_n|p\rangle, \tag{10}$$

where ϑ_n is the estimated random POD coefficients that describe the velocity field over $\vec{x}$, given the surface pressure, p and the empirical eigenfunctions. The estimated POD coefficient can be described as a series expansion with each additional term in the expansion containing increasing powers of the pressure condition.

$$\vartheta_n=b_{ni}p_i+c_{nij}p_ip_j+d_{nijk}p_ip_jp_k+\cdots \tag{11}$$

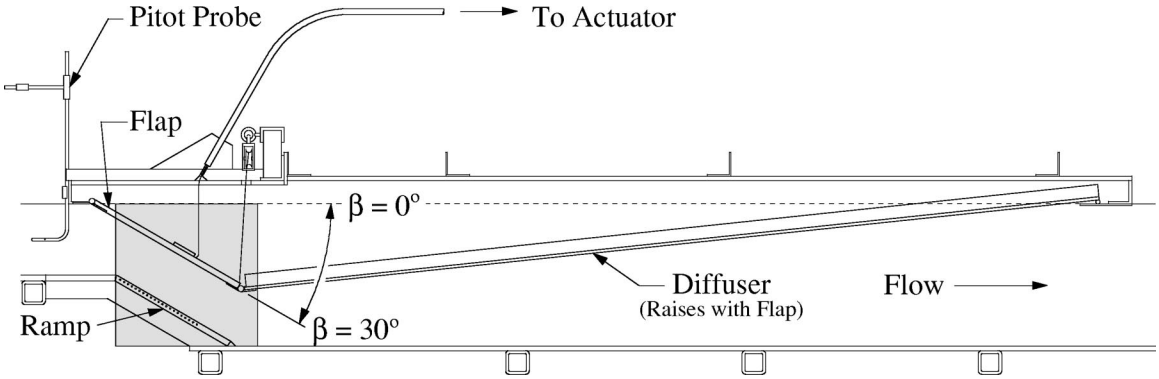

Fig. 1 The activewing test section with 22 static surface pressure taps on the spanwise centerline of the ramp, and a Pitot-static (differential) probe located at $z=-0.152$ m (-6 in.)

Equation (11) was truncated to include just the linear term plus the error associated with neglecting the higher order terms.

$$\vartheta_n = b_{ni} p_i + O[p_i^2] \tag{12}$$

The elements of b_{ni} are selected to minimize the mean square error, $e_{\vartheta_n} = \langle [\vartheta_n - a_n]^2 \rangle$, in the modified LSE by requiring that

$$\frac{\partial e_{\vartheta_n}}{\partial b_{ni}} = \frac{\partial \langle [b_{ni} p_i - a_n]^2 \rangle}{\partial b_{ni}} = 0 \tag{13}$$

and

$$\frac{\partial^2 e_{\vartheta_n}}{\partial b_{ni}^2} > 0. \tag{14}$$

The solution to this minimization problem is a linear system of equations, $\langle p_i p_j \rangle b_{ni} = \langle a_n p_j \rangle$, which can be written in matrix form as:

$$\begin{bmatrix} \langle p_1^2 \rangle & \langle p_1 p_2 \rangle & \cdots & \langle p_1 p_q \rangle \\ \langle p_2 p_1 \rangle & \langle p_2^2 \rangle & \cdots & \langle p_2 p_q \rangle \\ \vdots & \vdots & \ddots & \vdots \\ \langle p_q p_1 \rangle & \langle p_q p_2 \rangle & \cdots & \langle p_q^2 \rangle \end{bmatrix} \begin{bmatrix} b_{n1} \\ b_{n2} \\ \vdots \\ b_{nq} \end{bmatrix} = \begin{bmatrix} \langle a_n p_1 \rangle \\ \langle a_n p_2 \rangle \\ \vdots \\ \langle a_n p_q \rangle \end{bmatrix} \tag{15}$$

The selected elements of b_{ni} are then substituted back into Eq. (12) to estimate the random POD coefficient for each of the instantaneous pressure measurements. This operation yields a set of estimated POD coefficients which may be used to construct an estimate of the velocity, via Eq. (7) which has been modified to carry the time-dependence, as per Aubry [26]. For more details on the modified LSE method see Taylor [2].

4 Experiment

The geometry used in this experiment is a perturbed version of the traditional backward facing step flow with an inlet channel height, h, of 0.076 m (3 in.) and an outlet channel height of 0.152 m (6 in.). Figure 1 shows the backward facing ramp, as well as the adjustable flap, which were placed behind the step and above the ramp, respectively. Varying the position of the flap alters the adverse pressure gradient experienced by the flow. As the flap moves from a position parallel to the ramp to the fully raised position, the flow transitions from a curved channel flow, through a point of incipient separation, and ultimately to a fully separated flow. Figure 2 presents the coordinate system used throughout this study. For additional details regarding the facility, the reader is referred to Taylor [1].

The experiments consisted of six cases spanning 3 Reynolds numbers and two different inlet conditions. The first three experiments were performed at centerline velocities, measured 0.076 m (3 in.) upstream of the ramp apex, of 4 m/s (13.1 ft/s), 7 m/s (23.0 ft/s), & 10 m/s (32.8 ft/s) yielding Reynolds numbers based on step height, Re_h, of 2×10^4, 3.5×10^4, & 5×10^4. The reduced inlet channel (10 channel heights) produced a developing inlet flow approximating an external flow within the test section. The remaining three experiments were performed with a 30 channel height inlet extension which included a $0.04h$ tall, square edged, trip at the channel inlet.

For each experiment, 1024 statistically independent samples were obtained at 3 deg increments over the 30 deg range of the flap. Each sample included a measurement of the streamwise and wall-normal components of velocity using a Dantec FlowMap, 2100 PIV system in an x-y plane above the ramp and simultaneously the static surface pressure was measured at 22 locations on the ramp between $x_s=0$ and 105 mm (4.13 in.) in 5 mm (0.196 in.) increments.

Measurements of the inlet conditions were performed $2.5h$ upstream of the ramp apex using a Disa, 55M10 Constant Temperature Anemometer (CTA) with a Dantec, 55P15 boundary layer probe and a Kron-Hite Model, 3343 analog low-pass filter with a cut-off frequency of 2 kHz. The output signals were sampled at a rate of 5 kHz using a National Instruments, PCI-6071E A/D card with 12 bit accuracy and a personal computer.

The mean two-dimensionality of the flow in the span was verified to within ±0.1 m/s (±0.33 ft/s) over the full range of flap positions, inlet conditions, and Reynolds numbers. At 4 m/s (13.1 ft/s) the inlet flow was nearly laminar and the BL thickness was approximately 20% of the total channel height. As the flow rate

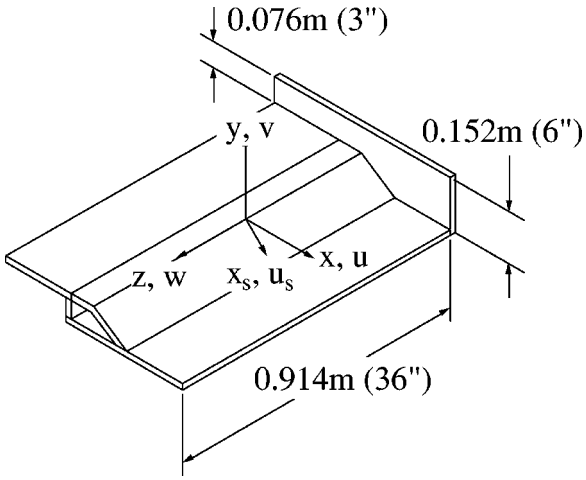

Fig. 2 The activewing coordinate system

was increased to 7 m/s (23.0 ft/s) and 10 m/s (32.8 ft/s) the boundary layers became turbulent and grew to thicknesses of approximately 35% and 40% of the total channel height respectively. Extending the inlet from 10*h* to 40*h* and adding a 0.04*h* tall trip to the upper and lower surfaces of the inlet at a location 40*h* upstream of the ramp apex resulted in turbulent flows with merged boundary layers at all three Reynolds numbers. The energy spectra for each of the flows with the additional inlet section exhibits an extended $k^{-5/3}$ region and a turbulence intensity of approximately 10% at the centerline.

The Dantec FlowMap 2100 Particle Image Velocimetry (PIV) system was used to acquire multi-point velocity measurements in a plane orthogonal to the ramp, where the potential for reverse flow precludes the use of traditional techniques, such as rakes of Constant Temperature Anemometry (CTA) probes. A ROSCO commercial fog generator was used to produce spherical liquid seed particles with diameters between 0.1 μm (3.9×10^{-6} in.) and 5 μm (2.0×10^{-4} in.) which would follow the follow the fluctuations in the flow up to a rate of roughly 5 kHz. The seed particulate was introduced directly upstream of the flow conditioning section through a 76.2 mm (3 in.)×609.6 mm (24 in.) settling tube which provided ample room for the glycerin particles to cool. The acquisition was delayed while the seed made a complete cycle through the facility thereby insuring a unifrom distribution of seed particles. A pair of pulsed NEWWAVE RESEARCH 120 mJ Nd:YaG lasers illuminated an x-y measurement plane normal at the spanwise centerline of the channel. The lasers were pulsed at time separation of 200, 108, and 33 μs for the three different Reynolds numbers which provided ample time for the fastest moving particles to traverse roughly 1/2 the width of the interrogation area between frames.

A Kodak Megaplus camera captured the pair of 1008×1008 images of the 15.24 cm×15.24 cm measurement window which covered the entire test section and yielded a magnification ratio of 151 μm/pixel (5.9×10^{-3} in./pixel). Each pair of images were partitioned into 41×41 interogation areas, each 32×32 pixel in size, with 25% overlap. Dantec's FlowManager 3.30 software was used to apply a Gaussian window, a digital bandpass filter, and then perform the cross-correlation as well as the sub-pixel interpolation necessary to accurately determine the statistical shift in the seed particles between frames. The estimated uncertainty in the PIV measurements, at the centerline of the inlet channel flow, was ±1% for the 4 and 7 m/s cases and ±2.3% for the 10 m/s case. The uncertainty increased in the low-speed recirculating region by roughly an order of magnitude.

An array of Modus T10 pressure transducers were used to mea-

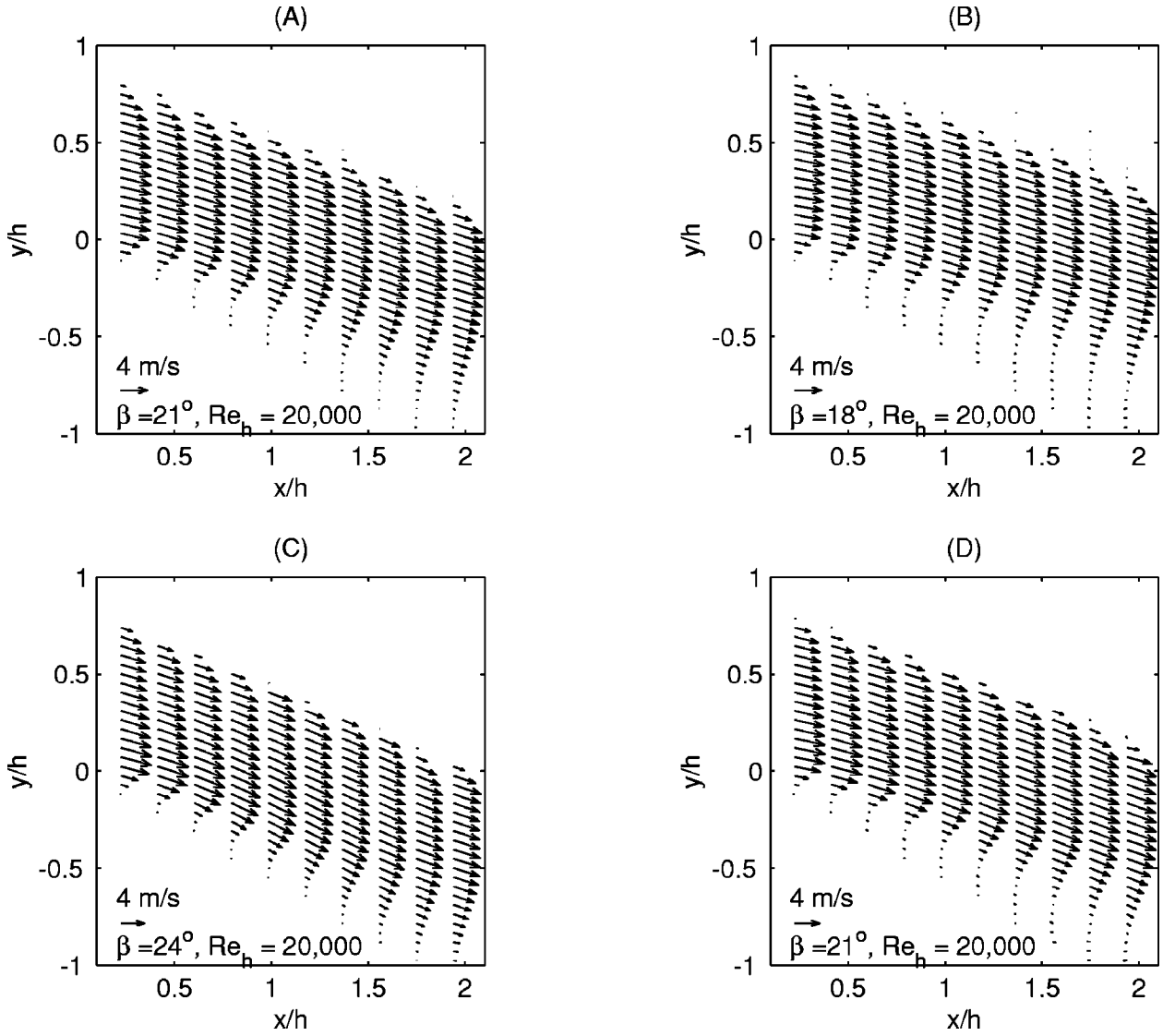

Fig. 3 Mean velocity near the point of incipient separation for the extended (*a*, *b*) and short (*c*, *d*) inlet with a $Re_h=2\times10^4$

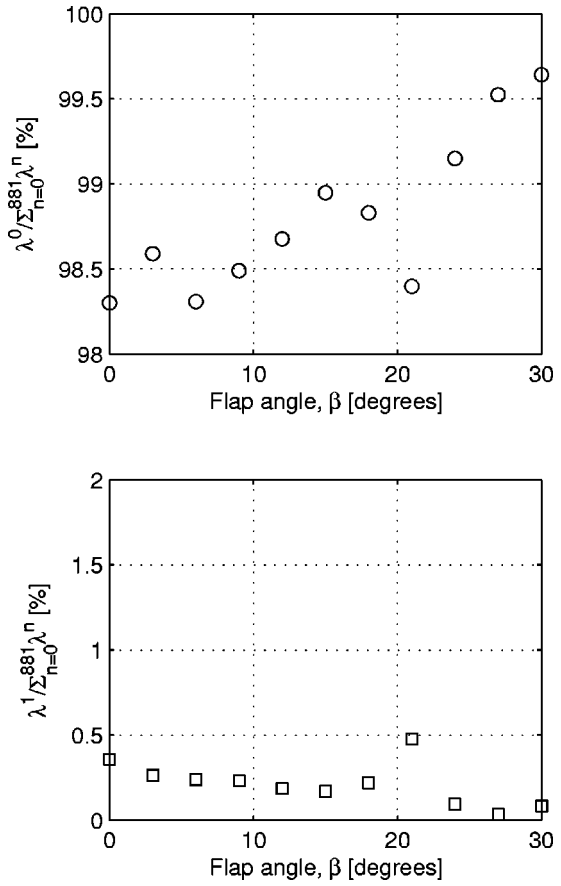

Fig. 4 Mean square energy captured by the first (upper) and second (lower) conditional pod modes at $Re_h=2\times10^4$ and with the extended inlet in place

sure the Pitot-static (differential) probe pressure, located at −0.076 m×0.038 m×−0.152 m (−3 in.×1.5 in.×−6 in.), and the 22 static surface taps located along the spanwise centerline of the ramp. These transducers were originally designed as draft sensors and therefore have a very small full scale range but are unable to resolve signals with frequencies greater than 10 Hz. Taylor [1] provide a discussion of the calibration procedures used with this pressure transducer array. To briefly summarize, a common manifold was connected to the 23 transducers and a uniform load was applied to the array via the static surface pressure tap at the apex of the ramp. The calibration procedure spans the full scale range, 24.9 Pa (0.1 in. H_2O), of the transducers and results in an instrument uncertainty of approximately ±0.25 Pa (±0.001 in. H_2O).

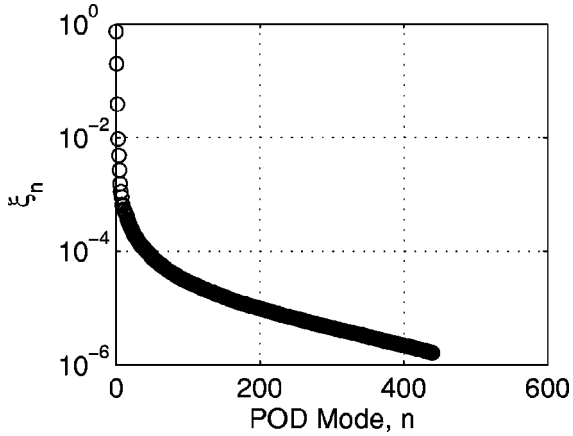

Fig. 5 The normalized mean square energy, $\xi_n=\lambda_n/\Sigma_{n=0}^{881}\lambda_n$, for the first N/2, or 441, of 882 composite modes at $Re_h=2\times10^4$

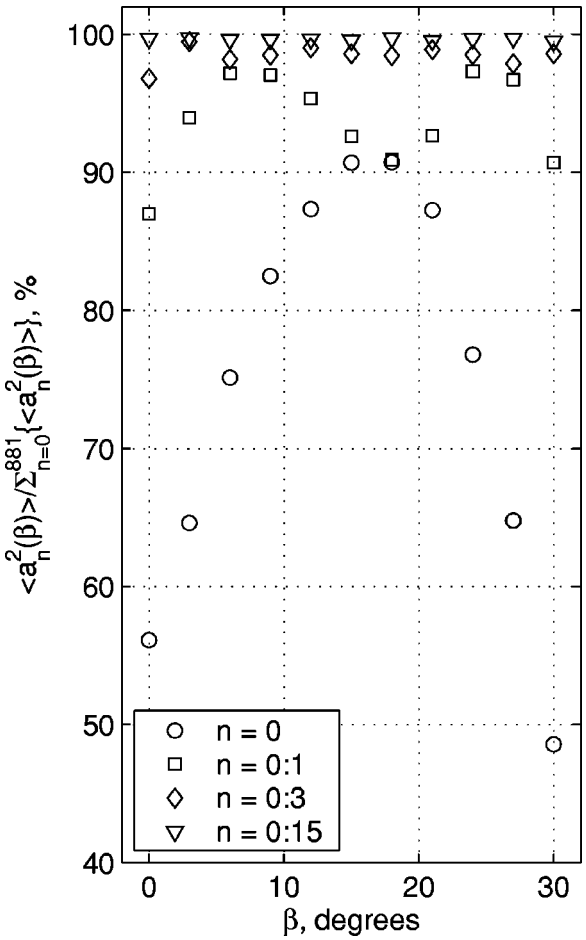

Fig. 6 Mean square energy captured by the first 1, 2, 4, and 16 composite eigenmodes as a function of the flap angle, β, using the velocity information at $Re_h=2\times10^4$ and with the extended inlet in place

5 Results

Determining the flap angle (β) associated with incipient separation was estimated by locating the point at which the wall normal shear stress, $\partial u_s/\partial y_s$, was minimized but remained positive over the length of the ramp. For the short inlet experiments the boundary layers were not as developed and separation occurred at an angle between $\beta=21$ deg and $\beta=24$ deg. For the extended inlet experiments the boundary layers were more developed and the point of incipient separation was delayed to $\beta\approx18$ deg. Figure 3 shows the flow in the test section prior to and near the incipient separation point for the extended and short inlet cases.

Jorgensen [6] showed that the ''conditional'' POD approach is optimal in the sense that for fixed flap angle, the number of modes necessary to capture a given percentage of the mean square energy in the flow is minimized. Figure 4 shows the energy contained in the first 2 of 882 ''conditional'' POD modes for the flow at 4 m/s (13.1 ft/s) and the extended inlet. This figure shows clearly that the first POD mode captures no less than 98% of the energy and

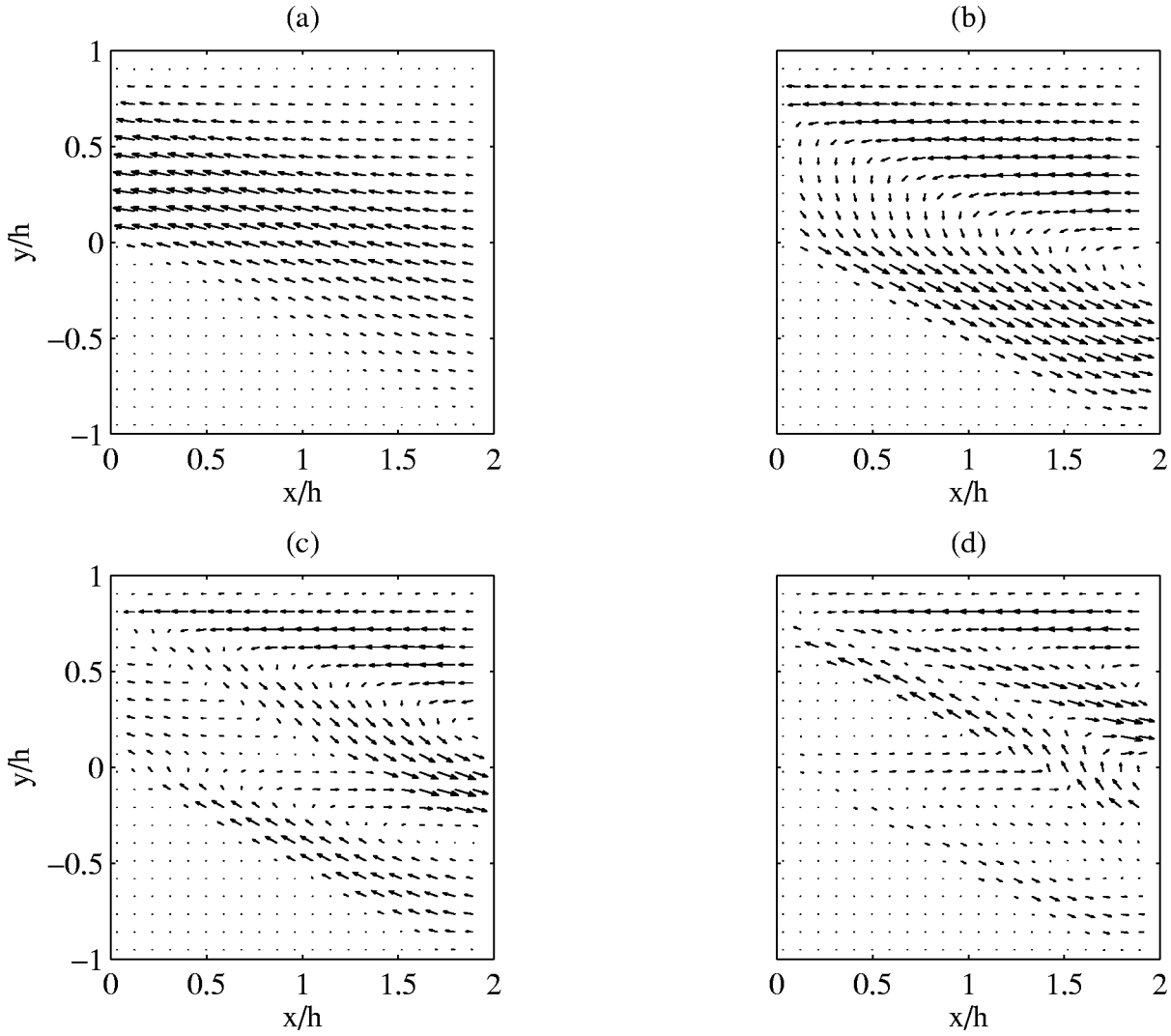

Fig. 7 Modes (*a*) 0, (*b*) 1, (*c*) 2, and (*d*) 3 of the 882 composite eigenfunctions which include information from both the short and extended inlet cases at $Re_h=2\times10^4$, 3.5×10^4, and 5×10^4

the second mode captures no more than 0.5%. Note that in this study we include the mean flow since we are interested in its low-dimensional description.

The ''conditional'' approach has two pitfalls that make it impractical for use in control applications. First the flap position, β, must be monitored for use in selecting the proper set of POD solutions. Second, introducing various control states, and/or dynamic flap motions, will result in additional degrees of freedom, each of which will have its own optimal POD solutions.

The ''composite'' approach is a compromise that trades the convergence rate for convenience. Rather than retain a set of eigenfunctions for each flap angle and then develop a technique for

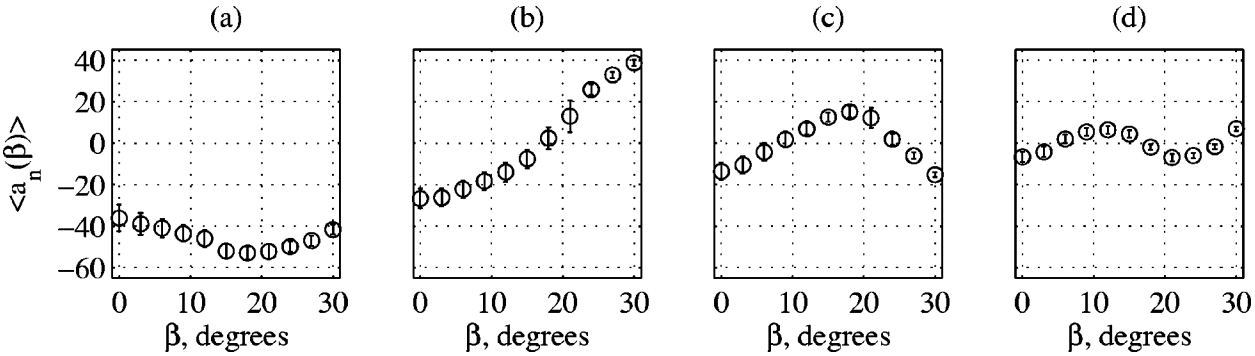

Fig. 8 Phase averaged POD expansion coefficients, $\langle a_n(\beta)\rangle$, for modes (*a*) 0, (*b*) 1, (*c*) 2 and (*d*) 3 at $Re_h=2\times10^4$ and with the extended inlet in place. Error bars indicate the magnitude of the fluctuations, 3σ, in the POD expansion coefficients.

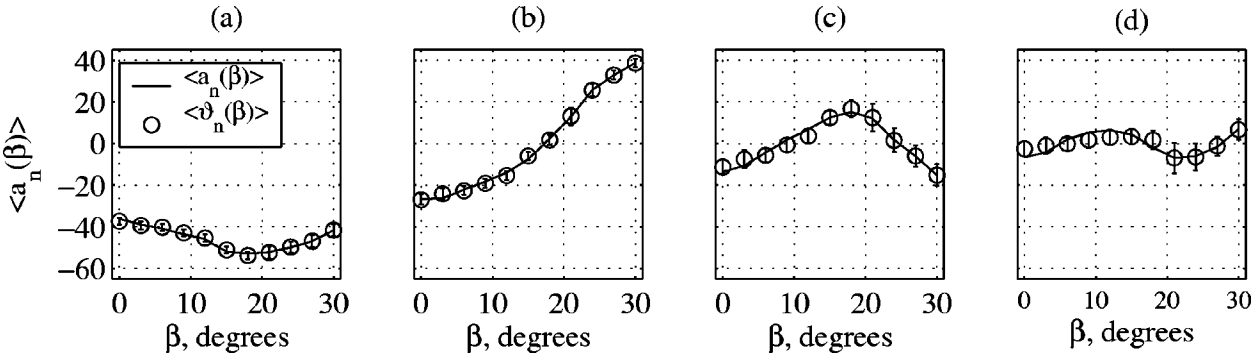

Fig. 9 Comparison of the phase averaged POD and estimated POD expansion coefficients for modes (*a*) 0, (*b*) 1, (*c*) 2 and (*d*) 3 at $Re_h=2\times10^4$. Error bars indicate the magnitude of the fluctuations, 3σ, in the estimated POD expansion coefficients.

interpolating between the various flap angles, the ''composite'' technique uses a single set of eigenfunctions that contains some information about the flow over a range of flap angles. Jorgensen [27] has recently proposed a new analysis technique, referred to as the SPOD, which falls between the ''conditional'' and the ''composite'' approach. The SPOD provides a mechanism to retain important, yet less energetic, structures while varying two flow parameters, e.g. Reynolds number and flap angle.

Figure 5 presents the eignevalue spectra from the ''composite'' technique. For the particular flow investigated, the first four modes capture ≈98% of the mean square energy in the flow. Note that for the results reported here, we ignore the position of the flap in the domain which leads to a negligible amount of spatial leakage (the spatial equivalent to temporal spectral leakage from time series analysis due to different size temporal windows) into the region above the flap.

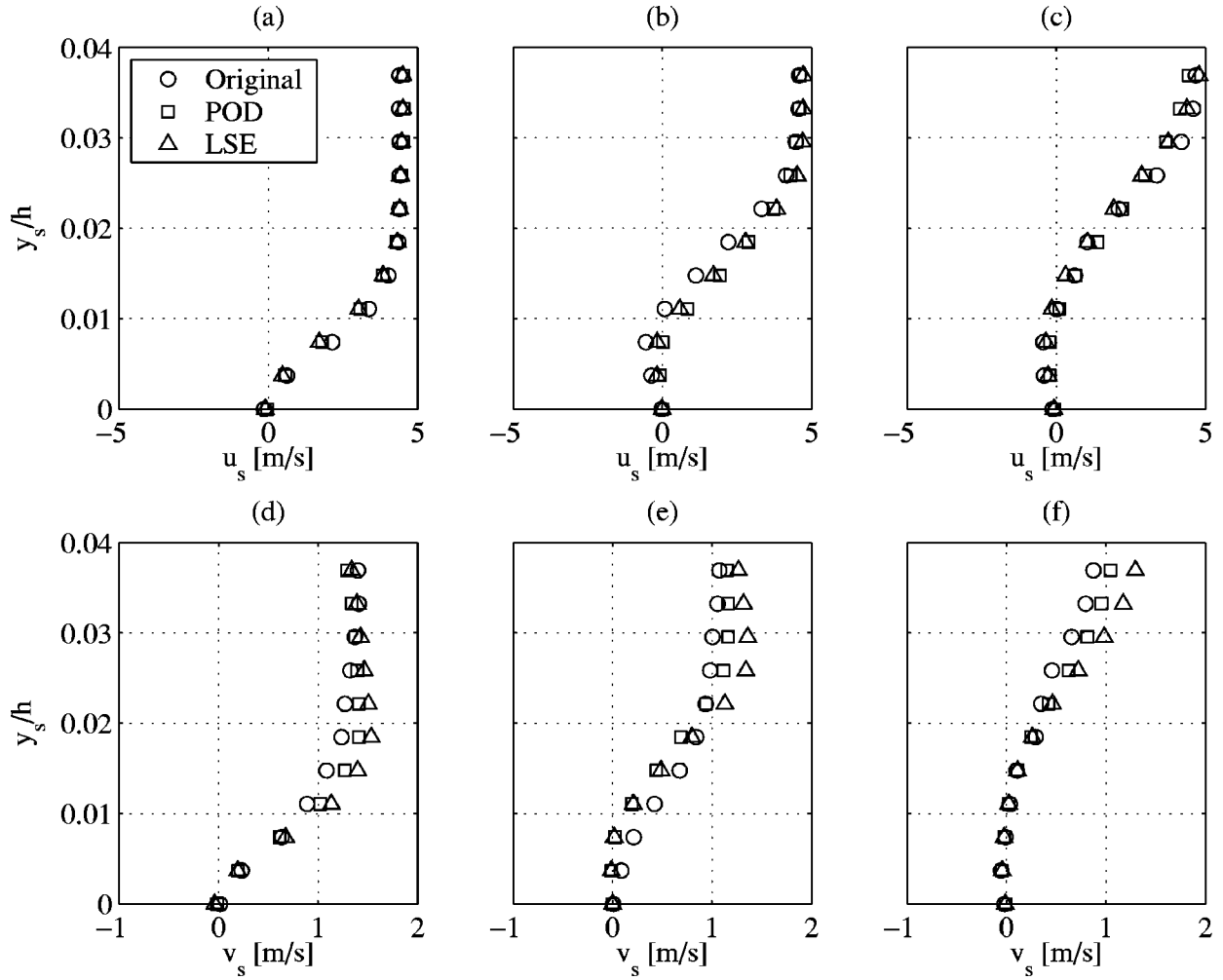

Fig. 10 Comparison of the wall normal velocity profiles on the ramped surface, $u_s(y_s/h)$ and $v_s(y_s/h)$, at (*a*, *d*) $x_s/h=0.34$, (*b*, *e*) $x_s/h=0.67$, and (*c*, *f*) $x_s/h=1.01$ with $\beta=21$ deg and $Re_h=2\times10^4$.

A comparison between the ''conditional'' and ''composite'' POD approaches can be made by comparing the convergence rates, or number of modes required to capture a significant portion of the mean square energy in the flow. Figure 6 was constructed by projecting 512 instantaneous measurements of the flow field at each flap angle onto the ''composite'' eigenfunctions to determine the random coefficients using a normalized form of Eq. (5),

$$\frac{\langle a_n a_n \rangle}{\Sigma_{n=0}^{881} \langle a_n a_n \rangle} \equiv \frac{\lambda^n}{\Sigma_{n=0}^{881} \lambda^n} = \xi_n . \tag{16}$$

Figures 7 and 8 show the first four ''composite'' POD eigenfunctions, and the mean value of the first four phase averaged POD coefficients as a function of flap angle. The 0th POD mode contains the mean flow and the 1st mode appears to serve as switch, or a strong indicator of flow separation. The combination of the first two modes appears to determine the presence of a recirculating region, a fully attached flow, or a state of incipient separation. When the flow is fully attached, $\beta=30$ deg, the coefficient of mode 1 has a positive mean value, with a magnitude approximately equal to the magnitude of mode 0. The product of the mode 1 coefficient and eignefunction result in a flow that travels down the ramp. As the flap is raised, the mode 1 coefficient decays, and at the point of incipient separation the magnitude of the mode 1 coefficient is 0. Continuing to raise the flap, causes the mode 1 coefficient become negative and the flow to travel up the ramp.

The desire to capture the characteristics of the flow without performing any intrusive measurements resulted in the development of the modified LSE. With each image acquired by the PIV system an external analog-to-digital converter, A/D, was triggered. This A/D sampled the surface pressure on the ramp from an array of 22 transducers. This information was used in conjunction with the POD coefficients to compute the modified LSE coefficients as shown in Eq. (15).

Figure 9 shows the first 4 phase-averaged POD coefficients, $\langle a_n(\beta) \rangle$, and the estimated POD coefficients, $\langle \vartheta_n(\beta) \rangle$. The transducers used in this study have a relatively low frequency response and were not expected to resolve any more than the first few modes which correspond to very large scale structures in the flow. The modified LSE approach is capable of resolving the first three POD coefficients (the mean, mode 0, and first two fluctuating modes). Beyond the third mode the transducers are only able to estimate the coefficients prior to the point at which the flow separates, approximately 21 deg.

Figure 10 presents a comparison of wall-normal velocity profiles for the original instantaneous field and the 4 mode POD reconstructions of the field using the phased averaged POD coefficients and the estimated POD coefficients, respectively. After the reconstruction was performed, the velocity fields were rotated and projected, using a bi-cubic interpolation routine, onto a uniform grid defined normal to the ramped surface. Figure 10 demonstrates the ability of the modified LSE technique to estimate the flow field along the length of the ramp using information from a small array of pressure taps and the two point statistics from the flow field. Perhaps more importantly, this method has the potential to provide velocity information from wall measurements which is critical for the flow sensing requirements of future active feedback flow control systems.

6 Summary and Future Work

A series of experiments were performed in the backward facing ramp facility with several different pressure gradients imposed by a flap above the ramp at 3 different Reynolds Numbers and with two different inlet channel configurations using a particle image velocimetry system and surface pressure instrumentation. Statistical POD based low-dimensional descriptions were constructed for a variety of imposed pressure boundary conditions. A comparison was made between a series of low-dimensional descriptions constructed for number of independent states of the flow and a ''composite'' low-dimensional description constructed such that it included information from broad range of flow states. This comparison showed that the use of an ''composite'' low-dimensional description was an advantageous compromise which traded the number of modes required to capture a given percentage of mean-square energy for increased robustness. While a low-dimensional construction for a single specific case required only 1 POD mode to capture 98% of the available energy (including the mean flow), the integrated low-dimensional approach was proven capable of capturing 98% of the energy in any of the cases using only 4 modes. A ''composite'' set of eigenfunctions used as the core of a dynamical systems model may result in much more robust system plants for future flow control investigations. In anticipation of future unsteady work, a technique has been introduced for estimating the instantaneous velocity field using surface pressure measurements and the two-point statistics from the flow field. This tool has been shown capable of estimating the first three POD modes for each of flap angle. It is believed that increasing the sensitivity and frequency response of the pressure instrumentation will likely extend the usable range of this tool to higher POD modes.

Acknowledgments

The authors would like to thank P. Holmes for his suggestion of using the composite (or phase-invariant) POD approach. They would also like to thank J.P. Bonnet, J. Delville, W.K. George, D. Rempfer and L. Ukeiley for insightful discussions on the use of wall pressure as the appropriate variable for estimating the POD coefficients and the general overall approach. Finally, J.A. Taylor would like to acknowledge the NASA Langley Research Center for funding portions of this study through the GSRP program.

References

[1] Taylor, J. A., 1999, ''Development of an 'Activewing' for the Validation of Active Flow Control Schemes to be Applied to the Control of Incipient Separation,'' Master's thesis, Clarkson University, Potsdam, NY, pp. 18–86.
[2] Taylor, J. A., 2001, ''Dynamics of Large Scale Structures in Turbulent Shear Layers,'' Ph.D. thesis, Clarkson University, Potsdam, NY, pp. 22–93.
[3] Taylor, J. A. and Glauser, M. N., 2002, ''Towards Practical Flow Sensing and Control via POD and LSE Based Low-Dimensional Tools,'' ASME FEDSM2002-31416, Montreal, Quebec, Canada.
[4] Lumley, J. L., 1967, ''The Structure of Inhomogeneous Turbulent Flows,'' In Yaglom and Tatarsky, editors, *Atmospheric Turbulence And Radio Wave Propagation*, Nauka, Moscow & Toulouse, France, pp. 166–178.
[5] Berkooz, G., Holmes, P., and Lumley, J. L., 1993, ''The Proper Orthogonal Decomposition in the Analysis of Turbulent Flows,'' Annu. Rev. Fluid Mech., **25**, pp. 539–575.
[6] Jorgensen, BO. H., 1997, ''Application of POD to PIV Images of Flow over a Wall Mounted Fence,'' In Sorensen, J. N., Hopfinger, E. J., and Aubry, N., editors, *IUTAM Symposium on Simulation and Identification of Organized Structures in Flows*, Lyngby, Denmark, pp. 397–407.
[7] Chapman, K. L., 1996, ''Structure Identification within a Transitioning Swept-Wing Boundary Layer,'' Ph.D. thesis, Clarkson University, Potsdam, NY, pp. 102–182.
[8] Chapman, K. L., Reibert, M. S., Saric, W. S., and Glauser, M. N., 1998, ''Boundary-Layer Transition Detection and Structure Identification Through Surface Shear-Stress Measurements,'' AIAA Paper 1998-0782.
[9] Rempfer, D., 2003, ''Low-Dimensional Modeling and Numerical Simulation of Transition in Simple Shear Flows,'' Annu. Rev. Fluid Mech., **65**(35), pp. 229–235.
[10] Eaton, E. L., 1999, ''An Examination of the Azimuthal Variation Using Multi-Point Measurements in the Axisymmetric Sudden Expansion,'' Ph.D. thesis, Clarkson University, Potsdam, NY, pp. 131–185.
[11] Fogleman, M., Lumley, J. L., Rempfer, D., and Haworth, D., 2003, ''Analysis of Tumble Breakdown in IC Engine Flows,'' Phys. Fluids., Killquem.
[12] Boree, J., Maurel, S., and Bazile, R., 2002, ''Disruption of a Compressed Vortex,'' Phys. Fluids, **14**, pp. 2543–2556.
[13] Adrian, R. J., 1977, ''On the Role of Conditional Averages in Turbulence Theory,'' In J. Zakin and G. Patterson, *Turbulence in Liquids: Proceedings of the Fourth Biennial Symposium on Turbulence in Liquids*, Science Press, Princeton, pp. 323–332.
[14] Cole, D. R., Glauser, M. N., and Guezennec, Y. G., 1991, ''An Application of Stochastic Estimation to the Jet Mixing Layer,'' Phys. Fluids, **4**(1), pp. 192–194.

[15] Ukeiley, L. S., Glauser, M. N., and Wick, D., 1993, ''Downstream Evolution of Proper Orthogonal Decomposition Eigenfunctions in a Lobed Mixer,'' AIAA J., **31**(8), pp. 1392–1397.
[16] Bonnet, J. P., Cole, D. R., Delville, J., Glauser, M. N., and Ukeiley, L. S., 1994, ''Stochastic Estimation and Proper Orthogonal Decomposition: Complementary Techniques for Identifying Structure,'' Exp. Fluids, **17**, pp. 307–314.
[17] Delville, J., Lamballais, E., and Bonnet, J. P., 2000, ''POD, LODS, and LSE: Their Links to Control and Simulations of Mixing Layers,'' ERCOFTAC Bulletin, No. 46, pp. 29–38.
[18] Boree, J., 2003, ''Extended Proper Orthogonal Decomposition: A Tool to Analyze Correlated Events in Turbulent Flows,'' Exp. Fluids, **35**, pp. 188–192.
[19] Lumley, J. L., 1970, ''Stochastic Tools in Turbulence.'' Academic Press, New York, NY.
[20] Glauser, M. N., Leib, S. J., and George, W. K., 1987, ''Coherent Structures in the Axisymmetric Jet Mixing Layer,'' In Durst et al., editor, *Turbulent Shear Flows 5*, Springer-Verlag, pp. 134–145.
[21] George, W. K., 1988, ''Insight Into the Dynamics of Coherent Structures from Proper Orthogonal Decomposition,'' In *Symposium on Near Wall Turbulence*, Dubrovnik, Yugoslavia, pp. 16–20.
[22] Moin, P., and Moser, R. D., 1989, ''Characteristic-Eddy Decomposition of Turbulence in a Channel,'' J. Fluid Mech., **200**, pp. 471–509.
[23] Glauser, M. N., and George, W. K., 1992, ''Application of Multipoint Measurements for Flow Characterization,'' Exp. Therm. Fluid Sci., **5**(11), pp. 617–632.
[24] Lumley, J. L., 1981, ''Coherent Structures in Turbulence,'' In R. E. Meyer, *Transition and Turbulence*, pp. 215–242.
[25] Berkooz, G., 1991, ''Turbulence, Coherent Structures, and Low Dimensional Models,'' Ph.D. thesis, Cornell University, Ithaca, NY.
[26] Aubry, N., Holmes, P., Lumley, J. L., and Stone, E., 1988, ''The Dynamics of Coherent Structures in the Wall Region of a Turbulent Boundary Layer,'' J. Fluid Mech., **192**, pp. 115–173.
[27] Jorgensen, H. BO., Sorensen, J. N., and Brons, M., 2003, ''Low-Dimensional Modeling of a Driven Cavity Flow with Two Free Parameters,'' Theoretical Computational Fluid Dynamics, **16**, pp. 299–317.

Measurements of Surface-Roughness Effects on the Development of a Vortex Produced by an Inclined Jet in Cross-Flow

M. I. Yaras[1]
[1]Associate Professor of Engineering,
Department of Mechanical and Aerospace Engineering,
Carleton University,
Ottawa, Canada K1S 5B6

This study examines the effects of surface roughness on the streamwise development of a vortex created by an isolated circular jet injected at 45 deg pitch and 90 deg skew into a crossflow. The study is motivated by the typical surface conditions encountered on in-service turbine blades of gas-turbine engines. Detailed measurements of the velocity field have been performed with a miniature four-wire probe at the jet exit plane, in the oncoming cross-stream boundary layer, and in a series of planes that capture the streamwise development of the vortex in the crossflow boundary layer up to about 15 jet-discharge diameters downstream of the jet. The paper presents the effects of surface roughness on the structure of the dominant streamwise vortex created by the interaction of the inclined jet with the mainstream, and documents the changes in the location, streamwise rate of change of circulation, and streamwise rate of diffusion of this vortex. Through these results, the change in the effectiveness of the vortex in energizing the boundary layer in the presence of surface roughness can be quantified. [DOI: 10.1115/1.1758260]

Introduction

Generation of streamwise vortices along the walls of flow paths, with the objective of manipulating the momentum distribution and/or heat transfer characteristics of the boundary layers developing on these walls, is a well-established practice [1–7]. Such vortices have also been considered for controlling larger scale flow features, such as secondary flows prevailing in curved ducts, to affect the overall total pressure losses and flow distortion levels [8,9].

Conventionally, such vortices are created by vanes or winglets set at an angle of attack relative to the local boundary layer flow. Since such vortex generators create an obstruction in the flow, there is a drag penalty associated with them in off-design operating regimes. This shortcoming has stimulated research in the development of low-profile vortex generators that produce the desired flow control with less drag penalty than their conventional counterparts [6,10,11,12].

An alternative to the solid vortex generators, that potentially does not suffer from parasitic drag, is based on the injection of fluid into the crossflow (main flow) through a hole on the surface. The jet of fluid is injected at a nonzero acute angle relative to the surface (known as the pitch angle), and is skewed relative to local crossflow direction. Complex vortical structures develop in the vicinity of the point of injection of a jet into the crossflow. These include a dominant streamwise vortex, an unsteady wake on the leeward side of the inclined jet, and a horse-shoe vortex wrapped around the jet. The dominant streamwise vortex possesses general features that are similar to those observed downstream of conventional solid vortex generators. The concept of vortex-generator jets (VGJs) was originally proposed by Wallis [13]. VGJs provide for variability in flow control, i.e. their effect can be readily adjusted by varying the jet velocity to meet changes in flow-control requirements, which of course includes the option of turning them off in operating regimes for which flow control is not required. VGJs have been adopted by industry at a rather slow pace since their first introduction by Wallis. This may be partly explained by their higher initial and operating costs in comparison to solid vortex generators. For such costs to be more-than-offset by the performance gains that can be achieved with VGJs through the active nature of this control mechanism, it is essential that the design parameters of VGJs be thoroughly understood.

There have been an increasing number of studies that have contributed to this understanding over the past two decades [14–19]. Through these studies, a number of VGJ design parameters, namely the jet-to-crossflow velocity (momentum) ratio, the pitch and skew angles of the jet, the jet diameter relative to the local boundary layer thickness, and the shape of the jet at discharge have been investigated in considerable detail. In addition to pressure, mean velocity and vorticity fields that have been most often used to study the physics of VGJ flows. More recent efforts have measured the turbulence properties of these flows as well [20,21].

In practical applications, an array of VGJs placed side-by-side can be used to establish flow control over a larger surface segment. Several studies in the published literature have focused on the effect of the lateral spacing of the VGJs on the resultant strength, decay rate and trajectory of the streamwise vortices, and the differences in co- versus contra-rotating vortex arrangements [19,22–25]. For a good summary of vortex-generator-jet studies tailored for boundary-layer separation control, the reader is referred to the review of Johnston [26]. Finally, there are recent efforts that have focused on the use of VGJs for heat transfer control purposes [27,28].

In practice, it is very likely that there will be some level of roughness on the surface over which boundary-layer control is sought through the use of VGJs. For example, the surface roughness on in-service turbine blades in gas-turbine engines can be as large as 300 μm (roughness peak to valley distance), which constitutes a substantial fraction of the boundary layer that is in average about 1mm-thick on smaller (with chord length of $\sim$2cm) blades [29]. Over such surfaces, increases in the streamwise decay and diffusion rates of the vortex produced by the VGJ would be

Contributed by the Fluids Engineering Division for publication in the JOURNAL OF FLUIDS ENGINEERING. Manuscript received by the Fluids Engineering Division October 30, 2002; revised manuscript received December 11, 2003. Associate Editor: A. K. Prasad.

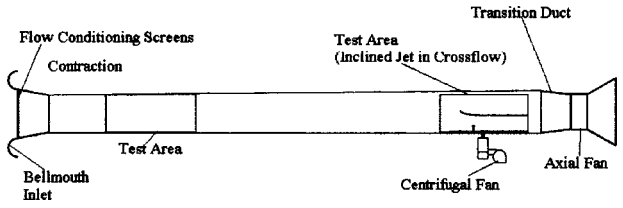

Fig. 1 Wind-tunnel schematic

expected due to increased aerodynamic resistance on the surface and, for roughness that protrudes beyond the wall region of the cross-flow boundary layer, modified turbulence structure of the boundary layer. To the author's knowledge, there does not exist a study in the published literature that has investigated this matter, hence the motivation for the present effort.

Experimental Apparatus

Wind Tunnel. In the planning of the experimental setup, emphasis was placed on the ability to acquire high-resolution and accurate measurements that would not only assist in the exploration of the flow physics but also be suitable as a benchmark for computational-fluid-dynamics studies that are being undertaken concurrently by the author. As such, the size of the isolated jet, hence the thickness of the oncoming cross-flow boundary layer, was chosen to be as large as our facilities permit. In the open-circuit tunnel used for the experiments, air enters through a bellmouth inlet, passes through a honeycomb and three flow-conditioning screens, a contraction of 3.75 area ratio, a 13 m-long section with a cross-section of 168 cm width and 112 cm height at the upstream end, and a cross-section of 168 cm$\times$121 cm at the downstream end, a rectangular-to-circular transition duct, and finally a section that houses the axial fan of the tunnel. The flow path of the tunnel is shown schematically in Fig. 1.

Test Section. The inclined-jet-in-crossflow test section is shown schematically in Fig. 2. It consists of a steel frame of 204 cm length, 167 cm width, and 71 cm height, housing a test surface with a single jet hole and an adjustable ceiling. The frame is sized to occupy the full length and full width of the rear test area in the wind tunnel. The test surface is made of 25.4 mm-thick medium-density fiber board. To allow positioning of the y-z probe traverse gear at multiple streamwise locations, the test surface is split into multiple segments as shown in the figure. Dowel pins are used between these segments to ensure absence of discontinuities in surface elevation at the interfaces, and the interfaces are sealed with tape to prevent leakage during testing. One of the surface

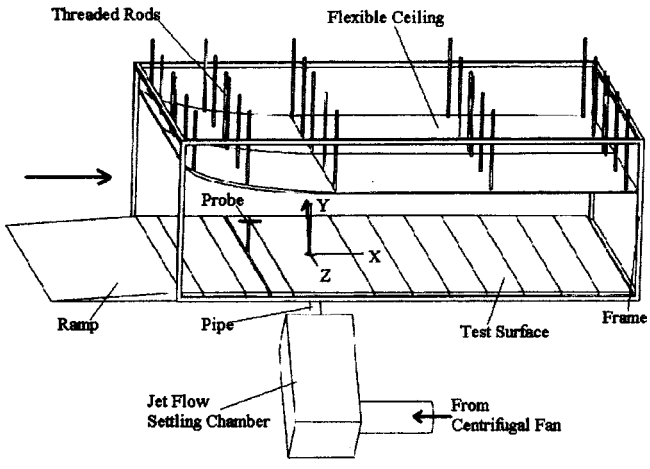

Fig. 2 Schematic of the inclined-jet-in-crossflow test section

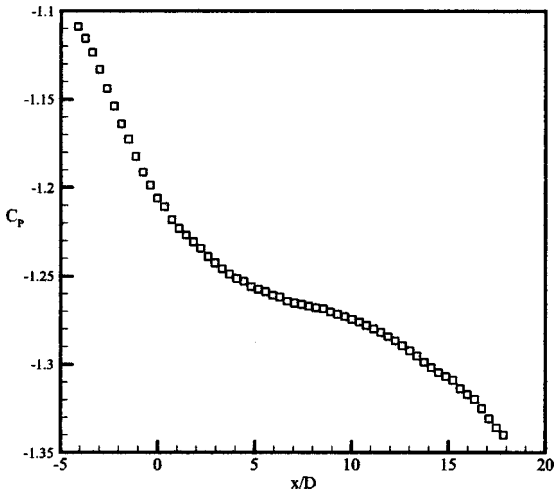

Fig. 3 Test surface static pressure distribution measured at $z/D=0$

segments contains the jet hole, positioned at half span. For the current study, the axis of the hole is oriented at 45 deg from the surface and 90 deg from the longitudinal (x) axis of the test section (i.e., 45 deg pitch and 90 deg skew). A 61 cm-long ramp of 2.4 deg inclination is installed ahead of the test surface leading edge to provide a smooth transition of the flow from the wind tunnel floor onto the test surface. The two-piece adjustable ceiling is made of 7.5 mm-thick fiberboard, and is suspended on a series of threaded rods. The purpose of the adjustable ceiling is to allow manipulation of the streamwise pressure distribution on the test surface. Variation of the streamwise pressure distribution is not part of the test matrix of the current study, hence the ceiling geometry is kept fixed in the shape shown in Fig. 2. As seen in the figure, the front portion of the ceiling provides a slightly converging flow path into the test section. Downstream of this region, the ceiling is kept at a constant distance of 47 cm from the test surface. For the present study, the jet hole center is positioned 67.3 cm (about $10D$) downstream of the leading edge of the ceiling, which places it right at the end of the converging section of the flow path. The static pressure distribution on the test surface in absence of a jet flow, measured with surface pressure taps along the test section centerline ($z=0$), is given in Fig. 3. The pressure coefficient, C_P, is obtained by referencing the surface static pressure to the free-stream stagnation pressure measured at ($x=-6.27D$, $y=3.66D$, $z=0$), and normalizing it by the dynamic pressure at that location. The stagnation and dynamic pressures at this reference location were measured with a pitot static probe. The freestream is noted to accelerate most rapidly up to $x=0$ where the ceiling levels off, with milder acceleration occurring beyond this point, caused by the streamwise growth of boundary layers on the ceiling, the test surface, and the test section side walls. The overall streamwise acceleration of the freestream from $x=-4D$ to $x=18D$ is noted to be 10 percent of the free-stream velocity at the reference location.

The airflow for the jet is supplied by a 5 hp centrifugal fan. Upon discharge from the fan, the air is diffused into a 28 cm $\times$28 cm$\times$60 cm stagnation chamber through a 15.6 cm-diameter basket diffuser. Halfway through this stagnation chamber, the air is passed through a layer of honeycomb, and then is accelerated into a galvanized steel pipe of 68.26 mm inner diameter (D) and 55 cm ($\sim 8D$) length through a bellmouth. The downstream end of this pipe is flanged to the MDF board forming the test surface, yielding a seamless transition from the pipe to the hole in the test surface. The centrifugal fan is operated at a constant speed. The jet velocity is manipulated by blocking the flow at the inlet of the fan with multiple layers of furnace filter. The layers of filter are

placed in a wire cage that attaches to the inlet of the fan, and the extent of flow blockage is controlled by adjusting both the number of filter layers and the amount of compression of these layers.

The measurement of the vortex development behind the inclined jet is performed both on a smooth test surface and on a surface populated with roughness elements. For the rough-surface configuration, the roughness elements consist of 25.4 mm ($\approx 0.372D$) diameter cylinders of 25.4 mm height. The elements are placed at 50.8 mm intervals (center-to-center) in spanwise (z) rows. These rows are placed 50.8 mm apart (center-to-center) in the streamwise (x) direction in a staggered pattern, covering an area extending from $x=2.79D$ to $x=21D$ over the full width of the test surface. The chosen roughness height is 1/6th of the thickness of the crossflow boundary layer measured at $x/D=-2$. This is compatible with the roughness-to boundary-layer-thickness ratios encountered on small turbine blades in gas-turbine engines, as compiled by Bons et al. [29].

Instrumentation. The primary sensor used to measure the 3-D velocity and turbulence fields throughout the test section is a miniature four-wire probe, controlled by a four-channel constant-temperature anemometer, both of which have been developed in-house. The four tungsten hot-wire sensors on the probe (each of 1.0 mm length and 5-micron diameter) are oriented at about 45 deg relative to the probe axis and are circumferentially positioned at 90 deg from each other to form the shape of a pyramid [30,31]. The four sensors collectively form a measurement volume of about 2 mm diameter. This volume is quite small compared to that of most commercial three- or four-wire probes, hence allows measurement of the flow with high resolution. The choice of four sensors instead of three was made to increase the range of flow misalignments for which the flow direction can be determined uniquely. Through measurements in the near field of a free jet, Lavoie and Pollard [31] have shown the four-wire probe to yield mean-flow and Reynolds stress information of accuracy comparable to that of conventional cross-wire probes. In the present work, calibration of the probe is based on the method of directional sensitivity functions, described by Dobbeling et al. [30], which has been demonstrated to be more accurate than alternative methods [31]. The directional sensitivity functions are determined through calibration of the probe on a probe-calibration apparatus with motorized motion in pitch and yaw. The flow direction is varied in 5 deg increments up to 45 deg of misalignment relative to the probe axis. Several sets of values are obtained for these functions over a flow velocity range varying from 5 m/s to 15 m/s, to cover the approximate velocity range anticipated in the experiments. The Reynolds number sensitivity of the directional sensitivity functions was found to be small within this range. The angular calibration was repeated regularly throughout the experiments to monitor for any possible changes in the sensor geometry that may occur accidentally during handling of the probe. Although the angular calibration of the probe should not change unless the sensor geometry is modified, the velocity calibration of each of the four sensors is prone to relatively rapid changes, primarily due to drift in the conditioning (analog signal amplification and offset) circuitry of the constant-temperature anemometer. For this reason, the velocity calibration, performed with the probe axis aligned to the flow direction in the probe calibration apparatus, was repeated frequently throughout the experiments. Based on the combined uncertainties of the angular and velocity calibrations of the probe (slight changes in the calibration curves between probe recalibrations; interpolation errors associated with the velocity calibration curves and directional-sensitivity calibration surfaces) the velocity magnitude and direction measured with this probe are judged to be within 2% and ± 1.5 deg of the actual values. For flow misalignments greater than about 30 deg relative to the probe axis, the uncertainty in the flow direction is closer to ± 2.5 deg. These uncertainties were estimated based on the procedure described by Moffat [32]. In this procedure, first the repeatability of the mean velocity and flow direction measurements was established at a range of locations within the VGJ flow field. These error estimates in velocity magnitude and flow direction were then combined with the uncertainty generated by the biquadratic interpolation scheme used in conjunction with the angular calibration surfaces, the 9th-order least-square interpolation curves used in conjunction with the velocity calibration data, and the variations in the angular and velocity calibration of the probe between calibration updates. The estimated uncertainties for the mean velocity magnitude and flow direction are noted to be consistent with those established by Lavoie and Pollard [31].

During the experiments, the effective cooling velocities of the four wire sensors are non-dimensionalized by the reference velocity at ($x=-4.44D$, $y=4.39D$, $z=0.0$). Prior to the measurements with the 4-wire probe, this reference velocity is correlated against the difference between two pressures, measured on the contraction of the tunnel with an MKS™ differential pressure transducer of +/-10 torr range. In order to correct the hot-wire signals for temperature variations as per the procedure described by Bearman [33] (typically a few degrees Celsius over the course of each test run), the temperature of the flow in the test section is measured with a thermocouple.

Data Acquisition. The signals from the four wires of the probe, the reference pressure difference, and the flow temperature are simultaneously sampled with an Analog Devices RTI-834L data acquisition card interfaced with a sample-and-hold amplifier. The system utilizes a 12-bit A/D converter. Although transient measurements are not intended for the reference temperature and reference pressure, these quantities are sampled together with the hot-wire signals at the same rate to simplify the structure of the data records. The hot-wire signals are low-pass analog filtered with a cut-off frequency that is set to half of the sampling rate.

At each measurement position of the four-wire probe, 18 cycles of measurements are acquired, with each sampling cycle consisting of 4,096 samples measured at a rate of 6,000 Hz. This sampling rate and total sample count have been verified to be adequate for statistical convergence of the mean velocity and turbulence data.

Measurement Locations and Traverse System. The first measurement plane is located at $x=-5.5D$ and is used to document the state of the oncoming mainstream boundary layer. The second measurement plane, located at $x=-2D$ establishes the extent of change in this boundary layer due to the contraction of the mainstream as it enters the test section. Five measurement planes located at $x=4.5D$, $7.5D$, $10D$, $13D$ and $15.5D$ are used to document the downstream development of the dominant vortex generated by the inclined jet. All of the measurement planes extend from $z=-6.74D$ to $z=3.52D$ laterally, and up to $y=4.54D$ from the test surface. These dimensions are larger than those that would be required to completely capture the vortex laterally and the full thickness of the cross-flow boundary layer. This was done to document the overall flow field in the test section, ensuring absence of any anomalies in the form of nonuniformity of the freestream or boundary layer properties along the width of the test section. To emphasize the flow field associated with the vortex, only a portion of these measurement planes will be presented herein. In each measurement plane, the first and second measurement points off of the test surface are located $y=6.6$ mm ($\sim 0.1D$) and $y=10$ mm, respectively. The next 14 measurement points in the y direction are spaced 10 mm apart, followed by 8 points of 20 mm spacing. In the lateral (z) direction, the spacing of measurement points is kept uniform at 10 mm. These spacings result in close to 1,700 measurement locations in each plane. For the case with surface roughness, the distribution of the measurement points in the y direction is adjusted such that the first point is located 6.6 mm above the top of cylinder-shaped roughness elements of 25.4 mm height. The four-wire probe is traversed in each measurement plane with its axis oriented longi-

tudinally, i.e. aligned with the x coordinate direction. The sensor wire configuration on the probe combined with the chosen calibration procedure allows reliable use of the probe for flow misalignments of up to 35 deg relative to the probe axis. The first measurement plane downstream of the inclined jet is placed at $x = 4.5D$, which has been found to be sufficiently far from the location of the jet discharge to yield flow angularity that remains within the calibration range of the probe when it is traversed as noted.

To document the flow conditions in the jet as it discharges from the test surface, the 4-wire probe is traversed parallel to the test surface with its axis aligned with the axis of the jet. The measurement grid is shaped elliptically to match the shape of the exit hole, and the jet is traversed slightly above the test surface ($y = 0.044D$) to allow the extension of the measurement grid to cover the complete cross section of the jet without probe/wall interference difficulties. Measurement points are slightly clustered towards the perimeter of the hole where larger gradients in the velocity distribution are anticipated. The measurement grid contains a total of 227 points.

All measurement planes are traversed with a gear that provides motorized motion of the probe in the y and z directions. The traverse gear is mounted to the test surface from below, and the probe is attached to a stem that protrudes through the test surface. As shown in Fig. 2, one of the test-surface segments contains a slot extending in the z direction to accommodate the probe stem. The probe position and its orientation relative to the reference axes are estimated to be accurate to within 0.2 mm and 0.1 deg, respectively.

Experimental Results and Discussion

The four-wire measurements of the present experiments have produced both mean-flow and turbulence information. Herein, the discussion of the effects of surface roughness on the flow field downstream of the inclined jet is based on the 3-D mean-velocity and vorticity fields. The turbulence field and its interaction with the mean-flow field will be presented in a follow-up paper.

Inclined Jet Discharge and Upstream Cross-Flow Conditions. The jet velocity field at discharge from the test surface is shown in Fig. 4*a*. In this plot, the velocity component aligned with the centreline of the jet, V_{x_j}, is shown as flood contours, and the secondary-flow motions perpendicular to the jet centreline are shown in vector format. The magnitude of the area-averaged velocity, $\overline{V}_{x_j}$, is shown as a vector to provide a reference for the magnitude of secondary-flow motions, thereby giving a sense for the angularity of the flow. Considerable axial-flow nonuniformity (25% to 135% of $\overline{V}_{x_j}$) is noted over the cross-section of the jet, with the axial velocity peaking on the leeward side with respect to the mainstream crossflow, biased towards the upper side of the jet relative to the test surface. The distribution of turbulence intensity is given in Fig. 4*b*. For most of the jet flow, the turbulence intensity averages to about 3.5%. On the windward side, interaction of the jet with the cross-flow is observed to yield high levels of turbulence. For reference, the jet flow in absence of crossflow was measured to consist of a core of uniform velocity, surrounded by a thin boundary layer along the perimeter, with 3.5% turbulence intensity in the core.

The observed distribution of axial velocity in the jet is related to the variation of static pressure along the perimeter of the jet at discharge. On the windward side, the pressure is expected to be relatively high due to deceleration of the mainstream cross-flow in that region, as it encounters the jet. As the mainstream makes its way around the inclined jet, it is expected to experience greater acceleration over the upper side of the jet, since on the lower side larger viscous forces would be present due to closer proximity of the flow region to the test surface. Consequently, the static pressure along the jet perimeter is expected to be relatively the lowest along the upper-leeward side, and the highest along the windward

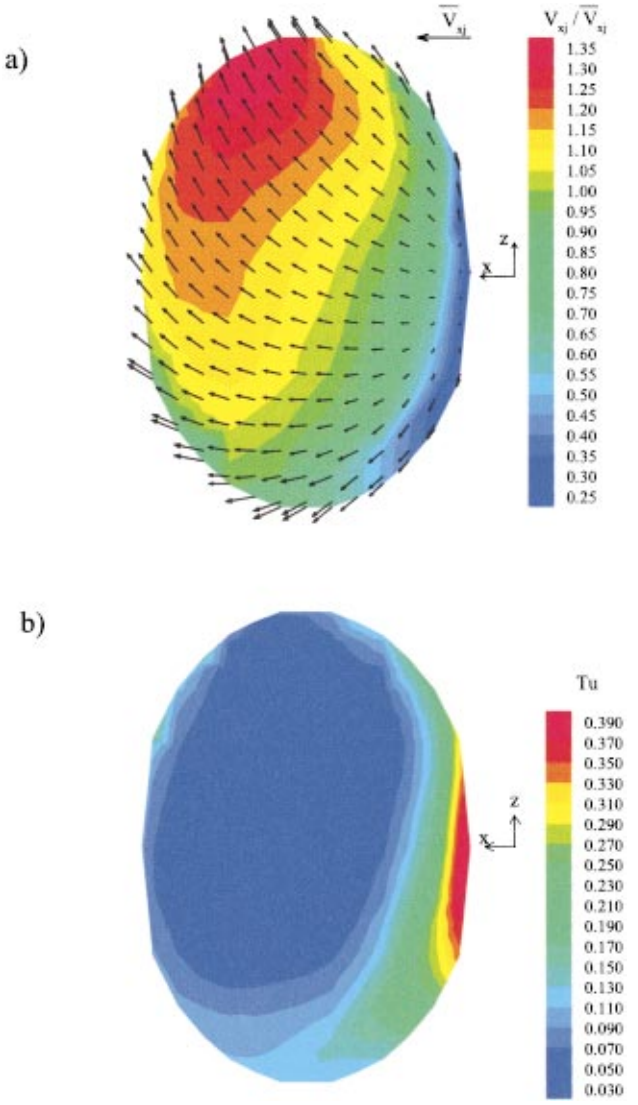

Fig. 4 ***a*) Velocity and *b*) turbulence intensity fields at jet discharge (uncertainties: ±2% for the velocity magnitude and ±1.5 deg. for the flow direction)**

side. The cross-flow motion within the jet shown in Fig. 4*a* is consistent with such spatial variation of static pressure. As mentioned earlier, the jet stream is produced by accelerating air from a settling chamber into a short pipe through a bellmouth. This design ensures close-to-uniform stagnation pressure distribution across the jet stream. Consequently, any nonuniformity in the axial velocity distribution observed at the jet discharge plane is expected to be due to differences in the amount of acceleration the jet fluid experiences, which in turn is caused by spatial variations in the static pressure ''boundary condition'' imposed on this fluid at the discharge plane. The spatial distribution of axial velocity in Fig. 4*a*, in relation to the expected static pressure distribution along the jet perimeter in this plane described above, is consistent with this argument.

The area-averaged axial velocity of the jet is calculated to be equal to 1.22 V_{ref}, where V_{ref} is the reference velocity measured in the freestream at $x/D = -4.44$, as described earlier. The jet flow Reynolds number based on the jet discharge diameter and the area averaged jet velocity is 46,400. The converging shape of the test-section ceiling (Fig. 2) results in slight acceleration of the freestream upstream of the location of jet discharge. This acceleration is measured to yield a post-acceleration freestream veloc-

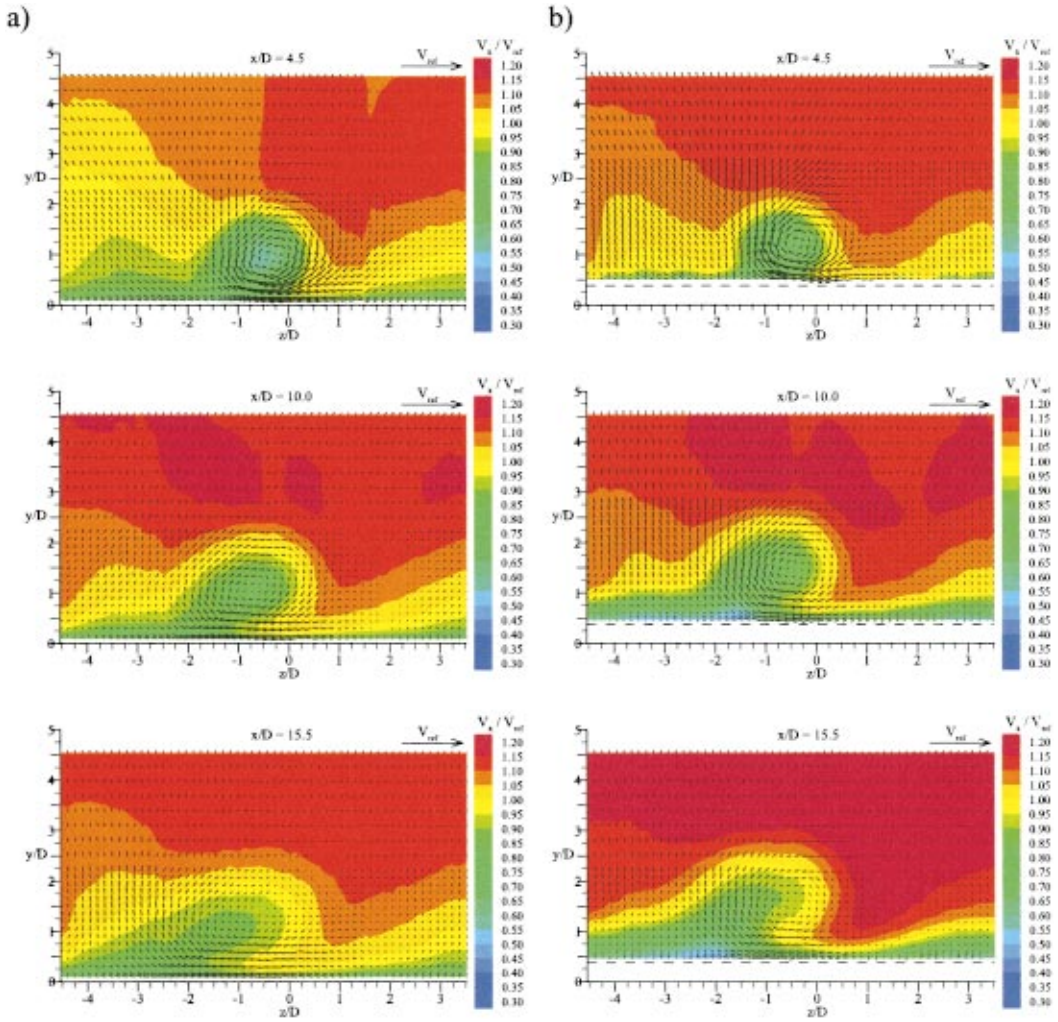

Fig. 5 Velocity field of the vortex produced by the inclined-jet/cross-flow interaction for smooth (*a*) and rough (*b*) surfaces (uncertainties: ±2% for the velocity magnitude and ±1.5 deg. for the flow direction)

ity that is 11% greater (as measured at $x/D=-2$) than the reference velocity. As a result, the jet-to-mainstream velocity ratio, based on the spatially-averaged jet axial velocity and the freestream cross-flow velocity at $x/D=-2$, is equal to 1.1. This, together with the present δ/D value of about 2.2, is a typical configuration when the vortex generated by the inclined jet is intended for boundary-layer control.

The mainstream cross-flow boundary-layer conditions upstream of the jet-discharge location were quantified through hot-wire measurements at $x/D=-2$ and $x/D=-5.5$. At $x/D=-2$, the displacement and momentum thicknesses, normalized by the diameter of the jet at discharge, D are determined to be 0.095 and 0.07, respectively. These values correspond to $z/D=0$, i.e. the lateral position of jet discharge. The variations in these integral quantities from $z/D=-4.5$ to 3.5 are within $\pm 10\%$, confirming the presence of a fairly 2-D cross-stream boundary layer. The resultant shape factor of the boundary layer is 1.36. This is slightly lower than the value of 1.4 prevailing at $x/D=-5.5$, due to the acceleration of the flow between these streamwise locations. The Reynolds number based on the momentum thickness and the free-stream velocity at $x/D=-2$ is 2600, and the boundary layer thickness is about $2.2D$.

Downstream Development of Velocity and Vorticity Fields. The velocity field in selective mainstream measurement planes for the smooth- and rough-surface cases, as viewed from upstream, is shown in Fig. 5. In the figure, the x-component of velocity, normalized by V_{ref} is shown as flood contours, and the in-plane velocity components are given as vectors. V_{ref} is also shown as a vector to provide a visual reference for the cross-flow velocity components.

The smooth-surface results appearing in the first column of the figure indicate that the inclined jet has completed its roll-up into a vortex by $x/D=4.5$. The interaction between the inclined jet and the mainstream leading to this single dominant vortex is fairly complex, as described by Barberopoulos and Garry [18] among others. The boundary-layer-energizing effect of the vortex is clearly visible in the figure, with the high-momentum fluid at some distance from the surface being convected towards the surface along the downward-sweeping side of the vortex. A similar effect on the axial-flow distribution is noted up to the last measurement plane at $x/D=15.5$, although the well-defined circular cross-flow pattern visible in the upstream measurement planes is no longer as distinct in this plane. Plots of the x-component of vorticity, given in Fig. 6, support these observations. The range of these plots is limited to vorticity of positive sign to yield a clearer illustration of the spatial extent of the streamwise vortex in question. It is noted that up to $x/D=10$, the vorticity field associated with this vortex maintains a near-circular perimeter. While the vortex is subjected to turbulent diffusion by the surrounding boundary layer fluid of the mainstream flow, its diffusion is also

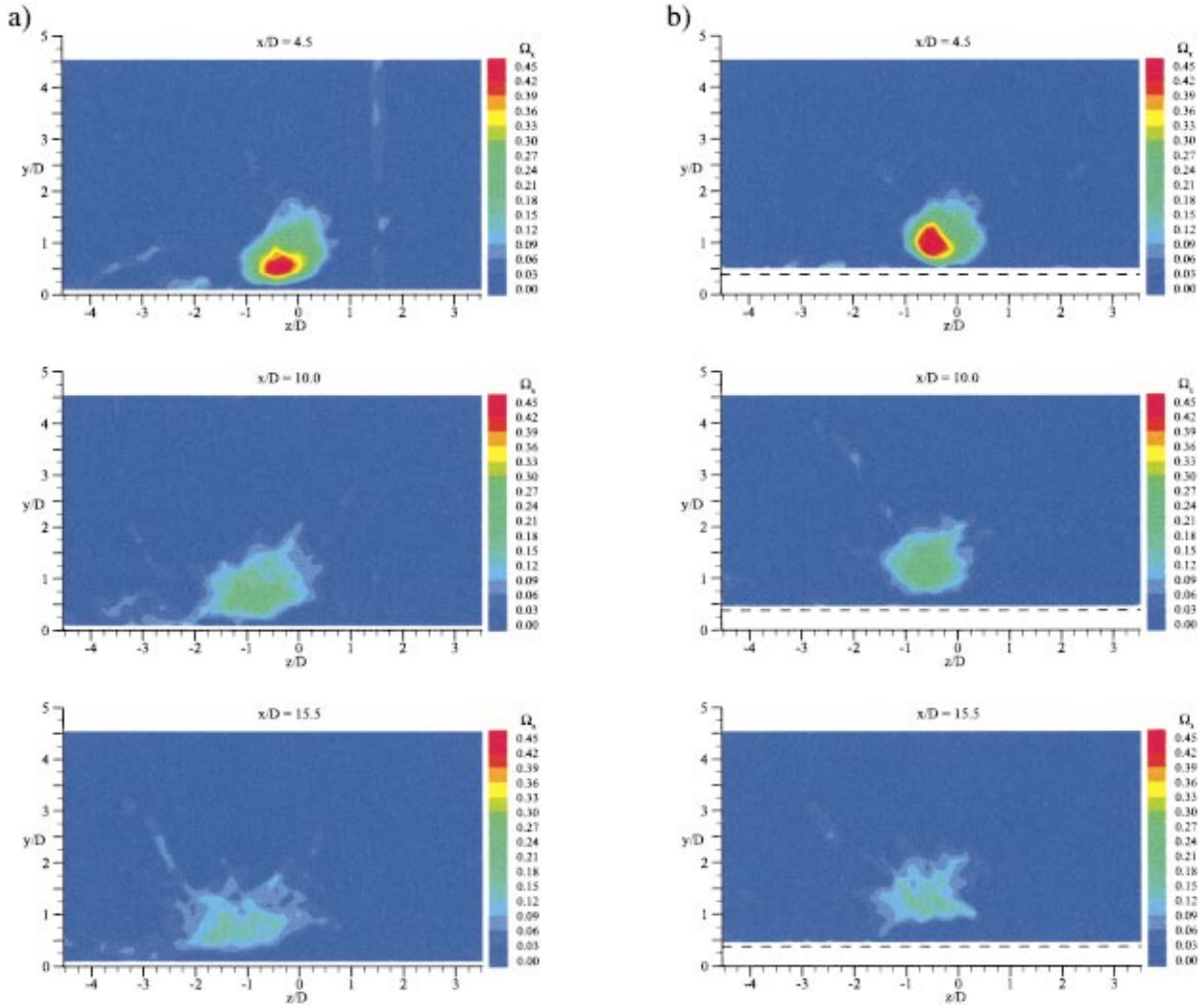

Fig. 6 Streamwise positive vorticity field of the vortex produced by the inclined-jet/cross-flow interaction for smooth (*a*) and rough (*b*) test surfaces (uncertainty in streamwise vorticity = ±0.02)

affected by its close proximity to the surface. Close proximity of the vortex to the surface results in the production of a cross-stream shear layer beneath the vortex, which separates from the surface on the upsweep side of the vortex. This shear layer and its 3-D separation affect the local turbulence field, hence the rate of diffusion of the vortex. Furthermore, cross-stream acceleration of the fluid near the surface results in the production of vorticity of opposite sign beneath the vortex. This vorticity accumulates in the lower portion of the upsweep side of the vortex as shown in Fig. 7 for the first mainstream measurement plane downstream of the inclined jet. Presence of this region of negative vorticity is responsible for the reduction of the circulation of the vortex with downstream distance. The rate of this decay is presented in the next section. Additionally, the region of negative vorticity is expected to induce a velocity on the vortex, which tends to move the vortex away from the surface. This effect is noted by comparing the

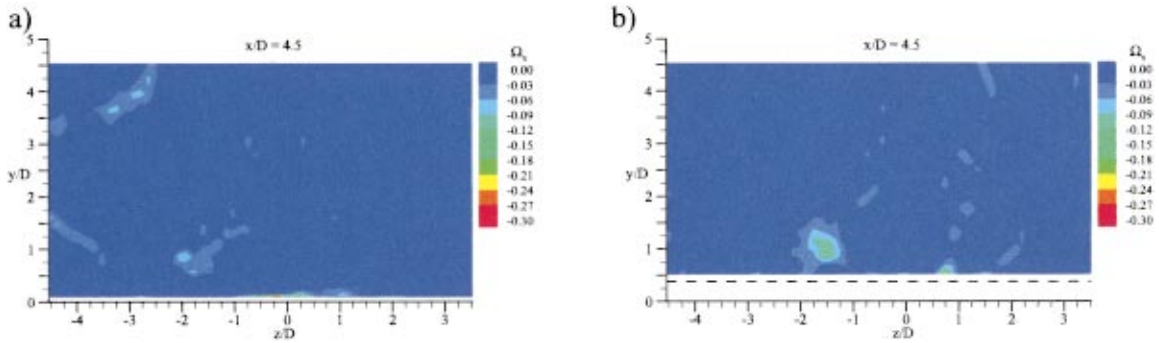

Fig. 7 Streamwise negative vorticity produced on the test surface by the vortex with smooth (*a*) and rough (*b*) surfaces (uncertainty in streamwise vorticity = ±0.02)

proximity to the surface of the region of positive vorticity associated with the vortex in each of the measurement planes shown in Fig. 6.

The discussion thus far has focused on the velocity and vorticity fields for the smooth test-surface case. The effect of roughness on these fields is observed by comparing the plots in the right columns of Figs. 5–7 to those in the left column of these figures. The horizontal dashed line on the plots for the rough-surface case represents the location of the top of the cylindrical roughness elements. The axial-velocity flood contours give the appearance of a somewhat more effective vortex in energizing the boundary layer for the rough-surface case. This is a misleading observation caused by a shift in the color bands of the flood plots between the smooth and rough-surface cases. This shift is due to the freestream axial velocity being slightly ($\sim 5\%$) higher across the test section with the rough surface, caused by the greater rate of growth of the mainstream boundary layer with downstream distance. The extent of cross-stream motion driven by the vortex is somewhat weaker in the presence of surface roughness, implied by the smaller region of positive vorticity at all streamwise positions in Fig. 6. Although the spatial extent of this vorticity field is smaller with the rough surface, the magnitude of vorticity within this region is very similar for the smooth and rough surfaces at all streamwise locations. This is consistent with the fact that presence of roughness on the test surface is expected to alter the turbulence field along the lower portion of the vortex, and the amount of vorticity of opposite sign produced between the vortex and the surface, both of which act along the perimeter of the vortex in affecting its diffusion and decay rates. Finally, the trends in Fig. 7 suggest production of larger amount of vorticity of negative sign on the rough surface under the influence of the cross-flow motion driven by the vortex. This, in turn, causes a larger displacement of the vortex away from the surface (even with reference to the top rather than base of the roughness elements) with downstream distance.

In the case of the smooth test surface, at streamwise locations corresponding to $x/D=4.5$, 10 and 15.5, the streamwise vortex is observed to be centered at $z/D=-0.35$, -0.6 and -0.6, respectively. For the rough-surface case, in the same measurement planes the vortex is centered at $z/D=-0.3$, -0.45 and -0.45. Considering its sense of rotation, the vortex is expected to migrate in the negative z direction with downstream distance, judged on the basis of the velocity induced on this vortex by its hypothetical mirror image below the test surface. Such consideration of an image vortex, as per inviscid-flow theory, ensures that the no-through-flow condition of the surface is satisfied mathematically. In reality, presence of viscous forces resulting from the no-slip condition yield lateral migration rates lower than those predicted by inviscid flow theory, mostly because of the reduction in the circulation of the vortex during its streamwise development. In the case of the rough test surface of the present study, the larger streamwise decay rate of the vortex caused by greater viscous forces is therefore one of the factors responsible for the reduced lateral migration of the vortex in this instance. A second factor responsible for this trend is the fact that the vortex is placed farther away from the test surface when roughness is present. This increases the distance of the vortex from its hypothetical image, thereby reducing the magnitude of the mutually induced lateral velocity in an inviscid sense.

Streamwise Decay of the Vortex. The streamwise variation of circulation, Γ, associated with the dominant streamwise vortex created by the interaction of the inclined jet with the mainstream cross-flow is shown in Fig. 8. In the calculation of circulation in each measurement plane, integration of the x-component of vorticity is performed only over the portion of the measurement plane occupied by the vorticity field of this vortex. This ensures that the resultant circulation values are not affected by the contribution of low-level vorticity (within the uncertainty range) over the remainder of the measurement plane. At $x/D=4.5$, the circulation of the

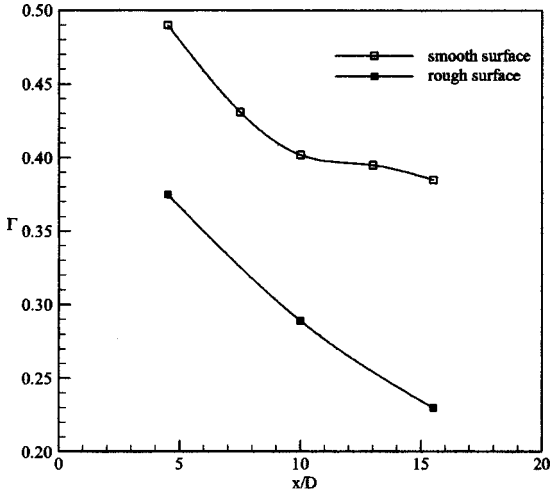

Fig. 8 Streamwise variation of circulation

vortex is noted to be substantially lower with the rough test surface. The rough portion of the test surface starts at $x/D=2.8$, hence the difference in the Γ values noted at $x/D=4.5$ is caused by the effect of the roughness elements on the vortex development over a rather short streamwise distance of $1.7D$. This observation is particularly interesting in view of the very similar decay rates of the vortex between $x/D=5$ and ~ 8 for the smooth- and rough-surface cases. When the vortex first encounters the roughness elements, its proximity to the test surface would be the same as with the smooth surface. As a result, the roughness elements would initially penetrate deeper into the core of the vortex than is the case farther downstream, where the vortex is centered farther away from the surface when roughness elements are present (Figs. 5, 6). This may explain the apparent higher rate of decay of the vortex upstream of $x/D=4.5$ when the test surface is rough. Beyond $x/D\approx 8$, the decay rate of the vortex is noted decrease with the smooth surface, whereas the decay rate remains nearly constant between $x/D=4.5$ and the last measurement location of $x/D=15.5$ when roughness is present. This highlights the effect of roughness on the generation of counter-sign vorticity on the surface beneath the vortex.

Despite the notable differences in the circulation of the streamwise vortex in its early stages of development with smooth and rough surfaces, and the effect of roughness on the streamwise rate

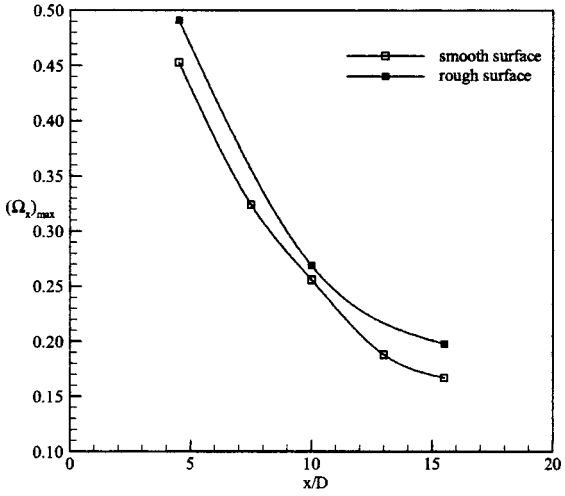

Fig. 9 Streamwise variation of maximum vorticity in the core of the vortex (uncertainty in streamwise vorticity $=\pm 0.02$)

of change of circulation, the peak streamwise vorticity measured at the center of the vortex, $\Omega_{x_{max}}$ is noted to be very similar for the two cases, as shown in Fig. 9. Although a slightly larger value of $\Omega_{x_{max}}$ is observed for the rough-surface case at all streamwise locations, this difference is very close to the estimated uncertainty in Ω_x. The differing trends in $\Omega_{x_{max}}$ and Γ is explained by the fact that the counter-sign vorticity generated between the vortex and the surface affects the vortex along its perimeter, hence streamwise decay of the vortex progresses radially inwards. The fact that the variation of $\Omega_{x_{max}}$ with streamwise distance is not sensitive to surface roughness even at $x/D=15.5$ suggests that at this streamwise position the diffusion of the vortex core continues to be driven by local turbulence and viscous stresses, unaffected by the decay mechanisms in effect along the perimeter of the vortex. Finally, the fact that the $\Omega_{x_{max}}$ values in the vortex core are very similar at $x/D=4.5$ for the smooth and rough surfaces may suggest that the formation (roll-up) of the vortex is already complete or nearly so as it first encounters the roughness elements at $x/D=2.8$.

Conclusions

The paper presents the results of an experimental study examining the effects of surface roughness on the streamwise development of a vortex created by an inclined jet in crossflow. It is shown that surface roughness affects the circulation of this vortex primarily in its early stages of development, with a relatively smaller effect on the rate of decay beyond about 5 jet diameters of streamwise distance. The vortex is observed to be positioned further away from the test surface in the presence of roughness, which in turn influences its location laterally. Despite the difference in the streamwise rate of change of circulation for smooth and rough surface conditions, the peak streamwise vorticity in the vortex is observed to remain unaffected by the roughness of the surface up to the last measurement location 15.5 jet diameters downstream of the jet discharge. This observation is shown to be consistent with the physical mechanism through which roughness is expected to affect the decay and diffusion of the vortex. The study has also highlighted the effect of the nonuniform static pressure distribution in the jet discharge plane, that results from the interaction of the crossflow and the jet stream, on the axial velocity distortion in the jet stream.

Acknowledgments

The author acknowledges the research grant of the Natural Sciences and Engineering Research Council of Canada in support of this project. The assistance of J. Sliwka, A. Proctor and S. Graveline in the construction of the test section, and of G.L. Davis in the preparation of Figs. 1 and 2 is also acknowledged.

Nomenclature

C_p = static pressure coefficient
D = diameter of the circular jet exit hole, measured perpendicular to the jet axis
Tu = turbulence intensity
V = local flow velocity, normalized by V_{ref}
$\overline{V}$ = area-averaged velocity
V_{ref} = reference velocity measured at $x=-4.44D$, $y=4.39D$, $z=0$
x, y, z = cartesian co-ordinates; refer to Fig. 2
Ω = vorticity, normalized by D and V_{ref}
Γ = circulation, normalized by D and V_{ref}
δ = cross-flow boundary layer thickness

Subscripts

ref = reference quantity measured at $x=-4.44D$, $y=4.39D$, $z=0$
x = component in the x direction
x_j = component aligned with the axis of the inclined jet at discharge

References

[1] Schubauer, G. B., and Spangenburg, W. G., 1960, "Forced Mixing in Boundary Layers," J. Fluid Mech., **8**, pp. 10–31.
[2] Pearcey, H. H., 1961, "Shock Induced Separation and Its Prevention," *Boundary Layer and Flow Control*, **2**, Pergamon, New York, pp. 1170–1344.
[3] Spangler, J. G., and Wells, C. S., 1964, "Effects of Spiral Longitudinal Vortices on Turbulent Boundary Layer Skin friction," NASA Contract Report 145.
[4] Shabaka, I. M. M. A., Mehta, R. D., and Bradshaw, P., 1985, "Longitudinal Vortices Embedded in Turbulent Boundary Layers, Part 1. Single Vortex," J. Fluid Mech., **155**, pp. 37–57.
[5] Pearcey, H. H., Rao, K., and Sykes, D. M., 1993, "Inclined Jets Used as Vortex Generators to Suppress Shock-Induced Separation," AGARD-CP-534, Computational and Experimental Assessment of Jets in Crossflow.
[6] McCormick, D. C., 1992, "Shock-Boundary Layer Interaction Control with Low Profile Vortex Generators and Passive Cavity," AIAA Paper No. 92-0064.
[7] Zhang, X., and Collins, M. W., 1993, "Flow and Heat Transfer in a Turbulent Boundary Layer through Jets," AIAA J., **31**(**9**), pp. 1590–1599.
[8] Reichert, B. A., and Wendt, B. J., 1993, "An Experimental Investigation of S-Duct Flow Control Using Arrays of Low Profile Vortex Generators," AIAA Paper No. 93-0018.
[9] Anderson, B. H., and Gibb, J., 1998, "Vortex-Generator Installation Studies on Steady-State and Dynamic Installation," J. Aircr., **35**, pp. 513–520.
[10] Wendt, B. J., and Hingst, W. R., 1994, "Measurements and Modeling of Flow Structure in the Wake of a Low Profile Wishbone Vortex Generator," AIAA Paper No. 94-0620.
[11] Rao, D. M., and Kariya, T. T., 1988, "Boundary-Layer Submerged Vortex Generators for Separation Control-An Exploratory Study," AIAA Paper No. 883546-CP.
[12] Ashill, P. R., Fulker, J. L., and Hackett, K. C., 2002, "Studies of Flows Induced by Sub Boundary Layer Vortex Generator," AIAA Paper No. 2002-0968.
[13] Wallis, R. A., 1952, "The Use of Air Jets for Boundary Layer Control," Aerodynamics Research Labs, Aero. Note 110 (N-34736), Melbourne Australia.
[14] Compton, D. A., and Johnston, J. P., 1992, "Streamwise Vortex Production by Pitched and Skewed Jets in a Turbulent Boundary Layer," AIAA J., **3**, No. 3, pp. 640–647.
[15] Selby, G. V., Lin, J. C., and Howard, F. G., 1992, "Control of Low-Speed Turbulent Separated Flow Using Jet Vortex Generators," Exp. Fluids, **12**, No. 6, pp. 394–400.
[16] Zhang, X., and Collins, M. W., 1993, "Flow and Heat Transfer in a Turbulent Boundary Layer Through Skewed and Pitched Jets," AIAA J., **31**, pp. 1590–1599.
[17] Zhang, X., and Collins, M. W., 1997, "Nearfield Evolution of a Longitudinal Vortex Generated by an Inclined Jet in a Turbulent Boundary Layer," ASME J. Fluids Eng., **119**, No. 4, pp. 934–939.
[18] Barberopoulos, A. A., and Garry, K. P., 1998, "The Effect of Skewing on the Vorticity Produced by an Airjet Vortex Generator," paper no. 2275, Aeronaut. J., pp. 171–177.
[19] Findlay, M. J., Salcudean, M., and Gartshore, I. S., 1999, "Jets in Crossflow: Effects of Geometry and Blowing Ratio," ASME J. Fluids Eng., **121**, pp. 373–378.
[20] Zhang, X., 1998, "Turbulence Measurements of a Longitudinal Vortex Generated by an Inclined Jet in a Turbulent Boundary Layer," ASME J. Fluids Eng., **120**, pp. 765–771.
[21] Khan, Z. U., and Johnston, J. P., 2000, "On Vortex Generating Jets," Int. J. Heat Fluid Flow, **21**, pp. 506–511.
[22] Johnston, J. P., and Nishi, M., 1990, "Vortex Generator Jets—A Means for Flow Separation Control," AIAA J., **28**, No. 6, pp. 989–994.
[23] Wendt, B. J., and Reichert, B. A., 1996, "Spanwise Spacing Effects on the Initial Structure and Decay of Axial Vortices," AIAA-96-2518-CP, pp. 1151–1161.
[24] Zhang, X., 1999, "Counter-Rotating Vortices Embedded in a Turbulent Boundary Layer with Inclined Jets," AIAA J., **37**, No. 10, pp. 1277–1284.
[25] Zhang, X., and Rona, A., 1999, "Measurements of Contra-Rotating Vortices in a Turbulent Boundary Layer," AIAA Paper No. 99-0555.
[26] Johnston, J. P., 1999, "Pitched and Skewed Vortex-Generator Jets for Control of Turbulent Boundary Layer Separation: A Review," Proceedings of the 3rd ASME/JSME Joint Fluids Engineering Conference, July 18–23, 1999, San Fransisco.
[27] Goldstein, R. J., and Jin, P., 2000, "Film Cooling Downstream of a Row of Discrete Holes with Compound Angle," ASME Turbo Expo 2000, Paper No. 2000-GT-248, Munich, Germany.
[28] Zaman, K. B. M. Q., 1998, "Reduction of Jet Penetration in a Cross-Flow by using Tabs," AIAA Paper No. 98-3276.

[29] Bons, J. P., Taylor, R. P., McClain, S. T., and Rivir, R. B., 2001, ''The Many Faces of Turbine Surface Roughness,'' ASME Turbo Expo 2001, Paper No. 2001-GT-0163, New Orleans, Louisiana.
[30] Dobbeling, K., Lenze, B., and Leuckel, W., 1990, ''Computer-aided Calibration and Measurements with a Quadruple Hotwire Probe,'' Exp. Fluids, **8**, pp. 257–262.
[31] Lavoie, P., and Pollard, A., 2003, ''Uncertainty Analysis of Four-Sensor Hot-Wires and Their Data-Reduction Schemes in the Near Field of a Turbulent Jet,'' Exp. Fluids, **34**, pp. 358–370.
[32] Moffat, R. J., 1982, ''Contributions to the Theory of Single-Sample Uncertainty Analysis,'' ASME J. Fluids Eng., **104**, pp. 250–260.
[33] Bearman, P. W., 1971, ''Corrections for the Effect of Ambient Temperature Drift on Hot-wire Measurements in Incompressible Flow,'' DISA Information Report No. 11, pp. 25–30.

Analysis and Modeling of Pressure Recovery for Separated Reattaching Flows

W. W. H. Yeung
School of Mechanical and Production Engineering,
Nanyang Technological University,
Singapore 639798

G. V. Parkinson
Department of Mechanical Engineering,
University of British Columbia,
Vancouver, Canada V6T 1Z4

Analyses have been carried out on the mean pressure data for separated reattaching flows downstream of a variety of 2-D bluff-bodies to reveal some similarity features. The step height has been identified as an important parameter in relationships such as the correlation between the reattachment length x_r and the initial shear-layer angle. The separation velocity (deduced from separation pressure c_{ps}) in the direction perpendicular to the upstream flow increases linearly with the reattachment length at fixed step heights. The streamwise location of the vortex center x_v (deduced from mean streamline plots) correlates with the location of minimum pressure x_m and each varies linearly with the reattachment length. Pressure force, moment and center of pressure induced by the standing vortex also increase with the reattachment length. An inviscid flow model of a rectilinear stationary vortex above a flat wall leads to a general form of the pressure recovery $(c_p - c_{p\,\min})/c_{p\,\max} - c_{p\,\min}) = (8/9)\hat{x}^2(\hat{x}^2+1)/(\hat{x}^2+1/3)^2 x_m <, < x_r$ where $0 \leqslant \hat{x}(1 = X_m/X_r)$ and $c_{p\,\max}$ and $c_{p\,\min}$ are respectively the maximum and minimum pressure coefficients. It is demonstrated that the present analyses allow the pressure distributions downstream of various fore-bodies to be realistically predicted.
[DOI: 10.1115/1.1758266]

1 Introduction

This paper considers some similarities of the mean pressure distribution arising from incompressible flow separating from a bluff body and reattaching on a flat solid surface downstream. This type of flow is of enormous engineering interest as it is often encountered in flow-measurement devices such as the orifice meters and on aerodynamic control surfaces. In particular, according to Roshko [1], the shear layers separating from a circular cylinder and reattaching on a downstream splitter plate reduce the pressure drag coefficient from 1.1 to 0.7 at a Reynolds number of 1.45×10^4. For low Reynolds numbers between 0.35×10^3 and 1.15×10^3, the overall drag coefficient of a rectangular cylinder is reduced from 2 to 1 when a splitter plate is added, as reported by Mansingh and Oosthuizen [2]. Recently, the experimental results of Fertis [3] and the numerical computation of Finaish and Witherspoon [4] show that the separated flow with subsequent vortex formation generated by a backward-facing step on the upper surface of an airfoil leads to considerable enhancements in lift and lift-to-drag ratio.

Some similarity features of such flow were earlier identified by Roshko and Lau [5], which reported the pressure measurements downstream of separated flow occurring behind a number of bluff bodies, as shown in Fig. 1*a*. Their hypothesis that the reattachment pressure rise depends on the velocity and pressure (U_e, p_e) approaching separation leads to a pressure coefficient $\tilde{c}_p = 2(p - p_e)/(\rho U_e^2)$ different from the ordinary pressure coefficient $c_p = 2(p-p_\infty)/(\rho U_\infty^2)$, which is based on the free-stream velocity U_∞ and pressure p_∞. The two coefficients are related by $\tilde{c}_p = (c_p - c_{pe})/(1-c_{pe})$, where $c_{pe} = c_p$ at $p = p_e$. Experimental measurements with thin boundary layers at separation, which are characterized by the reattachment pressure rise coefficient $\tilde{c}_{pm}$ (i.e. when p attains its maximum value p_m), can be well collapsed onto a single curve when plotted in terms of $\tilde{c}_p$ and the reduced distance coordinate x/x_r, where x is measured from the separation point. It is important to note that

1. when p_e is taken to be the minimum pressure, the combination, $\tilde{c}_p/\tilde{c}_{pm}$, is identical to the ordinate $c_p^* = (c_p - c_{p\,\min})/(c_{p\,\max} - c_{p\,\min})$ (where $c_{p\,\max}$ and $c_{p\,\min}$ are respectively the maximum and minimum pressure coefficients) used by Narayanan et al. [6] and Gai and Sharma [7] to achieve better collapse of pressure data of various separation conditions,
2. the theoretical basis for the single curve is limited in the literature.

Cherry et al. [8] measured the unsteady structure of such flow behind a number of 2-D bodies (see Fig. 1*b*). Their data on the reattachment length verses the angle of separation follow Simpson's [9] relation closely. Djilali and Gartshore [10] studied the size of a separation bubble behind a blunt thick plate at various initial shear-layer angles, as depicted in Fig. 1*c*. The trend of their data, although similar to that of [8], follows a different variation. Besides, it is unclear how flows at separation and reattachment may be linked.

The objective of the present study is to analyze the experimental data of separated reattaching flows available in the literature for the purpose of establishing relationships linking the pertinent parameters. The ultimate goal is to develop a mathematical model for predicting the pressure induced by the standing vortex. In the first part of this paper, a relation unifying those from [9] and [10] is proposed to provide the trend of the data from [8] and [10] by including the step height. Its validity is demonstrated by testing against data from [5] and Govinda Ram and Arakeri [11] (see Fig. 1*d* for fore-body shapes). A further step is taken to correlate the initial condition (i.e. the separation pressure) and final condition (i.e. the reattachment length) of this flow at fixed step heights. Such a relation is well supported by existent data. The reattachment length has also been correlated with the vortex-center location and minimum pressure distance x_m, pressure gradient at reattachment, force, moment and center of pressure.

Based on thin-airfoil theory, O'Malley et al. [12] proposed a constant-pressure/constant-vorticity model for inviscid, incom-

Contributed by the Fluids Engineering Division for publication in the JOURNAL OF FLUIDS ENGINEERING. Manuscript received by the Fluids Engineering Division January 31, 2003; revised manuscript received November 7, 2003. Associate Editor: J. Marshall.

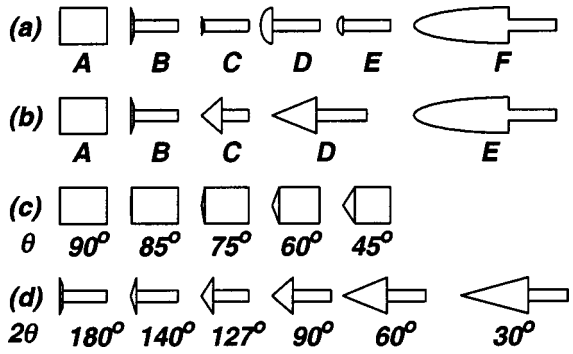

Fig. 1 Fore-body shapes used in various studies (with flow from left to right). (*a*) from [5], (*b*) from [8], (*c*) from [10], and (*d*) from [11].

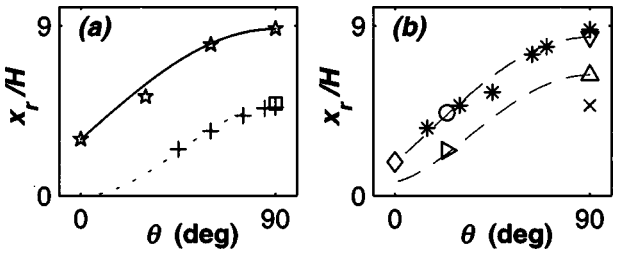

Fig. 3 Variations of reattachment length x_r/H with initial shear-layer angle θ. (*a*) ☆ for models *B* to *E* and □ for model *A* from [8], + for models from [10], ——: Eq. (1), ····: Eq. (2), (b) ×, ▽, △, ○, ▷, ◇ for models *A* to *F* from [5], — — —: Eq. (3), ∗ for models from [11].

pressible flow down a backward-step, providing some theoretical basis for reduced coordinates suggested by [5]. The second part of this paper is on inviscid models of a standing vortex, one with the vorticity tightly concentrated in a vanishing core and another with the vorticity proportional to the stream function and distributed over a finite core. Pressure distributions from [5,8,10–11] plotted in terms of c_p^* and $(x-x_m)/x_r$ are in favor of the model having a vanishing core. The last part of this paper is devoted to demonstrate how realistic the predicted pressure distributions can be when the similarity features are incorporated into the model.

2 Effects of Initial Shear-Layer Angle and Step Height

Figure 2*a* depicts the general flow configuration of the present study, identifying parameters such as step height h, maximum fore-body thickness H, thickness of splitter-plate t (i.e., $t+2h=H$), separation angle θ, reattachment length x_r and streamwise vortex location x_v. The experimental pressure distribution behind a wedge corresponding to $2\theta=60$ deg from [8] is shown in Fig. 2*b* together with parameters such as x_m, $c_{p\,\max}$, $c_{p\,\min}$ and separation pressure c_{ps}.

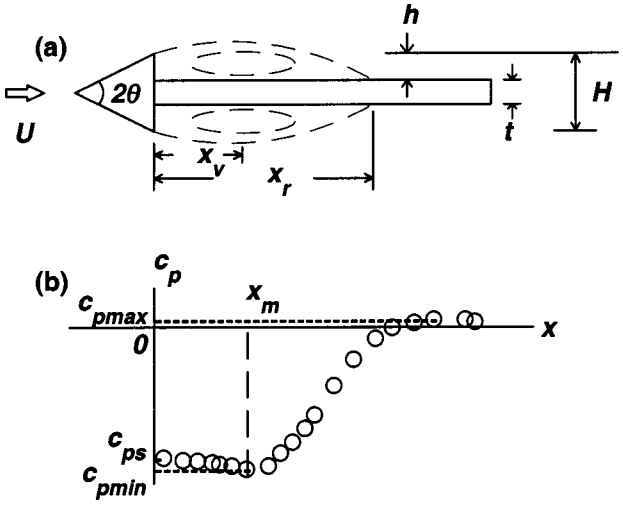

Fig. 2 Definitions of pertinent parameters used in the present study. (*a*) General flow configuration, (*b*) pressure distribution ($2\theta=60$ deg) from [8].

Simpson [9] presented a comprehensive review of two-dimensional turbulent separated flow. For a given wind-tunnel solid-blockage ratio, the reattachment length and the separation angle θ is proposed as

$$[x_r(\theta)-x_r(0\ \text{deg})]/[x_r(90\ \text{deg})-x_r(0\ \text{deg})]=\sin\theta \qquad (1)$$

where $\theta=0$ deg and $\theta=90$ deg correspond to the backward-facing step and the vertical fence with a splitter plate downstream, respectively. Data of models B to E from [8] (see Table 1 for values of θ and dimensionless step height h/H) are closely described by (1), as shown in Fig. 3*a*. The data point of model A ($h/H=0$) does not conform to (1) but follows data of the five cases from [10] (where $\theta=45$ deg,60 deg,75 deg,85 deg,90 deg, $h/H=0$) and the variant correlation

$$x_r(\theta)/x_r(90\ \text{deg})=\sin^2\theta \qquad (2)$$

The two sets of data are obviously segregated by the difference in step height, which is consistent with the dimensional analysis by Smits [13] where the splitter-plate thickness was considered as an important dimensionless group. Based on the step heights from [8] and [10], (1) and (2) can be unified to form

$$\frac{x_r(\theta,h/H)-x_r(0\ \text{deg},h/H)}{x_r(90\ \text{deg},h/H)-x_r(0\ \text{deg},h/H)}=\sin^n\theta \qquad (3)$$

where $x_r(0\ \text{deg},0)=0$ and $n=2-(1/0.37)(h/H)$. The validity of (3) is demonstrated in Fig. 3*b*, when plotted with data of models B, D and F from [5] and of six models from [11] with values of h/H listed in Table 1. If $x_r(0\ \text{deg},0.19)$ is linearly interpolated from $x_r(0\ \text{deg},0)$ and $x_r(0\ \text{deg},0.34)$, then (3) is also consistent with the data of models E and C, as shown in Fig. 3*b*. Note that θ for models D and E were estimated from the flow-visualization pictures in Lau [14].

Unlike the reattachment length, the separation pressure c_{ps} from [8] decreases with θ, a trend which is ''opposite'' to that of [10], further highlighting the significant influence from the step

Table 1 Details of models from references [[5], [8], [10] and [11]].

[5]			[8]			[10]			[11]		
Model	θ	h/H	Model	θ	h/H	Model	θ	h/H	Model	θ	h/H
F	0 deg	0.34	*E*	0 deg	0.44	–	45 deg	0	Triangular	15 deg	0.32
D	24 deg	0.34	*D*	30 deg	0.38	–	60 deg	0	‘‘	30 deg	0.32
B	90 deg	0.34	*C*	60 deg	0.37	–	75 deg	0	‘‘	45 deg	0.32
E	24 deg	0.19	*B*	90 deg	0.37	–	85 deg	0	‘‘	63.5 deg	0.32
C	90 deg	0.19	*A*	90 deg	0	–	90 deg	0	‘‘	70 deg	0.36
A	90 deg	0							‘‘	90 deg	0.36

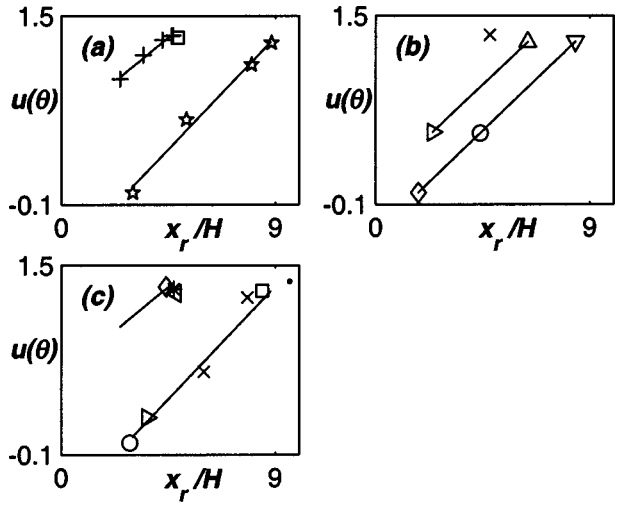

Fig. 4 Variations of initial shear-layer velocity $u(\theta)$ with reattachment x_r/H. (*a*) and (*b*) see legend of Fig. 3. (*c*) × for $\theta = 30$ deg and 90 deg from [13], ▷ for truncated airfoil from [14], ○ from [18], □ from [19], ● from [20], ◇ from [21], ◁ from [23], ——: least-square fit.

height. Instead of finding a relation linking the three parameters in each case, it is believed that separation may be linked to reattachment through c_{ps}, x_r, θ and h/H. In analyzing experimental data on separated flow (without downstream reattachment) around a flat plate at inclination α, Yeung and Parkinson [15] found that a "characteristic" wake width leading to a constant modified Strouhal number takes the form of $D^* = c\sqrt{1-c_{pb}(\alpha)}\sin\alpha$, where c is the plate length and $c_{pb}(\alpha)$ is the separation pressure at α. A similar expression [16] has also been identified for the flow around a symmetrical wedge. For separated reattaching flows where the prominent feature is the "coherent" vortex structure in the free shear layers (see Roshko [17]), x_r is the characteristic length. Data from [5,8,10] are reasonably collapsed in Figs. 4*a* and 4*b* by

$$\sqrt{1-c_{ps}(\theta)}\sin\theta = a(x_r/H) + b \tag{4}$$

where a and b are functions of h/H shown in Fig. 5*a*. Additional evidence for (4) can be found in Fig. 4*c*, where data are from [13–14,18–23]. The separation velocity in the direction normal to upstream flow, $\mu(\theta) = \sqrt{1-c_{ps}(\theta)}\sin\theta$, being linearly related to the characteristic length suggests that separated flows (with and without reattachment) are similar.

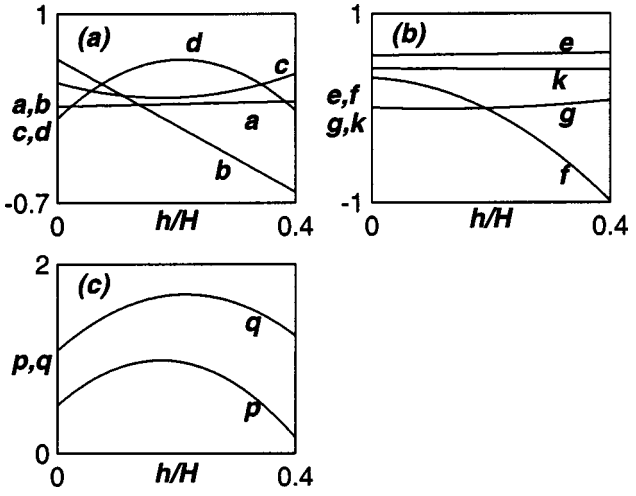

Fig. 5 Variations of coefficients (*a*) a, b, c, d, (*b*) e, f, g, k, (*c*) p, q with h/H.

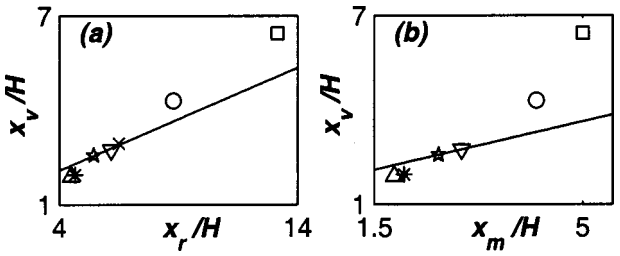

Fig. 6 Location of vortex center x_v/H vs. (*a*) reattachment length x_r/H, (*b*) location of minimum pressure (x_m/H). ○ from [20], ☆ from [24], ▽ from [25], × from [26], △ from [27], * from [29], □ from [30], ——: least-square fit of data from [24,25,26] where $h/H=1$.

3 Location of Standing Vortex

To gain an understanding of how the pressure recovers after separation, it is important to study the associated flow field. Roshko [1] postulated a kind of standing vortex formed on each side of the circular cylinder when placing a splitter plate along the center line of the wake. The existence of a vortex is clearly confirmed by the streamline plots such as those in [20,24–30]. If the vortex center x_v (measured from the separation point) is defined as the mean of leftmost and rightmost distances of the inner streamline from the separation point in [24–26] where the backward-facing step is the geometry (i.e., $h/H=1$), then from Fig. 6*a* $x_v/H = 0.32(x_r/H) + 0.79$, where the Reynolds number Re_H ranges between 5.5×10^3 and 5×10^5. It is interesting to note that when x_v and x_r were measured from the base of the backward-facing step, Acrivos et al. [31] concluded that $x_v/x_r \sim 1/3$ when $\mathrm{Re}_H > 30$. As gathered from these two expressions, increasing the Reynolds number has negligible effect on the gradient of the linear relation between x_v and x_r.

One effect of a stationary vortex hovering above a solid boundary is to induce a suction peak, as pointed out by Hummel [32] for the flow over a slender delta wing at large angles of attack. In fact, its relevance to separated reattaching flows was earlier pointed out when it (rather than the separation pressure) was used in [5] to define the reduced pressure coefficient. The location of such suction is explored here by correlating it with the streamwise location of the vortex from [24–25] (no pressure measurements from [26]), giving $x_v/H = 0.44(x_m/H) + 1.45$ in Fig. 6*b*. With the limited data available, the main purpose here is to emphasize the effect from the step height by including data from [20,27,29–30] of other geometrical shapes (where $h/H \neq 1$) in Figs. 6*a* and 6*b*. As such, the effect of the initial shear-layer angle (i.e., through x_r) on x_m should also be appropriately addressed by segregating data from [5,8,10] in terms of h/H, as shown in Fig. 7. In general, where

$$x_m/H = c(x_r/H) + d \tag{5}$$

where c and d are functions of h/H, as shown in Fig. 5*a*.

4 Force, Moment, Pressure Center and Pressure Gradient at Reattachment

Most of the pressure distributions cited above exhibit that c_p is negative from separation to reattachment. Even in the exceptional case, the backward-facing step, where $c_p > 0$ at reattachment, c_p is negative within most of the re-circulating zone. Therefore, the resulting pressure force has its direction pointing upward, explaining why the separated reattaching flow behind the step may enhance lift, as reported in [3,4].

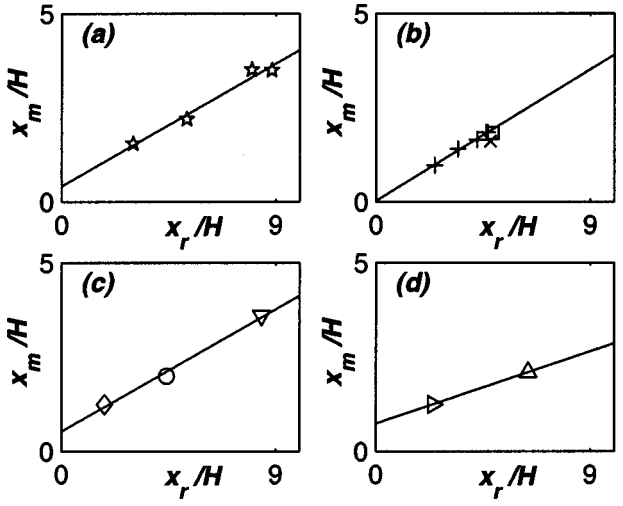

Fig. 7 Location of minimum pressure x_m/H vs. reattachment length x_r/H. See legend of Fig. 3, ——: least-square fit.

Similarities of overall pressure distributions from [5,8,10] are investigated through force coefficient $c_l = \int_{x=0}^{x_r}(-c_p)d(x/H)$, moment coefficient $c_m = \int_{x=0}^{x_r}(-c_p)(x/H)d(x/H)$ and center of pressure $x_g = c_m/c_l$. After taking the variation of step height into consideration, it is found that

$$c_l = e(x_r/H) + f \tag{6}$$

$$x_g = g(x_r/H) + k \tag{7}$$

while c_m behaves like a quadratic function of x_r/H, as shown in Figs. 8–9. Coefficients e, f, g and k are functions of h/H, as shown in Fig. 5*b*. In passing, (1) and (6) suggest that lift enhancement found in [3] may be optimized by increasing the angle of separation.

When studying the reattaching separated flow behind a vertical fence mounted on the wall of a wind tunnel, Fricke [33] proposed a lift coefficient similar to c_l but with the upper limit of integration replaced by the "distance downstream of separation to $c_p = 0$ position." His result, corresponding to $h/H = 1$, is $c_l = 0.69(x_r/H) - 2.5$, which is quite comparable to $c_l = 0.64(x_r/H) - 7.7$. The discrepancy in the intercept may be

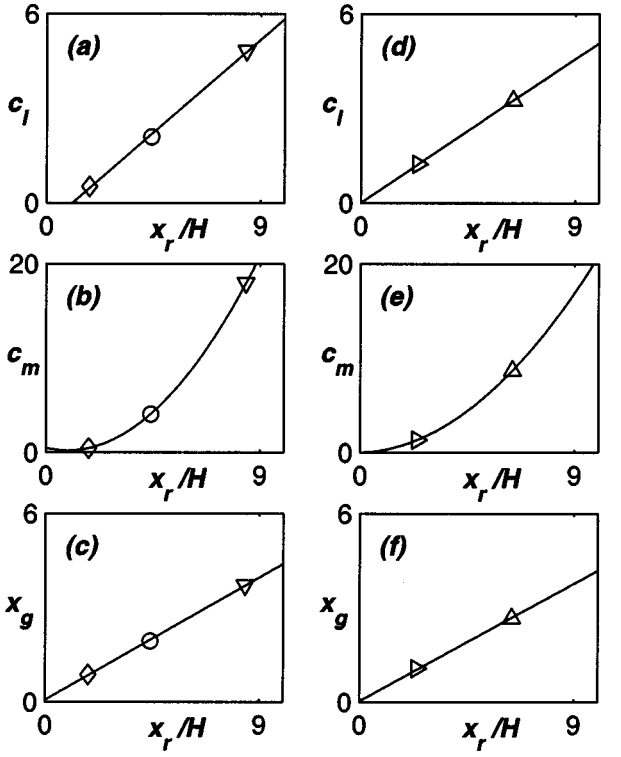

Fig. 9 Variations of force c_l, moment c_m and center of pressure x_g with reattachment length x_r/H from [5]. See legend of Fig. 3, ——: least-square fit.

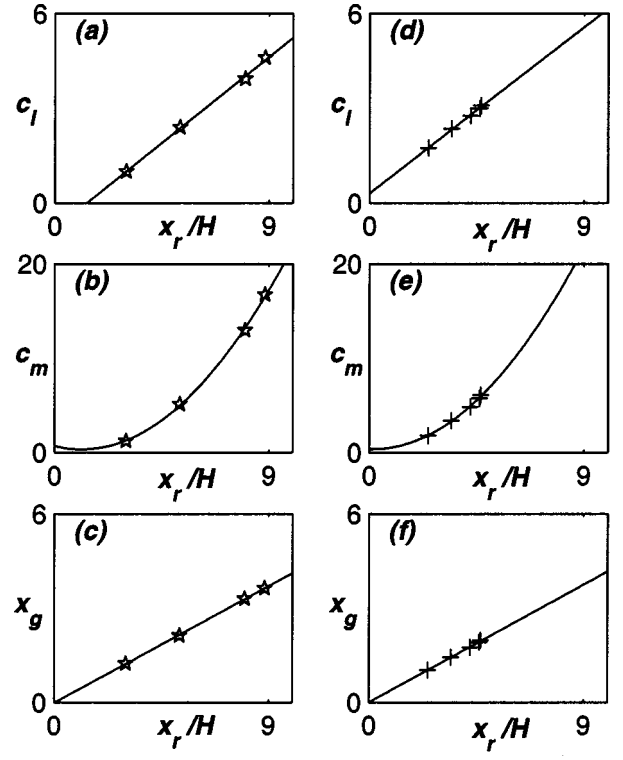

Fig. 8 Variations of force c_l, moment c_m and center of pressure x_g with reattachment length x_r/H. (*a*), (*b*), (*c*) from [8], (*d*), (*e*), (*f*) from [10]. See legend of Fig. 3, ——: least-square fit.

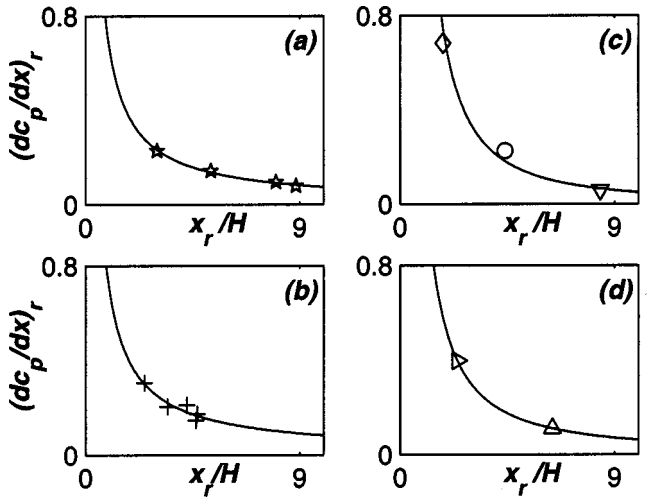

Fig. 10 Variations of pressure gradient at reattachment $(dc_p/dx)_r$ with reattachment length x_r/H. See legend of Fig. 3, ——: least-square fit.

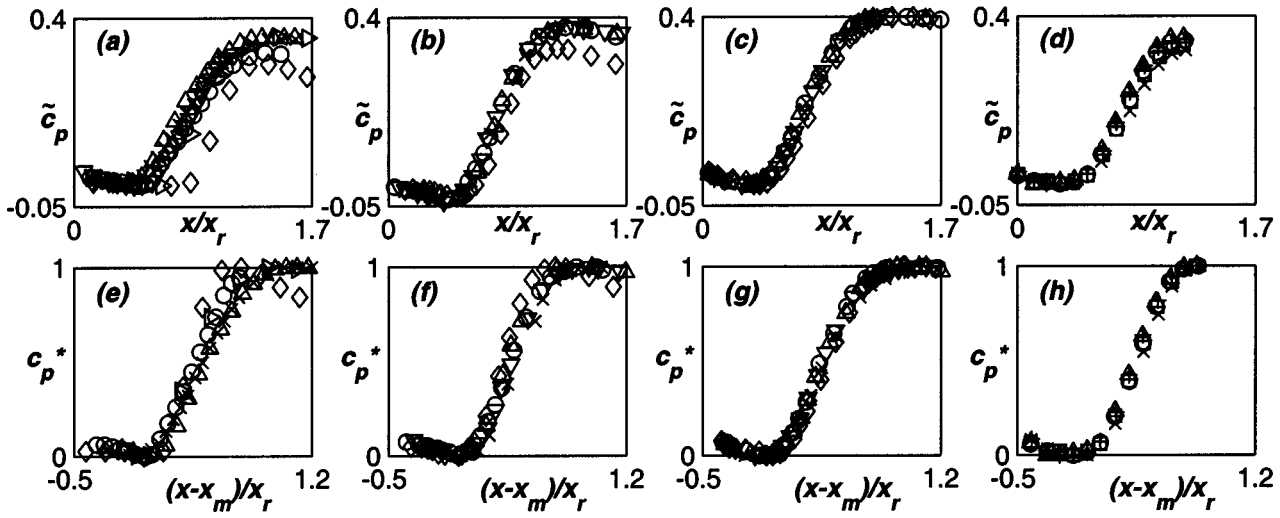

Fig. 11 Comparison of pressure distributions in two sets of reduced coordinates $(x/x_r, \tilde{c}_p)$ and $((x-x_m)/x_r, c_p^*)$. (*a*) and (*e*) from [5], (*b*) and (*f*) from [8], (*c*) and (*g*) from [10], (*d*) and (*h*) from [11].

caused by the differences in the solid blockage ratio (4%~8% in [33], 3%~5% in [5,8,10]) and the method to calculate c_l.

Streamwise pressure gradient has long been recognized as an important parameter in fluid flow. In the present study, the pressure gradient at flow reattachment is of particular interest. Measurements from [5,8,10] in Fig. 10 show that it is always positive and may be correlated with x_r as

$$\frac{dc_p}{d(x/H)} = \frac{p}{(x/H)^q} \quad \text{at } x = x_r \tag{8}$$

where p and q are functions of h/H, as shown in Fig. 5*c*.

5 Flow Models for Reduced Coordinates

After examining the similarities of pressure data in coordinates $(x/H, c_p)$, they are studied in reduced coordinates. Figure 11 compares the data from [5,8,10–11] plotted in terms of $(x/x_r, \tilde{c}_p)$ (as originally suggested in [5]) and $(\hat{x}, c_p^*)$, where $\hat{x} = (x-x_m)/x_r$, demonstrating that the latter can collapse data of thicker boundary-layer at separation without affecting others. From Fig. 11, it is obvious that c_p varies from its value at separation c_{ps} to its minimum value $c_{p\,\min}$ gradually over $0 < x < x_m$ and can be accurately represented by a simple linear variation

$$c_p = (c_{p\,\min} - c_{ps})\frac{x}{x_m} + c_{ps} \quad \text{or} \quad c_p^* = \frac{c_{p\,\min} - c_{ps}}{c_{p\,\max} - c_{p\,\min}}\frac{x_r}{x_m}\hat{x} \tag{9}$$

As for the downstream portion where $x_m < x < x_r$, the pressure recovers rapidly and non-linearly. The streamline plots from [20,24–30] suggest modeling the flow with a 2-D inviscid point vortex of strength Γ located at a distance L above an impermeable boundary $(y = 0, -\infty < x < \infty)$ in the presence of uniform flow U. The complex potential for this irrotational flow is $F(z) = Uz + (i\Gamma/[2\pi])\ln([z-iL]/[z+iL])$, where $z = x + iy$. If the vortex is stationary at $z = iL$, then its strength is uniquely determined by solving $(dF/dz) - (i\Gamma/[2\pi])(1/[z-iL]) = 0$. Applying Bernoulli's equation, c_p along the impermeable boundary can be written as $c_p = 1 - (1 - 4L^2/[x^2+L^2])^2$, which attains its minimum of -8 at $x = x_m = 0$ and maximum of unity at $x = x_r = \sqrt{3}L$. Within $0 < \hat{x} < 1$, it has the form

$$\frac{c_p - c_{p\,\min}}{c_{p\,\max} - c_{p\,\min}} = \frac{8}{9}\frac{\hat{x}^2(\hat{x}^2+1)}{(\hat{x}^2+1/3)^2} \tag{10}$$

The above-mentioned model represents the case where the vorticity is tightly concentrated in a vanishingly small core. Another limit of the vortex motion was discussed by Batchelor [34, p. 534] where the vorticity being proportional to the stream function is distributed over a finite circular area. The corresponding stream function in polar coordinates (r, θ) is $\psi = 2UJ_1(Kr)\sin\theta/[KJ_0(KP)]$ where $r \leq P$. Here J_0 and J_1 are Bessel functions and $KP = 3.8317$, the first zero of J_1. By choosing the center of the vortex to be the same as that of the previous model, it can be shown that $P = 2.081L$ and a comparison of streamlines (having the same stream-function values) from the two models is made in Figs. 12*a* and 12*b*. With the Bernoulli constant properly evaluated, $c_p = 1 - 4J_1^2(Kx)/[KxJ_0(KP)]^2$ along $\psi = 0\ (-P < x < P, y = 0)$, which reaches its minimum of about -5.16 at $x = x_m = 0$ and maximum of unity at $x = x_r = P$. Within $0 < \hat{x} < 1$, it has the form

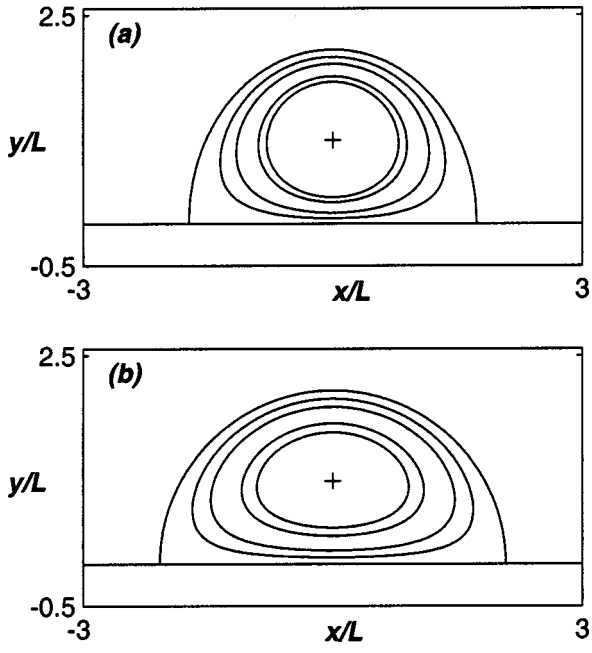

Fig. 12 Streamline patterns of (*a*) irrotational vortex and (*b*) vortex with vorticity. +: center of vortex.

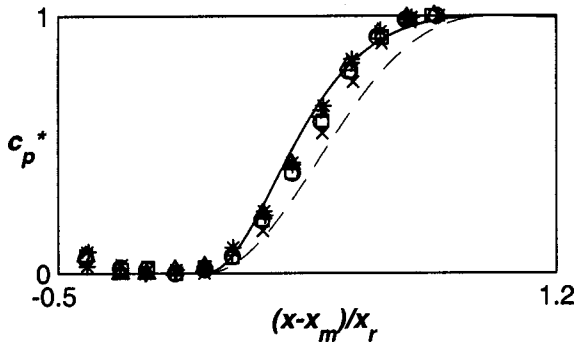

Fig. 13 A typical comparison of pressure distributions in c_p^* and $(x-x_m)/x_r$. ——: Eq. (10), — — —: Eq. (11), *, △, +, ○, □, × from [11].

$$\frac{c_p - c_{p\,\min}}{c_{p\,\max} - c_{p\,\min}} = 1 - \frac{4J_1^2(KP\hat{x})}{K^2P^2\hat{x}^2} \tag{11}$$

Figure 13 gives a typical comparison between data from [11] and the variations from (10) and (11) in reduced coordinates, indicating that the irrotational model is closer to the experimental data.

As shown in Fig. 11, pressure distributions plotted in reduced coordinates $\hat{x}$ and c_p^* are characterized by five parameters, namely x_m, x_r, c_{ps}, $c_{p\,\min}$ and $c_{p\,\max}$, which are not known a priori. However, they can by solved for by using conditions (4) to (8), where (9) and (10) are appropriately incorporated into c_p to produce

$$\left.\frac{dc_p}{d(x/H)}\right|_{x=x_r} = \frac{(c_{p\,\max} - c_{p\,\min})}{x_r/H}\,\frac{16\beta(1-\beta^2)}{(3\beta^2+1)^3} \tag{12}$$

$$c_l = \left[\frac{(c_{p\,\min}+c_{ps})}{2}(1-\beta) + \beta c_{p\,\min} + \frac{8}{3}\,\frac{\beta^3(c_{p\,\max}-c_{p\,\min})}{(3\beta^2+1)}\right]\frac{x_r}{H} \tag{13}$$

$$c_m = \left[\frac{c_{ps}}{2} + \frac{c_{p\,\min}-c_{ps}}{3}\right](1-\beta)^2\left(\frac{x_r}{H}\right)^2 + G\left(\frac{x_r}{H}\right)^2 \tag{14}$$

where

$$G = (c_{p\,\max} - c_{p\,\min})\left[\frac{4}{9}\,\frac{(-1+6\beta-3\beta^2)\beta^2}{(3\beta^2+1)} + \frac{4\ln(3\beta^2+1)}{27}\right] + \left(\beta - \frac{\beta^2}{2}\right)c_{p\,\min}, \quad \beta = 1 - \frac{x_m}{x_r}.$$

Realistic predictions, especially between separation and reattachment, as compared with data from [11] have been found and shown in Fig. 14.

6 Conclusion

After analyzing the mean pressure downstream of a variety of bluff bodies, it has been demonstrated in the present study that the dimensionless step height plays a vital role in the relation between the reattachment length and the initial shear-layer angle. Furthermore, given the step height, the separation-velocity in the direction normal to the freestream increases linearly with the reattachment length. While flow parameters such as the location of minimum pressure, pressure force, and the center of pressure also possess similar variations, the pressure gradient at reattachment is inversely proportional to the reattachment length.

Reduced coordinates involving x_m, x_r, c_{ps}, $c_{p\,\min}$ and $c_{p\,\max}$ are found to characterize the pressure variation regardless of forebody geometry and boundary-layer thickness at separation. Theoretical pressure distributions based on flow models of a stationary vortex (with and without vorticity) above a flat impermeable boundary have been worked out to give the relationship between the reduced coordinates. The variation from the irrotational model is closer to the experimental data. By incorporating the above-derived conditions into this relationship, it has been shown that the predicted pressure in the re-circulating zone agree reasonably with experimental data.

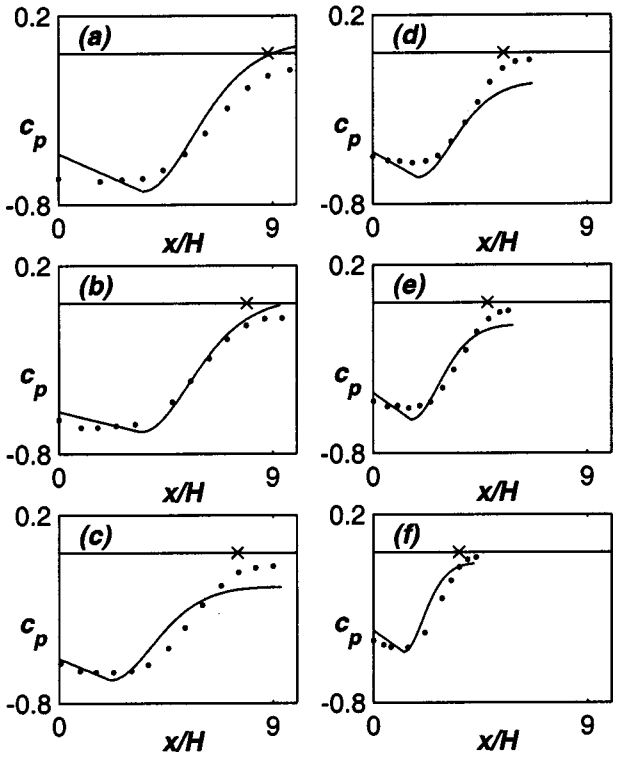

Fig. 14 Comparison of pressure distributions in c_p and x/H. ●: experimental data from [11] in (*a*)–(*f*) for $2\theta = 180$ deg, 140 deg, 127 deg, 90 deg, 60 deg, and 30 deg, ×: reattachment, ——: Eqs. (9) & (10).

Nomenclature

a,b,c,d,e, = functions of dimensionless step
f,g,k,p,q = height h/H
c_l = sectional lift coefficient, $\int_{x=0}^{x_r}(-c_p)d(x/H)$
c_m = sectional moment coefficient, $\int_{x=0}^{x_r}(-c_p)(x/H)d(x/H)$
c_p = mean pressure coefficient, $2(p-p_\infty)/\rho U^2$
c_{pe} = pressure coefficient approaching separation
$c_{p\,\max}$ = maximum pressure coefficient
$c_{p\,\min}$ = minimum pressure coefficient
c_{ps} = pressure coefficient at separation
$\tilde{c}_p$ = modified pressure coefficient, $(c_p - c_{pe})/(1-c_{pe})$
c_p^* = reduced pressure coefficient, $(c_p - c_{p\,\min})/(c_{p\,\max} - c_{p\,\min})$
F = complex potential
G = function of $c_{p\,\max}$, $c_{p\,\min}$ and β
H = maximum fore-body thickness, $2h+t$
h = step height
J_0, J_1 = Bessel functions of orders zero and one
K = constant in $J_1(KP)=0$, first zero
L = distance of vortex center from impermeable boundary
n = function of dimensionless step height
P = Radius of circular area
p = static pressure

p_∞ = freestream pressure
Re_H = Reynolds number, UH/ν
t = thickness of splitter plate
U = freestream velocity
x = streamwise distance downstream of separation
x_g = center of pressure, c_m/c_l
x_m = location of minimum pressure
x_r = location of reattachment
x_v = location of vortex center
$\hat{x}$ = reduced streamwise co-ordinate, $(x-x_m)/x_r$
z = complex number, $x+iy$
β = dimensionless parameter, $1-x_m/x_r$
Γ = strength of vortex
ν = kinematic viscosity of fluid
ρ = density of fluid
θ = separation angle
ψ = stream function

References

[1] Roshko, A., 1954, ''On the drag and shedding frequency of two-dimensional bluff bodies,'' NACA Tech. Note 3169.
[2] Mansingh, V., and Oosthuizen, P. H., 1990, ''Effects of splitter plates on the wake flow behind a bluff body,'' AIAA J., **28**, pp. 778–783.
[3] Fertis, D. G., 1994, ''New airfoil-design concept with improved aerodynamic characteristics,'' ASCE, J. Aerosp. Eng., **7**, pp. 328–339.
[4] Finaish, F., and Witherspoon, S., 1998, ''Aerodynamic performance of an airfoil with step-induced vortex for lift augmentation,'' ASCE, J. Aerosp. Eng., **11**, pp. 9–16.
[5] Roshko, A., and Lau, J. C., 1965, ''Some Observations on transition and reattachment of a free shear layer in incompressible flow,'' Proc. Heat Transfer and Fluid Mech. Inst., Stanford University Press, pp. 157–167.
[6] Narayanan, M. A. B., Khadgi, Y. N., and Viswanath, P. R., 1974, ''Similarities in pressure distribution in separated flow behind backward-facing steps,'' Aeronaut. Q., **25**, pp. 305–312.
[7] Gai, S. L., and Sharma, S. D., 1987, ''Pressure distributions behind a rearward facing segmented step,'' Exp. Fluids, **5**, pp. 154–158.
[8] Cherry, N. J., Hillier, R., and Latour, M. E. M. P., 1983, ''The unsteady structure of two-dimensional separated-and-reattaching flows,'' J. Wind. Eng. Ind. Aerodyn., **11**, pp. 95–105.
[9] Simpson, R. L., 1985, ''Two-dimensional turbulent separated flow,'' AGARDograph 287.
[10] Djilali, N., and Gartshore, I. S., 1991, ''Effect of leading-edge geometry on a turbulent separation bubble,'' AIAA J., **30**, pp. 559–561.
[11] Govinda Ram, H. S., and Arakeri, V. H., 1990, ''Studies on unsteady pressure fields in the region of separating and reattaching flows,'' ASME J. Fluids Eng., **112**, pp. 402–408.
[12] O'Malley, K., Fitt, A. D., Jones, T. V., Ockendon, J. R., and Wilmott, P., 1991, ''Models for high-Reynolds-number flow down a step,'' J. Fluid Mech., **222**, pp. 139–155.
[13] Smits, A. J., 1982, ''Scaling parameters for a time-averaged separation bubble,'' ASME J. Fluids Eng., **104**, pp. 178–184.
[14] Lau, J. C., 1965, ''Experimental study of the reattachment pressure rise at subsonic speeds,'' Ae. Eng. Thesis, California Institute of Technology.
[15] Yeung, W. W. H., and Parkinson, G. V., 1997, ''On the steady separated flow around an inclined flat plate,'' J. Fluid Mech., **333**, pp. 403–413.
[16] Yeung, W. W. H., and Parkinson, G. V., 2000, ''Base pressure prediction in bluff-body potential-flow models,'' J. Fluid Mech., **423**, pp. 381–394.
[17] Roshko, A., 1993, ''Perspectives on bluff body aerodynamics,'' J. Wind. Eng. Ind. Aerodyn., **49**, pp. 79–100.
[18] Bearman, P. W., 1965, ''Investigation of the flow behind a two-dimensional model with a blunt trailing edge and fitted with splitter plates,'' J. Fluid Mech., **21**, pp. 241–255.
[19] Arie, M., and Rouse, H., 1956, ''Experiments on two-dimensional flow over a normal wall,'' J. Fluid Mech., **1**, pp. 129–141.
[20] Castro, I. P., and Haque, A., 1987, ''The structure of a turbulent shear layer bounding a separation region,'' J. Fluid Mech., **179**, pp. 439–468.
[21] Saathoff, P. J., and Melbourne, W. H., 1989, ''The generation of peak pressures in separated/reattaching flows,'' J. Wind. Eng. Ind. Aerodyn., **32**, pp. 121–134.
[22] Sam, R. G., Lessmann, R. C., and Test, F. L., 1979, ''An experimental study of flow over a rectangular body,'' ASME J. Fluids Eng., **101**, pp. 443–448.
[23] Kiya, M., Sasaki, K., and Arie, M., 1982, ''Discrete-vortex simulation of a turbulent separation bubble,'' J. Fluid Mech., **120**, pp. 219–244.
[24] Moss, W. D., and Baker, S., 1980, ''Re-circulating flows associated with two-dimensional steps,'' Aeronaut. Q., **31**, pp. 151–172.
[25] Driver, D. M., Seegmiller, H. L., and Marvin, J. G., 1987, ''Time-dependent behavior of a reattaching shear layer,'' AIAA J., **25**, pp. 914–919.
[26] Kasagi, N., and Matsunaga, A., 1995, ''Three-dimensional particle-tracking velocimetry measurement of turbulence statistics and energy budget in a backward-facing step flow,'' Int. J. Heat Fluid Flow, **16**, pp. 477–485.
[27] Djilali, N., and Gartshore, I. S., 1991, ''Turbulent flow around a bluff rectangular plate. Part I: Experimental investigation,'' ASME J. Fluids Eng., **113**, pp. 51–67.
[28] Adams, E. W., and Eaton, J. K., 1988, ''An LDA study of the backward-facing step flow, including the effects of velocity bias,'' ASME J. Fluids Eng., **110**, pp. 275–282.
[29] Ota, T., and Itasaka, M., 1976, ''A separated and reattached flow on a blunt flat plate,'' ASME J. Fluids Eng., **98**, pp. 79–86.
[30] Good, M. C., and Joubert, P. N., 1968, ''The form drag of two-dimensional bluff-plates immersed in turbulent boundary layers,'' J. Fluid Mech., **31**, pp. 547–582.
[31] Acrivos, A., Leal, L. G., Snowden, D. D., and Pan, F. F., 1968, ''Further experiments on steady separated flows past bluff objects,'' J. Fluid Mech., **34**, pp. 25–48.
[32] Hummel, D., 1978, ''On the vortex formation over a slender wing at large angles of incidence,'' AGARD CP-247.
[33] Fricke, F. R., 1971, ''Pressure fluctuations in separated flows,'' J. Sound Vib., **17**, pp. 113–123.
[34] Batchelor, G. K., 1967, *An Introduction to Fluid Mechanics*, Cambridge University Press.

Backward-Facing Step Flows for Various Expansion Ratios at Low and Moderate Reynolds Numbers

G. Biswas*

M. Breuer

F. Durst

Lehrstuhl für Strömungsmechanik,
Universität Erlangen-Nürnberg Cauerstr. 4,
D-91058 Erlangen, Germany
e-mail: breuer@lstm.uni-erlangen.de

This paper is concerned with the behavior of flows over a backward-facing step geometry for various expansion ratios $H/h=1.9423$, 2.5 and 3.0. A literature survey was carried out and it was found that the flow shows a strong two-dimensional behavior, on the plane of symmetry, for Reynolds numbers $Re_D=\rho U_b D/\mu$ below approximately 400 (U_b =bulk velocity and D=hydraulic diameter). In this Reynolds number range, two-dimensional predictions were carried out to provide information on the general integral properties of backward-facing step flows, on mean velocity distributions and streamlines. Information on characteristic flow patterns is provided for a wide Reynolds number range, $10^{-4}\leqslant Re_D\leqslant 800$. In the limiting case of $Re_D\rightarrow 0$, a sequence of Moffatt eddies of decreasing size and intensity is verified to exist in the concave corner also at $Re_D=1$. The irreversible pressure losses are determined for various Reynolds numbers as a function of the expansion ratio. The two-dimensional simulations are known to underpredict the primary reattachment length for Reynolds numbers beyond which the actual flow is observed to be three-dimensional. The spatial evolution of jet-like flows in both the streamwise and the spanwise direction and transition to three-dimensionality were studied at a Reynolds number $Re_D=648$. This three-dimensional analysis with the same geometry and flow conditions as reported by Armaly et al. (1983) reveals the formation of wall jets at the side wall within the separating shear layer. The wall jets formed by the spanwise component of the velocity move towards the symmetry plane of the channel. A self-similar wall-jet profile emerges at different spanwise locations starting with the vicinity of the side wall. These results complement information on backward-facing step flows that is available in the literature. [DOI: 10.1115/1.1760532]

1 Introduction and Aim of Work

This paper is concerned with two- and three-dimensional backward-facing step flows and provides results obtained by thorough numerical computations for various expansion ratios and a wide Reynolds number range. Although numerous investigations have been carried out on this topic, an insightful and complete understanding of the physical origin of flow separation and vortex formation has hitherto been not clear. The major reason for this lies in the fact that an analytical treatment of the flow is not available and hence experimental and numerical investigations are involved. Most studies on backward-facing step flows were carried out for a limited number of relevant parameters such as Reynolds number $\mathrm{Re}_D=\rho U_b D/\mu$, expansion ratio H/h and aspect ratio W/h. Here $D=2h$ denotes the hydraulic diameter of the inlet channel with height h, H the channel height in the expanded region and W the channel width. Other definitions of the Reynolds numbers found in the literature will be provided in Section 3.1. Because of this situation, distributed results are available in various publications. Furthermore, the existing investigations are partially incomplete with respect to the relevant parameter sets and require extensions to provide the basis for a sufficiently detailed fluid mechanical knowledge of backward-facing step flows. This paper is a contribution to improve the present unsatisfactory situation, at least for the Reynolds number range $10^{-4}\leqslant \mathrm{Re}_D\leqslant 800$ and the expansion ratio range $1.9423\leqslant H/h\leqslant 3$. The flow obeys the laws of two-dimensionality on the vertical mid-plane, i.e. on the plane which is equidistant from the two side walls, up to a Reynolds number of 400. For this range of Reynolds numbers, a fairly complete description of the flow is provided. Attempts have been made to explain the mechanisms that are responsible for the difference in the prediction of primary recirculation length for two- and three-dimensional simulations.

The backward-facing step flow was already of interest even when fluid mechanical problems used to be addressed only by potential flow theory. As shown by Lee and Smith [1], potential flow theory permits the treatment of the backward-facing step flow yielding a streamline pattern which does not indicate any separation or recirculation region behind the step. Hence potential theory does not provide the generally expected separation of the flow at the upper corner of the step, nor does the lower corner yield a region of vortices as expected from the considerations of Moffatt [2]. Moffatt predicted under specified conditions the existence of a sequence of vortices near corners as shown in Fig. 1 for $\mathrm{Re}_D\rightarrow 0$. Early numerical predictions of backward-facing step flows, see, e.g., Roache [3], Taylor and Ndefo [4] and Durst and Pereira [5], did not show any separation at the upper corner of the step for low Reynolds numbers. However, a separated region was predicted at the lower corner that contained a single vortex only. A careful analysis of the flow in sudden expansions was carried out by Alleborn et al. [6] and it was indicated that, at least at low Reynolds numbers, the lower corner contains a sequence of Moffatt vortices. It was concluded by Alleborn et al. [6] that the earlier numerical predictions were carried out with insufficient numerical grid resolution to resolve the smaller vortices at the lower corner. Hence high-performance computers are needed to carry out detailed studies of backward-facing step flows, even at low Reynolds numbers. Furthermore, since the early work to predict the backward-facing step flows, new numerical methodologies such as the multigrid method (see, e.g., Brandt et al. [7], Hackbusch [8]) or local block refinement (see, e.g., Lange et al. [9]) have been introduced into computer programs for solving the

*Present address: Mechanical Engineering Department, Indian Institute of Technology, Kanpur-208016, India.

Contributed by the Fluids Engineering Division for publication in the JOURNAL OF FLUIDS ENGINEERING. Manuscript received by the Fluids Engineering Division March 6, 2003; revised manuscript received November 8, 2003. Associate Editor: F. F. Grinstein.

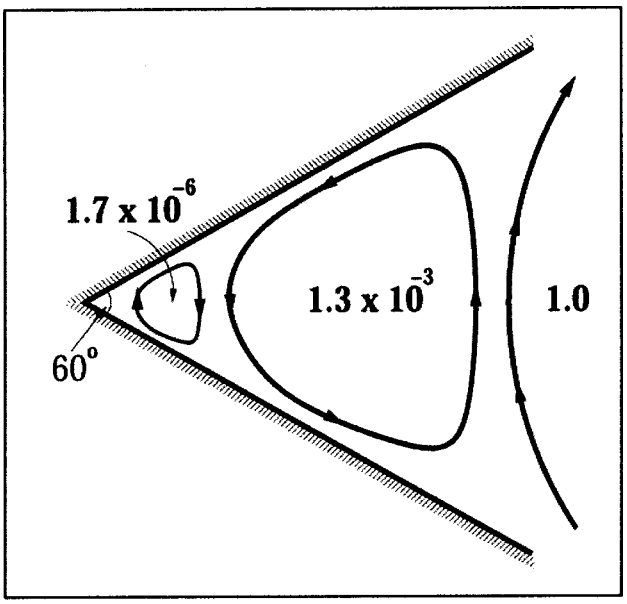

Fig. 1 Moffatt eddies in a concave corner for $2\alpha=60$ deg. The values describe the relative intensities (Moffatt [2]).

Navier-Stokes equations more efficiently with a faster convergence rate. It is also claimed that most of the numerical predictions on backward-facing step flows that have been carried out have not resolved the corner singularity at the step and its effect on the velocity field, see Ladevéze and Peyret [10].

Furthermore, the mechanisms that are responsible for increasing primary reattachment length resulting from the two-dimensional to three-dimensional flow transition are not completely understood. One possible reason for the difference in two- and three-dimensional predictions could be the effects initiated at the side walls of the channel, see Armaly et al. [11]. Durst et al. [12] have observed a symmetry-breaking bifurcation leading to one short and one long primary separation zone in a sudden-expansion flow.

This paper provides a brief literature survey carried out to summarize the existing knowledge on backward-facing step flows under the conditions mentioned above. The basic equations and their numerical solution methods, including the boundary conditions employed, are summarized in Section 3. In Section 4 the results are provided and the paper is concluded in Section 5.

2 Backward-Facing Step Flow: A Brief Literature Survey

The study of backward-facing step flows constitutes an important branch of fundamental fluid mechanics. The interest in such a flow was intensified with the experimental and numerical work of Armaly et al. [11]. They presented a detailed experimental investigation in a backward-facing step geometry for an expansion ratio $H/h=1.9423$, an aspect ratio $W/h=35$ and Reynolds numbers up to $\mathrm{Re}_D=8000$. The flow appeared to be three-dimensional above Reynolds numbers close to 400. Around this Reynolds number, they observed a discrepancy in the primary recirculation length between the experimental results and the numerical predictions. Also, around this Reynolds number, a secondary recirculation zone was observed at the channel upper wall. Armaly et al. [11] conjectured that the discrepancy between the experimental measurements and the numerical prediction was due to the secondary recirculation zone that perturbed the two-dimensional character of the flow. The normalized value of the reattachment length showed a peak at $\mathrm{Re}_D\approx1{,}200$. The decrease in recirculation length beyond a Reynolds number of 1,200 was attributed to the effect of Reynolds stresses.

Kim and Moin [13] computed the flow over a backward-facing step using a method that is second-order accurate in both space and time. They found a dependence of the reattachment length on Reynolds number in good agreement with the experimental data of Armaly et al. [11] up to about $\mathrm{Re}_D=500$. At $\mathrm{Re}_D=600$ the computed results of Kim and Moin [13] started to deviate from the experimental values. The difference was attributed to the three-dimensionality of the experimental flow around a Reynolds number of 600.

Gartling [14] developed a solution procedure using a Galerkin-based finite-element method for steady incompressible flow over a backward-facing step geometry. His results compared well, especially with respect to the bottom wall separation zone, with the results of Kim and Moin [13].

Lee and Mateescu [15] performed an experimental and numerical investigation of air flow over a two-dimensional backward-facing step for $\mathrm{Re}_D\leqslant3000$. The hot film sensor measurements at $\mathrm{Re}_D=805$ and expansion ratio $H/h=2.0$ were found to be in agreement with their numerical predictions with respect to the locations of the separation and reattachment points on the upper and lower walls.

Kaiktsis et al. [16] identified the bifurcation of two-dimensional laminar flow to three-dimensional flow as the primary source of discrepancies appearing in comparisons of numerical predictions and experimental data. They also observed that irrespective of the accuracy of the numerical schemes, the experimentally measured recirculation lengths (Armaly et al. [11]) were consistently underestimated above a Reynolds number of $\mathrm{Re}_D=600$. They found that all unsteady states of the flow are three-dimensional and develop for Reynolds number $\mathrm{Re}_D\geqslant\mathrm{Re}_c\approx700$. Furthermore, they detected that the downstream flow region is excited through the upstream shear layer with a characteristic frequency f_1. The supercritical states ($\mathrm{Re}_D>700$) were found to be periodic with another incommensurate frequency, f_2.

Durst et al. [12] observed the formation of secondary separation zones in the two-dimensional numerical simulations of a symmetric sudden-expansion flow. This observation is similar to what is found in the backward-facing step flow. Both the experiments and the predictions confirm a symmetry-breaking bifurcation leading to one short and one long primary separation zone.

Kaiktsis et al. [17] revisited the backward-facing step flow and found that the unsteadiness in step flow was created by convective instabilities. Another important conclusion of this study is that the upstream-generated small disturbances propagate downstream at exponentially amplified amplitude with a space-dependent speed in the range $700\leqslant\mathrm{Re}_D\leqslant2500$.

Heenan and Morrison [18] conducted experiments for a Reynolds number (Re_S) based on the step height S of 1.9×10^5 and suggested that while the flow is likely to be convectively unstable over a large region, the global unsteadiness, driven by the impingement of large eddies at reattachment is the cause of low frequency oscillations called *flapping*.

Le et al. [19] conducted direct numerical simulations of turbulent flows over a backward-facing step at a Reynolds number of $\mathrm{Re}_S=5100$ based on step height S and inlet free-stream velocity, and an expansion ratio of 1.2. The instantaneous velocity fields reveal the variation of reattachment length in the spanwise direction that oscillates about a mean value of 6.28 S. The flow exhibits strong streamwise vortical structures.

Kaltenbach and Janke [20] investigated the effect of sweep on the transitional separation bubble behind a backward-facing step using direct numerical simulation. In this context they also performed simulations for the unswept case at $\mathrm{Re}_S=3000$. The flow upstream of the step was laminar and shear-layer transition took place prior to reattachment. Comparing the results for zero sweep from two simulations using either steady inflow conditions or the same velocity profiles with superimposed low-amplitude random disturbances, they found out that the flow field downstream of the step is very sensitive to the type of inlet boundary conditions. The

changes in global flow features which are due to sweep, seem to be fairly independent of the specific transition scenario.

Williams and Baker [21] investigated laminar flow over a three-dimensional backward-facing step geometry. The full three-dimensional simulation of the geometry of Armaly et al. [11] for $100 \leqslant \mathrm{Re}_D \leqslant 800$ correctly predicts the reattachment lengths and confirms the effect of three-dimensionality. They also found that the side walls result in the creation of a wall jet, located at the lower channel wall and pointing from the side wall towards the channel mid-plane.

Chiang and Sheu [22] performed three-dimensional simulations of the laminar flow in a step geometry with an expansion ratio similar to that of Armaly et al. [11] for various Reynolds numbers and aspect ratios. They found that the flow at the plane of symmetry develops into a two-dimensional like profile only if the aspect ratios are increased up to 50 and higher.

Recently, Barkley et al. [23] carried out a three-dimensional linear stability analysis for the backward-facing step flow with an expansion ratio of 2. They showed that the primary bifurcation of the steady, two-dimensional flow is a steady, three-dimensional instability. Furthermore, the critical eigenmode is localized to the primary recirculation region consisting of a flat roll.

Nie and Armaly [24] presented the results of laminar forced convection flow in a backward-facing step geometry. They showed that the size of the primary recirculation zone and the maximum Nusselt number increase with increasing step height. They also indicated that the jet-like flow that develops near the side wall impinges on the stepped wall, causing a minimum to develop in the reattachment length near the side wall.

3 Numerical Methodology

3.1 Governing Equations. An incompressible fluid with constant fluid properties is assumed. The dimensionless governing equations expressing the conservation of mass and momentum are, in Cartesian coordinates x_j, as follows:

$$\frac{\partial u_j}{\partial x_j} = 0, \tag{1}$$

$$\frac{\partial u_i}{\partial t} + \frac{\partial (u_i u_j)}{\partial x_j} = -\frac{\partial p}{\partial x_i} - \frac{1}{\mathrm{Re}} \frac{\partial \tau_{ij}^{mol}}{\partial x_j} \tag{2}$$

where $i,j = 1-3$. The Cartesian velocity components are denoted u_j and the pressure p. τ_{ij}^{mol} describes the molecular momentum transport, which for a Newtonian fluid can be expressed by

$$\tau_{ij}^{mol} = -\mu \left(\frac{\partial u_i}{\partial x_j} + \frac{\partial u_j}{\partial x_i} \right). \tag{3}$$

The only non-dimensional parameter appearing in the governing equations is the Reynolds number. For the flow problem considered, the following definition is used:

$$\mathrm{Re} = \mathrm{Re}_D = \frac{\rho U_b D}{\mu}, \tag{4}$$

where ρ and μ are the density and the dynamic viscosity, respectively. As mentioned before, U_b denotes the bulk (average) velocity of the inlet flow, which corresponds in the laminar case to two-thirds of the maximum inlet velocity. In the present investigation the notation of Armaly et al. [11] is used, where D is chosen as the hydraulic diameter of the inlet channel, which is equivalent to twice its height, $D = 2h$. For the definition of the characteristic length, different options are used in the literature leading to the following additional definitions of the Reynolds number:

$$\mathrm{Re}_h = \frac{\rho U_b h}{\mu},$$

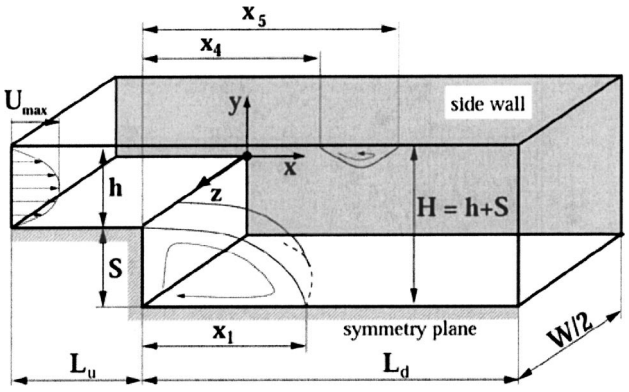

Fig. 2 Sketch of the flow configuration and definition of length scales

$$\mathrm{Re}_S = \frac{\rho U_b S}{\mu},$$

where h is the channel height upstream of the step and S denotes the step height (see Fig. 2). All three definitions are in use for backward-facing step flows, which requires a clear statement on the definition applied (here: Re_D in order to avoid confusion).

3.2 Geometry of the Flow Domain and Boundary Conditions. The geometry of the flow problem was chosen in accordance to the experimental setup of Armaly et al. [11] sketched in Fig. 2. The expansion ratio is defined by $H/h = 1 + S/h$, i.e., by the ratio of the channel height H downstream of the step to the channel height h of the inflow channel, where S denotes the step height. In addition to Armaly et al.'s expansion ratio of $H/h = 1.9423$, two other configurations with larger step heights S were considered, i.e., $H/h = 2.5$ and 3.0. For the three-dimensional predictions, the aspect ratio W/h was set to 35 and only half of the geometry is taken into account assuming symmetry at $z = W/2$. Furthermore, the two-dimensional computations are restricted to this symmetry plane. The assumption of spanwise symmetry in the three-dimensional computations was carefully checked by additional simulations based on periodic boundary conditions in spanwise direction. The predicted results for the plane of symmetry ($z = W/2$) using both types of boundary conditions were found to deviate negligibly, e.g., the discrepancies with respect to the computed length of the different recirculation regions were found to be about 0.01%.

Upstream and downstream of the step, the channel length is L_u and L_d, respectively. Note that in the present study all geometrical length scales are made dimensionless based on the channel height h. In order to simulate a fully developed laminar channel flow upstream of the step, a standard parabolic velocity profile with a maximum velocity $U_{\max} = 3/2 U_b$ is prescribed at the channel inlet ($x = -L_u$) for the two-dimensional model. For the three-dimensional simulations a curve fit of the experimental data of Armaly et al. [11] was used as the inlet conditions. In the laminar range, the measured profile of Armaly et al. was close to the solution of the fully developed duct flow with a rectangular cross-section (see White [25]) showing a slight deviation from the two-dimensional parabolic profile.

Based on a series of simulations carried out with different upstream lengths L_u showing no influence on the predicted results past the step for $L_u \geqslant 5h$, a distance of five times the channel height h upstream of the step expansion was verified to be absolutely sufficient. This coincides with data reported in the literature. At the outlet of the computational domain ($x = L_d$) the flow should be fully developed again. Hence, the application of simple outflow conditions assuming zero gradients of all flow variables is typically sufficient. However, to be on the safe side, we also tested a convective boundary condition (Orlanski [26]) at the outflow

Table 1 Grid-independence study at $Re_D=100$ $H/h=1.9423$ using five consecutively refined grid levels (finest grid=5, coarsest grid=1)

Grid Level	$\Delta y_{min}/h$	x_1/h	*Error*	*Error* [%]
Richardson extrapolation	–	2.70584	–	–
5	0.01	2.70305	0.0027933	0.103
4	0.02	2.69467	0.0111733	0.413
3	0.04	2.67253	0.0333133	1.231
2	0.08	2.61510	0.0907433	3.353
1	0.16	2.36366	0.3421833	12.646

plane, but that yielded no deviations to the Neumann condition. The convective boundary condition ensures that vortices can approach and pass the outflow boundary without significant disturbances or reflections into the inner domain. This property was justified based on large-eddy simulations (LES) for various flows (see, e.g., Breuer and Rodi [27] or Breuer [28,29]).

In the range of Reynolds numbers investigated, the flow is affected very little by the outflow length L_d assuming that the length of the flow development was correctly estimated before depending on the Reynolds number. As will be shown below, very short outflow length can be chosen for Reynolds numbers below $Re_D=1$, whereas for the highest value investigated L_d has to be increased to $L_d=32h$. Hence in all cases it was assured that on the one hand the upstream influence of the step does not reach the inflow plane and on the other hand that the flow is fully developed at the outlet section. At all solid walls Stokes' no-slip boundary conditions are applied.

3.3 Numerical Solution Method. For the spatial discretization of equations (1)–(3), a finite-volume method (*FASTEST-2D*) with a colocated arrangement of the variables was employed, as described by Demirdžić and Perić [30]. The convection and diffusion terms were evaluated using a central differencing scheme of second-order accuracy. As explained in detail in Breuer [29], a second-order accurate scheme is even appropriate for LES of turbulent flows and consequently is reliable for the simulation of laminar flows carried out within this study. For the pressure calculation, a pressure-correction equation taking mass conservation expressed by equation (1) into account was solved iteratively with equation (2). The entire procedure follows the well-known SIMPLE algorithm (" '*Semi-Implicit Method for Pressure Linked Equation*' ") proposed by Patankar and Spalding [31].

Details of the discretization and the pressure-velocity coupling are given by Demirdžić and Perić [30] and Perić et al. [32]. A nonlinear multigrid scheme was employed for convergence acceleration (see, e.g., Brandt et al. [7] and Hackbusch [8]). For parallel computations, a block-structured grid partitioning and a message-passing strategy were used as described by Durst and Schäfer [33]. In order to improve the accuracy of the numerical results without a decrease in efficiency and to optimize the utilization of the available computational resources, a local grid refinement technique was employed (see Lange et al. [9]). The numerical code *FASTEST-2D* was verified by a variety of predictions for different flow problems, especially for the laminar flow and heat transfer around two-dimensional cylinders at a wide range of Reynolds numbers, see e.g., Lange et al. [34,35], Durst et al. [36] and Shi et al. [37].

In order to investigate whether the predicted results are grid independent, extensive refinement studies were carried out. At least partially, the outcome should be presented here briefly. For that purpose we choose the simulations for expansion ratio $H/h=1.9423$ which were finally based on a grid with about 44,000 control volumes, i.e., the finest grid level (5) of five multigrid levels. In this case the cross-stream direction was resolved by 160 CVs using a wall-normal extension of the first CV of $\Delta y_{min}/h=10^{-2}$. Furthermore, computations on consecutively coarsened grid levels (4, 3, 2, 1) were carried out. As a typical result Table 1 shows the predicted length of the primary recirculation length x_1/h at $Re_D=100$ for all five grid levels. Based on the well-known Richardson extrapolation one can obtain an approximation of the exact solution also provided in Table 1. Using this exact value the absolute and relative errors of the numerical solution on all five grid levels can be determined. It is obvious that the errors monotonically converge towards zero and are only 0.103% on the fifth grid level. If the absolute error is plotted versus the grid spacing (not shown here) with a double-logarithmic scaling of the axes, the slope is as expected for a second-order scheme, at least for the finest grid levels 4 and 5. Additionally, other quantities were taken into account for these extensive refinement studies clearly demonstrating that the results presented in the paper are sufficiently accurate on the finest grid level. These grid-independence studies were repeated at different Reynolds numbers and expansion ratios. For the cases with larger expansion ratios $H/h=2.5$ and 3.0, the total grid resolution has to be increased to about 189,000 and 208,000 CVs, respectively. Further exceptions will be explained in Section 4.

Furthermore, in order to exclude all possibility of doubt, the predictions were partially re-run with a second finite-volume flow solver, *LESOCC*. This code is based on a 3-D finite-volume method for arbitrary non-orthogonal grids (Breuer and Rodi [27], Breuer [28,29]). In accordance with *FASTEST-2D*, all fluxes are approximated by central differences of second-order accuracy. However, time advancement is performed by a predictor-corrector scheme consisting of a low-storage multi-stage Runge-Kutta method (second-order accuracy) for the momentum equations and an implicit solution of the pressure correction equation. Hence the method is especially adapted for three-dimensional unsteady flows, but can also be used for two-dimensional and steady-state predictions. Furthermore, it is highly vectorized and additionally parallelized by domain decomposition allowing efficient computations on high-performance computers.

In the present study, *LESOCC* was used for the three-dimensional cases and the validation purpose mentioned above. For the three-dimensional predictions, a grid consisting of about 4.2 million CVs was employed. Similar to the two-dimensional computations, the wall-normal direction was resolved by 160 CVs, whereas for the spanwise extension 100 CVs were used. Of course, the grid was stretched towards all walls with smallest wall distances of the cell faces of $\Delta y_{min}/h=\Delta z_{min}/h=10^{-2}$. Consequently, a *x-y* cross-section of the grid for the three-dimensional cases was basically identical to the finest grid level of the corresponding grid for the two-dimensional predictions which was verified to be sufficiently fine above.

4 Results of Flow Predictions

For the presentation of the results we first start with the general description of the two-dimensional flow field presented for one expansion ratio and a wide range of Reynolds numbers. Then we address the issues related to various expansion ratios. Subsequently, we discuss in detail the flow fields for the three-dimensional simulations and identify the spatial spanwise structures. In a subsequent section, we attempt to predict some integral parameters of practical interest.

4.1 Two-Dimensional Predictions

4.1.1 Flow Field. Figure 3 shows streamlines of the steady-state flow field for an expansion ratio $H/h=1.9423$ (≈ 2) and a Reynolds number range $10^{-4} \leqslant Re_D \leqslant 10^2$. This expansion ratio was considered in the experimental study by Armaly et al. [11] and the same value has been used for a set of numerical computations. The flow over the backward-facing step is two-dimensional and non-oscillatory in the region of $Re_D \leqslant 400$. This observation was well supported by three-dimensional simulations additionally carried out using *LESOCC*. The results of the two-dimensional and three-dimensional computations are commensurate with the experiments of Armaly et al. [11].

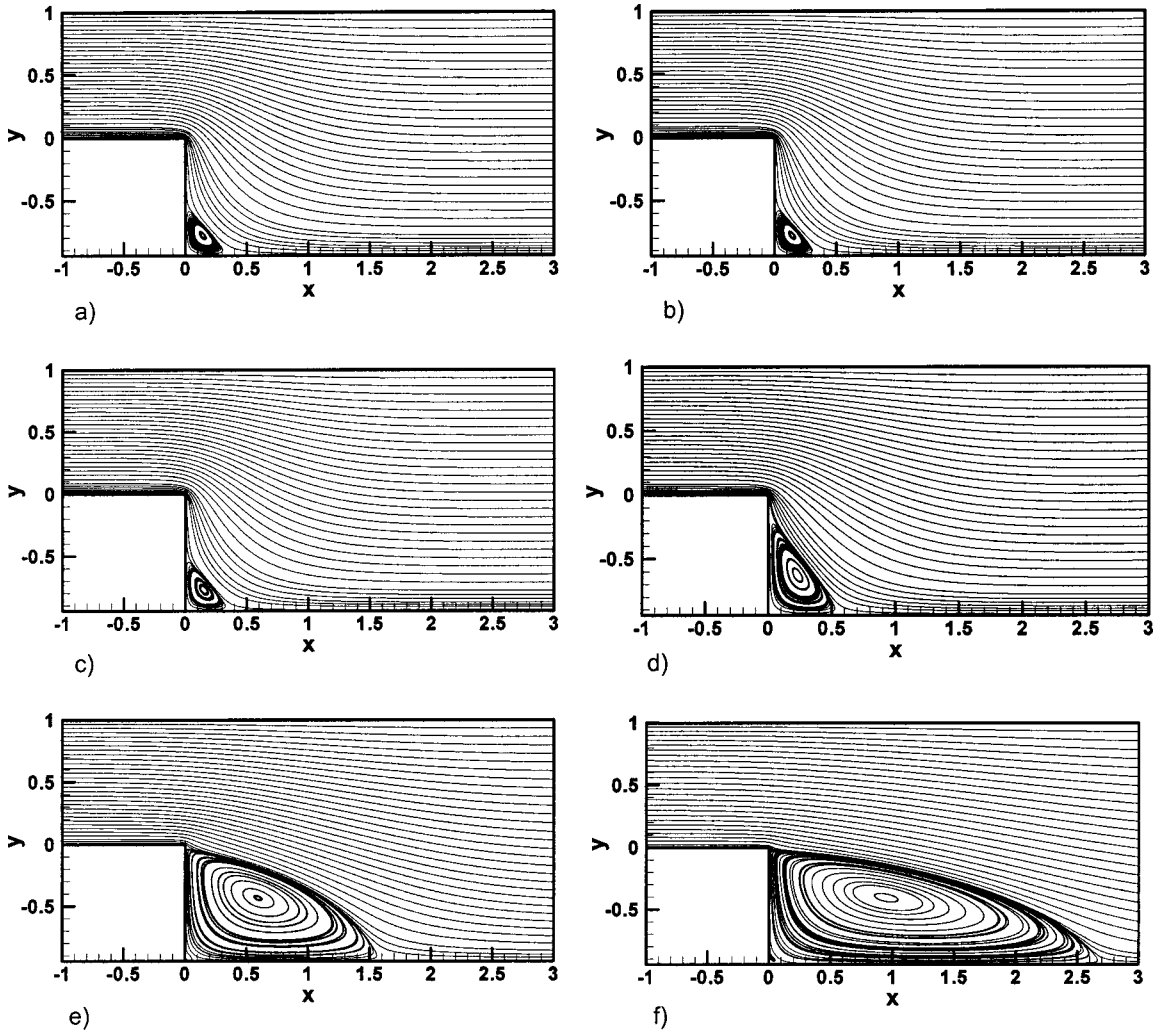

Fig. 3 Flow in the vicinity of the step. Expansion ratio $H/h=1.9423$; $10^{-4}\leq Re_D\leq 10^2$. (a) $Re_D=0.0001$; (b) $Re_D=0.1$; (c) $Re_D=1$; (d) $Re_D=10$; (e) $Re_D=50$; (f) $Re_D=100$.

In Fig. 3(*a*)–(*c*), the streamline patterns for $\mathrm{Re}_D=10^{-4}$, 10^{-1} and 1 are depicted. In all three cases shown, the flow follows the upper convex corner without revealing a flow separation. Furthermore, a corner vortex is found in the concave corner behind the step. In this range of very small Reynolds numbers ($10^{-4}\leq \mathrm{Re}_D \leq 1$), the size of this vortical structure is nearly constant varying between $x_1/h=0.350$ (for $\mathrm{Re}_D=10^{-4}$) and 0.365 (for $\mathrm{Re}_D=1$). Under these conditions, the effect of inertia forces can be assumed to be negligible compared with viscous forces often denoted as molecular transport. Hence the flow resembles the Stokes flow.

For a detailed analysis, the governing equations for the general case of Navier-Stokes flow given by Eqs. (1) and (2) are rewritten in a streamfunction-vorticity formulation eliminating the pressure:

$$\frac{\partial \psi}{\partial y}\frac{\partial \omega}{\partial x}-\frac{\partial \psi}{\partial x}\frac{\partial \omega}{\partial y}=\frac{1}{\mathrm{Re}_D}\nabla^2\omega \tag{5}$$

with

$$u=\frac{\partial \psi}{\partial y},\quad v=\frac{\partial \psi}{\partial x}\quad \text{and}\quad \omega=\frac{\partial u}{\partial y}-\frac{\partial v}{\partial x}. \tag{6}$$

The stream function ψ and the vorticity ω are related by

$$\omega=\nabla^2\psi. \tag{7}$$

For the description of creeping motion ($\mathrm{Re}_D\rightarrow 0$), the vorticity transport equation (5) reduces to the right-hand side of this equation, which in combination with Eq. (7) yields a biharmonic equation for the stream function ψ:

$$\nabla^4\psi=0. \tag{8}$$

This can be solved subject to appropriate boundary conditions. Based on analytical work, Moffatt [2] derived an expression for the complex stream function for the flow in the vicinity of sharp corners. In polar coordinates (r,θ) with the origin in the corner, the solution reads

$$\psi(r,\theta)=Kr^{\lambda}[\cos((\lambda-2)\alpha)\cos(\lambda\theta)-\cos(\lambda\alpha)\cos((\lambda-2)\theta)]. \tag{9}$$

The complex coefficient K is determined by the nature of the far-field flow. The complex exponent λ satisfies the nonlinear algebraic equation

$$\lambda\tan(\lambda\alpha)=(\lambda-2)\tan(\lambda-2)\alpha \tag{10}$$

where 2α defines the angle between two rigid boundaries. Under the condition $2\alpha<146$ deg Moffatt [2] showed the existence of an infinite sequence of closed eddies with decreasing size and strength in the sharp corner (see Fig. 1) now known as Moffatt eddies. Moffatt also demonstrated that even for finite Reynolds

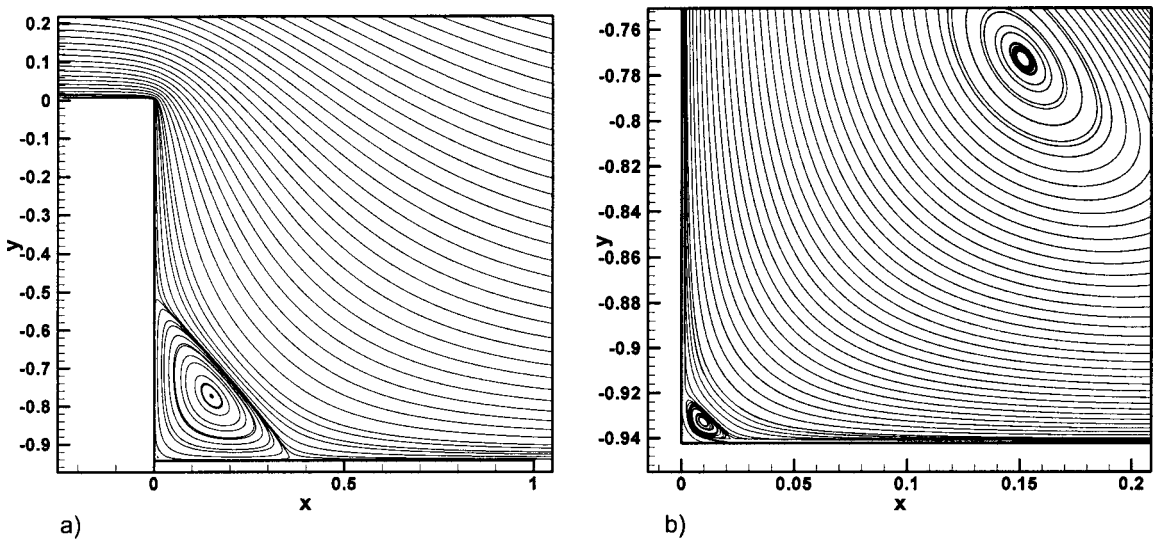

Fig. 4 Flow in the vicinity of the step. Expansion ratio $H/h=1.9423$; $Re_D=1$. (a) Zoom of the concave corner showing the first Moffatt eddy; (b) Increased zoom showing additionally the second Moffatt eddy.

numbers, the flow in the direct vicinity of the corner can still be described by the creeping flow assumption. It is therefore interesting to investigate whether for a finite Reynolds number, Moffatt vortices exist in the backward-facing step flow and whether they can be predicted by numerical solutions of the Navier-Stokes equations. Exemplarily the case of $\mathrm{Re}_D=1$ was chosen. At the upper convex corner of the step, $2\alpha=270$ deg and hence far beyond the critical value. In coincidence with the theory, no Moffatt eddy is found in the prediction. However, much more interesting is the lower concave corner with $2\alpha=90$ deg, where the condition on α for the existence of Moffatt eddies is satisfied.

Trying to capture the corner eddies numerically, a refined simulation applying the local grid refinement technique was carried out. The resolution in either direction near the corner point was taken as $\Delta x_{\min}/h=\Delta y_{\min}/h=0.001$. The entire domain was divided into seven different blocks and in total 310,784 control volumes were employed. Figure 4(*a*) depicts the streamlines in the vicinity of the corner showing the first corner vortex. Additionally, Fig. 4(*b*) shows a increased zoom of the corner region revealing that the second corner eddy (Moffatt eddy) could be resolved at the finite Reynolds number $\mathrm{Re}_D=1$. Based on Moffatt's considerations, an infinite sequence of eddies has to be expected but with reasonable resources it was not possible to resolve the third and subsequent eddies. This is due to the fact that the dimensions of successive eddies fall off in geometric progression with a ratio of $r_n/r_{n+1}=\exp(2.79)\approx 16.28$ for the α-value considered (Moffatt [2]). Here r_n and r_{n+1} are the distances of the center of the nth and $(n+1)$th eddy from the corner, respectively. The ratio of sizes of the first and second eddies found in the prediction are in close agreement with the theoretical value mentioned above. Moffatt also derived a measure for the intensity of consecutive eddies showing a fall-off with a geometric progression similar to the size. However, for a right-angle $(2\alpha=90)$ deg the eddy intensity drops more rapidly than the size at a ratio of $\exp(7.63)\approx 2059$. These considerations explain why the resolution of more than two corner vortices is extremely costly and hence was not taken into account.

Moffatt [2] noted in his paper that the size of the first corner vortex for $\mathrm{Re}_D\to 0$ is determined by conditions far from the corner where driving forces agitate the fluid. For the backward-facing step flow two important parameters are obviously responsible for the far-field flow. The first is given by the geometrical configuration, which can be defined by the expansion ratio h/H. The second is the Reynolds number. Figure 3 clearly demonstrates the effect of the Reynolds number for a fixed expansion ratio $H/h=1.9423$. As mentioned above, the size of the first eddy is nearly constant for all Reynolds numbers below $\mathrm{Re}_D=1$. This is also depicted in Fig. 5, showing the length x_1 of the first corner eddy behind the step (recirculation region) normalized by the step height S as a function of Re_D. However, for $\mathrm{Re}_D>1$ the corner vortex strongly increases in size. As a direct consequence, the corner vortex reaches up to the corner of the step at $\mathrm{Re}_D\approx 10$ and covers the complete face of the step. Hence a change in the entire flow structure is observed and the notation of a *corner vortex* has to be replaced by the notation *recirculation region*, which for $\mathrm{Re}_D>10$ better reflects the flow structure. With increasing Reynolds number the size of the recirculation region steadily increases.

In Fig. 6, streamline patterns for four different Reynolds numbers ($\mathrm{Re}_D=200$, 400, 600 and 800) are displayed, showing the increasing size of the recirculation region behind the step up to about $x_1/S\approx 12$ at $\mathrm{Re}_D=800$. Figure 7 shows the variation of reattachment length as a function of the Reynolds number. The agreement of the present predictions and the experimental results of Armaly et al. [11] for the vertical mid-plane ($z=W/2$) is excellent for $\mathrm{Re}_D\leqslant 400$. However, for $\mathrm{Re}_D\geqslant 400$ a discrepancy between computations and measurements at $z=W/2$ is visible,

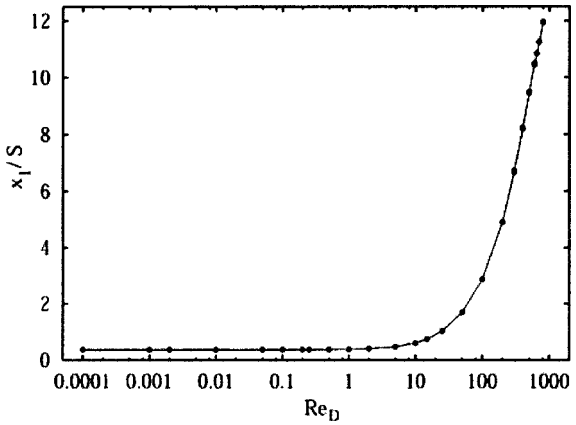

Fig. 5 Length x_1 of the first corner eddy behind the backward-facing step (expansion ratio $H/h=1.9423$) normalized by the step height S.

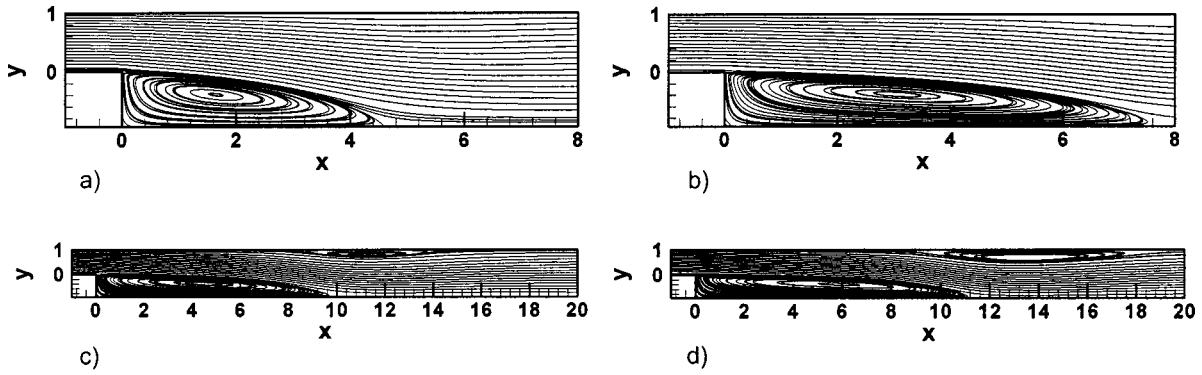

Fig. 6 Flow in the vicinity of the step. Expansion ratio $H/h=1.9423$; $200 \leq Re_D \leq 800$; two-dimensional simulations; (a) $Re_D=200$; (b) $Re_D=400$; (c) $Re_D=600$; (d) $Re_D=800$.

which obviously increases with Re_D. In order to improve these predictions, a variety of computations with different domain sizes, different resolutions and flow solvers (*FASTEST-2D* and *LESOCC*) were carried out. However, even on the finest grid and with an extremely long computational domain, the deviations observed between the measurements of Armaly et al. [11] and the present simulations could not be reduced. As expected from previous predictions by Armaly et al. and others (e.g. Kim and Moin [13]), which, however, used much coarser grid resolutions, the deviations mentioned above have to be attributed to the restriction to two-dimensional flow in the computations.

In addition to the primary recirculation zone, there exists a secondary recirculation zone near the upper wall for $Re_D>400$. The adverse pressure gradient due to the sudden expansion at the edge of the step induces this separated flow. In Figs. 6(*c*) and (*d*), the secondary recirculation region is clearly visible for $Re_D=600$ and 800, respectively. Figure 8 shows the starting position of the secondary recirculation zone (x_4/S) and the corresponding end (x_5/S) as a function of the Reynolds number. The size of the secondary recirculation zone increases with increasing Reynolds number while at the same time the flow structure is moving in a streamwise direction. Far downstream of the step, the flow recovers to a parabolic profile. However, at high Reynolds numbers such as $Re_D=800$, the flow recovery takes more than 20 step heights.

Figure 9 describes the variation of the primary reattachment lengths with Reynolds numbers for different expansion ratios, namely 1.9423, 2.5 and 3. At Reynolds numbers smaller than 400 the flow was predominantly two-dimensional. The reattachment lengths (x_1/h) increase with increase in the expansion ratio; for example, at a Reynolds number of 400, the reattachment lengths are 7.708, 10.214 and 12.409 for the expansion ratios of 1.9423, 2.5 and 3, respectively. The two-dimensional flow becomes unsteady with increasing Reynolds numbers. For an expansion ratio $H/h=1.9423$ the steady character of the two-dimensional backward-facing step flow was revealed over the entire Reynolds number range ($Re_D \leq 800$) investigated. For the case of expansion ratio $H/h=3$, the unsteadiness was observed at a Reynolds number of 500. The flow field demonstrated a low frequency oscillation at this Reynolds number.

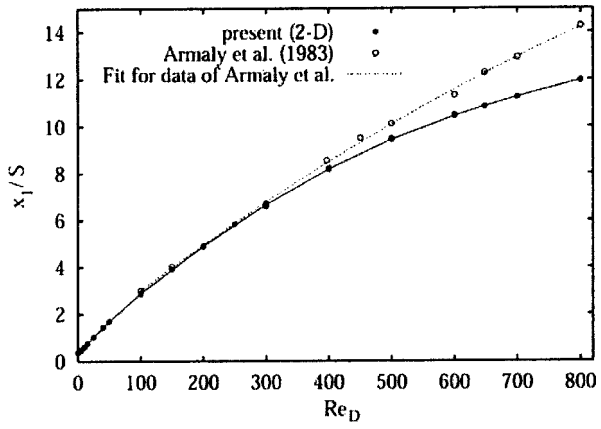

Fig. 7 Length x_1 of the primary recirculation region behind the backward-facing step (expansion ratio $H/h=1.9423$) normalized by the step height S

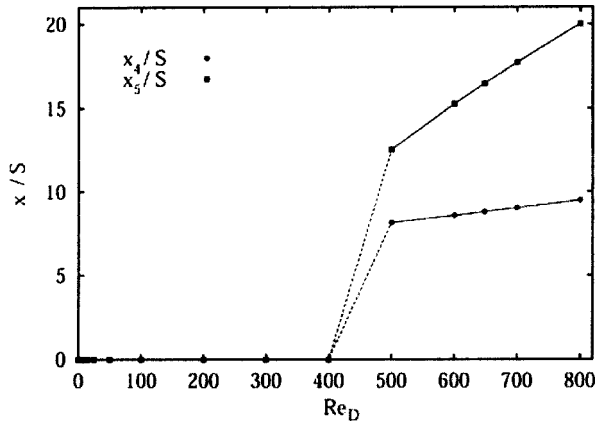

Fig. 8 Length x_4 and x_5 of the secondary recirculation region (on the roof) behind the backward-facing step (expansion ratio $H/h=1.9423$) n ormalized by the tep height S

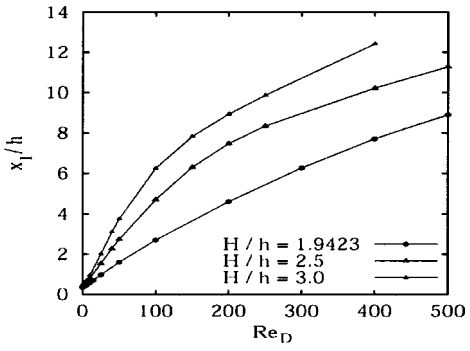

Fig. 9 Length of the primary recirculation region behind the backward-facing step x_1 for different expansion ratios, $H/h=1.9423$, 2.5, and 3.0

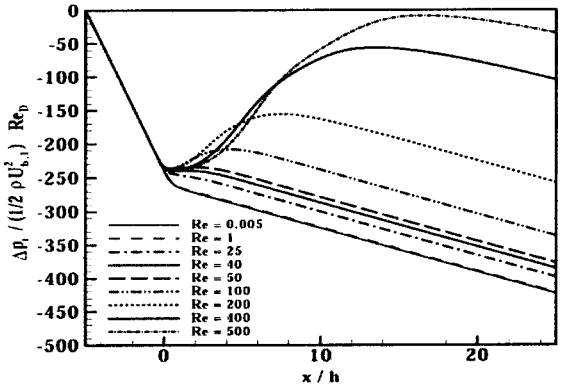

Fig. 10 Dimensionless pressure loss $\Delta p_t/(0.5\rho U_{b,1}^2)\cdot Re_D$ in the streamwise direction of the channel. Expansion ratio H/h=1.9423; Reynolds number range $5\cdot 10^{-3}\leqslant Re=Re_D\leqslant 5\cdot 10^2$.

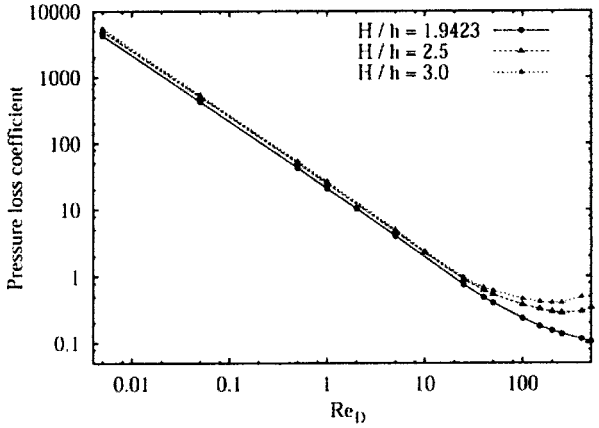

Fig. 11 Pressure loss coefficient ξ in the channel for different Reynolds numbers Re_D and expansion ratios H/h

4.1.2 Pressure Losses. An important engineering quantity for the design of channel systems with varying cross-sections is the pressure drop, which defines the performance of pumps required. For that purpose, the pressure drop in the backward-facing step geometry was evaluated for the expansion ratios and Reynolds numbers of interest in this study. Based on the two-dimensional simulations, the total pressure drops $\Delta p_t/(0.5\rho U_{b,1}^2)$ occurring on the axis of the channel are shown as a function of the Reynolds number in Fig. 10 for an expansion ratio $H/h=1.9423$. The pressure distributions for the Reynolds numbers range $0.005\leqslant \mathrm{Re}_D\leqslant 25$ are basically linear combinations of the pressure drops in the channels before and after the step, denoted Δp_1 and Δp_2, respectively. For a fully developed laminar channel flow, this irreversible pressure drop related to friction can be analytically determined as

$$\Delta p_1=\frac{\lambda}{\mathrm{Re}_D}\frac{L_u}{h}\frac{\rho}{2}U_{b,1}^2 \quad \text{and} \quad \Delta p_2=\frac{\lambda}{\mathrm{Re}_D}\frac{L_d}{H}\frac{\rho}{2}U_{b,2}^2, \tag{11}$$

where L_u and h are the length and height of the channel upstream of the step and L_d and H denote the length and height downstream of the step, as sketched in Fig. 2. The quantities $U_{b,1}$ and $U_{b,2}=U_{b,1}h/H$ describe the bulk (mean) velocities in either part of the channel. Based on the present definition of the Reynolds number [see Eq. (4)], the friction coefficient for the channel is $\lambda=48$. With regard to Eq. (11), the following aspects should be mentioned. First, it is obvious why for highly viscous flows (i.e. low Re_D) the pressure decreases linearly in streamwise direction showing different slopes in both parts of the channel. Additionally, it is clear why the dimensionless pressure drop in Fig. 10 was scaled with the Reynolds number Re_D leading to matching curves in the upstream channel over the entire Reynolds number range. If no other losses or gains are of importance, the pressure distributions are linear combinations of the pressure drops Δp_1 and Δp_2 as mentioned for $0.005\leqslant \mathrm{Re}_D\leqslant 25$.

However, this trend of streamwise pressure variation differs for $\mathrm{Re}_D>40$. In addition to the irreversible pressure drop discussed above, a reversible pressure rise near the step has to be taken into account because its relative importance increased. This pressure rise corresponds to the Bernoulli effect, associated with the decrease in mean velocity due to the sudden expansion:

$$\Delta p_{\exp}=\frac{\rho}{2}(U_{b,1}^2-U_{b,2}^2)=\frac{\rho}{2}U_{b,1}^2\left(1-\frac{h^2}{H^2}\right) \tag{12}$$

Hence the dimensionless pressure rise at the expansion $\Delta p_{\exp}/(0.5\rho U_{b,1}^2)$ is solely a function of the expansion ratio corresponding to the Bernoulli effect due to changes in the flow area. Owing to the special scaling in Fig. 10, the product increases with increasing Reynolds number. After reaching the peak, the streamwise pressure distribution in the channel follows again the same slope for all Reynolds numbers. Consequently, the total pressure drop in a backward-facing step geometry can be decomposed into

$$\Delta p_t=\Delta p_1+\Delta p_2-\Delta p_{\exp}+\xi\left(\frac{\rho}{2}U_{b,1}^2\right) \tag{13}$$

The last term in Eq. (13) takes into account the irreversible pressure drop occurring due to additional losses at the step. In contrast to Eq. (11) given for fully developed channel flow, a slightly modified formulation of Δp_2 is reasonable for the cases where a recirculation region is found behind the step:

$$\Delta p_2=\frac{\lambda}{\mathrm{Re}_D}\frac{(L_d-x_1)}{H}\frac{\rho}{2}U_{b,2}^2=\frac{\lambda}{\mathrm{Re}_D}\frac{(L_d-x_1)}{h}\left(\frac{h}{H}\right)^3\frac{\rho}{2}U_{b,1}^2, \tag{14}$$

where x_1 denotes the primary reattachment length determined as a function of Re_D and H/h in Fig. 9. Based on the determination of Δp_t by the predictions, the coefficient of irreversible pressure drop ξ was evaluated for various Reynolds number and expansion ratios. The results are shown on a double-logarithmic scale in Fig. 11. The value of ξ decreases with increasing Reynolds number. Higher expansion ratios produce higher coefficients of the irreversible pressure drop ξ, as expected.

4.2 Three-Dimensional Predictions: Flow Field. At relatively low Reynolds numbers ($\mathrm{Re}_D\leqslant 400$), the mid-plane flow field in a channel with an expansion ratio $H/h=1.9423$ is accurately predicted by two-dimensional simulations. Beyond a Reynolds number of about 400, the side wall influences the structure of the laminar flow behind the step. The measured reattachment lengths at the mid-plane and the predictions of two-dimensional simulations do not match. The discrepancies between the experimental result and the two-dimensional simulation are the consequence of the three-dimensionality that influences the flow structure at the mid-plane of the channel. In order to prove this, we compared the three-dimensional numerical simulation and the experimental results at three different Reynolds numbers, i.e., $\mathrm{Re}_D=397$, 648 and 800. The flow was found to be steady at these Reynolds numbers. Based on a nominally two-dimensional configuration assuming periodic boundary conditions in the spanwise direction, Kaiktsis et al. [16] observed an oscillatory behavior of the backward-facing step flow beyond $\mathrm{Re}_c\approx 700$. In the laboratory experiment of Armaly et al. [11] using a three-dimensional step geometry, the primary reattachment length exhibits a peak at $\mathrm{Re}_D\approx 1200$ followed by a subsequent decrease beyond this Reynolds number. This behavior can only be attributed to the action of the Reynolds stresses which must be present already for slightly

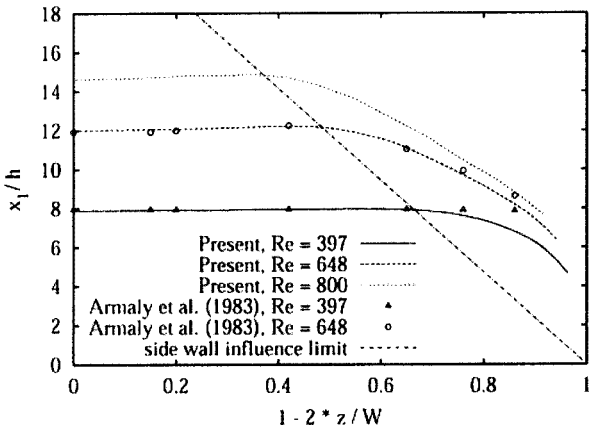

Fig. 12 Comparison of the spanwise location of the reattachment line past the backward-facing step at $Re=Re_D=397$, 648, and 800. Expansion ratio $H/h=1.9423$; aspect ratio $W/h=35$; present numerical 3-D simulation and experimental data of Armaly et al. [11].

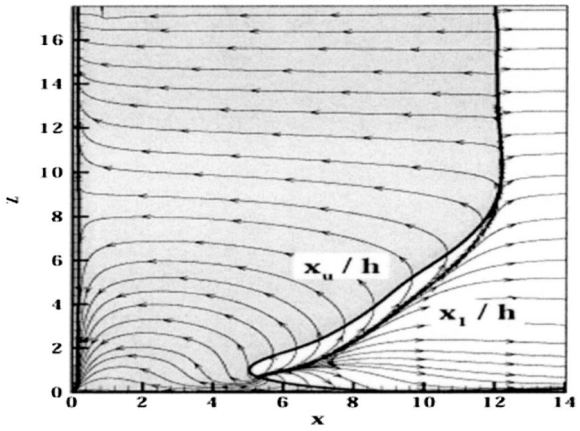

Fig. 14 Comparison between the boundary of the primary recirculation zone and the line of $\partial u/\partial y|_{wall}=0$. Flow past the backward-facing step at $Re_D=648$. Expansion ratio $H/h=1.9423$; aspect ratio $W/h=35$; (a) $y^*=0.046$; (b) $y^*=0.154$; (c) $y^*=0.273$; (d) $y^*=0.402$.

lower Reynolds numbers. This finding was complemented by our three-dimensional simulation at $Re_D=1300$. The unsteadiness of the flow was observed from the signals at different locations downstream of the expansion. In addition to the dominant frequency, f_1 another frequency, f_2, and the linear combination ($m_1 f_1 \pm m_2 f_2$, with integers m_1 and m_2) of f_1 and f_2 are present in the spectra. Hence in contrast to the observations of Kaiktsis et al. [16] for the two-dimensional configuration, the limit of steady flow in the three-dimensional case is expected to be at $Re_D \approx 1200$ characterized by the transitional regime ($1{,}200 < Re_D < 6{,}600$) found by Armaly et al. [11]. Consequently, the steady flow behavior predicted for $Re_D \leqslant 800$ is reasonable and in accordance with other simulations (e.g., Chiang and Sheu [22] and Williams and Baker [21]).

The comparison between the measured and predicted values of the primary reattachment lengths on the bottom wall (stepped wall) at $Re_D=397$ and 648, presented in Fig. 12, shows excellent agreement at different spanwise locations in the channel. For $Re_D=800$ no experimental data are provided by Armaly et al. [11]. Figure 12 also demonstrates the increasing side-wall effect with increasing Reynolds number. At $Re_D=397$ the influence of the side wall is visible up to about 36% of $W/2$, whereas about 54

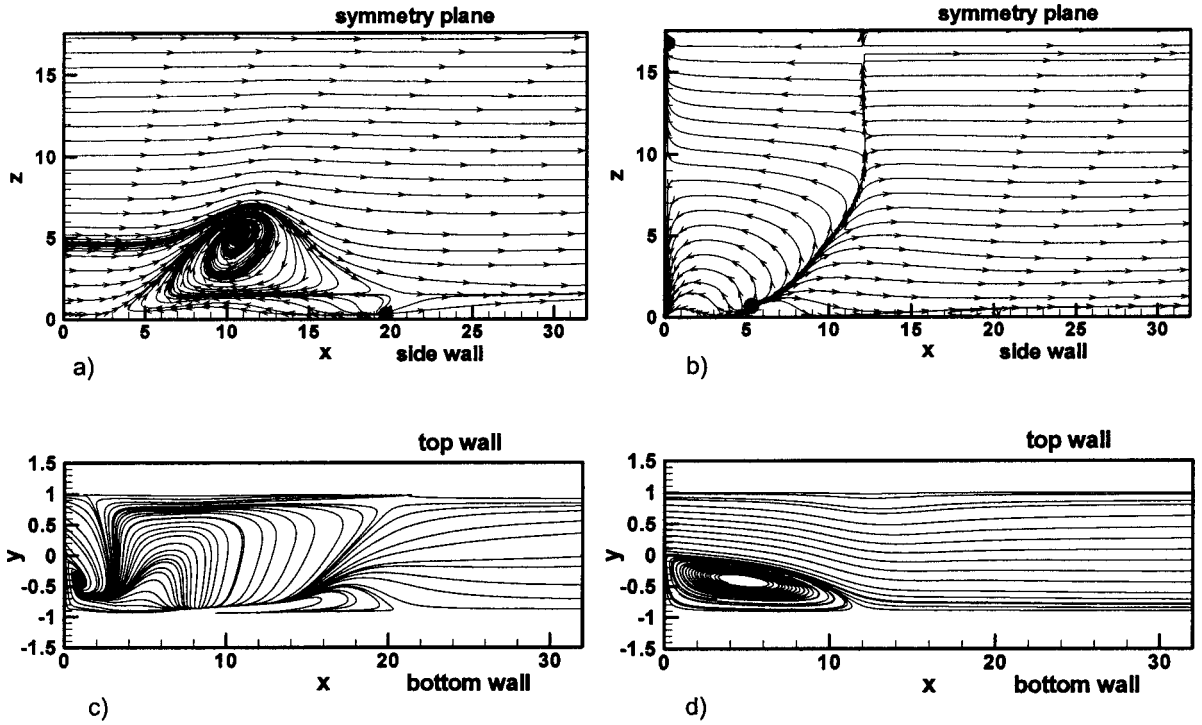

Fig. 13 Surface streamlines of the backward-facing step flow at $Re_D=648$. Expansion ratio $H/h=1.9423$; aspect ratio $W/h=35$; (a) Roof; (b) Bottom Wall; (c) Side Wall; (d) Symmetry Plane.

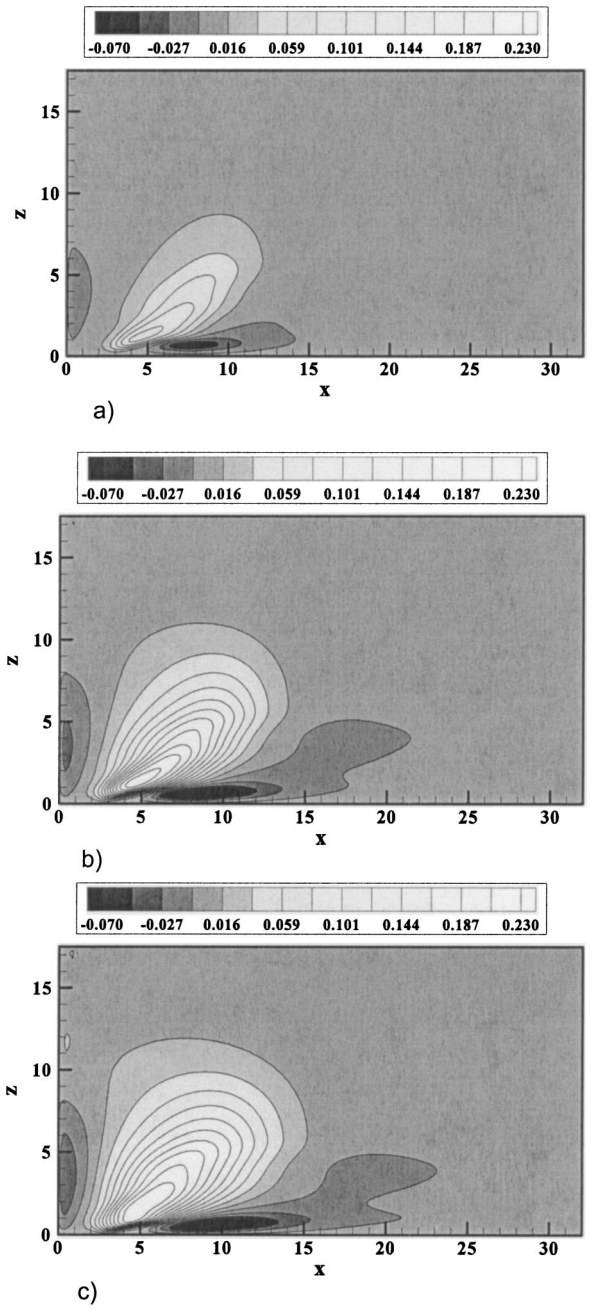

Fig. 15 Contours of the velocity component *w* on various *x-z* planes. *y denotes the dimensionless distance from the bottom wall; $H/h=1.9423$; $Re_D=648$**

and 66% are covered in case when $Re_D=648$ and 800, respectively. The results agree fairly well with predictions by Chiang and Sheu [22].

In order to understand the flow structure better, the limiting surface streamlines on the channel roof (Fig. 13(*a*)) and on the bottom (stepped) wall (Fig. 13(*b*)) are plotted at $Re_D=648$. The roof eddy extends about 40% of the width to the mid-plane. The limiting surface streamlines are the streamlines close to the surface (Hornung and Perry [38], Chiang and Sheu [22]). The kinematic aspects of the limiting surface streamlines are described by the singular points, namely nodes, saddle points and foci. The classification of critical points using local solutions of the Navier-Stokes equations was introduced by Oswatitsch [39]. The limiting streamlines diverge from the line of attachment. Usually this is known as positive streamsurface bifurcation. Figure 13(*b*) shows

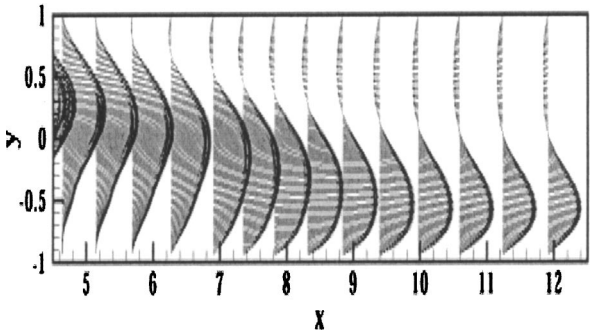

Fig. 16 Velocity vectors at a spanwise location of $z=1.05$; $H/h=1.9423$; $Re_D=648$

the diverging surface streamlines and the line of reattachment on the bottom wall for a Reynolds number of 648. Figures 13(*c*) and (*d*) depict the surface streamlines on the side wall and on the symmetric plane, respectively. The side wall shows the existence of a foci. All the surface streamlines spiral onto this point. The streamlines on the symmetric plane resembles with those of the two-dimensional simulation.

We have used the limiting streamlines to determine the boundary of the primary recirculation zone on the bottom wall (stepped wall) of the channel. As described by Chiang and Sheu [22], the surface streamlines tend to diverge from the line of attachment. The streamlines on both sides of this line of attachment move in opposite directions. Figure 14 shows that this boundary line (x_1/h) is different from the line (x_u/h) on which the gradient of the streamwise component of velocity at the wall ($\partial u/\partial y|_{wall}$) is zero. It is not incongruous to mention here that quantities such as x_1/h and x_u/h are identical for a two-dimensional flow. The effects of three-dimensionality culminate in the creation of a spanwise velocity component. This spanwise velocity component is responsible for the difference in the trajectory of the line that denotes the boundary of the primary recirculation region and the line on which $\partial u/\partial y|_{wall}$ is zero, particularly near the side wall. Moreover, it should be mentioned that these two lines are identical with each other over a span that extends a little more than about 50% of the half channel width in either direction of the symmetry plane. The discrepancies observed are more pronounced near the side wall where the *w* component of velocity is fairly strong. Another observation is that the reattachment length, based on the criterion of $\partial u/\partial y|_{wall}=0$ which defines a zero wall shear stress in the streamwise direction, increases near the side wall after attaining a minimum value. In fact, it reaches its maximum at the

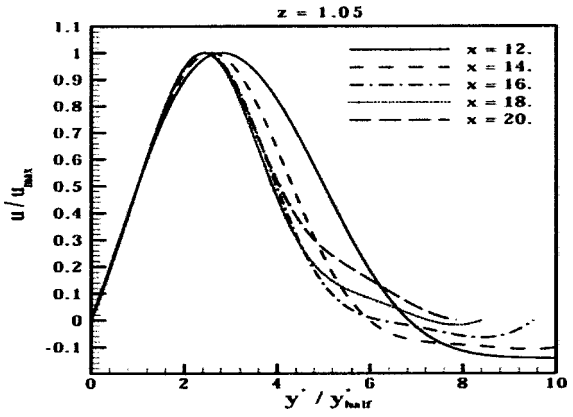

Fig. 17 Development of a wall jet in streamwise direction near the bottom wall. Spanwise location $z=1.05$; $H/h=1.9423$; $Re_D=648$; three-dimensional simulation.

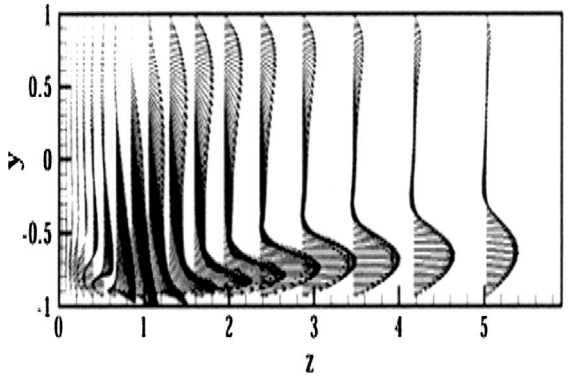

Fig. 18 Cross-stream velocity vectors at a streamwise location of $x=6$; $H/h=1.9423$; $Re_D=648$

side wall. The numerical data reveal this fact, even though it is not very evident from the figure. Our observation is well supported by Nie and Armaly [24].

The experiments of Armaly et al. [11] indicate that for an expansion ratio of 1.9423, the flow appears to be three-dimensional above $Re_D=400$. The transition to three-dimensionality is the primary source of discrepancies that appear in the comparison of two-dimensional computation and the experimental results above a Reynolds number of 400. In order to address the issues related to three-dimensionality, we resort to our three-dimensional simulation for $Re_D=648$. Figure 15 depicts the development of the spanwise component of velocity at four different horizontal planes located at $y^*=0.046$, 0.154, 0.273 and 0.402 from the bottom wall. Figures 15(*a*)–(*d*) show the gradual development of isolines of *w* velocity over different horizontal planes. The *w* velocity is initiated near the side wall, at the edge of the step as a consequence of development of a low-pressure zone and the fluid recirculation therein. The zone, influenced by the *w* velocity, grows larger as one moves in the perpendicular direction from the bottom wall. The maximum value of the *w* velocity is found to be 0.23.

The adverse pressure gradient due to the sudden expansion at the location of the step is responsible for the reverse flow together with the swirling motion in the spanwise direction, as shown by Williams and Baker [21]. They also showed the three-dimensional spiraling path from the side wall to the central symmetry plane. The swirling flow is responsible for the maximum and the minimum values that develop near the side wall in the spanwise distribution of the primary reattachment length (Fig. 12). The simulation for a Reynolds number of 648 shows a minimum around $(x=5;\ z=1)$. One noteworthy feature of the three-dimensional laminar flow is the shear layer that emanates adjacent to the step corner, impinges on the step wall and continues in the flow direction as a wall jet. Figure 16 shows the computed streamwise velocity profiles for a Reynolds number of 648 along the length of the channel at a spanwise location of $z=1.05$. After impingement, the flow continues downstream into the redeveloping flow region. A wall-jet-like characteristic feature is demonstrated during the redeveloping stage. The *u* velocity profile becomes self-similar in this regime. We investigate the *u* velocity profiles at a spanwise location of $z=1.05$ away from the side wall over the streamwise locations of $x=12$, 14, 16, 18 and 20. The *u* velocity profiles are normalized by $u_{\max}$, the local maximum value and the vertical distances from the bottom wall are normalized by y^*_{half}, the distance from the bottom wall to the location where the *u* velocity attains the value of local $u_{\max}/2$. Figure 17 illustrates the self-similar profiles at the lower part of the channel confirming the development of the wall-jet-like flow. The self-similarity holds good from the bottom wall until $y^*/y^*_{half}=3$. The maximum value of the *u* velocity profile at $x=12$ is 0.9867, whereas the maximum at $x=20$ is 0.6474.

Williams and Baker [21] found that yet another wall-jet-like profile forms at the step plane and grows in strength with increasing Reynolds number. They observed the presence of wall jet at the channel bottom wall, originated from the side wall and directed towards the channel mid-plane. The cross-stream velocity vectors (Fig. 18) at a streamwise distance of $x=6$ indicates that a wall-jet-like flow, in the spanwise direction, develops in the separating shear layer and moves towards the channel center. The formation of the wall jet in the spanwise direction is further demonstrated by our simulation at a Reynolds number of 648 in Figs.

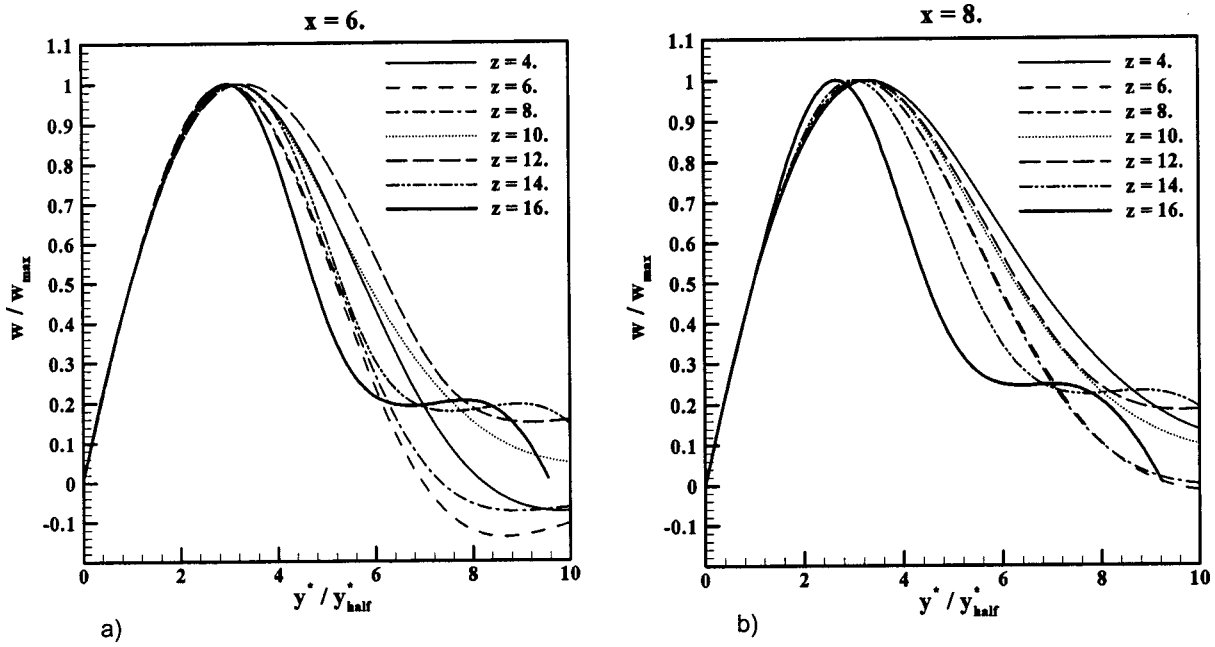

Fig. 19 Development of a wall jet in spanwise direction near the bottom wall. $H/h=1.9423$; $Re_D=648$. Steamwise locations: (a) $x=6$ (b) $x=8$.

19(*a*) and (*b*). The jet-like flow that develops in the spanwise direction is the culmination of the generation of the *w* velocity component from the side wall. The flow, predominantly the shear layer, emanates from the step edge and forms the separation zone at the sudden expansion. At about $x=5$, the flow impinges on the bottom wall, adjacent to the side wall and a jet-like flow emanates in the spanwise direction. The jet-like flow continues as a wall jet and interacts with the primary recirculation zone. We envisage the wall jet to exist at $x=6$ and 8. Figure 19(*a*) shows the self-similar wall-jet profile over various *z* locations at $x=6$. The *w* velocity distribution along *y* at a *z* location was normalized by $w_{\max}$, the maximum absolute value of the local *w* velocity distribution at that *z* location. The vertical distance from the bottom wall was expressed as y^* and this was normalized by y^*_{half}, the distance from the bottom wall to the point where the *w* velocity attains half of its maximum value. It is evident that the profiles at various *z* locations become self-similar in their bottom part, entailing the development of a wall jet up to the channel mid-plane. The deviation from a self-similar profile beyond $y^*/y^*_{half}=3.2$ can be explained by the difference in flow structure on the upper wall. Figure 19(*b*) reveals the same flow characteristics of the wall jets at various *z* locations at $x=8.0$. The value of $w_{\max}$ increases from 0.17 to 0.194 as one moves from $x=6$ to 8. However, a closer examination reveals that this maximum value of the *w* velocity decreases further downstream, say at $x=18$, and the wall-jet structure in the spanwise direction is no longer seen.

5 Conclusions

Laminar backward-facing step flow was investigated for a wide range of Reynolds numbers and expansion ratios by means of two- and three-dimensional simulations. The following conclusions can be drawn:

- For a wide range of Reynolds numbers, $10^{-4}\leqslant \mathrm{Re}_D\leqslant 1$, a corner vortex of nearly constant size is found in the concave corner behind the step. Based on the theory of Moffatt [2], an infinite sequence of closed eddies with decreasing size and strength is expected for $\mathrm{Re}_D\rightarrow 0$. In the present investigation, the first and second corner eddies were successfully predicted. Owing to the requirement for excessive computational resources, further eddies with decreasing strength could not be be captured with reasonable effort. Surprisingly, the phenomenon of creation of the Moffatt eddies (corner vortex) is not restricted to $\mathrm{Re}_D\rightarrow 0$ but is also evident at a finite Reynolds number of $\mathrm{Re}_D=1$.
- For the Reynolds number range $\mathrm{Re}_D\leqslant 400$ the flow past the backward-facing step can be predicted successfully by two-dimensional computations. The corner vortex observed for $\mathrm{Re}_D\leqslant 1$ reaches the step height at $\mathrm{Re}_D\approx 10$ (for $H/h=1.9423$) covering the entire face of the step. Hence the *corner vortex* steadily evolves into a *recirculation region* with increasing Re_D. Based on the two-dimensional predictions, excellent agreement with the experimental measurements of the flow field at the vertical mid-plane ($z=W/2$) is found for $\mathrm{Re}_D\leqslant 400$. As expected, this primary recirculation length increases non-linearly with increasing expansion ratio, H/h.
- As one of the most important engineering quantities for the design of a channel system, the pressure losses were evaluated for various expansion ratios and Reynolds numbers of interest in this study. The total pressure loss is subdivided into irreversible pressure drops related to friction in the channels before and after the step, the reversible pressure rise at the expansion and an irreversible pressure drop ξ occurring due to additional losses at the step. As expected, these losses increase with increasing step height *H* and decrease with increasing Reynolds number, except for $\mathrm{Re}_D>200$ and large expansion ratios, H/h.
- The three-dimensional predictions at three different Reynolds numbers ($\mathrm{Re}_D=397$, 648 and 800) were found to be in excellent agreement with the experimental results of Armaly et al. [11]. The effect of the side wall is evident for $\mathrm{Re}_D>400$, explaining the discrepancies observed between two-dimensional simulations and the experimental findings in the vertical mid-plane ($z=W/2$). In contrast to the observations of Kaiktsis et al. [16] an oscillatory behavior of the backward-facing step flow was found beyond $\mathrm{Re}_D\approx 1200$, which is in concurrence with the measurements of Armaly et al. [11].
- In the three-dimensional simulations it was observed that the boundary of the primary recirculation zone, determined by the surface streamlines on the bottom wall, is not identical with the line on which $\partial u/\partial y|_{wall}$ at the wall is zero.
- On the bottom wall, a wall jet in the streamwise direction with self-similar velocity profiles was identified as one of the main flow structures in the redeveloping region past the step. Furthermore, another wall jet in the spanwise direction, which is directed towards the channel mid-plane, was found near the bottom wall in the recirculation zone.

Acknowledgments

The stay of G. Biswas at LSTM Erlangen was supported by DAAD and KONWIHR (Competence Network on High-Performance Computing). The computations were carried out on the Fujitsu VPP 700 computer of the Leibniz Computing Center, Munich. This support is also gratefully acknowledged.

References

[1] Lee, Y. S. and Smith, L. C., 1986, *Analysis of power-law viscous materials using complex stream, potential and stress functions*, in Encyclopedia of Fluid Mechanics, vol. 1, Flow Phenomena and Measurement, ed. N. P. Cheremisinoff, pp. 1105–1154.
[2] Moffatt, H. K., 1964, *Viscous and resistive eddies near a sharp corner*, J. Fluid Mech., **18**, pp. 1–18.
[3] Roache, P. J., 1972, *Computational Fluid Dynamics*, Hermosa, New Mexico, pp. 139–173.
[4] Taylor, T. D., and Ndefo, E., 1971, *Computation of viscous flow in a channel by the method of splitting*, Proc. of the Second Int. Conf. on Num. Methods in Fluid Dynamics, Lecture Notes in Physics, vol. **8**, pp. 356–364, Springer Verlag, New York.
[5] Durst, F., and Peireira, J. C. F., 1988, *Time-dependent laminar backward-facing step flow in a two-dimensional duct*, ASME J. Fluids Eng., **110**, pp. 289–296.
[6] Alleborn, N., Nandakumar, K., Raszillier, H., and Durst, F., 1997, *Further contributions on the two-dimensional flow in a sudden expansion*, J. Fluid Mech., **330**, pp. 169–188.
[7] Brandt, A., Dendy, J. E., and Ruppel, H., 1980, *The multigrid method for semi-implicit hydrodynamic codes*, J. Comput. Phys., **34**, pp. 348–370.
[8] Hackbusch, W., 1985, *Multigrid Methods for Applications*, Springer, Berlin.
[9] Lange, C. F., Schäfer, M., and Durst, F., 2002, *Local block refinement with a multigrid flow solver*, Int. J. Numer. Methods Fluids **38**, pp. 21–41.
[10] Ladevéze, J., and Peyret, R., 1974, *Calcul numerique d'une solution avec singularité des equations de Navier-Stokes: écoulement dans un canal avec variation brusque de section*, J. Mech., **13**, no. 3, pp. 367–396.
[11] Armaly, B. F., Durst, F., Peireira, J. C. F., Schönung, B., 1983, *Experimental and theoretical investigation of backward-facing step flow*, J. Fluid Mech., **127**, pp. 473–496.
[12] Durst, F., and Peireira, J. C. F., and Tropea, C., 1993, *The plane symmetric sudden-expansion flow at low Reynolds numbers*, J. Fluid Mech., **248**, pp. 567–581.
[13] Kim, J., and Moin, P., 1985, *Application of a fractional-step method to incompressible Navier-Stokes equations*, J. Comput. Phys., **59**, pp. 308–323.
[14] Gartling, D. K., 1990, *A test problem for outflow boundary conditions—flow over a backward-facing step*, Int. J. Numer. Methods Fluids **11**, pp. 953–967.
[15] Lee, T., and Mateescu, D., 1998, *Experimental and numerical investigation of 2D backward-facing step flow*, J. Fluids Struct., **12**, pp. 703–716.
[16] Kaiktsis, L., Karniadakis, G. E., and Orszag, S. A., 1991, *Onset of three-dimensionality, equilibria, and early transition in flow over a backward-facing step*, J. Fluid Mech., **231**, pp. 501–528.
[17] Kaiktsis, L., Karniadakis, G. E., and Orszag, S. A., 1996, *Unsteadiness and convective instabilities in a two-dimensional flow over a backward-facing step*, J. Fluid Mech., **321**, pp. 157–187.
[18] Heenan, A. F., and Morrison, J. F., 1998, *Passive control of backstep flow*, Exp. Therm. Fluid Sci., **16**, pp. 122–132.
[19] Le, H., Moin, P., and Kim, J., 1997, *Direct numerical simulation of turbulent flow over a backward-facing step*, J. Fluid Mech., **330**, pp. 349–474.
[20] Kaltenbach, H.-J., and Janke, G., 2000, *Direct numerical simulation of flow separation behind a swept rearward-facing step at Re=3000*, Phys. Fluids, **12**(9), pp. 2320–2337.
[21] Williams, P. T., and Baker, A. J., 1997, *Numerical simulations of laminar flow over a 3D backward-facing step*, Int. J. Numer. Methods Fluids **24**, pp. 1159–1183.

[22] Chiang, T. P., and Sheu, T. W. H., 1999, *A numerical revisit of backward-facing step flow problem*, Phys. Fluids, **11**(4), pp. 862–874.
[23] Barkley, D., Gomes, M. G. M., and Henderson, R. D., 2002, *Three-dimensional instability in flow over a backward-facing step*, J. Fluid Mech., **473**, pp. 167–190.
[24] Nie, J. H., and Armaly, B. F., 2002, *Three-dimensional convective flow adjacent to backward-facing step—effects of step height*, Int. J. Heat Mass Transfer, **45**, pp. 2431–2438.
[25] White, F. M., 1991, *Viscous Fluid Flow*, 2nd ed., McGraw-Hill, New York.
[26] Orlanski, I., 1976, *A simple boundary condition for unbounded flows*, J. Comput. Phys., **21**, pp. 251–269.
[27] Breuer, M., and Rodi, W., 1996, *Large-eddy simulation of complex turbulent flows of practical interest*, In: Flow Simulation with High-Performance Computers II, ed. E. H. Hirschel, Notes on Numerical Fluid Mechanics, **52**, pp. 258–574, Vieweg Verlag, Braunschweig.
[28] Breuer, M., 1998, *Large-eddy simulation of the sub-critical flow past a circular cylinder: numerical and modeling aspects*, Int. J. Numer. Methods Fluids **28**, pp. 1281–1302.
[29] Breuer, M., 2002, *Direkte Numerische Simulation und Large-Eddy Simulation turbulenter Strömungen auf Hochleistungsrechnern*, Habilitationsschrift, Universität Erlangen-Nürnberg, Berichte aus der Strömungstechnik, ISBN 3-8265-9958-6, Shaker Verlag, Aachen.
[30] Demirdžić, I., and Perić, M., 1990, *Finite-volume method for prediction of fluid flow in arbitrary shaped domains with moving boundaries*, Int. J. Numer. Methods Fluids **10**, pp. 771–790.
[31] Patankar, S. V., and Spalding, D. B., 1972, *A calculation procedure for heat, mass and momentum transfer in three-dimensional parabolic flows*, Int. J. Heat Mass Transfer, **15**, pp. 1787–1806.
[32] Perić, M., Kessler, R., and Scheuerer, G., 1988, *Comparison of finite-volume numerical methods with staggered and colocated grids*, Comput. Fluids, **16**, pp. 389–403.
[33] Durst, F., and Schäfer, M., 1996, *A parallel blockstructured multigrid method for the prediction of incompressible flows*, Int. J. Numer. Methods Fluids **22**, pp. 549–565.
[34] Lange, C. F., Durst, F., and Breuer, M., 1998, *Momentum and heat transfer from cylinders in laminar flow at* $10^{-4} \leqslant Re \leqslant 200$, Int. J. Heat Mass Transfer, **41**, pp. 3409–3430.
[35] Lange, C. F., Durst, F., and Breuer, M., 1999, *Wall effects on heat losses from hot-wires*, Int. J. Heat Mass Transfer, **20**, pp. 34–47.
[36] Durst, F., Shi, J. M., and Breuer, M., 2002, *Numerical prediction of hot-wire corrections near walls*, J. Fluids Eng., **124**, pp. 241–250.
[37] Shi, J. M., Breuer, M., and Durst, F., 2002, *Wall effect on heat transfer from a micro cylinder in near-wall shear flow*, Int. J. Heat Mass Transfer, **45**, pp. 1309–1320.
[38] Hornung, H., and Perry, A. E., 1984, *Some aspects of three-dimensional separation, part I: streamsurface bifurcations*, Z. Flugwiss. Weltraumforsch., **8**(2), pp. 77–87.
[39] Oswatitsch, K., 1958, *Die Ablösungsbedingung von Grenzschichten*, In: Grenzschichtforschung, ed. H. Goertler, pp. 357–367, Springer Verlag Berlin/Göttingen/Heidelberg.

Christian Del Taglia[+]
Lars Blum
Jürg Gass
Yiannis Ventikos[++]
Dimos Poulikakos*

Laboratory for Thermodynamics in Emerging Technologics,
Swiss Federal Institute of Technology,
ETH-Zentrum, Sonneggstrasse 3, 8092 Zurich,
Switzerland

Numerical and Experimental Investigation of an Annular Jet Flow With Large Blockage

Unsteady 3-D numerical simulations and 3-D LDA measurements of an annular jet with a blockage ratio of 0.89 and Reynolds number 4400 are presented. At these flow conditions, the flow inside of the recirculation zone is asymmetric, with a preferential direction. Very good predictions of the velocity fluctuation values are achieved with the unsteady simulation technique in the same region, as the fluctuations are mainly large scale, structure dominated. A frequency near to 10 Hz is identified in the simulations, which is attributed to the principal shedding behavior of the vortical structures.
[DOI: 10.1115/1.1760533]

1 Introduction

Bluff-body flows are encountered in many fields of practical interest. In the case of turbulent flames, the existence of a zone dominated by intense recirculation, omnipresent in such flows, increases the mixing intensity and stabilizes the flame. Stability is a fundamental issue in gas turbine combustion, where extremely lean fuel-air mixtures are adopted for achieving low NO_x emissions [1,2]. These lean flames are often very close to the extinction limit. Another advantage of enhanced mixing is the reduced peak temperature and, consequently, the possibility of an additional reduction of thermal NO_x emission.

The axisymmetric bluff-body stabilized burner is a combustion device of practical relevance because it introduces highly strained and recirculating turbulent flows. It consists of a tube of diameter D_0 with a axisymmetric bluff-body of smaller diameter $D<D_0$ at the outlet. Disks, cones or cylinders are frequently used as bluff-bodies. The flow is forced to pass through the annular slot and to form an annular jet, Fig. 1a. Due to flow separation, a region of subatmospheric pressure is formed behind the disk, and a part of the annular jet is entrained in that region in a continuous strong recirculation.

Numerous experimental studies of the non-reacting time-averaged flow field in the recirculation zone of turbulent annular jets have appeared in the literature [3–7]. It has been found that the ratio of recirculation length to bluff-body diameter decreases with increasing blockage ratio D^2/D_0^2, while the ratio of reverse mass flow to total mass flow in the recirculation zone increases with increasing blockage ratio. The actual shape of the bluff-body influences the flow direction at the jet exit and therefore the recirculation length [3,6].

The turbulence intensity in the recirculation zone has been found to be particularly high (at least 30% of the local mean velocity [4]) and strongly anisotropic, becoming isotropic further downstream, after the reattachment point [3,4,6]. At the axial stagnation point, the radial stresses are larger than the axial stresses. This is due to the attenuation of the axial normal stresses in that region. Indeed, the production of axial normal stresses is a negative quantity at the stagnation point, since the axial velocity gradient is positive [6]. In the recirculation zone, the measured shear stresses do not vanish in the locations of zero velocity gradient [4]. Observations and measurements of this nature for the turbulence quantities lead to the conclusion that isotropic turbulence models (e.g., the standard k-ε model) are inadequate for appropriately capturing the Reynolds stresses [4,6].

Stroomer [7] and Aly and Rashed [8] investigated experimentally annular jets with a high blockage ratio. Stroomer was the only researcher who reported limited measurements inside the recirculation zone for such jets, where he also observed strongly anisotropic turbulence.

In contrast to the experimental works, the number of publications on turbulent annular jet simulations is very limited. McGuirk et al. [9], Durão et al. [10] and Akselvoll and Moin [11] studied the annular jet combined with a central jet (i.e., the coannular jet). Only Pope and Whitelaw [12] and Leschziner and Rodi [13] performed simulations on free (unconfined) annular jets, both works reporting results for a blockage ratio of 50%. In the latter work, very good predictions of the mean velocity on the symmetry axis were obtained, conducting axisymmetric steady simulations along with the skew-upwind differencing scheme and the quadratic, upstream-weighted differencing scheme.

One of the topics of the present work is the identification and the characterization of the flow asymmetry originating from the annular jet. Asymmetric flows originating from symmetric geometries and boundary conditions have been observed in the past [14–22]. The flow asymmetry is one of the possible solutions of the non-linear problem expressed by the Navier-Stokes equations [17]. Extensive experimental and numerical studies have been undertaken for the symmetric plane sudden expansion configuration [14,15,18–20]. A key observation is that for high expansion ratios or high Reynolds numbers, the flow is more prone to become and remain asymmetric.

For confined annular jets, flow asymmetry has been observed by Pinho and Whitelaw [16]. In their work, the blockage ratio was 50%. The authors performed LDA measurements of a water flow and a water-carboxy methyl cellulose mixture for analyzing the differences between Newtonian and non-Newtonian flows. In the range of Reynolds numbers between 400 and 6000 the pure water flow exhibited an asymmetric flow field. The authors identified oscillations with a Strouhal number of $St=0.094$ (the Strouhal number is the frequency normalized with the disk diameter and the annular jet velocity) in this range. They associated these oscillations to the propagation of instabilities shed from the disk edge, which are responsible for the asymmetry, as explained by Cherdron et al. [14]. In contrast to the results obtained for the symmetric plane sudden expansion, for which the asymmetry persists also in the turbulent regime [15], the confined annular jet shows a limited range of Reynolds numbers where the flow is asymmetric. Actually, as we shall show in the sequel, the symme-

[+]Air Flow Consulting AG, 8006 Zurich, Switzerland; e-mail: deltaglia@afc.ch
[++]Department of Engineering Science University of Oxford, U.K.
*Corresponding author. Phone: +41 1 63 22 738; e-mail: poulikakos@ltnt.iet.mavt.ethz.ch

Contributed by the Fluids Engineering Division for publication in the JOURNAL OF FLUIDS ENGINEERING. Manuscript received by the Fluids Engineering Division March 20, 2003; revised manuscript received January 5, 2004. Associate Editor: M. V. Ötügen.

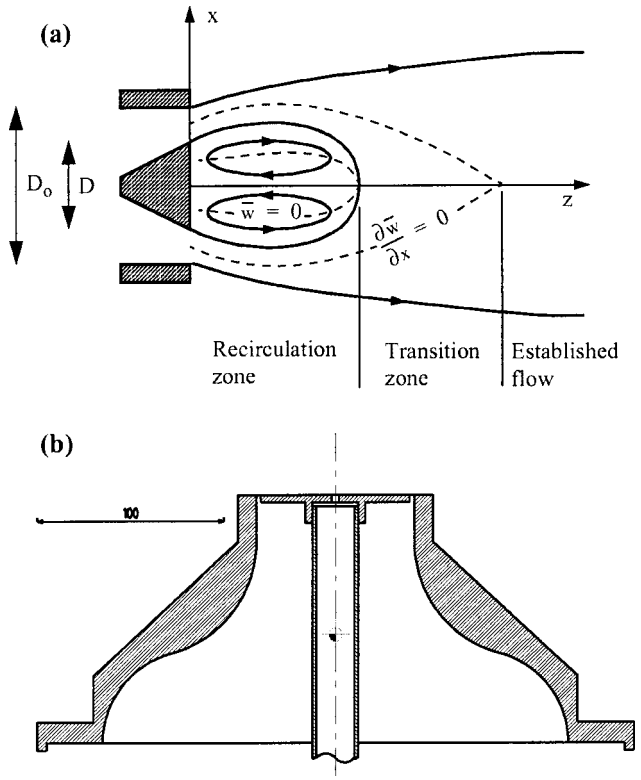

Fig. 1 (*a*) Sketch of an annular jet. (*b*) Cross-section of the annular jet device used in the experiments.

try breaking observed in the present unconfined annular jet is of a particularly complex nature, since it can be both spontaneous and forced.

To summarize, the present contribution deals with the numerical and experimental investigation of a non-reacting annular air jet with a blockage ratio of 89%. The experimental work consists of systematic three-dimensional LDA measurements of the flow field, whereas in the numerical work three-dimensional unsteady computations are employed. The objectives of this work are the following: to show the flow features (large scale asymmetry, fluctuating quantities and the existence of a characteristic vortex frequency) of the high blockage ratio jet under investigation by means of experimental and numerical data. Additionally, this work demonstrates that unsteady Reynolds Averaged Navier-Stokes (URANS) simulations can be, under certain requirements, a valuable tool for engineering design.

2 LDA Measurements

A cross-section of the upper part of the disk stabilized burner producing the air annular jet is shown in Fig. 1b. For the experimental part of this work we utilized the same burner device as in the measurements of Stroomer [7]. The disk diameter is $D=80$ mm and the inner tube diameter is $D_0=85$ mm, giving a blockage ratio of 0.89. After exiting the honeycomb (not shown), the air enters a contraction section and is forced to pass through the annular slot of width 2.5 mm. The air flow was fixed at such a rate that the axial bulk velocity at the slot exit was $U_0=13.2$ m/s. The accuracy of the thermal mass flow meter amounted to $\pm 2\%$. For the annular jet, the hydraulic diameter [4×(passage area)/(wetted perimeter)] is equal to D_0-D. Therefore, the Reynolds number based on the hydraulic diameter and the jet exit velocity was, in our case, 4400.

The burner had a second gas supply for an additional central flow through the 4 mm hole of the disk (Fig. 1b). However, in the present set of measurements, this hole was hermetically sealed.

The setup of the 3D-LDA system was described extensively by Flury [23]. It consists of a 5W Ar^+-Laser, which was operated in multiline mode at 2W, a two-component transmitting optics ($\lambda=514.5$ nm and 488 nm), an ordinary one-component transmitting optics ($\lambda=476.5$ nm) and the corresponding receiving optics. The optical system was mounted on an optical bench, which could be moved in three directions. Cross scattering was used to reduce the sphere equivalent diameter of the measurement volume down to 80 μm. The signals were processed by means of FFT analyzers. TiO_2 seeding particles of 1 μm mean diameter were used. The calibration factors of the three velocity components were determined by means of two independent ways: geometrically and by using a rotating disk. The difference in the results obtained by these two calibration techniques was always smaller than 4%.

The origin of the Cartesian coordinate system was fixed at the disk center. The symmetry axis of the disk was vertical and was chosen as the z-axis. The y-axis was parallel to the optical bench. The positioning accuracy of the measurement volume was 0.5 mm or better. The velocities were measured by scanning a grid with 11×9 nodes on the yz-plane. Additionally, measurements near to the jet nozzle were performed.

Approximately 50,000 shots were taken at each measuring point. From the collected shots, mean and r.m.s. values of the three velocity components could be computed. The errors in the mean values and in the r.m.s. values were within a $\pm 5\%$ range and a $\pm 10\%$ range, respectively.

Detailed measurements at the jet nozzle showed a quasi-parabolic radial profile of the axial velocity. However, differences of the order of $0.08U_0$ were observed in the peak values along the periphery of the annular nozzle. This indicates that a certain level of nonuniformity in the azimuthal distribution of the axial velocity at the jet nozzle must be taken into account. We shall expand on this point in the sequel.

It must be emphasized that Stroomer [7] used a two-component LDA system for measuring the axial and the radial velocity components, whereas the present experimental contribution deals with three-dimensional LDA measurements. The simultaneous measurement of three velocity components is critical for a accurate analysis of the flow structure, as shown in the sequel.

3 Numerical Simulations

3.1 Simulation Technique. Vortex shedding and convection is encountered in bluff-body flows, in which strong flow separation and recirculation are dominant. For the numerical simulation of these kind of flows, the Unsteady Reynolds Averaged Navier Stokes (URANS) simulation technique has been successfully employed in the past [24–27]. The technique is based on the Ensemble Averaged Navier Stokes equations, for which a model for the Reynolds stresses must be provided [24,27]. The reason for its success lies in the accurate direct computation of the large vortex structures, whereas the small and short time vortices are modeled.

For the simulation of the described annular jet flow three different models for the Reynolds stresses were used in this work: (1) the standard k-ε model based on the Boussinesq approximation (see Ref. [28]), (2) the Reynolds Stress Model of Speziale, Sarkar and Gatski (SSG-RSM, [29]), and (3) a no-model approach, for which the Reynolds stresses are assumed to be zero.

The results of the k-ε model are not shown here, as they were particularly poor as far as the large vortex fluctuations are concerned. Indeed, the local velocity oscillations presented us with a strong damping after a short initial transient. A large amount of dissipation is introduced in these computations through the turbulent viscosity ν_{eff}, which finally led the unsteady simulation to a steady state. Other works [25,27] have already observed that the standard k-ε model is very dissipative especially for unsteady flows with large scale unsteadiness, since the turbulent kinetic energy k is overpredicted. This is due to the large production term in the transport equation of k.

Table 1 Description of the three used meshes

	Central block			4 surrounding blocks			
	I	J	K	I	J	K	Total
Fine (F)	21	21	95	105	21	95	879,795
Medium (M)	17	17	72	78	17	72	402,696
Coarse (C)	13	13	58	64	13	58	202,826

The no-model approach represents a sort of "naive" Large Eddy Simulation (LES), as observed by Rodi [30]. LES is a technique commonly considered to be the most accurate in CFD for flows in the turbulent regime, because it computes the dynamics of the largest eddies directly and models the smallest eddies effects with a subgrid scale model. Since the effects of the smallest eddies are dissipative, it is argued that their effect can be artificially introduced by the numerical dissipation of the momentum equations spatial discretization scheme, namely through the coarseness of the computational grid compared to the smallest eddies size [30]. We shall emphasize at this point, that the fundamental equations solved in this approach are averaged in time, as we are dealing with the RANS technique. They do not reflect spatial filtering, as it is typical in LES.

The bulk of the results presented however come from the approach with the Reynolds Stress Model of Speziale, Sarkar and Gatski [29]. This approach, in a fashion very similar to the LES concept, delegates the large eddies to the momentum equations and assigns the modeling of the small eddies to the statistical (yet anisotropic) Reynolds Stress Model. It is obvious that for such a scheme to be consistent, the two energy ranges (large scale, momentum assigned and small scale, model assigned) must be sufficiently separated. This, as we shall see, is true for our system, where two orders of magnitude in the frequency separate the coherent from the statistical fluctuations.

The averaged quantities obtained with the unsteady simulation technique are generally affected by a statistical error, which is due to the limitation of the total simulated time interval. Indeed, the averages of distinct and contiguous time sub-intervals are slightly different from each other. In this work, the statistical error is given by the minimum and maximum velocity average value of three contiguous and equidistant time sub-intervals.

The analysis is limited to the post-transient state of the annular jet flow. In this state, the three velocity averages taken over three distinct and contiguous time sub-intervals are nearly the same. These averages also slightly differ from the average taken over the total time. In the simulation results, the condition to identify the post-transient state is that for each sub-interval, the difference between the sub-interval average and the overall average is less than the r.m.s. value of the sub-interval fluctuations.

3.2 Meshes and Boundary Conditions. For the computations, multiblock grids with three different mesh sizes were used. The grids consisted of five blocks in total. The block in the central region included the symmetry axis of the annular jet device, and four blocks were attached around the central block ("butterfly" configuration). The multiblock structure was preferred to a one block O-grid, because it provides greater cell size uniformity. The three different meshes have sizes of 202,826 points, 402,696 points and 879,795 points, and are referred in the sequel as coarse, medium and fine mesh, respectively (Table 1).

All three grids have the shape of a truncated cone, see for example Fig. 2. The axial expansion ratio of the grid is 1.05, starting from the bluff-body disk. So, the space between the grid points near to the disk is very small and cannot be recognized in Fig. 2. Figure 3 shows a cross section of the computational domain through the symmetry axis. In the same figure the boundary conditions and the dimensions are described.

It must be stressed that extensive steady-state computations have been carried out for testing the influence of the boundary conditions on the results. In one simulation, the region in the contraction tube below the bluff-body disk (see Fig. 1b) was included. It was shown that negligible differences in the mean values were observed when compared to the simulations which included only the region above the disk and a uniform annular jet of velocity U_0. Another simulation included a large free region to the side of the annular jet device, in order to test the air entrainment effect caused by the jet. It was shown that the same results are achieved when the large region is removed and replaced by a low velocity axial coflow, provided this coflow had a velocity below $0.1U_0$. Grids of different lateral and axial lengths, ranging up to 15D downstream, were tested and yielded, essentially, the same results with the grid and the boundary conditions used in the present work. An effect on the main flow pattern is observed only with domains smaller than 3 diameters. The effect is a contraction of the recirculation zone above the bluff-body disk.

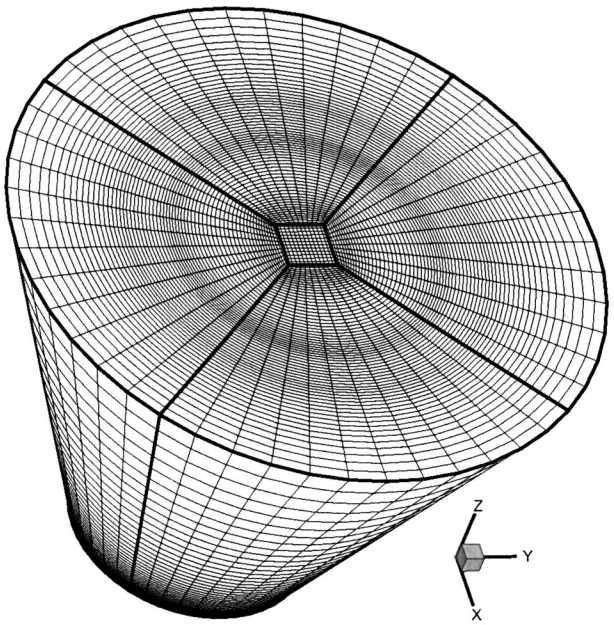

Fig. 2 Computational grid with approximately 200,000 mesh points. This grid is referred as *coarse grid*.

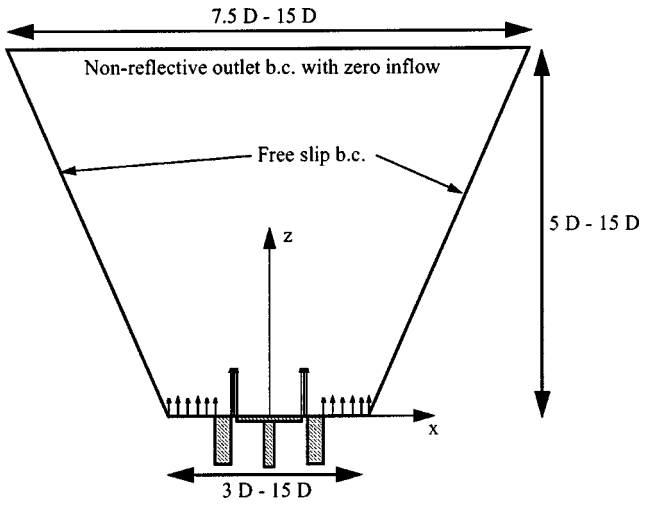

Fig. 3 Axial cross-section of the computational domain and boundary conditions

Table 2 Details of the unsteady simulations. *PC*800=PC Intel Pentium 3 (800 MHz) processor.

	No-model			k-ε	SSG-RSM		
	Grid C	Grid M	Grid F	Grid F	Grid C	Grid M	Grid F
Time step (seconds)	10^{-4}	10^{-4}	$4\cdot10^{-4}$	$4\cdot10^{-4}$	10^{-4}	10^{-4}	10^{-4}
Time step (D/U_0)	$1.7\cdot10^{-2}$	$1.7\cdot10^{-2}$	$6.6\cdot10^{-2}$	$6.6\cdot10^{-2}$	$1.7\cdot10^{-2}$	$1.7\cdot10^{-2}$	$1.7\cdot10^{-2}$
Space discretization order	2nd	2nd	2nd	2nd	2nd	2nd	2nd
Time discretization order	2nd	2nd	2nd	2nd	1st	1st	1st
Total time steps	16,000	11,000	6,700	3,700	25,000	3,200	5,600
Time steps past initial transient	12,000	11,000	6,000	···	20,000	3,200	4,000
CPU time per time step on PC800 (min.)	~3	7.5	~19	~14	~6	~12	~25

In Fig. 3, the smaller circular surface of the truncated cone (bottom) is put at the height of the bluff-body disk plane (at z/D =0). The larger circular surface (top) is the outlet of the computational domain. In our unsteady simulations, the flow at the annular jet nozzle was modeled with a uniform axial jet and the lateral air entrainment was modeled with a uniform low velocity coflow. The velocity of the uniform axial annular flow was U_0 =13.2 m/s (in z-direction) as the bulk velocity in the experiments (see Section 2). The coflow had a velocity of 0.5 m/s in axial direction and zero velocity in radial and azimuthal direction.

In the simulations with the Reynolds Stress Model, the turbulent intensity at the inflow surface was set to 10% with an integral length $l_0=0.06D$. This choice has been made guided by the measurements [7] in the nearest available position. The low velocity co-flow (external air entrainment) had a turbulent intensity of 5% and an integral length of 0.06D.

At the lateral surface of the truncated cone-shaped domain, a free-slip boundary condition was set. At the free-slip boundaries both the velocity gradients normal to the boundaries and the velocity component normal to the boundaries are zero. Moreover, for the Reynolds Stress Model simulations, this condition implies a zero diffusive flux imposed for the additional transport quantities. These additional quantities are the six Reynolds stresses τ_{ij} and the dissipation ε of the turbulent kinetic energy.

At the outlet, a non-reflective outflow boundary condition with zero inflow was put. Zero inflow means that a free-slip boundary condition is automatically put at the outlet boundary faces at which the momentum equations would result in an entering flow. This particular condition was chosen for reasons of numerical stability.

3.3 Summary of the Computations. The computations were performed using the finite volume code CFX-TASCflow. This platform employes a collocated grid scheme along with a pressure correction method for the pressure-velocity coupling. The space discretization scheme utilized was the second order skew upwind, which has demonstrated efficient behavior in a previous annular jet flow numerical study [13]. Due to constraints of the CFD code the computations with the SSG model were first order accurate in time. The solver uses the Incomplete Lower Upper (ILU) Factorization for the relaxation of the discretized equations at a specific time step.

Convergence is accelerated via the employment of an algebraic multigrid method, which is based on a W-cycle with 4 sweeps going down. The number of sub-iterations varies between 4 and 10. For each time step a certain number of iterations is performed until full convergence is achieved. Typically, the number of steps is 6.

Table 2 summarizes the performed computations. The time step is, depending on the simulation, 0.1 or 0.4 ms. The choice of the time step is based on the results obtained by Stroomer [7] and on typical Strouhal numbers of similar devices. Stroomer measured the velocity fluctuation frequencies of the flow coming out of exactly the same annular jet device, with the same Reynolds number. He reported a fundamental oscillation period of approximately 83 ms, which is at least 200 times larger than our timestep. For a confined annular jet Pinho and Whitelaw [16] found experimentally a value of St=0.094, which corresponds to an oscillation period of 64 ms (i.e., 160 times larger). Typical Strouhal numbers for simple bluff-body flows (i.e., flows past square, circular and triangular cylinders) are in the range 0.12–0.25 [27,30,31], which yield oscillation periods between 24 and 50 ms in our annular jet. Therefore, the time steps in the computations are sufficiently small to capture the main flow oscillations.

The unsteady computations needed to go through an initial transient before reaching the final stationary state characterized by oscillations around a steady time average. All postprocessing presented involves post-transient time series. Therefore, Table 2 specifies both the amount of totally collected time steps (fourth row) and the amount time steps in the post-transient state only (fifth row).

The stationary state was assumed to be reached, when all three velocity components averages taken over three distinct and contiguous time-sub intervals were nearly the same. Note that amounts in the fifth row of Table 2 reflect considerably large time lengths. Indeed the time intervals in the post transient state are at least 30 times larger than the time needed by the air flow to cover a distance equal to the disk diameter.

4 Results and Discussion

4.1 Mean Values. As a typical velocity signal of the unsteady computations, the instantaneous axial velocity on the symmetry axis at a distance of z/D=0.2 from the disk is plotted in Fig. 4. The signal is obtained from the simulations with the SSG-Reynolds Stress Model (SSG-RSM) and with the fine grid. It is characterized by stable oscillations. On the other side, the signal given by the no-model computations (not shown here) at the same position has larger amplitudes and has finer structures superimposed to the dominant fluctuations.

The time averaged axial velocity component on the symmetry axis is plotted in Fig. 5. Our and Stroomer's [7] experimental data are presented together with the results of our unsteady computations with the SSG-Reynolds Stress Model (SSG-RSM) and with the no-model approach.

The numerical results are based on the computations with grid F. The computations with the grids C and M give very similar predictions, indicating that the results, as far as this quantity is concerned, are fairly grid independent. The statistical errors (Section 3.1) of the computations are indicated with error bars. The fact that there is no significant difference between the axial profile computed with the two approaches points out, that the axial velocity component is relatively insensitive to the model used.

In the region near to the disk the axial velocity is negative due to the backflow of the recirculation. It becomes positive further downstream. The two modelling approaches employed for the

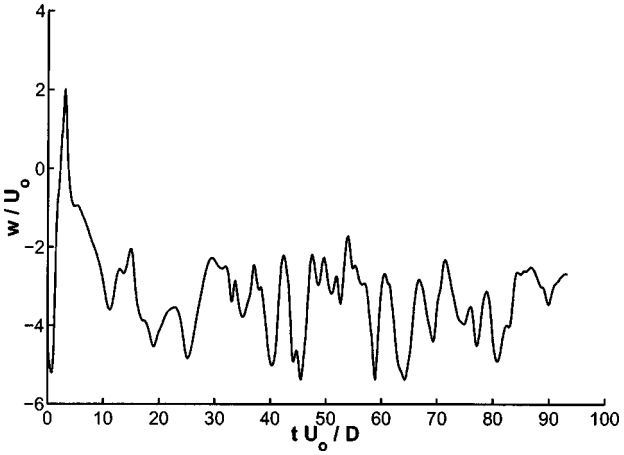

Fig. 4 SSG-RSM simulations: Axial velocity signal on the symmetry axis at z/D=0.2

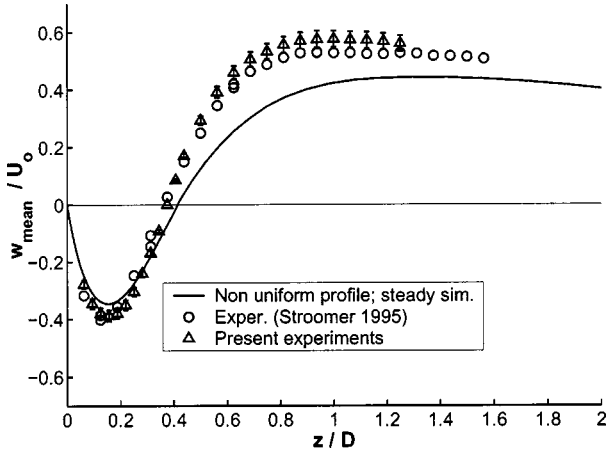

Fig. 6 Steady simulations with a nonuniform annular jet flow: Mean values of the axial velocity component on the symmetry axis

Reynolds stresses give the same results as far as the mean velocities are concerned. It can be observed that the position of the inversion point of the axial velocity component on the symmetry axis is overpredicted and the maximum reverse velocity is underpredicted. Test computations have shown that this discrepancy is due to the type of inlet boundary condition used in the computations. We used a uniform annular jet in the simulations, whereas the experiments show evidence of a relatively non-uniform mass flow in radial and azimuthal direction. More specifically, measurements in the vicinity of the jet exit of the device at different azimuthal positions showed a variation of the order of $0.08U_0$ in the peak values of the velocity. In order to test this hypothesis, three-dimensional steady simulations were conducted with a similar numerically imposed variance of the exit velocity at the jet periphery, according to Eq. (1):

$$w = (1 + 0.08 \sin \theta) U_0 \tag{1}$$

where w is the axial component of the velocity and θ is the azimuth.

The main result of these steady computations is that the velocity profile computed along the axis becomes very similar to the measured one (Fig. 6), in the critical recirculation region.

Effectively, what we showed with these computations is that when symmetry is broken in a forced manner, and at magnitudes that match experimental imperfections, the large scale features of the flow are captured satisfactorily [32].

Computations with other grids also show a decrease in the recirculation length by imposing a nonuniform velocity profile at the jet exit. However, since we shall discuss general features of this flow and in particular its (small and large scale) oscillating behavior, we shall focus on symmetrically forced configurations and spontaneously emerging asymmetries, from now on.

The annular jet asymmetry configuration we investigate, falls under the SO(2) symmetry group. It has been shown, and is well established now, that SO(2) flows can exhibit spontaneous symmetry breaking [22,33–37]. Moreover, recent results have provided strong evidence that, at least in certain cases, even minute, and effectively unavoidable, imperfections of the experimental rig cause symmetry breaking that manifests itself with responses that are disproportionally large with respect to the triggering disturbance [21,32,38–42].

The radial velocity on the symmetry axis is shown in Fig. 7. The numerical results are obtained from the no-model simulations. Both simulations and experiments give similar shapes: There is a maximum value near the upper border of the recirculation zone and an asymptotic decrease to zero further downstream. From the non-zero values of the radial component on the

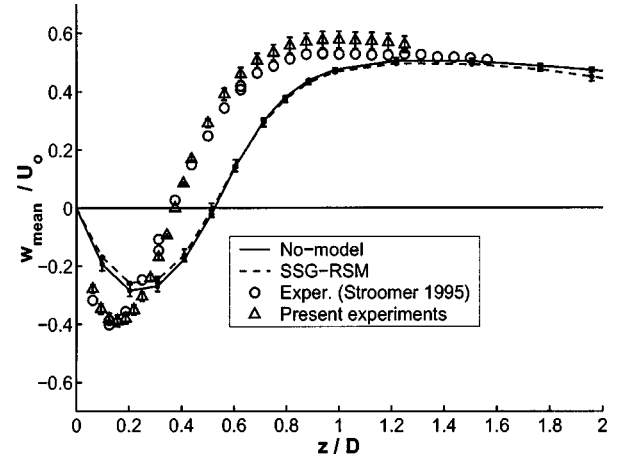

Fig. 5 Mean values of the axial (streamwise) velocity component on the symmetry axis. Results of unsteady simulations with a uniform annular jet.

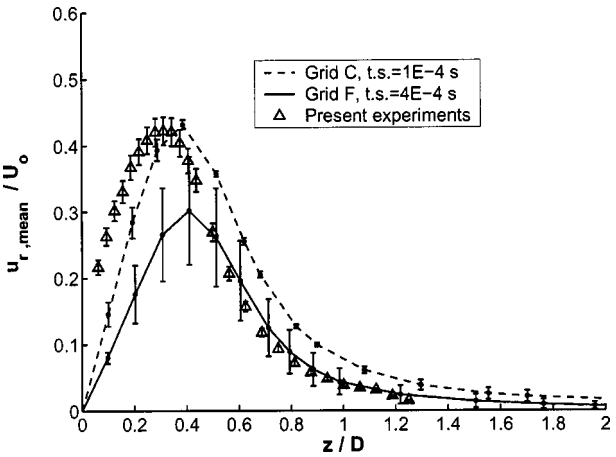

Fig. 7 Mean values of the radial velocity component on the symmetry axis (no-model approach)

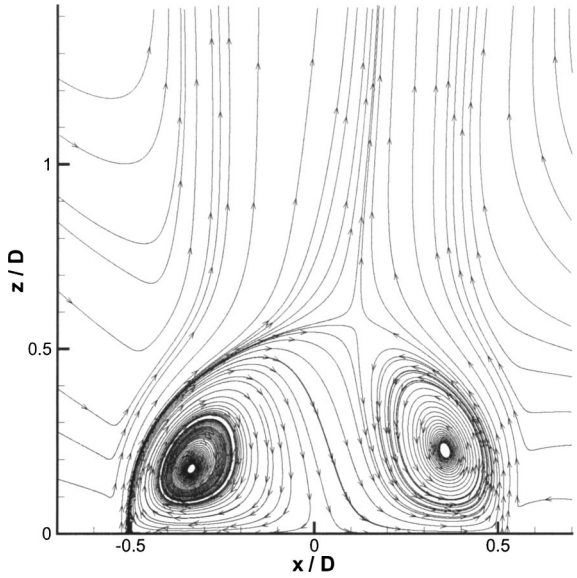

Fig. 8 SSG-RSM simulations: Streamlines of (u,w)-vectors on the xz-plane of the simulation coordinate system

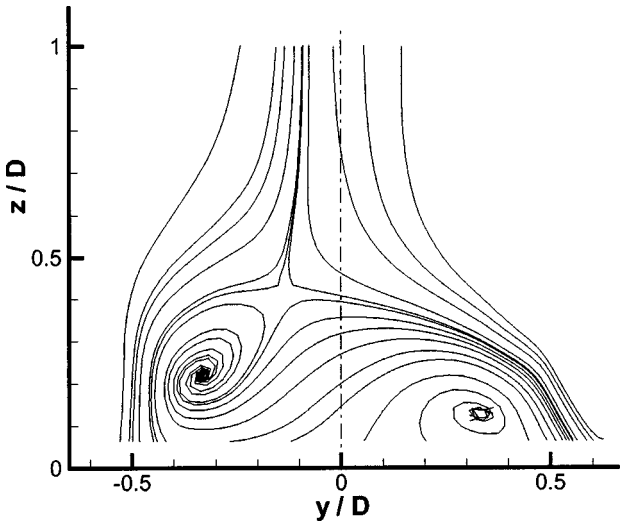

Fig. 9 LDA measurements: Streamlines of (v,w)-vectors on the yz-plane of the measurements coordinate system

symmetry axis it must be concluded that the mean flow is not axisymmetric in the region where the recirculation takes places.

The profile of the radial velocity on the symmetry axis (Fig. 7) is not fully grid independent. However, three-dimensional steady computations, for which a grid independence test has been performed, show the identical curve shape with deviations of only 20% from the unsteady simulations. So, also three-dimensional steady computations yield a non zero radial velocity profile on the symmetry axis, indicating a basic asymmetry in the flow field.

Figure 8 shows the streamlines of the (u,w)-vectors on the xz-plane through the symmetry axis, after averaging the results of the SSG-RSM simulations. The streamlines on the symmetry axis are not parallel to the axis itself. Part of the flow coming from the upper left region of the recirculation torus is moving to the lower right region, giving a net mass flow across the symmetry axis. The two cross sections of the recirculation torus have different shapes and positions. The stagnation point on this plane is located approximately at $x/D=0.15$ and $z/D=0.60$, i.e., it does not lie on the symmetry axis. The point at which the w-component is zero on the symmetry axis does not coincide with the stagnation point, as it is for axisymmetric flows.

As the computational domain is limited, and the velocity of the co-flow set at the boundary is small, a toroidal recirculation zone is present between the wake flow and the lateral sides of the computational domain. The downward flow towards the jet exit (left part in Fig. 8) is due to this recirculation. Of course, large velocity values of the co-flow would forbid the toroidal recirculation flow to be formed. However, such large velocity values would largely affect the wake flow, as extensive steady state computations have shown. We should mention that apart from examining the influence of the co-flow velocity magnitude, we have conducted a set of computations where the domain was extended peripherally outwards and below the disk section, therefore allowing for a more ''natural'' circulation development. The results however were essentially identical to the ones obtained with the co-flow approximation, significantly more expensive in computational time though.

The streamline plot of Fig. 8 was obtained after averaging the results of the unsteady Reynolds stress model computations. Qualitatively the same result, i.e., a net (asymmetric) flow from one annular jet side to the other is obtained in the unsteady computations with the no-model approach and with three-dimensional steady computations. Moreover, grid independent results of three-dimensional laminar computations at the same blockage ratio and at $Re=50$ show a stable and steady flow asymmetry of the same shape [43].

Essentially the same features of asymmetry are observed in the experiments, Fig. 9. Note that the coordinate system used in the measurements does not coincide with the coordinate system of the simulations, since the break of symmetry destroys the intrinsic azimuthal invariance of the problem. So, a comparison of the images is possible only on a qualitative basis. We should repeat here that the numerical results presented originate from computations where the break of symmetry is spontaneous (i.e. with a symmetric inflow boundary condition), whereas for the experiment this idealized condition is impossible (see previous discussion on magnitude of inflow asymmetry). In effect, one would expect a higher level of asymmetry in the experiment.

The analysis of the velocity vector orientation on the symmetry axis has shown that the fluid flows from one side of the annular jet to the opposite side, and that there is only one preferential direction. While the streamlines on a plane through this preferential direction are asymmetric (Fig. 8), the streamlines on the perpendicular plane (not shown in this work) have a nearly axisymmetric shape. A detailed description of the asymmetry phenomenology is out of the scope of this work and will be discussed elsewhere. However, we have evidence that it is caused by the imbalance of pressure and inertia forces for thin annular jets, and that it is triggered by perturbations generated in the vicinity of the disk [43].

4.2 Fluctuations. In the sequel, the values of the axial velocity fluctuations are presented. In the experiments, they are derived from the LDA signals as the r.m.s. of the instantaneous fluctuation around the mean. In the unsteady computations, they are computed on the basis of the large scale, coherent fluctuations and of the small scale, modeled fluctuations [27], according to the equation

$$w'_{tot}=((w'_{coh})^2+(w'_{mod})^2)^{1/2}=(\overline{(\langle w\rangle-w_{mean})^2}+\overline{\langle w'w'\rangle})^{1/2} \tag{2}$$

where w'_{tot} is the total, w'_{coh} the coherent and w'_{mod} the modeled fluctuation. The overbars in Eq. (2) mean time averaging over the total time interval. $\langle w\rangle$ is the instantaneous velocity value, w_{mean} is the time averaged velocity, and $\langle w'w'\rangle$ is the instantaneous value of the axial Reynolds stress. Note that the notation used is reflecting time averages, as it is common in the RANS technique, and not spatial filtering, adopted in LES.

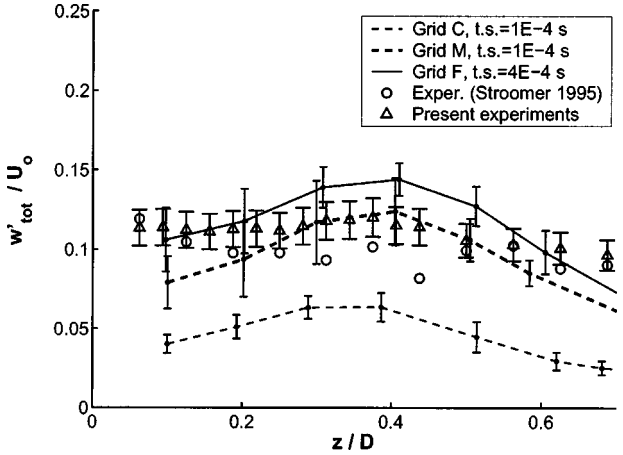

Fig. 10 No-model approach: Computed coherent fluctuations and experimental total fluctuations

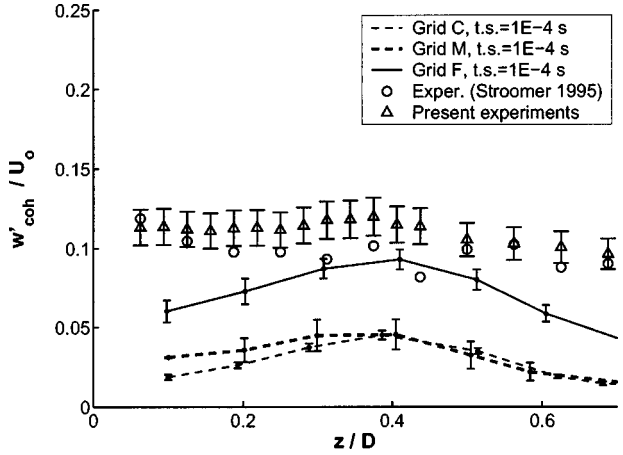

Fig. 11 SSG-RSM simulations: Computed coherent fluctuations and experimental total fluctuations

The coherent fluctuation is the r.m.s. of the instantaneous velocity fluctuation around the mean, whereas the modeled fluctuation is the square root of the Reynolds stress time average. Equation (2) is valid, as long as the small and large scale fluctuations are uncorrelated [28], which is generally the case in single frequency dominated vortex shedding flows.

The axial velocity fluctuations on the symmetry axis are shown in Fig. 10, for the no-model approach simulations, together with our experimental data and those of Stroomer [7]. As the no-model approach assumes that the Reynolds stresses are zero, the fluctuations are only coherent.

The coherent fluctuations of the no-model computations (Fig. 10) are obtained with different grid resolutions (202,826 (Grid C), 402,696 (Grid M) and 879,795 grid points (Grid F)). It can be seen that there is an asymptotic trend converging to a grid independent solution, i.e., the difference between the results of the grids M and F is smaller than the difference between the results of the grids C and M. So, the result of grid F is not strictly grid independent but very close to the grid independent solution. Finer grid discretization (probably exceeding 2–3 million points) would be necessary to obtain fully grid independent solutions. Such levels of discretization, when computed in a time-accurate, unsteady manner, are beyond our current computational capabilities.

The results obtained show a significant statistical spreading, which could be improved by collecting a longer signal history. Nevertheless, for the finer and medium grid there is evidence of large fluctuation values which agree with the experimental data satisfactorily, especially in the near disk zone, where recirculation takes place. In this zone, the experiments indicate axial turbulent fluctuations in the range $0.10-0.15U_0$. The results of the coarse grid are much lower than the other results, indicating that the numerical dissipation is too high.

For the simulations with the SSG-RSM the fluctuation components are presented separately, i.e., the coherent fluctuations in Fig. 11 and the turbulent fluctuations in Fig. 12. From these fluctuations the total fluctuations (Fig. 13) can be computed with Eq. (2).

Figure 11 shows the coherent fluctuations of the Reynolds stress model computations. The fine grid results are not fully grid independent. However, the grid independent solution will reasonably lie between the fine grid results (upper curve in Fig. 11) and the fluctuations of the no-model computations (upper curve in Fig. 10), as the Reynolds stresses have a dumping effect on the coherent fluctuations.

Figure 12 presents the modeled fluctuations of the Reynolds stress model computations. It can be reasonably stated, that the grid independent solution for the modeled fluctuations in the upper part of the recirculation zone (i.e., in the region $0.25<z/D<0.5$) is significantly smaller than the coherent fluctuations. From Fig. 12 it is evident, that nearer to the bluff-body disk ($0<z/D<0.25$) the grid independent modeled fluctuations will be large. Vice versa, the coherent fluctuations decrease to zero in this region, as the velocity decreases to zero near to the wall. So, by

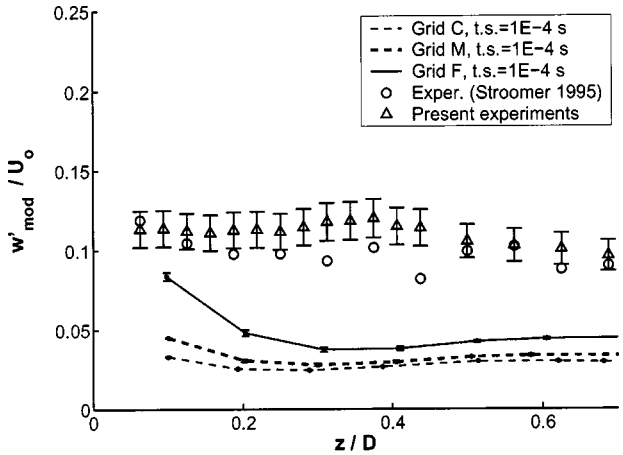

Fig. 12 SSG-RSM simulations: Computed modeled fluctuations and experimental total fluctuations

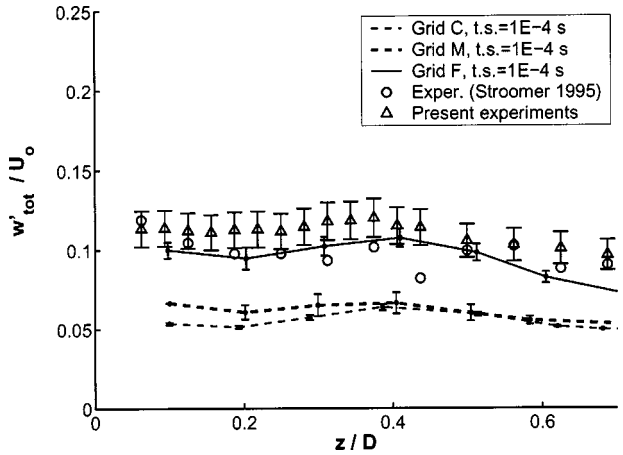

Fig. 13 SSG-RSM simulations: Computed total fluctuations and experimental total fluctuations

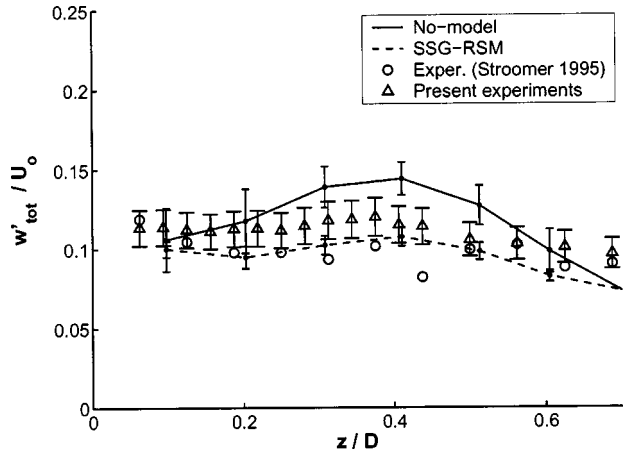

Fig. 14 Axial velocity fluctuations. Comparison of the two approaches for the Reynolds stresses.

comparing Figs. 11 and 12 it can be reasonably stated that near to the wall the fluctuations are due to small vortices (fine structures).

Some definitive trends can be recognized from these figures: the characteristics of the fluctuations are locally different. In the region near the disk ($0<z/D<0.25$) there is a large contribution of high frequency fluctuations (Fig. 12). The upper region of the recirculation zone ($0.25<z/D<0.5$) is dominated by small frequency coherent fluctuations. There, the computed (fine grid) coherent fluctuations reach values of $0.08U_0$ (Fig. 11). These features can not be observed by looking at the total fluctuations, which present a substantially flat profile (Fig. 13), and strengthen the need of unsteady simulations for this kind of bluff-body flows: a steady simulation would neglect the coherent large eddy fluctuations, which are responsible both for the large values of the total fluctuations and for the high fluctuation level in the upper recirculation region. Considering both coherent and modeled fluctuations leads to total fluctuations, which fit very well with our and Stroomer's [7] experimental data.

By comparing the coherent fluctuations of the SSG-RSM computations (Grid F in Fig. 11) and the total fluctuations of the no-model computations (Grid F in Fig. 10) the larger amplitudes of the no-model approach are evident. This shows that the computations are not dominated by numerical diffusion. Indeed, in presence of a large numerical diffusion we would not see any difference in the coherent fluctuations.

The fine grid results of the two approaches are shown in Fig. 14. Both approaches give similar high values of fluctuations in agreement with the experimental results. The no-model approach behaves better at the upper part of the recirculation zone ($0.25<z/D<0.5$). Nearer to the disk ($0<z/D<0.25$) this approach is not able to maintain a high level of fluctuation, as the profile decreases. Apparently, the zone near to the disk is characterized by both small and large scale fluctuations. The no-model approach is able to capture the large scale fluctuations, however, the intense small scale fluctuations are not captured, requiring higher grid resolution near to the disk. The turbulent approach is able to capture the trend of having a fluctuation maximum near to the wall. This observation is in accordance with new zonal trends in simulations, where the near wall regions are computed using URANS-type approaches (like our SSG-RSM) and the regions further away from the wall are modelled using LES-type approaches (more sophisticated, but of the same philosophy as our ''naive-LES'' no-model approach) [44–46].

4.3 Time Series Fourier Analysis. The previous sections dealt with statistical quantities of the annular jet flow. Detailed technical studies need also data on the flow dynamics. We focus here on the frequencies of coherent structures. In the particular case of the annular jet, these structures can be vortices passing periodically at the monitor point (i.e., vortex shedding), or boundary layers oscillating around the monitor point.

The frequencies are computed via the Fast Fourier Transform (FFT) of the auto-correlation function [47]. The computation of the auto-correlation function and of its FFT was performed numerically and based on the collected time history of the simulations.

The results of the FFT analysis based on the fine grid SSG-RSM simulations are presented in Fig. 15. Oscillation frequencies of $f=10$ Hz or a Strouhal number $St=f\cdot D/U_0=0.06$ can be observed. Simulations with other grid resolutions and with the no-model approach confirmed the existence of a specific frequency in the range 5–10 Hz ($St=0.03$–0.06). Strouhal numbers of flows past cylinders (see Section 3.3) are in the range 0.12–0.25. For a confined annular jet Pinho and Whitelaw [16] found a value of $St=0.094$.

Stroomer [7] measured a frequency of 12 Hz ($St=0.073$) for the same annular jet but with methane-air combustion. We must be aware that the frequency reported by Stroomer in the combustion case and the frequency obtained in these non-reacting flow simulations must not necessarily coincide. Indeed, different mean values and r.m.s. fluctuations values commonly appear in combusting flows due to strong changes in density and momentum. However, we can reasonably state that the orders of magnitude of the velocity and of the size of the large moving vortex structures are not changed by the presence of combustion. Therefore, similar frequencies should be expected in the reacting and non-reacting cases as is the case here.

5 Conclusions

The present contribution dealt with the simulations and the measurements of an air annular jet with a very high blockage ratio (89%) and a moderate Reynolds number ($Re=4400$). The experiments were performed using the three-dimensional LDA technique. Different points in the flow field were measured, and mean and r.m.s. values were computed. The simulations were based on the three-dimensional unsteady RANS technique. Different models for the Reynolds stresses were used.

A comparison of the mean velocities presented significant differences between the simulated and measured values, which proved to be the effect of asymmetries in the experimental jet exit velocities. When similar magnitude asymmetries were introduced to the numerical simulation, the comparison of mean velocities yielded very satisfactory results. However, experiments and simulations proved the existence of an asymmetric flow field inside of the recirculation zone, with a preferential flow direction. This strengthened the choice of performing simulations in a three-dimensional fashion for this flow. Indeed, two-dimensional simulations would artificially force axisymmetry.

The computed velocity fluctuations were in very good agreement with the experiments. For the comparison with the experiments, the total fluctuations had to be computed as the sum of the directly computed, large scale coherent fluctuations and the modeled, small scale fluctuations. It was shown that the fluctuations in the recirculation zone mainly consisted of fluctuations of large scale vortices, implicitly proving the necessity of performing the computations in an unsteady manner. Steady computations clearly underestimate the total fluctuations.

Fast Fourier frequency analysis based on the simulated velocity time series indicated the existence of large vortex structures oscillating at a frequency around 10 Hz, in good agreement with previous measurements.

Acknowledgments

The authors would like to thank the Swiss Federal Office of Energy (BFE) and Dr. A. Hintermann for the financial support, the Swiss manufacturer of heating equipment Ygnis AG for the coop-

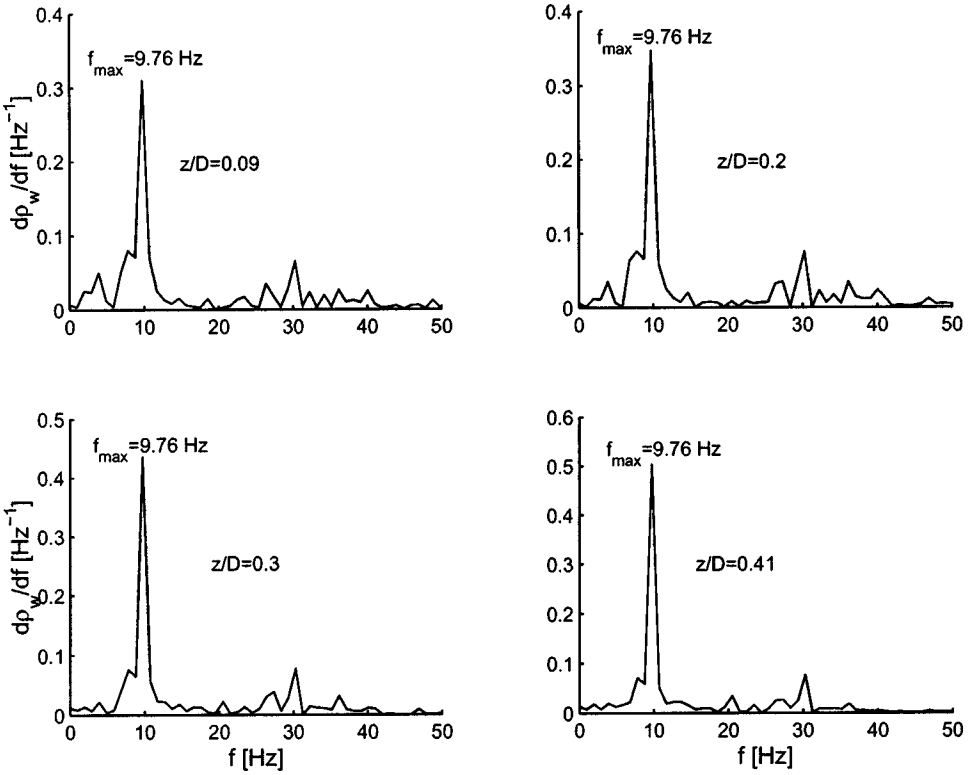

Fig. 15 Axial velocity component on the symmetry axis inside the recirculation zone. Fourier analysis of the auto-correlation functions [Ref. [47]] (fine grid, SSG-RSM). Oscillation frequencies at 9.76 Hz (Strouhal number St=0.06) can be observed.

eration and the Computational Services of ETH, Mr. T. Racic and Mr. A. Bongulielmi, for the computational facilities and their support.

References

[1] Bowman, C. T., 1992, ''Control of Combustion-Generated Nitrogen Oxide Emissions: Technology Driven by Regulation,'' Twenty-Fourth Symposium (International) on Combustion, The Combustion Institute, pp. 859–878.

[2] Turns, S. R., 1996, *An Introduction to Combustion*, McGraw-Hill International Editions.

[3] Davies, T. W., and Beér, J. M., 1971, ''Flow in the Wake of Bluff-Body Flame Stabilizers,'' Thirteenth Symposium (International) on Combustion, The Combustion Institute, pp. 631–638.

[4] Durão, D. F. G., and Whitelaw, J. H., 1978, ''Velocity Characteristics of the Flow in the Near Wake of a Disk,'' J. Fluid Mech., **85**, pp. 369–385.

[5] Ko, N. W. M., and Chan, W. T., 1978, ''Similarity in the Initial Region of Annular Jets: Three Configurations,'' J. Fluid Mech., **84**, pp. 641–656.

[6] Taylor, A. M. K. P., and Whitelaw, J. H., 1984, ''Velocity Characteristics in the Turbulent Near Wakes of Confined Axisymmetric Bluff Bodies,'' J. Fluid Mech., **139**, pp. 391–416.

[7] Stroomer, P. P. J., 1995, ''Turbulence and OH Structure in Flames,'' Ph.D. thesis, TU-Delft, Netherlands.

[8] Aly, M. S., and Rashed, M. I. I., 1991, ''Experimental Investigation of an Annular Jet,'' J. Wind. Eng. Ind. Aerodyn., **37**, pp. 155–166.

[9] McGuirk, J. J., Taylor, A. M. K. P., and Whitelaw, J. H., 1982, ''The Assessment of Numerical Diffusion in Upwind Difference Calculations of Turbulent Recirculating Flows,'' *Turbulent Shear Flows 3*, Selected Papers from the Third International Symposium on Turbulent Shear Flows, Editors: Bradbury, L. J. S., Durst, F., Launder, B. E., Schmidt, F. W., and Whitelaw, J. H., Springer-Verlag.

[10] Durão, D. F. G., Knittel, G., Pereira, J. C. F., and Rocha, J. M. P., 1991, ''Measurements and Modelling of Turbulent Near Wake Flow of a Disk With a Central Jet,'' Eighth International Symposium on Turbulent Shear Flows.

[11] Akselvoll, K., and Moin, P., 1996, ''Large-Eddy Simulation of Turbulent Confined Coannular Jets,'' J. Fluid Mech., **315**, pp. 387–411.

[12] Pope, S. B., and Whitelaw, J. H., 1976, ''The Calculation of Near-Wake Flows,'' J. Fluid Mech., **73**, pp. 9–32.

[13] Leschziner, M. A., and Rodi, W., 1981, ''Calculation of Annular and Twin Parallel Jets Using Various Discretization Schemes and Turbulence-Model Variations,'' ASME J. Fluids Eng., **103**, pp. 352–360.

[14] Cherdron, W., Durst, F., and Whitelaw, J. H., 1978, ''Asymmetric Flows and Instabilities in Symmetric Ducts With Sudden Expansions,'' J. Fluid Mech., **84**, pp. 13–31.

[15] Restivo, A., and Whitelaw, J. H., 1978, ''Turbulence Characteristics of the Flow Downstream of a Symmetric, Plane Sudden Expansion,'' ASME J. Fluids Eng., **100**, pp. 308–310.

[16] Pinho, F. T., and Whitelaw, J. H., 1991, ''Flow of Non-Newtonian Fluids Over a Confined Baffle,'' J. Fluid Mech., **226**, pp. 475–496.

[17] Goodwin, R. T., and Schowalter, W. R., 1996, ''Interactions of Two Jets in a Channel: Solution Multiplicity and Linear Stability,'' J. Fluid Mech., **313**, pp. 55–82.

[18] Drikakis, D., 1996, ''Bifurcation Phenomena in Incompressible Sudden Expansion Flows,'' Phys. Fluids, **9**(1), pp. 76–87.

[19] De Zilwa, S. R. N., Khezzar, L., and Whitelaw, J. H., 2000, ''Flows Through Plane Sudden Expansions,'' Int. J. Numer. Methods Fluids, **32**, pp. 313–329.

[20] Schreck, E., and Schäfer, M., 2000, ''Numerical Study of Bifurcation in Three-Dimensional Sudden Channel Expansions,'' Comput. Fluids, **29**, pp. 583–593.

[21] Sotiropoulos, F., and Ventikos, Y., 2001, ''The Three-Dimensional Structure of Confined Swirling Flows With Vortex Breakdown,'' J. Fluid Mech., **426**, 155–175.

[22] Yu Gelfgat, A., Bar-Yoseph, P. Z., and Solan, A., 2001, ''Three-Dimensional Instability of Axisymmetric Flow in a Rotating Lid—Cylinder Enclosure,'' J. Fluid Mech., **438**, pp. 363–377.

[23] Flury, M., 1999, ''Experimentelle Analyze der Mischungsstruktur in turbulenten nicht vorgemischten Flammen,'' Ph.D. thesis No. 13312, ETH Zurich, Switzerland.

[24] Franke, R., and Rodi, W., 1991, ''Calculation of Vortex Shedding Past a Square Cylinder With Various Turbulence Models,'' Eighth International Symposium on Turbulent Shear Flows.

[25] Kato, M., and Launder, B. E., 1993, ''The Modelling of Turbulent Flow Around Stationary and Vibrating Square Cylinders,'' Ninth International Symposium on Turbulent Shear Flows, Vol. 1.

[26] Durbin, P. A., 1995, ''Separated Flow Computations With the k-ε-v^2 Model,'' AIAA J., **33**, No. 4, pp. 659–664.

[27] Lakehal, D., and Thiele, F., 2001, ''Sensitivity of Turbulent Shedding Flows to Non-Linear Stress-Strain Relations and Reynolds Stress Models,'' Comput. Fluids, **30**, pp. 1–35.

[28] Wilcox, D. C., 1994, *Turbulence Modeling for CFD*, DCW Industries, Inc.

[29] Speziale, C. G., Sarkar, S., and Gatski, T. B., 1991, ''Modelling of Pressure-Strain Correlation of Turbulence: An Invariant Dynamical Systems Approach,'' J. Fluid Mech., **227**, pp. 245–272.

[30] Rodi, W., 1992, ''On the Simulation of Turbulent Flow Past Bluff Bodies,'' J. of Wind Engineering, **52**, pp. 1–17.

[31] Persillon, H., and Braza, M., 1998, ''Physical Analysis of the Transition to

Turbulence in the Wake of Circular Cylinder by Three-Dimensional Navier-Stokes Simulations,'' J. Fluid Mech., **365**, pp. 23–88.
[32] Ventikos, Y., 2002, ''The Effect of Imperfections on the Emergence of Three-Dimensionality in Stationary Vortex Breakdown Bubbles,'' Phys. Fluids, **14**(3), 13–16.
[33] Blackburn, H. M., and Lopez, J. M., 2002, ''Modulated Rotating Waves in an Enclosed Swirling Flow,'' J. Fluid Mech., **465**, 33–58.
[34] Marques, F., Lopez, J. M., and Shen, J., 2002, ''Mode Interactions in an Enclosed Swirling Flow: A Double Hopf Bifurcation Between Azimuthal Wavenumbers 0 and 2,'' J. Fluid Mech., **455**, 263–281.
[35] Marques, F., and Lopez, J. M., 2001, ''Precessing Vortex Breakdown Mode in an Enclosed Cylinder Flow,'' Phys. Fluids, **13**, 1679–1682.
[36] Blackburn, H. M., and Lopez, J. M., 2000, ''Symmetry Breaking of the Flow in a Cylinder Driven by a Rotating Endwall,'' Phys. Fluids, **12**, 2698–2701.
[37] Lopez, J. M., 1995, ''Unsteady Swirling Flow in an Enclosed Cylinder With Reflectional Symmetry,'' Phys. Fluids, **7**, 2700–2714.
[38] Spohn Mory, M., and Hopfinger, E. J., 1998, ''Experiments on Vortex Breakdown in a Confined Flow Generated by a Rotating Disk,'' J. Fluid Mech., **370**, pp. 73–99.
[39] Sotiropoulos, F., and Ventikos, Y., 1998, ''Transition From Bubble Vortex Breakdown to a Columnar Vortex in a Closed Cylinder With a Rotating Lid,'' Int. J. Heat Fluid Flow, **19**(5), pp. 446–458.
[40] Sotiropoulos, F., Ventikos, Y., and Lackey, T. C., 2001, ''Chaotic Advection in 3-D Stationary Vortex-Breakdown Bubbles: Śil'nikov's chaos and the devil's staircase,'' J. Fluid Mech., **444**, 257–297.
[41] Ventikos, Y., 2004, ''Emergence of Dominant Non-Axisymmetric Modes and Chaotic Advetion in Geometrically Forced Vortex Breakdown Flows: The Potential of Passive Structure Control,'' submitted, J. Fluid Mech. .
[42] Ventikos, Y., ''Excitable Modes in Forced Symmetry Breaking for a Cylindrical Container With one Rotating Endwall,'' in Nonlinear Dynamics in Fluids, Eds. F. Marqués and A. Meseguer, ISBN 84-95999-28-5, CIMNE Barcelona.
[43] Del Taglia, C., Blum, L., Gass, J., Ventikos, Y., and Poulikakos, D., 2004, ''Intrinsic Asymmeric Flows in Annular Jets,'' submitted to Phys. Fluids .
[44] Spalart, P. R., 2000, ''Strategies for Turbulence Modelling and Simulations,'' Int. J. Heat Fluid Flow, **21**, pp. 252–263.
[45] Spalart, P. R., 2002, ''Detached-Eddy Simulation, 1997–2000,'' Proceedings of the Euromech Colloquium 412, Munich, Germany, 4–6 October, 2000, Advances in LES of Complex Flows, R. Friedrich and W. Rodi (Eds.), Fluid Mechanics and its Applications, **65**.
[46] Spalart, P., Hedges, L., Shur, M., and Travin, A., 2002, ''Simulation of Active Flow Control on a Stalled Airfoil,'' Key note lecture, IUTAM Symposium ''Unsteady Separated Flows,'' Toulouse, France.
[47] Pope, S. B., 2000, *Turbulent Flows*, Cambridge University Press.

Instability of Inelastic Shear-Thinning Liquids in a Couette Flow Between Concentric Cylinders

O. Coronado-Matutti

P. R. Souza Mendes

M. S. Carvalho*
e-mail: msc@mec.puc-rio.br

Department of Mechanical Engineering,
Pontifícia Universidade Católica do
Rio de Janeiro,
Rua Marquês de São Vicente 225,
Gávea, Rio de Janeiro, RJ,
22453-900, Brazil

Circular Couette flow of inelastic shear-thinning materials in annuli is examined. The curved streamlines of the circular Couette flow can cause a centrifugal instability leading to toroidal vortices, well known as Taylor vortices. The presence of these vortices changes the hydrodynamic and heat transfer characteristics of the processes at which this type of flow occurs. Therefore, it is quite important to be able to predict the onset of instability. Most of the available theoretical and experimental analyses are for Newtonian and viscoelastic (dilute polymeric solutions) liquids. In this work, the effect of the shear-thinning behavior of high concentration suspensions on the onset of the Taylor vortices is determined theoretically by solving the conservation equations, constructing the solution path as the inner cylinder speed rises and searching for the critical conditions. This procedure avoids the need for a stability analysis of the flow and the solution of an eigenproblem. The differential equations were solved by the Galerkin/finite-element method and the resulting set of nonlinear algebraic equations, by Newton's method.
[DOI: 10.1115/1.1760537]

1 Introduction

Circular Couette flow in an annulus occurs in many practical applications, such as catalytic chemical reactors, filtration devices, liquid-liquid extractors, journal bearings, and the return flow of drilling mud between the rotating drill column and the stationary wall in oil and gas well drilling. The pioneering work of Taylor [1], showed that the pure azimuthal flow, i.e. a Couette flow, can evolve to a flow presenting recirculating vortex rings if the angular speed of the inner cylinder is above a critical value. This type of flow transition is known as Taylor instability.

The flow pattern can drastically affect the transport processes that occur in the applications mentioned earlier. In the case of continuous reactors, the yield is maximized if mixing in the transverse direction is large and in the longitudinal direction is small. Therefore, the process can be optimized by using annular flow through concentric cylinders rotating at angular speeds that Taylor vortices are present. In the case of well drilling, the transport of drilled cuttings, the diffusion of gas, and the build-up of mud cake on the formation wall are all affected by the characteristics of the flow between the rotating drill and the stationary bore hole wall.

The stability of Newtonian flow between concentric rotating cylinders has been extensively studied in the past, beginning with the pioneering work of Taylor [1]. The main goal was to determine experimentally and theoretically the critical operating condition at which toroidal vortices appear at different flow configurations. The critical conditions are usually reported in terms of a critical Taylor number $Ta \equiv \rho \omega_i r_i d/\mu$, where ω_i is the angular velocity of the inner cylinder, r_i its radius, d is the gap between the two cylinders, and ρ and μ are the liquid density and viscosity. The experimental investigations consisted of flow visualization to observe the different flow patterns. Important contribution were presented by Gravas and Martin [2]; Andereck et al. [3] and Lueptow et al. [4]. Theoretical prediction of the onset of instability is generally done by a linear stability analysis of the base flow, which leads to an eigenvalue problem. The first contributions used perturbation theory and were restricted to narrow gaps and axisymmetric disturbances. The methods were later extended to arbitrarily wide annular gaps. Important contribution were presented by Chandrasekhar [5]; Diprima [6] and Lee [7].

In many practical situations the liquid of interest is non-Newtonian and its rheological behavior may alter the critical speed at which the Taylor vortices appear. Muller et al. [8] observed that the torque on the outer cylinder of a Couette rheometer changed dramatically above a critical angular speed during simple viscosity measurements of a Boger liquid, i.e. a dilute high molecular weight polymer solution. Shaqfeh [9] presented a complete review of experimental and theoretical work on purely elastic Taylor instability. For concentrated polymer solutions, Larson [10] recognized that the critical Taylor number at the onset of instability is determined by a combination of elastic and shear-thinning effects. The effect of viscous heating on the stability of viscoelastic Taylor-Couette flow has also been investigated recently (see Al-Mubaiyedh et al. [11] and White and Muller [12]).

Although some drilling muds may present elastic behavior, most the water-based muds are a highly concentrated colloidal suspension of clay, with strong shear-thinning behavior and negligible elasticity, well described by a Generalized Newtonian Model with a Carreau viscosity function. Fewer studies have addressed the Taylor instability of an inelastic shear-thinning liquid. Miller [13] extended the stability analysis for the case of an infinitely thin annulus and non-Newtonian behavior described by a Generalized Newtonian Model. For this limiting case, the shear rate, and consequently the viscosity, is constant across the gap between the two cylinders. Lockett et al. [14] used a finite element code to determine the first bifurcation point for inelastic liquids in thin and wide annuli. The shear thinning behavior was described by the Power-law and Bingham models. These viscosity functions have anomalous behavior as the shear rate approaches zero, which may cause a problem when the non-Newtonian character is high or the gap between the cylinders is wide. The analysis takes into account the radial variation of the effective viscosity. The critical condition was determined by a linear stability analysis

*Corresponding author

Contributed by the Fluids Engineering Division for publication in the JOURNAL OF FLUIDS ENGINEERING. Manuscript received by the Fluids Engineering Division April 11, 2003; revised manuscript received January 5, 2004. Associate Editor: D. Siginer.

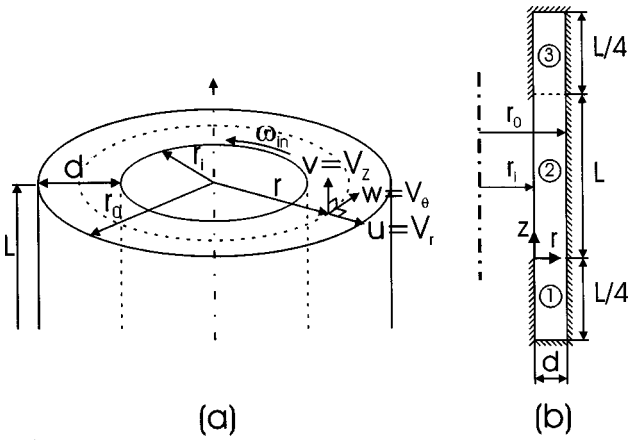

Fig. 1 Geometrical configuration of flow between concentric rotating cylinders

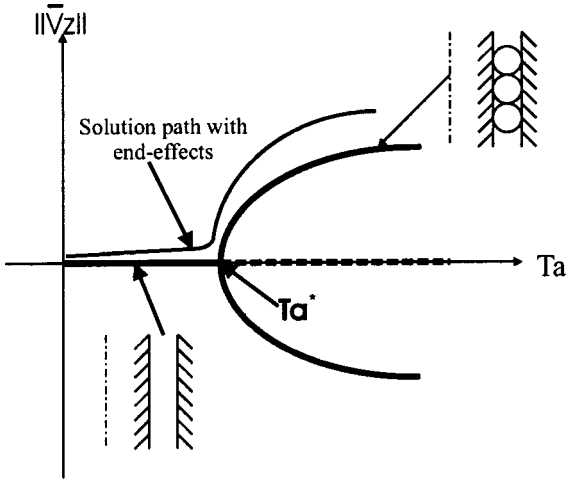

Fig. 2 Sketch of the phase diagram of the flow between concentric rotating cylinders. Continuous lines represent stable branches.

of the flow. At the bifurcation point the solution to the equations of motion changes character and the Jacobian matrix becomes singular.

The theoretical determination of critical Taylor number at the onset of the instability for Newtonian, viscoelastic or inelastic shear-thinning liquids leads to an eigenproblem. The evaluation of the spectrum (leading eigenvalues) of the Jacobian matrix is not simple.

In this work, the critical Taylor number for inelastic shear-thinning liquids at different geometrical configurations, i.e. inner-to-outer cylinder radius ratio r_i/r_o and different rheological parameters is determined. The shear-thinning character of the liquids was described by a Carreau model that avoids the anomalous behavior at low shear rates of the Power-Law and Bingham models. An alternative approach to evaluate the critical Taylor number, that avoids the solution of an eigenvalue problem, is proposed. The flow conditions at the onset of the instability is determined by tracking the solution path as the Taylor number rises and searching for the value at which the growth rate of the velocity field on the $r-z$ plane is maximum. At each flow condition, the system of differential equation was solved by the Galerkin/finite-element method. The resulting set of nonlinear algebraic equations is solved by Newton's method.

2 Mathematical Model

The configuration of the flow analyzed is shown in Fig. 1. The inner cylinder has a radius equal to r_i and it is rotating at a speed of ω_i. The radius of the outer cylinder is equal to r_o and it is stationary. The gap between the cylinders is $d=r_o-r_i$. Most of the papers presented in the literature assumed the annular space infinitely long, i.e. end effects were neglected. To do this numerically, one possibility is to explore the flow periodicity and solve for a finite domain with periodic boundary conditions. The shortcoming of this choice is the danger of obtaining solutions (e.g., vortex size) which depend and are modulated by the size of the domain. To circumvent this problem, we chose to employ a long but finite domain, with ''extensions'' at both ends, as illustrated in Fig. 1(*b*). The inner cylinder does not rotate in the extensions of the domain, i.e., there is a velocity discontinuity at $z=0$ and $z=L$.

Each of the extensions of the domain have an axial length equal to $L/4$, where L is the axial length of the domain of interest.

The relevant dimensionless parameters for this situation are:

1. Radius ratio, $\Pi \equiv r_i/r_o$
2. Aspect ratio, $\Gamma \equiv L/d$
3. Taylor number, $Ta \equiv \rho \omega_i r_i d/\mu$

The phase diagram of the flow states between infinitely long cylinders, as a function of Taylor number *Ta* is sketched in Fig. 2. The different flow states may be characterized by a norm of the axial component of the velocity field $\|\overline{v_z}\|$ (for example, the maximum absolute value of the axial velocity field). At low Taylor numbers, there is only one possible flow state, the trivial Couette flow without vortices, and therefore $\|\overline{v_z}\|=0$. At a critical Taylor number Ta^*, there is a bifurcation, and beyond that point, three flow states are possible. The flow without vortices, i.e., the pure Couette flow (with $\|\overline{v_z}\|=0$), becomes unstable (dashed line on the plot) and the stable states are those that contain recirculating vortices (continuous lines on the plot). Experiments have shown that just beyond the onset of the instability, the vortices formed are steady and axisymmetric.

The tactic used here to determine approximately the critical Taylor number is to automatically construct a solution path as a function of Taylor number by solving the complete momentum and continuity equations for steady, axisymmetric flow and using arc-length continuation. In the cases analyzed here, in which the length of the annulus space is finite, end effects, characterized by small vortices near the discontinuity of the angular speed of the inner cylinder, are present. Because of these recirculations, even at very small Taylor number, the norm of the axial velocity field will not be exactly equal to zero. The expected solution path is also sketched in Fig. 2 (thinner continuous line on the plot). It should lie close to the stable branches of the diagram. Near the critical Taylor number, it should show a sudden change in the norm of the velocity field, an indication of the onset of instability, i.e., the appearance of toroidal vortices.

2.1 Conservation Equations. The liquid motion is governed by the momentum and continuity equations for axisymmetric and steady flows.

$$\rho\left(v\frac{\partial u}{\partial z}-\frac{w^2}{r}+u\frac{\partial u}{\partial r}\right)=\frac{1}{r}\frac{\partial}{\partial r}(r\tau_{rr})-\frac{\tau_{\theta\theta}}{r}+\frac{\partial \tau_{zr}}{\partial z} \tag{1}$$

$$\rho\left(v\frac{\partial v}{\partial z}+u\frac{\partial v}{\partial r}\right)=\frac{1}{r}\frac{\partial}{\partial r}(r\tau_{rz})+\frac{\partial \tau_{zz}}{\partial z} \tag{2}$$

$$\rho\left(v\frac{\partial w}{\partial z}+\frac{uw}{r}+u\frac{\partial w}{\partial r}\right)=\frac{\partial \tau_{r\theta}}{\partial r}+\frac{2}{r}\tau_{r\theta}+\frac{\partial \tau_{z0}}{\partial z} \tag{3}$$

$$\frac{1}{r}\frac{\partial}{\partial r}(ru)+\frac{\partial v}{\partial z}=0 \tag{4}$$

The boundary conditions are:

$$r=r_i;0<z<L:\ u=0,\ v=0\ \text{and}\ w=\omega_i r_i$$

$$r=r_i;-L/4<z<0\ \text{and}\ L<z<L+L/4:\ u=v=w=0$$

$$r=r_o:\quad u=v=w=0$$

$$z=-L/4\ \text{or}\ z=L+L/4:\quad u=v=w=0$$

2.2 Non-Newtonian Model. As mentioned before, drilling mud is well described by the Generalized Newtonian Model. In this model, the stress tensor $\underline{\tau}$ is a non-linear function of the rate of deformation tensor $\underline{\underline{2D}}$:

$$\underline{\tau}=\eta(\dot{\gamma})\underline{\underline{2D}} \tag{5}$$

The viscosity dependence on shear rate can be represented by a Carreau viscosity function:

$$\frac{\eta-\eta_\infty}{\eta_0-\eta_\infty}=[1+(\lambda\dot{\gamma})^2]^{(n-1)/2} \tag{6}$$

η_0 is the viscosity at low shear rate, η_∞ is the viscosity at high shear rate, λ is a time constant, n is the power-law index. $\dot{\gamma}$ is the deformation rate, and it is given by

$$\dot{\gamma}=\sqrt{2\mathrm{tr}\underline{\underline{D}}^2}=\left\{2\left[\left(\frac{\partial v}{\partial z}\right)^2+\left(\frac{u}{r}\right)^2+\left(\frac{\partial u}{\partial r}\right)^2\right]+\frac{1}{2}\left[\left(\frac{\partial w}{\partial z}\right)^2+\left(\frac{\partial u}{\partial z}+\frac{\partial v}{\partial r}\right)^2+\left(\frac{\partial w}{\partial r}-\frac{w}{r}\right)^2\right]\right\}^{0.5} \tag{7}$$

2.3 Solution of the Differential Equations. The set of differential equations coupled with the constitutive model was solved by the Galerkin/finite-element method. The velocity and pressure field were represented in terms of basis functions:

$$u=\sum_{j=1}^{n}U_j\phi_j;\ v=\sum_{j=1}^{n}V_j\phi_j;\ w=\sum_{j=1}^{n}W_j\phi_j\ \text{and}\ p=\sum_{j=1}^{m}P_j\chi_j$$

Biquadratic basis functions ϕ_i were used to represent the velocity field and piece-wise linear discontinuous functions χ_i were used to represent the pressure field. The corresponding weighted residuals of the Galerkin's method are:

$$R^i_{mr}=\int_{\bar{\Omega}}\left\{\rho\left(v\frac{\partial u}{\partial z}-\frac{w^2}{r}+u\frac{\partial u}{\partial r}\right)\phi_i+\frac{\partial\phi_i}{\partial z}\tau_{rz}+\frac{\phi_i}{r}\tau_{\theta\theta}+\frac{\partial\phi_i}{\partial r}\tau_{rr}-\rho g\phi_i\right\}r|\underline{\underline{J}}|d\bar{\Omega}+BI;\quad i=1,\ldots n \tag{8}$$

$$R^i_{m\theta}=\int_{\bar{\Omega}}\left\{\rho\left(v\frac{\partial w}{\partial z}+\frac{wu}{r}+u\frac{\partial w}{\partial r}\right)\phi_i+\frac{\partial\phi_i}{\partial z}\tau_{\theta z}-\frac{\phi_i}{r}\tau_{r\theta}+\frac{\partial\phi_i}{\partial r}\tau_{\theta r}\right\}r|\underline{\underline{J}}|d\bar{\Omega}+BI;\quad i=1,\ldots n \tag{9}$$

$$R^i_{mz}=\int_{\bar{\Omega}}\left\{\rho\left(v\frac{\partial v}{\partial z}+u\frac{\partial v}{\partial r}\right)\phi_i+\frac{\partial\phi_i}{\partial z}\tau_{zz}+\frac{\phi_i}{r}\tau_{zr}\right\}r|\underline{\underline{J}}|d\bar{\Omega}+BI;\quad i=1,\ldots n \tag{10}$$

$$R^i_c=\int_{\bar{\Omega}}\left(\frac{u}{r}+\frac{\partial u}{\partial r}+\frac{\partial v}{\partial z}\right)\chi_i r|\underline{\underline{J}}|d\bar{\Omega};\quad i=1,\ldots m \tag{11}$$

Once all the variables are represented in terms of the basis functions, the system of partial differential equations reduces to simultaneous algebraic equations for the coefficients of the basis functions of all the fields. This set of equations is nonlinear and sparse. It was solved by Newton's method, which requires the evaluation of the full Jacobian matrix, viz.

$$\underline{C}^{(k)}=\underline{C}^{(k-1)}+\Delta\underline{C} \tag{12}$$

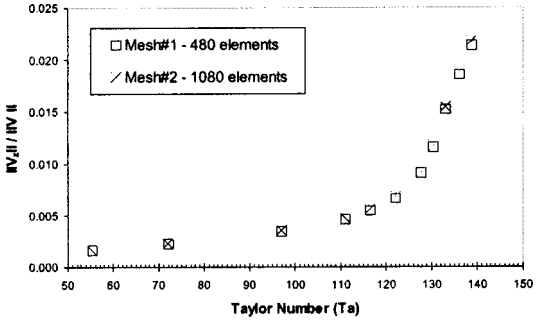

Fig. 3 Solution path computed with both meshes tested. The results are virtually insensitive to the level of discretization.

$$\underline{\underline{J}}\Delta\underline{C}=-\underline{R}(\underline{C}) \tag{13}$$

$\underline{C}$ is the vector of the unknowns coefficients of the basis functions for the velocity and pressure, $\underline{R}$ is the vector of the weighted residuals, and $\underline{\underline{J}}$ is the Jacobian matrix of sensitivities of the residuals to the unknowns:

$$J_{ij}=\begin{bmatrix}\frac{\partial R_{mz}}{\partial V_j} & \frac{\partial R_{mz}}{\partial W_j} & \frac{\partial R_{mz}}{\partial U_j} & \frac{\partial R_{mz}}{\partial P_j}\\ \frac{\partial R_{m\theta}}{\partial V_j} & \frac{\partial R_{m\theta}}{\partial W_j} & \frac{\partial R_{m\theta}}{\partial U_j} & \frac{\partial R_{m\theta}}{\partial P_j}\\ \frac{\partial R_{mr}}{\partial V_j} & \frac{\partial R_{mr}}{\partial W_j} & \frac{\partial R_{mr}}{\partial U_j} & \frac{\partial R_{mr}}{\partial P_j}\\ \frac{\partial R_c}{\partial V_j} & \frac{\partial R_c}{\partial W_j} & \frac{\partial R_c}{\partial U_j} & \frac{\partial R_c}{\partial P_j}\end{bmatrix}$$

The evaluation of the Jacobian entries include the derivative of the extra-stress components with respect to the coefficients of the velocity field, which is a function of the expression used to represent the viscosity dependence on shear rate, e.g.

$$\frac{\partial\tau_{rz}}{\partial U_j}=\frac{\partial\eta}{\partial U_j}\frac{\partial u}{\partial z}+\eta\frac{\partial\phi_j}{\partial z}=\frac{\partial\eta}{\partial\dot{\gamma}}\frac{\partial\dot{\gamma}}{\partial U_j}\frac{\partial u}{\partial z}+\eta\frac{\partial\phi_j}{\partial z}$$

The iteration proceeded until $\|\Delta\underline{C}\|+\|\Delta\underline{R}\|<10^{-6}$. At each Newton iteration, the linear system was solved using a frontal solver.

Newton's method converges quadratically when the residual norm is close to zero. In order to automatically construct solution paths at rising Taylor number in an efficient way a pseudo-arc-length condition method, as proposed by Bolstad and Keller [15] was used. The step in Taylor number was automatically controlled such that Newton's method did not take more than six iterations to converge.

The domain was divided into 480 elements (8 in the radial direction and 60 in the axial direction), which corresponded to 7,611 degrees of freedom. The elements were concentrated near both cylinders. Increasing the number of elements to 1,080 (16,815 degrees of freedom) did not change appreciably the computed solution path, and consequently the critical Taylor number at each flow condition. Figure 3 shows the solution paths at radius ratio $\Pi=0.9$ and Newtonian liquid computed with both meshes.

3 Results

The aspect ratio of the annular space was held constant at $\Gamma=10$ for all cases presented here. The critical Taylor number was determined as a function of the radius ratio and of the rheological properties of the liquid.

3.1 Newtonian Liquids. The solution path as Taylor number varies obtained at radius ratio $\Pi=0.6$ is shown in Fig. 4. Each

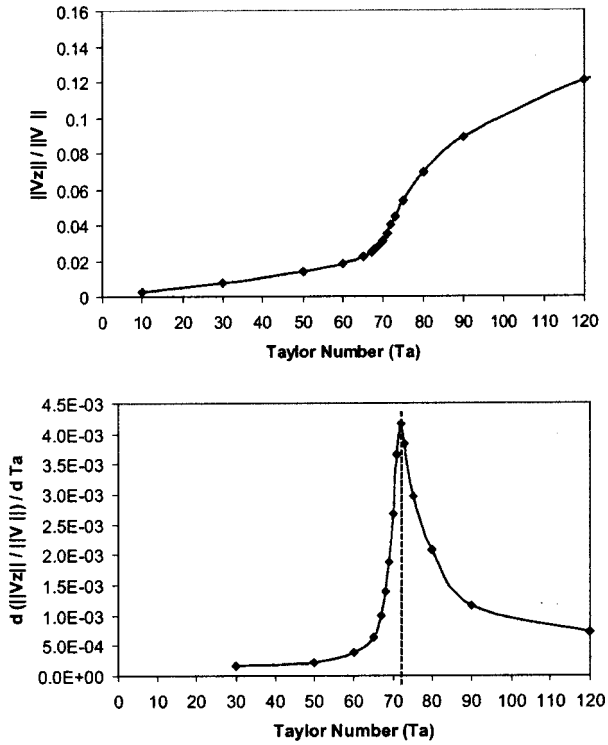

Fig. 4 (*a*) Solution path for Newtonian liquid as Taylor number rises. The radius ratio is $\Pi=0.6$. The flow states are characterized by the intensity of the flow in the axial direction. (*b*) Derivative of the flow intensity in the axial direction with respect to Taylor number. The critical condition is defined as the value at which the derivative is maximum.

flow state is characterized by the ratio of the norm of the axial velocity field to the norm of the tangential velocity field $\|V_z\|/\|V_\theta\|$, defined as

$$\|V_z\|/\|V_\theta\| = \frac{\Sigma_{i=1}^{nodes} |V_z|_i}{\Sigma_{i=1}^{nodes} |V_\theta|_i} \tag{14}$$

At small Taylor numbers, the norm of the axial velocity field is less than 1% of that of the azimuthal velocity. As mentioned before, the weak axial flow is caused by the small recirculation due to the end effects. At Taylor number close to 70, there is a sudden change on the growth rate of the norm of the axial velocity. This behavior indicates the onset of instability and the appearance of toroidal vortices. The critical Taylor number was chosen to be the value at which the derivative of the norm ratio with respect to the Taylor number is maximum, as illustrated in Fig. 4(*b*). For this situation, the critical Taylor number was $Ta^*=72.0$. Figure 5 shows the evolution of the projection of the streamlines on the $r-z$ plane, i.e. the vortex pattern, near the edges of the annular space as the Taylor number rises. The axial position $z=L$ corresponds to the end of the rotating portion of the inner cylinder. At $Ta=33.4$, there is only a recirculating flow near the edge of the annular space due to end effect. Far from the edges, there is no evidence of recirculation pattern. At Taylor numbers larger than the critical value, e.g. $Ta=80$, the presence of Taylor vortices is evident. The calculated aspect ratio of each recirculation cell was $h/d=0.99$ and agrees well with experimental measurements of Taylor [1].

A solution path similar to the one presented in Fig. 4 was constructed for Newtonian liquids at different radius ratios Π, and a critical Taylor number was estimated at each condition. The results are summarized in Fig. 6. The critical Taylor number rises as the gap between the two cylinders becomes narrower, i.e. as the

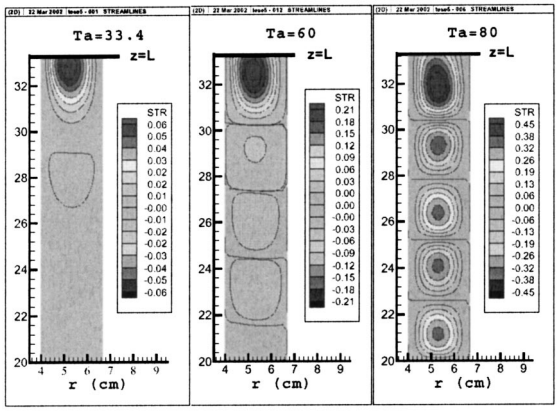

Fig. 5 Evolution of the vortex pattern as the Taylor number rises above the critical value. The radius ratio is $\Pi=0.6$.

radius ratio is increased. The azimuthal flow in narrow gaps is more stable than the flow in wide gaps between the two cylinders. The plot also shows the critical Taylor number obtained experimentally by different researchers and presented by Lueptow et al. [4] and the critical Taylor number obtained by Recktenwald et al. [16] using linear stability analysis. The agreement between the predictions reported here and the linear stability analysis is excellent. The maximum difference over the entire range of radius ratio was 1.2%.

The excellent agreement between the predictions using the simple approach described earlier in this work and the complete linear stability analysis validates the use of this method to determine the critical conditions for non-Newtonian flows, which is discussed next.

3.2 Shear-Thinning Liquids. In order to validate the procedure to determine the critical Taylor number for shear-thinning liquids, the predicted critical condition at $\Pi=0.95$ for Carreau model presented here are compared to those obtained by stability analysis for Power-Law liquids, reported by Lockett et al. [14]. Miller [13] showed that for infinitely thin annulus ($\Pi\rightarrow 1$), all Generalized Newtonian Models are equivalent if their non-Newtonian behavior is described by a parameter defined as $\Delta\beta \equiv d(\ln \eta)/d(\ln \dot{\gamma})$. Figure 7 shows this comparison. The critical conditions are represented by the definition of Taylor number used by Lockett et al. [14], i.e. $Ta_L \equiv \rho^2 \omega_i^2 r_i d^3/\eta^2(\dot{\gamma}_c)$. The character-

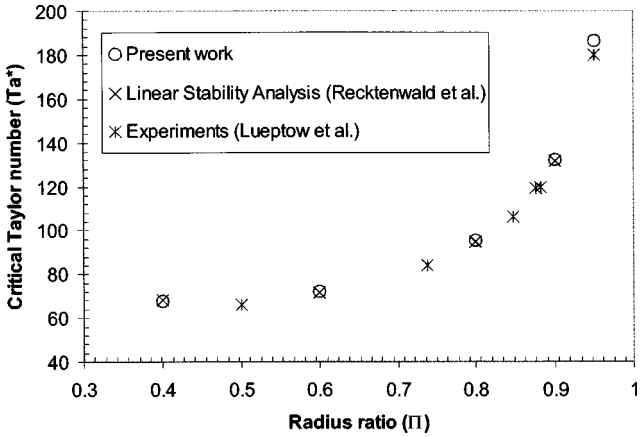

Fig. 6 Critical Taylor number for Newtonian liquids as a function of the radius ratio $\Pi \equiv r_i/r_o$

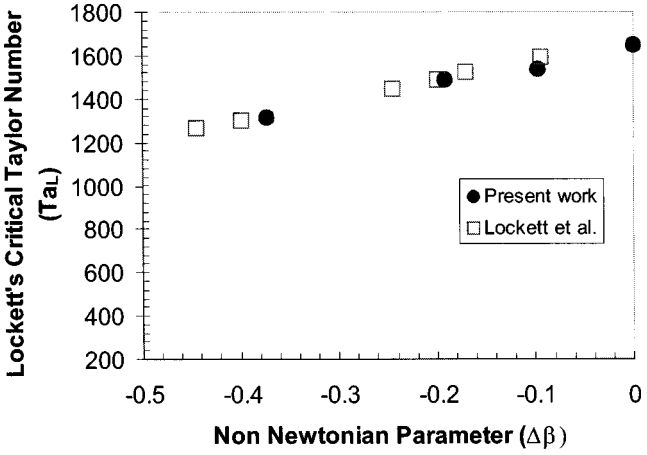

Fig. 7 Comparison of Lockett's critical Taylor number for inelastic shear-thinning liquids obtained in this work with those predicted by linear stability analysis

istic shear rate is defined as $\dot{\gamma}_c = \omega_i r_i / d$. The results of the simpler approach used here agree well with predictions obtained by linear stability analysis.

The effect of the shear-thinning behavior of the flowing liquid on the onset of Taylor instability was analyzed here by constructing solution paths similar to those presented in Fig. 4 at different rheological parameters of the Carreau viscosity function. The low shear viscosity was held constant and equal to $\eta_0 = 0.004$ Pa.s. The predicted critical Taylor number at a radius ratio of $\Pi = 0.95$ and different high-shear viscosity η_∞ and power-law index n is shown in Fig. 8. The Taylor number was defined in terms of the low shear viscosity, e.g. $Ta = \rho \omega_i r_i d / \eta_0$. At this radius ratio, the critical Taylor number for Newtonian liquid was $Ta^* = 189.6$. As the power-law index n and the high-shear viscosity η_∞ fall, the onset of the Taylor instability occurs at lower inner cylinder speed. In some cases, the critical speed can be close to half of the speed at which the vortices would occur with Newtonian liquids. One possible explanation for the early onset of instability in the case of inelastic shear-thinning liquids is that the local viscosity in regions of high shear rate can by much lower than η_0, due to the shear-thinning behavior of the liquid. Because the viscosity is a function of the shear rate, it is more appropriate to define a Taylor number based on a characteristic viscosity $\eta_c = \eta(\dot{\gamma}_c)$, called here the modified Taylor number, Ta_{mod}, and defined as:

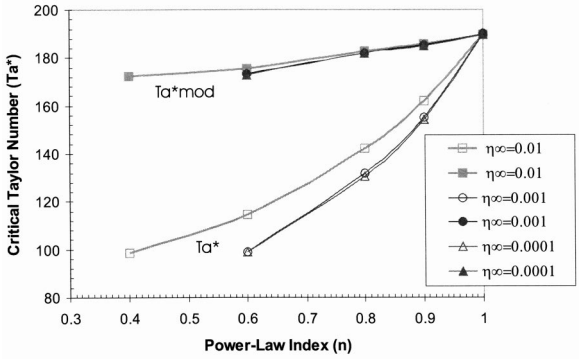

Fig. 8 Critical conditions at the onset of the instability as a function of the power-law index n and high-shear viscosity η_∞. $\lambda = 0.1$ s and $\Pi = 0.95$. The results are also presented in terms of a modified Taylor Number Ta_{mod}.

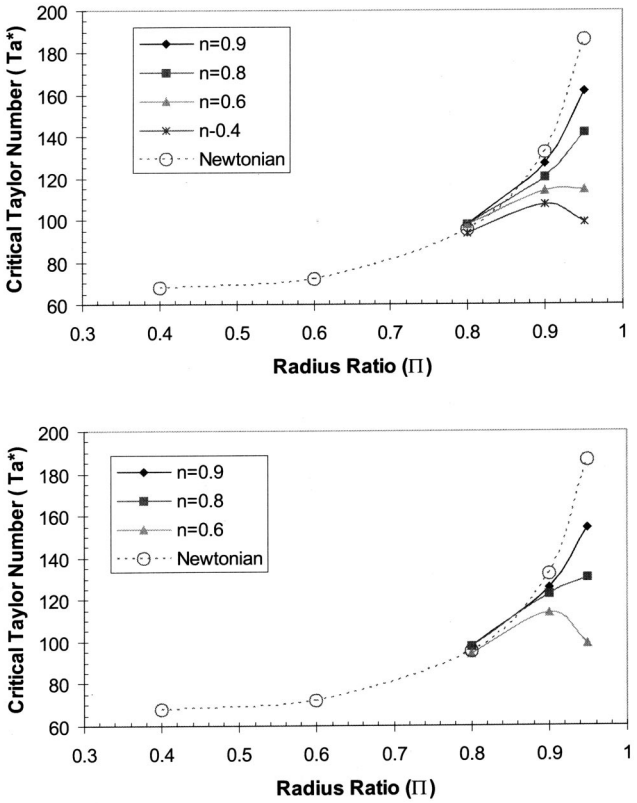

Fig. 9 Critical Taylor number as a function of the radius ratio Π and power-law index n. $\lambda = 0.1$ s. (*a*) $\eta_\infty = 0.01$ Pa.s and (*b*) $\eta_\infty = 0.0001$ Pa.s.

$$Ta_{mod} \equiv \frac{\rho \omega_i r_i d}{\eta(\dot{\gamma}_c)} \tag{15}$$

The characteristic shear rate is defined as $\dot{\gamma}_c = \omega_i r_i / d$. Figure 8 also presents the onset of the instability in terms of the critical modified Taylor number Ta^*_{mod}. If the shear-thinning behavior of the liquid is taken into account on the definition of the Taylor number, the variation of the critical value at the onset of Taylor instability becomes much less sensitive to the rheological parameters. For the cases analyzed in this work, the maximum relative variation of the critical modified Taylor number was approximately 9%. A similar approach was used by Ali et al. [17] when studying the stability of a dilute suspension of rigid spherical particles in cylindrical Couette flow.

The effect of radius ratio Π on the onset of the instability for inelastic shear-thinning liquids is presented in Fig. 9 at $\lambda = 0.1$ s, $\eta_\infty = 0.01$ and 0.001 Pa.s, and different values of the power-law index. For wide gaps, i.e. $\Pi < 0.8$, the shear-thinning behavior of the liquid does not affect the critical Taylor number for the parameter range explored here. The shear rates that occur in these cases are low enough that the viscosity everywhere in the flow is approximately equal to the low-shear viscosity η_0. At a fixed radius ratio, above $\Pi = 0.8$, the critical Taylor number falls as the power-law index decreases. The local liquid viscosity decreases as the power-law index falls, and hence the flow is less stable, i.e. the critical angular speed at the onset of the vortex formation falls. At low power-law indexes, e.g. $n = 0.4$ and $n = 0.6$, the effect of the radius ratio on the critical Taylor number is not monotonic. At radius ratio larger than $\Pi > 0.9$, the critical angular speed falls with rising radius ratio. For Newtonian liquids, as the gap of the annular space decreases, the flow becomes more stable. This tendency is also observed in the case of shear-thinning liquids up to a point. As the gap falls, the deformation rate in the flow rises and

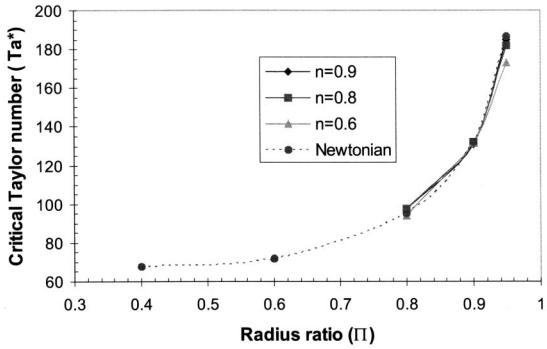

Fig. 10 Results presented in Fig. 9 in terms of the modified Taylor number, that takes into account the shear-thinning effect on the definition of the Taylor number

consequently the viscosity falls, making the flow less stable. The competition between these two opposite effects explain the nonmonotonic behavior.

Again, if the onset of the instability is presented in terms of the modified Taylor number, defined in Eq. (15), the predictions of the shear-thinning liquids are very close to that of the Newtonian flow, as illustrated in Fig. 10.

The effect of the time constant λ on the onset of Taylor vortices in presented in Fig. 11. The radius ratio was $\Pi = 0.95$, the high-shear viscosity was $\eta_\infty = 0.0001$ Pa.s, and the power-law index was $n = 0.8$. The critical conditions are also presented in terms of the modified Taylor number that takes into account the shear-thinning behavior of the liquid.

In the analysis presented here, if the shear-thinning behavior of the liquid is taken into account on the definition of the Taylor number of the flow, the variation of the critical value at the onset of the flow instability becomes much less sensitive to the rheological parameters. For the cases analyzed here, the maximum relative variation of the critical modified Taylor number was approximately 9%. Therefore, for an estimation of the critical angular speed at which the azimuthal flow of inelastic shear-thinning liquids between rotating cylinders becomes unstable, a modified Taylor number, defined in terms of a characteristic viscosity, can be used. The instability occurs at approximately $Ta^*_{mod} = Ta^*$ for Newtonian liquids.

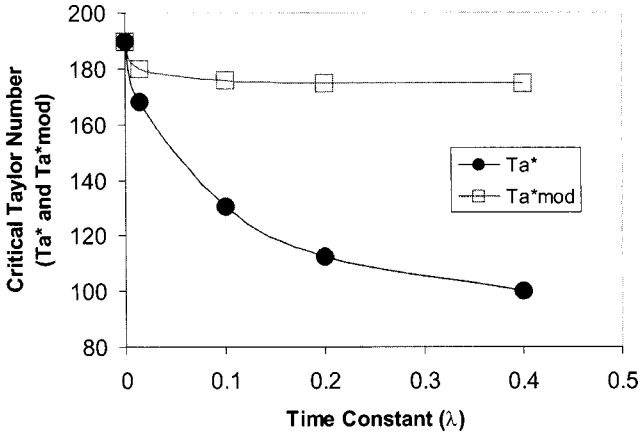

Fig. 11 Critical Taylor number as a function of the time constant of the Carreau viscosity function. $\eta_\infty = 0.0001$ Pa.s, $n = 0.8$ and $\Pi = 0.95$.

4 Final Remarks

The onset of Taylor vortices that completely changes the flow pattern between rotating concentric cylinders can affect the transport phenomena that occur in many practical applications. Taylor instability of Newtonian liquids has been extensively studied by theory and experiments. Recently, the instability of viscoelastic liquids flowing between rotating cylinders has received attention in the literature. However, in many applications, the flowing liquid is a suspension with shear-thinning behavior with no elasticity. The analysis of the effect of shear-thinning behavior alone on the Taylor instability is limited.

In this work, the critical operating condition at different geometrical configurations and rheological parameters is determined by tracking the solution path as the Taylor number rises and searching for sudden changes on the axial and radial velocity components. The simple procedure avoids the solution of eigenproblems and proved to be accurate. The system of differential equations that describes the flow is solved by the Galerkin/finite-element method and the resulting set of nonlinear equation is solved by Newton's method. The results show that if the variation of the viscosity is considered on the definition of the Taylor number, the critical Taylor number of Newtonian flow is a good estimation for the onset of the instability.

Acknowledgments

Oscar Coronado was supported with a scholarship from CAPES (Brazilian Department of Education). This work was funded by grants from CNPq (Brazilian Research Council) and FAPERJ (Science Foundation of the State of Rio de Janeiro).

References

[1] Taylor, G. I., 1923, "Stability of a viscous liquid contained between two rotating cylinders," Philos. Trans. R. Soc. London, Ser. A, 289–343.
[2] Gravas, N., and Martin, B. W., 1978, "Instability of viscous axial flow in annuli having a rotating inner cylinder," J. Fluid Mech., **86**(2), 385–394.
[3] Andereck, C. D., Liu, S. S., and Swinney, H. L., 1986, "Flow regimes in a circular Couette system with independently rotating cilinders," J. Fluid Mech., **164**, 155–183.
[4] Lueptow, R. M., Docter, A., and Min, K., 1992, "Stability of axial flow in an annulus with a rotating inner cylinder," Phys. Fluids A, **4**(11), 2446–2455.
[5] Chandrasekhar, S., "Hydrodynamic and hydromagnetic stability," *Dover Publications, Inc. New York* (1961).
[6] Diprima, R. C., 1960, "The stability of a viscous fluid between rotating cylinders with an axial flow," J. Fluid Mech., **9**(4), 621–631.
[7] Lee, M. H., 2001, "The stability of spiral flow between coaxial cylinders," Comp. Math. Appl., **41**, 289–300.
[8] Muller, S. J., Larson, R. G., and Shaqfeh, E. S. G., 1989, "A purely elastic transition in Taylor-Couette flow," Rheol. Acta, **28**, 499–503.
[9] Shaqfeh, E. S. G., 1996, "Purely Elastic Instability in Viscometric Flows," Annu. Rev. Fluid Mech., **28**, 129–185.
[10] Larson, R. G., 1989, "Taylor-Couette stability analysis for Doi-Edwards Fluid," Rheol. Acta, **28**, 504–510.
[11] Al-Mubaiyedh, U. A., Sureshkumar, R., and Khomami, B., 2002, "The effect of viscous heating on the stability of Taylor-Couette flow," J. Fluid Mech., **462**, 111–132.
[12] White, J. M., and Muller, S. J., 2003, "Experimental studies on the effect of viscous heating on the hydrodynamic stability of viscoelastic Taylor-Couette flow," J. Rheol., **47**(6), 1467–1492.
[13] Miller, C., "A Study of Taylor-Couette Stability of Viscoelastic Fluids," *Ph.D. Thesis, University of Michigan* (1967).
[14] Lockett, T. J., Richardson, S. M., and Worraker, W. J., 1992, "The stability of inelastic non-Newtonian fluids in Couette flow between concentric cylinders: a finite-element study," J. Non-Newtonian Fluid Mech., **43**, 165–177.
[15] Bolstad, J. H., and Keller, H. B., 1986, "A multi-grid continuation method for elliptic problems with folds," SIAM (Soc. Ind. Appl. Math.) J. Sci. Stat. Comput., **7**(4), 1081.
[16] Recktenwald, A., Lucke, M., and Muller, H. W., 1993, "Taylor vortex formation in axial through-flow: Linear and weakly non-linear analysis," Phys. Rev. E, **48**, 4444.
[17] Ali, M. E., Mitra, D., Schwille, J. A., and Lueptow, R. M., 2002, "Hydrodynamic stability of a suspension in cylindrical Couette flow," Phys. Fluids, **14**(3), 1236–1243.

An Air Curtain Along a Wall With High Inlet Turbulence

Brandon S. Field

Eric Loth*
e-mail: e-loth@uiuc.edu
phone: 217-244-5581

Department of Aeronautical
and Astronautical Engineering,
University of Illinois Urbana-Champaign,
104 S. Wright Street,
Urbana, IL 61801

A downward blowing isothermal wall jet at moderate Reynolds numbers (1,500 to 8,500) with significant inflow turbulence (ca. 6%) was investigated. The flow configuration is an idealization of the air curtains of refrigerated display cases. Flow visualization using particle seeding was employed to identify the flow field eddy dynamics. Particle Image Velocimetry was used to examine the velocity fields in terms of mean and fluctuating values. These diagnostics showed that the air curtain entrainment was dominated by a large variety of eddies that engulfed ambient air into the air curtain. The velocity fields generally showed linear spreading, significant deceleration and high turbulence levels (ca. 25%). It was observed that the air curtain dynamics, velocity fields and growth were not significantly sensitive to Reynolds number variation between Re=3,800 and Re=8,500. However, at low air velocities (Re=1,500), the curtain was found to detach, leading to a large air curtain thickness and high curtain entrainment.
[DOI: 10.1115/1.1758265]

Introduction

Refrigerated air curtains are used on supermarket display cases to keep ambient air from entering the case. According to some estimates, 75% of the refrigeration load comes from air curtain entrainment [1], although some energy calculations done by the refrigeration industry have put the air curtain entrainment contribution as high as 90%. In addition to the sensible and latent heat load, the humidity of the entrained air accelerates the frosting on the evaporator coils, making entrainment critical to minimize for overall system performance. Therefore, understanding the development of the basic flow pattern, an isothermal wall jet, can provide critical information to help reduce the energy load on display cases.

Air curtain entrainment in display cases results from the shear layer mixing between the quiescent ambient room air and the refrigerated air curtain. The air curtain tends to ''ride'' along the front of the products, and is supported by flow through a porous wall at the back of the refrigerator case, such that the flow is approximately a planar wall jet. It should be noted that while the reduced density associated with refrigeration can cause some flow modification, the isothermal condition is a reasonable first approximation since the flow is momentum dominated, i.e. typical air curtains are characterized by Richardson numbers much less than unity [2].

For wall jets, the Reynolds number can be defined based on the height of the curtain inlet, H, as follows:

$$\mathrm{Re}=\frac{V_{jet}\rho_{jet}H}{\mu_{jet}} \tag{1}$$

In equation (1), V_{jet} is the mean stream-wise velocity of the initial curtain and ρ_{jet} and μ_{jet} are the density and viscosity of the initial curtain air respectively.

Previous Studies on Air Curtains and Wall Jets. Based on the typical jet flow rates, the Reynolds number based on curtain inlet height is about 5,000 and the typical curtain lengths are about ten jet widths [2]. Thus, air curtains tend to reside in the transitional flow regime: not fully-developed turbulence, but not a laminar flow either. In addition, it should be noted that the initial turbulence levels at the beginning of the air curtain are typically high, e.g. 6% [2], since previously studied wall jets at this Reynolds number are restricted to low inflow turbulence intensity (ca. $<1\%$ or less).

Typically, previous studies of air curtains have only focused on case-specific configurations and have been applied investigations, i.e. a fundamental flow description was not their objective. For example, George and Buttsworth [3], conducted experiments and simulations which included models for components such as fans and the evaporator coils. Characterization of entrainment by temperature measurements at various distances along the curtain indicated that the simulations of the amount of entrainment in the air curtain were underpredicted by the laminar model and overpredicted by the turbulent model. This was attributed to the air curtain being in the transitional flow regime and little information was available concerning the velocity distribution details. Similarly, Cortella et al. [4] examined air curtain flows but experimental measurements were again limited to temperature distributions (no velocity measurements were performed).

In general, when velocity measurements have been performed for air curtain flows, the flow diagnostic techniques employed did not allow for high enough resolution to characterize the quantitative velocity profiles and turbulence levels. One exception to this is the study by Navaz et al. [5] which employed Particle Image Velocimetry (PIV) to validate a computational simulation of refrigerated display case. Small parametric variations of initial air curtain temperature and speed were performed on the display case. A qualitative comparison was shown between the experimentally measured mean velocity profiles and the calculated profiles. However, the experimental uncertainty of the velocity measurements was too high to quantitatively report distributions of turbulence levels. In addition, the geometry employed in the experiment and in the computational model was complex and specific to a particular display case model (as is the case in the above studies), such that it was difficult to develop a fundamental understanding of the underlying fluid physics of air curtains in general.

There are a few fundamental wall-jet studies that are relevant to the simplified air curtain geometry. Bajura and Catalano [6] produced dye streak visualization and hot-film anemometry measurements of low Reynolds number transitional wall jets in a water tunnel with a low turbulence inflow. The natural transition of these low Reynolds number wall jets (Re=200 to 600) was found to pass through five stages, starting with the formation of vortices on the outer shear layer, the pairing of these vortices, and the jet detaching from the wall as a result of these vortex pairings. After

*Corresponding author
Contributed by the Fluids Engineering Division for publication in the JOURNAL OF FLUIDS ENGINEERING. Manuscript received by the Fluids Engineering Division December 12, 2002; revised manuscript received January 5, 2004 Associate Editor: M. V. Ötügen

Table 1 Curtain Reynolds numbers of different test conditions.

Test Condition	Reynolds Number
One low-speed fan	1,500
Two low-speed fans	3,800
One high-speed fan	4,600
Two medium-speed fans	7,600
Two high-speed fans	8,500

detachment, three-dimensional turbulent structures were present and then the upstream flow was again made laminar and reattached, until another vortex pair occurred.

Shih and Gogineni [7] also documented low Reynolds number wall jet dynamics, this time with an acoustically forced air jet at a Reynolds number of 1,000. It was found that the vortices pair and eject in a similar manner to the above studies, causing an immediate transition to turbulence. By adjusting the forcing frequency, the separation length between the vortex pairs could be controlled to reduce or increase the vortex interaction.

Hsiao and Sheu [8] documented the wall jet transition from laminar to turbulent at different Reynolds numbers by investigating water jets of varying Reynolds number, from Re=300 to 30,000. Transition was shown to occur when small perturbations in the outer layer of the wall jet grow into vortices. For the range of Reynolds numbers between 1,500 and 5,000, the primary instability was found to have a length scale on the order of the nozzle width and caused a strong interaction between the inner and outer layers. This is when the turbulence levels in the inner layer can surpass those of the outer layer. Although this study included Reynolds numbers typical of air curtains, only low inflow turbulence levels ($<0.7\%$) were considered, whereas the turbulence levels of refrigerated air curtains typically are significantly higher.

Study Objective. The above studies indicate that no detailed flow visualization and velocity experiments have been conducted for wall-bounded air curtains at the Reynolds number and streamwise distances typical of refrigerated display cases with high inflow turbulence levels. The object of this study was to study the dynamics and development of transitional planar isothermal wall jets with uniform initial mean jet velocity and high initial turbulence. As such, the display case air curtain was simplified to a wall jet to retain the general properties of the curtain while eliminating case-specific issues particular to each manufacturer. The high initial turbulence levels, which result from the design of the display cases, are retained in order to allow relevance to display case flows (and contrast with the previous fundamental wall jet studies of low inflow turbulence). High resolution non-intrusive Particle Image Velocimetry measurements of the air curtain were performed to obtain detailed statistics of the air curtain development. In addition, flow visualization of the curtain interface was used to provide dynamic illustrations of the physics inside the curtains. Reynolds numbers from 1,500 to 8,500 were investigated, which covers the applicable ranges for most refrigerated display case air curtains.

Methods

Flow Facility. While a conventional display case was employed to ensure relevance, several modifications were made to create a more fundamental flow field. The air curtain is created by forcing air in the duct at the top of the case into a deflector turning the flow downward through a honeycomb to produce the initial velocity profile. The case schematic is shown in Fig. 1. Note that the x direction is oriented downwards along the jet. A new deflector was made to produce a more uniform velocity profile, eliminating case-specific features of the air curtain, while retaining the characteristic high inflow turbulence levels. The height of the curtain inlet, H, was 120 mm wide. To create a wall jet configuration,

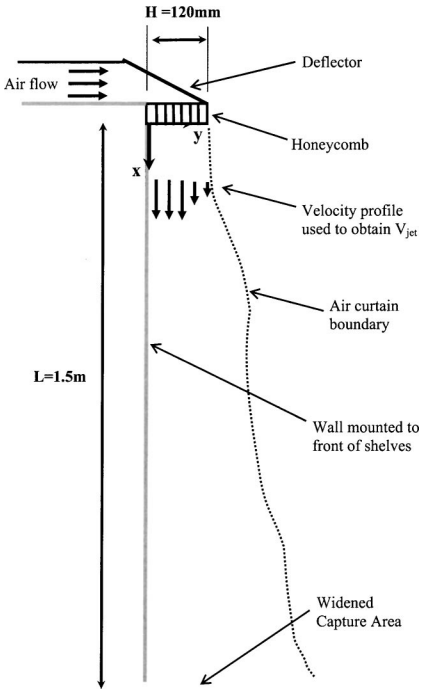

Fig. 1 Idealizations made to the display case

a wall was mounted to the front of the shelves to idealize the front of the products in a fully stocked case. The capture area of the case at $x/H=13$ was widened so as to minimize return configuration effects. Finally, one of the side walls of the case was replaced by a plexiglass window to enable visibility along the air curtain. A photograph of the lab set up can be seen in Fig. 2.

The air curtain speed was varied by changing the blades of the two fans that provided the circulation of air through the case. Three different pairs of fan blades were available of the same diameter but with different cambers. The fan blades provided commercially with the case produced the fastest flow, and are called the ''high-speed'' fans. The two other sets of fan blades produced successively slower curtains, and are called ''medium-speed'' and ''low-speed'' fans. To achieve slower flow with the

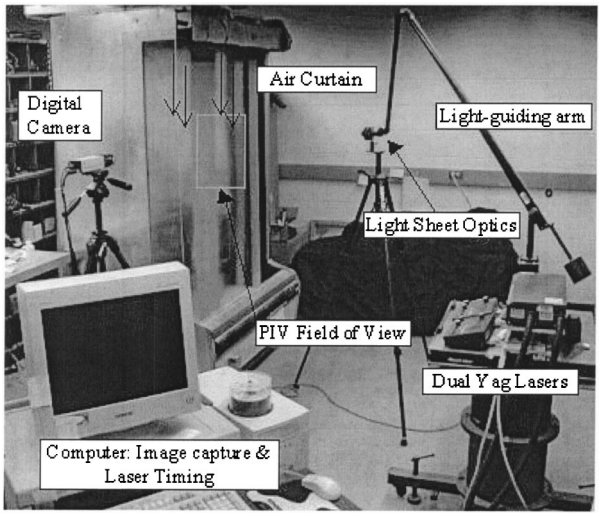

Fig. 2 Photograph of laboratory showing display case, lasers, camera and computer for PIV collection

low-speed and high-speed fans, one of the fan motors was disconnected. The curtain Reynolds numbers resulting from these test conditions are shown in Table 1.

Velocimetry Measurements and Flow Visualization. Particle Image Velocimetry (PIV) consists of a double-pulsed laser sheet illuminating the cross section of a seeded airflow. A cross-correlation digital camera takes two pictures of the illuminated seed particles in quick succession and correlates the differences in particle position to calculate a two-dimensional velocity vector field, using a LaVision system. Trace particle seeding of the air flow was accomplished with 30μm glass particles, Microspheres by 3M. For PIV measurements, both the air curtain (by injection upstream of the deflector) and the ambient air (by a distributed external release) were seeded uniformly [2]. For visualization of the air curtain interface, only the air curtain was seeded (however the technique used the same camera and lasers as in the PIV setup). The Stokes number of these seed particles was calculated to be sufficiently small ($\ll 1$), allowing the particles to faithfully adjust to changes in the flow velocity. A cross-correlation PIV calculation was used, as is discussed by Keane and Adrian [9].

Since the curtain length was larger than the field of view of the camera, several fields of view were taken to cover the entire curtain. For each field of view, 500 cross-correlation images were taken to ensure the quality of the velocity statistics. This produced 500 vector fields at each location along the curtain. In the PIV vector calculation algorithm, if a sufficient number of particles were not found within the interrogation spot a vector could not be computed for that point, in which case, that point was omitted from both the average and the fluctuation calculations. Mean velocity profiles were produced by time-averaging 15 horizontal rows of velocity vector data, centred about the row of interest. Turbulence statistics were calculated by averaging a the deviation from the mean using a nine-point stencil around the vector of interest.

The curtain thickness, $\delta(x)$, was defined from the velocity profiles as the y distance (from the wall) where the streamwise velocity reduced to 25% of the maximum streamwise velocity, i.e. $\delta(x)=y$ occurs at $V_x(y)/V_{x,\max}=0.25$. The curtain thickness was then normalized by the curtain inlet height, H. The velocities were normalized by V_{jet}, which was defined herein as the average streamwise velocity at the downstream location $x=H$.

Results

Flow Visualizations. From the flow visualization, the primary trend in the curtain development is a growth of curtain width and eddy sizes as the flow proceeded from the jet exhaust at the top of the curtain to the return vent at the bottom. The shear layer interface is dominated by strong vortex structures that can be seen as combinations of protrusions and indentions forming a wave pattern along the outer layer of the curtain. Figure 3 is a simplified sketch of the observed curtain eddies from the visualizations of the curtain interface, which (as will be shown) was more representative of a shear-layer interface than a boundary-layer interface. It is inside the indentations that the ambient air primarily gets engulfed and entrained into the curtain.

Figure 4 is a typical instantaneous particle flow visualization from the Re=3,800 air curtain at two streamwise locations. The streamwise development of the curtain and the eddy sizes of the entrainment process can be qualitatively seen from the images. As the curtain progresses downward, both the curtain thickness and the eddies grow. At the top of the curtain, the curtain thickness is roughly the same size as the curtain inlet, H, and the eddies along the curtain interface are a variety of sizes, as large as H but typically smaller. At $x/H=2$, a protrusion-indentation combination can be clearly seen engulfing ambient air. By $x/H=7$, the jet width and the most discernable eddy structures are visibly larger, with a large protrusion visible at $x/H=7.5$. These eddies are expected to stem from a combination of two sources: the shear interface instability (as in Kelvin-Helmholtz waves) and the internal turbulence of the exiting jet. As will be shown later, the initial curtain turbulence is quite high and thus may serve as a primary driver of the edge instabilities in a similar manner to the acoustically forced wall jets of [7].

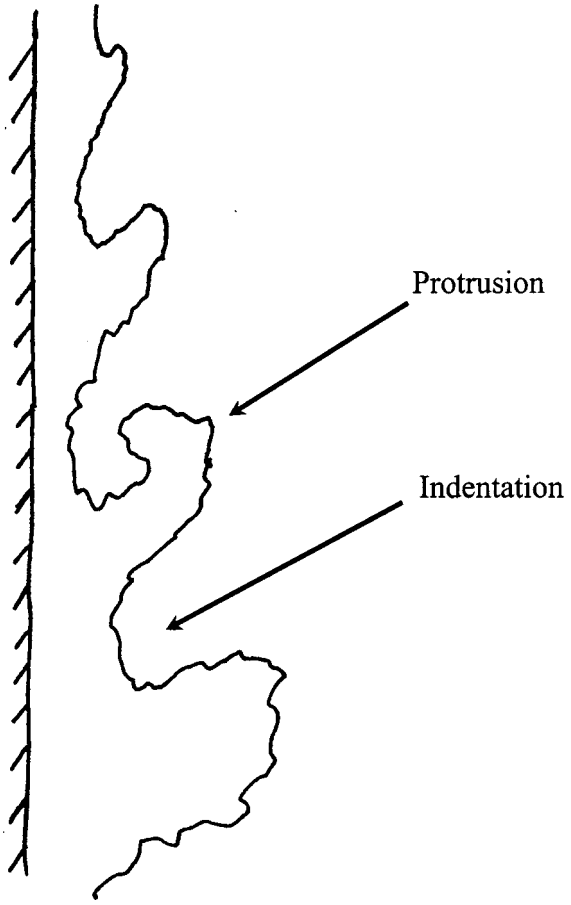

Fig. 3 Sketch of curtain edge showing basic eddy features

Figure 5 shows an animation sequence from the particle visualization of the Re=3,800 air curtain near the inlet. The development of a variety of eddies can be seen along with the engulfment of ambient air into the curtain in a broad range of structure length scales. Certain features are followed as they move down the curtain, indicated by numbered arrows. Features 1 and 3 are both indentations that move with the curtain, growing and deforming as they move through the field of view. Feature 2 is a protrusion that has deeply penetrated the ambient air and is moving much more slowly than the interior of the air curtain. In fact, the feature actually moves slightly upstream in the latter part of the sequence. This is consistent with velocity measurements (discussed in the next section) which show that there is significant negative and positive vertical velocity fluctuations far from the wall, i.e. high rms and a low mean at $y>\delta$. The complexity in the flow visualizations suggests a highly nonlinear flow as compared to the numerical simulations of [4] and [10] which found no significant eddies until approximately $x/H=8$ at similar Reynolds number curtains. However, neither study included high initial turbulence levels. From these visualizations of the flow, it was noted that the entrainment is dominated by vigorous and unsteady eddy engulfment of ambient air into the curtain indentations by the eddies.

For the Reynolds number 3,800, 4,600, 7,600, and 8,500 air curtains, there were no significant qualitative differences in the overall flow character (in terms of either spatial development or structure dynamics). As will be demonstrated by the velocity statistics, the curtain growth and non-dimensional turbulence levels

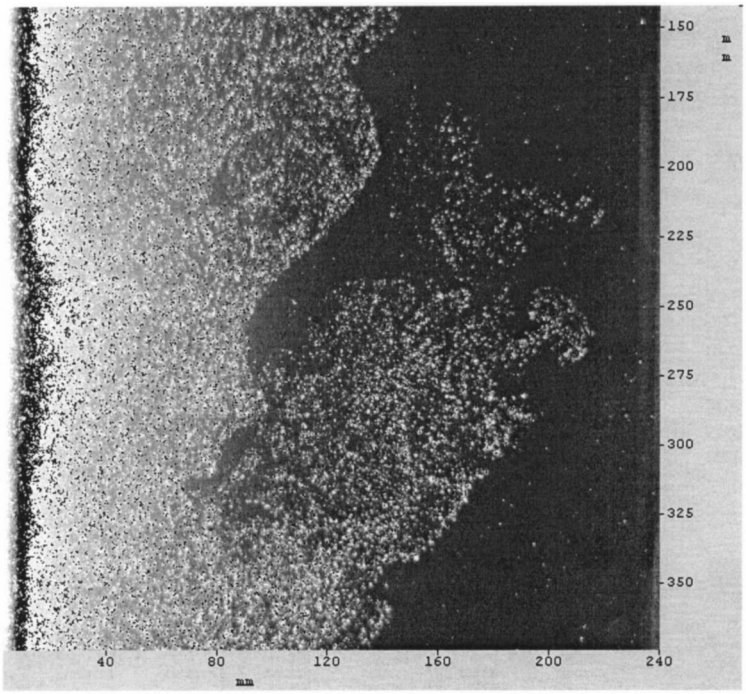

x/H=2

x/H=3

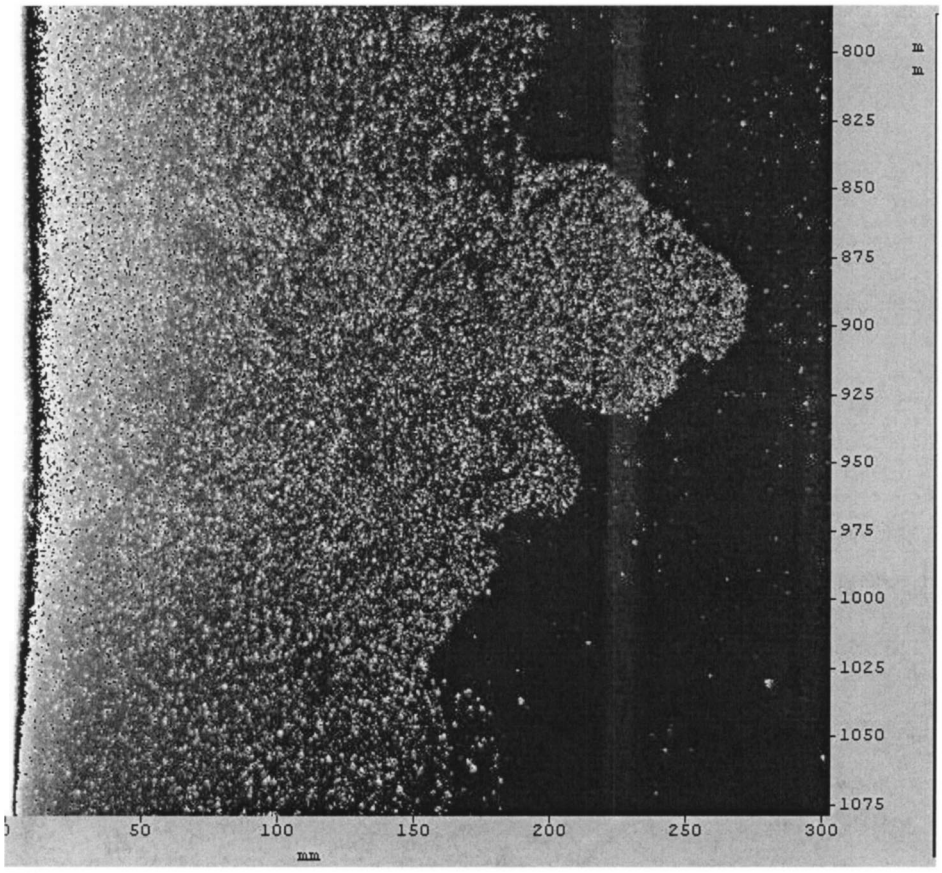

x/H=7

x/H=8

Fig. 4 Particle visualizations from Re=3800 curtains

are the same for these curtains. However when the curtain Reynolds number was reduced to 1,500, the curtain dynamics changed dramatically. At Re=1,500, the curtain would not stay continuously attached to the wall, typically pulling away and thus spilling and recirculating into the ambient field. At some times this detachment would occur rapidly, within one or two inlet heights of the

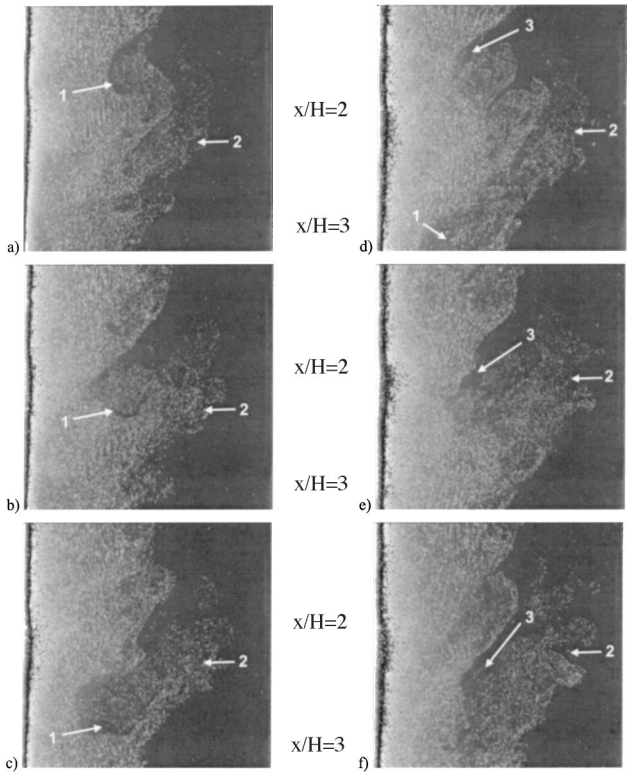

Fig. 5 *(a–f)*: Sequential particle visualizations of the Re=3800 curtain with an inter-frame time interval of 0.133 sec. Moving flow features are labeled.

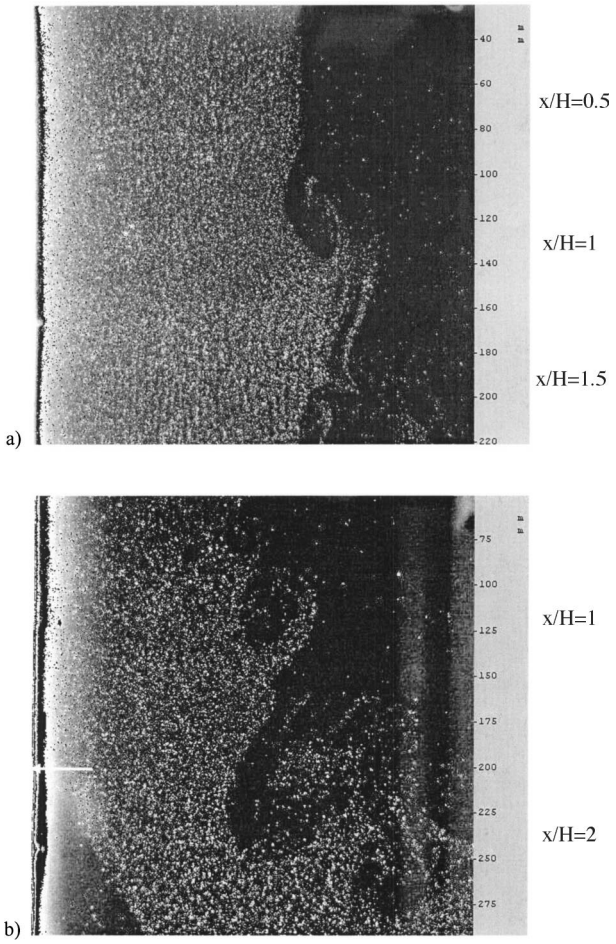

Fig. 6 Particle visualizations from inlet of Re=1,500 curtain with *a*) delayed and *b*) rapid detachment

inlet, and at other times detachment would be delayed, not occurring until $x/H=4$ or even further downstream. Figure 6*a* shows a sample flow visualization near the inlet of the Re=1,500 curtain during a period of delayed detachment when the curtain remained attached to the wall for at least two inlet heights downstream. A small eddy can be seen at $x/H=1$ engulfing ambient air, but the inflow does not indicate high unsteadiness at this instant. Figure 6*b* shows an image taken when the curtain rapidly detached from the wall with the location of detachment indicated by an arrow. More dramatic engulfment structures can be seen on the outer edge of the curtain, suggesting that the instantaneous inflow disturbances were higher than that found in Figure 6*a*. In fact, even minor physical interactions with the curtain (e.g. at $y\sim 2\delta$) could cause the curtain to detach further upstream at this Reynolds number, indicating a high sensitivity to instabilities at this condition.

Similar detachment of a wall jet has been previously observed by Bajura and Catalano [6] but at lower Reynolds numbers (200-800) with negligible inflow turbulence. This study determined the detachment to be a result of the vortex pairing between the outer and inner layers at moderate Reynolds numbers. In particular, the sketch produced in Figure 8 of Bajura and Catalano shows the pairing of inner and outer vortices and subsequent ejection of the vortices from the jet. This process is similar to the detachment process observed in the current study, but herein a greater range of scales and flow complexity was generally noted. Detachment of a wall jet was also photographed in Fig. 3 of Shih and Gogineni [7] of an acoustically forced wall jet of Re=1,000, where the wall jet detachment occurred around x/H of 4. Similarly, the present study indicated outer layer vortices which quickly formed on the edge of the curtain at Re=1,500 (Figs. 6*a* and 6*b*) for both the cases of rapid detachment and delayed detachment. This indicates that the high inflow turbulence associated with the current flow act similar to the acoustic forcing. In summary, the present wall jet had a lower limit of curtain velocity below which attachment and curtain integrity could not be ensured.

Velocity Measurements. Figure 7 is a false-color composite of the time-averaged streamwise velocity contours for the Re =8,500 curtain. The qualitative curtain growth can be seen as the high-velocity core gradually decays and the momentum spreads as it progresses downward. Thus the mean momentum of the flow is continuously diffused outward. All of the air curtains from Re =3800 to Re=8500 developed in a similar fashion.

From these time-averaged velocities, the streamwise velocity profiles normalized by the mean velocity of that curtain, V_{mean}, were obtained at various x/H locations down the curtain. Figure 8 shows the initial velocity profile and initial turbulence levels at $x/H=1$ for an air curtain of Re=4,600. The initial turbulence levels inside the curtain are about 6%, which is much higher than most unforced wall jets. The peak turbulence location coincides with the location of maximum mean velocity shear as is typically found for wall jets. Figure 9*a* shows the quantitative velocity profiles for the Re=4,600 curtain. As the velocity profiles widen, the peak velocity decreases, and the diffusion rate increases linearly with x/H. This appears qualitatively consistent with the velocity profiles reported by Hsiao and Sheu [8] for Re=3,770. For all of the curtains within Reynolds numbers of 3,800 to 8,500, a similar profile evolution of the curtain momentum was obtained as will be shown later. This indicated a relatively weak dependence on Reynolds number for this regime.

Figure 9*b* shows the average velocity profiles for a Re=1,500 curtain that rapidly detached. At $x/H=1$, the curtain is not com-

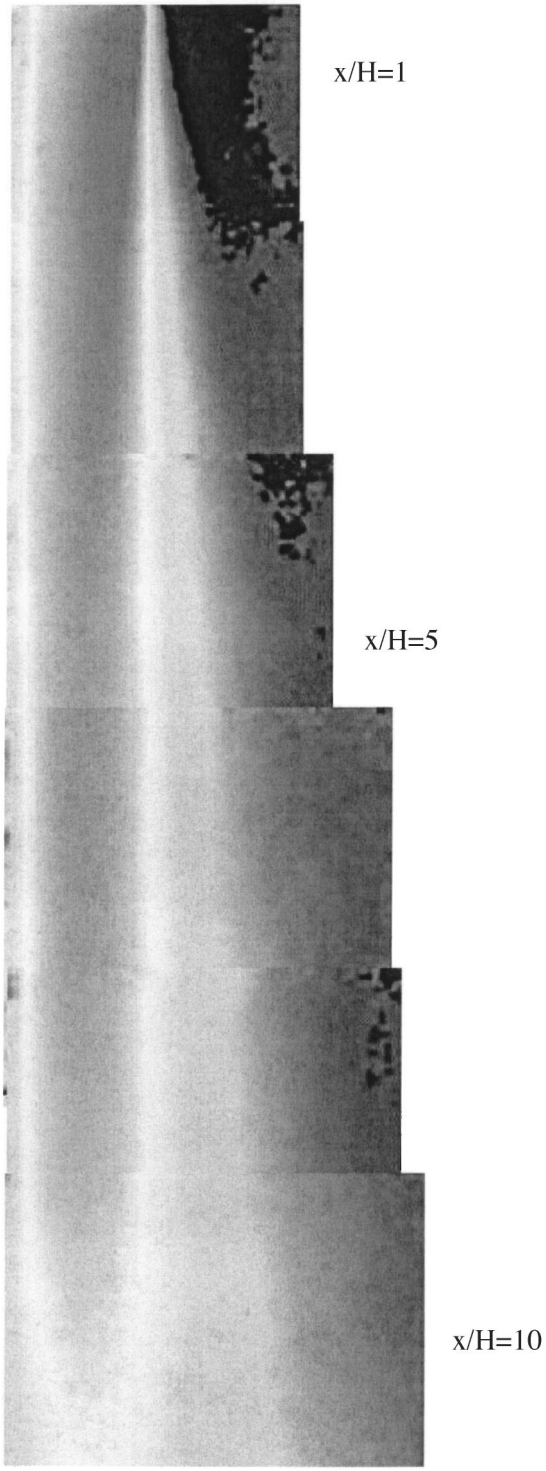

Fig. 7 Streamwise velocity contours for Re=8,500 curtain where highest velocities are red and lowest are black

pletely detached, but by $x/H=2.2$, the effect of detachment can be clearly seen. Further down the detached curtain, $x/H>4$, the streamwise velocities taper off to yield nearly stagnat conditions along the wall ($y/H<0.5$) and the peak velocity location is at a large transverse distance. Thus the curtain integrity was completely lost.

As mentioned above, the profile evolution for Re of 3,800 to 8,500 is similar. Figure 10 shows the average velocity profiles for all of the curtains at the downstream $x/H=5$ location. The similarity of the velocity distributions indicates that the nondimensional rate of momentum diffusion is approximately constant within this range of Reynolds numbers for the curtain. This similarity continued at all downstream x/H locations. The Re $=1,500$ curtain, which was detached from the wall, is the exception.

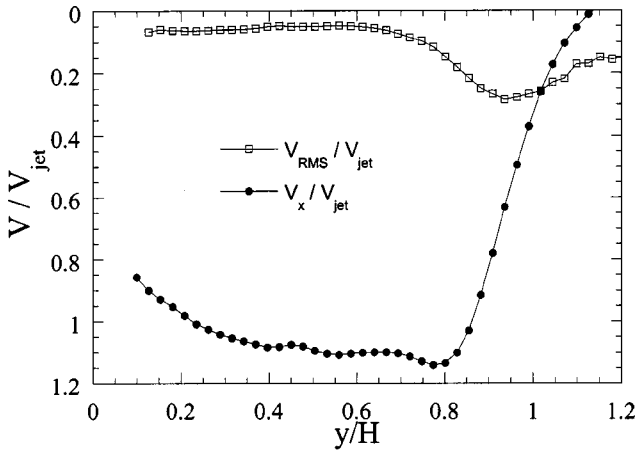

Fig. 8 Initial streamwise velocity and RMS velocity profiles for $x/H=1$ for Re=4600 curtain

In Fig. 11, a plot of the downstream turbulence levels for the Re=3,800 curtain is presented. The turbulence levels inside the

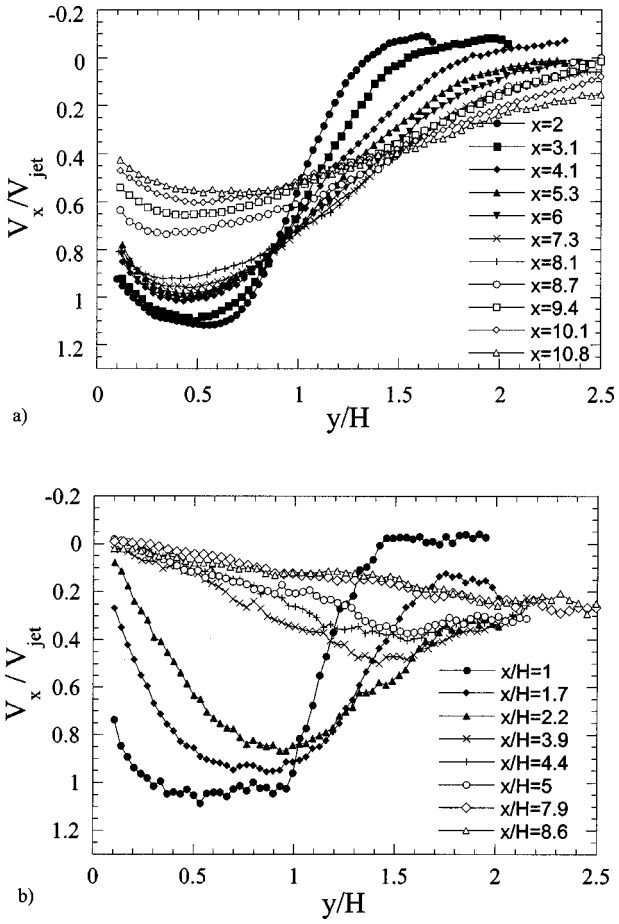

Fig. 9 Evolution of streamwise velocity profiles for *a*) Re=4600 and *b*) Re=1500 curtains

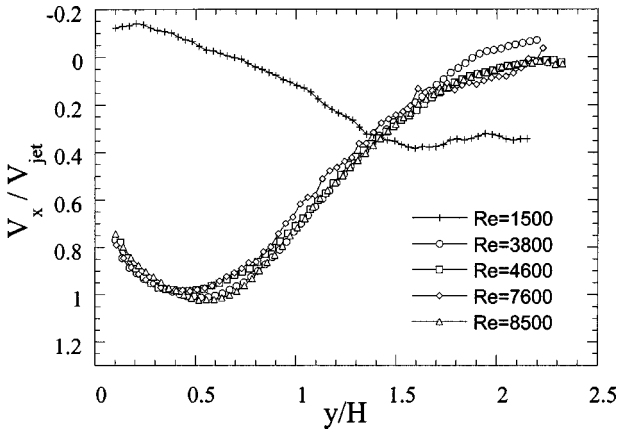

Fig. 10 Streamwise velocity profiles for curtains at $x/H=5$

curtain are around 10% (with the some peaking near the wall) and these levels are highest (up to 25%) in the mixing region (near y/H=1). These peak locations are consistent with the regions of maximum velocity gradient observed in the mean velocity statistics away from the wall, and show that significant mixing with the ambient flow was occurring. As noted previously, the magnitude of the turbulence intensity levels is much higher than typically observed in fully developed wall jets or modelled in numerical simulations. These high values of turbulence intensity are attributed to the high initial turbulence values of the air curtain not present in other studies. Indeed, the forced wall jet study of Gogineni et al. [11] used a forcing intensity of 6% to obtain phase-locked results. This indicates a similarity between the present inlet turbulence and the forced wall jets. In addition, that while the turbulence near the wall shows some peaking (as in boundary-layer flows), the free-shear layer dynamics tend to dominate the bulk of the flow, and in particular the entrainment near the curtain edge.

Using the average velocity profiles, values for the curtain thickness, $\delta(x)$, were calculated as shown in Fig. 12. For the Re =1,500 curtain, the curtain thickness for both the rapid and delayed detachment cases are plotted separately, but both cases indicate rapid thickening as compared to the other higher Re cases. Downstream of $x/H=4$, the detachment was too severe to allow quantification of the curtain thickness. As expected from the velocity profiles shown in Figure 10, the curtain thicknesses for the curtains with Re=3,800 through 8,500 grew at the same rate,

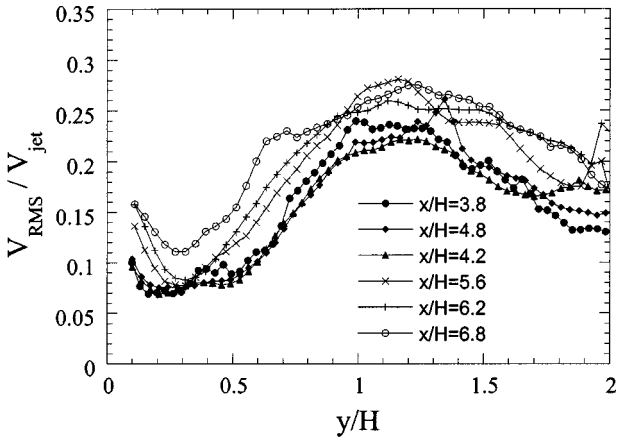

Fig. 11 Evolution of turbulence intensity levels for Re=3800 curtain

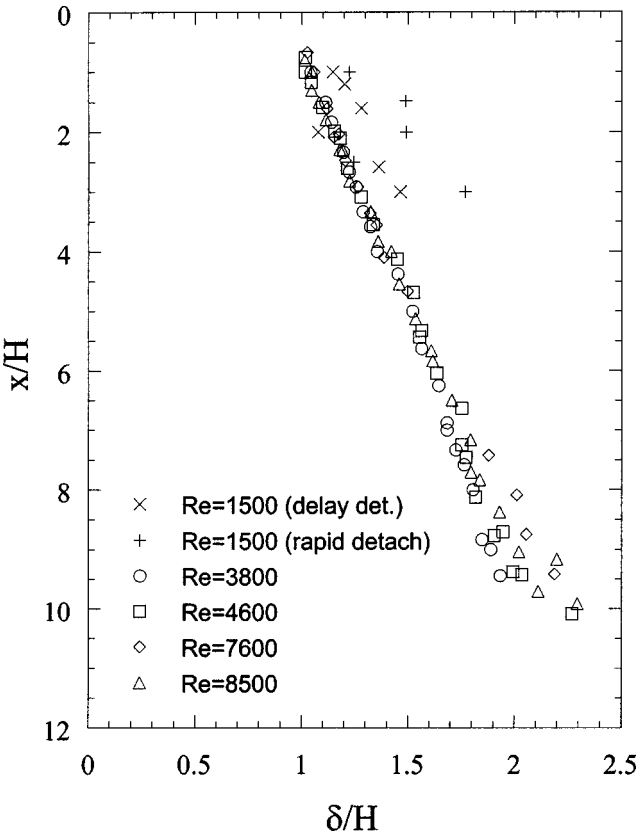

Fig. 12 Curtain thickness development for curtains

although some deviation was noted at the most downstream locations where there was a tendency for the large Re cases to have somewhat larger δ values.

As such, the air curtain dynamics and momentum distribution in the Re=3,800 to 8,500 range are not largely affected by the Reynolds number of the air curtain. This is significant because the mass entrainment rate is proportional to the curtain speed, so by slowing the curtain, the rate of entrainment of the ambient humid air can be linearly decreased. Therefore, one way to minimize the thermal entrainment (and the associated energy losses) is to reduce the jet velocity (and thus Re), but only in the regime where attachment can be ensured.

Conclusions

An air curtain from a refrigerated display case was simplified as an isothermal wall jet to examine the basic fluid dynamics at work in the Re=1,500 to 8,500 range typical of such air curtains. The curtain entrainment was seen to be dominated by eddy engulfment of ambient air. The eddies were primarily attributed to two sources, the initial high turbulence in the jet exhaust and the shear layer instabilities of the air curtain. The thickness of the air curtain was calculated from the velocity profiles and was found to grow roughly independent of Reynolds number for Reynolds numbers from 3,800 to 8,500. However, detachment of the air curtain from the wall was observed to occur for the Re=1,500 curtain. This was similar to the detachment process previously observed in laminar wall-jets as well as in acoustically driven turbulent wall-jets. This indicates a lower limit of the present air curtain velocity exists below which air curtain integrity can not be ensured, at least at these high inflow turbulence level conditions.

Acknowledgments

This study was funded by the Air Conditioning and Refrigeration Center at the University of Illinois at Urbana-Champaign (UIUC). The refrigerated display case used in the study was provided by Hussmann Co. in Bridgeton, MO. Pega Hrnjak of UIUC provided valuable assistance with the configuration of the refrigeration case.

References

[1] Adams, P. 1985, ''The intereffect of supermarket refrigeration and air conditioning,'' ASHRAE CH-85-09 No. 1, pp. 423-433.
[2] Field, B., 2001, *Entrainment in Refrigerated Air Curtains*, University of Illinois, Masters Thesis.
[3] George, B., and Buttsworth, D., 2000, ''Investigation of an open refrigeration cabinet using computational simulations with supporting experiments,'' Proceedings of the ASME International Mechanical Engineering Congress and Exposition, Nov 2000.
[4] Cortella, G., Manzan, M., and Comini, G., 2001, ''CFD simulation of refrigerated display cabinets,'' Int. Journal of Refrigeration, **24**, pp. 250–260.
[5] Navaz, H. K., Faramarzi, R., Gharib, M., Dabiri, D., and Modarress, D., 2002, ''The application of advanced methods in analyzing the performance of the air curtain in a refrigerated display case,'' ASME J. Fluids Eng., **124**, pp. 756–764.
[6] Bajura, R., and Catalano, M., 1975, ''Transition in a two-dimensional plane wall jet,'' J. Fluid Mech., **70**, pp. 773–799.
[7] Shih, C., and Gogineni, S., 1994, ''Experimental study of perturbed laminar wall jet,'' AIAA J., **33**, pp. 559–561.
[8] Hsiao, F-B., and Sheu, S., 1996, ''Experimental studies on flow transition of a plane wall jet,'' Aeronaut. J., **100**, pp. 373–380.
[9] Keane, R., and Adrian, R., 1992, ''Theory of cross-correlation analysis of PIV images,'' Applied Science Research, **49**, pp. 191–215.
[10] Bhattacharjee, P., and Loth, E., 2001, ''Simulation of thermal air curtain entrainment,'' Proceedings of the ASME Fluid Engineering Division Summer Meeting, New Orleans, May 2001.
[11] Gogineni, S., Visbal, M., and Shih, C., 1999, ''Phase-resolved PIV measurements in a transitional plane wall jet: a numerical comparison,'' Exp. Fluids, **27**, pp. 126–136.

A. Britan

A. V. Karpov
Research Engineer

Department of Computational Mechanics,
Volgograd University,
Volgograd, Russia

E. I. Vasilev
Professor
Department of Computational Mechanics,
Volgograd University,
Volgograd, Russia 400062,
Volgograd, str. 2nd Prodolnaja, 30

O. Igra
Professor

G. Ben-Dor
Professor

E. Shapiro

The Pearlstone Center for Aeronautical
Engineering Studies,
Department of Mechanical Engineering,
Ben-Gurion University of the Negev,
Beer Sheva, Israel

Experimental and Numerical Study of Shock Wave Interaction With Perforated Plates

The flow developed behind shock wave transmitted through a screen or a perforated plat is initially highly unsteady and nonuniform. It contains multiple shock reflections and interactions with vortices shed from the open spaces of the barrier. The present paper studies experimentally and theoretically/numerically the flow and wave pattern resulted from the interaction of an incident shock wave with a few different types of barriers, all having the same porosity but different geometries. It is shown that in all investigated cases the flow downstream of the barrier can be divided into two different zones. Due immediately behind the barrier, where the flow is highly unsteady and nonuniform in the other, placed further downstream from the barrier, the flow approaches a steady and uniform state. It is also shown that most of the attenuation experienced by the transmitted shock wave occurs in the zone where the flow is highly unsteady. When solving the flow developed behind the shock wave transmitted through the barrier while ignoring energy losses (i.e., assuming the fluid to be a perfect fluid and therefore employing the Euler equation instead of the Navier-Stokes equation) leads to non-physical results in the unsteady flow zone. [DOI: 10.1115/1.1758264]

1 Introduction

It is well known that different ducts and channels act as a structured wave-guide. When such channels lead to protected area or objects it is possible to reduce the pressure acting on them by the colliding shock wave. This pressure reduction can be achieved by introducing various types of barriers inside the channel, before the protected objects, e.g., perforated plates and/or screens. When a planar shock wave collides, head-on, with an obstacle two processes take place simultaneously. One part of the shock wave is reflected head-on from the obstacle, whereas the other part is transmitted through the open parts of the obstacle. The first process is usually referred to as *shock wave reflection* from the obstacle and the second one as *shock wave diffraction* through the obstacle generating a nonsteady flow behind it. The resulted wave pattern depends on the strength of the incident shock wave M_s, and on the relative area blockage (or porosity, ε) caused by the barrier $\varepsilon = A_{op}/A_{tot}$, where A_{op} is the cross section of the duct that is open to the flow and A_{tot} is the total cross section of the duct. By proper choice of the barrier geometry one can control the strength of the transmitted shock wave. While this idea is employed for protection against both accidental and planned explosion (Lind et al. [1]) the initial unsteady flow developed inside the duct, behind the transmitted shock wave, is not fully understood. In the case of a slit-like obstacle (e.g., a plate blocking part of a two-dimensional duct, like the one shown schematically in Fig. 1), the starting flow developed behind the transmitted shock wave is similar to that obtained while passing through a very short, rough converging-diverging nozzle; Franks [2]. As shown subsequently an important feature in such transient flows is the free jet generated by the flow expansion and subsequent separation that take place downstream of the barrier/nozzle exit plane.

The present paper has three different goals. First, and foremost, is a detailed study of the unsteady flow developed behind a transmitted shock wave that resulted from head-on collision of an incident shock wave with a slit-like barrier, e.g., the one shown in Fig. 1.

The second goal is answering the question: is it acceptable to model the flow as being inviscid and nonconductive as was done in Britan and Vasiliev [3] and in Igra et al. [4,5]?

The justification for employing this assumption is that in such short flow duration the amount of energy losses due to friction (viscous losses) and heat transfer is negligibly small in comparison with the flow kinetic energy. For assessing the importance of these loss mechanisms on the starting-flow developed behind the transmitted shock wave; in the present study the flow simulation is conducted twice. First, by modeling the flow as being inviscid (Euler equations) and thereafter, solving the real flow, i.e., being viscous and heat conductive (Navier-Stokes equations). Comparison is made between the two numerical solutions and experimental findings.

The third goal is to extend the model proposed for a slit-like barrier to barriers of different geometries, for example those shown in Fig. 2. While doing so attention is given to the following important features of the transient pressure field:

1. The distance effect (pressure traces were recorded at different distances downstream from the barrier).
2. The time effect (how pressures change behind the transmitted and thereafter, behind the reflected shock wave as they pass the recording pressure transducers).

Contributed by the Fluids Engineering Division for publication in the JOURNAL OF FLUIDS ENGINEERING. Manuscript received by the Fluids Engineering Division December 6, 2002; revised manuscript received October 31, 2003. Associate Editor: W. W. Copenhaver

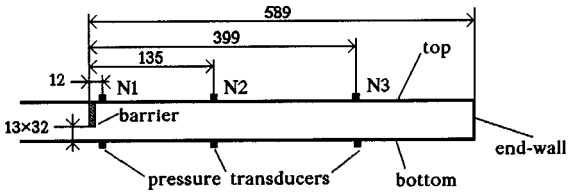

Fig. 1 Schematic description of the investigated 2-D conduit

3. The geometrical configuration (variations in the pressure amplitude associated with changes in the geometry of the open spaces of the barrier).

Porous plates with a single rectangular or circular hole were tested as well as perforated plates having different hole's spacing and holes number. However, all tested plates had the same porosity ($\varepsilon = 0.4$).

2 Theoretical Background

2.1 The Flow Field. Numerical simulations were conducted for the flow developed inside the conduit shown in Fig. 1. This is a 2-D flow; a flow between two parallel plates inside which a slit-like barrier is installed. This barrier blocks 60% of the flow cross-section area, i.e., it results in a porosity of $\varepsilon = 0.4$. Pressure histories were calculated along the conduit top and bottom walls.

2.2 Governing Equations. The governing, 2-D equations, expressing conservation of mass, momentum and energy are given in (1)–(3). These are known as the Navier-Stokes equations. Once the viscous and heat transfer term are eliminated the set reduces to the Euler equations, which are the governing equations for the perfect gas case.

$$\rho_t + \nabla \cdot (\rho \mathbf{V}) = 0 \tag{1}$$

$$(\rho \mathbf{V})_t + \nabla \cdot (\rho \mathbf{V}\mathbf{V}) + \nabla p = \nabla \cdot \ddot{\tau} \tag{2}$$

$$E_t + \nabla \cdot ((E+p)\mathbf{V}) = (\nabla \cdot \ddot{\tau}) \cdot \mathbf{V} + S + \nabla \cdot (\hat{k} \nabla T) \tag{3}$$

Here the specific total energy, E, is given by

$$E = \frac{1}{p(\gamma - 1)} + \frac{1}{2}\rho V^2$$

The gas is assumed to behave as a perfect gas, i.e., it has a simple equation of state, $p = \rho RT$.

For a two-dimensional flow of an ideal gas, having a velocity vector $V = (u, v)$, the friction force, $\nabla \cdot \ddot{\tau}$, and the irreversible energy dissipation S are expressed as follows:

$$\nabla \cdot \ddot{\tau} = \frac{1}{3}\begin{pmatrix} 6(\mu \boldsymbol{u}_x)_x + 3(\mu(\boldsymbol{u}_y + \boldsymbol{v}_x))_y - 2(\mu(\boldsymbol{u}_x + \boldsymbol{v}_y))_x \\ 3(\mu(\boldsymbol{u}_y + \boldsymbol{v}_x))_x + 6(\mu \boldsymbol{v}_y)_y - 2(\mu(\boldsymbol{u}_x + \boldsymbol{v}_y))_y \end{pmatrix}$$

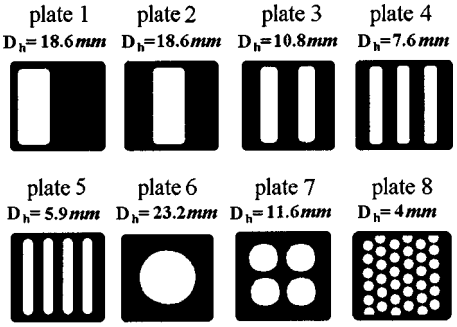

Fig. 2 Geometry of perforated barriers used in the shock tube experiments (all have the same porosity $\varepsilon = 0.4$)

$$S = \frac{\mu}{3}[2(\boldsymbol{u}_x - \boldsymbol{v}_y)^2 + 2(u_x^2 + v_y^2) + 3(\boldsymbol{u}_y + \boldsymbol{v}_x)^2]$$

The effective viscosity and thermal conductivity, μ and λ, are composed of the molecular part (μ_m and λ_m) and the turbulent part (μ_T and λ_T) as follows:

$$\mu = \mu_m + \mu_T; \quad \lambda = \lambda_m + \lambda_T;$$

$$\lambda_m = \frac{\mu_m}{(\gamma - 1)Pr}; \quad \lambda_T = \frac{\mu_T}{(\gamma - 1)Pr_T}$$

The molecular viscosity is given by $\mu_m = \mu_0 (T/T_0)^{0.85}$ where μ_0 is the viscosity at a reference temperature T_0. The turbulent viscosity can be expressed in term of k and ε as $\mu_T = \rho C_\mu k^2 \varepsilon^{-1}$. Here k expresses the kinetic energy in the turbulent flow and ε is the energy dissipation rate.

The specific values of k and ε are obtained from the solution of the following two equations:

$$(\rho k)_t + \nabla \cdot (\rho \mathrm{kV}) = \nabla \cdot (\mu_k \nabla k) + \rho C_\mu S \frac{k^2}{\varepsilon} - Dk - \varepsilon \tag{4}$$

$$(\rho \varepsilon)_t + \nabla \cdot (\rho \varepsilon V) = \nabla \cdot (\mu_\varepsilon \nabla \varepsilon) + \rho C_{\varepsilon 1} C_\mu S k - C_{\varepsilon 1} D\varepsilon - C_{\varepsilon 2} \frac{\varepsilon^2}{k} \tag{5}$$

$$D = \frac{2}{3}\nabla \cdot V = \frac{2}{3}(u_x + v_y), \quad \mu_k = \mu_m + \frac{\mu_T}{\sigma_k}, \quad \mu_\varepsilon = \mu_m + \frac{\mu_T}{\sigma_\varepsilon}.$$

For details see Launder and Spalding [6]. The following constants were used in the present solution of (1)–(5):

$$C_\mu = 0.09, \quad C_{\varepsilon 1} = 1.5, \quad C_{\varepsilon 2} = 1.9,$$

$$\sigma_k = 1, \quad \sigma_\varepsilon = 1.3, \quad \mathrm{Pr_T} = 0.9.$$

It was noted by Baldwin and Lomax [7] that in vicinity to the conduit's wall (4) and (5) provide wrong values for k and ε. Therefore, in these regions k and ε were evaluated using the model proposed by Cebeci and Smith [8] with Baldwin and Lomax modification [7].

2.3 Boundary and Initial Conditions. In the Euler Eqs. (1)–(3), the slip boundary condition ($u_n = 0$) was used along all conduit walls. In the Navier-Stokes equations (1)–(5), which was used only for solving the flow downstream of the slit-like barrier, zero slip conditions for the gas velocity along the walls was imposed. The viscous stress normal to the conduit wall is related to the pressure gradient via the relation $\partial p/\partial n = (\nabla \cdot \ddot{\tau})_n$. The heat flux to the wall was set to zero, i.e., treating the flow as being adiabatic: $\partial T/\partial n = 0$.

The initial gas pressure prior to the arrival of the incident shock wave is set at 1 bar (air, $\gamma = 1.4$). The pre-shock channel wall temperature, as well as that of the undisturbed air is set at 298 K. Initial density and sound speed are denoted as ρ_0 and a_0. The initial turbulent background $k = 10^{-4} a_0^2$, $\mu_T = 2.25\mu_m$. In all computations, the incident shock wave Mach number is 1.435.

3 Numerical Method

W-modification of Godunov's scheme for a system of conservation equations which employs the flux-corrections at the 2-D stencil has been used in the present numerical calculations. In the following only the general idea of the scheme is described. More details can be found in Vasiliev [9]. Consider a system of hyperbolic equations written in a conservative form:

$$\frac{\partial \omega}{\partial t} + \frac{\partial f(\omega)}{\partial x} + \frac{\partial g(\omega)}{\partial y} = 0, \tag{6}$$

where $\omega(x, y, t)$ is an m-component vector and $f(\omega)$ and $g(\omega)$ are the vectors of the fluxes. Then, the first-order Godunov scheme applied to the modified equation:

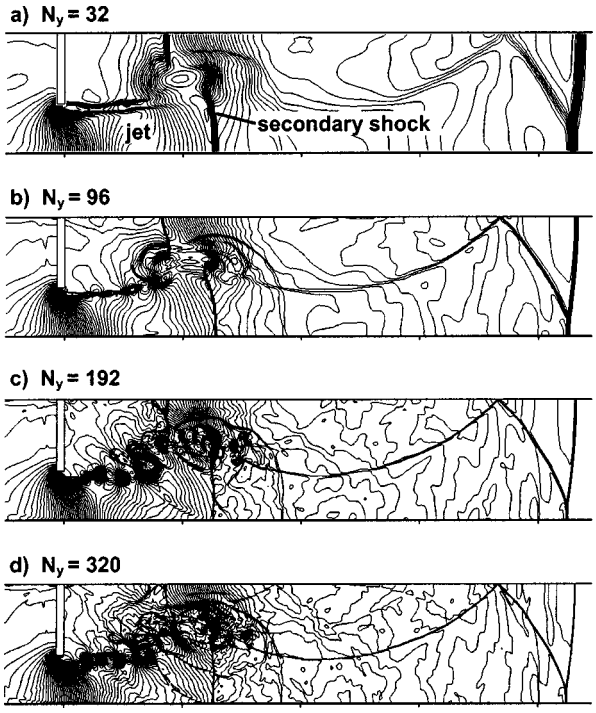

Fig. 3 Effect of the mesh size on the resulted flow field

$$\frac{\partial \omega}{\partial t} + \frac{\partial f(\omega+\alpha)}{\partial x} + \frac{\partial g(\omega+\beta)}{\partial y} = 0,$$

provides a second-order-accurate in space and in time solution of equation (6) if

$$\alpha = \frac{\Delta x}{2} \operatorname{sgn} \frac{\partial f(\omega)}{\partial \omega} \frac{\partial \omega}{\partial x} + \frac{\Delta t}{2} \frac{\partial \omega}{\partial t}$$

and

$$\beta = \frac{\Delta y}{2} \operatorname{sgn} \frac{\partial g(\omega)}{\partial \omega} \frac{\partial \omega}{\partial y} + \frac{\Delta t}{2} \frac{\partial \omega}{\partial t}$$

The nonlinear approximation of the terms α and β during the numerical solution is performed using a W-stencil with orientation depending on the flow velocities (i.e. eigenvalues of the matrices $\partial f(\omega)/\partial \omega$ and $\partial g(\omega)/\partial \omega$).

This scheme was modified to solve the Navier-Stokes Eqs. (1)–(5) using a splitting method. The viscous terms were approximated using an explicit scheme with central differences in space and a two-step Runge-Kutta method in time. The stiff source terms in k-ε Eqs. (4) and (5) were approximated using an exponential interpolation in time. At high turbulent viscosity one time step Δt for solving the inviscid gas equations included several sub-steps to account for the viscous contribution during the splitting procedure. The same procedure was applied to the heat transfer term in the energy Eq. (3); the number of the required sub-steps was estimated for stability of the marching method.

4 Numerical Results

4.1 The Transient Flow, Predictions of the Inviscid Solution. The main objective of this section is to study the flow patterns observed during the starting flow downstream from the barrier. Simulations are conducted for four different variants of the square computational grids. Resulted flow pictures are presented in Fig. 3 by lines of constant density (isopycnics). The value N_y appearing on top of each drawing indicates the size of the vertical grid. It corresponds to either 1, 3, 6, or 10 cells per 1 mm of length. The density step in these figures is $\Delta\rho = 0.33\rho_0$. At $t=0$ the front of the incident shock wave coincides with the flow entrance to the barrier, the barrier's thickness is 2 mm. In the observed time ($t=340\ \mu$s) the diffraction of the incident shock wave over the barrier was completed. The flow in the considered stage shows the appearance of a secondary upstream-facing shock wave, which matches between the high Mach number and low pressure downstream of the barrier and the lower velocity and high pressure prevailing behind the transmitted shock [3].

The next important detail, which is clearly visible in the flow pattern, is a jet stream. It is essentially unsteady and composed of numerous small vortexes, which appear at different locations on each of the simulations shown in Fig. 3. These vortexes interact with the secondary shock wave and give rise to a series of weak shocks directed towards the jet. Such new interactions increase the jet instability, which in turn generates oscillations in the flow variables over the whole flow field downstream the slit-like barrier. Close inspection of their amplitude shows that peak oscillations are observed in vicinity of the leading part of the jet, in the flow region close to the secondary shock wave. Spectral analysis reveals a decrease in their frequency and an expansion of the frequency band with reduction in the mesh size. These observations support a turbulent nature of the flow pattern shown in Fig. 3. Judging from this figure it is apparent that the smaller the mesh size (larger N_y) is, the higher is the resolution of the simulated flow in vicinity to the jet stream and shock waves. Since the number and the dimension of these details depend on the mesh size any attempts to resolve accurately the phenomena using Euler simulations is doomed to end in a failure.

4.2 Navier-Stokes Solution. The head-on collision of a planar shock wave with a slit-like barrier was simulated using Navier-Stokes Eqs. (1)–(5) in the region downstream from the barrier and Euler equations in the region upstream from the barrier. Numerical results obtained when using computational grid of 2700×96 are shown in Figs. 4–6. In these figures the flow evolvement, upstream and downstream of the slit-like barrier, is shown from the moment when the incident shock wave hits the barrier (at $t=0$) and up to $t=3{,}280\ \mu$s thereafter. In the considered case, the slit-like barrier blocks significant part of the duct cross-section (60%), this results in a strong reflected shock wave from the barrier. Downstream from the slit the transmitted shock wave is clearly observed. As could be expected a strong rarefaction wave is evident between these two shock waves (see Fig. 4 at $t=30\ \mu$s). As a result, at $t=30\ \mu$s the shape of the reflected and the transmitted shock waves are convex. During the time interval $170\ \mu\text{s} \leqslant t \leqslant 210\ \mu$s the oblique interaction of the shock waves with the conduit walls results in a Mach reflection configuration on both sides of the barrier. The vortex sheds from the slit's edge interacts with the diffracted shock wave, seen in Fig. 4 downstream from the barrier. This interaction leads to the vortex breakup. The vortex breakup creates a series of unsteady vortices that detach from the slit edge and strongly affect the downstream flow. Series of the secondary shocks that match between the high pressure prevailing behind the transmitted/reflected shock waves and the low pressure that exist in the expanding flow is also visible in Fig. 4 (at $t=210\ \mu$s and $t=250\ \mu$s). These shocks are responsible for the flow separation at the bottom and formation of the unsteady vortex, which slowly moves downstream from the barrier and shifts the jet towards the conduit topside. The jetting observed in Fig. 4 (at $t=210\ \mu$s) under the vortex accelerates the flow to a supersonic, over-expanded flow. Above the vortex the backward flow is also supersonic. The strong shock seen at the upper wall, at $t=250\ \mu$s and weak separation at $t=430\ \mu$s support this conclusion.

With proceeding time, at $t=430\ \mu$s, the transmitted and the reflected shock waves propagated further away from the barrier and approaches a planar front while the unsteady vortex becomes rather weak. Hence, the first stage in the starting process could be regarded as being completed. Now, the flow field evolved downstream from the barrier can be divided in two different zones. In

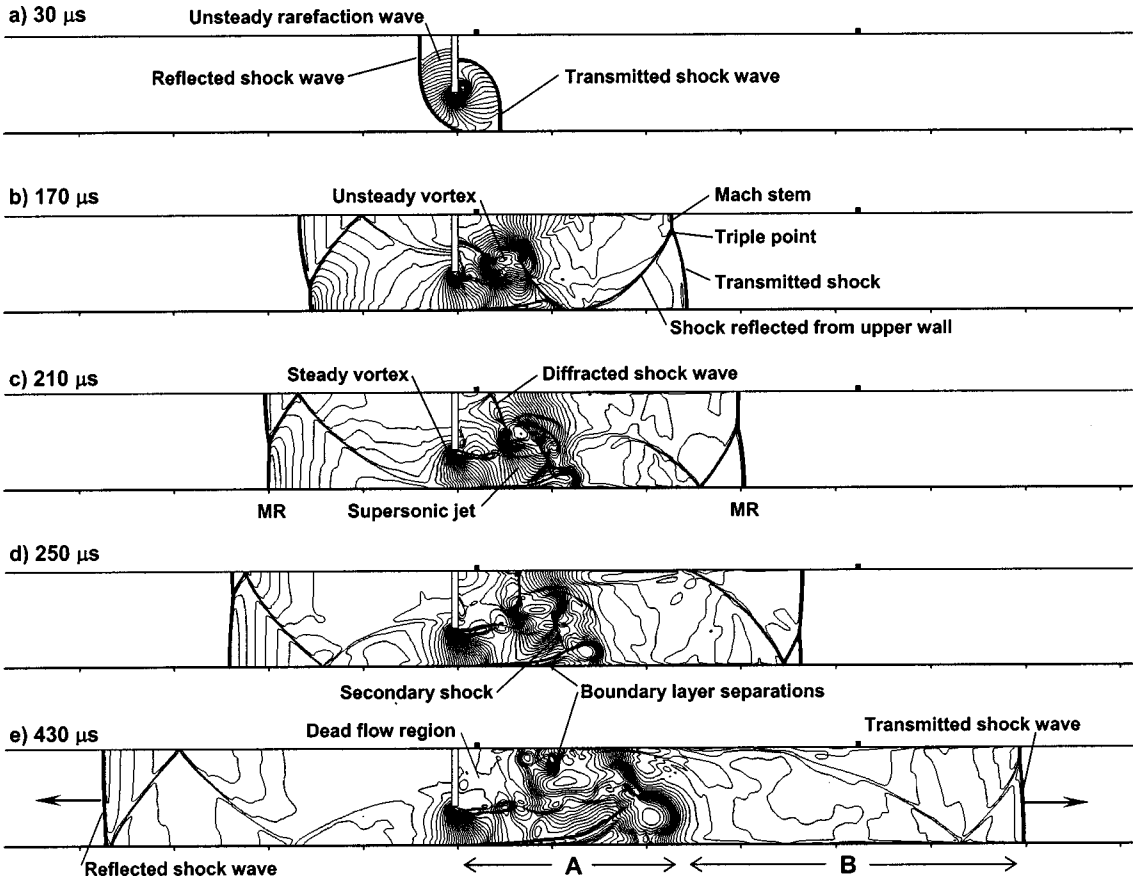

Fig. 4 Computed isopycnics plots showing the initial stage of the flow generated by the transmitted shock wave

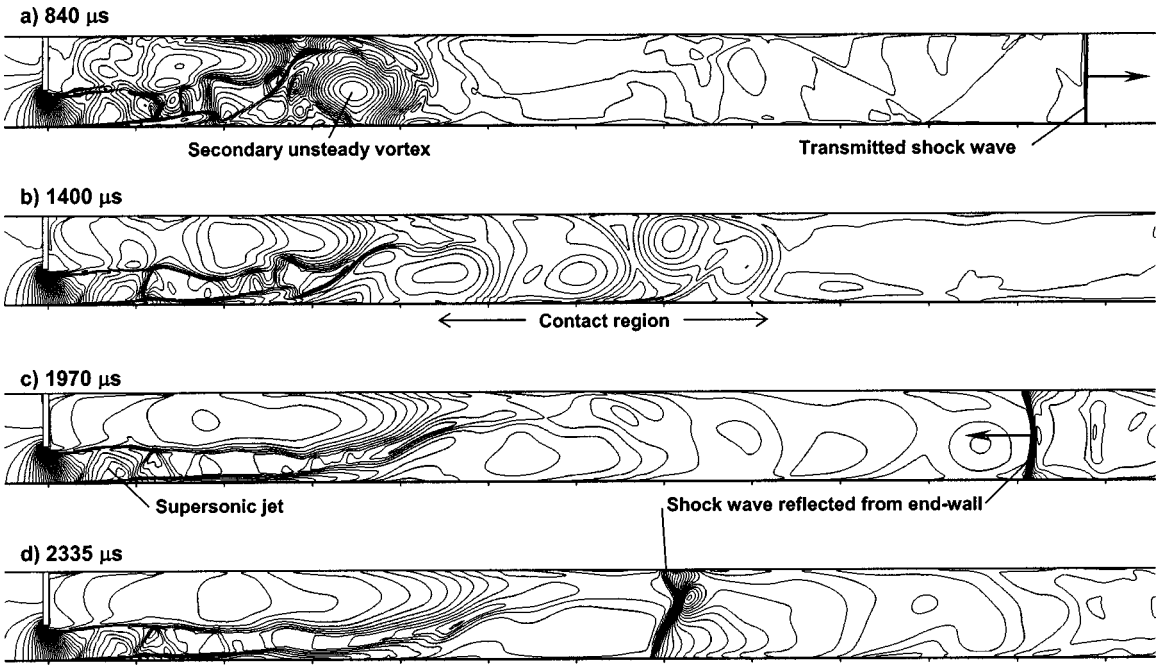

Fig. 5 Computed isopycnics plots showing the intermediate stage of the flow generated by the transmitted shock wave

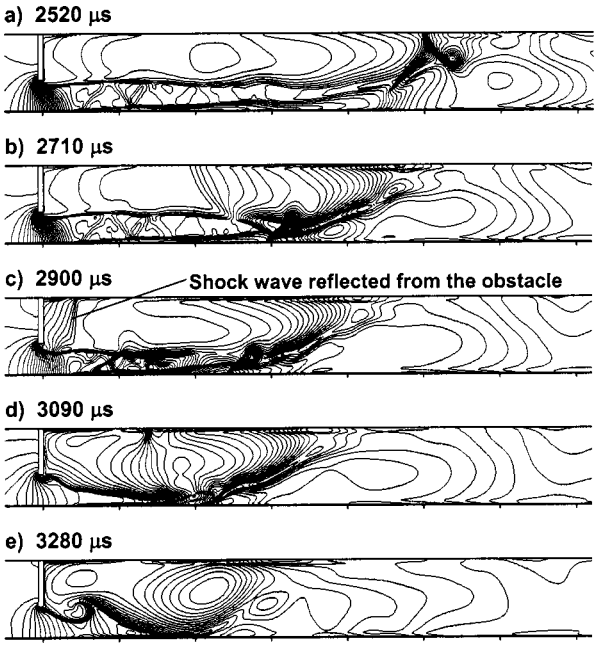

Fig. 6 Computed isopycnics plots showing the final stage of the flow generated by the transmitted shock wave

zone A, the expending jet and the dead flow region are the dominant features. The flow in this zone is highly turbulent due to the many vortexes that comprise this flow.

On the other hand, zone B contains a quasi-uniform gas flow which was compressed and heated by the transmitted shock wave, see Fig. 4 at $t=430\ \mu$s.

The second stage in the flow starting process is shown in Fig. 5. At $t=840\ \mu$s the two zones mentioned earlier have extended. Now the transmitted shock wave has a planar front and the flow behind it is almost uniform. It is apparent that in the considered time zone A is a region of very turbulent flow, composed of multiple wave reflections from the conduit walls which interact with the remaining vortices. With increasing time the turbulence in zone A subsides and a clear formation of a jet-flow through the orifice (produced by the slit-like barrier) is evident; see Fig. 5 at $t\geqslant 1{,}400\ \mu$s. At $t=1{,}400\ \mu$s the transmitted shock wave passed the observed part of the flow field and now the flow behind it is almost a steady 1-D flow. With proceeding time the transmitted shock wave reaches the conduit end-wall and is reflected back into the quasi-steady, one-dimensional flow of zone B.

The duration of a quasi-steady flow at any pressure recording station N_i ($I=1,2,3$), downstream of the barrier can be estimated by $\Delta t_s=t_e-t_{start}$ where t_e is the time elapsed since the transmitted shock wave passed the considered pressure recording station and t_{start} is the duration of the starting process at this station. Note, that the time duration Δt_s (at a given pressure recording station), is largely governed by the distance from the barrier to the conduit end-wall. In real experiments, once the transmitted shock wave reaches the conduit end-wall it reflects back and thus restricts the steady flow duration.

Figures 5 and 6 contain information about the dynamics of the reflected shock wave from the duct's end wall. At an early time after the reflection of the transmitted shock wave from the end-wall, at about $t=1{,}900\ \mu$s (a time not shown in Fig. 5), the front of the reflected shock wave is almost planar indicating that it propagates into a quasi-uniform flow. With increasing time the reflected shock wave continues its propagation in the quasi-uniform flow region, facing less uniform flow. This causes a change in the geometry of the shock wave front, from a planar to a concave front shape, see Fig. 5 at $t=1{,}970\ \mu$s. The concave shape of the reflected shock wave become more pronounce as it propagates toward the highly nonsteady, nonuniform region close to the barrier, see Fig. 5 at $t=2{,}335\ \mu$s. Once the reflected shock wave reaches the highly turbulent region near the barrier it splits to a lambda-shaped shock which terminates at the jet region, see Fig. 6 at $t=2{,}520\ \mu$s. Now the flow is obviously nonuniform, the lateral asymmetry in the flow is clearly visible in Fig. 6 at the considered time and thereafter. With increasing time the strength of the reflected shock wave quickly reduces until its complete decay as is evident in Fig. 6 at $t=3{,}280\ \mu$s. Judging from Figs. 4–6 it is apparent that the jet evolvement with time has a dominant effect on the transient phenomena of the flow prevailing in the region behind the slit-like barrier. The length of zone A, as well as that of a contact region, which separates between zone A and zone B, increases with time; until it reaches a maximum length. In the present case, this maximum is about ten times the slit open space ($\approx 10h, h=13$ mm). This is reached at about $t=1{,}400\ \mu$s. Thereafter, it remains constant until the arrival of the reflected shock wave, at $t=2{,}710\ \mu$s. (Hence, the quasi-steady flow duration in zone A based on the present data is about $\Delta t=2{,}710\ \mu\text{s}-1{,}400\ \mu\text{s}=1{,}300\ \mu$s).

4.3 Pressure Histories at Various Stations Downstream of the Barrier. So far the behavior of the unsteady flow developed behind the slit-like barrier was observed via isopycnics mapping. It could also be evaluated from observing pressure histories computed at different locations inside the conduit, downstream of the barrier. Specifically, in locations N1, N2, and N3 shown in Fig. 1. The obtained pressure histories are shown in Fig. 7; results shown in Fig. 7*a* refer to the conduit bottom side while the results of Fig. 7*b* are for the conduit top side. It should be noted that different starting time is used in Figs. 4–6 and in Fig. 7. While $t=0$ in Figs. 4–6 indicates the time of arrival of the incident shock wave at the barrier, in Fig. 7 the pressure traces start when the transmitted shock wave reaches the considered pressure ''recording'' station (N1, N2, or N3). The first pressure jump is that experienced across the transmitted shock. Different pressure oscillations are observed thereafter along the three pressure traces. The pressure histories shown in Fig. 7*a* are for pressures computed along the conduit's bottom wall. Results obtained for station N1 are strongly affected by the unsteady flow expansion through the orifice (the open part of the slit-like barrier) since this is the closest station to the barrier. This explains the fast pressure decrease shown in Fig. 7*a*, see trace marked N1, immediately behind the pressure jump across the shock front; this front is marked as 1.

The pressure history computed at station N1 but in the configuration shown in Fig. 7*b* is different from that shown in Fig. 7*a*; see Fig. 7*b* for trace N1. Now the pressure is computed along the conduit upper wall and as a result, for a short time period (less than 100 μs) a constant pressure prevails behind the front of the transmitted shock wave. Immediately thereafter, the pressure reduces to a sub-atmospheric level, see point 2 in Fig. 7*b* trace N1. This is not surprising since now the pressure at location N1 is strongly influenced by the rarefaction wave that follows the triple point of the Mach configuration shown in Fig. 4 at $t=170\ \mu$s.

After this reduction to sub-atmospheric pressure level a sharp pressure jump, at point 2, which restores the pressure to its quasi-steady level is evident in Fig. 7*b* for trace N1. This pressure jump is due to the arrival of the diffracted shock wave at station N1; see Fig. 4 at $t=210\ \mu$s. With proceeding time the slit generated vortex and the waves observed at early flow time either decayed or swept downstream leaving behind a relatively uniform flow at station N1 (see Fig. 7*b*) from shortly after point 2 until point 3. During this period almost a constant pressure is evident (about 0.25 bar) along trace N1 in Fig. 7*b*. The pressure jump seen at point 3 is due to the arrival of the shock wave reflected from the conduit end wall and thereafter reflected back from the slit-like barrier. This reflected shock wave is clearly observed in Fig. 6 at $t=2{,}900\ \mu$s. A relatively high pressure (about 2.5 bar) prevails behind this reflected shock wave; see Fig. 7*b*.

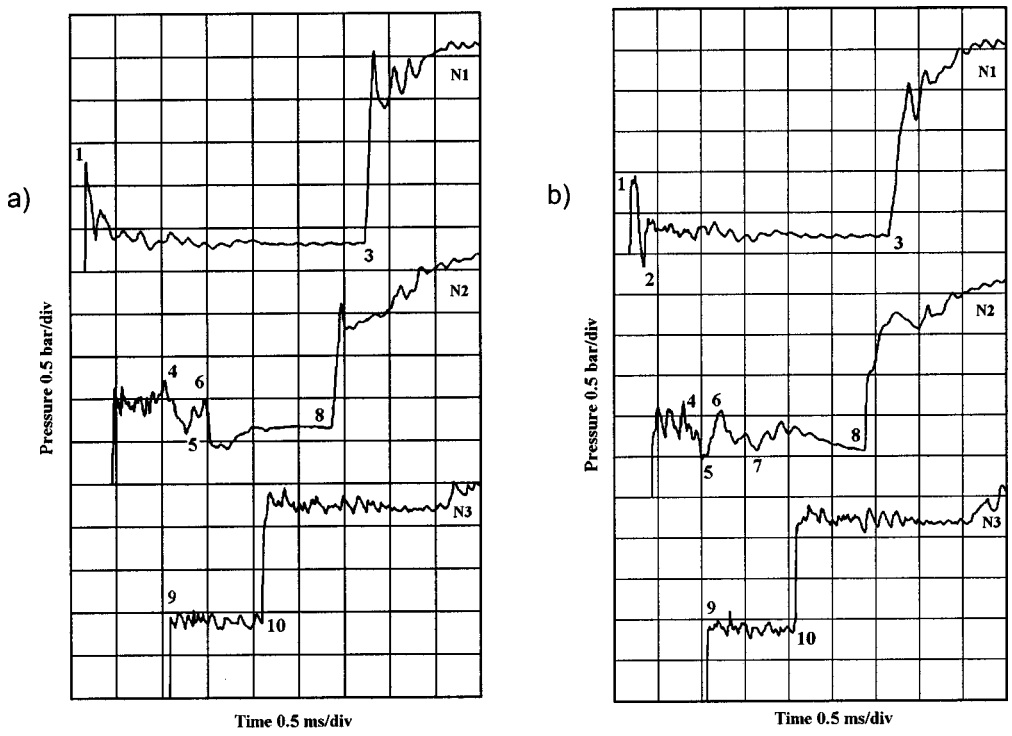

Fig. 7 Computed wall pressure histories for bottom (*a*) and top (*b*) of the conduit shown in Fig. 1

In summary, it is clear from the simulations shown in Figs. 4–6 and in Fig. 7 that at early time after the head-on collision of the incident shock wave with the slit-like barrier a region of sub-atmospheric pressure exist, for a short time, behind the barrier (trace N1 in Fig. 7*b*). This low pressure supports the jet emerging from the slit-like barrier; which is visible in Fig. 5. The jet divides the flow field into two different sections. The lower part is occupied by the jet stream while the top region contains a fairly uniform flow as is evident from Fig. 5 and 6 up to a time $t < 2{,}900\ \mu$s. This region of a fairly uniform pressure is clearly seen in Fig. 7, trace N1.

The flow behavior at station N2 can be deduced from the isopycnics shown in Figs. 4–6 and the appropriate pressure history at this station, shown in Fig. 7. It is apparent from trace N2 in Fig. 7 that for a short time after the passage of the transmitted shock wave at this station a fairly uniform, high-pressure zone exists until point 4 marked on this trace. This is also visible in Fig. 4 at $t = 430\ \mu$s where station N2 is seen closely behind the transmitted shock wave. The isopycnics appearing in this zone indicate changes in density, explaining the pressure variations seen in Fig. 7*b* between the front of the transmitted shock wave and point 4. The larger pressure fluctuations observed in Fig. 7*b* between points 4 and 6 are due to the arrival of the nonsteady portion of the post-shock flow, (see Fig. 5 at $t = 840\ \mu$s), at station N2. The pressure reduction observed in Fig. 7*b* after point 6 is a direct result of the jet stream that reached the considered station and is the dominant feature there until the arrival of the reflected shock from the conduit end wall, see Fig. 5. Once the shock wave, reflected from the conduit end wall, reaches station N2 a pressure jump is expected through the shock front. This indeed is the case in point 8 in Fig. 7. The reflected shock from the conduit end wall is shown in Fig. 6 at $t = 2520\ \mu$s, shortly before it reaches station N2.

While at early time after the arrival of the transmitted shock wave at station N2 (for $210\ \mu\text{s} < t < 840\ \mu$s) the flow behind the shock is fairly uniform, at latter times it is definitely not 1-D. This is also evident when comparing Fig. 7*a* with 7*b*. While shortly after the passage of the transmitted shock wave at station N2 both traces show similar behavior (from the shock front and up to point 6), later different pressure histories are exhibit in the two traces.

Pressure measuring station N3 is located further away from the slit-like barrier. As a result the flow at this station is fairly uniform as is evident from Figs. 5 and 6. Therefore it is not surprising that very similar pressure histories are shown, for station N3, in Figs. 7*a* and 7*b*. In both, the transmitted and the reflected (from the end wall) shock waves are clearly seen; these shocks are separated by uniform flow zone (constant pressure).

4.4 Comparison Between Viscous and Inviscid Solutions The flow developed behind the transmitted shock wave, downstream of the slit-like barrier is initially highly unsteady as is evident from Figs. 4–6. It is reasonable to assume that in such flows energy dissipation via viscous and heat transfer processes plays a meaningful role. To assess the importance of these processes the numerical solution of (1)–(3) was repeated using the same initial condition but omitting the viscous and heat transfer terms from (1)–(3). Results obtained for pressure histories at stations N1, N2, and N3, for the bottom and the top sides of the conduit shown in Fig. 1, are shown in Fig. 8. Comparing computed pressure histories obtained for viscous flow (Fig. 7) with those obtained for a similar inviscid flow (Fig. 8) reveals the following:

Almost identical pressure histories, between points 1–3 (along trace N1) and 9–10 (along trace N3), are shown in Figs. 7 and 8. Hence, in vicinity of the first and the third pressure recording stations, until the arrival of the reflected shock from the conduit end wall, viscous effects do not play an important role.

This is not the case when pressure histories, shown in Figs. 7 and 8 at station N2 are compared. While the location of points 4 and 8 are very similar the pressure variations between these points are very different. Ignoring the loss mechanism results in pressure fluctuations throughout the obtained pressure history, see trace N2 in Fig. 8. The strongest pressure fluctuations are visible at the jet stream area, i.e., between points 4 and 8 in Fig. 8.

Unlike the viscous solution, in the inviscid case pressure fluctuations, which started at the jet stream zone, are maintained even

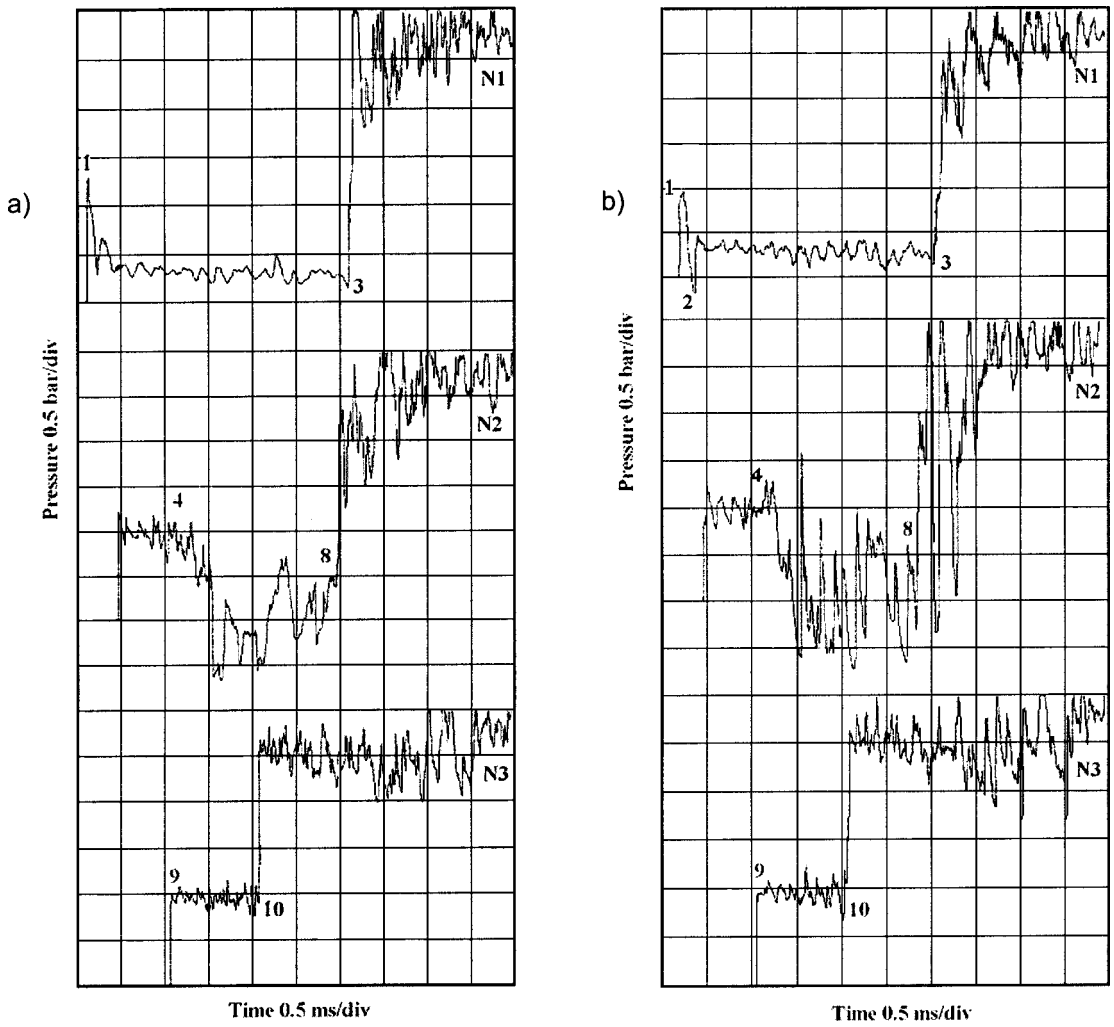

Fig. 8 Computed wall pressure signals for bottom (*a*) and top (*b*) of the conduit shown in Fig. 1. Computed pressures are based on the Euler equations.

behind the reflected shock wave from the conduit end wall. For understanding the reason for these pressure fluctuations the flow shown in Fig. 5 (for the viscous case) is shown in Fig. 9 (pressure contours) for a similar inviscid case. Comparing these two figures reveals that in the inviscid case (Fig. 9) strong vortices are detached from the slit-like barrier and together with the shock waves propagate downstream. Eventually, they fill the entire conduit cross-section. The weak shock waves generated in the vortices region, in turn, move toward the transmitted shock wave (Fig. 9*b*). These weak shocks are responsible for pressure oscillations observed along trace N3, between points 9 and 10 in Fig. 8*b*. Comparing Fig. 8*b* with Fig. 7*b* one notices that these oscillations are much stronger in the inviscid flow case.

The vortices trail does not evolve into a jet stream, like in the viscous case; see Fig. 9 and Fig. 5 at $t \geqslant 1{,}400$ μs. Due to the fact that in the inviscid case the flow behind the transmitted shock wave is dominated by vortices, the reflected shock from the conduit end wall obtains a much more curved front; compare Fig. 9 with Fig. 5, both at $t = 2{,}335$ μs. In summary, in the considered flow (flow duration of about 3 ms) the gas viscosity is the main mechanism in subsiding the vortices trail, developed behind the transmitted shock wave, and altering it into a jet stream. Omitting the gas viscosity results in nonphysical flow behavior between the slit-like barrier and the transmitted shock wave.

5 Experimental Results

5.1 Pressure Field Behind the Slit-Like Barrier. So far only numerical results were shown and discussed. In order to confirm the validity of these results experiments were conducted using the conduit shown in Fig. 1. The experiments were conducted in a 32 mm by 32 mm cross-section shock tube. The slit-like barrier was placed between the flanges connecting the test-section to the driven section of the shock tube. For preventing gas leakage through this connection rubber gaskets were glued between the two flanges.

In order to improve repeatability of experiments, the shock tube was equipped with a fast opening pneumatic valve having a rise-time of about 1 ms. The velocity of the transmitted shock wave and the overpressure behind it were measured using three 603H Kistler pressure transducers located at stations N1, N2 and N3 shown in Fig. 1. The output of the pressure transducers were farther stored using a data acquisition system which has a sampling rate of 500 KHz per channel.

The scatter in the incident shock wave Mach number was about 1% (Britan et al. [10]). The uncertainty in the measured velocity of the incident shock wave is estimated to be less than 0.7% and the uncertainty in overpressure measurements is estimated to be less $\pm 7\%$.

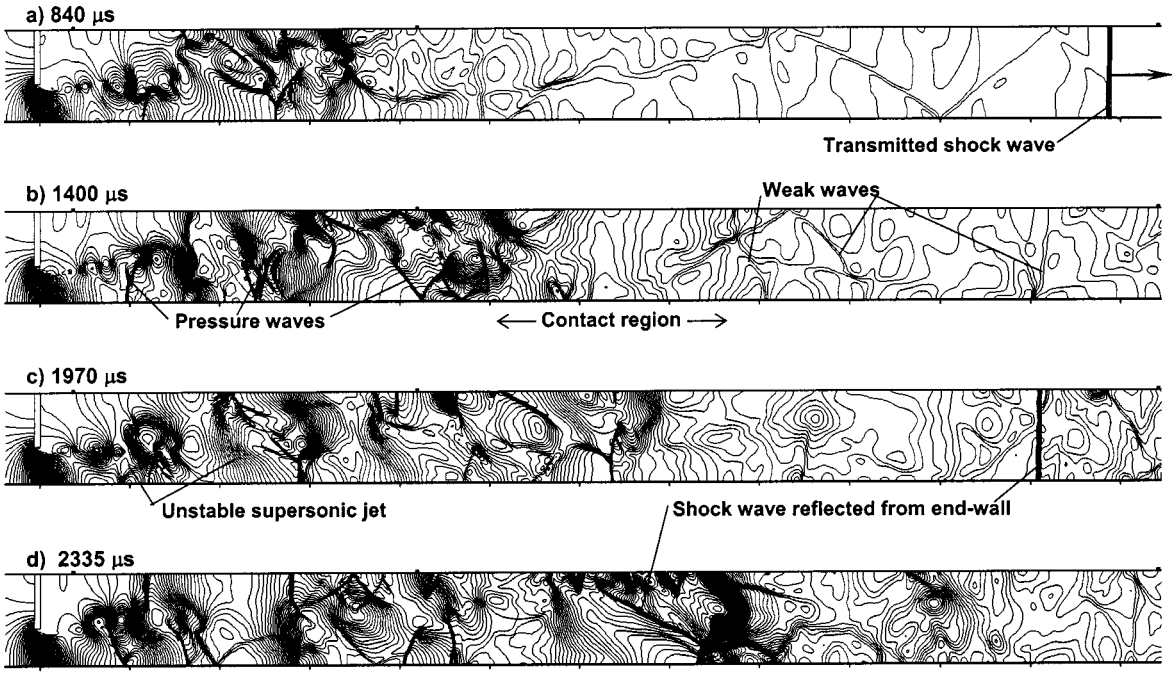

Fig. 9 Computed isobars plots showing the intermediate stage of the flow generated by the transmitted shock wave. Computations are based on the Euler equations.

Typical examples of recorded pressure histories are given in Figs. 10 and 11 along with appropriate numerical simulations. The numerical simulations are based on the flow model given in (1)–(5), i.e., a model that includes viscous and heat losses. Results shown in Fig. 10 are for the bottom transducers shown in Fig. 1. Fig. 10*a* shows simulations presented earlier and in Fig. 10*b* the recorded pressure histories, at stations N1, N2, and N3 are shown. It is clear from these figures that the present simulations reconstruct accurately the recorded pressures throughout most of the investigated flow duration. The physical model used and its numerical solution also simulates the shocks' (transmitted and reflected from the conduit end wall) velocities accurately. The same is true for the results shown in Fig. 11, which show computed and measured pressure histories along the conduit's upper wall. This confirms the validity of the proposed physical model (1)–(5) and its numerical solution. It also confirms the importance of including loss mechanism in modeling such a complex flow.

5.2 Shock Wave Attenuation Caused by the Barrier's Geometry. It is well known that shock wave attenuation resulting

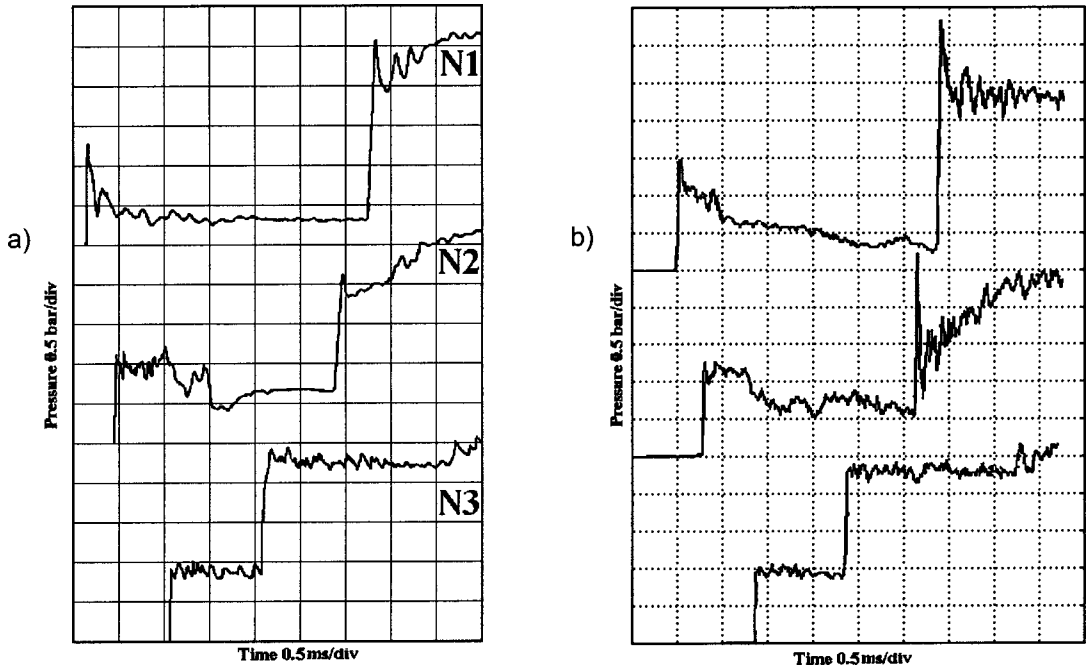

Fig. 10 Comparison between computed (*a*) and measured (*b*) wall pressure at the conduit's bottom wall. Computations are based on the Navier-Stokes equations.

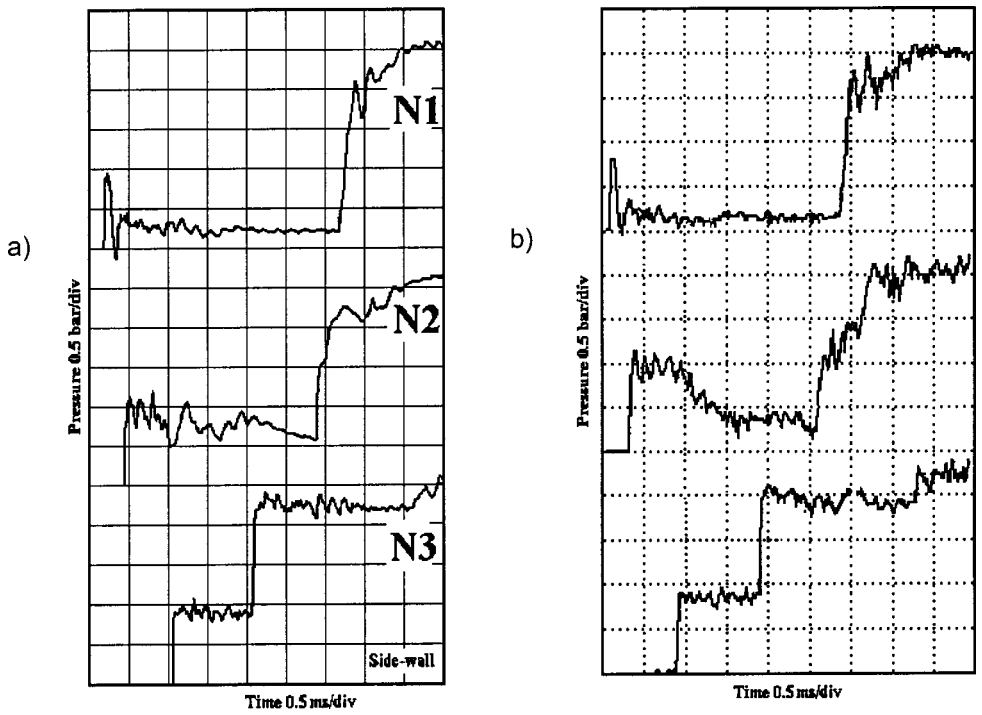

Fig. 11 Comparison between computed (*a*) and measured (*b*) wall pressure at the conduit's upper wall. Computations are based on the Navier-Stokes equations.

from its passage through a barrier depends on the barrier's porosity, ε. It also depends on the shape of the open spaces in the barrier, through which the flow passes, and the space distribution of these open spaces. The barrier discussed so far had only one rectangular opening. In order to assess the effect of the open spaces geometry and distribution, experiments were conducted with barriers having a constant porosity $\varepsilon=0.4$, but having different hydraulic diameter D_h, $D_h=4S/\Pi$ (where S is the area of the open space in the barrier and Π is the perimeter of the open space). A set of barriers having the same porosity ($\varepsilon=0.4$) but different D_h's were tested in our shock tube; the tested set is shown in Fig. 2.

During each experiment pressure histories were recorded at different distances downstream from the barrier. Results from these experiments are given in Fig. 12. Each plot appearing in Fig. 12 contains three pressure histories recorded at different positions downstream of the barrier. The distance of each recording station is given in a non-dimensional form, i.e., in term of x/D_h, where x is the distance of the pressure measuring station from the barrier. It is apparent from Fig. 12 that for the four different barriers tested, the recorded pressure histories are mostly influenced by the distances of the recording station from the barrier. Similar pressure histories are seen at equal distances x/D_h, downstream of the barriers. Close to the barrier (when $x/D_h<0.5$), the recorded pressure histories is similar to that shown in Fig. 7*b*, trace N1. That is, an initial unsteady spike followed by a quasi-steady flow where the pressure Δp is relatively small, $\Delta p \ll \Delta p_s$, see Fig. 12. As mentioned earlier, such a pressure trace is typical to a jet dominated flow, marked as zone A in Fig. 4. The flow in this zone is inhomogeneous, non-isotropic with maximum production of turbulent kinetic energy due to the jets and the wakes produced by the barrier (the perforated plate, see also Honkan and Andreopoulos [11]). It is apparent from Fig. 12 that with increasing distance away from the barrier the transient flow approaches a state of steady, uniform flow. At a distance of $x/D_h \geq 7.2$ the recorded pressure history reaches equilibrium amplitude Δp_ε. Based on results shown in Fig. 12 it is plausible that the flow developed behind the transmitted shock wave depends mostly on one non-dimensional parameter, x/D_h.

Additional support to this statement is given in Fig. 13, where a summary of all obtained results is presented in a non-dimensional form. The parameter k ($k=\Delta p/\Delta p_i$ where Δp_i is the pressure jump across the incident shock wave before reaching the barrier) is a measure to the shock wave attenuation caused by the barrier. Results shown in Fig. 13 were gathered from experiments done with the eight barriers shown in Fig. 2 (for all $\varepsilon=0.4$) and for two different incident shock wave Mach numbers, $M_s=1.46\pm0.01$ and $M_s=1.58\pm0.01$. The dotted line in Fig. 13 is the numerical simulation for the considered case ($\varepsilon=0.4$ and $M_s=1.435$). It is clear from Fig. 13 that all experimental findings are closely scattered around a single line indicating that the shock attenuation (k) could be expressed in term of x/D_h. Furthermore, the largest changes in k are experience close to the barrier, where $x/D_h<7$, while for $x/D_h>10$ the flow reaches steady conditions. There is also a fairly good agreement between the numerical simulation and the experimental findings although the simulation was conducted only for $M_s=1.435$. It should be noted the experimental results show no real dependence on the incident shock wave Mach number in the investigated range.

6 Conclusions

The present paper studies the head-on collision of an initially planar shock wave with protective porous barrier placed inside a straight conduit. In the experimental part a shock tube was used as the conduit. Particular attention has been given to the numerical analysis of the shock wave interactions with a slit like barrier using a high-resolution shock capturing scheme for viscous and inviscid flows. In the experimental part several barriers having different shape and different dimension of the spaces open to flow (which affect the value of hydraulic diameter D_h) were investigated. The pressure prevailing downstream of these barriers, over

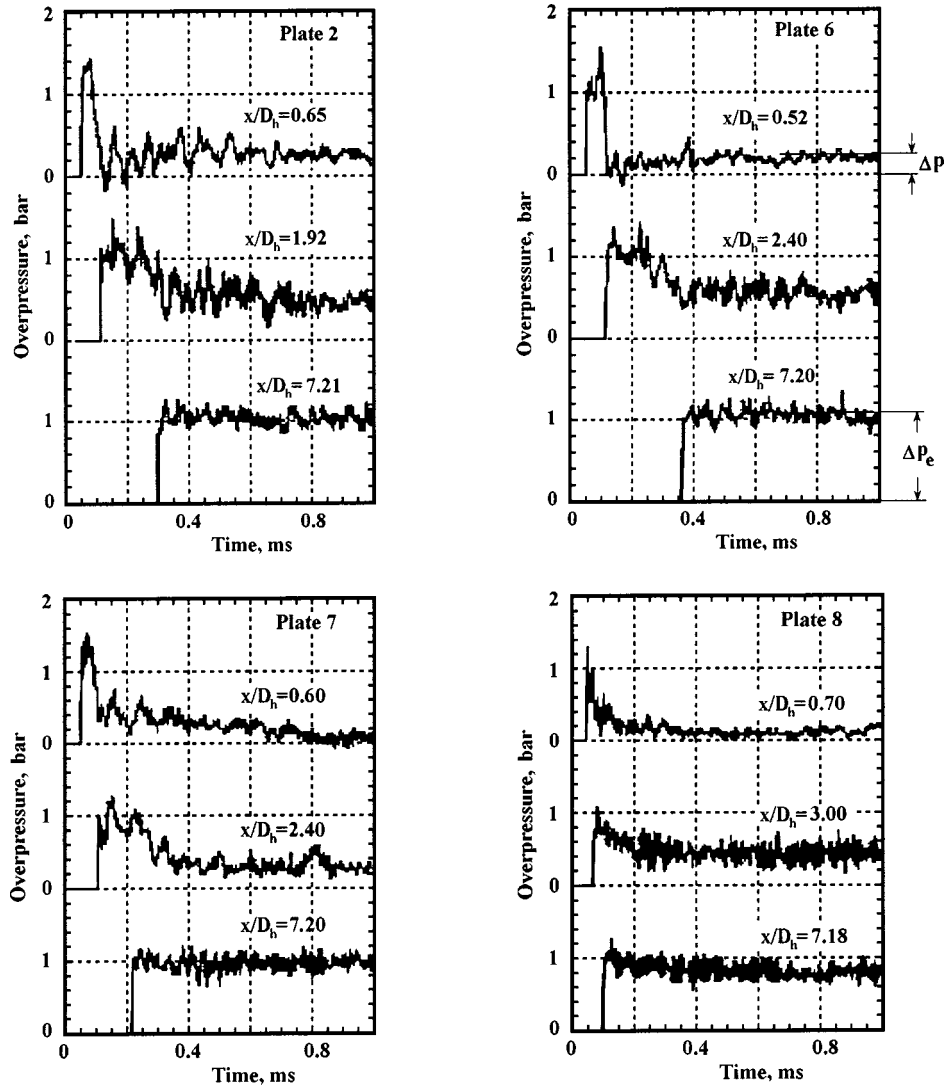

Fig. 12 Pressure signals recorded at different distances downstream of the barrier

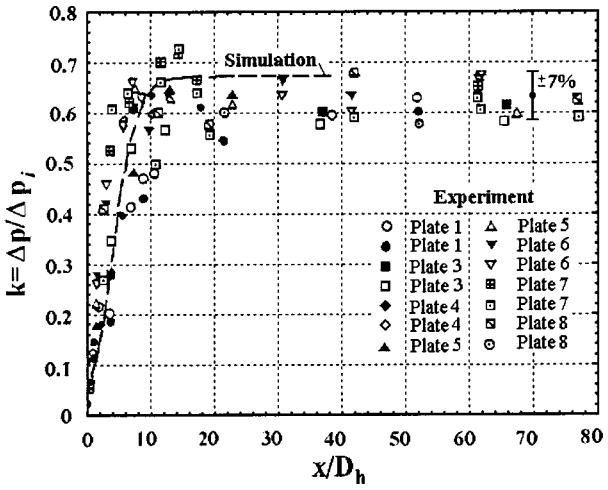

Fig. 13 Attenuation coefficient *k* vs the non-dimensional distance from the barrier x/D_h. Close points $M_s=1.46\pm0.01$, open points $M_s=1.58\pm0.01$. Error Bar shows the measured uncertainty at the 95% confidence level [12].

a wide range of hydraulic diameters, was recorded. It was found that most of the pressure recovery takes place close to the barrier, i.e., at $0<x/D_h<7$. In this zone the flow is highly non-steady and nonuniform. For longer distances downstream from the barrier ($x/D_h>7$) the flow approaches a steady one-dimensional state. For such large distances the specific shape of the barrier (perforated plate) has practically no influence on the pressure recovery (recorded pressures), as long as the porosity is kept at a constant value. The present numerical results and the recorded pressures indicate the importance of the viscous terms (appearing in the conservation equations) in generating the observed complex flowfield behind the porous barrier.

Acknowledgment

Appreciation is expressed to Mr. V. Shlimak for help in the experiments. The authors would like to acknowledge the Israel Science Foundation under grant no. 190/01-1 and United State-Israel Binational Science Foundation under grant no. 1999248 and the INTAS Foundation under grant no. 2000-0050 for support that made this research possible.

References

[1] Lind, C., Cybyk, B. Z., and Boris, J. P., 1999, ''Attenuation of shocks: High Reynolds number porous flows,'' In Proc. 22nd Int. Symp. On Shock Waves Eds. G. J. Ball, R. Hiller and G. T. Roberts, pp. 1138–1140. Imperial College, London UK.

[2] Franks, W. J., 1957, ''Interaction of a shock wave with a wire screen,'' UTIA Tech. Note No. **13**.

[3] Britan, A., Vasiliev, E. I., 1985, ''The peculiarity of the starting flow in the profiling nozzle of shock tube,'' Dokladi Akademii Nauk SSSR, **281**, No. 2 pp. 295–299 (in Russian).

[4] Igra, O., Falcovitz, J., Reichenbach, H., and Heilig, W., 1996, ''Experimental and numerical study of the interaction between a planar shock wave and square cavity,'' J. Fluid Mech., **313**, pp. 105–130.

[5] Igra, O., Wu, X., Falcovitz, J., Meguro, T., Takayama, K., and Heilig, W., 2001, ''Experimental and Numerical Study of Shock Wave Propagation Through Double-Bend Duct,'' J. Fluid Mech., **437**, pp. 255–282.

[6] Launder, B. E., and Spalding, B., 1972, ''Mathematical Models of Turbulence,'' New York: Academic Press.

[7] Baldwin, B. S., Lomax, H., 1978, ''Thin Layer Approximation and Algebraic Model for Separated Turbulent Flows,'' AIAA paper 78–257, Huntsville, Alabama, USA.

[8] Cebeci, T., Smith, A. M. O., 1974, ''Analysis of Turbulent Boundary Layers,'' New York: Academic Press.

[9] Vasiliev, E. I., 1996, ''A W-modification of Godunov's method and its application to two-dimensional non-stationary flows of a dusty gas,'' Comp. Math. Phys., **36**, pp. 101–112. Translation from Zh. Vychisl. Mat. Mat. Fiz., **36**, pp. 122–135.

[10] Britan, A., Ben-Dor, G., Igra, O., and Shapiro, H., 2001, ''Shock waves attenuation by granular filters,'' Int. J. Multiphase Flow, **27**, pp. 617–634.

[11] Honkan, A., and Andreopoulos, J., 1992, ''Rapid compression of grid-generated turbulence by a moving shock wave,'' Phys. Fluids A, **4**, pp. 2562–2572.

[12] Losev, S. A. 1976 ''On convolution of information obtained in the shock tube researches'' Scientific report of Institute of Mechanics MSU, No. 43, pp. 3–21.

Xinwei Song
Mechanical and Aerospace Engineering Department,
Virginia Artificial Heart Institute,
University of Virginia,
Charlottesville, VA USA

Amy L. Throckmorton
Biomedical Engineering Department,
Virginia Artificial Heart Institute,
University of Virginia,
Charlottesville, VA USA

Houston G. Wood*
Mechanical and Aerospace Engineering Department,
Virginia Artificial Heart Institute,
University of Virginia,
Charlottesville, VA USA

James F. Antaki
Associate Professor
Biomedical Engineering and Computer Science,
Carnegie Mellon University,
Pittsburgh, PA USA

Don B. Olsen
Utah Artificial Heart Institute,
Salt Lake City,
UT USA

Quantitative Evaluation of Blood Damage in a Centrifugal VAD by Computational Fluid Dynamics

This study explores a quantitative evaluation of blood damage that occurs in a continuous flow left ventricular assist device (LVAD) due to fluid stress. Computational fluid dynamics (CFD) analysis is used to track the shear stress history of 388 particle streaklines. The accumulation of shear and exposure time is integrated along the streaklines to evaluate the levels of blood trauma. This analysis, which includes viscous and turbulent stresses, provides a statistical estimate of possible damage to cells flowing through the pump. Since experimental data for hemolysis levels in our LVAD are not available, in vitro normalized index of hemolysis values for clinically available ventricular assist devices were compared to our damage indices. This approach allowed for an order of magnitude comparison between our estimations and experimentally measured hemolysis levels, which resulted in a reasonable correlation. This work ultimately demonstrates that CFD is a convenient and effective approach to analyze the Lagrangian behavior of blood in a heart assist device. [DOI: 10.1115/1.1758259]

Introduction

Left ventricular assist devices (LVADs) have been used as a possible bridge-to-transplant treatment for patients with heart disease and congestive heart failure. Several of these devices, such as the DeBakey axial VAD®, Jarvik 2000®, Medtronic Biomedicus® assist system, and the Berlin Incor I®, were designed and developed during the last few decades with successful animal and clinical trials [1–4]. Almost all of the LVADs currently being developed are continuous flow rotary blood pumps, and these devices provide supplemental mechanical circulatory support to the native left ventricle. The prospects of these devices for long-term support of patients, as an alternative means to transplantation, is dependent on excellent blood compatibility. Therefore, it is essential to quantify levels of blood trauma for successful design of rotary blood pumps.

Hemolysis, the breakdown or destruction of red blood cells, causes the contained protein hemoglobin (Hb) to be released into the surrounding medium [5–6]. Hemoglobin readily binds oxygen in the lungs and delivers it to the peripheral tissues to ensure cellular metabolic function. Continuous destruction of red cells reduces the blood's ability to transport oxygen, increasing risk of morbidity to the patient. In addition to preventing hemolysis, the design of the blood flow path must also minimize possibilities of flow stagnation.

Flow stagnation or conditions where blood pools in one location for a period of time while in contact with a foreign surface may activate the body's coagulation cascade and potentially result in an immunologic response [6]. This cascade activation may produce blood clots or thrombi. Release of a thromboemboli into the blood stream could lead to the obstruction of capillary beds, possible stroke conditions, and likely death of surrounding oxygen deprived tissue and muscle.

Prior experimental studies have revealed that both Reynolds turbulent and viscous shear stresses throughout the pump contribute to blood damage [7–13]. Reynolds stresses occur as a result of momentum transfer due to the turbulent flow conditions. Viscous shear stresses, however, arise because of the intermolecular frictional forces within the fluid itself. In this study, these stresses are considered to describe the level of trauma experienced by the blood as it travels through the LVAD.

Numerous studies have reported on fluid induced hemolysis [9–23]. According to these studies, techniques for predicting or measuring the levels of hemolysis fall into three categories: computational fluid dynamics (CFD) [19–21], flow visualization [15,17,18], and in vitro blood tests [5,9,16,18]. CFD analysis, a straightforward and cost-effective approach, enables the prediction of shear stresses through the fluid flow field and has been widely used as a design tool for artificial heart pumps [24–30]. Flow visualization using particle image velocimetry (PIV) provides measurements of the fluid velocity field that can validate CFD results; however, neither CFD nor flow visualization can intrinsically provide measures of blood damage. To directly measure red cell destruction requires in vitro experiments in which whole blood is circulated, sampled, and analyzed for released hemoglobin.

Earlier experimental investigations utilized rotating viscometers, cone-and-plate viscometers, flow jets, pulsating gas bubble tests, and oscillating wire experiments to analyze the effects of shear stresses on blood samples, including human and animal blood [5,9]. The plasma free hemoglobin level was measured using the cyanmetheglobin method, and the ratio of free hemoglobin content to total plasma hemoglobin was calculated, which corresponds to the extent of hemolysis. These experiments demon-

*Corresponding author

Contributed by the Fluids Engineering Division for publication in the JOURNAL OF FLUIDS ENGINEERING. Manuscript received by the Fluids Engineering Division April 1, 2003; revised manuscript received November 17, 2003 Associate Editor: Y. Tsujimoto.

strated damage threshold values ranging from 150 to 400 Pa and even larger magnitudes, depending on the exposure duration and the equipment used [5,22]. A maximum shear stress value of 250 Pa has been widely used as the design criterion in the development of LVADs [21,22]. Researchers in the field of artificial heart technology have only recently explored exposure time and its relation to shear stress.

An early attempt to mathematically describe hemolysis included the following relationship by Blackshear et al. [31]:

$$(\tau^2)(t) = C_1 \tag{1}$$

where τ is the shear stress, t denotes the exposure time, and C_1 signifies a constant of proportionality. This relationship was derived based on experimental evidence. These results indicated that hemolysis is proportional to the time of exposure and the square of the shear stress.

Giersiepen et al. [32] improved the previous model and developed a simple but effective correlation between shear stress, exposure time and the extent of damage to erythrocytes as given by the power law:

$$dHb/Hb = C \cdot \tau^{\alpha} \cdot T^{\beta} \tag{2}$$

Here, Hb is the hemoglobin content, dHb represents the damaged hemoglobin content, τ signifies the characteristic scalar stress, T is the stress exposure time, and C, α, β correspond to constants that can be obtained by regressing experimental data. Therefore, researchers obtain different values for the constants depending on experimental conditions. The values $C = 3.62 \times 10^{-5}$, $\alpha = 2.416$, and $\beta = 0.785$ have been used by Mitamura et al. [19] for their study of rotary blood pumps; but, in that study, τ only took into account the turbulent Reynolds stresses. They assumed that these stresses dominated the viscous stresses occurring in the pump. This group measured hemolysis levels in vitro and calculated dHb/Hb ratios, which demonstrated a reasonable correlation.

In another study [9], a different set of constants was found to be $C = 1.8 \times 10^{-6}$, $\alpha = 1.991$, and $\beta = 0.765$. These constants were obtained by regression of experimental data taken with an exposure time of 0.0034 to 0.6 s for shear stresses between 40 and 700 Pa in a Couette viscometer. This range of investigation is comparable to the flow conditions in blood pumps.

Apel et al. [23] applied a Lagrangian approach to assess the stress distribution and related exposure time in a microaxial blood pump. The viscous stresses were found to dominate the flow field compared to the Reynolds stresses. They determined the coordinates of each streakline using Euler forward integration of the particle velocity, as shown:

$$x_{i,t} = x_{i,t-1} + \frac{dx_{i,t-1}}{dt}\,\delta t \tag{3}$$

$$\text{with } \frac{dx_{i,t-1}}{dt} = v_{i,p}$$

where $x_{i,t-1}$ corresponds to the particle location at the preceding time step, δt is the time step, $v_{i,p}$ denotes the local velocity of the fluid element i, which starts from the pump's inlet and ends at the pump's outlet behind the trailing edge.

In this study, we focus on the effects of high stress because of rotation and high-speed jets, which could damage the membrane of the red blood cells (referred to as shear induced hemolysis). The power law model of blood damage and the Euler forward integration approach were implemented to assist in our estimation of hemolysis in an artificial heart pump.

Materials and Methodology

Blood Properties. Blood consists of a suspension of cells, primarily including erythrocytes or red blood cells, in a Newtonian medium, plasma. The volume percentage of erythrocytes to plasma is approximately 45% while platelets comprise 1% [33]. Red blood cells measure 6–8 μm in diameter by 2.2 μm in thickness with a distinctive biconcave shape cell. This biconcave cell can deform into a number of configurations without stretching the cell membrane beyond sustaining levels of damage. This inherent deformability allows red cells to maneuver through the smaller diameter vessels with ease. These red blood cells average a volume of 91.5 μm^3 and surface area of 141.6 μm^3 with an average lifespan of 120 days.

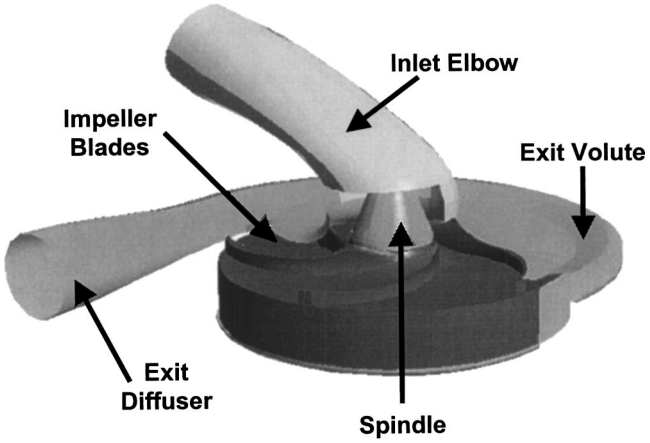

Fig. 1 Centrifugal Blood Pump Prototype-CF4b: This VAD includes an inlet elbow, spindle, impeller, clearance region between the rotor and housing, exit volute and diffuser.

For this study, blood is modeled as an incompressible continuous medium having Newtonian rheological properties, instead of a suspension of cells. Blood behaves as a Newtonian fluid for shear rates greater than 100 s^{-1} [34]. Preliminary studies and their comparison to experimental data have shown that the assumption of Newtonian behavior holds within the range of shear rates found in this study [35,36]. Therefore, a constant viscosity of 0.0035 Pa-s and density of 1050 Kg/m^3 were used for each CFD simulation [21,22,24].

Centrifugal Blood Pump. This article investigates blood trauma in a magnetically suspended centrifugal pump, $Cf4b$ (Medquest Products, Inc.), as shown in Fig. 1. The $Cf4b$ represents the fourth generation developmental prototype of a permanently implantable LVAD [35,36]. The flow path consists of an inlet elbow, impeller, clearance regions and an exit volute. The inlet elbow is a curved pipe specifically developed to link to the impeller eye and enhance vertical washing and spatially uniform flow. The impeller contains five rotating blades and ejects blood into the exit volute. It is fully suspended by magnetic bearings within the pump's housing. As a result, a blood-filled clearance exists between the impeller and housing due to the magnetically levitated design. The pressure gradient between the volute and inlet causes retrograde flow through this clearance. Therefore, a small proportion (approximately 10%) of blood recirculates through the pump. The thickness of the back clearance gap is designed to create a balance between minimizing exposure time, yet preventing excessive regurgitant flow. A wider gap would both reduce pump efficiency and expose a larger proportion of blood to the elevated shear stress within this region, while a thinner gap would increase the rate of blood damage within this region.

This VAD features an impeller with a diameter of 47 mm, rotating at a nominal speed of 2,500 RPM. This rotational speed generates a pressure rise of 100 mmHg at 6 LPM. We analyzed trauma levels for this design point during steady flow conditions.

Hemolysis. Distortion of erythrocytes occurs as they pass through peripheral blood vessels, many of which have a diameter less than that of a traveling cell. Red cells tolerate bending and

folding to maneuver in the peripheral vessels; but, if appreciable stretching of the membrane occurs, the cell could be irreversibly damaged or potentially destroyed. Though regulated, the cell membrane is fairly permeable to water, oxygen, carbon dioxide, glucose, urea, and certain other substances; it is impermeable to hemoglobin [6,33]. Therefore, an indicator of erythrocyte damage is the amount of hemoglobin released into the plasma. This trauma is directly related to the impinging shear stress and exposure time to such stress.

In this study, the numeric relation between hemolysis, shear stress and exposure time was implemented as given by regressed experimental data from Heuser et al. [9]:

$$dHb/Hb = 1.8\times 10^{-6}\cdot \tau^{1.991}\cdot T^{0.765} \tag{4}$$

This relationship includes turbulent and viscous stresses. As erythrocytes travel through the pump, they experience time-varying shear stresses. An integrative approach is used to cumulatively estimate the damage to red cells:

$$D = \int_{inlet}^{outlet} 1.8\times 10^{-6}\cdot \tau^{1.991}\cdot dT^{0.765} = \sum_{inlet}^{outlet} 1.8\times 10^{-6}\cdot \tau^{1.991}\cdot \Delta T^{0.765} \tag{5}$$

Where D symbolizes the blood damage index and is a measure of the possibility of erythrocytes being damaged. *Inlet* and *outlet* correspond to the entrance and exit faces of the blood pump in the computational model.

Computational Fluid Dynamics. The CFD analysis utilized four software programs: *BladeGen, TurboGrid, Build* and *TASCflow*. All of these programs are commercially available through Ansys Inc. (Canonsburg, PA, USA) *BladeGen*, a turbo-machinery design tool, allows easy generation of an impeller geometry and graphic manipulation of the impeller design parameters. *TurboGrid* and *Build* were used to generate the structured computational grids. The Reynolds averaged Navier-Stokes equations were solved using *TASCflow*, a finite-element-finite volume numerical solver, to characterize the flow field.

For each simulation, the incremental time step, or the relaxation factor in a steady-state study, was specified as 0.001-0.005 with a maximum normalized convergence residual of 1×10^{-4} [21,22,24]. Previous grid convergence studies provided insight into appropriate regional grid densities for the computational model [14,22,37,38]. The computational model consists of approximately 400,000 grid elements with 100,000 located in the impeller region, which is arguably the most important section of the VAD. The computational grid density is also comparable to the size employed for a number of other blood pump CFD models [39]. Furthermore, the grid had no twisted elements or negative volumes and acceptable aspect ratios. Discretization in *TASCflow* involved a modified linear profile selection coupled with a physical advection correction. In turbulent flow conditions, which are expected in the $Cf4b$ pump with Reynolds numbers on the order of 10^5, the value of scalar variables continuously fluctuates. The instantaneous value of any scalar quantity can be expressed as the sum of a mean and fluctuating component. *TASCflow* does not directly solve for the fluctuating component, but, rather, expresses this component in terms of its mean values. The expression of the instantaneous scalar quantities in terms of mean values is referred to as Reynolds-Averaging [40–41].

With conditions of constant density, the Reynolds-Averaging form of conservation of mass equation can be reduced to [41]:

$$\frac{\partial \overline{U_i}}{\partial x_i} = 0 \tag{6}$$

Applying the Reynolds-Averaging process for incompressible fluids, Eq. (12) shows the conservation equation describing the mean momentum:

$$\frac{\partial}{\partial t}(\rho \overline{U_i}) + \frac{\partial}{\partial x_j}(\rho \overline{U_i U_j}) = -\frac{\partial \overline{P}}{\partial x_i} - \frac{\partial}{\partial x_j}(\overline{\tau_{ij}} + \rho \overline{u_i' u_j'}) \tag{7}$$

The Reynolds stress tensor, $\rho \overline{u_i' u_j'}$, results from the averaging procedure using the nonlinear convection term on the left side of the equation. This tensor is considered one of the most difficult quantities to calculate or estimate in turbulence modeling [40–41]. *TASCflow* applies an eddy viscosity approximation to relate the Reynolds-averaged stresses and turbulent fluctuating terms to the mean flow variables. This approximation yields the following relationship:

$$\rho \overline{u_i' u_j'} = -\mu_t\left(\frac{\partial \overline{U_i}}{\partial x_j} + \frac{\partial \overline{U_j}}{\partial x_i}\right) + \frac{2}{3}\rho \delta_{ij} k \tag{8}$$

where μ_t is the turbulent viscosity and k is the turbulent kinetic energy term. For a Newtonian fluid, Reynolds-Averaging yields the averaged viscous stress tensor for an incompressible fluid:

$$\overline{\tau_{ij}} = -\mu_v\left(\frac{\partial \overline{U_i}}{\partial x_j} + \frac{\partial \overline{U_j}}{\partial x_i}\right) \tag{9}$$

The turbulent viscosity (μ_v) and turbulent kinetic energy term are estimated by selecting the appropriate turbulence model.

Turbulence Modeling. Turbulent flow conditions consist of many swirling eddies. The largest eddies are composed of much smaller eddies, which can also be broken down further into even smaller eddies. The kinetic energy generated by eddies at the smallest possible level is converted to heat through a process called viscous dissipation [40–41]. The time and length scales of the smallest eddies are orders of magnitude greater than the time and length scales of molecular motion. Therefore, viscous dissipation can be considered independent of molecular motion. Turbulence models in CFD codes solve the nonlinear Reynolds stress tensor in the Navier-Stokes equation by approximating turbulent flow conditions for this viscous dissipation and kinetic energy transfer [40–41]. The determination of the nonlinear terms in the momentum and mass equations requires statistical averaging of the unknown quantities. In general, one and two-equation based turbulence models are used throughout industry. *TASCflow* includes a number of different turbulence models, such as the k-ε model.

***k*-ε Turbulence Model.** The k-ε turbulence model solves the equations for k, the turbulent kinetic energy, and ε, the dissipation rate of k [40]. The dissipation rate of k or ε is also defined as the amount of k per mass and time converted to internal fluid energy by viscous motion. Several research groups have used the k-ε turbulence model for CFD simulations to design their artificial heart pumps [12,13,21,22,26,29,30]. Once the values of k and ε are known, the turbulent viscosity can be calculated as follows:

$$\mu_t = \rho c_\mu \frac{k^2}{\varepsilon} \tag{10}$$

where c_μ is a model constant. Along with the k-ε model, we selected a logarithmic wall function to characterize and reasonably resolve near-wall flow conditions.

Over the past several years, we have employed the k-ε turbulence model for the design of our centrifugal LVAD prototypes. A third generation design prototype (Cf3 pump) was built and experimentally tested prior to optimization and production of the Cf4b prototype [21,22,34,35]. Laser flow measurements by particle image velocimetry (PIV) in the back clearance regions of the

CF3 pump resulted in the acquisition of fluid velocity components, which correlated within 10–15% of CFD results using the k-ε model turbulence model [34,35]. PIV measurements for the impeller and clearance regions of the Cf4b prototype are currently underway, but are not available for direct comparison to CFD results at this time. Once the flow measurement results are available, this choice of turbulence model will be rigorously evaluated.

In addition to calculating averaged velocity flow fields and pressure gradients, *TASCflow* includes the ability to determine the shear stress at any nodal location in the flow field. Qualifying and quantifying the shear stress within the pump allows designers to estimate whether hemolysis or thrombosis may occur and adjust design parameters accordingly to reduce the likelihood of occurrence.

To account for the 3-D nature of the shear field, we adopted scalar stresses as originally introduced by Bludszuweit [12,13]:

$$\tau=\left(\frac{1}{6}\sum\ (\tau_{ii}-\tau_{jj})^2+\sum\ \tau_{ij}^2\right)^{1/2} \tag{11}$$

Lagrangian tracking was employed to consider the shear history of particles (cells). The particle displacement is calculated using forward Euler integration of the particle velocity over time step (δt) similar to the approach adopted by Apel et al. [23] and discussed earlier.

Boundary Conditions. For each simulation, steady-state flow conditions were assumed to ensure constant boundary conditions and velocities in time. A uniformly distributed mass flow rate was specified along the inflow boundary face. The no-slip boundary condition was applied to the stationary walls so that the fluid velocity values along the boundary would equal zero. Similarly, the outflow pressure was specified to be constant at 20,000 Pascals to establish the outlet boundary condition. A stationary wall boundary was applied to the internal housing regions of the pump; the rotor (impeller blades, hub, region for the magnetic bearings) was specified as rotating walls in the counterclockwise direction to correspond with the blade orientation. The frozen rotor interface was applied to link regions of differing reference frames and allows flow to cross the interface without executing circumferential averaging. Therefore, the frozen rotor characterization preserves the profile of wake and core flow field from the impeller region into the exit volute.

Each simulation particle was released at the inlet port of the computational model. A total of 388 particle streaklines were tracked and recorded, which was the maximum number of particles that the server (Sun Dual 450 MHz with 1G Byte RAM) could accommodate for this calculation. The 388 particles were uniformly distributed and released over the surface area of the inlet face such that they filled the entire grid region.

Results

Based on convergence of each simulation, the blood damage index (D) was computed according to Eq. (5). Figure 2 shows the isotimic plot of the scalar shear stress along the blade-tip surface. This surface has historically demonstrated the highest level of shear in the heart pump (maximum value of 250 Pa). Figures 3 and 4 illustrate several representative streaklines, colored according to exposure time and shear stress, respectively.

Most, 322 of 388, blood particles took less than 0.19 seconds to travel completely through the pump. The mean residence time was 0.34 s with a maximum residence time of 5.3 s due to a possible vortex region. Figures 5 and 6 demonstrate the particle distributions of exposure time and blood damage index, respectively. The mean value of the blood damage index was found to be 0.21% with a maximum value of approximately 2.04%. For 313 of 388 particles, the blood damage index remained less than 0.16%. This

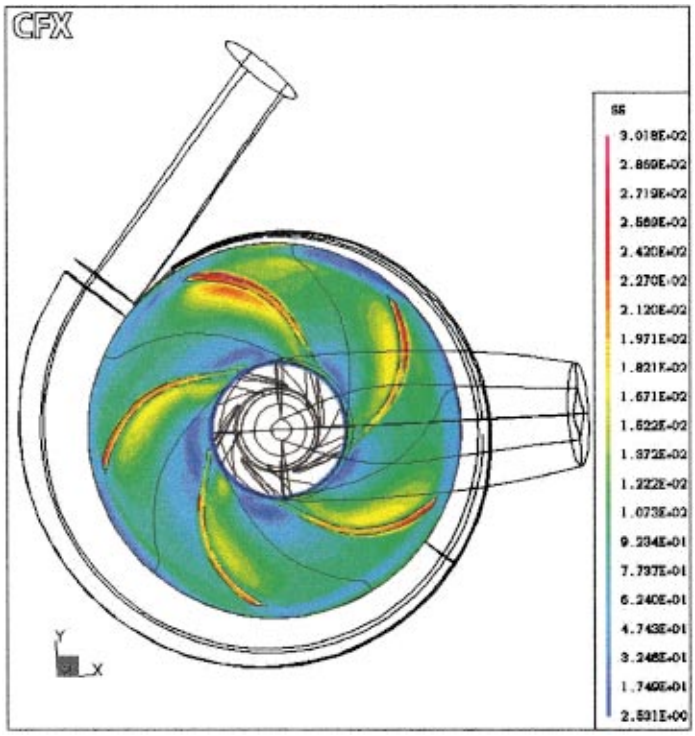

Fig. 2 Isotimic Plot of Shear Stress along Blade-tip Surface: This surface along the tip of the blade shows the highest levels of shear stresses in the pump. Higher shear stresses exist along the trailing edge of the impeller region prior to the entering the exit volute and directly along the blades, particularly at the trailing edge. Maximum shear stress values of 250 Pa are found in this plane.

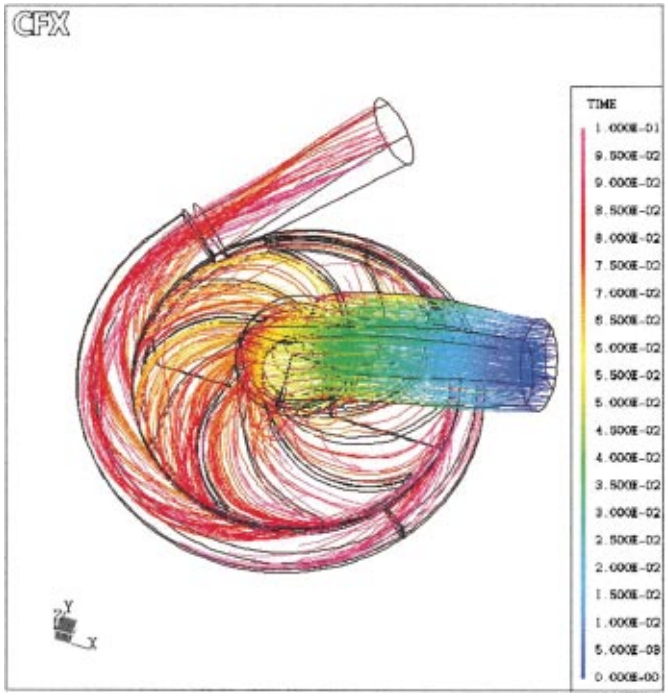

Fig. 3 Streaklines Colored by Exposure Time: Particles released at the inlet port of the computational model and travel through the pump for a given residence time.

low blood damage index indicates that cells traveling along these streaklines are not likely to be ruptured. For the remaining 75 particles with damage index values ranging from 0.21% to 2.04%, there is a greater possibility of damage to the particles, especially at the higher end.

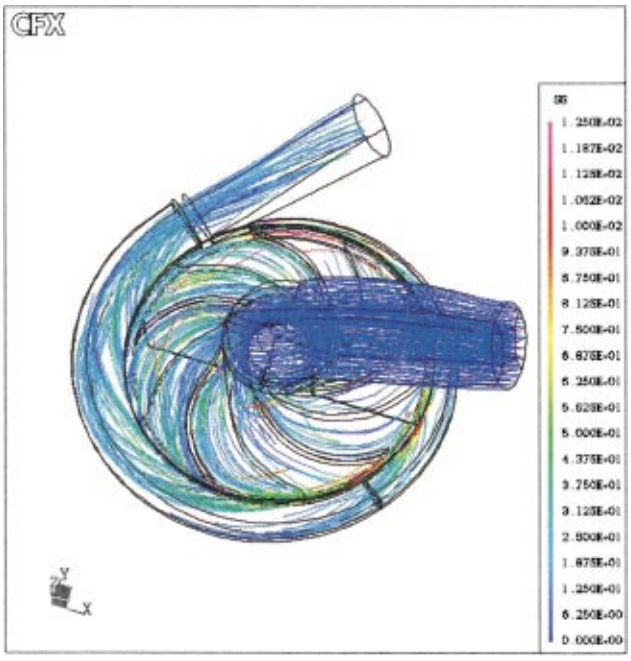

Fig. 4 Streaklines for 388 Particles, Colored by Shear Stress: Particles released at inlet port and travel along streaklines or pathlines during steady state flow conditions. Shear stress values are plotted for each nodal location along the streakline for each particle.

Figures 7–11 depict the shear information of one particle along their streaklines. Each figure includes the shear stress ($\tau^{1.991}$) on the ordinate plotted with the exposure time ($T^{0.765}$) on the abscissa, according to Eq. (4). The area under the curve represents the blood damage index for that particular particle. This analysis was executed for each particle. These figures illustrate a few selected particles and results from the streakline analysis over a wide range of damage indices. Table 1 specifically delineates each particle and corresponding damage index. These particles were randomly selected to illustrate a range of damage indices. As would be expected, particle #2 with a damage index of 1.22% has

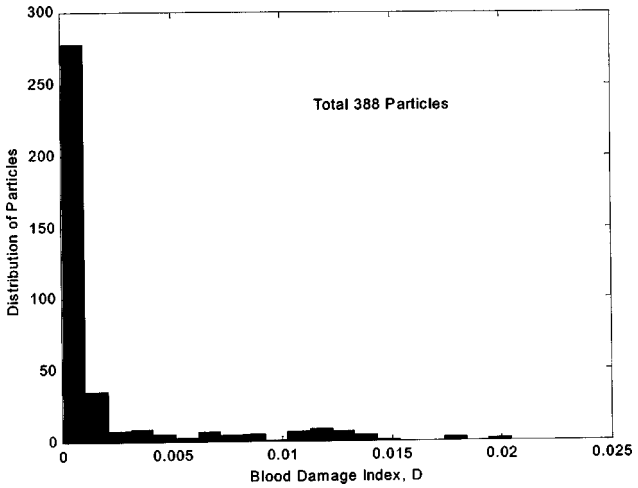

Fig. 5 Distribution of Blood Damage Index for Population of 388 Pathlines Studied: Maximum blood damage indices averaged 2% for only a few particles. Most particles experienced a damage index less than 0.5%.

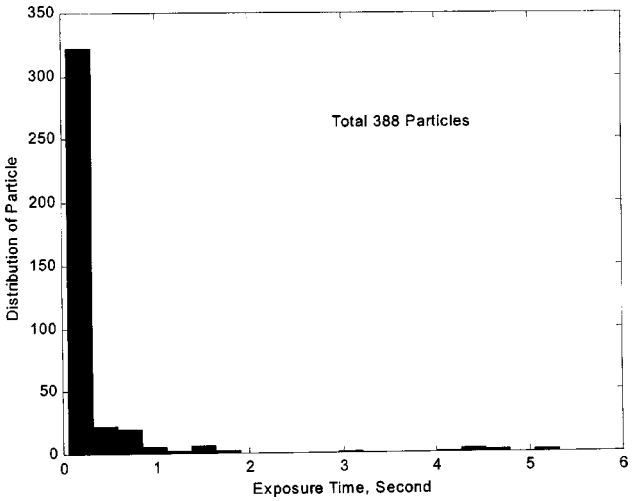

Fig. 6 Distribution of Exposure Time for Population of Particles Studied: Approximately 322 of the 388 particles in this study took less than 0.19 s to travel through the computational flow model. Average residence times are 0.34 second with a maximum exposure time of 5.3 s due to a possible vortex region.

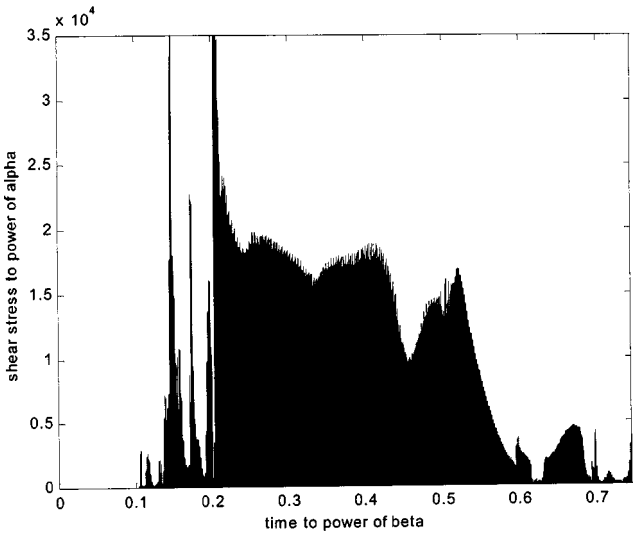

Fig. 8 Shear stress power versus time for particle #2

far more area under the curve (ie. higher shear stress, longer exposure time) on Fig. 8 than particles #1, #3, and #10 as seen in Figs. 7, 9, and 11.

Additionally, this blood damage analysis allows designers to easily calculate the rate of change in the shear stress over time. Due to the discrete nature of the data points, the slope can be readily determined and plotted as shown in Figs. 12 and 13 for particles #2 and #3, respectively. The rate of change in the shear level over time can also have a large impact on hemolysis [5,9,11]. Dramatic increases and abrupt decreases in the shear rate may lead to red cell rupture or significant damage. Figures 12 and 13 display the exposure of these particles to abrupt changes in the shear rate ($d\tau/dt$), which contribute to their overall damage indices and increase the likelihood of particle damage or trauma.

Normalized Index of Hemolysis. The equation developed by Koller and Hawrylenko [42] is often used to express blood damage as a normalized index of hemolysis (NIH) as shown here:

$$NIH(g/100L) = \frac{\Delta fHb \times V \times (1-(Ht/100)) \times 100}{\Delta t \times Q} \quad (12)$$

where ΔfHb is the increase in plasma free Hb concentration (g/L) during the test period, Δt represents the duration of the test period (min), Ht denotes the hematocrit (%), V corresponds to the blood volume in the test circuit (L), and Q symbolizes the flow rate (LPM). This equation is employed in designing heart pumps as well as other medical devices, such as oxygenators [43–44].

Since the purpose of this paper is primarily to illustrate a technique and experimental data is not readily available regarding the Cf4b LVAD, we derived an order of magnitude estimate of the damage indices for clinically available blood pumps to compare with our Cf4b computational model by using results from Mitamura et al. [19]. This research group showed a correlation between the Hb and damaged Hb content to experimentally measured NIH in vitro values according to:

$$NIH = (0.00015)\frac{dHb}{Hb} \quad (13)$$

Their regression analysis included an r-squared value of 0.87, which indicates a reasonable correlation, for five samples from a

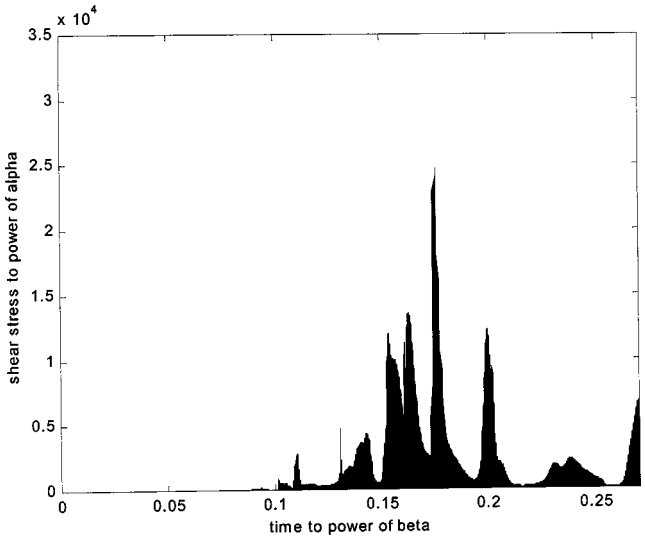

Fig. 7 Shear Stress Power Versus Time for Particle #1

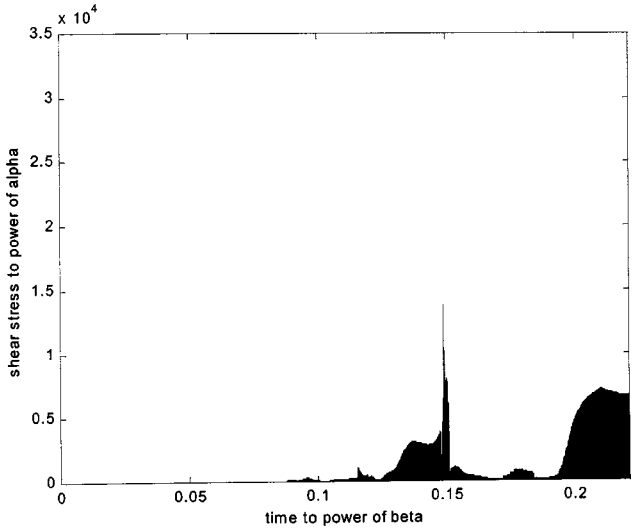

Fig. 9 Shear stress power versus time for particle #3

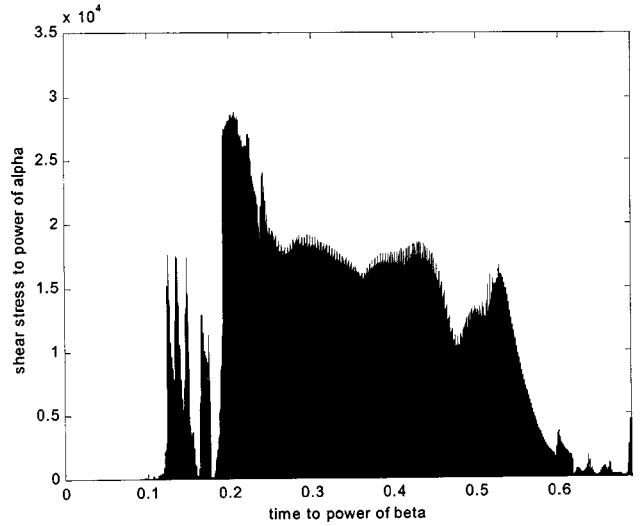

Fig. 10 Shear stress power versus time for particle #9

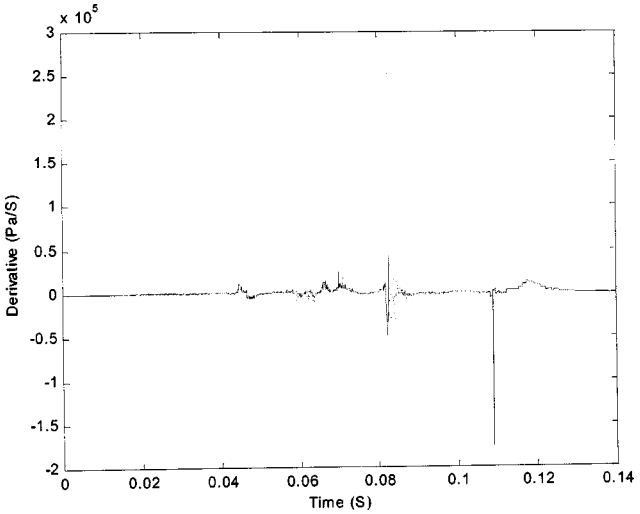

Fig. 12 Shear rate ($d\pi/dt$) over time for particle #2

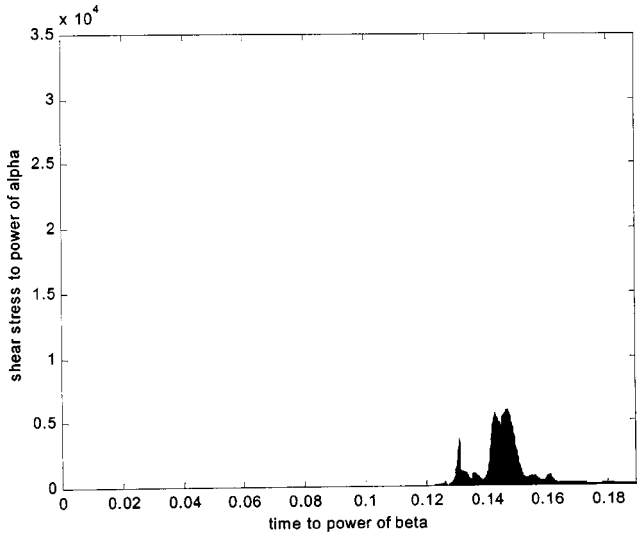

Fig. 11 Shear stress power versus time for particle #10

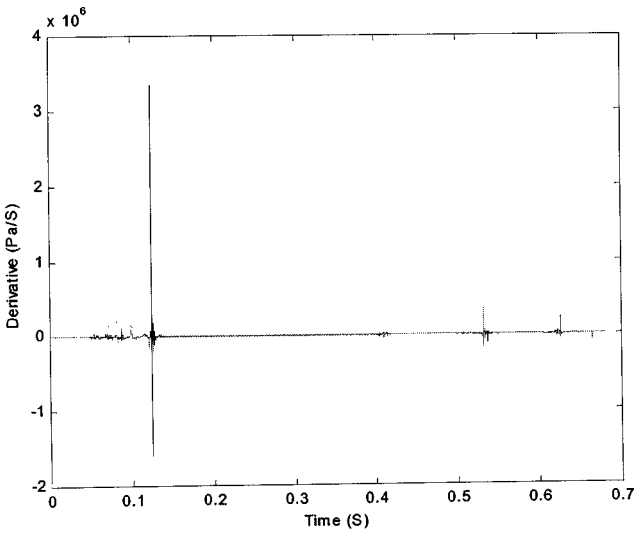

Fig. 13 Shear rate ($d\pi/dt$) over time for particle #3

mock loop circuit. They tested fresh bovine blood flow of 5 LPM while maintaining a pressure of 100 mmHg at a physiologic temperature for three hours. Equation (13) was applied to our results in order to estimate dHb/Hb values for five clinically available blood pumps.

Numerous in vitro hemolysis studies have been conducted on existing VADs. Table 2 displays a list of clinically available centrifugal pumps with their corresponding NIH values and estimated dHb/Hb or damage indices according to Eq. (19). These NIH values were obtained in vitro using fresh bovine blood in a test loop under conditions of 6 LPM at 120 mmHg for six hours at room temperature (21°C) [45].

The maximum value of our damage index was estimated to be approximately 2%. This value is of the same order of magnitude as the indices approximated for the clinically available VADs, which lends credence to the approach introduced in this paper for estimating blood damage. Several improvements, however, should be made to enhance this blood damage model: (1) experimental NIH values from mock loop testing (2) more realistic constant

Table 1 Selected Particles and Corresponding Damage Indices

Particle	Damage Index	Figure
#1	0.087%	7
#2	1.22%	8
#3	0.045%	9
#9	1.26%	10
#10	0.013%	11

Table 2 *In Vitro* NIH Values of Clinically Available Centrifugal Blood Pumps and Estimations of dHb/Hb

Centrifugal Pump	NIH value (g/100L)	dHb/Hb
Biomedicus BP-80 (Medtronic)	0.00070	5%
Isoflow (St. Jude Medical)	0.00096	6%
HPM-15 (Nikkiso)	0.00066	4%
Capiox CX-SP45 (Terumo)	0.00090	6%

values for dHb/Hb expression based on experimental evidence for the Cf4b (3) flow measurements and oil streaking to determine local shear stresses in the Cf4b prototypes (4) in vivo blood damage results from animal testing.

Conclusions

Quantifying levels of blood damage within LVADs is essential to ensuring a reliable and effective VAD reaches market. This study describes a cumulative approach to evaluate the stress-induced hemolysis occurring in a miniature centrifugal blood pump using CFD technology. We analyzed scalar shear stresses and the exposure time of these particles to such stress levels in the pump. A Lagrangian particle tracking technique was used to obtain the stress history of 388 representative particles along their streaklines. An integrative computation makes it possible to consider the damage history of each particle.

The results suggest this blood pump prototype has an acceptable level of hemolysis for steady-state flow simulations. The maximum damage index found in this study is the same order of magnitude as those estimated in clinically available VADs. Future experiments that measure the flow conditions through the pump and estimate levels of shear stress may enable the validation of these damage index estimations. Benchtop blood bag testing will also provide insight into hemolysis levels in the VAD. Additionally, exploring the results for a transient translational sliding interface computational case, which allows the impeller real-time rotation, would also enable more sophisticated computational analyses of potential damage index values. Transient CFD simulations would reflect a more realistic implant scenario because they account for variation in the relative position between the blades and housing.

In general, CFD was shown to be an effective and useful tool for the general assessment of stress induced hemolysis in a LVAD based on the results of this study.

Acknowledgments

The authors wish to acknowledge the financial support for this work provided by the Utah Artificial Heart Institute, Department of Health and Human Services, National Institutes of Health, the National Heart, Lung, and Blood Institute: Grant number: R01 HL64378-01, and the National Science Foundation ITR/ACS (ACI-0086093).

References

[1] Noon, G. P., Morley, D. L., Irwin, S., Abdelsayed, S. V., Benkowski, R. J., and Lynch, B. E., 2001, ''Clinical experience with the MicroMed DeBakey ventricular assist device.'' Ann. Thorac. Surg., **71**(3 Suppl), S133–8.

[2] Tamez, D., Conger, J. L., Jacobs, G., Gregoric, I., Inman, R. W., Radovancevic, B. R., Moore, S. M., Eya, K., Eichstaedt, H., Jarvik, R., and Frazier, O. H., 2000, ''In vivo testing of the totally implantable Jarvik 2000 heart system.'' ASAIO J., **46**(2), 168.

[3] Throckmorton, A. L., Allaire, P. E., Gutgesell, H. G., Matherne, G. P., Olsen, D. B., Wood, H. G., Allaire, J. H., and Patel, S. M., 2002, ''Pediatric Circulatory Support Systems.'' ASAIO J., **48**, 216–221.

[4] Muller, J., Weng, Y., Goettel, P., Nuesser, P., Kilic, A., Arndt, A., Merkel, J., and Hetzer, R., ''The First Implantations in Patients of the InCor I Axial Flow Pump with Magnetic Bearings.'' 10th Congress of the International Society for Rotary Blood Pumps. Osaka, Japan. 13 September 2002.

[5] Leverett, L. B., Hellums, J. D., Alfrey, C. P., et al. 1972, ''Red blood cell damage by shear stress.'' Biophys. J., **12**, 257–73.

[6] Blackshear, P. L., and Blackshear, G. L., Mechanical Hemolysis. In: Skalak, R., Chien, S., eds. Handbook of Bioengineering. New York: McGraw-Hill, 1987, 15.1–9.

[7] Toshitaka, Y., Akio, F., Fujio, M., et al. 2001, ''Influence of static pressure and shear rate on hemolysis of red blood cells.'' ASAIO J., **47**(4), 351–3.

[8] Richardson, E., 1975, ''Application of a theoretical model for hemolysis in shear flow.'' Biorheology, **12**, 12–37.

[9] Heuser, G., and Opitz, R., 1980, ''A couette viscometer for short time shearing in blood.'' Biorheology, **17**, 17–24.

[10] Schima, H., Muller, M. R., Papantonis, D., et al. 1992, ''Minimization of hemolysis in centrifugal blood pump: Influence of different geometries.'' Int. J. Artif. Organs, **16**(7), 521–9.

[11] Yeleswarapu, K. K., Antaki, J. F., Kameneva, M. V., et al. 1995, ''A mathematical model for shear-induced hemolysis.'' Artif. Organs, **19**(7), 576–582.

[12] Bludszuweit, C., 1995, ''Model for a general mechanical blood damage prediction.'' Artif. Organs, **19**, 583–589.

[13] Bludszuweit, C., 1995, ''Three-dimensional numerical prediction of stress loading of a blood particles in a centrifugal pump.'' Artif. Organs, **19**, 590–596.

[14] Song, X., Wood, H. G., and Olsen, D. B., ''CFD Study of the 4th Generation Prototype of a Continuous Flow Ventricular Assist Device,'' ASME J. Biomech. Eng., **126**(2), 180-7.

[15] Weinicke, J. T., Meier, D., Mizuguchi, K., et al. 1995, ''A fluid dynamic analysis using flow visualization of the Baylor/NASA implantable axial flow blood pump for design improvement.'' Artif. Organs, **19**(2), 161–77.

[16] Pohl, M., Samba, O., Wendt, M. O., et al. 1998, ''Shear stress related hemolysis and its modeling by mechanical degradation of polymer solutions.'' Int. J. Artif. Organs, **21**(2), 107–13.

[17] Yamane, T., Asztolos, B., Nishida, M., et al. 1998, ''Flow visualization as a complementary tool to hemolysis testing in the development of centrifugal blood pump.'' Artif. Organs, **22**(5), 375–80.

[18] Masuzawa, T., Tsukiya, T., Endo, S., et al. 1999, ''Development of design methods for a centrifugal blood pump with a fluid dynamics approach: results in hemolysis tests.'' Artif. Organs, **23**(8), 757–61.

[19] Mitamura, Y., Nakamura, H., and Sekine, K., 2000, ''Prediction of hemolysis in rotary blood pumps with computational fluid dynamics analysis.'' J. Congestive Heart Failure Circulatory Support **1**(4), 331–336.

[20] Toshitaka, Y., Kenji, S., Akio, F., et al. 2000, ''An investigation of blood flow behavior and hemolysis in artificial organs.'' ASAIO J., **46**(5), 527–31.

[21] Anderson, J. B., Wood, H. G., Allaire, P. E., et al. 2000, ''Numerical Studies of Blood Shear and Washing in a Continuous Flow Ventricular Assist Device.'' ASAIO J., **46**(4), 486–94.

[22] Anderson, J. B., ''Computational Flow Analysis of a Ventricular Assist Device.'' Master Thesis, School of Engineering and Applied Science, University of Virginia, Charlottesville, Virginia, 1999.

[23] Apel, J., Paul, R., Klaus, S., et al. 2001, ''Assessment of hemolysis related quantities in a microaxial blood pump by computational fluid dynamics.'' Artif. Organs, **25**(5), 341–47.

[24] Wood, H. G., Anderson, J., Allaire, P. E., McDaniel, J. C., and Bearnson, G., 1999, ''Numerical solution for blood flow in a centrifugal ventricular assist device.'' Int. J. Artif. Organs, **22**, 827–836.

[25] Pinotti, M., and Rosa, E. S., 1995, ''Computational prediction of hemolysis in a centrifugal ventricular assist device.'' Artif. Organs, **19**, 267–273.

[26] Takiura, K., Masuzawa, T., Endo, S., et al. 1998, ''Development of design methods of a centrifugal blood pump with in vitro tests, flow visualization, and computational fluid dynamics: results in hemolysis tests.'' Artif. Organs, **22**, 393–398.

[27] Thomas, D. C., Butler, K. C., Taylor, L. P., et al. 1997, ''Continued development of the Nimbus/University of Pittsburgh axial flow left ventricular assist system.'' ASAIO J., **43**, M564–M566.

[28] Antaki, J. F., Ghattas, O., Burgeen, G. W., and He, B., 1995, ''Computational flow optimization of rotary blood pump components.'' Artif. Organs, **19**, 608–615.

[29] Allaire, P. E., Wood, H. G., Awad, R. S., and Olsen, D. B., 1999, ''Blood flow in a continuous flow ventricular assist device.'' Artif. Organs, **23**, 769–773.

[30] Miyazoe, Y., Sawairi, T., Ito, K., et al. 1998, ''Computational fluid dynamic analyses to establish design process of centrifugal blood pumps.'' Artif. Organs, **23**, 381–385.

[31] Blackshear, P. L., Dormen, F. D., and Steinbach, J. H., 1965, ''Some mechanical effects that influence hemolysis.'' ASAIO Trans., **XI**, 112–117.

[32] Giersiepen, M., Wurzinger, L. J., Opitz, R., and Reul, H., 1990, ''Estimation of shear stress-related blood damage in heart valve prostheses-in vitro comparison of 25 aortic valves.'' Int. J. Artif. Organs, **13**(5), 300–306.

[33] Thomas, H. D. Engineering Design of the Cardiovascular System Mammals. Prentice Hall Inc. 1991.

[34] Day, S. W., McDaniel, J. C., Wood, H. G., Allaire, P. E., Landrot, N., and Curtas, A., 2001, ''Particle image velocimetry measurements of blood velocity in a continuous flow ventricular assist device.'' ASAIO J., **47**(4), 406–411.

[35] Day, S. W., McDaniel, J. C., Wood, H. G., Allaire, P. E., Song, X., Lemire, P. P., and Miles, S. D., 2002, ''A prototype HeartQuest ventricular assist device for particle image velocimetry measurements.'' Artif. Organs **26**(11), 1002–1005.

[36] Lemire, P. P., McDaniel, J. C., Wood, H. G., Allaire, P. E., Landrot, N., Song, X., Day, S. W., and Olsen, D. B., 2002, ''The Application of Quantitative Oil Streaking to the HeartQuest Left Ventricular Assist Device.'' Artif. Organs, **26**(11), 971–973.

[37] Curtas, A. R. ''Computational Fluid Testing for the Design and Development of a Heart Assist Pump.'' Masters Thesis, University of Virginia, May 2000.

[38] Curtas, A. R., Wood, H. G., Allaire, P. E., McDaniel, J. C., et al. 2002, ''CFD Modeling of Impeller Designs for the HeartQuestTM LVAD.'' ASAIO J., **48**, 552–561.

[39] Apel, J., Neudel, F., and Reul, H., 2001, ''Computational Fluid Dynamics and Experimental Validation of a Microaxial Blood Pump.'' ASAIO J., **47**, 552–558.

[40] Kundu, P. K., and Cohen, I. M., *Fluid Mechanics*, 2nd Edition. New York: Academic Press, 2002.

[41] Warsi, Z. U. *Fluid Dynamics: Theoretical and Computational Approaches*, 2nd Edition. Boca Raton: CRC Press, 1999.

[42] Koller, T., and Hawrylenko, A., 1967, ''Contribution to the in vitro testing of

pumps for extracorporeal circulation.'' J. Thorac. Cardiovasc. Surg., **54**, 22–29.
[43] Naito, K., Mizuguchi, K., and Nose, Y., 1994, ''The need for standardizing the index of hemolysis.'' Artif. Organs, **18**(1), 7–10.
[44] Kawahito, S., Maeda, T., Yoshikawa, M., Takano, T., Nonaka, K., et al. 2001, ''Blood trauma induced by clinically accepted oxygenators.'' ASAIO J., **47**, 492–495.
[45] Naito, K., Suenaga, E., Cao, Z. L., Suda, H., Ueno, T., Natsuaki, M., and Itoh, T., 1996, ''Comparative hemolysis study of clinically available centrifugal pumps.'' Artif. Organs, **20**(6), 560–563.

Yuka Iga
Research Associate
Institute of Fluid Science, Tohoku University,
2-1-1, Katahira, Aoba-ku, Sendai, Miyagi,
980-8577, Japan
Phone: +81-22-217-5229
Fax: +81-22-217-5229
e-mail: iga@ifs.tohoku.ac.jp

Motohiko Nohmi
Senior Researcher
Ebara Research Co., Ltd,
11-1, Haneda Asahi-cho, Ohta-ku, Tokyo,
144-8510, Japan
Phone: +81-3-3743-6314
Fax: +81-3-3743-6578
e-mail: nohmi@ebara.co.jp

Akira Goto
Director
Ebara Research Co., Ltd,
4-2-1, Honfujisawa, Fujisawa, 251-8502, Japan
Phone: +81-466-83-7608
Fax: +81-466-82-9371
e-mail: goto05296@erc.ebara.co.jp

Toshiaki Ikohagi
Professor
Institute of Fluid Science, Tohoku University,
2-1-1, Katahira, Aoba-ku, Sendai, Miyagi,
980-8577, Japan
Phone: +81-22-217-5228
Fax: +81-22-217-5229
e-mail: ikohagi@ifs.tohoku.ac.jp

Numerical Analysis of Cavitation Instabilities Arising in the Three-Blade Cascade

Three types of cavitation instabilities through flat plate cascades, which are similar to "forward rotating cavitation," "rotating-stall cavitation" and "cavitation surge" occurring in high-speed rotating fluid machinery, are represented numerically under the three-blade cyclic condition. A numerical method employing a locally homogeneous model of compressible gas-liquid two-phase medium is applied to solve the above flow fields, because this permits the entire flow field inside and outside the cavity to be treated through only one system of governing equations. In addition, the numerical method suites to analyze unsteady cavitating flow with a long time evolution. From the calculated results of the present numerical simulation with wide range of cavitation number and flow rate, we obtain a cavitation performance curve of the present three-blade cyclic cascade, analyze the aspects of unsteady cavitation, and discuss the characteristics and mechanisms of cavitation. [DOI: 10.1115/1.1760539]

Introduction

Cavitation is a phenomenon in which liquid evaporates and vapor bubble occurs in the region where the pressure of the liquid falls off under vapor pressure. Cavitation is usually observed in areas of the high-speed fluid machinery such as propellers and pumps, where the flow accelerates and the pressure decreases. Sheet cavitation, which includes strong unsteady phenomena such as cyclic cloud cavity shedding under a certain cavitation condition, causes a large-scale oscillation in fluid machinery, reduces the performance, and becomes a cause of damage. Furthermore, phenomena called cavitation instabilities are caused by mutual interference between the cavitation and the fluid machine systems, where the original unsteadiness of cavitation increases. Actually, these become a cause of serious accidents involving fluid machinery.

An analysis of cavitation instabilities that occur around the impeller of fluid machine systems is an important subject in the field of design and development of high-speed fluid machinery. Cavitation instabilities are roughly classified into two categories. One is generally called ''local instability,'' which is caused by mutual interference between cavitation and impeller, and the other is generally called ''system instability'' which is caused by mutual interference between cavitation and the entire turbopump system. The former includes rotating cavitation, alternate blade cavitation, asymmetric cavitation, and rotating-stall cavitation. These cavitations are two-dimensional instabilities. The latter includes cavitation surge, which is a one-dimensional instability. The alternate blade cavitation is a peculiar phenomenon of the impeller having even number of blades. Rotating cavitation and rotating-stall cavitation are an unstable phenomena with nonuniform cavity area in each blade, which propagates toward the circumferential direction of the impeller. This becomes a cause of the asynchronous axial vibration, resulting in a decrease in performance and damage to the turbopump.

A lot of experimental and theoretical analyses of such cavitation instabilities in the turbopump have been performed. Bhattacharyya, et al. [1] investigated the rotor-dynamic force of the three-blade cavitating inducer. Tsujimoto, et al. [2] experimentally observed various types of cavitation instabilities in the inducer, such as cavitation in back flow vortices, attached nonuniform cavitation, rotating cavitation and cavitation surge, and mapped their occurrences. Hashimoto, et al. [3] showed maps of occurrence, spectrum analysis of inlet pressure and time evolution of cavity area for each blade in the turbopump inducer of the LE-7 engine of the Japanese H-II rocket, in which various cavitation instabilities exist, including backward rotating cavitation. Friendrichs, et al., [4] considered a mechanism of rotating cavitation occurring in the centrifugal pump. Shimura, et al. [5] investigated the relationship between rotating-stall cavitation and the slope of the performance curve in the LE-7 inducer. Yoshida et al. [6] performed an experimental investigation on the four-blade inducer having an alternate cutback impeller in order to suppress rotating cavitation. In addition, in the field of theoretical analysis, Stripling [7] and Jakobsen [8] indicated head break-downs of the cavitating turbopump by analysis of the flat plate cascade, and Acosta [9]

Contributed by the Fluids Engineering Division for publication in the JOURNAL OF FLUIDS ENGINEERING. Manuscript received by the Fluids Engineering Division May 2, 2003; revised manuscript received February 9, 2004. Associate Editor: Y. Tsujimoto.

determined the mass flow gain factor and cavity compliance that are transfer functions for the analysis of instability in the cavitating inducer. Later, Tsujimoto [10] indicated a relationship between rotating cavitation and mass flow gain factor, and reported the existence of two modes in rotating cavitation: forward-rotating cavitation and backward-rotating cavitation, which was later confirmed experimentally. Watanabe, et al. [11] performed three-dimensional analysis of rotating cavitation in the inducer. Horiguchi, et al. [12] reported the occurrence condition of alternate cavitation. Fujii, et al. [13] predicted the cavitation instability having the propagation velocity ratio of 0.5, which occurs in the range where the performance curve becomes to have positive slope. Same phenomenon was previously found by Shimura et al. experimentally [5]. Furthermore, Tsujimoto, et al. [14] indicated unified theoretical treatment of various instabilities in turbomachinery.

As mentioned above, researchers regarding cavitation instabilities in the turbopump have been advanced actively. However, particularly in experimental investigations of rocket engines, economic and time considerations remain problematic. In addition, in theoretical analysis at the present stage, because no existing cavitation model can describe the cloud cavity shedding caused by the break-off phenomenon of sheet cavitation, the unsteady cavitating flow is difficult to analyze strictly. On the other hand, in recent years, large-scale computations have been realized with the increasing sophistication and speed of computers. Thus, improvement in the prediction of cavitation instabilities via numerical simulation is expected. Furthermore, in the design and development of high-speed fluid machinery, numerical analysis is expected for not only cost reduction of the experiment but also for acquisition of detailed fluid information of the flow fields inside the fluid machinery, which was not previously obtainable experimentally. In the last several years, the development of cavitation model and computational code that can solve the unsteady cavitating flows inside turbomachinery is try to advance. Joussellin, et al. [15] simulated rotating cavitation and alternate blade cavitation occurring in four-blade cyclic cascade by applying a two-dimensional unsteady numerical method with cavitation model by barotropic state law. Also through the comparison with the experimental data of four-blade turbopump inducer, it was shown that the trend of the occurrence range of the rotating cavitation was predicted by numerical simulation. The authors [16] simulated propagating phenomena of cavitation, which corresponds to the rotating cavitation through three-blade cyclic cascade, and discussed the difference of the results obtained in different conditions in inlet boundary. Coutier, et al. [17] performed three-dimensional numerical analysis of turbopump inducer by incorporating above cavitation model [16] to 3-D commercial code, and the numerical results were compared with experimental data regarding the head drop range and vaporized area. Song [18] reproduced spiral vortex sheet cavitation downstream of the hub in the calculation of three-dimensional Francis turbine. At present, some commercial codes that can simulate cavitating flow have been proposed, and the prediction accuracy has been compared and examined (see for example, by Dupont, et al. [19]). However, the commercial codes are difficult to analyze quantitatively the strong unsteady cavitating flowfields that occur in turbopumps yet.

Under the above-mentioned circumstances, in the present study, the authors have numerically simulated cavitation instabilities occurring in three-blade cyclic cascade. From the calculated results in wide ranges of cavitation number and flow rate, we obtained a cavitation performance curve of the present three-blade cyclic cascade. The aspects of unsteady cavitation in the flow fields are analyzed in detail, and the relationship between a number of cavitation instabilities and the slope of the performance curve are shown. In addition, the mechanisms of propagation phenomena of nonuniform cavities are discussed.

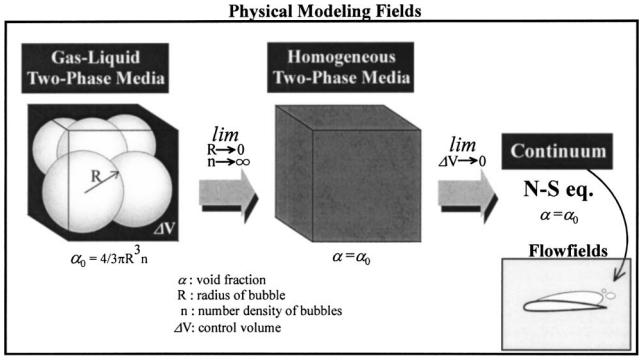

Fig. 1 Concept of physical modeling of the locally homogeneous model

Numerical Method for Cavitating Flow

Physical Modeling. The equation of state for the liquid phase with compressibility can be expressed using the following form proposed by Tammann [20]:

$$p_l + p_c = \rho_l K_l (T_l + T_0), \tag{1}$$

where p_l, ρ_l and T_l are the pressure, density and temperature of the liquid (the subscript l representing the liquid phase), p_c and T_0 are the pressure and temperature constants of the liquid and K_l is the liquid constant. When the gas phase is assumed to be an ideal gas, the equation of state is

$$p_g = \rho_g R_g T_g, \tag{2}$$

where R_g is the gas constant and the subscript g represents the gas phase.

In the ''locally homogeneous compressible gas-liquid two-phase model'' presented by authors [21], the gas-liquid two-phase medium inside the cavity is treated as a locally homogeneous pseudo-single-phase medium. The model concept is shown in Fig. 1. By assuming a limiting case of the two-phase medium, the radius of bubbles being infinitely small, the number of bubbles being infinitely large with the local void fraction (volume fraction of gas phase) α being held constant, furthermore the control volume being infinitely small, the two-phase medium can be considered as a continuum. Then, the equations of a continuum can be applied to the two-phase medium and it becomes easy to treat. Applying this model to the mixture condition inside the cavity, it is expected that unsteady and complex cavity flows can be simulated by the method similar to a continuum. The mixture density ρ of a two-phase medium is expressed by linearly combining gas phase density ρ_g and liquid phase density ρ_l with the local void fraction α,

$$\rho = (1-\alpha)\rho_l + \alpha\rho_g. \tag{3}$$

Then, assuming the local equilibrium conditions, $p_l = p_g = p$, $T_l = T_g = T$, the equation of state becomes, from Eqs. (1), (2), and (3),

$$\rho = (1-\alpha)\frac{p+p_c}{K_l(T+T_0)} + \alpha\frac{p}{R_g T}. \tag{4}$$

Also, the following relationship is obtained between the local void fraction α and the quality (mass fraction of the gas phase) Y:

$$\rho(1-Y) = (1-\alpha)\rho_l, \quad \rho Y = \alpha\rho_g. \tag{5}$$

Using Y from Eq. (5), the equation of state for a locally homogeneous two-phase medium can be expressed as

$$\rho = \frac{p(p+p_c)}{K_l(1-Y)p(T+T_0) + R_g Y(p+p_c)T}. \tag{6}$$

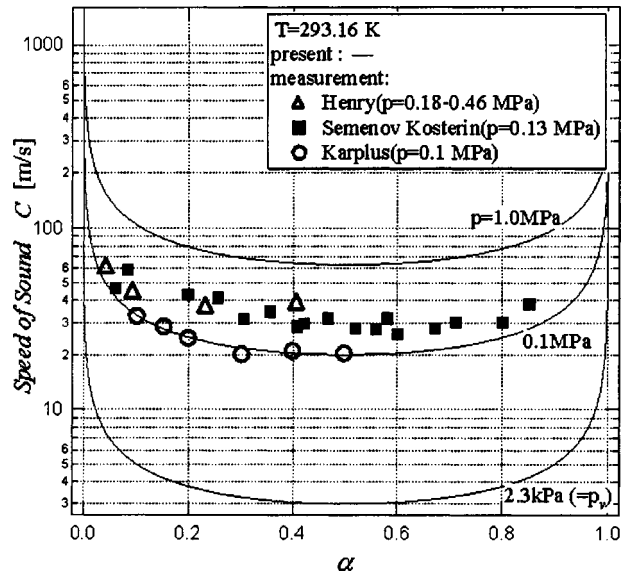

Fig. 2 Speed of sound under isothermal condition

Since the temperature change of the usual cavity flow in water is negligible, the speed of sound C under isothermal conditions is expressed as

$$C^2=\frac{dp}{d\rho}=\left.\frac{\partial p}{\partial \rho}\right|_{\substack{Y=\text{const}\\ T=\text{const}}}=\frac{p(p+p_c)}{\rho}\times\frac{YR_g(p+p_c)+(1-Y)K_lp}{YR_g\{(p+p_c)^2-K_lp\}+Y(1-Y)\rho K_lR_gp_cT_0+K_lp^2} \tag{7}$$

In Fig. 2, the relationship between the speed of sound C and the void fraction α at 20°C is shown for different pressures. Also, measurement values of the speed of sound by Karplus [22] for a surrounding pressure of 0.1 MPa and by others are shown in Fig. 2. The calculated values correspond well with these measurements, and represent the general tendency of speed of sound in mixture condition that takes lower value than that of gas phase.

Mathematical Modeling. The governing equations for the two-phase medium mentioned above are the 2-D compressible Navier-Stokes equations to which the mass conservation law of the gas phase is added. They are expressed as follows in curvilinear coordinates (ξ,η);

$$\frac{\partial \boldsymbol{Q}}{\partial t}+\frac{\partial(\boldsymbol{E}-\boldsymbol{E}v)}{\partial \xi}+\frac{\partial(\boldsymbol{F}-\boldsymbol{F}v)}{\partial \eta}=\boldsymbol{S}, \tag{8}$$

where the unknown variable vector $\boldsymbol{Q}$, the flux vectors $\boldsymbol{E}$ and $\boldsymbol{F}$, the viscous flux vectors $\boldsymbol{E}v$ and $\boldsymbol{F}v$ and source term vector $\boldsymbol{S}$ are

$$\boldsymbol{Q}=\frac{1}{J}\begin{pmatrix}\rho\\ \rho u\\ \rho v\\ \rho Y\end{pmatrix},\quad \boldsymbol{E}=\frac{1}{J}\begin{pmatrix}\rho U\\ \rho uU+\xi_x p\\ \rho vU+\xi_y p\\ \rho UY\end{pmatrix},$$

$$\boldsymbol{F}=\frac{1}{J}\begin{pmatrix}\rho V\\ \rho uV+\eta_x p\\ \rho vV+\eta_y P\\ \rho VY\end{pmatrix},$$

$$\boldsymbol{E}v=\frac{1}{J}\begin{pmatrix}0\\ \xi_x\tau_{xx}+\xi_y\tau_{xy}\\ \xi_x\tau_{yx}+\xi_y\tau_{yy}\\ 0\end{pmatrix},\quad \boldsymbol{F}v=\frac{1}{J}\begin{pmatrix}0\\ \eta_x\tau_{xx}+\eta_y\tau_{xy}\\ \eta_x\tau_{yx}+\eta_y\tau_{yy}\\ 0\end{pmatrix},$$

$$\boldsymbol{S}=\frac{1}{J}\begin{pmatrix}0\\ 0\\ 0\\ \Gamma\end{pmatrix} \tag{9}$$

where, Γ denotes the source term with respect to phase change. J is the Jacobian and U and V are contravariant velocity components in curvilinear coordinates as expressed by

$$J=\frac{1}{\xi_x\eta_y-\eta_x\xi_y},\quad U=\xi_x u+\xi_y v,\quad V=\eta_x u+\eta_y v, \tag{10}$$

and u and v are the velocity components in Cartesian coordinates (x,y). The mixture viscosity coefficient μ for two-phase medium [23] is given by

$$\mu=(1-\alpha)(1+2.5\alpha)\mu_l+\alpha\mu_g. \tag{11}$$

In the present analysis, for simplicity, evaporation is supposed to take place instantaneously when pressure decreases under vapor pressure. In addition, vapor and gas are assumed to be of the same gas phase. Therefore, Γ in Eq. (9) that corresponds to phase change represents the following operation. In the region of $p<p_v$, the values of pressure and mass fraction of gas phase is rectified as

$$p\rightarrow p_v,\quad Y\rightarrow Y^*. \tag{12}$$

Here, p_v is vapor pressure, and Y^* is a modified mass fraction which is obtained from the equation of state (6) while ρ is satisfying the mass conservation.

Numerical Method. In the present study, unsteady cavity flows are simulated by the solution of the above governing equation (8) using the finite difference method. It is also necessary to simulate stably high-speed cavity flows with such discontinuities as a gas-liquid interface having a large density jump. Thus, the TVD scheme is used to preserve the monotonicity of the solution. Specifically, the explicit TVD-MacCormack scheme (Yee [24]) with 2nd-order accuracy in time and space is used. By the way, no turbulence model is applied in this study because there are no reliable turbulence models for two-phase flow.

The overall solution procedure is:

1. Calculate the new ρ, u, v, and Y from Eq. (8) using the TVD-MacCormack scheme
2. Substitute the above ρ and Y in the equation of state (6) of the gas-liquid two-phase medium to get the new p
3. Rectify the values of Y and p in the vicinity of vapor pressure using the instantaneous equilibrium condition assumption as shown in Eq. (12).
4. Modify the values of ρ, Y, u, v and p by applying boundary conditions
5. Return to step (1) for next time step

Computational Conditions. In the present study, the cyclic boundary condition is imposed at every three cascade passages in order to analyze the instabilities arising in the three-blade cyclic cascade. One cascade passage has 263×71 mesh points, two chord lengths from the inlet boundary to the leading edge of the hydrofoil, and three chord lengths from the trailing edge to the outlet boundary. The boundary layer is sufficiently resolved by clustering the grid to the wall with the minimum grid width of $0.1\times h/\sqrt{\mathrm{Re}}$. The hydrofoil geometry is a flat plate with no thickness, and the cascade arrangement is set at a pitch-chord ratio $h/c=0.5$ and a stagger angle of $\gamma=75$ deg. In this computation,

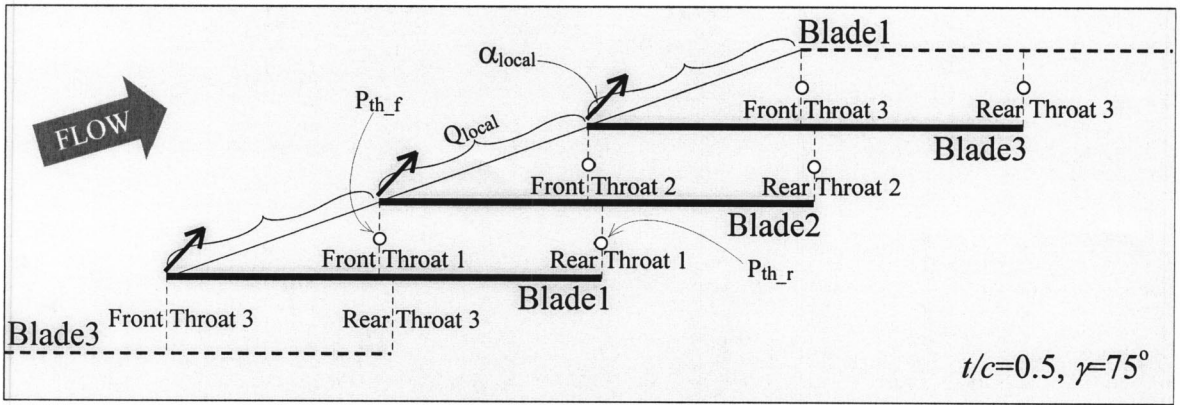

Fig. 3 Schematic diagram of present flat plate cascade with three blades cyclic condition

as shown in Fig. 3, the blades are dubbed Blade 1, Blade 2 and Blade 3 in the direction opposite that of rotation of the cascade, which corresponds to the tangential velocity direction of the cascade. The cascade throat located above Blade 1 is called Throat 1. Likewise, Throat 2 and Throat 3 exist along the direction opposite the direction of rotation of the cascade. A constant total pressure condition and constant angle of attack condition are applied to the inlet boundary, and the constant static pressure condition is applied to the outlet boundary. In addition, a non-slip condition is assumed on the wall boundary. Flow coefficient ϕ is adjusted by inflow angle and reference values are estimated all in the inlet boundary.

Results and Discussion

Cavitation Characteristics of the Present Three-Blade Cyclic Cascade. In Fig. 4, the relationship between the time-averaged static pressure coefficient ψ and the σ of the present three-blade cyclic cascade is shown for four flow coefficients ϕ $=0.105$, 0.141, 0.176 and 0.213. When the plot points are tied to each flow coefficient, head breakdowns, in which the head falls off drastically under a certain σ, are clearly present in the cascade. Where, the static pressure coefficient $\phi=0.105$ is decreasing along with the increase of σ and this is contrary to the qualitative characteristic of ϕ. Only in this case, the rapid decline of the inlet Mach number is observed in the higher σ range, the reason is conceivable that the inlet boundary condition is not appropriate in higher ϕ and σ range. However in the lower σ range, because the Mach number recovers even in the higher ϕ, it is believed that the calculated results possess higher reliability. In the meanwhile, in lower σ regions in Fig. 4, static pressure coefficient is reversed between the higher flow rate and the lower flow rate. By reading the values of static pressure coefficient at each σ value from this graph, which is smoothly re-lined as an approximated curve, the performance curve for the horizontal axis of flow coefficients ϕ can be obtained in Fig. 5. The ψ-ϕ performance curve has a stable negative slope above in higher ϕ and σ region. Here, notice the region in which the performance curve has an unstable ''positive'' slope in the case of the lower flow rate and the lower σ. In usual rotating machinery in the noncavitating condition, an unstable

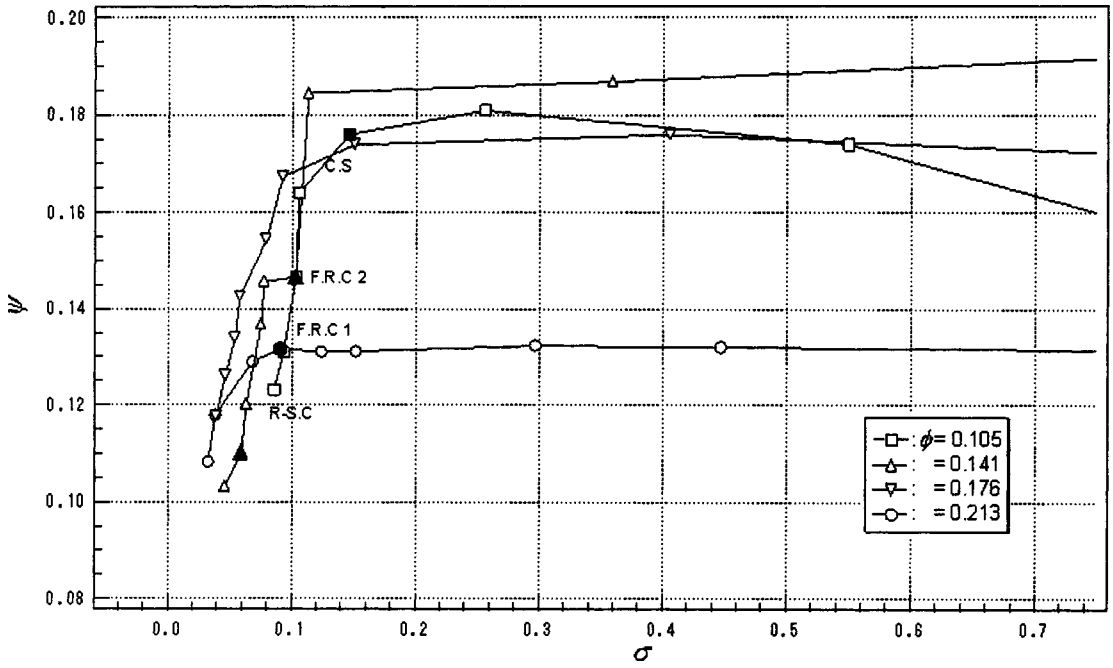

Fig. 4 Time averaged static pressure coefficient versus cavitation number (present three blades cyclic cascade; $h/c=0.5$, $\gamma=75$ deg)

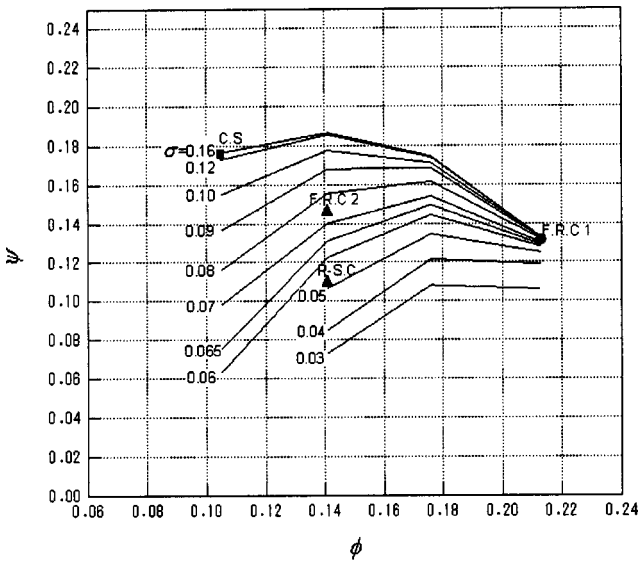

Fig. 5 Time averaged static pressure coefficient versus flow coefficient (present three blades cyclic cascade; $h/c=0.5$, $\gamma=75$ deg)

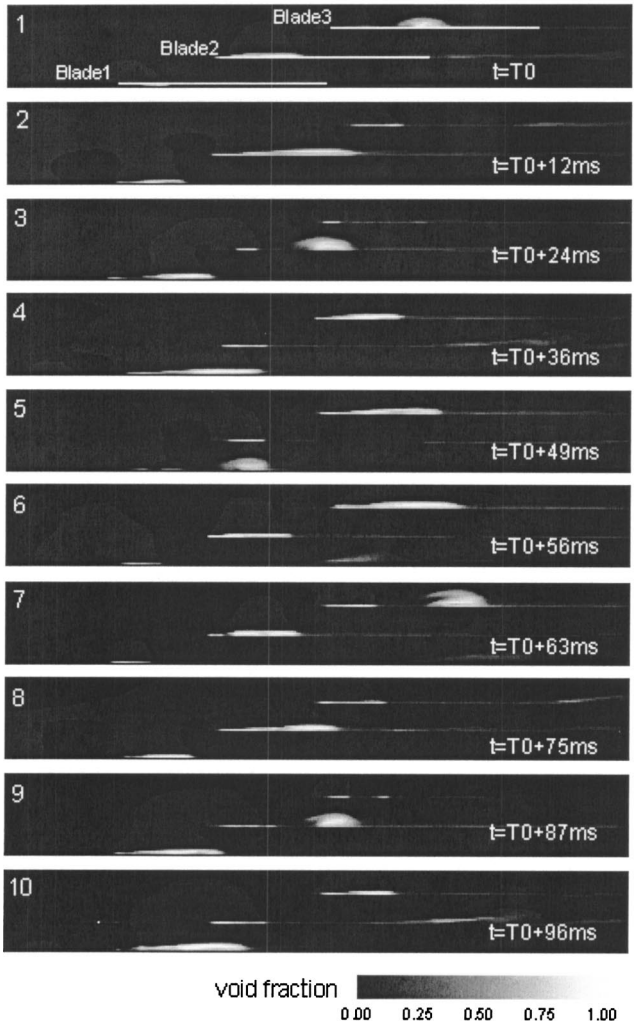

Fig. 6 Time evolution of void fraction contours around three blades ($\phi=0.213, \psi=0.131, \sigma=0.091$)

phenomenon, such as rotating-stall, occurs in region where the performance curve has a positive slope. Even if the performance curve has a negative slope in the higher σ range, rotating-stall cavitation occurs when the σ decreases and the slope of performance curve becomes positive [5,13]. On the other hand, cavitation surge and forward and backward rotating cavitation are independent of the slope of the performance curve. In other words, they occur in regions of both negative and positive slope.

Almost of the results shown in Fig. 4 are difficult to determine what kind of instabilities is occurring because the unsteady phenomena having very strong nonlinearity are occurring. Next, from those results, special attention is given to four cases of ($\phi=0.213, \sigma=0.091$), ($\phi=0.141, \sigma=0.103$), ($\phi=0.141, \sigma=0.059$) and ($\phi=0.105, \sigma=0.046$) denoted in Figs. 4 and 5 which are clearly determined what kind of instabilities are occurring, and the aspects and characteristics of cavitating flowfields are analyzed.

Forward Rotating Cavitation (Super-Synchronous). The aspects of cavitation in the three-blade cyclic cascade are investigated. At first, the time evolution of the void fraction contour in $\phi=0.213$ and $\sigma=0.091$ is shown in Fig. 6. This case is indicated by a filled circle denoted as F.R.C 1 in Fig. 4, and is located in the region of negative slope of the performance curve in Fig. 5. In this case, sheet cavities grow slightly beyond the front throat of the cascade, and break off from the leading edge of the blade. However, their break-off is not simultaneous. The break-off phenomena occurs in the following order: in Blade 3 at the time of frame 1 in Fig. 6, in Blade 2 at frame 3, in Blade 1 at frame 5, and again in Blade 3 at frame 7. Thereafter, the phenomena are repeated in the same order. Along with the cycle, the sheet cavity on next blade located above the break-off blade reaches its maximum in the order of Blade 3-Blade 2-Blade 1. That is, a nonuniform cavity area propagates in the direction of rotation of the cascade. Usually, local instabilities are classified as shown in Fig. 7. In a stationary frame, the propagation velocity ratio of super-synchronous forward rotating cavitation is greater than 1, the ratio of alternate blade cavitation and asymmetric cavitation are equal to 1. The propagation velocity ratios of sub-synchronous forward rotating cavitation and rotating-stall cavitation are between 0 and 1, and the ratio of backward-rotating cavitation is less than 0. In this case, the tangential velocity of the cascade is 11.4 m/s, and the propagating velocity of the nonuniform cavitation is 2.38 m/s on the cascade. In a stationary frame, the propagation velocity ratio between the velocity of the nonuniform cavity area and the tangential velocity of the cascade is estimated as 1.18. Therefore,

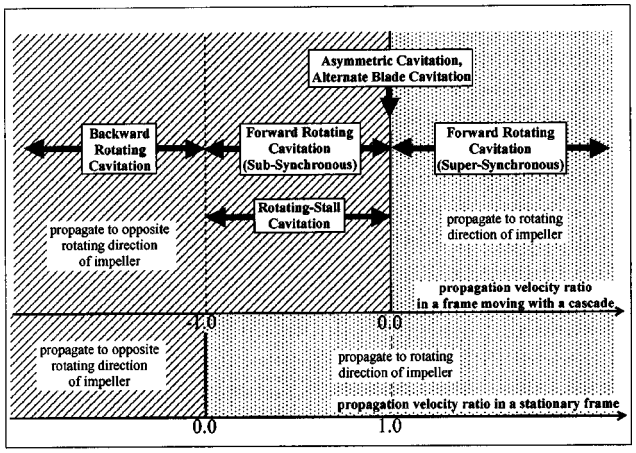

Fig. 7 Classification of cavitation instabilities under propagation velocity ratio of nonuniform cavity area

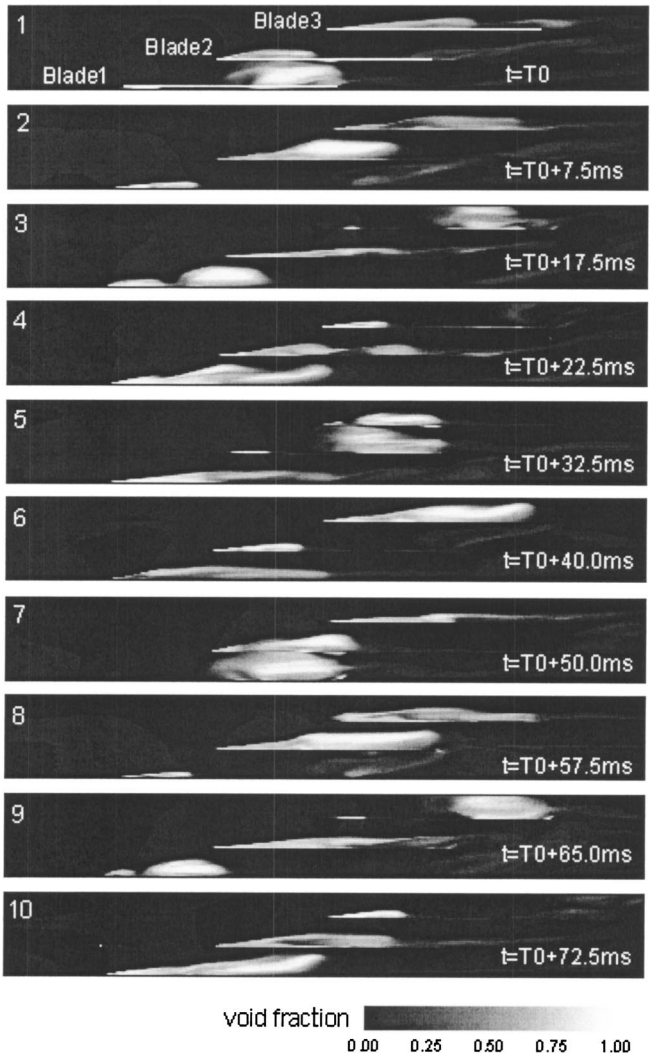

Fig. 8 Time evolution of void fraction contours around three blades ($\phi=0.141, \psi=0.147, \sigma=0.103$)

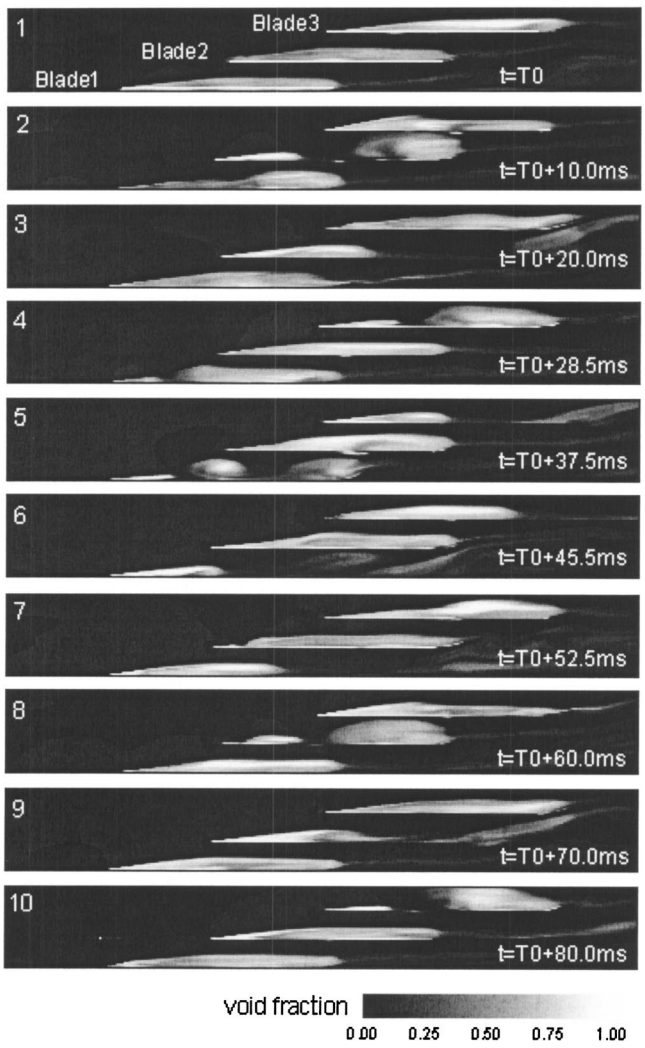

Fig. 9 Time evolution of void fraction contours around three blades ($\phi=0.141, \psi=0.110, \sigma=0.059$)

judging from the value the ratio, it is considered that a cavitation instability corresponding to super-synchronous forward rotating cavitation occurs.

Next, the time evolution of the void fraction contour in the three-blade cyclic cascade at $\phi=0.141$ and $\sigma=0.103$ is shown in Fig. 8. This case is also indicated by an upper filled triangle denoted as "F.R.C 2" in Fig. 4. In this case, sheet cavities grow much longer than in the previous case of forward rotating cavitation near the rear cascade throat and the cavities also break off from leading edge of the blade. The break-off phenomena occur respectively in the following order: in Blade 1 at the time of frame 1 in Fig. 8, in Blade 3 at frame 3, in Blade 2 at frame 5, and again in Blade 1 at frame 10. Therefore, a nonuniform cavity area propagates in the direction of rotation of the cascade. At this time, the tangential velocity of cascade is 11.9 m/s, and the propagating velocity of the nonuniform cavitation is 3.04 m/s on the cascade. When observed in a stationary frame, the propagation velocity ratio is estimated as 1.26. Therefore, it is considered that super-synchronous forward rotating cavitation occurs. This case is located in the region of unstable positive slope of the performance curve in Fig. 5. From the locations of the above two cases of forward rotating cavitation in the performance curve, it is confirmed that there is the possibility that rotating cavitation occurs in the regions of both negative and positive slope of the performance curve.

Rotating-Stall Cavitation. Furthermore, time evolution of void fraction contour in the three-blade cyclic cascade at $\phi=0.141$ and $\sigma=0.059$ are shown in Fig. 9. This case is indicated by a lower filled triangle denoted as "R-S.C" in Fig. 4. The sheet cavities are comparatively larger than the previous two cases of forward-rotating cavitation, and they grow about one chord length. The break-off phenomenon occurs in order as follows: in Blade-2 at the time of frame 2 in Fig. 9, in Blade 3 at frame 4, in Blade 1 at frame 5, and again in Blade 2 at frame 8. Because there exist two maximum sheet cavities simultaneously in this case, attention is given to the minimum sheet cavity, the cavity locating on the break-off blades becomes minimum in the order of Blade 1-Blade 2-Blade 3. That is, in contrast to the two previous cases, an nonuniform cavity area propagates to the opposite direction of rotation of the cascade. At this time 11.2 m/s, and the propagating velocity of the nonuniform cavitation is -1.88 m/s on the cascade. Then, the propagation velocity ratio of nonuniform cavity area is estimated as 0.83, in a stationary frame. Besides, this case is in the region of positive slope of the performance curve in Fig. 5. Therefore, this cavitation instability corresponds to rotating-stall cavitation.

Cavitation Surge. In Fig. 10, time evolutions of distribution of void fraction contour in the three-blade cyclic cascade at $\phi=0.105$ and $\sigma=0.046$ are shown. This case is indicated by a filled square denoted as C.S in Fig. 4. In this case, sheet cavities are

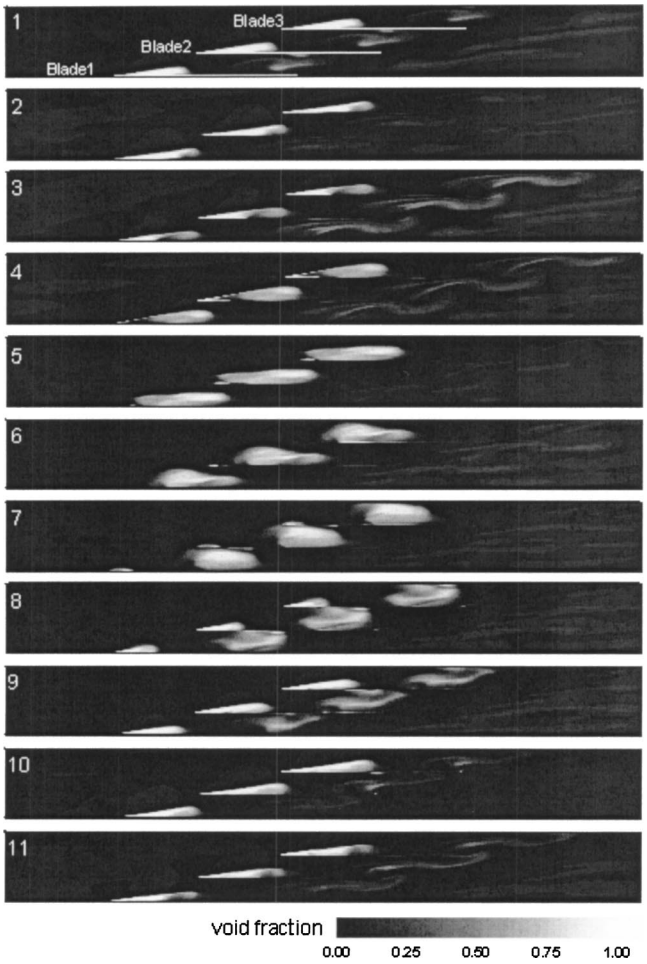

Fig. 10 Time evolution of void fraction contours around three blades (Time Interval=2.5 ms, $\phi=0.105, \psi=0.176, \sigma=0.146$)

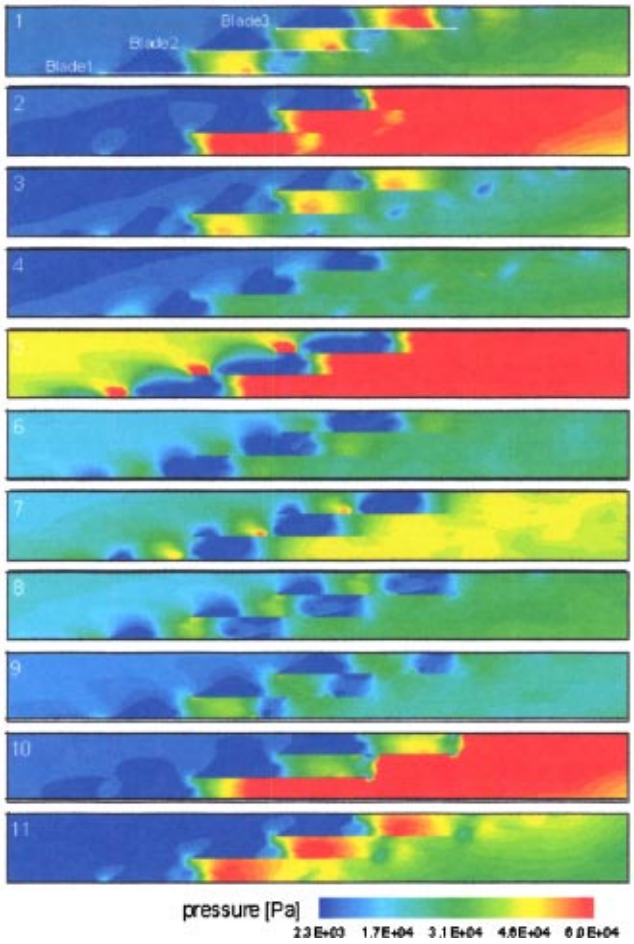

Fig. 11 Time evolution of pressure distribution contours around three blades (Time Interval=2.5 ms, $\phi=0.105, \psi=0.176, \sigma=0.146$)

shorter than for all previous cases, but the thickness is slightly wider because the mass flow rate is the lowest. From Fig. 10, the three sheet cavities break off simultaneously from each leading edge and cloud cavities are shed downstream at almost the same size. The frequency of break-off in this case is calculated as 47 Hz from the aspect of the cavity. The time evolution of the pressure distribution corresponding to Fig. 10 is shown in Fig. 11. The pressure downstream of the cascade increases instantaneously at a certain time, which is caused by the simultaneous collapses of the three cloud cavities at the time of frames 2 and 10. Then, the pressure gradients in the closer regions of the sheet cavities become steeply induced by the pressure increase in downstream, re-entrant jets are caused inside the sheet cavities by the steep pressure gradients at frames 3 and 11. Each three sheet cavities repeat the same unsteady cycles regularly in the same phase by the occurrence of the re-entrant jets. This pulsation phenomenon with cavity break-off is thought to correspond to cavitation surge because pressure vibration accompanied by the pressure waves propagating to the flow direction occurs, which is not seen in other cases.

Oscillation Characteristics of Flowfield in Cavitation Instabilities. In order to investigate the condition of the cavitating flowfield in detail, the temporal changes of the various fluid information in the flow field are shown in Fig. 12. This figure shows that, from top to bottom, the lift coefficient C_L of each blade, the local pressure at the center of the front cascade throat p_{th}-f and the rear cascade throat p_{th}-r, the local flow angle α_{local} near the leading edge of each blade, the local mass flow rate Q_{local} from blade to blade, the velocity in the inlet boundary U_{in}, the pressure at inlet boundary p_{in}, and the total cavity volume V_c, respectively estimated in the places denoted in Fig. 3. The figure shows, from left to right, (a) forward rotating cavitation 1 corresponding to the case of Fig. 6, (b) forward rotating cavitation 2 corresponding to the case of Fig. 8, (c) rotating-stall cavitation corresponding to the case of Fig. 9, and (d) cavitation surge corresponding to the case of Fig. 10, respectively.

In the case of (a) F.R.C1, the amplitude of fluctuations is small on the whole, because the occurring sheet cavities are small-scale. The values of C_L decrease in the order of Blade 3-Blade 2-Blade 1. Correspondingly, the fluctuations of p_{th}-f and α_{local} propagate toward the direction of rotation of the cascade. p_{th}-r fluctuate with a shorter cycle than that of cavity break-off.

In the case of (b) F.R.C2, although most fluid information around three blades fluctuates greater than that in (a), U_{in} and p_{in} fluctuate as little as (a). However, notice that the fluctuations of each Q_{local} propagate in the opposite direction of rotation of the cascade, although the other information propagates toward the direction of rotation. In addition, the period of fluctuation of Q_{local} is two-third that of other fluctuations. For example, when the increase of α_{local} propagates from Blade 3 to Blade 2, the decrease of Q_{local} propagates in the order of Blade 1-Blade 2-Blade 3. The propagation velocity of the nonuniform local mass flow rate is estimated to be -6.40 m/s based on the fluctuation period. At this time, the propagation velocity ratio observed in stationary frame is calculated as 0.45. This value corresponds to that of rotating-stall. Therefore, it can be said that a rotating-stall

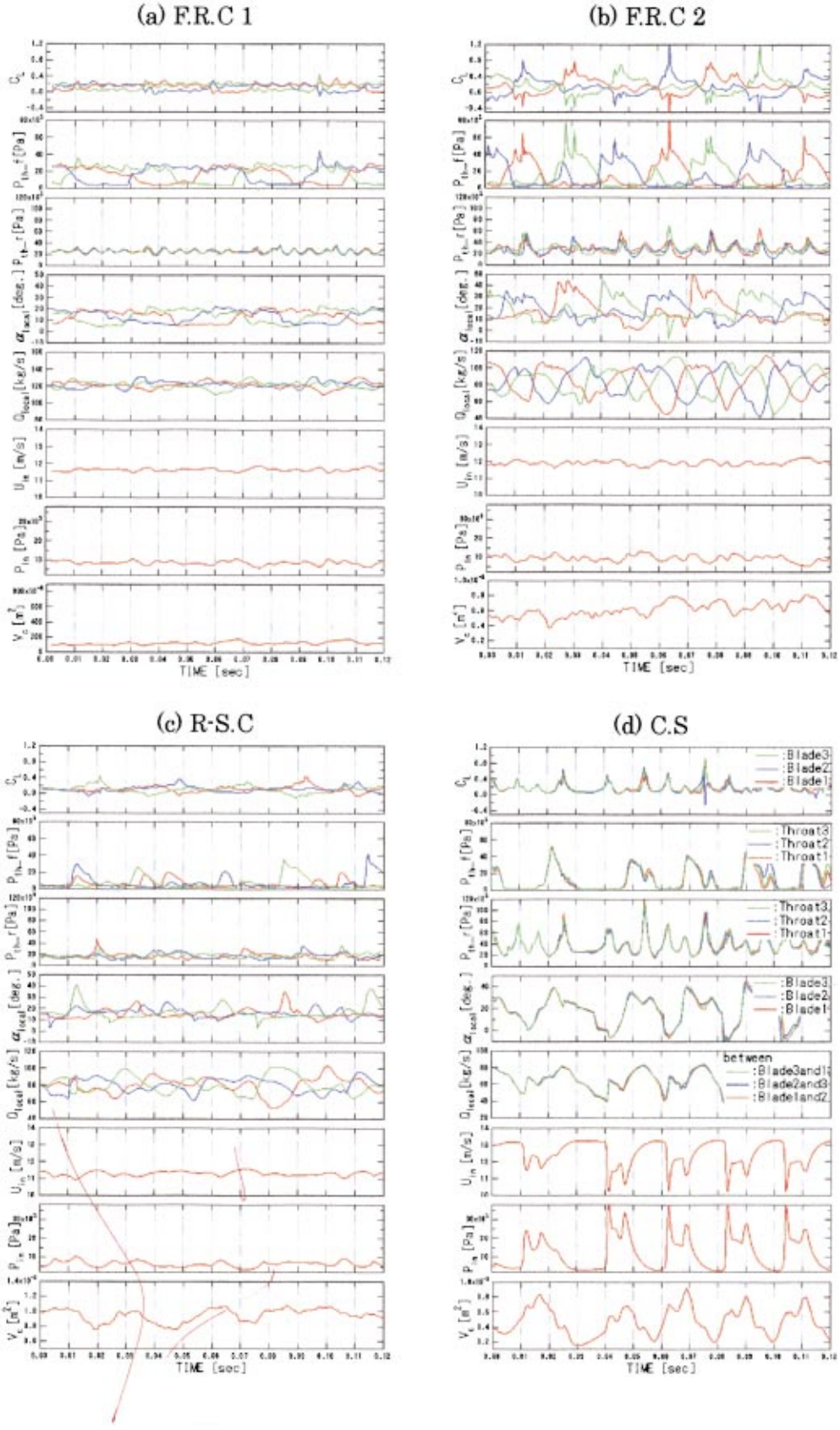

Fig. 12 Time evolution of lift coefficients of three blades, local pressures at the center of front cascade throat, local pressures of rear throat, local flow angles near the leading edge, local mass flow rate between blade to blade, velocity and pressure in inlet boundary, and total cavity volume, respectively from top to bottom

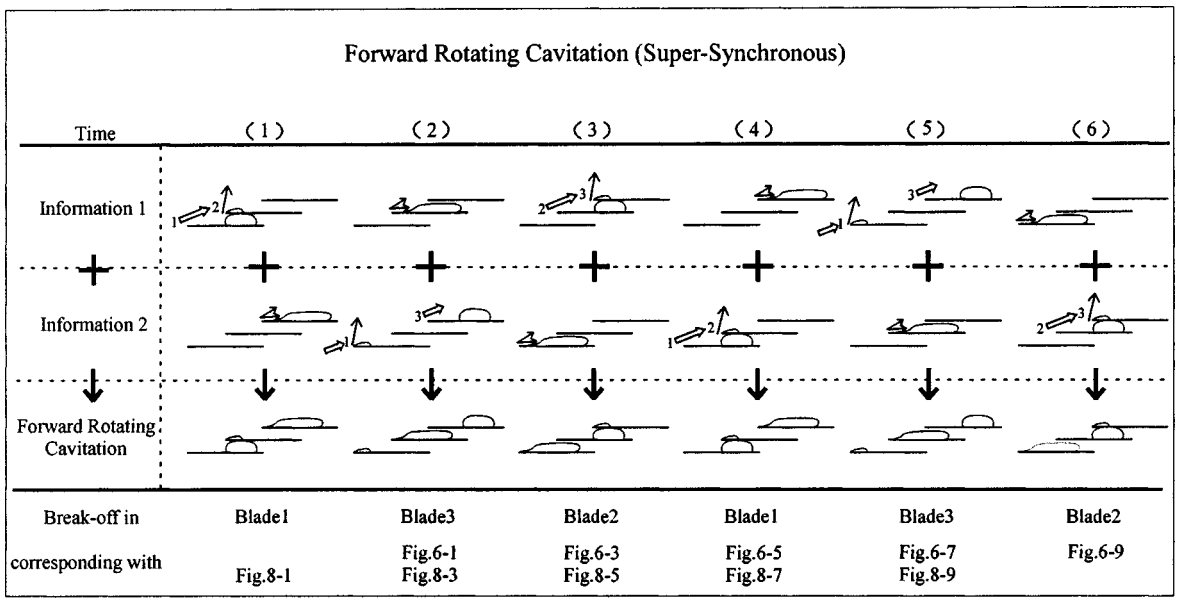

Fig. 13 Schematic aspect in super-synchronous forward rotating cavitation

of rotating fluid machinery in the noncavitating state occurs simultaneously with forward rotating cavitation. This fact corresponds to have the positive slope in the ψ-ϕ performance curve of Fig. 5.

In the case of (c) R-S.C, although V_c is larger than that of the two previous cases of (a) and (b), the fluctuations of fluid information are rather small. This is because the sheet cavities tend to be stable as they approach a condition of supercavitation. Besides, the period of fluctuations becomes longer for the same reason. The regularity of each fluctuation and the wave shapes are somewhat broken in this case. However, careful observation reveals that the fluctuations of C_L, p_{th}, α_{local}, and Q_{local} propagate toward the opposite direction of rotation of the cascade.

The case of (d) C.S differs from the previous three cases, in that each of the three fluctuations around the cascade are having the same period and phase. In addition, many sharp waves exist as a pulse shape in the inlet boundary and the amplitudes are very large. This may be attributed to the fact that the pressure waves generated downstream of the cascade by the simultaneous collapse of the three cloud cavities propagate upstream, as seen in the pressure contours of Fig. 11. Thus, the oscillation characteristic of the flowfield in cavitation surge is predicted in this case.

Mechanisms of Rotating Cavitation. Next, the mechanisms of cavitation instabilities are discussed, especially for super-synchronous forward rotating cavitation and rotating-stall cavitation in the present study. Generally, it is thought that the propagation of fluid information (such as disturbances in pressure and velocity) is caused by the mutual interaction between the variation of cavity volume and the leading edge of the next blade that adjoins on the side of opposite the direction of rotation [4]. In the present study, the fluid information in Blade 1 is assumed to propagate to Blade 2 by mediating Front Throat 1, judging from the relationship between local front-throat pressure and local flow angle near the leading edge shown in Fig. 12, and from the corresponding aspects of cavitation. The relationship is the same as the result for the one-blade cyclic cascade reported in the previous study by the present authors [21]. In the following, Front Throat 1 is called simply Throat 1.

First, the schema of the basic propagation pattern is shown in the upper-column of Fig. 13. During the time of (1) to (3), the information of break-off in Blade 1 propagates to Blade 2, and break-off is caused in Blade 2.

1. The sheet cavity, which separates from the leading edge of Blade 1, moves downstream between Blade 1 and Blade 2. When the sheet cavity has passed Throat 1, the local pressure in Throat 1 increases immediately since the throat width becomes wide instantaneously. The increase in the local pressure in Throat 1 causes an immediate increase in the local flow angle near the leading edge of Blade 2 which adjoins Throat 1.

2. The growth of the sheet cavity in Blade 2 is prompted by the immediate increase in local flow angle near the leading edge of Blade 2, after which, the flow angle decreases gradually.

3. The instability of the cavity surface near the leading edge induced by the fluctuation of the local flow angle [21] causes break-off in Blade 2, and then the sheet cavity in Blade 2 separates from the leading edge of Blade 2 and moves downstream.

As a result, the break-off information in Blade 1 propagates to Blade 2. After which, a similar basic pattern of propagation spreads from blade to blade in the direction opposite of rotation of the cascade as shown in the upper-column of Fig. 13. The break-off information is dubbed ''Information 1.''

Next, the mechanism of super-synchronous forward rotating cavitation occurring in the present three-blade cyclic cascade is discussed, taking into account the above mentioned basic pattern of propagation. At the time of Fig. 13 (1), attention is given to the behavior of the sheet cavity in Blade 3. The local flow rate between Blade 2 and Blade 3 decreases due to the growth of the sheet cavity in Blade 2, which is caused by the immediate increase in local flow angle near the leading edge of Blade 2. Then, the fluid that is pushed aside flows into and between Blade 3 to Blade 1. As a result, the increasing flow rate between Blade 3 and Blade 1 causes the local flow angle near the leading edge of Blade 3 to decrease at the time (1) in the middle-column. Next, the induced fluctuation of the local flow angle near the leading edge of Blade 3 causes instability of the cavity surface, and the sheet cavity breaks off from Blade 3 as shown in the middle-column (2). Afterward, the break-off in Blade 3 which is indicated as ''Information 2'' in the middle column, propagates from blade to blade being independent of ''Information 1.'' Because of the propaga-

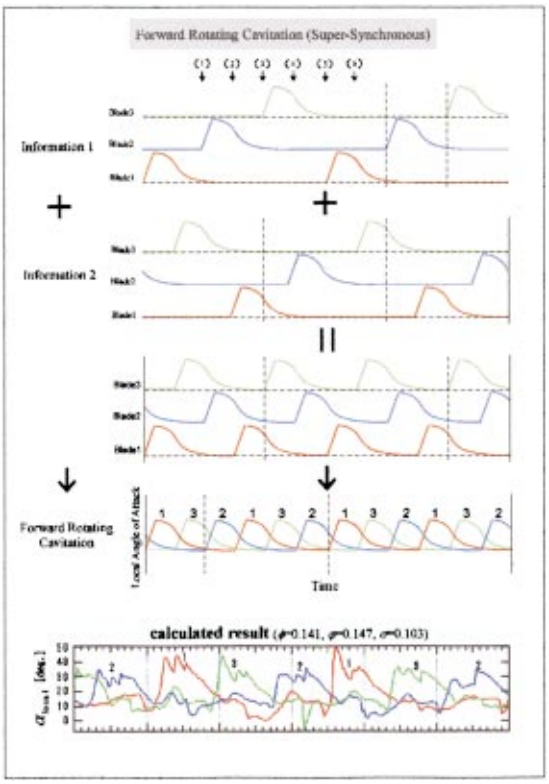

Fig. 14 Schematic time evolution of local flow angle near the leading edge in super-synchronous forward rotating cavitation

tion of two different sets of information, the aspect of cavitation in three-blade cyclic cascade is as in the lower-column of Fig. 13. The order of the break-off accords to that of the calculated results in Figs. 6 and 8, where the break-off occurs in the order of direction of rotation of the cascade as Blade 3-Blade 2-Blade 1. We consider that this may be the mechanism of super-synchronous forward rotating cavitation in the present three-blade cyclic cascade. In Fig. 14, the corresponding schema of time evolution of the local flow angle near the leading edge is shown. Superimposition of ''Information 1'' and ''Information 2,'' results in the peaks of local flow angles taking the order of direction of rotation of the cascade as Blade 3-Blade 2-Blade 1. The tendency resembles that of the lowest-column of Fig. 14, which are the calculated results of forward rotating cavitation shown in Fig. 8.

On the other hand, in the case of rotating-stall cavitation, at the time when the flow angle of Blade 2 immediately increases due to the increase in local pressure in Throat 1, the flow rate between Blade 2 and Blade 3 does not decrease because the sheet cavity of Blade 2 has already grown sufficiently. Therefore, the local flow angle near the leading edge of Blade 3 is not influenced. As a result, ''Information 2'' does not occur. Therefore, the rotating-stall cavitation in the present three-blade cyclic cascade is considered to be a phenomenon in which only one break-off information propagates in the direction opposite of the rotation of the cascade, according to the basic pattern of propagation in the upper-column of Fig. 13.

Conclusions

Various cavitation instabilities arising in flat plate cascade under the three-blade cyclic condition can be simulated by the present numerical method, and the unstable cavitation characteristics are analyzed for a wide range of flow conditions. In addition, the mechanisms of propagation of disturbance in the present three-blade cyclic cascade were discussed. The results obtained in present study can be summarized as follows:

1. Three types of cavitation instabilities arising in the three-blade cyclic cascade were reproduced in the present simulation for wide ranges of cavitation number and flow rate. These correspond to ''super-synchronous forward rotating cavitation,'' ''rotating-stall cavitation,'' which are generally called local instabilities, and ''cavitation surge'' which is generally called system instability.
2. In the region of lower cavitation number and flow rate, the ψ-ϕ performance curve of the present cascade having unstable positive slope was reproduced. In addition, rotating-stall cavitation was confirmed to occur in the above-mentioned positive-slope region of the ψ-ϕ performance curve, and forward rotating cavitation was confirmed to occur in the region of either negative or positive slope.
3. In the flow field in which a cavitation surge occurs, the amplitudes of fluctuation of the various fluid information becomes very large because of the resonance, and the velocity and pressure in the inlet boundary fluctuates, with numerous sharp waves, as a pulse shape because of the instantaneous pressure increase downstream of the cascade induced by the simultaneous collapse of three cloud cavities.
4. It is considered that the fluid information propagates because of the interaction between a change in cascade throat width due to the variation of cavity volume and local flow angle near the leading edge of the blade that adjoins the side opposite the direction of rotation. Considering the mechanisms of cavitation instabilities, rotating-stall cavitation is considered to be a phenomenon in which break-off information propagates in the direction opposite of the rotation of the cascade, according to the basic propagation pattern. Also, the propagation in forward rotating cavitation is explained by superimposing two basic propagations of different break-off information.

Acknowledgments

The numerical simulation was conducted using the supercomputer ORIGIN 2000 in Advanced Fluid Information Center, Institute of Fluid Science, Tohoku University.

References

[1] Bhattacharyya, A., Acosta, A. J., Brennen, C. E., and Caughey, T. K., 1997, ''Rotordynamic Forces in Cavitating Inducers,'' ASME J. Fluids Eng., **119**, pp. 768–774.
[2] Tsujimoto, Y., Yoshida, Y., Maekawa, Y., Watanabe, S., and Hashimoto, T., 1997, ''Observations of Oscillating Cavitation of an Inducer,'' ASME J. Fluids Eng., **119**, pp. 775–781.
[3] Hashimoto, T., Yoshida, M., Watanabe, M., Kamijo, K., and Tsujimoto, Y., 1997, ''Experimental Study on Rotating Cavitation of Rocket Propellant Pump Inducers,'' J. of Propulsion and Power, **13-4**, pp. 488–494.
[4] Friedrichs, J., and Kosyna, G., 2002, ''Rotating Cavitation in a Centrifugal Pump Impeller of Low Specific Speed,'' ASME J. Fluids Eng., **124**, pp. 356–362.
[5] Shimura, T., Yoshida, M., Kamijo, K., Uchiumi, M., and Yasutomi, Y., 2002, ''A Rotating Stall Type Phenomenon Caused by Cavitation in LE-7A LH2 Turbopump,'' JSME International J., Series B, **45-1**, pp. 41–46.
[6] Yoshida, Y., Tsujimoto, Y., Karaoka, D., Horiguchi, H., and Wahl, F., 2001, ''Effects of Alternate Leading Edge Cutback on Unsteady Cavitation in 4-Bladed Inducers,'' ASME J. Fluids Eng. , **123**, pp. 762–770.
[7] Stripling, L. B., 1962, ''Cavitation in Turbopumps-Part 2,'' ASME J. Basic Eng., pp. 339–350.
[8] Jakobsen, J. K., 1964, ''On the Mechanism of Head Break-down in Cavitating Inducer,'' ASME J. Basic Eng., pp. 291–305.
[9] Acosta, A., J., 1975, ''The Dynamic Transfer Function for a Cavitating Inducer,'' ASME publication, 75-WA/FE-16.
[10] Tsujimoto, Y., Kamijo, K., and Yoshida, Y., 1993, ''A theoretical Analysis of Rotating Cavitation in Inducers,'' ASME J. Fluids Eng., **115**, pp. 135–141.
[11] Watanabe, S., Yokota, K., Tsujimoto, Y., and Kamijo, K., 1999, ''Three-Dimensional Linear Analysis of Rotating Cavitation in Inducers Using an Annular Cascade Model,'' ASME J. Fluids Eng., **121**, pp. 866–871.
[12] Horiguchi, H., Watanabe, S., and Tsujimoto, Y., 2000, ''A Theoretical Analysis of Alternate Blade Cavitation in Inducers,'' ASME J. Fluids Eng., **122**, pp. 156–163.
[13] Fujii, A., Semenov, Y., and Tsujimoto, Y., 2003, ''Analysis of Rotating Choke in an Inducer,'' JSME Trans., **69–680**, pp. 764–771, in Japanese.
[14] Tsujimoto, Y., Kamijo, K., and Brennen, C. E., 2001, ''Unified Treatment of Flow Instabilities of Turbomachines,'' AIAA J. of Propulsion and Power, **17-3**, pp. 636–643.
[15] Joussellin, F., Courtot, Y., Coutier-Delgosha, O., and Reboud, J. L., 2001,

''Cavitating Inducer Instabilities: Experimental Analysis and 2D Numerical Simulation of Unsteady Flow in Blade Cascade,'' Proc. CAV2001, B8.002, Pasadena, CA, USA.
[16] Iga, Y., Nohmi, M., Goto, A., Shin, B. R., and Ikohagi, T., 2002, ''Numerical Analysis of Unstable Phenomena of Cavitation in Cascade with Finite Blade Numbers,'' Proc. The 9th International Symp. on Transport Phenomena and Dynamics of Rotating Machinery, Honolulu, Hawaii, USA. CD-ROM FD-ABS-128.
[17] Coutier-Delgosha, O., Morel, P., Fortes-Patella, R., and Reboud, J. L., 2002, ''Numerical Simulation of turbopump Inducer Cavitating Behavior,'' Proc. The 9th International Symp. on Transport Phenomena and Dynamics of Rotating Machinery, Honolulu, Hawaii, USA.
[18] Song, C. C. S., 2002, ''Current Status of CFD for Cavitating Flows,'' Proc. The 9th International Symp. on Transport Phenomena and Dynamics of Rotating Machinery, Honolulu, Hawaii, USA.
[19] Dupont, P., and Okamura, T., 2002, ''Cavitating Flow Calculation in Industry,'' Proc. The 9th International Symp. on Transport Phenomena and Dynamics of Rotating Machinery, Honolulu, Hawaii, USA.
[20] Chen, H. T., and Colins, R., 1971, ''Shock Wave Propagation Past an Ocean Surface,'' J. Comput. Phys., **7**, pp. 89–101.
[21] Iga, Y., Nohmi, M., Goto, A., Shin, B. R., and Ikohagi, T., 2003, ''Numerical Study of Sheet Cavitation Break-off Phenomenon on a Cascade Hydrofoil,'' ASME J. Fluids Eng., **125**, pp. 643–651.
[22] Karplus, H. B., 1958, ''The velocity of sound in a liquid containing gas bubbles,'' Armour Research Foundation of Illinois Institute of Technology, C00-248.
[23] Beattie, D. R. H., and Whally, P. B., 1982, ''A Simple Two-Phase Frictional Pressure Drop Calculation Method,'' Int. J. Multiphase Flow, **8-1**, pp. 83–87.
[24] Yee, H. C., 1987, ''Upwind and Symmetric Shock-Capturing Schemes,'' NASA-TM, 89464.

Condensation During Discharging of Pneumatic System

Jin Ying-zi
Zhejiang Institute of Science and Technology,
HangZhou, ZheJiang Province, 310033, PRC
Tel: 86-0571-88495237,
Fax: 86-0571-88495134
e-mail: kimyongzha@hotmail.com

Wang Zu-wen
Harbin Institute of Technology,
Harbin, Heilongjiang Province, 150001, PRC
Tel: 86-0451-86415883,
Fax: 86-0451-86415224
e-mail: zwwang@hope.hit.edu.cn

Bao Gang
School of Mechatronics,
Harbin Institute of Technology,
Harbin, Heilongjiang Province, 150001, PRC
Tel: 86-0451-86413446,
Fax: 86-0451-86415224
e-mail: bg@pneucen.hit.edu.cn

In order to make sure what factors have an effect on condensation, a mathematical model has been established for the discharging process of a pneumatic system using the fluid grid theory, an analytic equation has been derived to determine the maximum humidity of air during discharging of pneumatic system, and an analytic equation has been established as the first necessary condition for the determination of internal condensation in a pneumatic system. Flowing air may produce water droplets in a pneumatic system when the system satisfies the first necessary condition. An analytic equation has been developed as the second necessary condition for determination of internal condensation in a pneumatic system by introducing stroke and establishing an analytic equation for the stroke. The water droplets produced by satisfaction of the first necessary condition form drops of water inside the system when the system satisfies the second necessary condition. Internal condensation does not occur when the system does not satisfy the first necessary condition, and internal condensation occurs only when the system satisfies both conditions at the same time. The experimental results indicate that the points of internal condensation, external condensation and no condensation exhibit a regular distribution on the plane formed by the dimensionless volume of the discharging pipe and the average velocity of air, and the plane can then be divided into regions, providing a graphic discrimination method for determination of condensation in a pneumatic system.
[DOI: 10.1115/1.1758261]

1 Introduction

Condensation occurs in a pneumatic system when water droplets are produced as the air pressure reaches or exceeds the saturated steam pressure during expansion. It can be divided into internal condensation (water droplets inside a component) and external condensation (water droplets outside a component). When condensation occurs in a pneumatic system, the life of its components is decreased while the failure rate of the system is increased. The discrimination of condensation in a pneumatic system is therefore of great significance.

Zhang Hu-ping [1] analyzed the condensation during the discharging of a pneumatic system using the bond graph theory and the cold shrinkage theory, discussed the conditions for condensation with experimental results, and suggested the condensation shrinkage boundary curves for no condensation.

Prof. Wang Zu-wen [2] studied the mechanism of condensation in a pneumatic system through experiments, pointed out different factors and their effects on condensation, and suggested measures to prevent condensation.

This research indicates that condensation in a pneumatic system is a complicated phenomenon involving many factors. The size and shape of the pneumatic components, such as the volume of a cylinder, the inner diameter and the length of a discharging pipe, will affect the humidity and velocity of air in a pneumatic system during discharging. The initial status of the compressed air, such as the temperature, the humidity and the pressure will also influence its humidity and velocity. The air humidity and velocity during discharging will determine condensation status during discharging directly. The major contributions of this paper include: (1) Analytic equations are derived for the pressure, mass flow rate, and noncondensational maximum humidity of air during discharging using the fluid grid theory; (2) The first necessary condition is proposed for the condensation in a pneumatic system using the equilibrium condensation theory. Water droplets are produced when a system satisfies the first necessary condition; (3) An air stroke concept is introduced and the equation for calculating the air stroke is derived. The second necessary condition is proposed for the condensation in a pneumatic system according to the concept of the air stroke. The water droplets produced in the system will be kept in the system and internal condensation occurs when a system satisfies the first and the second necessary condition. The two necessary conditions proposed in this paper are directly determined by both the size and shape of system components and the initial state of the compressed air of the system. A large number of experimental results indicate that the points at which internal condensation, external condensation, and no condensation create a certain regular pattern on the plane formed by the dimensionless volume and average velocity of discharging pipes. A graphic discrimination method is therefore proposed for determination of condensation in a pneumatic system.

Contributed by the Fluids Engineering Division for publication in the JOURNAL OF FLUIDS ENGINEERING. Manuscript received by the Fluids Engineering Division January 10, 2001; revised manuscript received September 5, 2003. Associate Editor: L. Mondy.

2 Establishment of Mathematical Model

2.1 Basic Equations. It is established through analysis of experimental phenomena that internal condensation occurs in a system consisting of a smaller container and a longer air pipe. A model as shown in Fig. 1 is used for study on air flow in an air pipe.

It is assumed that [3]

1. The air flow in the container is a uniform flow except near the outlet.
2. The air flow is an axisymmetric flow without tangential velocity.
3. The air flow is a small disturbance.
4. Viscous force is small because of the compressibility of air.
5. The inside diameter of pipe is smaller than the wave length of the air flow.
6. The pipe length is so much greater than the inside diameter of the pipe that the effect of the pipe end is neglected.
7. The mass force is neglected.

The continuity Eq. (3) that satisfies assumptions 1–7 is

$$\frac{\partial \rho}{\partial t} + \frac{\partial (\rho u)}{\partial x} = 0 \tag{1}$$

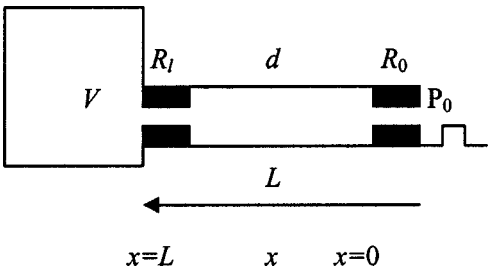

Fig. 1 Schematic diagram of discharging of pneumatic system

It is assumed [3]: ⟨1⟩ $\partial^2 u/\partial x^2 \ll \partial^2 u/\partial r^2$, ⟨2⟩ $u \cdot \partial u/\partial x \ll \partial u/\partial t$, namely $du/dt = \partial u/\partial t$.

The N-S equation and energy Eq. (3) that satisfies assumptions 1–7 is then:

$$\frac{\partial u}{\partial t} = -\frac{1}{\rho} \cdot \frac{\partial p}{\partial x} + \frac{v}{r} \cdot \frac{\partial}{\partial r}\left(r \frac{\partial u}{\partial r}\right) \tag{2}$$

$$\rho c_p \frac{\partial T}{\partial t} = \frac{\partial p}{\partial t} + \frac{K}{r} \cdot \frac{\partial}{\partial r}\left(r \frac{\partial T}{\partial r}\right) \tag{3}$$

The ideal gas state equation is

$$p = \rho R_g T \tag{4}$$

2.2 Approximate Solution to Basic Equation. The lossless fluid model is used, i.e. it is assumed that [3]

1. The air viscosity in the pipeline is so much smaller that it can be neglected, i.e. $\nu = 0$.
2. There is no heat exchange between air and pipe wall, i.e. $K = 0$, and no heat exchange between air inside and outside of the pipe.
3. The radial distribution of air temperature is uniform, i.e. $\partial T/\partial r = 0$.
4. For nonsteady flow, $\rho \partial u/\partial t \gg u \partial \rho/\partial x$.

From Eqs. (1), (2), (3), and (4)

$$\frac{\partial P}{\partial x} = -\frac{s}{A} Q, \quad \frac{\partial Q}{\partial x} = -\frac{As}{a^2} P \tag{5}$$

The series impedance Z, parallel admittance Y, propagation constant Γ, and characteristic impedance Z_c are than as follows

$$Z = \frac{1}{A} s, \quad Y = \frac{A}{a^2} s, \quad \Gamma = \frac{s}{A}, \quad Z_c = \frac{a}{A} \tag{6}$$

It is assumed that

1. The impedance at the beginning of pipe is $Z_0(s)$ when $x = 0$ and the impedance at the end of pipe is $Z_L(s)$ when $x = L$.
2. Disturbing pressure $P_0(s)$ is a step signal, and its quadrant function is $P_0(s) = p_0/s$.
3. $Z_0(s) = Z_c(s)$, and the expression of solution to Eq. (5) is then as shown below.

$$P(x,s) = \frac{p_0(sh\Gamma(s)(L-x) + Z' ch\Gamma(s)(L-x))}{s(1+Z')(ch\Gamma(s)L + sh\Gamma(s)L)} \tag{7}$$

$$Q(x,s) = \frac{p_0(ch\Gamma(s)(L-x) + Z' sh\Gamma(s)(L-x))}{s(Z_c(s) + Z_L(s))(ch\Gamma(s) + sh\Gamma(s)L)} \tag{8}$$

where

$$Z' = \frac{Z_L(s)}{Z_c(s)} \tag{9}$$

Solving Eq. (7) and Eq. (8) by the traveling wave method, the variation in pressure and mass flow rate are:

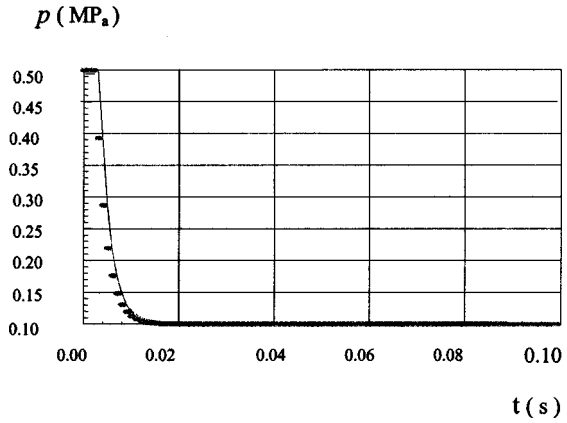

Fig. 2 Comparison between calculated and experimental results obtained with lossless pipeline model and average friction pipeline model (at outlet of small container)

$$\Delta p(x,t) = \frac{p_0}{2}\{U(t-\tau_1) + BU(t-\tau_2)\} \tag{10}$$

$$\Delta q(x,t) = \frac{p_0}{2Z_c}\{U(t-\tau_1) - BU(t-\tau_2)\} \tag{11}$$

where

$$B = 1 - (1-\eta)e^{-s_0(t-\tau_2)} \tag{12}$$

$U(t-\tau)$: unit function $U(t-\tau) = \{^{1, t>\tau}_{0, t<\tau}$, and τ_1, τ_2: are propagation time of wave, respectively.

$$\tau_1 = \frac{x}{a}, \quad \tau_2 = \frac{(2L-x)}{a} \tag{13}$$

$$\eta = \frac{R_L - Z_c}{R_L + Z_c}, \quad s_0 = \frac{A \cdot a}{V}, \quad R_L = \frac{a}{A_1} \tag{14}$$

The pressure and mass flow rate are

$$p = p(x,t) = p_s + \Delta p(x,t), \quad q = q(x,t) = \Delta q(x,t) \tag{15}$$

2.3 Comparison Between Experimental and Calculated Results. The pressure during discharging of the pneumatic system is calculated using the approximate solution in this paper, and is then compared with the actual measurement. The result of this comparison indicates that there is a very good agreement between the calculated result obtained with the lossless fluid pipeline model and the actual measurement, as shown in Fig. 2. The air pressure curves shown on the figure are the results of calculations made with $V = 3.20(\text{cm}^3)$, $d = 2.5(\text{mm})$, $L = 1.3(\text{m})$. The dotted lines stand for experimental results, while the solid lines stand for the results of calculation.

For the study of condensation during discharging of pneumatic systems, the following may be used:

1. A lossless pipeline model.
2. The flow impedance at the beginning of pipe is a flow resistance, equal to the characteristic impedance.
3. The flow impedance at the end of pipe is a flow resistance plus flow capacitance in series. The pressure and mass flow rate can then be calculated using Eqs. (10), (11), and (15).

3 Theoretical Discriminant for Internal Condensation

3.1 First Necessary Condition for Internal Condensation The following is obtained using the adiabatic state equation, Clapayron's equation, and the ideal gas state equation:

$$T=T(x,t)=\frac{\sqrt[k]{p_s}p^{(1-1/k)}}{R_g\rho_s} \tag{16}$$

From the definition of relative humidity, Clapayron's equation and Dalton's law, the relative humidity of gas before condensation occurs is as follows [1]:

$$\varphi=\varphi(x,t)=\frac{px_0}{(x_0+0.622)p_{\infty(T)}} \tag{17}$$

where $p_{\infty(T)}$ is obtained using experimental Eq. (4)

$$p_{\infty(T)}=10^{11.4051-2353/T} \tag{18}$$

When $t>2l-x/a$, $U(t-\tau)=1$. The step of pressure during discharging is negative, so $p_0<0$. The partial derivative of the temperature and humidity to x and t can be obtained from Eq. (10), Eqs. (16) and (17) as shown below.

$$\frac{\partial T}{\partial x}<0, \quad \frac{\partial \varphi}{\partial x}>0, \quad \frac{\partial T}{\partial t}<0, \quad \frac{\partial \varphi}{\partial t}>0 \tag{19}$$

Let $t=TS$, where TS is the total discharging time. It is assumed that the discharging process ends when the air pressure is (1 +0.00001) times ambient pressure.

Let $x=L$, the discharging time can be obtained using Eq. (10).

$$TS=\frac{L}{a}-\frac{\ln\left(-\dfrac{2p_a}{p_0(1-\eta)10^5}\right)}{s_0} \tag{20}$$

The maximum humidity of air at the outlet of container during discharging is obtained using Eq. (21):

$$\varphi_{\max}=\varphi(L,TS)=\frac{x_0p(L,TS)}{(x_0+0.622)10^{11.4051-2353/T(L,TS)}} \tag{21}$$

where

$$p(L,TS)=p_s+\frac{p_0}{2}[2-(1-\eta)e^{-s_0(TS-L/a)}] \tag{22}$$

$$T(L,TS)=\frac{\sqrt[k]{p_s}p^{(1-1/k)}(L,TS)}{R_g\rho_s} \tag{23}$$

According to the equilibrium condensation theory (5), equilibrium condensation means the cold shrinkage which occurs when the vapor pressure reaches the saturated status. The first necessary condition for internal condensation can be expressed that the maximum humidity of air at the outlet of container should be equal to 100%. But condensation does not necessarily occur in the system under this condition because the water droplets produced in the system will move with the air flow.

3.2 Second Necessary Condition for Internal Condensation. The air discharging velocity at the outlet of the pipe could be calculated by [4–6]:

$$u=\frac{q}{\rho\cdot A_1} \tag{24}$$

The case of $t>2l-x/a$ is discussed.

The partial derivatives of absolute values of mass flow rate and velocity to x are obtained using Eqs. (11) and (24).

$$\frac{\partial|q|}{\partial x}<0, \quad \frac{\partial|u|}{\partial x}<0 \tag{25}$$

The average velocity of air at the outlet of container during discharging time is obtained as shown below.

$$u_m=\frac{k\sqrt[k]{p_s}[p_{s0}^{-1/k+1}-p_{a0}^{-1/k+1}]}{A_1Z_cs_0\rho_s(k-1)TS} \tag{26}$$

where

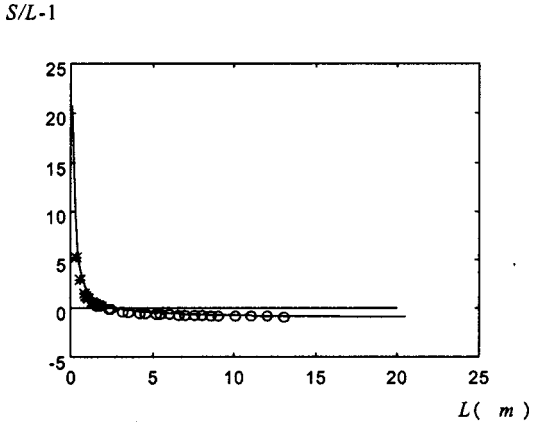

Fig. 3 Discrimination of internal condensation based upon dimensionless stroke and experimental results

$$p_{s0}=p_s+\frac{p_0}{2}(1+\eta) \tag{27}$$

$$p_{a0}=(p_a+10^{-5}p_a) \tag{28}$$

S, the distance covered by the air at the outlet of container during discharging time is obtained as shown below.

$$S=\frac{k\sqrt[k]{p_s}[p_{s0}^{-1/k+1}-p_a^{-1/k+1}]}{A_1Z_cs_0\rho_s(k-1)} \tag{29}$$

By introducing a dimensionless stroke $\overline{S}$

$$\overline{S}=\frac{S}{L}=\frac{k\sqrt[k]{p_s}[p_{s0}^{-1/k+1}-p_a^{-1/k+1}]}{LA_1Z_cs_0\rho_s(k-1)} \tag{30}$$

The temperature of the air drops dramatically during discharging as a result of the expansion of the air. It happens quite often that the temperature of the air drops below the dew point, as the temperature of the air in the system is very low, and when this happens, the first condition for internal condensation is satisfied. When the velocity of the air is high, the droplets flow out from the system through the pipe, and as a result, internal condensation does not occur. In order to judge whether internal condensation will occur when the first necessary condition ($\varphi_{\max}=100\%$) is satisfied, stroke can be used. If the stroke is comparatively longer than the pipe, it can be expected that the droplets will flow out from the systems, and internal condensation will not occur. If the stroke is shorter than the pipe, it may be expected that droplets will remain in the system and internal condensation will occur.

The second necessary condition for internal condensation is as follows

$$S\leqslant L \quad \text{or} \quad \overline{S}\leqslant 1 \tag{31}$$

When the pneumatic system satisfies the first and the second necessary conditions simultaneously, the internal condensation will occur.

3.3 Comparison Between Experimental and Calculated Results. The relationship between dimensionless stroke and length of discharge pipe according to Eq. (30) is shown in Fig. 3 where $V=3.62\ \text{cm}^3$, $d=2.5$ mm, $d_1=0.7$ mm. Here the solid line stands for the calculated results, while symbols "○" and "*" stand for the experimental results of internal condensation and non-condensation respectively. They show experimental results of internal condensation/non-condensation in different experimental configurations. Because of the small volume, the rapid discharging process, and the low air temperature, the first necessary condition would be satisfied without doubt. According to the second necessary condition, the experimental results spread in the region

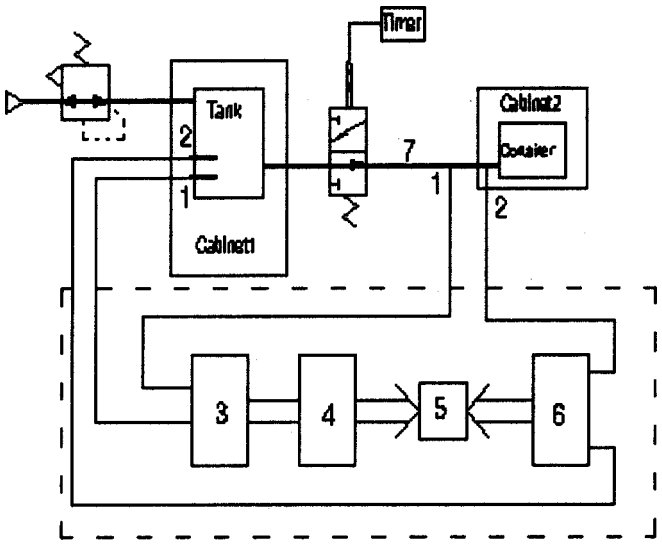

Fig. 4 Experimental setup:
1: Pressure transducer
2: Temperature transducer
3: Strain gauge
4: Recorder
5: Computer
6: HY8021 date-sampling card
Container 1: Experimental container,
Cabinet1: Constant temperature cabinet,
Cabinet2: Constant temperature and humidity cabinet
7: Charge (discharge) pipe

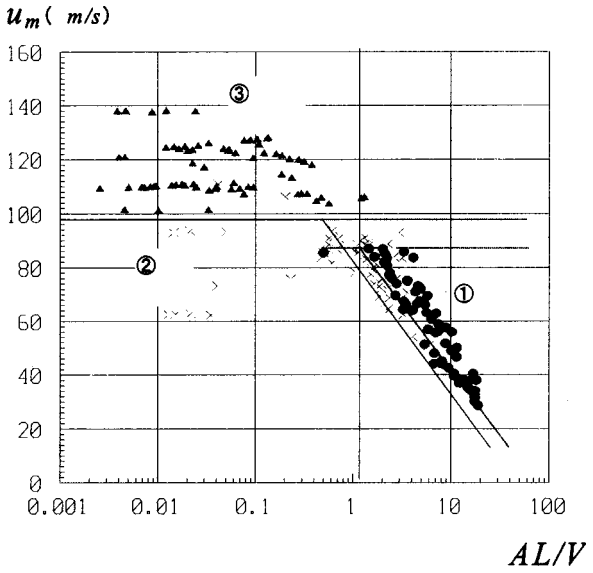

Fig. 5 Graphic discrimination method

$S/L>1$ will not create condensation. While if the experimental results drop into the region $S/L\leqq 1$, internal condensation occurs.

The experimental and calculated results show that the second necessary condition for internal condensation can be used for discrimination of internal condensation by checking if there are water droplets resulting from expansion of air remain in the system.

The experimental results were obtained using different lengths of discharging pipe. In this experiment, a total of 56 different lengths of discharging pipe, varying from 100 mm to 12950 mm, were chosen and optimized for experimental configuration. Figure 3 shows that the 56 result points are close each other. It indicates that the experimental data has repeatability.

4 Experimental Research and Graphic Discrimination Method

4.1 Experimental Research. The experimental setup, shown in Fig. 4, consists of an air supply including air compressor, air-cooled cooler, cooling dehumidifier, relief valve, shutoff valve, reversing valve, tank for air supply, experimental container, timer and a certain length of pipe, strain gauge, recorder, computer.

The charging process begins when the reversing valve opens and the air flows into the container. When the predetermined charging time has elapsed, the discharging process begins. When the predetermined discharging time has elapsed, the process is repeated. System elements such as the pipe and container can be checked for internal or external condensation after the charging and discharging process is repeated several times.

The air supply pressure can be adjusted by the relief valve during the experiment. The air supply has a pressure of 0.5 Mpa, a dew point of 2°C~3°C, an inlet temperature of 15°C, an ambient temperature of 25°C, and an ambient humidity of 35% ~40%.

The charging and discharging time is set by the timer. The repetitions of charging and discharging are recorded by a counter. The charging and discharging pipes are transparent pipes cut to the required length. The air supply temperature can be adjusted using a constant temperature and humidity cabinet. The dew point of the air supply can be controlled by an air-cooled cooler. The pressure sensor type PGM-10KC is used. The air temperature is measured by a thermistor. The temperature and humidity of the air supply is measured by a hygrothermograph. And the dew point is measured by a dew thermometer.

In the author's experimental configuration, a total of 20 cylinders of different volumes ranging from 1922.66 mm^3 to 206,088 mm^3 were used. For every volumetric size of cylinder, there are four different inner diameters of the discharge pipes, namely 2 mm, 4 mm, 5 mm, and 6 mm. Combining the different cylinders with the different inner diameter pipes, a total of 80 combinations could be configured. For every combination, more than 10 lengths of the discharging pipe varying from 100 mm to 20,000 mm were chosen, optimized for the experiment. This allowed for the selection of lengths so that those near the critical values of condensation and noncondensation would vary by no more than 10 mm. More than 1000 experiments were made. For every single experimental configuration, the experimenter observed the water droplets on the exterior and interior of the pipe during eight hours of continuous operation.

4.2 Graphic Discrimination Method for Condensation The partial differential of the air average velocity to s_0 and L/a at the outlet of the container can be obtained using Eqs. (26) and (20) as shown below.

$$\frac{\partial u_m}{\partial s_0}<0, \quad \frac{\partial u_m}{\partial (L/a)}<0 \tag{33}$$

The results of experimental data processing with $s_0\times L/a = A\cdot L/V$ as lateral coordinate and air average velocity u_m as longitudinal coordinate show that the experimental points at which internal condensation, external condensation or noncondensation occurs in a system with different elements, form a graph as shown in Fig. 5. The symbols *, ▲, and × stand for points of internal condensation, external condensation and noncondensation respectively, and the areas labeled ①, ②, and ③ stand for regions of internal condensation, external condensation and noncondensation, respectively.

Observing the spread of experimental results, it can be noted that:

Table 1 Experimental scheme and results in regions ①, and ② and ③

	Region ①		Region ②		Region ③	
V (cm^3)	3.62	10.8	3.62	10.8	235.4	137.4
d_1 (mm)	0.7		0.7		1.1	
d (m)	2.5		2.5		4	6
L (m)	8	10	1.5	3	0.15	0.1
$\log(AL/V)$	2.34	1.51	0.7	0.3	0.008	0.021
u_m (m/s)	45.5	62.4	75	76.5	93.2	108.7
Result	Internal condensation		Non-condensation		External condensation	

1. when the average air velocity is faster than 102 m/s, exterior condensation happens. It is called the exterior condensation area and was denoted as ③;

2. when the average air velocity is slower than 102 m/s, it is an interior/noncondensation area;

3. when the average air velocity is slower than 88 m/s, and the experimental results are located to the right of line $u_m = -500\log(AL/V)/297 + 10{,}000/99$, interior condensation occurs and was donated as ①;

4. when the average air velocity is within 88 m/s and 102 m/s, or it is slower than 102 m/s, and experimental results are located to the left of line $u_m = -500\log(AL/V)/297 + 100/9$, no condensation occurs and was donated as ②.

To verify the discrimination method, a few points from region ①, region ②, and region ③ were chosen. Table 1 shows the experimental specific conditions and results.

Experimental results in Table 1 show that condensation can be determined from the three regions shown in Fig. 5, when the ambient humidity remains unchanged. The regions may move up or down when the ambient humidity changes dramatically.

The experimental results obtained with systems of different volumes and discharge pipes of different inner diameters and lengths are shown in Fig. 5 including a total of 385 experimental points. The abscissa is a combination of structural parameters of the system instead of a single physical system. A combination may represent several physical systems (3–4 in this paper). It can therefore be concluded that the experimental results in the internal condensation region ①, no condensation region ② and external condensation region ③ have their generality.

The experimental results in Fig. 5 were obtained when the air supply conditions and the environmental factors were fixed values. If these air supply conditions and the environmental conditions change, the experimental results may change. The authors' primary research indicated that there is a borderline between the condensation region and the no condensation region, and the borderline may move in parallel according to the air supply conditions and the environmental factors.

5 Conclusion

In this paper, analytic equations for the first necessary condition and the second necessary condition are proposed to predict condensation in a pneumatic system. Only the structural size & shape of system components and the initial characteristics of the compressed air are needed to determine the maximum humidity and stroke during discharging. If the maximum humidity equals 100%, and the system satisfies the first necessary condition, droplets are produced in the system. When the stroke is less than or equal to the length of the discharging pipe, the system satisfies the second necessary condition. In this condition, the droplets produced by satisfying the first necessary condition stay in the system and internal condensation occurs.

Experimental results indicate that the experimental points for internal condensation, external condensation and no condensation create an regular pattern on the plane formed by the dimensionless volume and average velocity of discharging pipes, and this pattern can be used for prediction of condensation in a pneumatic system.

Nomenclature

a = Speed of sound
A = Cross section of pipe
A_1 = Effective sectional area at the outlet of container
d = Inside diameter of pipe
d_1 = Internal diameter of orifice at outlet of container
k = Specific heat ratio
K = Thermal conductivity of fluid
L = Pipe length
p = Pressure
P = Laplace's transform of pressure
p_a = Ambient pressure
p_0 = Pressure step value
p_s = Initial system pressure
$p_\infty(T)$ = Saturated vapor pressure in infinite plane
$P_0(s)$ = Quadrant function of disturbing pressure
q = Mass flow rate
Q = Laplace's transform of mass flow rate
R = Flow resistance of pipe
R_e = Reynolds number
R_g = Gas constant
R_l = Flow resistance at the end of pipe
R_T = Turbulent resistance
R_0 = Flow resistance at the beginning end of pipe
s = Laplacian
S = Stroke
s_0 = General parameter of system
$\bar{S}$ = Dimensionless stroke
T = Temperature
u = Axial velocity
u_m = Average velocity of air
V = Volume of container
Y = Parallel admittance
Z = Series impedance
Z_c = Characteristic impedance of pipe
$Z_l(s)$ = Flow impedance at the end of pipe
$Z_0(s)$ = Flow impedance at the beginning end of pipe
Γ = Propagation constant
η = Reflectance for flow resistance at the end of pipe
ν = Kinematic viscosity
ρ = Density
ρ_s = Initial density of system
τ = Propagation time of wave
φ = Relative humidity
χ_0 = Initial absolute humidity

Coordinate: x-axial coordinate, r-radial coordinate, t-time coordinate.
Subscript: 0-parameter at the beginning end of pipe, L-parameter at the end of pipe, s-Initial parameter.

References

[1] Zhang, Hu-ping, 1995, "Study on Condensation of Water Vapor in Pneumatic Systems" (in Japanese), Sophia University Doctoral dissertation (Japan), Tokyo, Japan.

[2] Wang Zu-wen, 1991, "Study on the Condensation in Pneumatic System" (in

Japanese), SMC Technical Papers (Japan), ER-STM-91-5, Tokyo, Japan, pp. 1–2.
[3] Luo Zhi-chang, 1988, ''Fluid Grid Theory'' (in Chinese), China Machine Press, Beijing, China.
[4] Zhou, Jin-Shang, 1982, ''Basic Atmosphere Physics,'' (in Chinese), Meteorology Press, Beijing, China.
[5] Zhang, Hu-Ping, 1993, ''Study on the condensation of Water in a pneumatic System,'' Proceeding of the Second JHPS International Symposium on Fluid Power. Tokyo, Japan.
[6] Hydraulic and Pneumatic Industry Academic of Japan, 1985, ''Practical Pneumatic Technology,'' (in Japanese), Industry press of Japan, Tokyo, Japan.

Takero Hirochi
e-mail: hiro@toba-cmt.ac.jp
Toba National College of Maritime Technology,
1-1 Ikegami,Toba, Japan

Yasuhiro Maeda

Shuichi Yamada

Masataka Shirakashi

Masaru Hattori

Nagaoka University of Technology,
1603-1 Kamitomioka,
Nagaoka, Japan

Akihiro Saito
Niigata Technical College,
1719 Fujihashi, Kashiwazaki, Japan

Flow Patterns of Ice/Water Slurry in Horizontal Pipes

The authors have observed flow patterns of ice/water slurry flow through horizontal circular pipes, and measured pressure loss for small diameter pipes, using three classes of ice particles. The slurry flows are classified into three patterns, dispersed-particle flow, cluster flow, and column flow. They are presented on a plane of two dimensionless parameters, the ice fraction f and the ratio of mixing energy to cohesion energy, π_{mix}. The pressure loss for small diameter pipes is estimated accurately by the formula proposed in previous studies by the present authors based on experimental data for larger pipes. [DOI: 10.1115/1.1760541]

1 Introduction

A new cool thermal energy transportation system utilizing ice/water mixture flow is under development to increase the energy carrying capacity of the medium in future district cooling systems. Many experimental studies have been conducted to clarify the flow and heat transfer characteristics of ice/water slurry [1–4]. In a previous study, the present authors have shown that the flow pattern of an ice-particle (or snow)/water mixture in a circular pipe is quite different from the usual flow of a solid-particle/water slurry flow due to the cohesive nature of the ice-particles. The authors proposed experimental formulas to predict pressure losses through horizontal and vertical pipes [4]. However, the parameters governing the various flow patterns specific to ice/water slurry are still unclear because a reliable method to estimate the cohesion strength of ice particles in water has not been developed. In addition, pressure loss data are still lacking for small diameter pipes, with an inner diameter of approximately 25 mm, commonly used to supply cool thermal energy to the terminal consumers in practical district cooling systems.

The specific aim of the present work is to investigate the relationship between flow patterns and cohesion strength, and to give a formula estimating pressure loss in such small diameter pipes.

2 Samples

Three types of ice particles of different size are used as samples because the cohesion strength depends strongly on particle size. Polypropylene beads with size and density comparable to those of the ice particles are also used for comparison. Photographs of the samples are shown in Fig. 1. The mean diameters d_p and densities ρ of the samples are:

a. Chipped ice ($d_p = 10$ mm, $\rho = 917$ kg/m^3), made in a commercial refrigerator;

b. Granulated snow ($d_p = 3$ mm, $\rho = 917$ kg/m^3), gathered from local spots in winter or made by cracking ice chips, and sieved out in each case. The sieve mesh size is 5 mm;

c. Fresh snow ($d_p = 1$ mm, $\rho = 917$ kg/m^3), gathered within 24 hours after snowfall; and;

d. Polypropylene beads ($d_p = 4$ mm, $\rho = 908$ kg/m^3), used as reference because of their non-cohesiveness.

3 Cohesion Strength

The cohesion strength of ice particles in a slurry flow should be defined as resistance stress, which could be obtained by a tensile or shearing test performed in 0°C water on a test piece formed with ice particles. However, such tests were unsuccessful because the ice-particle test pieces were not strong enough to bear the tensile or shearing tests. So far, only the compression test on a cylindrical test piece devised earlier by the present authors [5] could provide definite information on the value of cohesion strength among ice particles. Therefore, compressive yield stress is used in this paper as a measure of the cohesive nature of ice particles.

Figure 2 shows the ice particle cylinder compression test procedure. The test piece is formed in the air by softly and naturally packing the particles in a circular pipe mold with an inner diameter of 65 mm and a length of 65 mm. It is placed on the bottom of vacant cold-water bath, and the mold is removed leaving the test piece without giving deformation to the test piece, as shown in Fig. 2 (1). A ram suspended by two setting pins is put on the upper surface of the test piece without adding load on it (Fig. 2 (2)). After adding 0°C water to fully submerge the test piece as in Fig. 2 (3), the load w is added abruptly by pulling off the setting pins (Fig. 2 (4)).

In the case of chipped ice, the test piece scatters into particles upon submersion in water. Hence, the yield stress of chipped ice test piece can be estimated by the following equations, assuming that it is broken by the compression due to the buoyancy:

$$\sigma_y \leqq V_i(\rho_w - \rho_i)g/(\pi d_0^2/4), \tag{1}$$

$$V_i = f(\pi d_0^2/4)h_0, \tag{2}$$

where,
V_i : substantial volume of ice in a test piece;
f : ice packing fraction in volume;
=0.5 for the chipped ice;
ρ_w : density of water;
ρ_i : density of ice;

Contributed by the Fluids Engineering Division for publication in the JOURNAL OF FLUIDS ENGINEERING. Manuscript received by the Fluids Engineering Division August 3, 2003; revised manuscript received December 19, 2003. Associate Editor: D. Siginer.

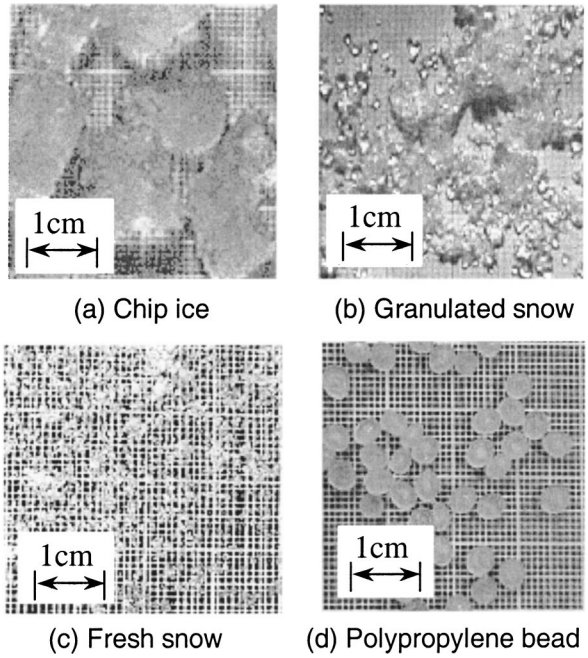

Fig. 1 Test particles

d_0: initial diameter of test piece; and,
h_0: initial height of test piece.

The granulated and fresh snow test pieces are compressed slightly while their diameter remains unchanged when the load w is small. When w is increased, the upper part of the test pieces are crushed into particles and the lower part with a height h remains almost unchanged in diameter. When w is larger than a certain value, the test piece is completely crushed into particles. Since this fracture behavior of the ice-particle cylinder in the compression test resembles that of brittle materials, it seems reasonable to assume that the compressive yield stress σ_y in the compression test is proportional to the shearing yield stress τ_y from the theory of strength of materials. Hence, the following values of σ_y determined from the results of the compression test is used in Section 5.2 as the measure of the cohesion strength of ice particles, since the relative magnitude is needed for the dimensional analysis.

Figure 3 shows the relationship between the compression ratio

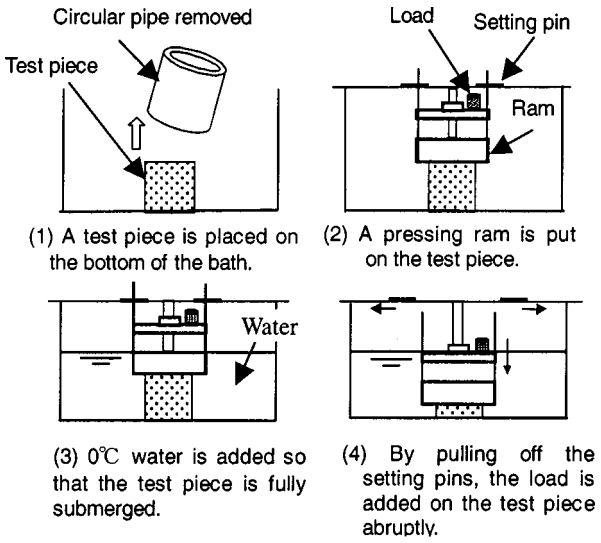

Fig. 2 Procedure of the compression test

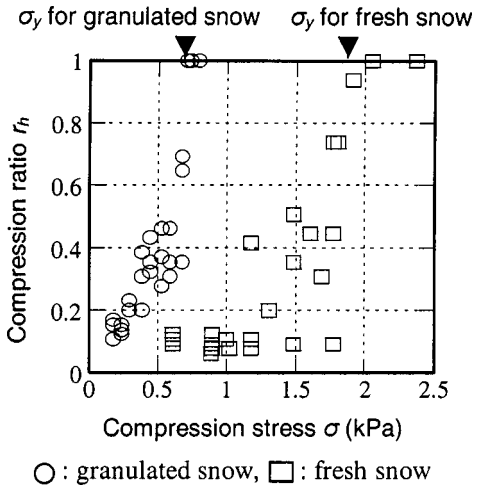

Fig. 3 Relationship between compression ratio r_h and compressive stress σ

r_h and the compression stress σ defined by

$$r_h = (h_0 - h)/h_0, \tag{3}$$

$$\sigma = w/(\pi d_0^2/4), \tag{4}$$

where
h: test piece height after adding the load w.

The initial diameter d_0 is used to define the stress σ, since the change in diameter is small during compression.

The data in Fig. 3 scatter considerably due to the fact that the size and shape of the ice particles are not so precisely controlled. However, the magnitude of σ is definitely different for the granulated and the fresh snows. The compressive yield stress σ_y is determined as the lowest value of σ at $r_h = 1$, i.e. when the test piece is crushed completely.

The compressive yield stresses of test pieces are thus determined as indicated in Fig. 3, giving the following values:

a. Chipped ice, $\sigma_y \leqslant 0.03$ kPa,
b. Granulated snow, $\sigma_y = 0.7$ kPa,
c. Fresh snow, $\sigma_y = 1.9$ kPa.

In the following analysis, we use the maximum value, 0.03 kPa, for chipped ice.

4 Experimental Apparatus for Pipe Flow

The flow pattern of ice/water slurry flow through horizontal circular pipes was observed and the pressure loss was measured for three small diameter pipes, with an inner diameter of $D = 26$, 35, 50 mm. As seen in Fig. 4, the motion of ice particles was recorded by a video camera mounted on a carrier moving with a velocity equal to the flow velocity.

Transparent acrylic pipes, used for the observing section, were set in a square-cross-section jacket filled with water to remove lens effect.

The ice-fraction f was measured by an instrument developed by the present authors based on the electric conductivity method [6]. The flow rate of slurry Q was measured by an electro-magnetic flow meter and the flow velocity U was defined as $U = 4Q/(\pi D^2)$. The pressure difference between two 1 mm diameter pressure holes set at the upstream and downstream ends of the test section was measured using a pressure transducer.

5 Flow Patterns

5.1 Observation of Flows. Figure 5 shows three flow patterns for chipped ice/water slurry with an ice fraction $f = 20\%$, in

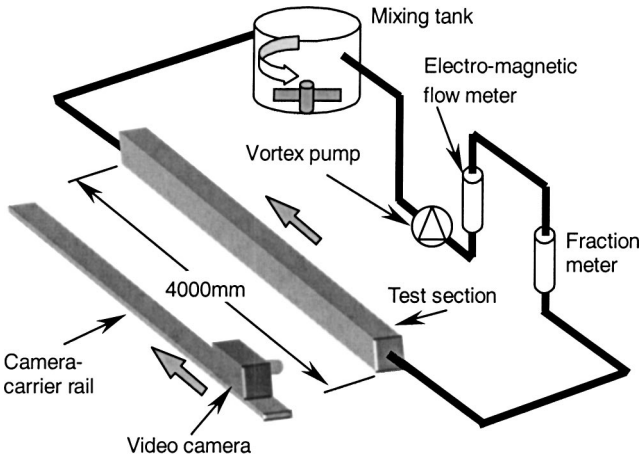

Fig. 4 Pipeline diagram

a pipe with an inner diameter $D=35$ mm. The frames were taken at 0.3 s intervals by a camera moving at the same speed as that of the flow. The flow direction is from right to left, and the flow velocity was decreased gradually from (*a*) to (*c*). The diagram at the bottom of each column illustrates the flow pattern.

When the flow velocity U is high enough, ice particles do not coalesce and dispersed particles move separately, as seen in Fig. 5(*a*). When a particle approaches the pipe wall, another moves from the wall to the center simultaneously, showing that ice particles are carried by the mixing motion of turbulent vortices.

At a medium velocity (Fig. 5(*b*)), ice particles coalesce to form clusters, which move with velocity U in the pipe at positions somewhat closer to the upper wall due to their buoyancy, keeping their shape almost unchanged.

When the velocity is even lower, the clusters coalesce and become axially continuous, forming a column as seen in Fig. 5(*c*). This ice-particle column also moves with a velocity U and its shape does not change during the observation period.

When the ice fraction is very high, the ice-particle column fills the whole cross section of the pipe and becomes a solid bar with considerable strength. An example of this flow, which was observed at the outlet of a test plant pipeline for the hydraulic conveying of snow, is shown in Fig. 6. A long solid snow-particle column is seen to flow out continuously at the pipe exit, which, subsequently, is broken into pieces due to gravity.

Figure 7 shows the slurry flow of polypropylene particles (some beads are colored for observation), which have a density close to that of ice, but not the cohesive nature. At a high flow velocity the motion of ice particles and polypropylene beads is similar, as seen by comparing Fig. 5(*a*) and Fig. 7. However, the flow patterns of the ice-particle slurry at lower flow velocities, as seen in Fig. 5(*b*) and (*c*), were not observed for the polypropylene-bead slurry flow. Gravity plays an important role in non-cohesive, coarse particle slurry, as demonstrated by the bead slurry. Their flow patterns can be classified into categories related to pressure loss and velocity as shown in Fig. 8 [7]. In ice/water slurry flows, gravity has only a slight influence and the flow patterns are quite different due to particle cohesion at low flow velocities.

In ice/water slurry, ice particles were moving at almost the same velocity, irrespective of the flow velocity and ice fraction. This behavior is quite different from that of ordinary rigid-particle/water slurry, in which the particles are likely to deposit on the bottom of pipes and to accumulate, creating stationary or slowly moving layers.

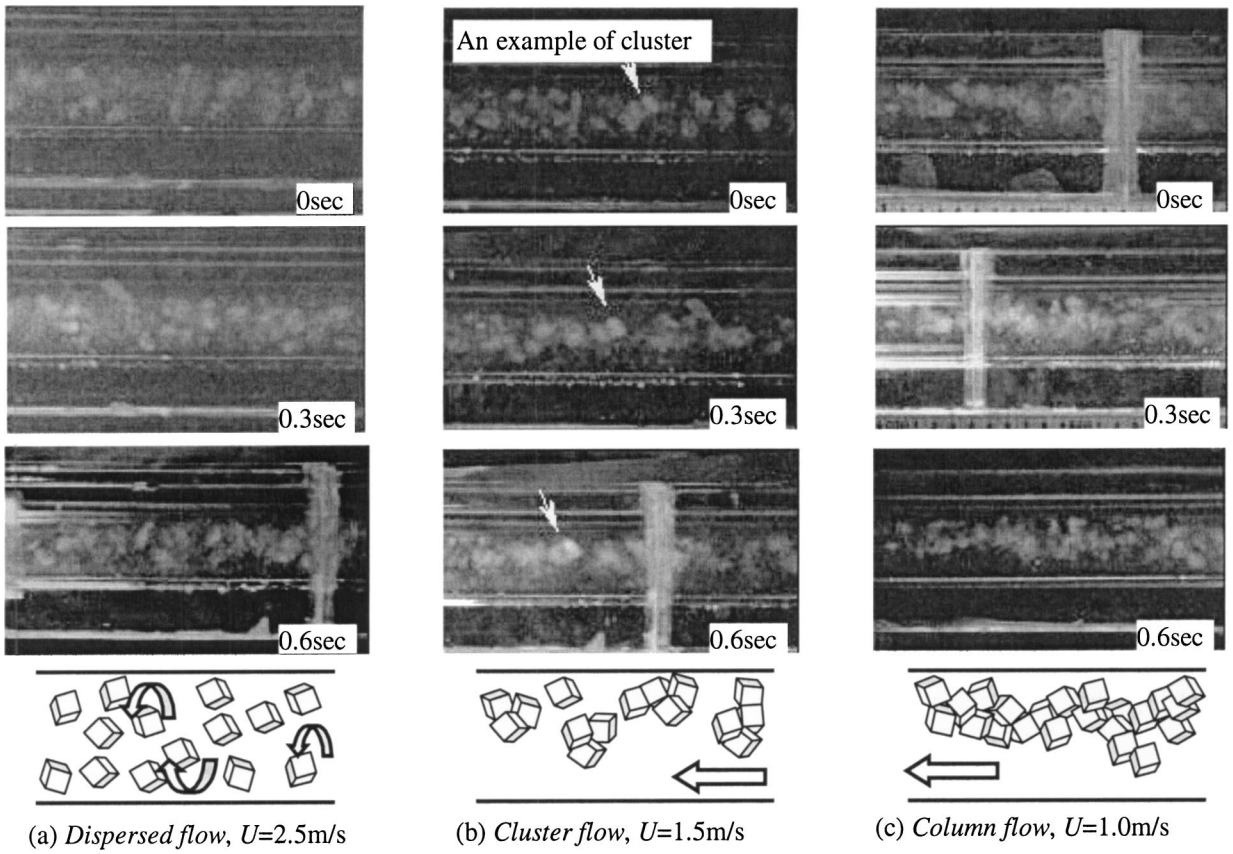

Fig. 5 Flow pattern of ice/water slurry for chipped ice ($D=35$ mm, $f=20\%$)

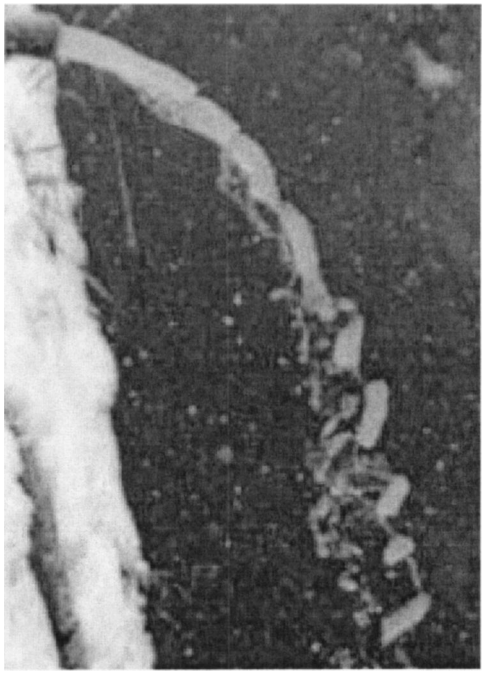

Fig. 6 High ice-fraction column flow at a pipeline outlet

Consequently, ice/water slurry flow can be classified into the following three patterns:

1. *Dispersed-particle flow*: Ice particles do not coalesce, moving separately. This is equivalent to the pseudohomogeneous flow of ordinary solid/liquid slurry two-phase flow, as shown in Fig. 8.
2. *Cluster flow*: Ice particles coalesce to form clusters and flow through a pipe, keeping their shapes un-deformed.
3. *Column flow*: The clusters coalesce to form an axially continuous column. In the case of high fraction, this flow becomes a cylindrical rigid body filling the pipe.

The transition of these patterns with a drop in pressure is shown in Fig. 9. When the flow velocity is decreased from a high enough value, the flow pattern changes from *dispersed-particle flow to cluster flow*, and then to *column flow*. Given the same pipe diameter D and particle diameter d_p, the boundary values of velocity decrease with ice fraction f.

When Fig. 8 is compared with Fig. 9, two remarkable differences can be found between them:

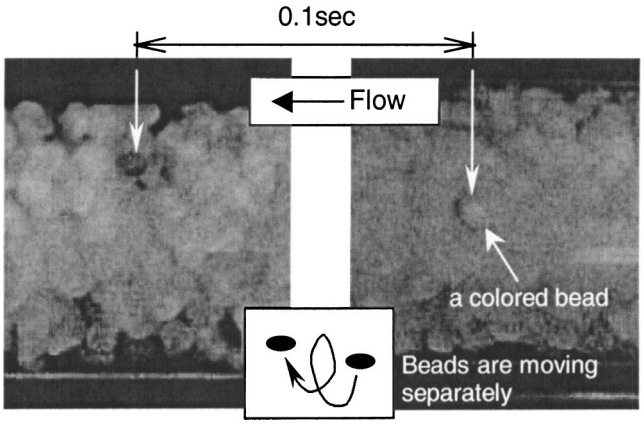

Fig. 7 Pseudo-homogeneous flow of beads (D=35 mm, U=1.5 m/s, f=20%) (The camera is moving with the flow)

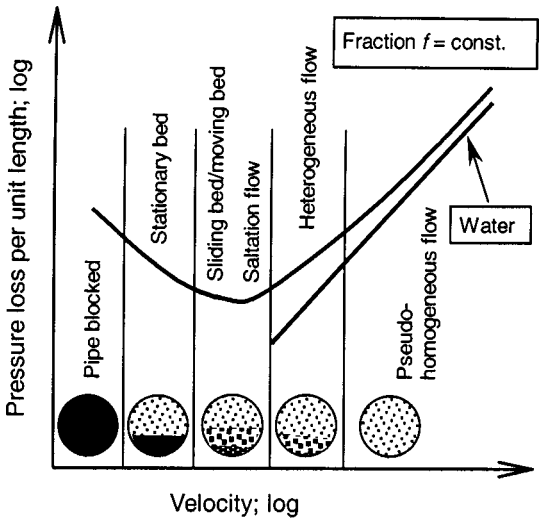

Fig. 8 Usual solid/liquid two-phase flow patterns

1. The saltation and the stationary bed flows in Fig. 8 are not observed in ice/water slurry, however, the cluster and the column flows appear instead.
2. The pressure loss of the ice/water slurry increases with the velocity, i.e., no minimum appears in the pressure loss curve. This profile of the pressure drop curve also suggests that the cohesive nature of ice-particle dominates the ice/water slurry flow, while gravity is dominant in ordinary solid/liquid slurry flow.

5.2 Dimensionless Numbers. Usually the Froude number Fr is adopted as the parameter dominating the patterns of solid/liquid flows, as Fr is the ratio of the agitating effect of flow to the settling effect of particles due to gravity. However, observation of ice/water slurry flows shows that the influence of gravity is small and the cohesion of ice is dominant. Hence, in addition to the ice fraction f, a new dimensionless parameter that includes the cohesion strength of ice particles must be introduced for ice/water slurry.

For this purpose, a flow condition is assumed to be specified by pipe diameter D, flow velocity U, ice fraction f, ice particle diameter d_p, and its cohesion strength τ_y. Where particles are dispersed over the entire pipe cross-section, as in Fig. 10, the energy required to disperse particles for pipe length L is

$$E_{mix} = SD\tau_y \tag{5}$$

where

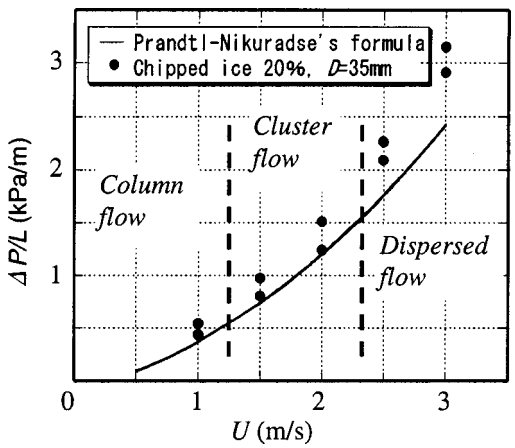

Fig. 9 Pressure loss and flow patterns vs. velocity

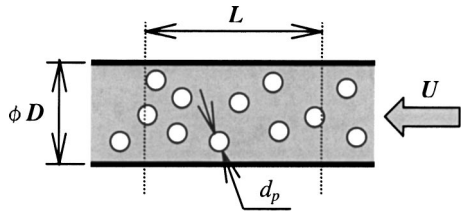

Fig. 10 Schematic diagram of flow

S: Total of surface of dispersed particles

If we denote the volume of an ice particle by v_p and its surface s_p, then the total volume of ice particles V_i and their total number N_i are,

$$V_i=(\pi/4)D^2Lf \tag{6}$$

$$N_i=V_i/v_p \tag{7}$$

Hence,

$$S=s_pN_i=s_p(V_i/v_p)=(\pi/4)D^2Lf(s_p/v_p) \tag{8}$$

By substituting Eq. (8) into Eq. (5) and representing the energy in terms of unit volume, we have

$$e_{mix}=E_{mix}/((\pi/4)D^2L)=Df\tau_y(s_p/v_p) \tag{9}$$

The ratio of surface to volume s_p/v_p depends on the shape of the particles and distribution of particle size. If all of the particles are spheres with identical diameters, then $s_p/v_p=6/d_p$. Hence, it is assumed that s_p/v_p is proportional to $1/d_p$ with d_p defined as the mean particle diameter. Since e_{mix} is the energy required to disperse the particles per unit volume, the ratio of agitating energy of flow $\rho_wU^2/2$ to e_{mix} can be a parameter governing the flow patterns. According to the conventional definition of the Froude number, a non-dimensional parameter is defined as the square-root of the ratio by the following equation:

$$\pi_{mix}=\sqrt{((\rho_wU^2d_p)/(f\sigma_yD))} \tag{10}$$

Here, the cohesion strength τ_y is replaced by σ_y, the compressive yield stress, and proportional factors are neglected because they are not essential.

The flow patterns observed in this work, i.e. for pipes with diameters $D=26$, 30, 50 mm and three kinds of ice particles, are all plotted on the $\pi_{mix}-f$ plane in Fig. 11. The results for a $D=80$ mm pipe obtained in the earlier work on the hydraulic conveying of snow [8] are also included in Fig. 11. The regions of the three flow patterns are well separated in the plane irrespective of D. However, the consistency is rather poor among slurries of different particles. This may be attributed to the fact that the size and shape of ice particles cannot be represented accurately by the mean diameter d_p, and that σ_y obtained by the compression test does not closely represent the cohesion strength of particles in slurry flow.

6 Pressure Losses

Pressure loss data are reduced to the excess pressure loss coefficient ϕ, and plotted against the Froude number Fr, defined by the following equations:

$$\phi=(i-i_w)/(fi_w) \tag{11}$$

$$Fr=U^2/(gD|1-s|) \tag{12}$$

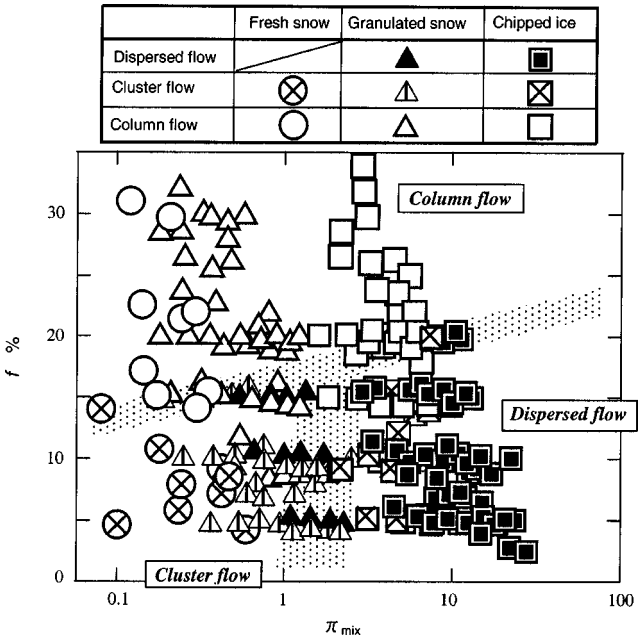

Fig. 11 Flow patterns of ice/water slurry (D=26,30,50,80 mm) (Particles: fresh snow, granulated snow, and chipped ice)

where

- i: pressure drop per unit length for mixture flow;
- i_w: pressure loss per unit length for water flow;
- f: ice fraction;
- U: mean velocity;
- g: acceleration due to gravity;
- D: inner pipe diameter; and,
- s: specific density of ice (=0.917).

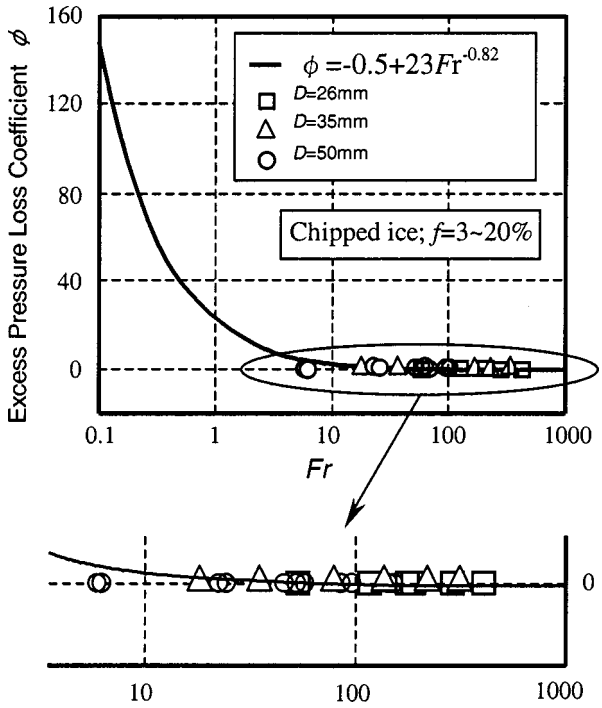

Fig. 12 Excess pressure loss coefficient

Figure 12 shows the excess loss coefficient of chipped ice/slurry for the three pipes with inner diameter $D=26$, 35, 50 mm. The results of the other slurries, i.e. fresh snow, granulated snow and polypropylene bead, collapsed on the same region, and are thus omitted here. The solid line represents the following empirical formula obtained from experiments using larger PVC pipes, $D=80$ mm [4]:

$$\phi = -0.5 + 23Fr^{-0.82} \tag{13}$$

Results of the present work, seen in Fig. 12, agree strongly with the solid line regardless of particle type and pipe diameters. The pressure loss is almost the same as that of pure water because *Fr* is large in this experiment due to small pipe diameter. To be noted is that the pressure loss for the chipped ice slurry, whose diameter (10 mm) is nearly half the pipe diameter, is almost the same as that of pure water.

Note that when *Fr* is larger than 106, Eq. (13) becomes negative, that is, pressure loss becomes smaller than that of pure water flow. This phenomenon has been confirmed in some studies of solid/liquid flow [9,10]. As the experimental results may have some dispersion in our ice/water slurry, the critical value is not strictly 106.

7 Conclusions

The conclusions of this work are summarized below:

1. The flow behavior of ice/water slurry in pipes is quite different from usual solid-particle/liquid slurries due to the cohesion strength among ice particles.
2. The flows of the ice/water slurry are classified into three patterns: *column flow, cluster flow* and *dispersed-particle flow*. While the dispersed-particle flow is equivalent to the pseudo-homogeneous flow, the column and the cluster flows are characteristic of ice/water slurry, and are not observed in ordinary solid/liquid flow.
3. The criteria of these flow patterns are presented on a plane of two dimensionless parameters, i.e. the ice-fraction *f* and the mixing parameter π_{mix}.
4. The pressure loss of ice/water slurry through small diameter pipes, say two or three times larger than the particle diameter of chipped ice, is predicted accurately by the formula previously proposed by the present authors [11].

References

[1] Larkin, B., and Young, J. C., 1989, ''Influence of ice slurry characteristics on hydraulic behavior,'' Proc. 80th Annual. Conf. IDHCA, pp. 340–351.
[2] Onojima, H., Takemoto, Y., Fukushima, M., and Takemoto, K., 1991, ''A study on the hydraulic transportation of ice-water mixture for district cooling system,'' Proc. 1st ASME/JSME Fluids Eng. Conf., 118, pp. 241–246.
[3] Winters, P. J., and Kooy, R. J., 1991, ''Direct freeze ice slurry district cooling system evaluation,'' Official Proc., Annunciation Conference of IDHCA, 18, pp. 381–398.
[4] Kawada, K., Shirakashi, M., and Yamada, S., 2001, ''Flow characteristics of ice/water slurry in a horizontal circular pipe,'' SEPPYO, **63**, pp. 11–19.
[5] Hirochi, T., Yamada, S., and Shirakashi, M., 2002, ''Cohesive nature of ice particles and blocking phenomenon of ice/water slurry,'' J. the Japanese Society of Snow and Ice; SEPPYO, **64-4**, pp. 453–460.
[6] Kitahara, T., Shirakashi, M., and Kajio, Y., 1993, ''Development of a snow-fraction meter based on the conductometric method,'' Ann. Glaciol., **18**, pp. 60–64.
[7] Masuyama, T., 2000, ''Measurement of solid concentration in solid-liquid two-phase flow in pipes,'' Japanese J. Multiphase Flow, **14-3**, pp. 263–292.
[8] Kawada, Y., Shirakashi, M., and Takahashi, S., 1996, ''Characteristics of ice/water mixture flow in horizontal circular pipes,'' Proc. 9th International Symposium on Transport Phenomena in Thermal-Fluids Engineering, Singapore, pp. 909–914.
[9] Shirakashi, M., Tokunaga, Y., and Hashimoto, T., 1987, ''Pressure loss reduction due to mixing of coarse particles in a pipe flow,'' Bull. JSME, **53–490**, pp. 1672–1676.
[10] Knodel, B. D., France, D. M., Choi, U. S., and Wambsganss, M. W., 2000, ''Heat transfer and pressure drop in ice-water slurries,'' Appl. Therm. Eng., **20**, pp. 677.
[11] Shirakashi, M., Kawada, Y., and Takahashi, S., 1995, ''Characteristics of ice/water slurry mixture in horizontal circular pipe,'' Bull. JSME, **61–585**, pp. 1632–1639.

A Numerical Analysis of Vapor Flow in Concentric Annular Heat Pipes

A. Nouri-Borujerdi
e-mail: anouri@sharif.edu

M. Layeghi

School of Mechanical Engineering,
Sharif University of Technology,
P.O. Box 11365-9567,
Tehran, Iran

A numerical method based on the SIMPLE algorithm has been developed for the analysis of vapor flow in a concentric annular heat pipe. The steady-state response of a concentric annular heat pipe to various heat fluxes in the evaporator and condenser sections are studied. The fluid flow and heat transfer in the annular vapor space are simulated using Navier-Stokes equations. The governing equations are solved numerically, using finite volume approach. The vapor pressure and temperature distributions along a concentric annular heat pipe are predicted for a number of symmetric test cases. The vapor flow reversal and transition to turbulence phenomena are also predicted. The results are compared with the available numerical data and have shown good agreement in all cases. Therefore, the vapor flow model developed in this paper has shown good accuracy and convergence behavior in the range of low to moderate radial Reynolds numbers.
[DOI: 10.1115/1.1760549]

1 Introduction

Heat pipes are the most effective passive method of transferring heat available today. Heat pipes can transmit heat at high rates and have a very high thermal conductance. They can transfer heat with low temperature drop and quick response time in a wide range of temperature.

A concentric annular heat pipe (CAHP), as shown in Fig. 1, consists of two concentric pipes of different diameters attached to each other by means of end caps, which create an annular vapor space between the two pipes. Wick structures are placed on both the inner surface of the outer pipe and the outer surface of the inner pipe. There are, however, only a limited number of works concerning the CAHP in the literature. CAHPs are more effective than conventional heat pipes and can be used in many applications including energy conversion systems, cooling of diesel-engine pistons [1], cooling of electronic equipments [2], air conditioning devices, heat recovery systems, furnace applications, high performance space applications, temperature and humidity control, etc.

The vapor flow in heat pipes has been investigated by various authors in the past 40 years. A basic theory was developed by Cotter [3] which has been used since then as a basis for heat pipe design. The flow of vapor was studied in one-dimensional form by Busse [4]. Bankston and Smith [5] modeled the flow of vapor using the stream function and vorticity formulation and determined numerically the pressure and velocity ditributions. Rohani and Tien [6] studied the influence of pressure drop on the temperature distribution in heat pipes using sodium as a working fluid. In their analysis the momentum equations were used in terms of stream function and vorticity coupled with the energy equation in terms of enthalpy. Chi [7], Dunn and Reay [8], and Faghri [9] have published many techniques, theories and applications of different heat pipe structures. Faghri [10] analyzed a two-dimensional, steady and incompressible flow of vapor in a CAHP. A parabolic form of the governing equations of motion was used for the solution of the vapor flow in the evaporator, adiabatic, and condenser sections of the heat pipe. He assumed a zero axial velocity at the evaporator inlet and a fully developed profile at the inlet of the adiabatic and condenser sections. Due to these assumptions, an implicit marching finite difference method is possible. Faghri and Parvani [11] have also studied all features of the laminar vapor flow in a CAHP using a complete two-dimensional incompressible model. Faghri [12,13] also compared various models for vapor flow analysis in the CAHPs. He found that there is no substantial difference between the parabolic and elliptic models but the elliptic model provides more complete simulation of vapor flow than the parabolic model. He experimentally compared the performance characteristics of a copper-water CAHP with a conventional one with the same outer diameter. He reported 80 percent increase in heat transfer for the CAHP case.

In this paper, a numerical method based on an innovative SIMPLE algorithm has been used for the analysis of vapor flow in the CAHPs. Here, the main object is the verification of this innovative SIMPLE algorithm and not dealing with the physics of the operation in annular heat pipes or making some developments in the previous models. The algorithm is developed based on a staggered grid system in order for the study of the dynamics of incompressible vapor flow at low and moderate radial Reynolds numbers in annular heat pipes, for both symmetric and asymmetric heat addition or rejection conditions. Symmetric heat addition and rejection condition is a condition such that all radial Reynolds numbers in the evaporator and condenser sections are the same. Any other condition is considered as an asymmetric condition. QUICK differencing scheme [14] due to its higher accuracy are used for the treatment of convective fluxes, while central differencing scheme is employed for diffusive fluxes. The vapor pressure and temperature distributions along a CAHP are predicted for a number of symmetric and asymmetric test cases. The vapor flow reversal and transition to turbulence are also predicted. The proposed SIMPLE algorithm has shown good convergence behavior at low and moderate radial Reynolds numbers, and even near the transition to turbulence.

2 Governing Equations

If we introduce a general variable ϕ, the conservative form of mass, momentum and energy equations for a laminar steady vapor flow in cylindrical coordinate system can be written in a general form as:

$$\frac{1}{r}\frac{\partial}{\partial r}\left[r\left(\rho v\phi-\Gamma_\phi\frac{\partial\phi}{\partial r}\right)\right]+\frac{\partial}{\partial z}\left[\rho w\phi-\Gamma_\phi\frac{\partial\phi}{\partial z}\right]=S_\phi \quad \text{for} \quad \phi=1,w,v,T \tag{1}$$

where Γ_ϕ and S_ϕ for various conservation equations are given in Table 1.

Contributed by Fluids Engineering Division for publication in the JOURNAL OF FLUIDS ENGINEERING. Manuscript received June 9, 2003; revised manuscript received December 11, 2003. Associate Editor: F. Grinstein.

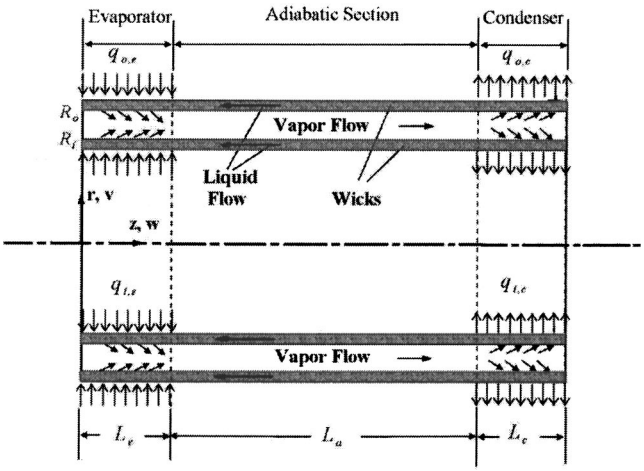

Fig. 1 Schematic of a CAHP and coordinate system

k and C_p are thermal conductivity and heat capacity of the vapor at constant pressure respectively. The boundary conditions of the vapor flow in the annular space are defined as follows (Fig. 1).

$$w(0,r)=v(0,r)=0, \tag{2a}$$

$$w(L,r)=v(L,r)=0, \tag{2b}$$

$$w(z,R_i)=w(z,R_o)=0 \tag{2c}$$

$$v(z,R_i)=V_i(z), \tag{2d}$$

$$v(z,R_o)=V_o(z), \tag{2e}$$

$$P(0,r)=0 \tag{2f}$$

if the end caps of the heat pipe are insulated, then

$$\frac{\partial T}{\partial z}(0,r)=\frac{\partial T}{\partial z}(L,r)=0 \tag{2g}$$

where $L=L_e+L_a+L_c$.

The evaporation and condensation are modeled as a uniform injection and suction at the liquid-vapor interface with no phase change assumption.

In this case, the radial blowing and suction velocities at the inner and outer liquid-vapor interface are computed as:

$$V_j(z)=\begin{cases}\pm V_{j,e} & if\ \ 0<z<L_e\\ 0 & if\ \ L_e<z<L_e+L_a\\ \mp V_{j,c} & if\ \ L_e+L_a<z<L\end{cases} \tag{3}$$

$$V_{j,e}=\frac{\dot{q}_{j,e}}{2\pi R_j L_e \rho h_{fg}}, \tag{4a}$$

Table 1 Γ_ϕ and S_ϕ for various conservation equations

Equation	ϕ	Γ_ϕ	S_ϕ
continuity	1	0	0
z—momentum	w	μ	$-\frac{\partial p}{\partial z}$
r—momentum	v	μ	$-\frac{\partial p}{\partial r}-\mu\frac{\partial}{r^2}$
energy	T	$\frac{k}{C_p}$	S_T

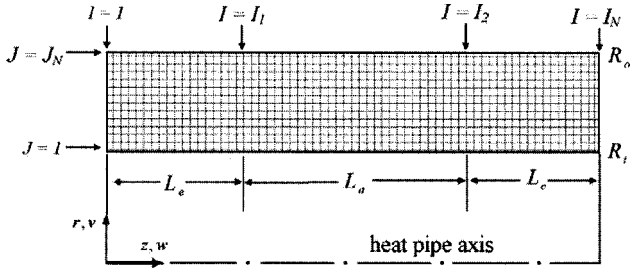

Fig. 2 Grid arrangement in the vapor flow domain

$$V_{j,c}=\frac{\dot{q}_{j,c}}{2\pi R_j L_c \rho h_{fg}} \tag{4b}$$

the subscript $j=i$, o indicates the locations of the prevailing velocities and heat transfer at the inner and outer walls, respectively. $\dot{q}_{j,e}$ and $\dot{q}_{j,c}$ are heat addition to the evaporator and heat rejection from the condenser sections, respectively. $\pm$ signs express the direction of the radial blowing and suction velocities.

The temperature at the vapor-liquid interface of the evaporator and condenser is calculated approximately using Clausius-Clapeyron equation.

$$T_{\text{int}}=\frac{1}{\frac{1}{T_{sat}}-\frac{R}{h_{fg}}\ln\frac{P}{P_{sat}}} \tag{5}$$

P_{sat} and T_{sat} are taken as a reference point and are equal to the condition of the vapor-liquid interface at the end of the evaporator. R is the vapor constant.

3 Method of Solution

The governing equations are discretised using a finite volume approach. Only axial symmetric by the annular vapor space is considered in the numerical analysis (Fig. 2). For the numerical analysis a uniform mesh size is used with 40×80 cells for the results of Fig. 4 and with 40×200 for other figures.

Typical computational cells for a scalar and vector variables are shown in Fig. 3. Node *P* is located at the center of the central cell and nodes *E, W, S and N* are located at the center of the neighboring cells. Nodes *EE, WW, SS and NN* are the neighboring nodes of *E, W, S,* and *N*. To yield a discretized equation at a nodal point *P*, multiplying Eq. (1) by r and integrating over the two-dimensional control volume of the cell *P* gives:

$$\int_w^e\left\{\left[r\left(\rho v\phi-\Gamma_\phi\frac{\partial\phi}{\partial r}\right)\right]_n-\left[r\left(\rho v\phi-\Gamma_\phi\frac{\partial\phi}{\partial r}\right)\right]_s\right\}dz + \int_s^n r\left\{\left[\left(\rho w\phi-\Gamma_\phi\frac{\partial\phi}{\partial z}\right)\right]_e-\left[\left(\rho w\phi-\Gamma_\phi\frac{\partial\phi}{\partial z}\right)\right]_w\right\}dr = \int_w^e\int_s^n rS_\phi dz dr \tag{6}$$

The face values in diffusion and convective terms are discretized by using the central and QUICK differencing schemes [14], respectively. For example, these values for east face of the cell ρ will be

$$\left(\Gamma_\phi\frac{\partial\phi}{\partial z}\right)_e=\Gamma_e\frac{\phi_E-\phi_P}{z_E-z_P} \tag{7}$$

$$F_e\phi_e=\left(\frac{6}{8}\phi_P+\frac{3}{8}\phi_E-\frac{1}{8}\phi_W\right)F_e^+ +\left(\frac{6}{8}\phi_E+\frac{3}{8}\phi_P-\frac{1}{8}\phi_{EE}\right)F_e^- \tag{8}$$

Similar expressions are used for the other faces. Substituting Eqs. (7,8) into Eq. (6), the final generalized discretization equation is as follows.

$$a_P\phi_P=\sum_{nb} a_{nb}\phi_{nb}+b_\phi \tag{9}$$

where the subscript *nb* refers to the neighboring nodes of the node *P*. Finally, the following coefficients are derived.

$$a_E=D_e-\frac{3}{8}F_e^+-\frac{6}{8}F_e^--\frac{1}{8}F_w^-,$$

$$a_W=D_w+\frac{3}{8}F_w^-+\frac{6}{8}F_w^++\frac{1}{8}F_e^+,$$

$$a_N=D_n-\frac{3}{8}F_n^+-\frac{6}{8}F_n^--\frac{1}{8}F_s^-,$$

$$a_S=D_s+\frac{3}{8}F_s^-+\frac{6}{8}F_s^++\frac{1}{8}F_n^+,$$

$$a_{EE}=\frac{1}{8}\overline{F}_e,\quad a_{WW}=-\frac{1}{8}F_w^+$$

$$a_{NN}=\frac{1}{8}\overline{F}_n,\quad a_{SS}=-\frac{1}{8}F_S^+$$

$$a_P=a_E+a_W+a_N+a_s+a_{EE}+a_{WW}+a_{NN}+a_{SS}$$

$$b_\phi=\frac{r_n^2-r_s^2}{2}(z_e-z_w)\overline{S}_\phi$$

where the superscript fluxes F_k^+ and F_k^- $(k=n,s,e,w)$ are defined as follows

$$F_k^+=\max(0,F_k), \tag{10a}$$

$$F_k^-=-\max(0,-F_k) \tag{10b}$$

In the above equations, the diffusive and convective terms are defined as follows.

$$D_e=\Gamma_e r_P\frac{r_n-r_s}{z_E-z_P}, \tag{11a}$$

$$D_w=\Gamma_w r_P\frac{r_n-r_s}{z_P-z_W}, \tag{11b}$$

$$D_n=\Gamma_n r_n\frac{z_e-z_w}{r_N-r_P}, \tag{11c}$$

$$D_s=\Gamma_s r_s\frac{z_e-z_w}{r_P-r_S} \tag{11d}$$

$$F_e=\rho r_P(r_n-r_s)w_e, \tag{11e}$$

$$F_w=\rho r_P(r_n-r_s)w_w, \tag{11f}$$

$$F_n=\rho r_n(z_e-z_w)v_n, \tag{11g}$$

$$F_s=\rho r_s(z_e-z_w)v_s \tag{11h}$$

Now we define the correction $\phi'(=w',\ v'$ or $P')$ as the difference between the correct field $\phi\ (=w,\ v$ or $P)$ and the guessed field $\phi^*(=w^*,\ v^*$ or $P^*)$.

$$w_e=w_e^*+d_e(P_P'-P_E'), \tag{12a}$$

$$w_w=w_w^*+d_w(P_W'-P_P') \tag{12b}$$

$$v_n=v_n^*+d_n(P_P'-P_N'), \tag{12c}$$

$$v_s=v_s^*+d_s(P_S'-P_P') \tag{12d}$$

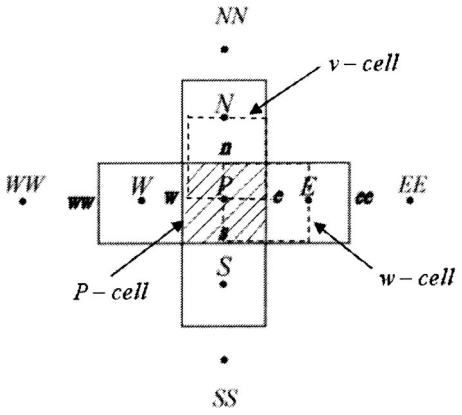

Fig. 3 Schematic of the computational cells and nodes

$$P_k=P_k^*+P_k',\quad k=P,N,S,E,W \tag{12e}$$

where

$$d_e=\frac{r_p(r_n-r_s)}{(a_p)_e},\quad d_w=\frac{r_p(r_n-r_s)}{(a_p)_w},$$

$$d_n=\frac{r_n(z_e-z_w)}{(a_p)_n},\quad d_s=\frac{r_s(z_e-z_w)}{(a_p)_s}$$

With a guessed pressure field P^*, discretised Eq. (9) for the dashed control volumes around the faces *e*, *w*, *n* or *s* in Fig. 3 yields for example for *e* as:

$$(a_P)_e w_e^*=\sum_{nb} a_{nb}w_{nb}^*+r_p(r_n-r_s)(p_P^*-p_E^*) \tag{13}$$

If we follow the same procedure in Ref. [15], the pressure correction equation is

$$a_{P,P}P_P'=a_{P,E}P_E'+a_{P,W}P_W'+a_{P,N}P_N'+a_{P,S}P_S'+b_P' \tag{14}$$

where $a_{P,E}$, $a_{P,W}$, $a_{P,N}$, $a_{P,S}$, $a_{P,P}$, and b_P' are given by the following equations.

$$a_{P,E}=\frac{\rho[r_p(r_n-r_s)]^2}{(a_P)_e}, \tag{15a}$$

$$a_{P,W}=\frac{\rho[r_p(r_n-r_s)]^2}{(a_P)_w}, \tag{15b}$$

$$a_{P,N}=\frac{\rho[r_n(z_e-z_w)]^2}{(a_P)_n}, \tag{15c}$$

$$a_{P,S}=\frac{\rho[r_s(z_e-z_w)]^2}{(a_P)_s} \tag{15d}$$

$$a_{P,P}=a_{P,E}+a_{P,W}+a_{P,N}+a_{P,S} \tag{15e}$$

$$b_P'=\rho[(z_e-z_w)(r_sv_s^*-r_nv_n^*)+(r_n-r_s)r_p(w_w^*-w_e^*)] \tag{15f}$$

4 Solution Procedure

The solution procedure of the discretised equations is based on a line-by-line iteration method in the axial and radial directions using a tri-diagonal matrix solver. The sequence of numerical steps based on SIMPLE algorithm is as follows.

1. Initialize the velocity, pressure, and temperature fields (w^*,v^*,T^*,P^*).
2. Solve Eqs. (9) for $\phi=u$ and *w*.
3. Solve Eq. (14) for P'.
4. Correct the velocity and pressure fields by Eqs. (12*a*–*d*).

Table 2 Design parameters of the CAHP

Dimensions (mm)	Fluid Properties
$L_e = 200$	$h_{fg} = 2251.2 \frac{\text{kJ}}{\text{kg}}$
$L_a = 600$	$C_p = 2.034 \frac{\text{kJ}}{\text{kg K}}$
$L_c = 200$	$\rho = 0.5974 \frac{\text{kg}}{\text{m}^3}$
	$\mu = 121.00e-7$ Pa.sec
$R_o = 23.3$	$k = 0.0248 \frac{\text{W}}{\text{m.K}}$
$R_i = 14.85$	$T_{sat} = 373.15$ K

5. Solve Eq. (9) for $\phi = T$.
6. Check Eq. (16) for convergence, if it is satisfied, calculations will be ended. Otherwise, replace w^*, v^*, T^*, P^* and return to step 2 and repeat the above procedure until convergence is achieved.

The accuracy of the numerical solution is checked first by summation of the absolute value of the relative errors should be equal or less than 10^{-4}. Second, the spot value should approach a constant value. The relative error, *RE*, in the numerical procedure is defined as:

$$RE = \sum_{cells} \left| \frac{\phi^{n+1} - \phi^n}{\phi^{n+1}} \right|, \quad \phi = w, v, P, T \tag{16}$$

where superscript n refers to the previous iteration.

5 Results and Discussion

A computer program has been developed for predicting the velocity, temperature, and pressure fields of vapor along the annular space of a copper-water CAHP. Using this program, various symmetric and asymmetric heat addition and rejection conditions have been analyzed for the design parameters as given in Table 2.

Figs. 4*a–c* show the vapor flow streamlines along the CAHP at low and moderate radial Reynolds numbers ($\text{Re}_r = \rho v_j R_j / \mu$). The radial Reynolds number is based on the radial blowing or suction vapor velocity at the inner or outer vapor walls in the evaporator or condenser section. Also, for a symmetric condition, the radial Reynolds numbers of the evaporator and condenser are the same. The axial velocity profile becomes fully developed in a short distance and stays parabolic all along the length of the heat pipe. In addition, Figs. 4*a–b* show that flow reversal does not occur in the condenser at low radial Reynolds numbers. But this result is not generally correct for all heat pipes. It should be noted that the location where the shear stress becomes zero is called the flow reversal point. Faghri and Parvani [11] have reported that this result is valid only when the condenser zone is short. For the heat pipes with longer condenser lengths, flow reversal may occur for lower radial Reynolds numbers. Experimental prediction of the radial Reynolds number corresponding to the occurrence of flow

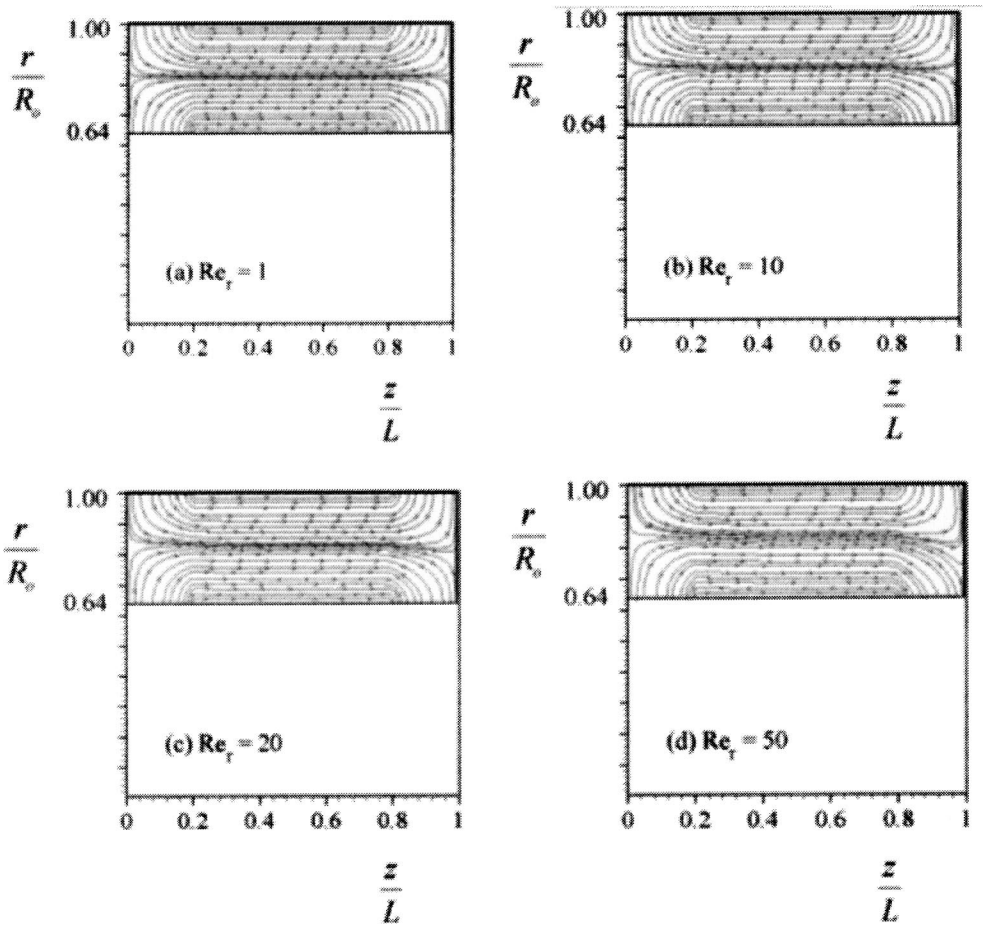

Fig. 4 Streamlines in the annular space at low to moderate vapor Reynolds numbers

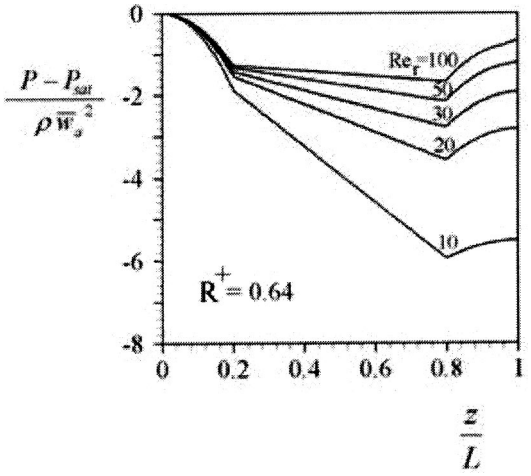

Fig. 5 Normalized vapor pressure distribution along the annular space centerline

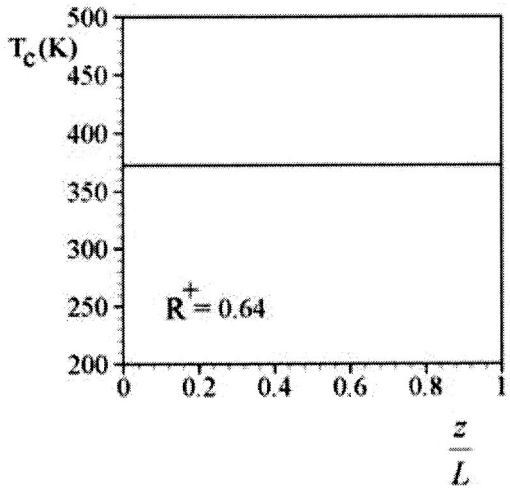

Fig. 7 Vapor temperature distribution along the annular space centerline

reversal in a heat pipe is quite complicated. But with the aid of numerical simulation, one can predict the flow reversal condition satisfactorily.

For the heat pipe analyzed here, this condition takes place on the outer pipe wall at radial Reynolds number very close to $Re_r = 19.9$. However, in other situations this condition depends strongly on the length of the condenser section. As the radial Reynolds number increases, the absolute value of the shear stress along the inner and outer wall increases too. The numerical analysis have shown that for the radial Reynolds number $Re_r \approx 19.9$, the shear stress becomes zero at a point very close to the end of the condenser ($z \approx 0.987$m). However, as the radial Reynolds number increases, the flow reversal point moves backward toward the adiabatic section. Under this condition, the reversed flow region extends from the flow reversal point to the end of the condenser. Due to the evaporation and condensation and vapor-liquid interface interactions, the real condition in a heat pipe can be more different from that assumed in the present analysis.

Figure 5 illustrates the pressure distribution along the annular space centerline for various radial Reynolds numbers. It can be seen that as the radial Reynolds number increases, the pressure distributions shift up without considerable change in their overall shapes. As the radial Reynolds number increases the pressure in the condenser section is more recovered. For the pressure drop in the adiabatic section, the present analysis is very close to the fully-developed pressure drop in Hagen-Poiseuille flow. Because pressure decreases linearly along the adiabatic section.

Figures 6a-b depict the normalized pressure distribution along the CAHP for two values of $R^+ = 0.2$ and 0.8 and various radial Reynolds numbers. It is concluded that the present results are in very good agreement with the results presented by Faghri [12]. This demonstrates that the present numerical analysis is sufficiently accurate for predicting the pressure distribution at low and moderate radial Reynolds numbers.

Figure 7 shows the temperature distribution of the annular vapor space centerline. Since the pressure drop along the heat pipe is very small at the low and moderate Reynolds numbers, the present analysis predicts very small temperature drop along the inner and outer walls of the heat pipe (below 0.1°C). This result seems to be logical, as a result of the assumption of thermodynamic equilibrium at the vapor-liquid interface and using Clausius-Clapeyron equation.

5.1 Transition to Turbulence. It is assumed that transition to turbulence may take place in the annular space when the axial

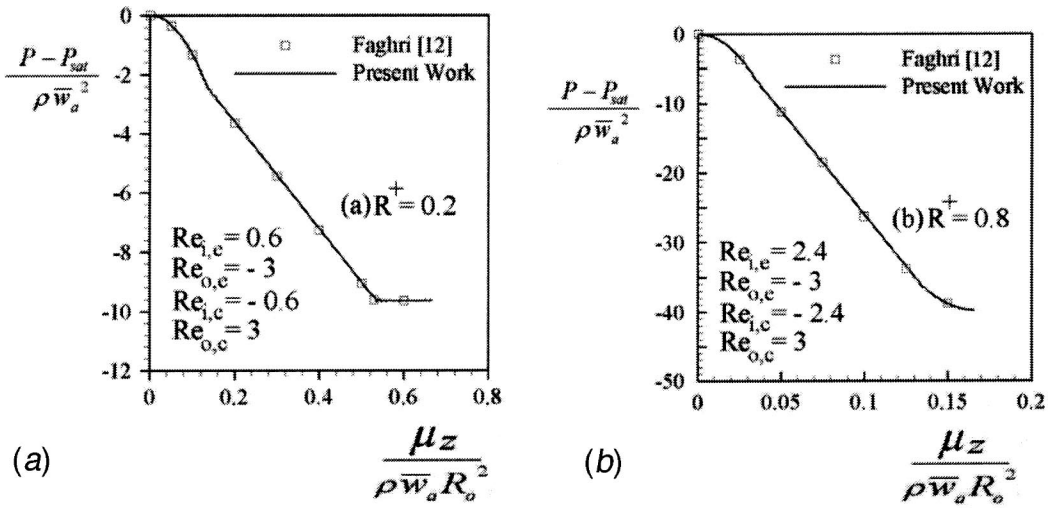

Fig. 6 Normalized vapor pressure distribution along the CAHP (*a*) low radial Reynolds numbers, (*b*) moderate radial Reynolds numbers

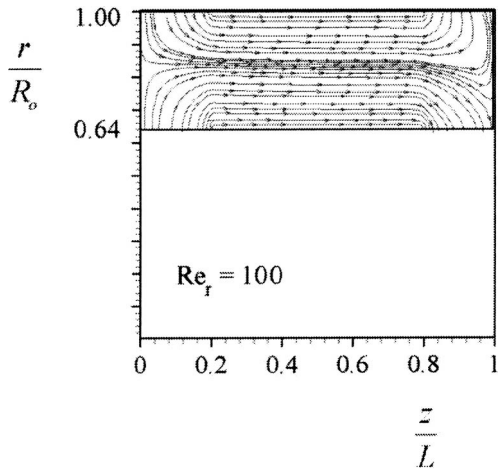

Fig. 8 Streamline in the annular vapor space

Reynolds number based on hydraulic diameter $(D_o - D_i)$ and the mean axial velocity $\overline{w_a}$ in the adiabatic section reaches to $\mathrm{Re}_{a,z} = 2300$. Rohani and Tien [6] assumed the value $\mathrm{Re}_{a,z} = 2100$ for a conventional heat pipe. However, this is not generally true for all heat pipes and depends strongly on the flow disturbance and wall conditions. Schlichting [16] has recommended the value 2000 for the transitional Reynolds number, in a non-circular channel. Below this value, the flow seems to be insensitive to the upstream disturbances and always remains laminar. Since the present numerical solution was stable and well-behaved up to, and even above the value 2300, this value is adopted here for the transitional Reynolds number. The axial Reynolds number and the mean axial velocity $\overline{w_a}$ in the adiabatic section can be found as:

$$\mathrm{Re}_{a,z} = \frac{\rho \overline{w}_a D_h}{\mu} = \frac{4L_e}{R_o + R_i}\left(|\mathrm{Re}_{i,e}| + |\mathrm{Re}_{o,e}|\right) \tag{18}$$

$$\overline{w_a} = \frac{\dot{q}_{i,e} + \dot{q}_{o,e}}{\pi \rho (R_o^2 - R_i^2) h_{fg}} \tag{19}$$

For an axial Reynolds number of 2300 and for a symmetric condition, the correpsonding radial Reynolds number of the heat pipe is $\mathrm{Re}_r = 54.8$. Above this value of radial Reynolds number, the laminar flow analysis using a coarse grid may not be valid and accurate prediction of the vapor flow needs experimental work or direct numerical simulation.

Fig. 8 represents the calculated results for $\mathrm{Re}_r = 100$. It is interesting to note that although the radial Reynolds number is higher than the transitional value, $\mathrm{Re}_r = 54.8$, but the numerical results seems to be acceptable and the convergence behavior is also good. The corresponding pressure distribution at $\mathrm{Re}_r = 100$ has been shown in Fig. 5. The large pressure recovery can be seen at the condenser section due to the flow reversal phenomenon. The flow regime seems to be still laminar. Because, the stability limits for laminar flows of this class have not yet been established. However, flows with injection have been found to retain laminar velocity profiles at axial Reynolds numbers greater than 10^5, as mentioned by Bankston and Smith [5]. This subject should be more studied numerically or experimentally for vapor flow analysis in both conventional and CAHPs. However, at higher radial Reynolds numbers, the flow reversal phenomenon may promote the transition to turbulence and needs to be more studied.

5 Conclusion

It has been shown that the incompressible vapor flow and heat transfer in a CAHP can be accurately simulated using the present numerical model. The QUICK differencing scheme has been used in the discretisation process and it has been found that its accuracy is acceptable, at least for moderate radial Reynolds numbers. The proposed SIMPLE algorithm has shown good convergence behavior at low and moderate radial Reynolds numbers and even near the nominal transition to turbulence or higher axial Reynolds number ($\mathrm{Re}_{a,z} = 2300$). It has been also demonstrated that the numerical model works well for the prediction of vapor flow reversal and presents reasonable results even near the transition to turbulence of vapor flow. However, further studies and more complete models are needed to predict these phenomena for a real condition in a CAHP. The presented numerical method was used to analyze the steady-state vapor flow and heat transfer in a CAHP for a number of symmetric and asymmetric heat addition and rejection conditions. The results have been compared with the available numerical data which have been done in the literature and have shown good agreement in all cases. Due to the small pressure drop along the heat pipe at low and moderate radial Reynolds numbers, the present analysis predicts very small vapor temperature drop along the heat pipe.

Nomenclature

C_p = heat capacity at constant pressure
D = diameter
h_{fg} = latent heat of vaporization
k = thermal conductivity
L = length
P = pressure
$\dot{q}$ = heat transfer
r = radial coordinate
R = gas constant, pipe radius
R^+ = radius ratio, R_i/R_o
Re = Reynolds number
S = source term
T = temperature
v = radial vapor velocity
w = axial velocity
z = axial coordinate

Greek Symbols

ϕ = general variable
μ = viscosity
ρ = density

Subscripts

a = adiabatic, axial
c = condenser, centerline
e = evaporator
h = hydraulic
i = inner wall
int = interface
o = outer
r = radial
z = axial
max = maximum

Superscripts

$-$ = mean
0 = initial value
$+$ = dimensionless

References

[1] Wang, Q., Cao, Y., Wang, R., Mignano, F., and Chen, G., 2000, "Studies of a Heat Pipe Cooled Piston Crown," ASME J. Eng. Gas Turbines Power, **122**, pp. 99–105.
[2] Peterson, G. P., 1994, *An Introduction to Heat Pipes: Modeling, Testing, and Applications*, John Wiely, New York.
[3] Cotter, T. P., 1965, *Theory of Heat Pipes*, Los Alamos Scientific Laboratory Report No. LA-3246-MS.
[4] Busse, C. A., 1967, "Pressure Drop in the Vapor Phase of Long Heat Pipes," *Proc. 1967IEEE Thermionic Conversion Specialist Conf.*, Palo Alto, California, p. 391.

[5] Bankston C. A. and Smith H. J., 1971, ''Incompressible Laminar Flow in Cylindrical Heat Pipes,'' *ASME PAPER 17-WA/HT-15*.
[6] Rohani, A. R., and Tien, C. L., 1974, ''Analysis of the Effects of Vapor Pressure Drop on Heat Pipe Performance,'' *International Journal of Heat Mass Transfer*, **17**, pp. 61–67.
[7] Chi, S. W., 1976, *Heat Pipe Theory and Practice*, Hemisphere, Washington, D.C.
[8] Dunn, P. D. and Reay, D. A., 1982, *Heat Pipes*, Pergamon, Oxford.
[9] Faghri, A., 1995, *Heat Pipe Science and Technology*, Taylor & Francis, Washington, D.C.
[10] Faghri, A., 1986, ''Vapor Flow Analysis in a Double-walled Concentric Heat Pipe,'' Numer. Heat Transfer, **10**, pp. 583–595.
[11] Faghri, A., and Parvani, S., 1988, ''Numerical Analysis of Laminar Flow in a Double-walled Annular Heat Pipe,'' J. Thermophys. Heat Transfer, **2**, pp. 165–171.
[12] Faghri, A., 1989, ''Performance Characteristics of a Concentric Annular Heat Pipe Part II-Vapor Flow Analysis,'' ASME J. Heat Transfer, **111**, pp. 851–857.
[13] Faghri, A., and Thomas, S., 1989, ''Performance Characteristics of a Concentric Annular Heat Pipe: Part I-Experimental Prediction and Analysis of the Capillary Limit,'' ASME J. Heat Transfer, **111**, pp. 844–850.
[14] Ferziger, J. H. and M. Peric, 1999, *Computational Methods for Fluid Dynamics*, 2nd ed., Springer-Verlag, Berlin Heidelberg.
[15] Patankar, S. V., 1980, *Numerical Heat Transfer and Fluid Flow*, Hemisphere, New York.
[16] Schlichting, H., 1979, *Boundary Layer Theory*, Mc-Graw-Hill, New York.

Simulation of Spray Transfer Processes in Electrostatic Rotary Bell Sprayer

Kyoung-Su Im

Ming-Chia Lai*

Sheng-Tao John Yu

Department of Mechanical Engineering,
Wayne State University,
Detroit, Michigan 48202, USA

Robert R. Matheson, Jr.
Dupont Herberts Automotive Systems,
Troy, Michigan 48007, USA

A numerical study of the spray transfer processes in an electrostatic rotary bell applicator (ESRB) has been conducted utilizing code for a newly developed simulation code. This code consists of three modularized solvers: a fluid flow solver, a spray dynamics solver, and an electrostatic solver. The development of the code consisted of the following steps. First, the flow solver designed for an unsteady three-dimensional Navier-Stokes equation was developed to simulate the shaping airflow with the initial condition and the boundary condition supported by experimental data. Second, the particle trajectory solver, which interacts with the airflow by momentum coupling, was developed to apply the spray transport processes. Finally, the electrostatic solver was developed to calculate the electrostatic field within the two phase flow field. The integrated code created by combining those three solvers was then applied to simulate the paint spray transport processes according to the operating conditions of interest. The numerical results show that the spray shape is very sensitive to changes in the charge to mass ratio. The voltage setting is a dominant operating parameter affecting the numerical transfer efficiency. The voltage range studied was 0 kV to 90 kV. In addition, the transfer efficiency decreases as the shaping airflow rate increases. However, a high shaping airflow rate produces a more uniform distribution of spray mass on the target plane. [DOI: 10.1115/1.1758263]

1 Introduction

The trend in the current automotive finishing industry is to use more ESRB applicators because of their higher transfer efficiency. However, it is only recently that the bell applicators have achieved some success in the application of metallic base-coats. Compared with the pneumatic spray gun, the ESRB produces a darker and duller appearance but a much higher transfer efficiency.

It is well known that the application of an electric charge will change the apparent color of some metallic paints to varying degrees [1]. However, the mechanisms are not well defined. Previous studies have suggested that improper flake orientation during flow transportation and differing concentrations of flakes in the deposited paint contribute to the discoloration. Nevertheless, the optimal operating conditions at which the droplet size and flake content are most uniform at the target surface depend on the entire paint transfer process. These conditions also change with the properties of the paint and the target surface.

The paint transfer efficiency, defined as the ratio of the mass of solid paint deposited on the target to that dispersed from the applicator, is a metric for the efficiency of the paint application process. An improvement in transfer efficiency results in savings to automotive manufacturers as a result of less paint usage and lower costs of paint sludge disposal. Therefore, manufacturers are motivated to continuously improve the paint application process. The ESRB applicators, operating under ideal conditions, can achieve high transfer efficiency, typically up to 90%.

The distribution of the paint spray by bell applicator can roughly be divided into three different regions: near field, transport field, and target field as shown in Fig. 1.

The atomization, the air ionization, and the electrostatic charge of the liquid particles are physical phenomena of the *near-bell field*. The flow physics in the *transport field* include the swirling turbulent flow (shaping-air flow), the spray dynamics, and the electrostatic field. The transport field occupies the largest region between the bell cup and the work piece. The swirling turbulent flow induced from the ESRB atomizer is highly unsteady and very complex [2,3]. The spray dynamics coupled with the shaping air is an extremely complicated phenomenon. In order to calculate the mass, momentum, and energy exchange between the spray particles and the airflow, the drop sizes, velocities and temperatures must be accounted for.

The interactions between the charged drops and airflow and among spray drops are important physical aspects of the flow. In the transport region, the following three interacting mechanisms are of concern:

1. The motion of the paint particles is influenced by the drag of the shaping air, the background electric field, and the repulsive forces from other charged particles.
2. The moving charged particles influence the overall electric field.
3. The flow field is influenced by the drag force from paint particles.

The physics of the *target field* is characterized by the rheology of film formation (drop deposition), the transfer efficiency, and the influence of the downdraft on the paint deposition and over-spray. It is very difficult to develop a validated model including all three regions. Therefore, our numerical modeling of the paint spray has only focused on the simulation of the transport field with the initially developed electric field. In the transport region, the electric field, which has a force much higher than the aerodynamic force, strongly affects the spray particles. In addition, the shaping airflow and the spray particles interact via mass, momentum, and energy exchange. However, the electric field and shaping airflow are only related through the spray particles. Figure 2 explains the relationships among these three dynamic elements.

Since the electric field responds instantaneously to the change of the spatial distribution of charged particles, the response time (Δt_e) between the electric field and the spray particle is much less than that between the shaping air and spray particle (Δt_f). Thus, we can assume that the electric response time is negligible (Δt_e

*Corresponding author: Mechanical Engineering Department, Wayne State University, 5050 Anthony Wayne Drive, Detroit, MI 48202. e-mail: lai@eng.wayne.edu.

Contributed by the Fluids Engineering Division for publication in the JOURNAL OF FLUIDS ENGINEERING. Manuscript received by the Fluids Engineering Division September 13, 2002; revised manuscript received February 4, 2004. Associate Editor: S. Balachanda.

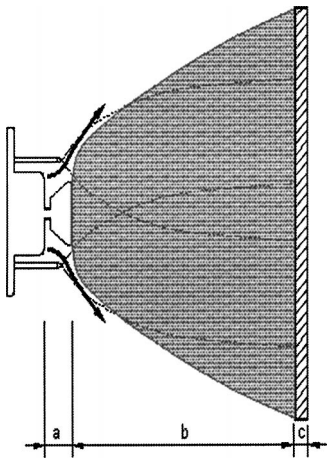

Fig. 1 Regions: *a*) near field, *b*) transport field, and *c*) target field of the paint spray

$\cong 0$) in the present simulation. As a result, the finite time (Δt_f), with which the droplet drag responds to the convection speed, becomes the pacing parameter in the present numerical simulation. In other words, the Courant number or Courant-Friedrichs-Lewy (CFL) number constraint will be the most important parameter to control the numerical simulation.

1.1 Previous Numerical Studies in ESRB Spray. Almost all reported research addresses spray simulations for combustion applications, where nozzle injection of hydrocarbon fuel is used as an input parameter and how the spray disperses is the information sought. The work discussed herein is unique in that it addresses how a dispersed spray deposits onto a substrate surface.

Bellan [4] proposed using electrical charge for soot control in a diesel engine. A one-dimensional analytical solution of an expanding spherical shell showed the effect of self-repulsion.

True [5] used a 2-D, quasi-axisymmetric, steady-state, Lagrangian, analytical solution for the monodispersed droplets in a homogeneous disc control volume to solve the radial expansion rate and the axial drag force of a divergent spray plume.

Elmoursi et al.[6] reported several charge simulation results including the particle trajectory. As a first step, they developed a Laplacian model to evaluate the electric field between the bell and the paint target. The space from the bell to the target and the size of target were used as parameters, which strongly influenced the electric field. They also developed an unbounded space charge field model to calculate the electrical characteristics of an electrostatic painting system. In addition, a particle trajectory model derived from Newton's second law was developed to calculate a single drop trajectory. From their simulation results, they found that increasing space charge has a stronger effect on the deposition field than increasing the applied potential. In the particle trajectory model, they didn't include the aerodynamic effects. Moreover, they considered the paint cloud to be made up of single size droplets only.

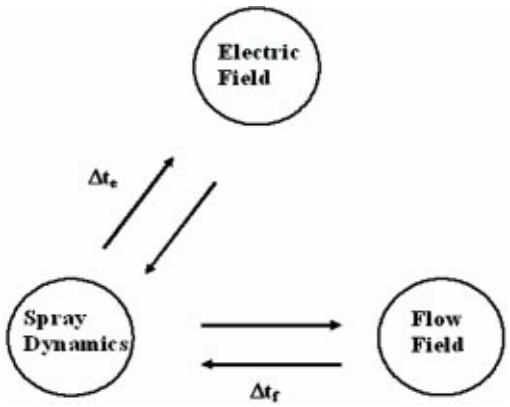

Fig. 2 The interactions of three main processes in transport field

Grace and Dunn [7] used a similar assumption as True [5] and simulated a charged spray plume using 2-D axisymmetric Eulerian steady-state approximation. The spray plume expansion rate (radial-to axial velocity ratio) was in relatively good agreement with the experiment, but the penetration speed was underpredicted.

It should be noted that the above studies use monodisperse droplet size and charge. In addition, only stagnant ambient air conditions are used. Thus, no momentum coupling between the gas phase and the dispersed phase was considered.

Recently, Shrimpton et al. [8] used a combined Eulerian/Lagrangian formulation to couple the continuous and discrete phases. The effect of the electrical field and the droplet space charge was incorporated into a pressure-implicit with splitting of operators (PISO) solver through the use of source terms. The model is used to simulate a capillary tube injection of ethanol onto a flat plate, for which reliable drop diameter and velocity information was obtained using Phase Doppler Particle Analyzer (PDPA). They reported that there is large uncertainty concerning the drop charge model and that the spray dynamics is extremely sensitive to the initial condition. They also found that dielectric force is negligible. However, only the spray shape data were reported for comparison with the experiment, which showed an overestimated radial velocity and an underestimated axial component.

Miller et al.[9] reported an ESRB simulation using the solid bell model, which is the first transport research in painting spray. Their flow solver was based on the PowerFlow (from Exa corporation), in which the fluid motion is determined through a series of particle collisions and advections on a regular lattice grid instead of solving the Navier–Stokes equation. The particle trajectory solver including electrostatic force was developed using a 4th-order Runge-Kutta method. Using this package, they reported that the influence of bell speed, charge-to-mass ratio, and electric potential showed good qualitative trends compared to experimental results. However, the shaping air distribution was confined narrowly around the bell about 3 mm radially away from the bell cup.

Huang et al.[10] used KIVA-3V to simulate the ESRB processes with some success, although the computational time is quite long. Therefore, further improvement in the simulation of ESRB paint transfer process is greatly needed.

1.2 Present Approach. There are so far no integrated simulation results for the ESRB paint transfer process in terms of the momentum coupling, the stochastic particle distribution, and effects of an electric field. Therefore, the goal of the present study is to conduct a fully integrated numerical simulation of ESRB paint spray transport process using a modern computational fluid dynamics (CFD) method, the space-time CE/SE method. To achieve this, three numerical components have been developed as follows: 1) a flow solver to simulate the compressible turbulent flow of the shaping air, 2) a spray solver to solve the particle dynamics, and 3) a Poisson's solver to calculate the electric field. These modules were coupled together within the software program to simulate the coupling effects of the shaping airflow, the paint spray dynamics, and electrostatic field.

2 Navier-Stokes Solver

Recently, Chang [11] reported a novel numerical framework for solving conservation laws, namely, the method of Space-Time Conservation Element and Solution Element, or the CE/SE method for short. The method is based on an equal-footing treatment of space and time in calculating flux balance in a space-time

domain. The method is not an incremental improvement of a previously existing method and it differs substantially from other well-established CFD methods. The design principles of the CE/SE method have been extensively illustrated in the cited references.

In this study, a variation of the original CE/SE method was used to solve the ESRB painting problem. The algorithm of the present modified CE/SE method is even simpler than the original CE/SE method. Nevertheless, all advantageous features of the original CE/SE method have been retained, including a unified treatment of space and time, accurate calculation of the space-time flux, high-fidelity resolution of unsteady flow motions, and full compliance with the physics of initial value problems. The present modified method is also extended to solve Navier-Stokes equations.

Finally, a brief comparison between the original and the modified CE/SE method is provided as the background of the current study. In the original CE/SE method, the flow variable u and its spatial gradient u_x are considered as unknowns that are solved simultaneously. Therefore, for equations in one spatial dimension, two CEs at each grid point are constructed to derive two discrete equations for u and u_x. Similarly, three and four CEs at each grid point are needed in two and 3-D cases, respectively. As compared to the original CE/SE method, in the modified CE/SE method [12], only one CE at each grid point is employed for equations in one, two and three spatial dimensions. Thus, the CE in the present method is used to calculate u only and the gradient variable u_x is calculated by a central difference method. Accordingly, the logic of the modified CE/SE scheme is simple and can be easily implemented. As such, it can serve as an alternative solver for time-accurate solutions in well-established CFD codes.

In the present calculation, we combine fluid dynamics equations into a compact vector form. The governing equations with momentum coupling term can be cast into the following form [13]:

$$\frac{\partial \mathbf{u}}{\partial t}+\frac{\partial \mathbf{f}}{\partial x}+\frac{\partial \mathbf{g}}{\partial y}+\frac{\partial \mathbf{h}}{\partial z}-\frac{\partial \mathbf{f}_{vm}}{\partial x}-\frac{\partial \mathbf{g}_{vm}}{\partial y}-\frac{\partial \mathbf{h}_{vm}}{\partial z}=\mathbf{S} \tag{1}$$

where

$$\mathbf{u}=\begin{Bmatrix}\rho\\ \rho u\\ \rho v\\ \rho w\\ E_t\end{Bmatrix},\mathbf{f}=\begin{Bmatrix}\rho u\\ \rho u^2+p\\ \rho uv\\ \rho uw\\ (E_t+p)u\end{Bmatrix},\mathbf{g}=\begin{Bmatrix}\rho v\\ \rho uv\\ \rho v^2+p\\ \rho vw\\ (E_t+p)v\end{Bmatrix},$$

$$\mathbf{h}=\begin{Bmatrix}\rho w\\ \rho uw\\ \rho vw\\ \rho w^2+p\\ (E_t+p)w\end{Bmatrix},$$

$$\mathbf{f}_{vm}=\begin{Bmatrix}0\\ \tau_{xx}\\ \tau_{xy}\\ \tau_{xz}\\ u\tau_{xx}+v\tau_{xy}+w\tau_{xz}+q_x\end{Bmatrix}$$

$$\mathbf{g}_{vm}=\begin{Bmatrix}0\\ \tau_{xy}\\ \tau_{yy}\\ \tau_{yz}\\ u\tau_{xy}+v\tau_{yy}+w\tau_{yz}+q_y\end{Bmatrix},$$

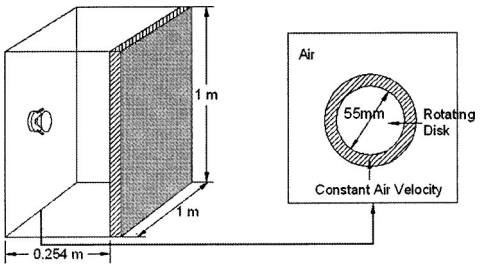

Fig. 3 A schematic of the computational domain

$$\mathbf{h}_{vm}=\begin{Bmatrix}0\\ \tau_{xz}\\ \tau_{yz}\\ \tau_{zz}\\ u\tau_{xz}+v\tau_{yz}+w\tau_{zz}+q_z\end{Bmatrix},\quad\text{and}\quad\mathbf{S}=\begin{Bmatrix}0\\ S_{px}\\ S_{py}\\ S_{pz}\\ 0\end{Bmatrix} \tag{2}$$

are the main flow variable, flux, viscous, and source term vectors, respectively. The corresponding equations are mass, the momentum (x,y,z), and energy equations. The vector **S** is the term defining momentum exchange with particles, which is modeled as follows:

$$S_{pi}=-\sum_k \langle D_k(\mathbf{u_g})(\mathbf{u_g}-\mathbf{u}_{pk})\delta(\mathbf{x}-\mathbf{x}_{pk})\rangle \tag{3}$$

where k is number of each particle, $\delta(x)$ is the three-dimensional Dirac delta function, and $D_k(\mathbf{u})$ is the drag function, which will be described following section. In addition, more detailed description for the momentum exchange term can be found in [14].

In recent research, Fureby and Gristein [15] introduced a new technique called monotonically integrated large eddy simulation (MILES) instead of the normal large eddy simulation. In the MILES method, unfiltered Navier-Stokes equations are solved with high resolution algorithms in which the functional reconstruction process replaced the flow physics of the sub grid scale (SGS) on the grid scale flow. Thus, they proved that the algorithms with nonlinear, high-frequency filters can dispense with explicit SGS models. The CESE method in present research employed one of the MILES techniques in a sense that first, the SEs in the algorithm provide the filtering effects to the flow with designed grid structure, and second, nonlinear weighted functions (nonlinear filters) built into the numerical scheme.

In the setting of the boundary conditions in the flow solver, three conditions are used at $x=0$ plane (see Fig. 3): i) constant angular speed on the bell disk surface, (ii) constant velocities, which are supported by experiment, near the bell disk zone, and (iii) non-reflective conditions except the area of (i) and (ii). In addition, the non-slip conditions are employed on the target plane and non-reflective conditions are applied to other planes.

3 The Spray and the Electrostatic Solver

In the transport field of ESRB spray flow, the particle volume fraction in the shaping airfield is quite small: that is, the spray is sparse compare to other sprays such as diesel and gasoline spray in automotive engine. As a result in this present study, no particle coalescence or particle breakup is considered and no particle collisions are considered. In addition, the initial breakup of liquid sprays is also not considered. Thus, the initial conditions such as drop size distributions, positions, and velocities are independently specified.

The discrete particle technique was used in the numerical calculation. Thus, each numerical particle is representing, in a statistical sense, a number of paint droplets having the same stochastic characteristics of droplet locations, velocities, sizes, and temperatures.

Table 1 Numerical Test Conditions

Rpm ×1000	Airflow Rate	V_{t1} (m/s)	V_{t2} (m/s)	V_{x1} (m/s)	V_{x2} (m/s)	Re_D
25	150	26.21	26.94	11.9	11.2	269387.8
	300	42.40	44.75	20.7	18.7	269387.8
50	150	33.16	31.54	14.7	16.4	538738.1
	300	57.45	54.96	24.5	22.0	538738.1

Based on the above assumptions, each particle, individually labeled by subscript k, is considered to obey the following equations:

$$\frac{d\mathbf{x}pk}{dt} = \mathbf{u}_{pk} \tag{4}$$

$$m_k \frac{d\mathbf{u}_{pk}}{dt} = m_k\mathbf{g} + D_k(\mathbf{u}_g)(\mathbf{u}_g - \mathbf{u}_{pk}) \tag{5}$$

where $\mathbf{x}_{pk}$ is the particle position, $\mathbf{u}_{pk}$ is its velocity, m_k is its mass, $\mathbf{g}$ is its gravity, and $D_k(\mathbf{u}_g)$ is drag function, which can be approximated by the simplified expression

$$D_k = 6\pi\mu_g r_k + \frac{1}{2}\pi r_k^2 \rho_g C_D |\mathbf{u}_g - \mathbf{u}_{pk}| \tag{6}$$

where μ_g is viscosity, ρ_g is density in the gas phase, and r_k is the radius of the kth particle. In Eq. 6, the drag coefficient C_D is determined by particle Reynolds number [14] and gives,

$$C_D = \frac{24}{\mathrm{Re}_k}[1.0 + 0.167\,\mathrm{Re}_k^{2/3}] \quad \text{for } \mathrm{Re}_k < 10^3$$
$$= 0.424 \quad \text{for } \mathrm{Re}_k > 10^3. \tag{7}$$

The particle Reynolds number is evaluated by relative velocity between the surrounding gas and particle, i.e.,

$$\mathrm{Re}_k = \frac{2r_k|\mathbf{u}_g - \mathbf{u}_{pk}|\rho_g}{\mu_g}. \tag{8}$$

There are many ways to obtain a specified size distribution when injecting particles. The method used in this study is similar to the KIVA code, where the Monte Carlo method is used to get a stochastic injection with a random number generator using predefined particle distribution function [16].

In modeling the interaction between the electrical field and the droplet dynamics, the spray electric field due to the presence of the charged droplets in the space between the bell and target is not considered. Only electrostatic forces from six electrodes are considered and the constant charge density of particles was assumed. Based on the assumptions, the electric force, which is a driving force applied to paint droplets flying through the electrostatic field, is given by,

$$\mathbf{F}e = q\mathbf{E}_e \tag{9}$$

where $\mathbf{E}_e$ is the electric field density due to the external electrodes. Note that the spray electric field due to the presence of the charged droples in the space is not included. Adding this electric force into the Eq. 5, the spray particle trajectory equation is modified by;

$$\frac{d\mathbf{u}_{pk}}{dt} = \mathbf{g} + D_k(\mathbf{u}_g)(\mathbf{u}_g - \mathbf{u}_{pk})/m_k + \frac{q}{m_k}\mathbf{E}_e. \tag{10}$$

The charge-to-mass ratio, q/m_k, is used as an input parameter for the simulation. Note that the electric field density can be calculated by using the gradient of the electrostatic potential. Thus, first, the electrostatic potential field from six electrodes should be calculated and the resultant equation is given by

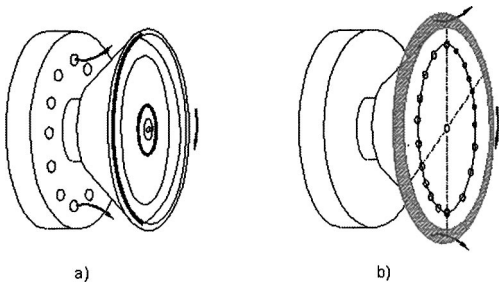

Fig. 4 Bell atomizers: *a*) original, *b*) numerical

$$\Phi(x,y,z) = \frac{\Phi_o}{4\pi}\sum_{k=1}^{k=6}\left(\frac{1}{R_{k+}} - \frac{1}{R_{k-}}\right) \tag{11}$$

where Φ_o is the initial point source potential on the each electrode, R_{1+}, R_{2+}, . . . , R_{6+} are the location of positive point sources and R_{1-}, R_{2-}, . . . , R_{6-} are the position of negative point image sources.

4 Results and Discussion

Figure 3 is a schematic description of the computational domain. The dimensions of the calculation domain are 0.254 m ×1 m×1 m. The work piece, i.e., target, is located at x = 0.254 m from the bell cup surface. For the purpose of numerical simulation, the surface of the rotating bell coincides with the computational surface at $x=0$. Thus, the plane at $x=0$ consists of (i) bell surface (55mm), (ii) input air velocity, and (iii) ambient air. These zones are shown on the right in Fig. 3.

The original bell disk, Fig. 4(*a*), is modified to the solid models as shown in Fig. 4(*b*). In a real bell, the shaping air is provided from the small holes annularly designed on the back wall, but in the model the shaping air velocity is supported by experimental data, which is measured from close to the bell edge to the zero velocity point. The liquid flow of the rotating bell is controlled by the number of injected particles from the injection holes along the edge of the bell disk surface. The number of ligaments measured from microscopic images [2] is used as the number of injection holes.

Cartesian coordinates are used for the numerical calculation. The total number of grid cells is about 703,601, which has a dimension of 41×131×131 as shown in Fig. 5. The calculation of

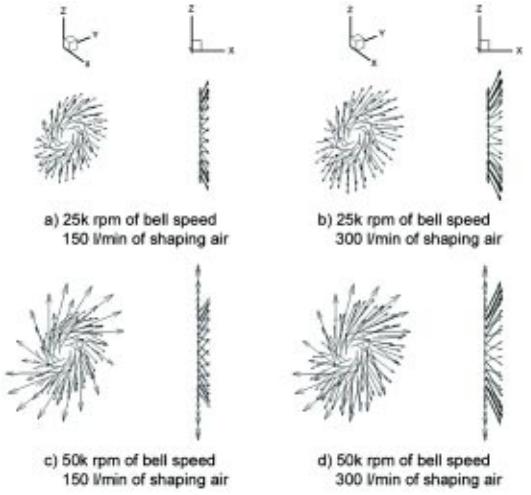

Fig. 5 Initial and boundary conditions reconstructed from experimental data

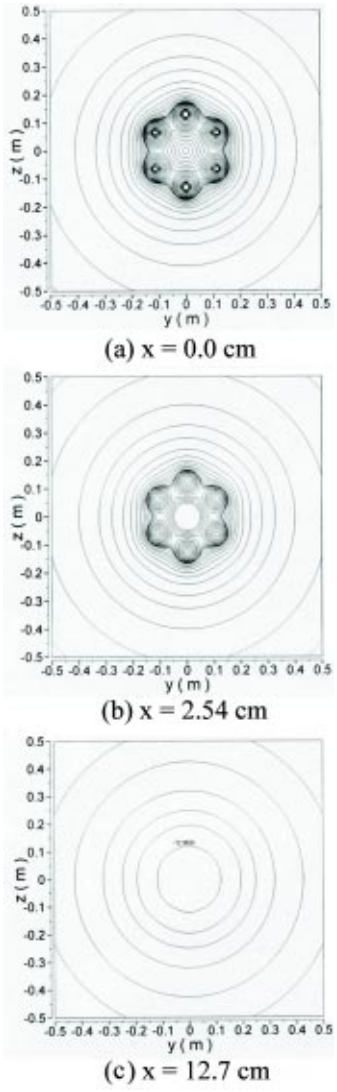

Fig. 6 Electrostatic potential contours at different positions

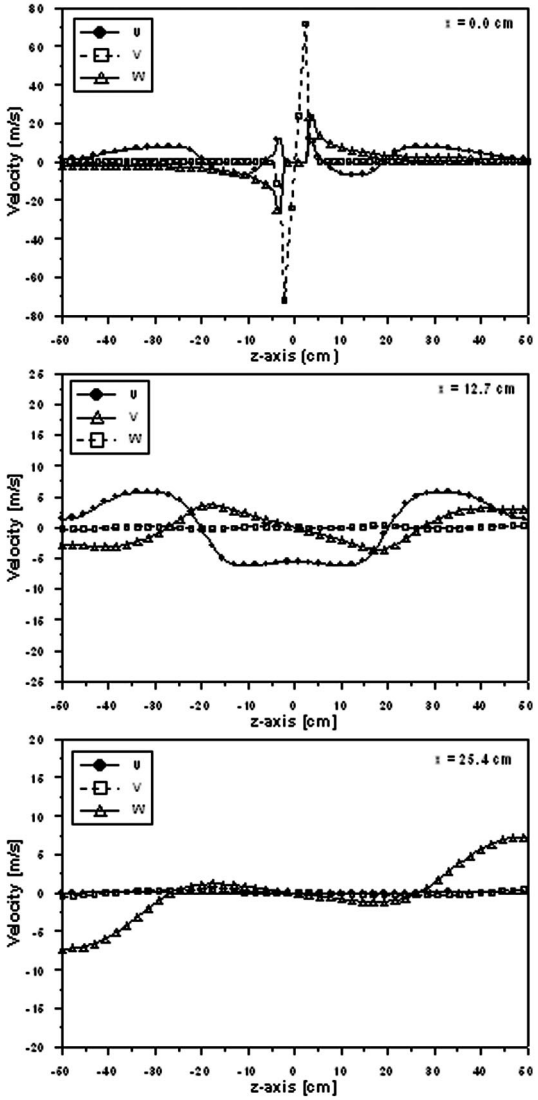

Fig. 7 Velocity components (u,v,w) on the z-axis at y=center

the electrostatic potential, the electric force, and the particle trajectory was executed in Lagrangian coordinates.

Table 1 shows the test matrix for the numerical simulation. To provide an initial and boundary condition at $x=0$ plane (see Fig. 3), we directly measure the shaping air velocity at several points by using a two-component PDPA systems. After obtaining this experimental data, we reconstructed the velocity data on the constant air velocity zone assuming symmetry about the x-axis (see Fig. 3). Figure 5 graphically illustrates the initial conditions corresponding to the bell speed and the shaping airflow rate.

Figure 6 shows the electrostatic potential contours of 90 kV settings plotted on y-z planes corresponding to different axial positions; ($x=0$, 2.54, and 12.7 cm) from the bell surface. The high potential cores around the six electrodes are clearly seen at $x=0.0$ cm and 2.54 cm. However, the potential cores disappear at the center plane of the axial direction, i.e., $x=12.7$ cm and weak electrostatic fields remain, indicating that the electrostatic force by the electrodes is only dominant in the region close to the bell surface. Beyond this area, the charge to mass ratio for each particle, held constant in the present study, may be important as a driving force.

The ESRB spray is a 3-D turbulent flow with a complex rotational flow. Thus, instead of analysis of the 3-D flow field, we plotted three velocity components along the z-axis. Figure 7 displays the time averaged velocity distribution of three components corresponding to the bell speed of 25k rpm and the shaping airflow rate of 150 l/min when the flow was fully developed. Each velocity component represents the physical characteristics of axial (U), swirl (V), and shearing (W) flow, respectively. The high swirl velocity (72 m/s) at the initial plane ($x=0.0$ cm) rapidly reduced and almost disappeared at $x=12.7$ cm. In contrast, the shearing velocity is symmetrically distributed at the center axial location. The axial velocity is even more complicated. The back flow can be seen near the center axis. After this back flow, a large air entrainment area can be seen. Near the target, shearing velocities are dominant with small axial and very small swirl velocity (less than 1 m/s).

In addition to the velocity components in the x and z directions, there is a rotating velocity about the bell axis due to high rotational speed of the bell cup. Figure 8 shows the angular speeds of the shaping airflow at different axial locations with the airflow rate of 150 l/min and the rotating bell speed of 25k rpm. In the plane of the bell edge, the angular speed is highest (2618 rad/s) close to the bell cup and decreases sharply away from the bell. Only 1.27 cm from the bell cup to downstream axially, the maximum angular speed is down to 360 rad/s. Far from the bell, the peak angular speed is reduced due to the reducing swirl momen-

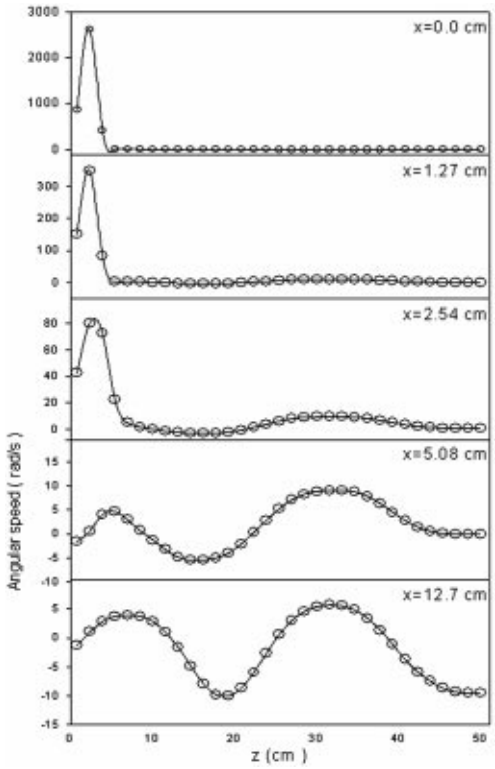

Fig. 8 Air flow angular velocity in the *z*-direction at different axial positions

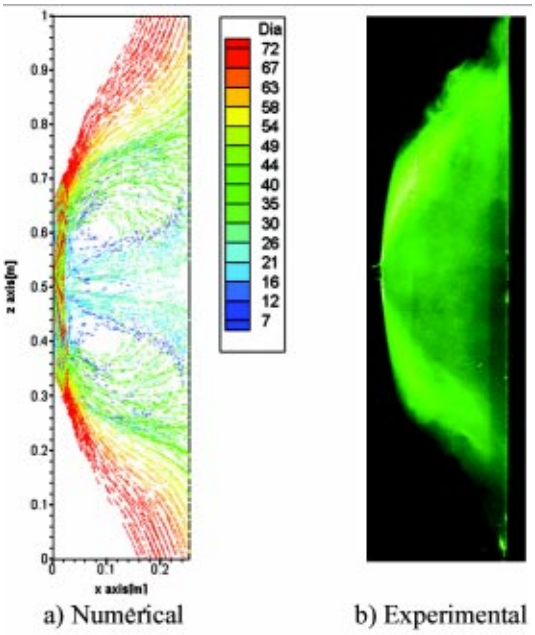

Fig. 9 Comparison of the numerical and experimental spray characteristics at the following operating condition: 150 l/min of shaping air, 50k rpm of bell speed, 90kv of electric force, and 150 ml/min liquid flow rate

tum. The profile of angular speed shows that different parts of the flow rotate at different angular speeds, indicating the presence of a central vortex. At $x=12.7$ cm, half of the total length, the angular speed shows a wave profile, indicating that circulating flow toward the target and the reflected circulating flow from the target coexist at this plane.

In the modeling of the spray flow, a stochastic particle injection based on the Monte Carlo method is used to get the predefined particle distribution, i.e., the χ-squared distribution. The initial velocity of each particle is given by the tangential speed at the bell edge and the initial position is specified by ligaments that are evenly distributed along the circumference divided by total numbers. The time step of the particle motion was chosen based on the flow field, which is five times bigger than that of the particle time step.

Figure 9 compares the computational spray flow with the experimental results on the x-z plane at the mid-point distance along the y-axis for the operating conditions of 150 l/min of shaping air, 50k rpm of bell speed, 90kv of electric force, and 150 ml/min of liquid flow rate. The injected Sauter mean radius of the numerical calculation was 30μm. An important observation here is that a re-circulating flow is created between the bell cup and the target due to the strong shaping air flowing over the bell cup. In addition, larger droplets stay on the outside of the spray, while smaller droplets are readily entrained into the re-circulating zone. Similar qualitative trends are seen in the experimental image on the right-hand side.

Figure 10 illustrates the effects of the charge to mass ratio ($q/m=0.0$, 0.5, 1.0 μC) under operating conditions of 150 l/min of shaping air, 25k rpm of bell speed, 90kV of electric setting, and 150 ml/min of liquid flow rate. At $q/m=0.0$, most of the droplets are distributed according to the air flow pattern, i.e., small droplets are inside of the spray and larger droplets are outside of the spray. In addition, part of the large droplets are outside of the target surface; these large droplets become over spray. Increasing the electric force makes most of particles distribute on the target, indicating that higher electric force tends to concentrate the spray pattern on the center, and thus, increasing the spray transfer efficiency.

Figure 11 shows the sensitivity of the spray flow to the bell speeds at 150 l/min of shaping air, 90kV of electric setting, and 150 ml/min of liquid flow rate. With increasing bell speed, the spray angle becomes wider and a large number of the small droplets are entrained into the airfield, indicating that higher bell speed reduces the transfer effects but gives more of an even distribution of the spray particles on the target.

The effects of numerical transfer efficiency (TE), defined as the ratio of the total mass of drops on the target to the total mass of

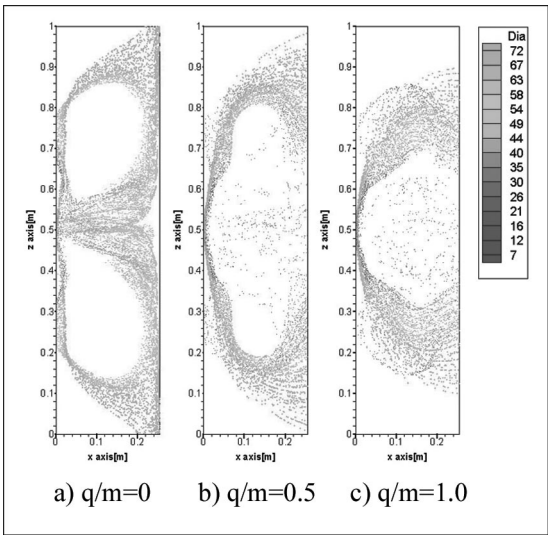

Fig. 10 Sensitivity of the spray flow to charge to mass ratio at the following operating condition: 30k rpm of bell speed, 150 l/min of shaping air, 90kV of electric setting, and 150 ml/min of liquid flow rate

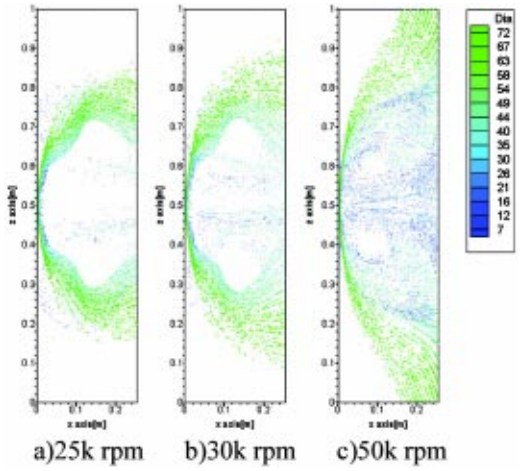

Fig. 11 Sensitivity of the spray flow to bell speed at the following operating conditions: 150 l/min of shaping air, 90kV of electric force, and 150 ml/min of liquid flow rate

injected drops, on operating conditions are shown in Table 2. The injected and deposited drop mass were corrected for 100 ms after an initial injection was started, when the flow was fully developed. For simplicity, no bounced model in this study is applied. When the spray particles arrive at the target, i.e., $xp > \text{xwall}$, those particles are collected to calculate the spray mass.

$$TE = \frac{Total\ Mass\ of\ drops\ on\ the\ target}{Total\ Mass\ of\ Injected\ drops} = \frac{m_{td}}{m_{ti}} \tag{12}$$

In a zero voltage condition, i.e., no electrical force, the numerical TE is only about 44%. When the electrical force is increased to 80 kV, with a $q/m = 1.0\ \mu C$ of the charge to mass ratio, the numerical TE is suddenly increased to 90%. The TE increases up to 94% at 90 kV at the same charge to mass ratio. These simulation results indicate that the electrical force is critical to the transfer efficiency. As the shaping airflow rate increases to 300l/min and other parameters remain the same, the TE decreases about 19% from that at 90 kV. This may be due to the high airflow rate; most of the spray drops are dispersed to the outside of the spray reducing the TE. In addition, the TE also decreases when the bell rotational speed is increased from 25k to 50k rpm with the same parameters as 90kV. As the bell speed is increased, the swirl momentum of the particles is increased and thus, the spray particles are easily dispersed to the outside.

Figure 12 illustrates the mass distribution along the z-direction on the target plane for 5ms after the spray flow was fully developed. The shaping airflow rate is changed from 150 l/min to 300 l/min, Fig. 12(a) to (b), and the bell speed is changed from 25k rpm to 50k rpm, Fig. 12(b) to (c), from the reference conditions, i.e., 1,50ml/min of liquid flow rate, 90k of voltage setting, 150l/min of airflow rate, and 25k rpm of bell speed. When increasing the shaping airflow rate, a more uniform distribution is observed on the target indicating that increasing the shaping airflow rate reduces the TE as discussed the above. On the other hand, even though increasing the bell speed makes the small particles move into the spray center, it does not seem to influence the uniformity.

Table 2 Numerical transfer efficiency

0 kV	80 kV	90 kV	300 l/min	50 k rpm
44%	90%	94%	75%	82%

Default conditions: 150 ml/min of liquid flow rate, 90 kV of high voltage setting, 150 l/min of shaping airflow rate, and 25 k rpm of bell speed.

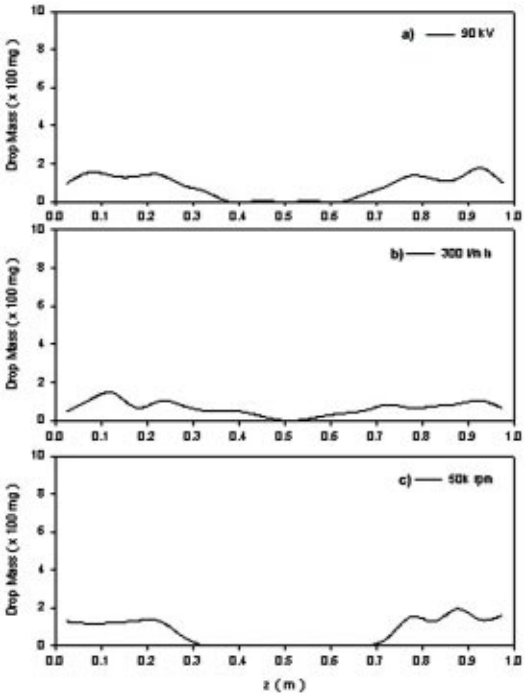

Fig. 12 Drop mass distribution on the target plane along *z*-axis direction at *y*=center

By making the spray angle wider, a large amount of the big particles are deposited on the outside of the target and a portion of them are also passed over the target, causing a reduction of the spray transport.

5 Conclusions

A numerical simulation of the spray transfer process in an electrostatic rotary bell applicator was performed using modern CFD method, the space-time CE/SE scheme. The newly developed numerical code, which is coupled together among three different modules, was applied to simulate the shaping airflow, spray particle dynamics, and electrostatic forces in conjunction with known experimental data. Based on the present results, the following findings can be summarized;

1. The spray shape is critically sensitive to changing the charge to mass ratio and electric force.
2. The electric force is an important parameter influencing the numerical transfer efficiency.
3. Although the numerical transfer efficiency was decreased by increasing the shaping airflow rate, the spray mass distribution became more uniform on the target.

The present work will be a steppingstone for more detailed model developments of the ESRB spray transfer process.

Nomenclature

C_D = Drag coefficient
D_k = Drag function
E_e = Electric field density
E_t = Total energy
e = Internal energy
F_e = Electric force
f_m, g_m, h_m = Flux vectors
$f\nu_m, g\nu_m, h\nu_m$ = Viscous flux vectors
p = Pressure

q/m = Charge to mass ratio
Δt_e, Δt_f = Response time
u, v, w = x, y, and z Velocity
u_m = Flow variables
$\vec{u}_p$ = Particle velocity vector
V_t = Tangential velocity
V_x = Axial velocity
$\vec{x}_p$ = Particle position vector
Φ = Electrostatic potential
γ = Specific heat
μ = Viscous coefficient
ρ = Density
τ = Shear stress
ω = Angular velocity (rad/s)

Subscript

d = Droplet
e = Electrode
f = Fluid
g = Gas
k = Particle index
p = Particle
o = Initial or constant value

References

[1] Bell, C. C., and Hochberg, J., 1981, ''Mechanisms of Electrostatic Atomization, Transport, and Deposition of Coatings,'' *Proc. 7th International Conference in Organic Science and Technology*, Athens, Greece.

[2] Im, K.-S., Lai, M.-C., Liu, Y., Sankagiri, N., Loch, T., and Nivi, H., 2001, ''Visualization and Measurement of Automotive Electrostatic Rotary-Bell Paint Spray Transfer Processes,'' J. Fluid Mech., **123**, pp. 237–245.

[3] Liu, Y., Lai, M.-C., Im, K.-S., Shankagiri, N., Loch, T., and Nivi, H., 1999, ''An Experimental Investigation of Spray Transfer Processes in an Electrostatic Rotating Bell Applicator,'' SAE Transaction Journal of Material Manufacturing, **107**(5), pp. 1235–1243.

[4] Bellan, J., 1983, ''A New Approach to Soot Control in Diesel Engines by Fuel-Drop Charging,'' Combust. Flame, **51**, pp. 117–119.

[5] True, M. A., 1983, ''Modeling of Electrostatic Spray Plumes,'' IEEE Transaction on Industry Applications, IA-19 **5**, pp. 754–758.

[6] Elmoursi, A. A., 1989, ''Laplacian Fields of Bell-Type Electrostatic Painting Systems,'' IEEE Transaction on Industry Application, **25**(2), pp. 234–240.

[7] Grace, J. M., and Dunn, P. F., 1994, ''Droplet Motion in an Electrohydrodynamic Fine Spray,'' *Proc. 6th International Conference on Liquid Atomization and Spray Systems*, Rouen, France, pp. 1002–1009.

[8] Shrimpton, J. S., Watkins, A. P., and Yule, A. J., 1997, ''A Turbulent, Transient Charged Spray Model,'' *Proc. 7th International Conference on Liquid Atomization and Spray Systems*, Seoul, Korea, pp. 820–827.

[9] Miller, R., Strumolo, G., Babu, V., Braslaw, J., and Mehta, M., 1998, ''Transient CFD Simulations of a Bell Sprayer,'' *Proc. of the IBEC'98*, 4, pp. 29–37.

[10] Huang, H., Lai, M.-C., Meredith, M., 2000, ''Simulation of Spray Transport from Rotary Cup Atomizer using KIVA-3V,'' *the 10th International KIVA User's Group Meeting*, Detroit.

[11] Chang, S. C., 1995, ''The Method of Space-Time Conservation Element and Solution Element—A New Approach for Solving the Navier Stokes and Euler Equations,'' J. Comput. Phys., **191**, pp. 295–324.

[12] Zhang, Z.-C., Yu, S.-T., Chang, S. C., Himansu, A., and Jorgenson, P. C. E., 1999, ''A Modified Space-Time CE/SE Method for Solving Euler and Navier-Stokes Equations,'' *AIAA Paper 99–3277*.

[13] Anderson, D. A., Tannehill, J. C., and Pletcher, R. H., 1984, *Computational Fluid Mechanics and Heat Transfer*, Hemisphere.

[14] Dukowicz, J. K., 1980, ''A Particle-Fluid Numerical Model for Liquid Sprays,'' J. Comput. Phys., **35**, pp. 229–253.

[15] Fureby, C., and Grinstein, F. F., 1999, ''Monotonically Integrated Large Eddy Simulation of Free Shear Flow,'' AIAA J., **37**(5), pp. 544–556.

[16] Amsden, A. A., O'Rourke, P. J., and Butler, T. D., 1989, ''KIVA-II: A Computer Program for Chemically Reactive Flows with Sprays,'' *Los Alamos National Laboratory Report*, LA-11560-MS.

Experimental and Numerical Development of a Two-Phase Venturi Flow Meter

Eugênio S. Rosa
Faculty of Mechanical Engineering-FEM,
State University of Campinas, UNICAMP,
CEP. 13081-970, Campinas, São Paulo, Brazil

Rigoberto E. M. Morales
Thermal Sciences Laboratory-LACIT,
Academic Department of Mechanics-DAMEC,
Federal Center of Technological Education of Paraná—CEFET/PR,
CEP. 80230-901, Curitiba, Paraná, Brazil

An algebraic model is developed access the gas and the liquid flow rates of a two-phase mixture through a Venturi tube. The flow meter operates with upward bubbly flows with low gas content, i.e., volumetric void fraction bellow 12%. The algebraic model parameters stem from numerical modeling and its output is checked against the experimental values. An indoor test facility operating with air-water and air-glycerin mixtures in a broad range of gas and liquid flow rates reproduces the upward bubbly flow through the Venturi tube. Measurements of gas and liquid flow rates plus the static pressure acroos the Venturi constitute the experimental database. The numerical flow modeling uses the isothermal, axis-symmetric with no phase change representation of the Two-Fluid model. The numerical output feeds the Venturi's algebraic model with the proper constants and parameters embodying the two-phase flow physics. The novelty of this approach is the development of each flow meter model accordingly to its on characteristics. The flow predictions deviates less than 14% from experimental data while the mixture pipe Reynolds number spanned from 500 to 50,000. [DOI: 10.1115/1.1758267]

1 Introduction

Multiphase flow meters measure, at line conditions, the volumetric or the mass rate of each component in a multiphase stream. They have applications in many industrial processes such as power plants, chemical plants and, in particular, on the segment of the exploration and production of the oil industry. They attend to four main demands: reservoir management by continuous monitoring of the flow rates at each well; custody transfer metering allowing the production of one field to be mixed with the production from another when the owners are different; process controlling when gas lift or vapor injection are used and, fiscal metering.

Research and development programs on multiphase metering started back during the 1980s in universities and research centers motivated by the oil industry needs. A brief review of their applications, operational principles, and shortcomings are in Jamieson [1], Costa e Silva et al. [2] and Falcone et al. [3]. Nowadays there are commercial multiphase flow meters available. They partially fulfill the demand of the oil industry. In fact, no single type of metering or metering approach can hope to cover all the applications. The difficulties arise when dealing with complex interfaces, turbulent flow field, data transmission, and available working space and environmental conditions to mention a few constraints met by the successful applications.

This work addresses to multiphase metering for bottom well applications. The development of multiphase meter operating in dowhole sites allows the follow-up of reservoir depletion, the performance assessment of each well, the production shut down and real time optimization of production by gas-lift. This type of application has flow with low gas void fraction and elevated pressure and temperature. The working environment and the dowhole space set constraints on the electronics and on the sizes of the mechanical parts turning the available multiphase meters not feasible to this scenario. To overcome these difficulties it was decided to turn back to the use of Venturi tube with pressure and temperature transducers as the main components of the multiphase meter for this application. The choice is based on the compliance of the size and shape of the Venturi tube with the dowhole site, the absence of moving parts and to the availability and the reliability of the pressure and temperature transducers for dowhole applications.

In fact, it is well known the use of the Venturi tube as a two-phase flow meter Graf [4], but there are no general relationships for differential pressure across Venturi. Its main limitation lies on the dependence of empirical constants, which in turn depends on experimental data. The applications for distinct flow rates, line size, or fluid properties are not straightforward since they depend on new experimental test campaigns. The objective of the paper is to exploit the use of numerical modeling to render an algebraic model employing discharge coefficient and other related flow meter parameters instead of estimating them through experimental tests. In principle, this approach will allow the development of each application on its own merits.

As a first approach to the subject matter experimental tests were performed. A vertical ascendant dispersed bubbly flow through a Venturi tube at near atmospheric pressure and ambient temperature with void fractions ranging from 2% to 12% is produced under laboratory-controlled conditions. Signals of the differential pressure and of the gas and liquid flow rates form the experimental database to access the reliability of the numerical modeling for the Venturi.

There are reported in the literature two approaches to develop the one-dimensional transport equations applied to dispersed bubbly flows: one of them is the Two-Fluid model described by Ishii [5] and Drew [6] and the other is the Interstitial Velocity approach reported in Kowe et al. [7]. Using the Two-Fluid model, Lewis and Davidson [8] and Kuo and Wallis [9] employed one-dimensional momentum equation to predict the trajectory of a bubble through a nozzle. More recently, Dias et al. [10] used similar formulation to describe the average concentration and velocities of a swarm of bubbles through a vertical nozzle. The 1-D modeling includes the influence of transverse gradients by means of covariance coefficients Ishii, [11]. Using the Interstitial Velocity approach Couet et al., [12] modeled a two-phase bubbly-droplet flow through a contraction. Boyer and Lemonnier [13] adapted the Interstitial Velocity model to predict air-water and oil-water flows and compared the experimental pressure drop against the predicted values. The later authors argue of a superior performance of the Interstitial Velocity model when compared to the Two-Fluid model. On the other hand Dias [14] and Dias et al.

Contributed by the Fluids Engineering Division for publication in the JOURNAL OF FLUIDS ENGINEERING. Manuscript received by the Fluids Engineering Division February 20, 2003; revised manuscript received November 30, 2003. Associate Editor: S. L. Ceccio.

[15] found the Two Fluid 1-D modeling sensitive to the inlet void profile, i.e., the model accuracy depends on how truthful are the transversal gradients transmitted to the model by the covariance coefficients.

The appeal of the 1-D models is due to the low computational cost. Represented by a set of ordinary differential equations they are readily solved by standard integration routine available in computational packages. On the other hand, they lack of information related to transversal gradients, wall friction factor, and turbulence effects, which are transmitted by means of covariance coefficients, which in turn come from experimental data. To better represent the physics of the flow and to be less dependent on experimental data, it was decided to use an axis-symmetric version of the Two-Fluid model as a numerical tool to model the vertical ascendant bubbly flow through the Venturi.

The structure of the paper is as follow. The experimental apparatus is in Section 2. Section 3 lauches the algebraic model, i.e., an evaluation procedure by which the gas and liquid flow rates are determined. The Two-Fluid model equations plus the additional equations for the turbulence modeling are in section 4. Section 5 gives details of the numerical implementation and Section 6 shows the results. The conclusions and final comments are in Section 7.

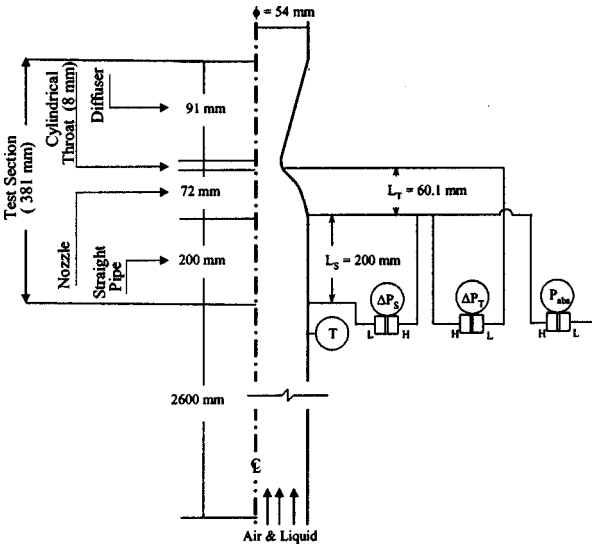

Fig. 2 Test section dimensions

2 Experimental Apparatus

The experimental setup reproduces a vertical, ascendant bubbly flow in a convergent-divergent section of a Venturi tube at near atmospheric pressure and at ambient temperature. The setup primary objective is to render an experimental database to validate the algebraic and numerical models. For reference the schematic of the apparatus is on Fig. 1. The mixing of gas and liquid takes place in a chamber, located at the lower end of the vertical pipe. On the chamber, the gas enters through an inner porous media and mixes with the liquid in an annular space. This arrangement produces uniform bubbles at the mixing chamber in the full range of gas and liquid flow rates. After the mixing, the bubbly flow develops upward along a vertical, straight Plexiglas pipe, 54 mm ID, and 50 diameters long, to reach the Venturi section. At the Venturi's outlet, there is another straight pipe, 30 diameters long. It connects the Venturi's outlet to the upper receiving tank open to the atmosphere. The upper tank acts as a gas-liquid separator: the gas stream vents to the atmosphere while the liquid returns to the lower liquid storage tank.

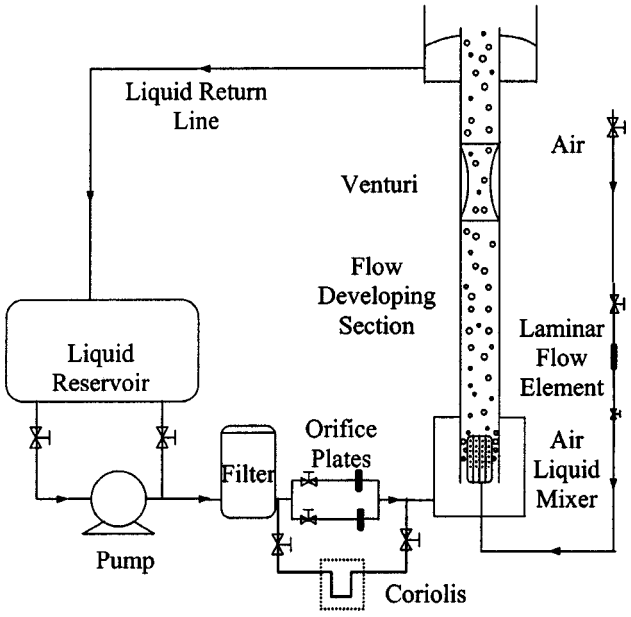

Fig. 1 Schematic of the experimental setup

The experimentals tests employ two pairs of working fluids: air and water and air plus a mixture of glycerin 72% in volume and water, hereafter referred as glycerin mixture for short. The densities of the phases are as follow: air is determined using ideal gas law; water is of 999 kg/m^3 and glycerin mixture is of 1190 kg/m^3. The viscosities of the water and of the glycerin mixture are of 1 cP and 30 cP, respectively. Finally, the surfaces tensions of the air-water and of the air-glycerin mixtures are 70 dynes/cm and 40 dynes/cm, respectively. A stainless steel centrifugal pump displaces the liquids. The air came from a compressed air supply. One Merian® laminar flow element, accurate within 1.5% measures the airflow. To measure the water volume flow rate one used two orifice plates previously calibrated to within 2%. Finally, a Micro Motion® Coriolis flow meter with an uncertainty of 1% measures the glycerin mixture mass rate. The experimental ranges of air and liquid superficial velocities (referred to the pipe cross section area) are, respectively, $J_G = 2$ cm/s to 11 cm/s and $J_L = 25$ cm/s to 100 cm/s. The averaged bubble size is of 3 mm and 2 mm for the air-water and air-glycerin mixture systems, respectively.

The test section consists of a straight pipe 200 mm long followed by the Venturi tube with 181 mm long, as shown on the schematic in Fig. 2. The convergent Venturi section is 72 mm long, with an inlet diameter, D, of 54.0 mm and throat diameter, D_T, of 30.3 mm rendering an area contraction ratio of 3:1. The Venturi throat and divergent sections have axial lengths of 8 mm and 101 mm. At the test section are measured the absolute temperature and pressure plus two differential pressures. The liquid phase always fills the pressure transducers connecting lines. Three pressure taps with 1.5 mm diameter holes and spacing L_S and L_T of 200 mm and 60.1 mm, respectively, transmit the signals to the pressure transducers ΔP_S and ΔP_T. The absolute pressure, P_{abs}, and ΔP_S and ΔP_T have a common pressure tap. The high- and low-pressure transducers terminals are labeled in Fig. 2 as H and L. Two differential pressure transducers, made by Valadyne® and calibrated against a hydrostatic water column, measures the differential pressures. The range of the pressure differences is of 3 mm H_2O to 20 mm H_2O for ΔP_S and of 100 mm H_2O to 650 mm H_2O for ΔP_T. The respective absolute uncertainties are of ± 0.5 mm H_2O and ± 5 mm H_2O.

The density of the upward gas-liquid column varies with time depending on the relative motion between the phases and on the

Table 1 Experimental data for air-water, (A@W), system

Run #	J_G^X (cm/s)	J_L^X (cm/s)	ΔP_S^X (mmH_2O)	ΔP_T^X (mmH_2O)	$\dot{m}^X$ (kg/s)	Re_D (- - -)	$\varepsilon_{\Delta PS}^X$ (%)	$\varepsilon_{\Delta PT}^X$ (%)	ε_m^X (%)
#1A@W	2.44	25.8	8.50	38	0.591	12901	6	13	2
#2A@W	4.21	26.1	15.27	38	0.598	13058	3	13	2
#3A@W	2.23	51.4	3.58	144	1.177	25696	14	3	2
#4A@W	4.46	51.4	9.43	148	1.178	25718	5	3	2
#5A@W	6.18	51.1	13.70	148	1.170	25534	4	3	2
#6A@W	7.47	51.2	16.56	149	1.172	25579	3	3	2
#7A@W	2.87	75.9	2.86	310	1.739	37967	17	2	2
#8A@W	4.51	76.1	5.48	316	1.743	38053	9	2	2
#9A@W	7.09	76.3	10.21	324	1.746	38129	5	2	2
#10A@W	10.22	76.6	15.63	336	1.754	38301	3	1	2
#12A@W	7.09	103.6	6.75	590	2.373	51804	7	1	2
#13A@W	10.19	103.6	10.17	604	2.373	51806	5	1	2
#15A@W	14.58	103.1	15.00	623	2.363	51579	3	1	2

Table 2 Experimental data for air-glycerin mixture, (A@G), system

Run #	J_G^X (cm/s)	J_L^X (cm/s)	ΔP_S^X (mm H_2O)	ΔP_T^X (mm H_2O)	$\dot{m}^X$ (kg/s)	Re_D (- - -)	$\varepsilon_{\Delta PS}^X$ (%)	$\varepsilon_{\Delta PT}^X$ (%)	ε_m^X (%)
1A@G	2.68	26.0	12.2	36	0.715	562	4	14	1
2A@G	4.15	25.7	21.0	36	0.705	554	2	14	1
3A@G	2.58	53.9	6.7	173	1.482	1165	7	3	1
4A@G	4.00	53.4	11.3	179	1.469	1154	4	3	1
5A@G	6.04	51.9	17.4	185	1.425	1120	3	3	1
9A@G	7.47	77.7	15.8	410	2.137	1679	3	1	1
10A@G	10.12	77.8	20.3	427	2.140	1682	2	1	1

air concentration inducing a pressure fluctuation on the feeding lines. Flow restrictions (orifices) inserted before the mixing chamber at the air and liquid feeding lines reduce this influence. The test begins adjusting a proper air and liquid flow rates. The data acquisition procedure starts after the whole setup achieves steady state.

A data acquisition board ATMIO-16, from National Instruments, acquire and store the measurement of pressure, temperature and phases flow rate at a sampling rate of 500 Hz. The output data are the time-averaged signals. The test runs totals 20, being 13 for the air-water system and 7 to the air-glycerin mixture. The experimental results are in Tables 1 and 2 but the data analysis is postponed to Section 6.

3 The Algebraic Model for Evaluation of the Phases Flow Rates

In a multiphase metering system is necessary to make *n* independent measurements in order to determine the flow rates of the *n* components. For the present case, there are just the gas and the liquid phases. The independent measurements will be two differential pressure signals, ΔP_T and ΔP_S, representing the pressure difference between the inlet to the Venturi's throat and the upstream to the Venturi inlet, respectively. Additionally, is also taken the absolute pressure and temperature to get the proper values of the transport properties. For reference, the pressure taps locations are in Fig. 2. The task of the algebraic model is to determine the stream velocity of each phase having as input just the two differential pressure signals. As its own name suggests, the model is constituted by algebraic equations whose parameters arise from numerical simulations. The following paragraphs outline the procedure.

3.1 Inlet Void Fraction. The ΔP_S signal helps to determine the cross-section averaged void fraction, $\langle \alpha_G \rangle$ at the inlet. By its turn, ΔP_S depends on the hydrostatic pressure of the mixture plus the pressure drop due to the wall friction force, ΔP_τ defined by the force balance: $\Delta P_\tau . A_S = \tau_w (\pi D L_S)$. Here, A_S, L_S, and τ_w are the Venturi inlet cross-section area, the spacing between pressure taps and the wall shear stress, correspondingly. Since the liquid phase fills the transducers lines, (see Section 2), ΔP_S expresses as:

$$\Delta P_S = \rho_L g L_S - [\rho_m g L_S + \Delta P_\tau], \tag{1}$$

where $\rho_m e \rho_L$ are, respectively, the mixture and the liquid densities and g is the gravitational constant. The mixture density is determined as a function of the inlet average cross-section void fraction $\langle \alpha_G \rangle$ and the densities of each phase:

$$\rho_m = (1 - \langle \alpha_G \rangle) \rho_L + \langle \alpha_G \rangle \rho_G , \tag{2}$$

where ρ_G is the gas density. From Eqs. (1) and (2), $\langle \alpha_G \rangle$ is:

$$\langle \alpha_G \rangle = \frac{\Delta P_S}{g L_S \Delta \rho} \cdot \lambda, \tag{3}$$

where $\Delta\rho$ is the phase density difference, $\Delta \rho = (\rho_L - \rho_G)$ and λ is a void fraction correction factor to $\langle \alpha_G \rangle$ due to the pressure drop put forth by the wall friction,

$$\lambda = 1 + \frac{\Delta P_\tau}{\Delta P_S}. \tag{4}$$

The estimate of λ comes from numerical flow simulation by running the code for distinct phase velocities. The data set for λ is conveniently expressed as a function of the Martinelli's parameter X in the form of:

$$\lambda = \lambda(X) \quad \text{where} \quad X^2 = \frac{(\Delta P_\tau)_L}{(\Delta P_\tau)_G} \tag{5}$$

beeing $(\Delta P)_L$ and $(\Delta P)_G$ are the gas and liquid pressure drop due to wall friction estimated using single-phase friction factor:

$$(\Delta P)_k = 4 \cdot \left(\frac{L_S}{D} \right) \cdot C_f \cdot \frac{1}{2} \rho_k J_k^2, \quad C_f = C_f \left(\frac{\rho_k J_k D}{\mu_k} \right),$$

k indicates the phase ($k=G$ gas phase or $k=L$ liquid phase), μ is the phase dynamic viscosity, J is the phase superficial velocity as defined in Eq. (10) and C_f is the Fanno friction factor coefficient. Section 6 discloses the fitting form for the function λ.

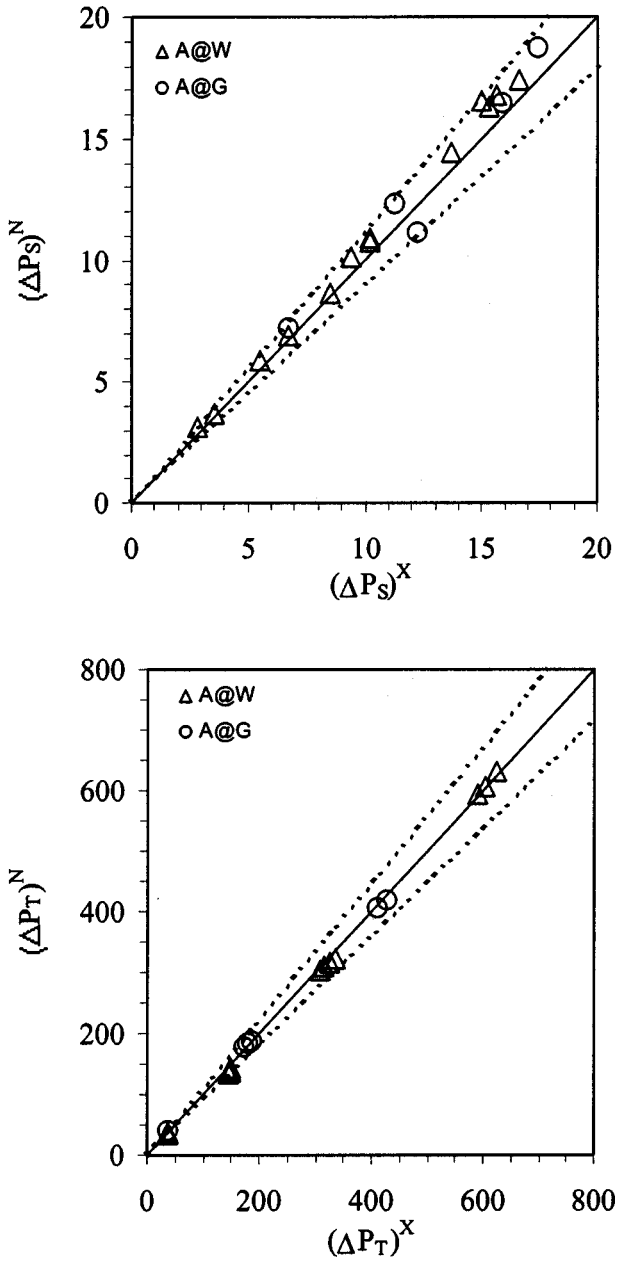

Fig. 3 Numerical versus experimental values of ΔP_S and ΔP_T

3.2 Mixture Mass Flow Rate. The gas and liquid mixture is treated as incompressible. The Venturi convergent section accelerates the mixture causing the pressure drop, similar to single phase flows. Patterning the established relationship between flow rate and pressure drop for a single-phase area obstruction flow meters, the mixture mass flow rate, $\dot{m}$ is determined as:

$$\dot{m} = C_d E \sqrt{2\rho_m \Delta P_T^*}, \tag{6}$$

where C_D is the two-phase discharge coefficient, E is the approaching velocity factor $E = A_T/\sqrt{1-\beta^4}$ being A_T the Venturi throat cross-section area and β the throat to pipe diameter ratio $\beta = D_T/D$ and finally, ΔP_T^* represents the pressure drop caused by the mixture hydrostatic column, by the flow acceleration and by the wall friction. To compose ΔP_T^* from ΔP_T signal, see Fig. 2 for schematic, is necessary to add the hydrostatic pressure exerted by the liquid column L_T:

$$\Delta P_T^* = \Delta P_T + \rho_L g L_T. \tag{7}$$

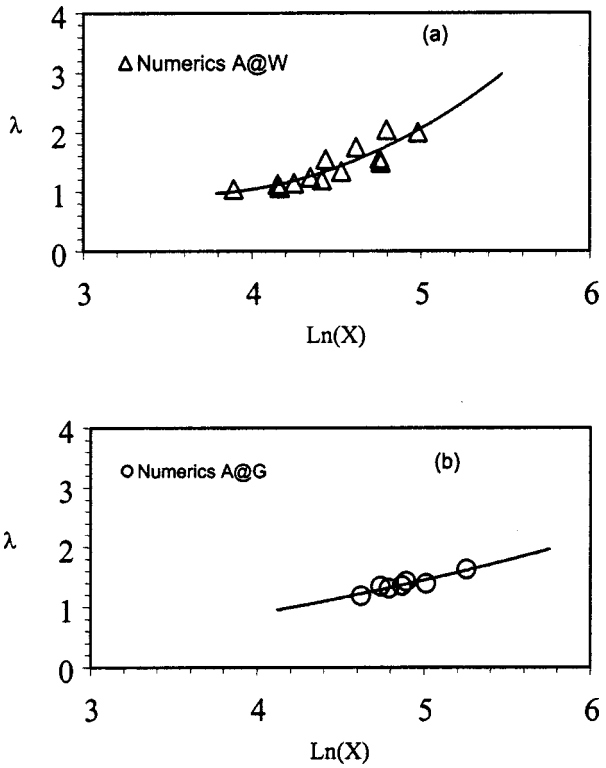

Fig. 4 Void fraction correction factor λ as a function of the Martinelli's parameter for air-water (*a*) and air-glycerim (*b*) systems. The open symbols are numerical data and the solid line is the curve fitting.

The discharge coefficient comes from Eq. (6) with all the variables related to its determination arising from a numerical database. The flow simulation uses distinct pairs of J_G and J_L as input conditions and the output is the mixture mass flow rate, the void fraction, the mixture density and ΔP_T^*. The ratio between the actual to the frictionless mass flow rate of a homogeneous mixture defines the discharge coefficient. It brings to Eq. (6) the effects of the turbulence, wall friction, slip velocity, phase velocity profiles, interfacial forces such as drag, virtual mass, lateral forces, and interfacial pressure forces. One of the usefulness of the numerical simulation is the possibility to model most of all physical flow mechanisms. The C_D represents a lumped parameter, which carries to the algebraic model all this information. For the algebraic model, C_D is conveniently expressed as a function of the pipe Reynolds number,

$$C_D = C_D(\mathrm{Re}_D) \quad \text{where} \quad \mathrm{Re}_D = \frac{4\dot{m}}{\pi D \mu_L}, \tag{8}$$

The fitting of the numerical data for $C_D \times \mathrm{Re}_D$ is in Section 6.

3.3 Gas and Liquid Superficial Velocities. The mixture mass flow rate evaluated by Eq. (6) is given by the sum of each phase mass flux which, expressed in terms of the densities, velocities and area, is in the form:

$$\dot{m} = (J_L \rho_L + J_G \rho_G) A_S, \tag{9}$$

J_L and J_G are the superficial gas and liquid velocities evaluated at the Venturi inlet and defined as:

$$J_G = Q_G/A_S \quad \text{and} \quad J_L = Q_L/A_S, \tag{10}$$

being Q_G and Q_L the gas and liquid volumetric flow rates.

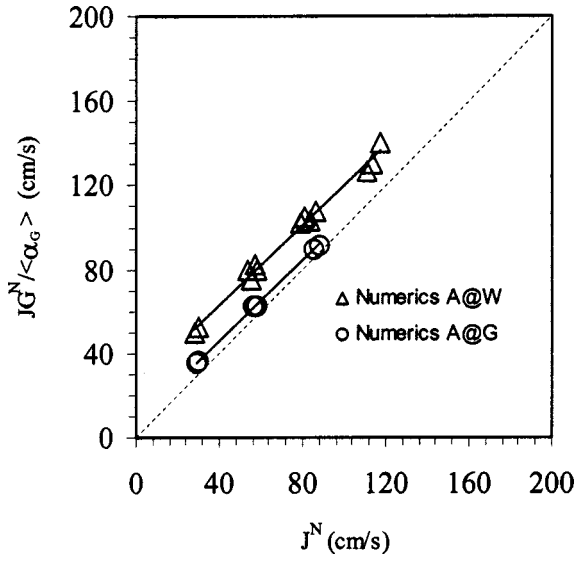

Fig. 5 Gas velocity against the mixture superficial velocity for air-water and air-glycerim systems. The open symbols are numerical data and the solid lines represent curve fitting.

To solve for the superficial phase velocities, it is necessary to have an extra equation for Eq. (9). The kinematic law enforced by the drift flux model, Zuber and Findley [16], supplies the missing information:

$$\frac{J_G}{\langle\alpha_G\rangle} = C_0 \cdot (J_G + J_L) + V_{GJ}, \tag{11}$$

where C_0 is a parameter associated with the phase distribution and V_{GJ} is the drift flux velocity. The values of C_0 and V_{GJ} are also determined from the numerical flow simulations. Solving Eqs. (9) and (11) determine the superficial phase velocities (Fig. 5):

$$\begin{bmatrix} \rho_L A_S & \rho_G A_S \\ -\langle\alpha_G\rangle C_0 & 1-\langle\alpha_G\rangle C_0 \end{bmatrix} \begin{bmatrix} J_L \\ J_G \end{bmatrix} = \begin{bmatrix} \dot{m} \\ \langle\alpha_G\rangle V_{GK} \end{bmatrix}. \tag{12}$$

The coefficients of the linear equation system are either known parameters such as area and densities or variables determined through the numerical flow simulation.

3.4 Evaluation Procedure. The evaluation of J_G and J_L is not straightforward since several parameters in Eq. (12) also depend on the superficial velocities. The phase velocities are determined recursively starting from initial guesses for C_D and λ. The following evaluation algorithm summarizes the iterative procedure.

1. Input data: ΔP_S and ΔP_T from experimental data, drift flux parameters C_0 and V_{GJ} from numerical flow simulations, and the initial guesses to C_D and λ taken as 0.6 and 1, respectively, suffice.
2. Evaluate void fraction $\langle\alpha_G\rangle$ and the mixture density, ρ_m, Eqs. (2) and (3).
3. Evaluate mixture mass flow rate, $\dot{m}$, Eq. (6).
4. Evaluate the pipe Reynolds number, Re_D and the discharge coefficient, C_D, Eq. (8).
5. Check if the calculated C_D value differs less than 0.01% than its assigned value. If false, return to Step 2 otherwise continue.
6. Solve Eq. (12) to determine the superficial phase velocities, J_G and J_L.
7. With the superficial velocities of Step 6 evaluate Lockhart parameter, X^2, Eq. (5), using Fanno's single-phase pipe friction factors.
8. Determine the void fraction correction factor, λ, Eq. (5).
9. Check if the calculated λ value differs less than 0.01% than its previous value. If false, return to Step 2 otherwise continue.
10. End of the procedure, the mixture mass flow rate, the inlet void fraction, and the gas and liquid superficial velocities determined.

4 The Two-Fluid Model

The Two-Fluid model embodies the interfacial exchanges in the mass, momentum and interfacial transport equations, Ishii [5] and Drew [6]. In steady-state isothermal flows with no phase change, these equations reduce, after some definitions and operations, to the forms of Eqs. (13) to (14):

$$\nabla \cdot (\alpha_k \rho_k \mathbf{V}_k) = 0 \tag{13}$$

$$\nabla \cdot (\alpha_k \rho_k \mathbf{V}_k \mathbf{V}_k) = -\alpha_k \nabla p_k + \nabla \cdot [\alpha_k (\tau_k + \tau_k^{\mathrm{Re}})] + \alpha_k \rho_k \mathbf{g} + (p_{ki} - p_k) \nabla \alpha_k + \mathbf{M}_{ki} \tag{14}$$

In the above equations the subscript $_k$ indicates the phase ($_{k=G}$ or $_{k=L}$, gas or liquid) and the subscript $_{ki}$ defines proper values of the variables at the interface, like the velocity and the pressure of phase $_k$ at the interface. The density is ρ, $\mathbf{V}$ represents the mean velocity vector field, p is the pressure, $\mathbf{g}$ is the gravitational force, τ is the stress tensor, $\mathbf{M}_{ki}$ is the generalized interfacial force, which couple the two phases. The phase local volumetric concentration is α_k, therefore $\alpha_G + \alpha_L = 1$. The local void fraction refers to the α_G volumetric concentration.

One used a rather complete formulation of the Two-Fluid model to represent the flow and the various forces acting to distribute the phases over the flow domain. A balance between the radial pressure forces, the lateral lift, and the turbulence forces sets up the lateral distribution of the phases. The interplay among the inertia, the gravity, the wall shear, the drag and the virtual mass forces along the axial direction establishes the pressure gradient. Furthermore, for the bubbly flow regime is considered that only the liquid phase is in contact with the walls. Therefore, the near wall flow is treated as a single-phase flow; the non-slip condition is enforced for the laminar flow regime while the standard wall law is used to bridge the flow to the fully turbulent regime. In order to solve Eqs. (13) and (14) one has to constitute this system with proper relations.

4.1 The Stress Tensor. The viscous and the turbulent shear stresses are:

$$\tau = \rho_L (\nu_L + \nu_T)[\nabla V_L - \nabla V_L^T] - \frac{2}{3} \kappa \cdot \delta_{ij}, \tag{15}$$

where ν_L and ν_T represent the liquid phase kinematic and turbulent viscosity, κ is the turbulent kinectic energy and δ_{ij} is the Kronecker delta. The contribution of the dispersed phase is negligible for its great density difference and also by its low concentration. In order to solve the phasic momentum equations, it is necessary to define closure laws for the turbulent viscosity. Following Bertodano et al. [17], the turbulent viscosity is a linear superposition of the turbulent viscosity due to the Reynolds stress plus an enhancement due to the bubble induced turbulence:

$$\nu_T = \nu_{BI} + \nu_{SI}. \tag{16}$$

The bubble induced turbulent viscosity model stems from the concept of mixing length,

$$\nu_{BI} = C_{\mu b} \alpha_G d |\mathbf{V}_G - \mathbf{V}_L|, \tag{17}$$

where $C_{\mu b}$ is equal to 0.69 and d is the mean bubble diameter. Conversely, the shear induced turbulent viscosity arises accordingly to the κ-ε model:

$$\nu_{SI} = C_\mu \kappa^2 / \varepsilon. \tag{18}$$

In Eq. (18), ε is the dissipation rate of turbulent kinetic energy and the value of C_μ is equal to 0.09. The turbulent kinetic energy and

its dissipation rate come from the simultaneous solution of the two-phase version of the standard κ-ε model, Bertodano et al., [17]:

$$\nabla\cdot(\alpha_L\mathbf{V}_L\kappa)=\nabla\cdot\left[\alpha_L\left(\nu_L+\frac{\nu_T}{\sigma_\kappa}\right)\nabla\kappa\right]+\alpha_L(P-\varepsilon)+\nabla\cdot\left(\frac{\nu_T}{\sigma_\alpha}\kappa\nabla\alpha_L\right) \tag{19}$$

$$\nabla\cdot(\alpha_L\mathbf{V}_L\varepsilon)=\nabla\cdot\left[\alpha_L\left(\nu_L+\frac{\nu_T}{\sigma_\varepsilon}\right)\nabla\varepsilon\right]+\alpha_L\left(\frac{\varepsilon}{\kappa}\right)(c_{\varepsilon1}P-c_{\varepsilon2}\varepsilon)+\nabla\cdot\left(\frac{\nu_T}{\sigma_\alpha}\varepsilon\nabla\alpha_L\right) \tag{20}$$

where $\sigma_\kappa=1.0$; $\sigma_\varepsilon=1{,}314$; $\sigma_\alpha=1.0$, $c_{\varepsilon1}=1.44$; $c_{\varepsilon2}=1.92$. P is the kinetic energy production term:

$$P=\nu_{SI}[\nabla\mathbf{V}_L+\nabla\mathbf{V}_L^T]:\nabla\mathbf{V}_L \tag{21}$$

The values of κ and ε near the wall come from the standard the single phase κ-ε model using the assymptotics limits of the wall law.

4.2 The Interfacial Pressure Term. The pressure at the interface, p_{Li}, for the liquid phase is:

$$p_{Li}=p_L-C_{pi}\rho_L(\mathbf{V}_G-\mathbf{V}_L)^2, \tag{22}$$

where p_L is the bulk liquid pressure.

This expression results from the solution of a non-viscous flow around a sphere. In this case the coefficient C_{pi} is 0.25. Lance and Bataille [18] suggested values between 0.5~0.7 for actual bubbly flows. The present work uses C_{pi} equals to 1.5 for laminar flow regime, while for turbulent flow regime follows Bertodano et al. [17]. That is $C_{pi}=C_{vm}/2$, where C_{vm} is the virtual mass force coefficient, to be defined in the next section. Furthermore, the pressure does not vary in the gas phase, $p_{Gi}=p_G$ but there is a jump at the interface due to the surface tension, γ, effect, $p_{gi}-p_{li}=4\gamma/d$.

4.3 The Interfacial Forces. The generalized interfacial force acting on the phase k, $\mathbf{M}_{ki}$, has the contribution of the drag force, $\mathbf{M}_k^d$, and the non-drag force, $\mathbf{M}_k^{nd}$. The drag force arises due to the relative displacement of the bubble. The drag force on a bubble of diameter d is

$$\mathbf{M}_L^d=-\mathbf{M}_G^d=\frac{3}{4}\frac{C_d}{d}\rho_L\alpha_G(\mathbf{V}_G-\mathbf{V}_L)|\mathbf{V}_G-\mathbf{V}_L| \tag{23}$$

where Cd is the drag coefficient and its expression are in Kuo and Wallis [9].

The non-drag force accounts for the lateral forces and the virtual mass force. A lateral force, $\mathbf{M}_L^L=-\mathbf{M}_G^L$, arises when the bubble displaces through a liquid with a nonuniform velocity distribution. In an upward bubbly flow, it acts to displace the bubble toward the wall:

$$\mathbf{M}_L^L=-\mathbf{M}_G^L=C_L\rho_L\alpha_G(\mathbf{V}_G-\mathbf{V}_L)\times(\nabla\times\mathbf{V}_L). \tag{24}$$

According Lahey et al. [19], the lift coefficient C_L varies between 0.05 and 0.1 in air-water bubbly flows. The values for C_L, which produced the best results, are of 0.1 for laminar flow regime and 0.4 to turbulent flow regime.

The virtual mass force is proportional to the relative fluid acceleration, Drew and Lahey, [20]:

$$\mathbf{M}_L^{VM}=-\mathbf{M}_G^{VM}=C_{vm}\rho_L\alpha_G[\mathbf{V}_G\nabla\mathbf{V}_G-\mathbf{V}_L\nabla\mathbf{V}_L]. \tag{25}$$

Various authors used different values for the virtual mass coefficient, C_{VM}. Drew and Lahey [20] suggested 0.5; Kuo and Wallis [9] used values within the range 2.0~3.0, and Lance and Bataille [18] indicated 1.2~3.4. The employed C_{VM} value is of 2.0 for all flow regime simulations.

5 The Numerical Method

The transport equations are discretized using the control-volume formulation, Patankar [21]. The computational domain encompasses a flow developing section, the Venturi convergent section, plus the cylindrical throat section. The developing section allows the numerical solution to evolve similarly to the experimental phenomena and reach the Venturi entrance with transversal profiles alike. The axial direction transports the flow information dominating the physical processes at the Venturi's convergent section. With the absence of choking, this feature allows to place the throat section as the domain outlet since the downstream flow exerts no effects at the convergent section. Furthermore, the experimental data input come from the Venturi's convergent section. The grid is cylindrical-polar with 140×27 volumes along the axial and radial directions, respectively. The radial grid spans from the centerline to the pipe wall with 27 volumes uniformly spaced. The axial grid has three regions. The first one has 40 volumes corresponding to the developing pipe section with 2,500 mm (40 D) long. The second region is coincident with the straight pipe section upstream the Venturi where ΔP_S is measured. It has 20 volumes with 200 mm (3.7 D). Finally, the third region corresponds to the convergent and throat sections of the Venturi tube. It is 80 mm (1.5 D) long with 80 volumes equally spaced.

The numerical problem is set-up within the environment of the CFD package Phoenics® 3.3. It is a transport equations solver with Two-Fluid model capability. The transport equations set is assembled using the elliptic solver with an implicit scheme for the pressure-correction (SIMPLEST), staggered grid and upwind scheme for the advection terms. The Inter-Phase Slip Algorithm, IPSA, solves the system of algebraic equations for two-phase flow, Spalding [22]. A Pentium IV, 1.5 GHz processor preformed the calculations. The averaged CPU time is three hours for each run.

6 Results

This section displays data coming from experiments, from numerical simulations and also from the algebraic model. For clearness purpose the variables are labeled with super-indexes to identify their origin. The super-indexes *X*, *N* and *M*, attached to each variable indicates if it come from e*X*perimental, *N*umerical or algebraic *M*odeling.

Prior to the data outputs, is necessary to define the experimental, the numerical and the algebraic model relative errors to aid the data analysis. The relative experimental error, or better saying the experimental uncertainty, is defined for a generic variable ϕ as the ratio between the absolute uncertainty of the variable and its most probable value, in terms of percentage it expresses as:

$$\varepsilon_\phi^X=100\cdot\left(\frac{\pm\Delta\phi^X}{\overline{\phi^X}}\right), \tag{26}$$

on the other hand, the numerical and the algebraic model relative errors, ε_ϕ^N and ε_ϕ^M express the relative difference between the experimental and the numerical or the experimental and the modeled values of a generic variable ϕ:

$$\varepsilon_\phi^N=100\cdot\left(\frac{\phi^X-\phi^N}{\phi^X}\right)\quad\text{or}\quad\varepsilon_\phi^M=100\cdot\left(\frac{\phi^X-\phi^M}{\phi^X}\right). \tag{27}$$

The results are presented on the four following sections. The first one regards to the experimental data. The second section presents the numerically determined database and the corresponding curve-fitting functions. A direct comparison of the modeled and experimentally determined flow rates is on the third section. Finally, the forth section draws a simplified version of the algebraic model and develops an uncertainty analysis.

6.1 Experimental Data. Tables 1 and 2 summarize the experimental database for the air-water and air-glycerin mixture experiments. The label of each run has a number followed by three

Table 3 Numerical results for air-water, (A@W), system

Run #	ΔP_S^N (mm H_2O)	ΔP_T^N (mm H_2O)	$\Delta P\tau$ (mm H_2O)	$\langle\alpha_G\rangle$ (- - -)	C_D (- - -)	λ (—)	$\varepsilon_{\Delta PS}^N$ (%)	$\varepsilon_{\Delta PT}^N$ (%)
1A@W	8.6	35	0.56	0.049	0.567	1.065	−1	6
2A@W	16.3	36	0.63	0.080	0.581	1.039	−7	5
3A@W	3.7	134	1.78	0.028	0.785	1.488	−2	7
4A@W	10.2	137	1.99	0.059	0.790	1.196	−8	7
5A@W	14.4	140	2.08	0.075	0.786	1.144	−5	5
6A@W	17.4	142	2.17	0.094	0.791	1.124	−5	4
7A@W	3.1	302	3.11	0.028	0.847	2.000	−9	2
8A@W	5.9	308	3.26	0.043	0.849	1.554	−7	3
9A@W	10.9	317	3.67	0.069	0.852	1.337	−7	2
10A@W	16.8	322	4.00	0.095	0.862	1.239	−7	4
12A@W	6.9	593	7.20	0.056	0.874	2.039	−3	0
13A@W	10.7	608	8.01	0.078	0.875	1.746	−6	−1
15A@W	16.5	630	8.63	0.104	0.869	1.541	−10	−1

letters, which represent the air-water system (A@W), or the air-glycerin system (A@G) for short. The numbering links the test to specific phases velocities. Therefore, coincident test numbering between the (A@W) and (A@G) systems means tests with the same superficial gas and liquid velocities. Each table has seven columns. The second to the fifth column represent the experimentally determined values of the air and liquid superficial velocities in centimeters per second and the pressure differences ΔP_S^X and ΔP_T^X, as measured by the line transducers, in millimeters of water column. The mass flow rate and the pipe Reynolds number are in columns 6 and 7 evaluated accordingly to Eqs. (9) and (8). Columns 8 thru 10 report the relative uncertainty of ΔP_S^X, ΔP_T^X and $\dot{m}^X$.

The A@W and A@G database consist of sub-sets with constant liquid superficial velocity with increasing gas velocities in order to access the influence of the gas and liquid content on the overall flow meter performance. A distinguished characteristic between databases is the liquid viscosity. The A@W system has pipe Reynolds number ranging from 13,000 to 52,000, typically on the turbulent flow regime. On the other hand, the A@G system has pipe Reynolds number within 500 and 1700, typical of laminar flow regime.

Keeping constant the liquid velocity, the ΔP_S^X values increase as the gas velocity increases. This behavior is in agreement with Eq. (1) since the increase of the gas velocity decreases the mixture density. Although the A@G have higher friction pressure drop than A@W system, it also have a higher liquid density, which overrides the ΔP_τ increase producing ΔP_S^X outcome up to 50% greater than the one observed for the same pair of velocities in the A@W system. The experimental relative uncertainty, $\varepsilon_{\Delta PS}^X$, spans from 2% to 17%.

The ΔP_T^X, following Eq. (6), is the outcome from the difference of the throat pressure drop and the hydrostatic pressure exerted by the liquid column between pressure taps. Since the hydrostatic pressure exerted by the liquid column, $(\rho_L g L_T)$, is constant through all the tests, the ΔP_T^X is directly proportional to the throat pressure drop. Considering the low inlet void fraction and the density difference between phases of three orders of magnitude, ΔP_T^X is mainly sensitive to the liquid flow rate and weakly on the airflow rate. The experimental relative uncertainty, $\varepsilon_{\Delta PT}^X$, spans from 1% to 14%.

The superficial gas velocities for A@W and A@G databases ranged from 2 cm/s to 14 cm/s with a relative uncertainty of 1.5%. The liquid superficial velocities ranged from 26 cm/s to 105 cm/s for the A@W database and from 25 cm/s to 77 cm/s for the A@G database with uncertainties of 2% and 1% for the A@W and A@G database, respectively. Finally, the mixture mass flow rate, $\dot{m}$, ranges from 0.5 kg/s to 2.4 kg/s with a relative uncertainty of 2% for the A@W and of 1% for the A@G.

6.2 Numerical Outputs and Correlation Functions. Tables 3 and 4 exhibit the numerically determined values for the A@W and A@G systems. The second and third columns have the differential pressure estimates of ΔP_S^N and ΔP_T^N as the output of the Two-Fluid model using the experimental values of J_G^X and J_L^X as input data. The numerical outputs pattern the experimental data. A comparison between the experimental and numerical pressure differences outcomes is in the scatter plot of Fig. 3. The x and y axes reports, respectively, the experimental and numerical values of ΔP_S and ΔP_T and the dashed lines represent $\pm 10\%$ bounds. Most of the numerical estimates are within the $\pm 10\%$ interval. The biggest deviations occur for the lower liquid velocity range. In general, the numerical data show a tendency to over-predict the ΔP_S^N for both systems: A@W and A@G. On the other hand, the ΔP_T^N values are underpredicted for the A@W system but overpredicted to the A@G system if one consider the low liquid velocities points on the test grid. Considering the high liquid velocity data, the estimates break even or reverse the observed tendency. Comparing the experimental uncertainty and the numerical relative error is possible to say that most of the numerical estimates, ΔP_S^N and ΔP_T^N, are within the experimental uncertainty bounds. The fact that $\Delta P_S^N > \Delta P_S^X$ is equivalent to $(\rho_m g L_S + \Delta P\tau)^X > (\rho_m g L_S + \Delta P\tau)^N$ but one can go no further than this on the analysis since it depends implicitly on $\langle\alpha_G\rangle$ and explicitly on $\Delta P\tau$ which are variables numerically determined. To draw an analysis to the experimental and numerical differences found in

Table 4 Numerical results for air-glycerin mixture (A@G), system

Run #	ΔP_S^N (mm H_2O)	ΔP_T^N (mm H_2O)	$\Delta P\tau$ (mm H_2O)	$\langle\alpha_G\rangle$ (- - -)	C_D (- - -)	λ (- - -)	$\varepsilon_{\Delta PS}^N$ (%)	$\varepsilon_{\Delta PT}^N$ (%)
1A@G	11.1	42	3.91	0.076	0.580	1.352	9	−16
2A@G	22.1	41	4.08	0.116	0.589	1.185	−5	−14
3A@G	7.2	180	4.52	0.041	0.795	1.628	−7	−4
4A@G	12.3	184	4.77	0.064	0.791	1.388	−9	−3
5A@G	18.8	188	5.78	0.097	0.774	1.308	−8	−2
9A@G	16.5	406	7.07	0.083	0.850	1.428	−4	1
10@G	23.3	419	8.04	0.111	0.853	1.345	−15	2

ΔP_T is even more cumbersome since its overall value depends on the mixture density, the flow velocities and the friction pressure drop.

The pressure drop due to the wall friction on the straight section of length L_S is on the fourth column of Tables 3 and 4. Considering the same pair of superficial velocities, the $\Delta P\tau$ outcome for the A@W system is always smaller than the one from A@G system due to the viscosity differences between the systems. The $\Delta P\tau$ grows as the liquid or the gas velocities increases. Keeping constant the liquid velocity $\Delta P\tau$ has less than one-fold increase with the increase of the gas velocity as observed in Tables 3 and 4. The void fraction correction term, λ, defined in Eq. (4) arises from the 2th and 4th columns in Tables 3 and 4. The behavior of λ is similar for A@W and A@G systems. As seen in Tables 3 and 4, λ decreases as J_G increases for a constant superficial liquid velocity. The λ dependence on J_G and J_L is well represented by the Martinelli's parameter X as shown in Fig. 4*a-b*. The parameter λ grows with increasing X for the A@W and A@G systems. The open symbols represent the numerically determined values and the solid line is the curve fitting. The linear regression equations for the A@W and A@G systems are in Eqs. (28) and (29), respectively:

$$\lambda = 0.5932 \cdot [Ln(X)]^2 - 4.3127 \cdot Ln(X) + 8.7989, \qquad (28)$$

$$\lambda = 0.0751 \cdot [Ln(X)]^2 - 0.1229 \cdot Ln(X) + 0.1825. \qquad (29)$$

The inlet averaged void fraction, $\langle \alpha_G \rangle$ is in the fifth column of Tables 3 and 4. It results from the averaging process of the local void fraction, numerically determined, along the Venturi inlet cross section. For a constant liquid velocity, the averaged void fraction increases as the gas velocity increases. The $\langle \alpha_G \rangle$ in A@G system is always higher than the A@W system considering the same phase velocities for both systems. This behavior is due to the reduction of the slip velocity in A@G system owing to the increase of the liquid viscosity. The drift flux constants, C_0 and V_{GJ}, stem from the linear fit of the gas velocity, $J_G/\langle \alpha_G \rangle$ versus the mixture superficial velocity J, as shown in Fig. 5. Successive numerical flow simulations using distinct pairs of inlet velocities, J_G and J_L, generate the necessary database to determine the drift flux constants. Despite of the differences between the A@W and A@G systems regarding flow regime (laminar/turbulent) and fluid-particle regime (distorted/spherical) the values of the distribution parameter are very close. In fact the determined values of C_0 are of 0.952 for the A@W and of 0.960 for the A@G. The near unit C_0 value indicates that the profiles of local variables α_G and j are alike. On the other hand, the determined drift velocities for the A@W and A@G systems are of 24.9 cm/s and 7.5 cm/s, respectively. The mean drift velocity, V_{GJ}, has a strong dependence on the liquid viscosity, which in turn is also related to the flow regime and the fluid-particle regime. The V_{GJ} values for the A@W and A@G systems compare with the 21 cm/s and 7 cm/s values found from the drift velocity correlations for infinitum media, Ishii [11]. The gas-liquid mixture for A@G system has an almost homogeneous behavior due to the low V_{GJ} value. Figure 5 has the homogeneous flow line for reference.

The discharge coefficient is on column 6 of Tables 3 and 4. For increasing Reynolds, C_D grows from 0.58 to 0.87 and from 0.56 to 0.86 for the A@W and A@G systems, respectively. At turbulent flow regime, high Reynolds numbers, C_D shows an asymptotic behavior similar to the ASME single-phase nozzles. Figure 6*a-b* shows a scatter plot of the C_D numerical values on the *y*-axis against the pipe Reynolds number on the *x*-axis. The solid lines in Fig. 6 represent the curve-fitting equations of C_D as a function of Re_D, which for A@W and A@G systems are in Eqs. (30) and (31), respectively:

$$C_D = -0.14[Ln(\mathrm{Re}_D)]^2 + 3.0825 Ln(\mathrm{Re}_D) - 16.095. \qquad (30)$$

$$C_D = -0.0983[Ln(\mathrm{Re}_D)]^2 + 1.6016 Ln(\mathrm{Re}_D) - 5.6133 \qquad (31)$$

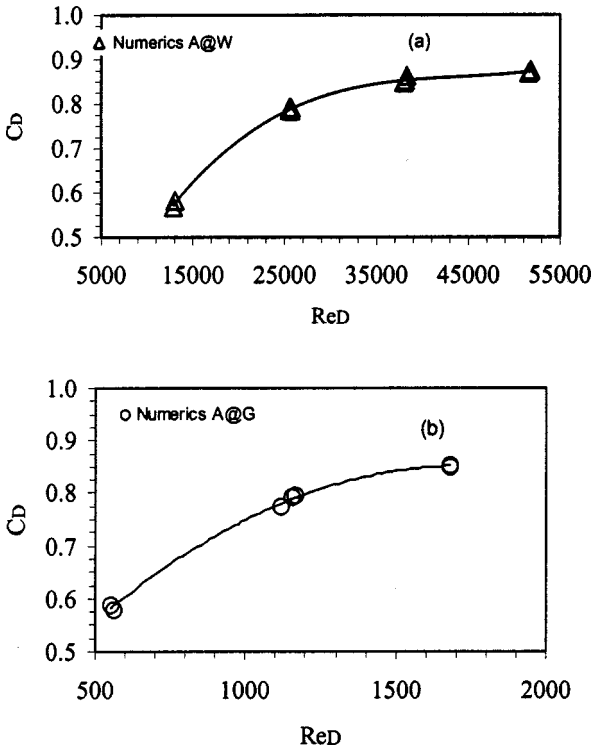

Fig. 6 Discharge coefficient as a function of the pipe Reynolds number for air-water (*a*) and air-glycerin mixtures (*b*) systems. The open symbols are numerical data and the solid line is the curve fitting.

6.3 The Evaluation of the Phases Flow Rates. The flow rate evaluation comes from the algorithm in Section 3.4. It uses as input data the experimental values of ΔP_T^X and ΔP_S^X, the phase transport properties, the correlation equations for $\lambda = \lambda(X)$ and $C_D = C_D(\mathrm{Re}_D)$ and the drift flux parameters, C_0 and V_{GJ}. The evaluation routine start with initials guesses to λ and C_D. The routine outcomes are the values of J_G^M, J_L^M and $\dot{m}^M$ as shown on the 2nd thru the 4th columns on Tables 5 and 6 for the A@W and A@G systems. Also, the model relative errors are shown in Tables 5 and 6, as defined in Eq. (27) for J_G^M, J_L^M and $\dot{m}^M$.

The Figures 7, 8 and 9 display, in the sequence, the comparison of the model outputs: J_G^M, J_L^M and $\dot{m}^M$ against the experimentally values. For the set of Figs. 7 thru 9, the solid line represent the locus of a perfect match between the model and experimental

Table 5 Model estimates for air-water, (A@W), system phase velocities

Run #	J_G^M (cm/s)	J_L^M (cm/s)	$\dot{m}^M$ (kg/s)	ε_{JG}^M (%)	ε_{JL}^M (%)	ε_m^M (%)
1A@W	2.7	29	0.673	−9	−14	−14
2A@W	4.3	28	0.650	−1	−9	−9
3A@W	2.4	54	1.245	−9	−6	−6
4A@W	5.0	54	1.231	−13	−5	−5
5A@W	6.6	53	1.215	−7	−4	−4
6A@W	7.6	53	1.208	−2	−3	−3
7A@W	3.0	78	1.782	−3	−2	−2
8A@W	4.8	78	1.781	−7	−2	−2
9A@W	7.8	77	1.773	−9	−2	−2
10A@W	10.7	77	1.775	−5	−1	−1
12A@W	7.7	103	2.366	−9	0	0
13A@W	10.4	103	2.369	−2	0	0
15A@W	13.7	104	2.372	6	0	0

Table 6 Model estimates for air-glycerin, (A@G), phase velocities

Run #	J_G^M (cm/s)	J_L^M (cm/s)	$\dot{m}^M$ (kg/s)	ε_{JG}^M (%)	ε_{JL}^M (%)	ε_m^M (%)
1A@G	2.4	25	0.699	11	2	2
2A@G	3.7	25	0.686	10	3	3
3A@G	2.6	49	1.344	1	9	9
4A@G	4.0	50	1.371	−1	7	7
5A@G	5.8	50	1.374	3	4	4
9A@G	8.5	81	2.228	−14	−4	−4
10A@G	10.6	83	2.279	−5	−7	−7

values and the dashed lines indicates ±10% error bound. The numerical and experimental values are along the *y* and *x* axes correspondingly.

The estimates of the gas superficial velocities for the A@W and A@G systems have an average relative error of 6% and 7%, respectively. The gas phase highest relative error is of 13% and belongs to the A@W system. The liquid superficials velocities for the A@W and A@G systems exhibit average relative errors of 4% and 5% respectively. Considering the A@W system, the match between the model and experimental liquid velocity is better than 6% with the exception of points #1 and #2. On the other hand, for the A@G system the liquid velocity relative errors spans from −7% to +9%. The model output for the A@W system show a tendency to over-predict the gas and the liquid velocities. Meanwhile, for the A@G system it does not show any definite tendency to the gas velocities estimates but under-preditics the liquid velocity. Finally, the relative errors of the mass flow rate are a mirror of the ones found to the liquid superficial velocity.

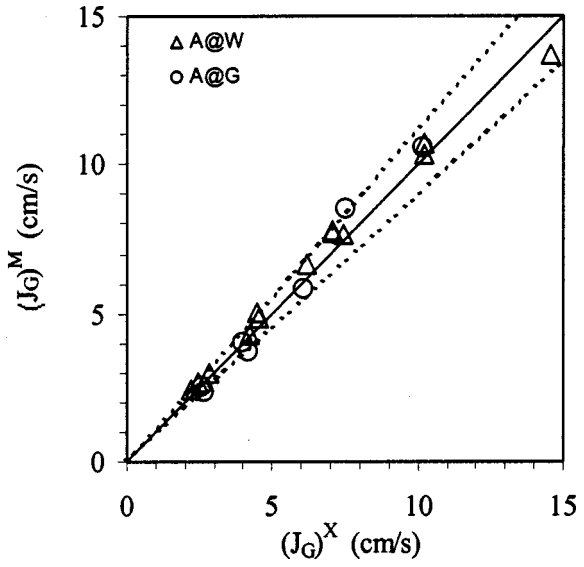

Fig. 7 Comparison between the predicted (J_G^M) and experimental (J_G^X) gas superficial velocity

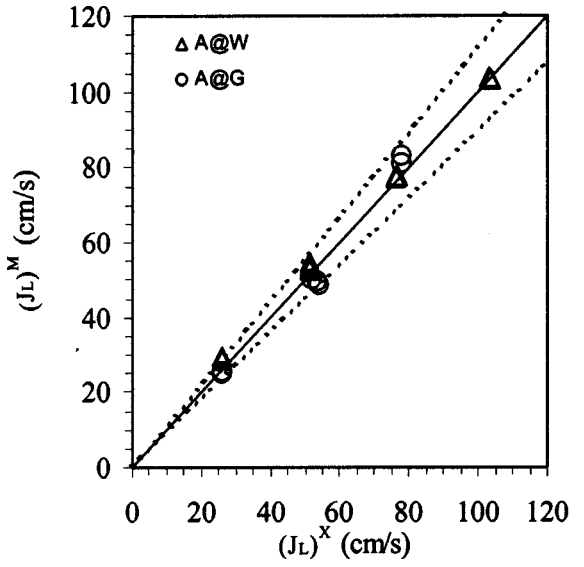

Fig. 8 Comparison between the predicted (J_L^M) and experimental (J_L^X) liquid superficial velocity

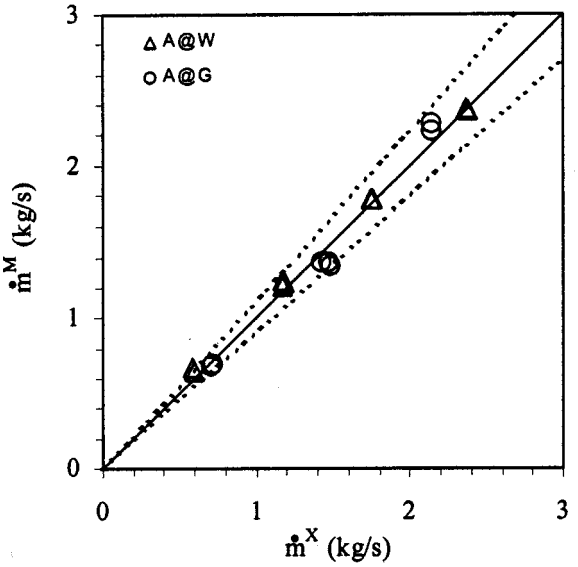

Fig. 9 Comparison between the predicted ($\dot{m}^M$) and the experimental ($\dot{m}^X$) mixture mass flow rate

A further inspection on the mass flow rate, Tables 5 and 6, reveals that it doesn't change with the gas velocity changes within three figures after the decimal point. This is correct because in the present study the gas density is three orders of magnitude less than the liquid density. Therefore, changes in $\dot{m}$, Eq. (9), due to J_G variations appears on the fourth decimal place.

6.4 Further Simplification on the Algebraic Model and the Uncertainty Analysis. Applications with great density difference between phases allow the algebraic model to be simplified. Considering $\rho_G \ll \rho_L$, then the mixture density, Eq. (2), turns to be:

$$\rho_m \cong (1-\langle \alpha_G \rangle)\rho_L, \tag{32}$$

the inlet cross section void fraction becomes,

$$\langle \alpha_G \rangle \cong \frac{\Delta P_S}{g L_S \rho_L} \cdot \lambda, \tag{33}$$

and the mixture mass flow rate, Eq. (9), reduces to

$$\dot{m} \cong J_L \rho_L A_S. \tag{34}$$

The neglect of the gas phase density allows the liquid velocity to be evaluated without an explicit dependence of the gas velocity. Using Eqs. (6), (32) and (34), J_L is approximatelly

$$J_L \cong \frac{C_D E}{\rho_L A_S} \sqrt{2(1-\langle \alpha_G \rangle)\rho_L \Delta P_T^*}, \tag{35}$$

once J_L is determined by Eq. (34), J_G stems from the drift flux relation, Eq. (11), as:

Table 7 Absolute uncertainties of λ, C_D, C_0 and V_{GJ}

Variable	Unit	Absolute A@W	Uncertainty A@G
$\Delta\lambda$	(- - -)	±0.1	±0.03
ΔC_D	(- - -)	±0.01	±0.006
ΔC_0	(- - -)	±0.05	±0.02
ΔV_{GJ}	(cm/s)	±3.8	±1.2

Table 8 Sensitivity analysis of λ and C_0 on the phase flow rates

	λ ± 0.1		$C_0 \pm 0.05$	
	A@W	A@G	A@W	A@G
J_G	±10.0%	±11.0%	±4.7%	±5.4%
J_L	±1.1%	±1.2%	±0.001%	±0.001%
$\dot{m}$	±1.1%	±1.2%	±0.001%	±0.001%

$$J_G \cong \frac{\langle \alpha_G \rangle}{(1-\langle \alpha_G \rangle C_0)} \cdot (C_0 \cdot J_L + V_{GJ}). \tag{36}$$

This low pressure approximation lets to cast the algebraic model in a simpler and uncoupled set of equations. The equation set discloses, in an explicit way, the functional dependence of J_G and J_L on the experimentally and numerically determined variables. The inlet averaged void fraction, Eq. (33), depends on the experimental measurement of ΔP_S and on the numerically estimated parameter λ. The liquid superficial velocity, Eq. (36), depends on the experimentally determined ΔP_T^*, on the discharge coefficient which comes from numerical simulation alone, plus on the averaged inlet void fraction which, by its turn, stems from experimental and numerical estimates. At last, but not the least, the gas superficial velocity, Eq. (36), reveals no direct dependence on experimentally determined variables such as ΔP_S or ΔP_T^*. In fact J_G has an implicit dependence on these variables which comes through J_L, $\langle \alpha_G \rangle$ and on the drift flux constants. The former set has the influence of experimental and numerical estimates while the drift flux constants arise solely through the numerical simulations.

The nested form which the experimentally and numerically determined variables are in Eqs. (33) thru (36) imparts a strong influence on the uncertainty of the $\langle \alpha_G \rangle$, J_G and J_L measurements. Employing the approximation $(1-\langle \alpha_G \rangle) \approx (1-\langle \alpha_G \rangle)^2 \approx 1$, the relatives uncertainties of $\langle \alpha_G \rangle$, J_L and J_G, Coleman and Steele [23], express as:

$$\varepsilon_{\langle \alpha_G \rangle} \cong \sqrt{\varepsilon_{\Delta P_S}^2 + \varepsilon_\lambda^2} \tag{37}$$

$$\varepsilon_{J_L} \cong \sqrt{\varepsilon_{C_D}^2 + \left(\frac{1}{2}\langle \alpha_G \rangle \varepsilon_{\langle \alpha_G \rangle}\right)^2 + \left(\frac{1}{2}\varepsilon_{\Delta P_T}\right)^2}, \tag{38}$$

$$\varepsilon_{J_G} \cong \left(\frac{\langle \alpha_G \rangle J_L}{J_G}\right) \sqrt{\varepsilon_{J_L}^2 + \left(\frac{V_{GJ}}{J_L}\right)^2 \varepsilon_{V_{GJ}}^2 + + \varepsilon_{C_0}^2 + \left(\frac{J_G}{\langle \alpha_G \rangle J_L}\right) \varepsilon_{\langle \alpha_G \rangle}^2}, \tag{39}$$

Equations (38) and (39) are estimates of J_L and J_G uncertainties based on the uncertainties of experimentally and numerically determined variables. Tables 1 and 2 report the uncertainties of the experimentals variables ΔP_T^X and ΔP_S^X for the A@W and A@G systems. On the other hand, the uncertainties of the numerically determined variables, C_D, $\langle \alpha_G \rangle$, C_0 and V_{GJ} are tough to estimate from first principles. It would require extensive grid test, numerical modeling analysis concerning the problem geometry and also ways to estimate these variables other than the numerical simulation. Since these matters are not the objective of this work, the remedy is to access, partially, the uncertainty of the numerically determined variables considering only the deviations between the algebraic fit and the numerical data. Under these constraints, the estimates of the absolute uncertainties of λ, C_D, C_0 and V_{GJ} are in Table 7. They suffice to get the estimates of the J_L and J_G uncertainties.

The algebraic model's sensitivity with respect to the parameters λ and C_0 is in Table 8 regarding variations of one uncertainty interval. For λ changing within ±0.1 around its mean value the estimates for J_G, varies as much as ±11% while J_L and $\dot{m}$ stays bounded by ±1.2%. On the other hand, for C_0 changing within ±0.05 around its mean value produces changes up to ±5.4% in J_G but negligible changes in J_L and $\dot{m}$. Equations (38) and (39) supports the higher model's sensitivity to the J_G estimates as compared against J_L.

Equations (38) and (39) can be further simplified if one consider a homogeneous mixture, $\langle \alpha_G \rangle = J_G/(J_G+J_L)$ and $\langle \alpha_G \rangle \ll 1$. Under these approximations, $\langle \alpha_G \rangle J_L/J_G \approx 1$ and the relative uncertainty of J_L and J_G turn to be:

$$\varepsilon_{J_L} \cong \sqrt{\varepsilon_{C_D}^2 + \left(\frac{1}{2}\varepsilon_{\Delta P_T}\right)^2}, \tag{40}$$

$$\varepsilon_{J_G} \cong \sqrt{\varepsilon_{J_L}^2 + \left(\frac{V_{GJ}}{J_L}\right)^2 \varepsilon_{V_{GJ}}^2 + \varepsilon_{C_0}^2 + \varepsilon_{\langle \alpha_G \rangle}^2}, \tag{41}$$

The first-order approximation of the J_L and J_G uncertainties, Eqs. (40) and (41), lead to the conclusions: i) the uncertainty liquid phase flow rate does not depend on the uncertainties of the void fraction and of the gas flow rate but only on the uncertainties of two parameters: the inlet to throat pressure difference and on the discharge coefficient, ii) the uncertainty of the gas measurement is sensitive to all the six variables related to the problem if one consider replacing Eqs. (37) and (40) into Eq. (41); iii) it is more probable to get a lower uncertainty on the liquid phase measurement rather than on the gas phase measurement.

7 Conclusion

The operational principle of the two-phase Venturi meter requires only two measurements of pressure differences and the knowledge of the gas-liquid transport properties; all other needed flow parameters are supplied through numerical flow simulation. The application is constrained to vertical ascendant gas-liquid flow in bubbly flow regime. An algebraic model determines the phases flow rates. Numerical flow simulation, employing finite volume technique and the Two-Fluid model, determines the algebraic model parameters which namely are: the void fraction correction term, λ, the discharge coefficient of the Venturi, C_D and the drift flux constants, C_0 and V_{GJ}. The algebraic model outputs are the gas and the liquid superficial velocities, the mixture mass flow rate, and the inlet averaged gas void fraction.

The strongest point of the numerical flow simulation is its potential to estimate the model parameters considering the specific characteristics of each Venturi tube and its application. The finite volume code employing the Two-Fluid model is efficient to handle characteristics such as: Venturi geometry and its contraction ratio, turbulent and laminar flow regime, distorted and spherical bubble regime, viscous and less viscous liquids and flows with slip velocities to almost homogeneous mixture to mention a few. The algebraic model accuracy is tested against experimental data. The mean deviation between the estimated and the experimental measurements of J_G, J_L and $\dot{m}$ is of ±7%, ±5%, and ±5%, respectively considering both experimental database: the air and water and the air and glycerin mixture. The liquid and gas phase velocities depend, respectively, on four and six variables when considering low pressure and low void fraction applications. The liquid phase velocity needs two experimental and two numerically determined variables while the gas phase velocity needs two experimental and four numerically determined. Therefore, the former tend to have a lower uncertainty than the last.

Despite of the success in combining experimental data and numerical modeling to launch an algebraic model to two-phase flow rate prediction, there are areas that demand more development. To start with, it is necessary to mention the need for studies regarding the chocking conditions at the Venturi throat; they will be useful to design the Venturi contraction ratio and to avoid working in flow regimes other than the bubbly flow regime. The second point regards applications with high pressures, typically 100 Bar to 300 Bar, where the gas density is no longer negligible when compared with liquid density. It is necessary to access the reliability of the Two-Fluid model as well as the turbulence model under these hyperbaric conditions. These steps are necessary to develop the flow meter for dowhole application. This application will demand further knowledge of the transport properties and most of all, the need to introduce phenomenological modeling to enhance the flow prediction when working with oil, water, and gas simultaneously.

Acknowledgments

This work received support from FINEP-CTPETRO funds and from Petrobras under the Grant no. 650.4.010.00.7.

References

[1] Jamieson, A. W., 1998, ''Multiphase Metering—The Challenge of Implementation,'' 16th North Sea Flow Measurement Workshop, Gardermoen, Norway, Oct. 1998.
[2] Costa E. Silva, C. B., Silva Filho, J. A. P., Borges Filho, M. J. and Mata, J. D., 2000, ''Multiphase Flow Metering Technology Updated,'' The 10th International Conference on Flow Measurement-Flomeko, Salvador-Brazil, June 4–8 in CD ROM.
[3] Falcone, G., Hewitt, G. F., Alimonti, C., and Harrison, B., 2002, ''Multiphase flow metering: current trends and future developments,'' J. Pet. Technol., **54**, pp. 77–84.
[4] Graf, W. A., 1967, ''A modified Venturimeter for Measuring Two-Phase Flow,'' J. Hydraul. Res., **5**, pp. 161.
[5] Ishii, M., 1975, *Thermo-Fluid Dynamics of Two-Phase Flow*, Eyrolles, France.
[6] Drew, D. A. 1992, ''Analytical modeling of multiphase flows,'' Lahey-Jr. R. T. editor, ''Boiling Heat Transfer: Modern Developments and Advances,'' pp. 31–83, Elsevier Science.
[7] Kowe, R., Hunt, J. C. R., and Hunt, A., Couet, B., and Bradburry, L. J. S., 1988, ''The effects of bubbles on the volume fluxes and pressure gradients in unsteady and non uniform flows of liquids,'' Int. J. Multiphase Flow, **14**, pp. 587–606.
[8] Lewis, D. A., and Davidson, J. F., 1985, ''Pressure drop for bubbly gas-liquid flow through orifice plates and nozzles,'' Chem. Eng. Res. Des., **63**, pp. 149–156.
[9] Kuo, J. T., and Wallis, G. B., 1988, ''Flow of bubbles through nozzles,'' Int. J. Multiphase Flow, **14**(5), pp. 547.
[10] Dias, S. G., França, F. A. and Rosa, E. S., 1999, ''Lateral and Axial Void Fraction evolution in bubbly flows inside a vertical short converging nozzle,'' Proc. Of the Second Int. Symposium on Two-Phase Flow Modelling and Experimentation, Rome, Italy, May 23–26.
[11] Ishii, M., 1977, ''One-dimensional drift-flux model and constitutive equations for relative motion between phases in various two-phase flow regimes,'' Technical Report Argonne National Lab., ANL-77-47, October.
[12] Couet, B., Brown, P., and Hunt, A., 1991, ''Two-phase bubbly-droplet flow through a contraction: experiments and unified model,'' Int. J. Multiphase Flow, **17**(3), pp. 291–307.
[13] Boyer, C., and Lemonier, H., 1996, ''Design of a flow metering process for two-phase dispersed flows,'' Int. J. Multiphase Flow, **22**(4), pp. 713–132.
[14] Dias, S. G., 1998a, ''Phase distribution in axi-simmetrical bubbly flow: numerical solution with the Two-Fluid Model and experimental validation with a new method using a double sensor probe,'' Ph.D. Thesis, Faculty of Mechanical Engineering, State University of Campinas.
[15] Dias, S. G., França, F. A. and Rosa, E. S., 1998b, ''The progress of the void fraction, bubble size and bubble velocity in a short vertical nozzle under the occurrence of bubbly flows,'' 3rd Int. Conference on Multiphase Flow, ICMF'98, Lyon, France, June 8–12.
[16] Zuber, N., and Findlay, J. A., 1965, ''Average Volumetric Concentration in Two-Phase Flow Systems,'' ASME J. Heat Transfer, **Nov.**, pp. 453–468.
[17] Bertodano, M. L., Lahey, R. T., and Jones, O. C., 1994, ''Development of a κ-ε model for bubbly two-phase flow,'' ASME J. Fluids Eng., **116**, March, pp. 128–134.
[18] Lance, M., and Bataille, J., 1991, ''Turbulence in the liquid phase of a uniform bubbly air-water flow,'' J. Fluid Mech., **222**, pp. 95–118.
[19] Lahey, Jr., R. T., Bertodano, M. L., and Jones, O. C., 1993, ''Phase distribution in complex geometry conduits,'' Nucl. Eng. Des., **141**, pp. 177–201.
[20] Drew, D. A., and Lahey, Jr., R. T., 1987, ''The virtual mass and lift force on a sphere in rotating and straining inviscid flow,'' Int. J. Multiphase Flow, **13**(1), pp. 113–121.
[21] Patankar, S., 1980, *Numerical Heat Transfer and Fluid Flow*, Hemisphere, USA.
[22] Spalding, B. D., 1994, *The Phoenics Encyclopedia*, CHAM, UK.
[23] Coleman, H. W., and Steele, W. G., 1999, ''Experimentation and Uncertainty Analysis for Engineers,'' 2nd Ed., John Wiley & Sons.

Sayavur I. Bakhtiyarov
Research Professor
Department of Mechancal Engineering,
Auburn University, AL 36849-5341

Mihai Dupac
Graduate Student
Department of Mechanical Engineering,
Auburn University, AL 36849-5341

Ruel A. Overfelt
Philpott-WestPoint Stevens Professor of
Mechanical Engineering
Department of Mechanical Engineering,
Auburn University, AL 36849-5341

Sorin G. Teodorescu
Research Scientist
Lynntech, Inc.,
College Station, TX 7784

On Electrical Conductivity Measurements of Molten Metals by Inductive Technique

In this paper, we propose a new relationship between the opposing mechanical torque and the electric conductivity of a rotating liquid specimen in a permanent external magnetic field of constant induction, which includes the effect of fluid flow. The proposed relationship was applied to describe the experimental data for a conductive specimens rotating in a permanent magnetic field. [DOI: 10.1115/1.1760542]

Introduction

Inductive techniques for measuring electrical resistivity are contactless and thus prevent chemical reactions between molten samples and contacting probes, which occur in the direct methods. The method is based on the phenomena that when a metal sample rotates in a magnetic field (or the magnetic field rotates around a stationary sample), circulating eddy currents are induced in the sample, which generate an opposing torque proportional to the electrical conductivity of the sample [1]. In liquid metals and alloys the applied magnetic field also causes significant rotation of the liquid in the crucible, which consequently decreases the angular velocity between the field and the sample [2]. However, the technique requires a reliable relationship between the electrical resistivity of the metal sample and the measured torque values. Braunbeck [3] proposed the following relationship between the opposing mechanical torque (T) and the electric conductivity of a liquid specimen (σ) in a rotating DC external magnetic field of induction B_0:

$$T=\frac{\pi}{4}\sigma\omega LR^4B_0^2-\frac{\pi}{192}\frac{1}{\eta}\sigma^2\omega LR^6B_0^4, \tag{1}$$

where L and R are length and radius of the specimen, respectively; ω is the angular velocity of the rotating magnetic field; and η is the viscosity of the liquid specimen. The magnetic induction and the radius of the specimen can be selected so that the second term in equation (1) will become negligibly small compared with the first term for measurements on metals with unknown viscosity [4].

Spitzer et al. [5] studied electromagnetic stirring in continuous casting of round strands. A finite difference model was developed for the computation of the flow field in continuous casting through the simultaneous solution of the Navier-Stokes equations, the continuity equation, and the Maxwell equation. The authors also presented a simplified analytical model for an infinitely long cylinder. In addition, experimental data on the rotation of liquid mercury in Plexiglas cylinder subject to a rotating magnetic field was shown for comparison. Spitzer et al. [5] found that the wall shear stresses from the numerical model and the analytical model agreed very well with the experimental data for liquid mercury. It is indicated that the flow field in the vicinity of the Plexiglas wall was predicted precisely. Thus from Spitzer et al. [5]

$$\tau_w=\frac{1}{8}\sigma\omega R^2B_0^2. \tag{2}$$

However, Spitzer et al. [5] correctly point out that more complex convection effects in the interior of the samples could not be adequately predicted from the simple analytical theory and resolution of these effects required use of the numerical model. Since the wetted area is $2\pi RL$, the torque per unit length exerted on the crucible from the magnetic interaction should be

$$\frac{T}{L}=\frac{\pi}{4}\sigma\omega R^4B_0^2. \tag{3}$$

Equation (3) is the same as the first term in equation (1) from Braunbeck [3].

Equations (1)–(3) were derived under the assumption that a magnetic field rotates around a metal sample. Recently we proposed a new relationship between the opposing mechanical torque and the electric conductivity of a rotating liquid specimen in a permanent external magnetic field of constant induction [6]. The purpose of this study is introduction of the fluid flow effect on the torque-electrical conductivity relationship for the sample rotating in a permanent magnetic field.

Mathematical Modeling

In our previous work [6], we considered the steady motion of a conducting fluid with constant physical properties in a cylindrical crucible with radius R and length L, which is rotating about its vertical axis with an angular velocity ω, in the presence of gravity, an applied magnetic field and a radiative heat source (Fig. 1). The transverse magnetic field imposed upon the rotating melt was assumed to be stationary and uniform. In addition to the applied magnetic field, there was a second magnetic field produced by the induced electric currents in the conducting fluid. To simplify the computation, the melt is considered to be electrically and thermally conducting and incompressible.

The numerical computations of the continuity and Navier-Stokes equations combined with Maxwell equation and Ohm's law under above mentioned assumptions and Boussinesq approximation, the following expression to relate the applied torque and the electrical conductivity of sample was obtained [6]:

Contributed by the Fluids Engineering Division for publication in the JOURNAL OF FLUIDS ENGINEERING. Manuscript received by the Fluids Engineering Division October 27, 2003; revised manuscript received January 5, 2004. Associate Editor: D. Siginer.

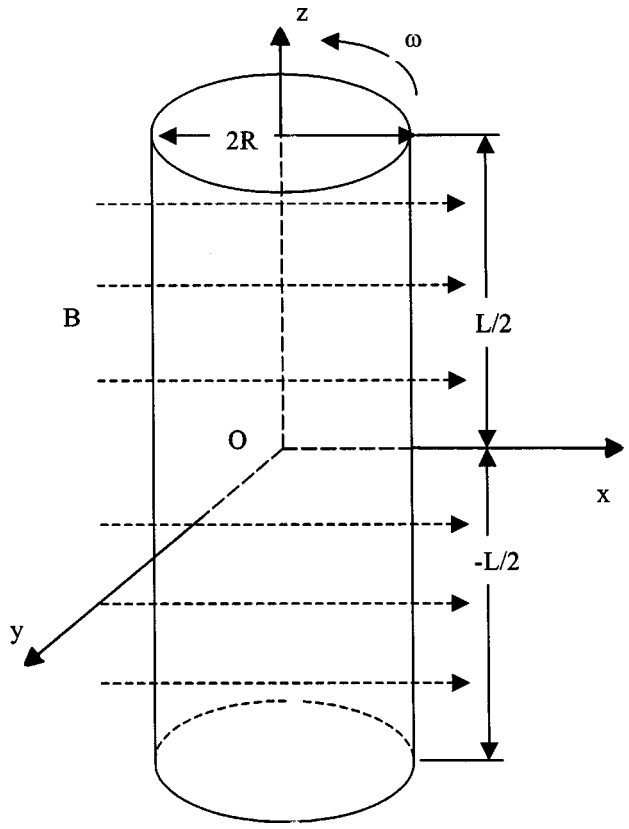

Fig. 1 Geometry of cylindrical crucible used for mathematical modeling

$$T=\frac{2}{3}\sigma\omega LR^4B_0^2. \tag{4}$$

Introducing the fluid motion with angular velocity $\omega_F=f(r)$ in the first approximation (a similar technique was used by Braunbeck [3]) we can write

$$dT=\frac{8}{3}\sigma(\omega-\omega_F)LB_0^2r^3dr. \tag{5}$$

On the other hand, from the hydrodynamics of the rotational fluid, the internal friction can be expressed as

$$dT=-2\pi L\eta\frac{d}{dr}\left(r^3\frac{d\omega_F}{dr}\right)dr. \tag{6}$$

Combining Eqs. (5) and (6), we can write

$$-2\pi L\eta\frac{d}{dr}\left(r^3\frac{d\omega_F}{dr}\right)=\frac{8}{3}\sigma(\omega-\omega_F)LB_0^2r^3 \tag{7}$$

or

$$\frac{d}{dr}\left(r^3\frac{d\omega_F}{dr}\right)=-\frac{4\sigma}{3\pi\eta}(\omega-\omega_F)B_0^2r^3. \tag{8}$$

The solution of the differential Eq. (8) with the following boundary conditions:

$$\begin{cases} r=0 \\ \dfrac{d\omega_F}{dr}=0 \end{cases} \quad \text{and} \quad \begin{cases} r=R \\ \omega_F=0 \end{cases} \tag{9}$$

will result in:

$$\omega_F=\frac{\sigma}{6\pi\eta}B_0^2\omega(R^2-r^2). \tag{10}$$

Substituting expression (10) into Eq. (5) will give:

$$dT=\frac{8}{3}\sigma\left(\omega-\frac{\sigma}{6\pi\eta}B_0^2\omega(R^2-r^2)\right)LB_0^2r^3dr \tag{11}$$

or

$$dT=\left(\frac{8}{3}\sigma\omega LB_0^2r^3-\frac{4}{9}\frac{\sigma^2}{\pi\eta}B_0^2\omega(R^2-r^2)LB_0^2r^3\right)dr. \tag{12}$$

Integrating equation (12) from 0 to R, the final expression for the applied torque on the cylinder will be:

$$T=\frac{2}{3}\sigma\omega B_0^2R^4L-\frac{1}{27\pi}\frac{1}{\eta}\sigma^2\omega B_0^4R^6L. \tag{13}$$

Results and Discussions

When fluid motion is ignored, a comparison of the derived equation (4) with the equation (3) obtained by Braunbeck [3] shows that a damping torque caused by induced circulating eddy currents in the permanent external magnetic field of constant induction (T_p) is 1.17 times less than that caused by the induced eddy currents in the rotating magnetic field (T_r):

$$T_r=1.17T_p. \tag{14}$$

The torques caused by the fluid motion effect in the permanent external magnetic field of constant induction (T_p^f) and in the rotating magnetic field (T_r^f) are defined by the second terms on the right hand side of the equations (13) and (1), respectively. A comparison of these two torques shows that a damping torque caused by fluid flow in the rotating magnetic field (T_r^f) is 1.39 times more than that caused by the fluid flow in the permanent external magnetic field (T_p^f):

$$T_r^f=1.39T_p^f \tag{15}$$

Recently, Bakhtiyarov et al. [7–9] developed a rotational contactless inductive technique to measure both a viscosity and an electrical conductivity of liquid metals. Preliminary tests conducted with low melting point metals (lead and tin), alloys (A319, A356, LMA-158), and binary systems (Pb/Sn) showed a good agreement with data from the literature. LMA-158 is a low melting alloy, which consists of 50% bismuth, 26.7% lead, 13.3% tin and 10% cadmium. The melting temperature of this composite is 70°C, hardness is 12 by Brinell, thermal expansion is 0.27%. This

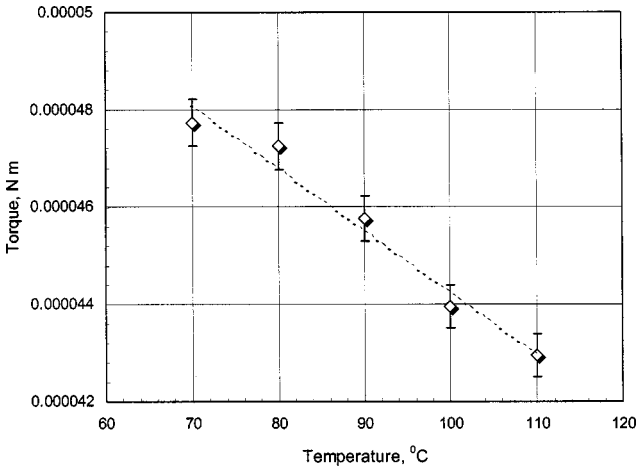

Fig. 2 Variation of measured torque values with temperature for LMA-158 alloy ($B_0=0.1$ T and $\omega=10$ s^{-1}) [7]

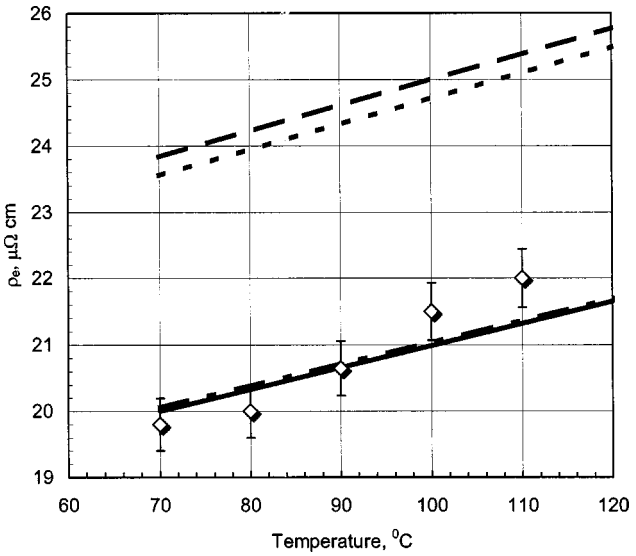

Fig. 3 Variation of electrical resistivity of LMA-158 alloy with temperature ($B_0=0.1$ T and $\omega=10\ s^{-1}$): ◇-experimental data obtained by Bakhtiyarov and Overfelt [7]; - - - - simulations by Braunbeck Eq. (3); — — — simulations by Braunbeck Eq. (1); —— simulations by Eq. (4); — - — - — simulations by Eq. (13).

composite material can be melted under hot water and can be recovered and tested over and over again. The variation of the measured damping torque caused by induced circulating eddy currents with temperature for cylindrical sample (19.05 mm diameter and 38.1 mm long) of LMA-158 composite is shown in Fig. 2 [7]. Figure 3 shows the variation of the electrical resistivity ($\rho_e = 1/\sigma$) estimated from the torque measurements for the same size cylindrical samples of the pure metals (Pb and Sn) of known electrical conductivity, against the temperature, along with simulations made according to equation (13) and Braunbeck equation (1). As seen from this figure, Eq. (13) describes the experimental data obtained in permanent external magnetic field of constant induction, better than equation (1) derived for rotating DC external magnetic field. It is appear that in case of the permanent magnetic field the contribution of fluid motion effect onto damping torque values is less than in the case of rotating DC external magnetic field.

Conclusions

A new relationship between the opposing mechanical torque and the electric conductivity of a rotating liquid specimen in a permanent external magnetic field of constant induction is proposed. It is shown that the proposed relationship describes the experimental data for rotating specimen better than Braunbeck formula derived in the assumption that a magnetic field rotates around a stationary metal sample.

Acknowledgments

The authors gratefully acknowledge the financial support received from NASA's Space Product Development Office at Marshall Space Flight Center under Cooperative Agreement No. NCC8-240.

Nomenclature

B_0 = magnetic field induction
L = length of the specimen
R = radius of the specimen
T = mechanical torque
η = viscosity of liquid metal
σ = electric conductivity of liquid specimen
τ_w = wall shear stress
ω = angular velocity of the rotating magnetic field
ω_F = angular velocity of the rotating fluid as a function of the distance r

References

[1] Iida, T., and Guthrie, R. I. L., 1988, *The Physical Properties of Liquid Metals*, Clarendon Press, Oxford, pp. 227–229.
[2] Moffatt, H. K., 1965, "On Fluid Flow Induced by a Rotating Magnetic Field," J. Fluid Mech., **22**, p. 521–528.
[3] Braunbeck, W., 1932, "Eine Neue Methode Elektrodenloser Leitfähigkeitsmessung," Zeitschrift für Physik, **73**, pp. 312–334.
[4] Takeuchi, S., and Endo, H., 1962, "The Electric Resistivity of the Metals in the Molten State," Trans. Jpn. Inst. Met., **3**, pp. 30–35.
[5] Spitzer, K.-H., Dubke, M., and Schwerdtfeger, K., 1989, "Rotational Electromagnetic Stirring in Continuous Casting of Round Strands," Metall. Trans. B, **17B**, pp. 119–131.
[6] Teodorescu, S. G., Dupac, M., Bakhtiyarov, S. I. and Overfelt, R. A., 2001, "Numerical Simulations of Fluid Flow during Electromagnetic Stirring of Aluminum," *Proc. ASME IMECE*, eds. D. A. Siginer and S. I. Bakhtiyarov, New York, NY, pp. 1–5.
[7] Bakhtiyarov, S. I., and Overfelt, R. A., 1999, "Electrical Conductivity Measurements in Liquid Metals by Rotational Technique," J. Mater. Sci., **34**(5), pp. 945–949.
[8] Bakhtiyarov, S. I., and Overfelt, R. A., 1999, "Measurements of Liquid Metal Viscosity by Rotational Technique," Acta Mater., **47**(17), pp. 4311–4319.
[9] Bakhtiyarov, S. I., Overfelt, R. A., and Teodorescu, S. G., 2001, "Electrical and Thermal Conductivity of A319 and A356 Aluminum Alloys," J. Mater. Sci., **36**, pp. 1–6.

Control of Volumetric Flow-Rate of Ball Valve Using V-Port

Ming-Jyh Chern*
Assistant professor

Chih-Cheng Wang
Graduate student

Department of Mechanical Engineering,
National Taiwan University of Science and Technology,
Taipei 106, Taiwan

The control of volume flow rate in a ball valve is very important when a ball valve is utilized in a piping system. It is difficult to linearly control the flow rate in a ball valve without external devices. V-ports are employed to achieve this purpose. In order to investigate the effects of V-port on the volume flow rate and flow features, 3-D numerical simulations and experiments were conducted to observe the flow patterns and to measure performance coefficients when V-ports with various angles were used in a piping system. Three V-ports with angles 30 deg, 60 deg, and 90 deg were studied. It was found that V-ports with angles 30 deg and 60 deg make the flow rate proportional to the valve opening. However, V-ports increase the pressure loss between the inlet and the exit of a ball valve. In addition, V-ports with a small angle such as 30 deg increase the possibility of cavitation compared with flows without V-ports. [DOI: 10.1115/1.1760536]

1 Introduction

Valves are commonly used in piping systems. One objective of valves is to control the flow rate in a piping system. Linear control of flow rate in a piping system is an important issue in valve design. The V-port is one method used to control the flow rate linearly through a valve (Hutchison [1]). However, the effect of V-ports on fluid flows through a valve in a piping system is still unclear. The main purpose of this study is to investigate the fluid flows which are controlled by a full-port 1/4 turn valve with a V-port. The variation of fluid flows and the effect on relevant performance coefficients due to a V-port are presented in this study.

Fluid flows through a valve have been studied by several researchers. Due to the fast progress of the flow visualization and measurement techniques, it becomes possible to observe the flows inside a valve and to estimate the performance of a valve. Mertai et al. [2] established a water tunnel system to conduct a performance test of a V-sector ball valve. They used a Laser Doppler Velocimetry (LDV) measuring system to investigate flows in ball valves. Davis & Stewart [3] employed a closed-loop piping system to test and observe flows passing through a globe control valve.

The flow visualization can provide flow patterns through a valve in a piping system, especially the cavitation phenomenon. Visual structures of vortices in flows inside a ball valve can be obtained from the results of flow visualization. These vortices mainly determine the energy loss (or the pressure drop). Chern & Wang [4] utilized particles and a laser sheet to visualize flow patterns through a ball valve. Cavitation phenomena were observed at certain valve openings.

Computational approaches are getting popular in this area due to the dramatic progress of digital computers and numerical algorithms. Computational fluid dynamics (CFD) has become an important tool for design of fluid machinery. It has also been applied to valve research. For example, Kerh et al. [5] utilized the finite element method to simulate transient interaction of fluids and structures in a control valve. Mertai et al. [2] adopted a commercial package, FLUENT™, to investigate the flow around a V-sector ball valve. van Lookeren Campagne et al. [6] used a commercial package, AVL-Fire™, to simulate flows containing bubbles in ball valves. Davis & Stewart [7] adopted FLUENT™ to study the flows in globe control valves. For three-dimensional analysis, Huang & Kim [8] utilized FLUENT™ to simulate turbulent flows in a butterfly valve, in which the k-ε model was employed for turbulence consideration. Chern & Wang [4] employed a commercial package, STAR-CD™, to investigate fluid flows through a ball valve and to estimate relevant coefficients of a ball valve.

In the previous study (Chern & Wang [4]), a performance test procedure for a ball valve has been established using both the experimental and the numerical approaches. Good agreements in flow patterns were obtained between the experimental and the numerical results. In addition, relevant performance coefficients for ball valves were estimated using experimental measurement and numerical simulation. In this work, the linear volume flow rate control on a ball valve was studied. In order to assess the possibility of controlling the performance of a ball valve, a plate

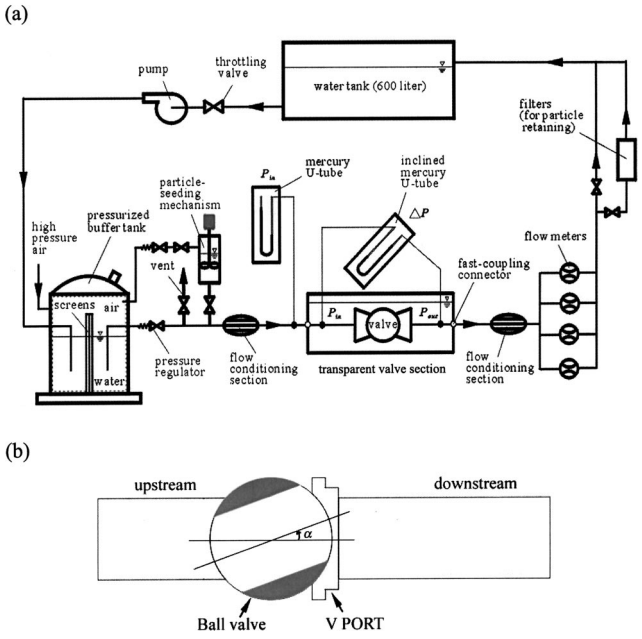

Fig. 1 Schematic diagram of the experiment apparatus: (*a*) the closed-loop water tunnel system (*b*) test section including the acrylic ball valve and the V-port

*Corresponding author: Department of Mechanical Engineering, National Taiwan University of Science and Technology, 43 Sec. 4 Keelung Road, Taipei 106, Taiwan; Phone: +886-2-27376496; Fax: +886-2-27376460; e-mail: mjchern@mail.ntust.edu.tw

Contributed by the Fluids Engineering Division for publication in the JOURNAL OF FLUIDS ENGINEERING. Manuscript received by the Fluids Engineering Division April 8, 2003; revised manuscript received November 8, 2003; Associate Editor: M. V. Ötügen.

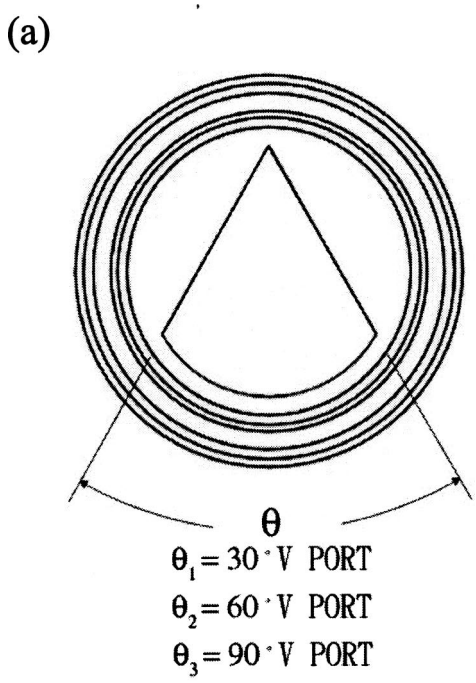

Fig. 2 Pictures of V-ports with various angles. The ratio of the open, A_V, of a V-port relative to the opening of a ball valve without a V-port is proportional to the angle, θ, as shown in (*c*)

Table 1 Coefficients in the *k*-ε turbulence model

C_μ	σ_k	σ_ε	$C_{\varepsilon 1}$	$C_{\varepsilon 2}$
0.09	1.00	1.29	1.44	1.92

with a V-shaped opening was placed at the downstream exit of the valve. The flow changes induced by the V-port were visualized numerically and experimentally. Effects of a V-port on the performance coefficients were measured and correlated with visualized flow fields.

2 Experimentals

The visualization and measurement of flows in a valve with a V-port was conducted in a close-loop water piping system. Figure 1(*a*) gives a schematic diagram of the close-loop water tunnel

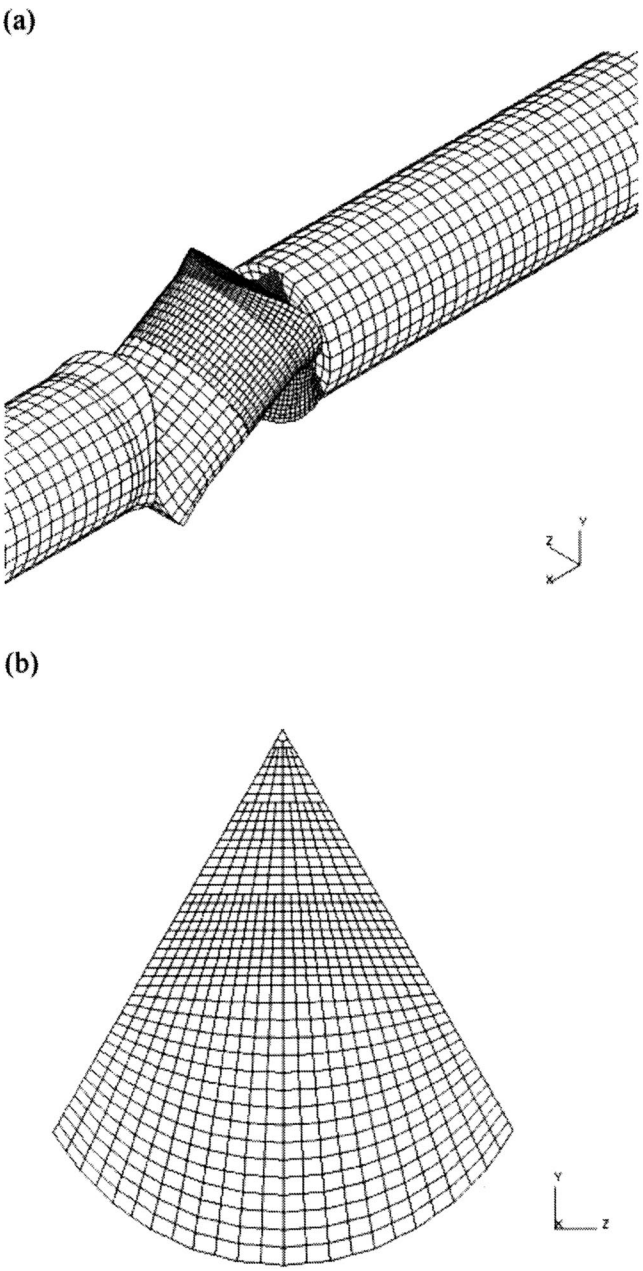

Fig. 3 The 3-D computational mesh including the piping system, the ball valve, and the V-port

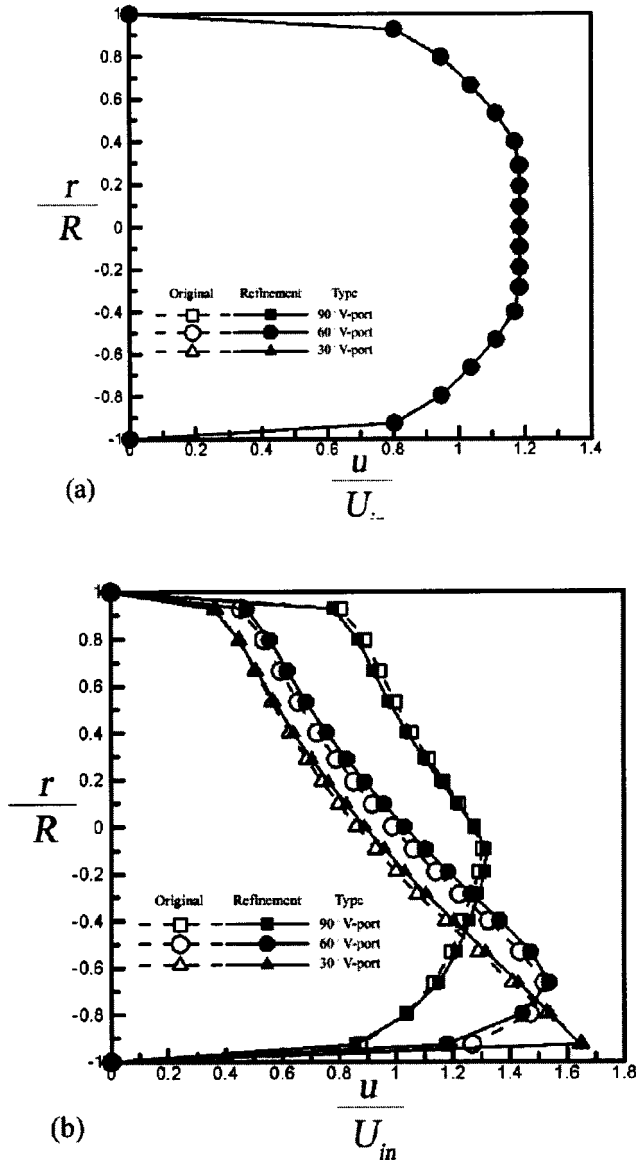

Fig. 4 Grid size independency tests for cases with 90 deg, 60 deg and 30 deg V-ports. *R* is the radius of the circular pipe and *r* refers to the *y*-direction. (*a*) The axial velocity profile at the section 2D in front of the valve (*b*) the axial velocity profile 6D behind the valve

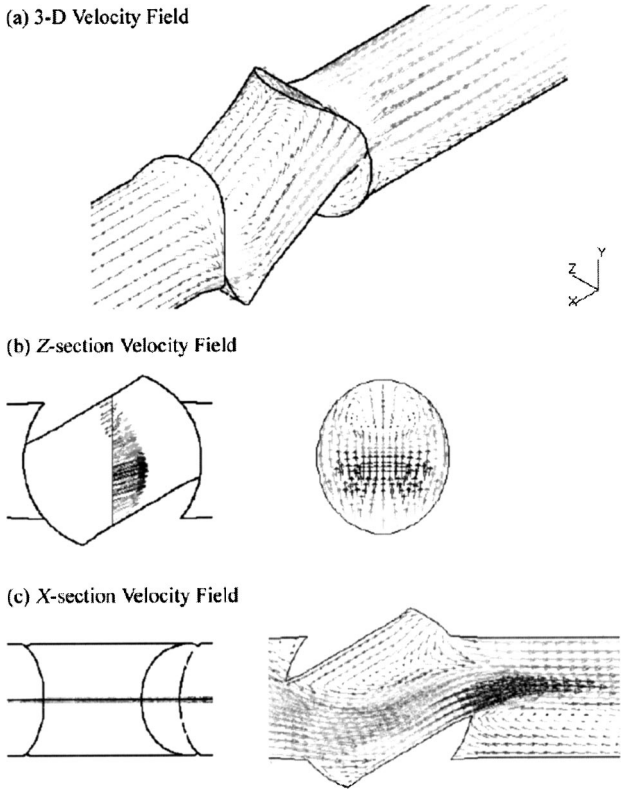

Fig. 5 Velocity fields at various sections

system. The clean water contained in a reservoir tank of 600-liter was drawn by a high pressure pump and discharged to a pressurized buffer tank. The water goes sequently through a pressure regulator, an upstream flow conditioning section, a transparent valve section, a downstream flow conditioning section, through several flow meters, a filer, and then recirculates back to the reservoir tank. The upstream pressure is provided by high pressure air which is supplied to the buffer tank from an air-compressor system. The pressurized water then passes through a pressure regulator. This setup maintains a stable pressure at the valve inlet, which is ideal for valve operation. The test section, as shown in Fig. 1(*b*), includes a plexyglas tube, the acrylic ball valve, and the V-port. The acrylic model of the ball valve of nominal diameter 59.4 mm (2 inches) is CNC machined. The rotating angle of the valve, α, is 0 deg, when the valve is fully open. Moreover, α is 90 deg, when the valve is completely closed. The opening of the valve is denoted as ϕ. ϕ is linear interpolated with respect to α. When α is 0 deg and 90 deg, ϕ is 100% and 0%, respectively. The transparent test section is connected to the upstream and downstream pipes via the specially-designed fast-coupling mechanisms. The laser-light beam emitted from an 5W argon-ion laser is transmitted through an optical fiber and then connected to a 20 deg laser-light sheet expander. The laser-light sheet is adjusted to a thickness of about 0.5 mm. In order to compensate for the difference in the refraction indices between the air and the curved plexyglas, a rectangular glass tank filled with still water is enclosed around the whole test section. By using this method, the refraction of the laser-light sheet is effectively reduced.

V-ports with various angles, as shown in Figs. 2(*a*) and 2(*b*), were made of stainless steel. Three V-ports with angles 30 deg, 60 deg, and 90 deg were manufactured. The relationship between the normalized open area of a V-port and its angle, θ, is shown in Fig. 2(*c*). A_V and A refer to the area of a V-port and the area of a ball valve at θ=180 deg, respectively. The relationship is not linear as shown in Fig. 2(*c*).

When the valve performance is tested, the static pressures, P_{in} is measured at a distance 2D upstream of the valve by using the mercury manometers. The diameter of the pipe, D, is 38 mm and is used as the characteristic length of Reynolds number. The pressure drop, ΔP, across the value is also detected by an inclined mercury U-tube manometer as shown in Fig. 1. The measuring points of the inclined manometer are at 2D upstream and 6D downstream of the valve (ANSI/ISA-75.02-1996). The volume flow rate, q, is measured by several calibrated turbine flow meters which are installed downstream of the valve. The ranges of operation for pressure and inlet velocity are 0.5 to 1.8 bars (gauge) and 2 to 10 m/s, respectively. In terms of the Reynolds number, Re_D, it covers from 0.64×10^5 to 3.18×10^5.

The particle tracking flow visualization method (PTFV) is employed to reveal the flow patterns. When the flow visualization is conducted, plastic particles made of polystyrene (PS) are used to scatter the laser light via a particle seeding mechanism. The diameters of the polystyrene particles are between 30 to 70 μm and the specific weight is 1.03 at 25°C. Ignoring the effect of turbulent

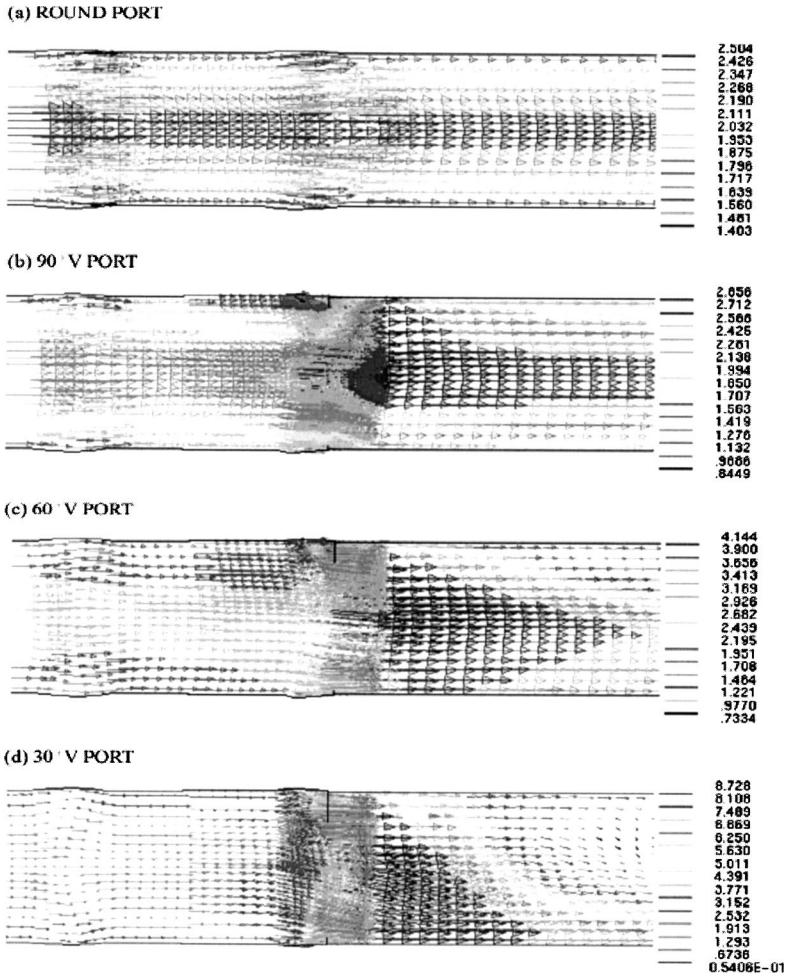

Fig. 6 Flow patterns of computational results at Re=0.64×10^5 and α=0 deg

diffusion, the relaxation time constant is estimated to be less than 6.25×10^{-5} s and the Stokes number is in the order of 10^{-6} within the range of experiment so that slip between the flow and particles could be neglected (Richard & John [9]). A digital camera and a Charge-Coupled Devices (CCD) camera are used to take the pictures of path line patterns and the animations of the flows.

3 Numerical Method

Fluid flows through the ball valve with V-ports are simulated numerically. Incompressible and viscous fluids are considered in the model. Fluids have to conserve mass and momentum, so the continuity equation and the Navier-Stokes equations are used as governing equations. Since the inlet velocity varies from 2 m/sec to 10 m/sec, corresponding Reynolds numbers from 0.64×10^5 to 3.18×10^5 reveal that flows studied are turbulent. In addition, no energy transfer is considered. Uniform temperature through the fluid flow is postulated.

To deal with turbulent flows, the Reynolds averaged approach is utilized to decompose mean quantities and fluctuations for all of the physical variables. Therefore, 3-D governing equations can be denoted as

$$\frac{\partial U_j}{\partial x_j}=0, \quad j=1\sim3, \tag{1}$$

where U is the mean velocity and the subscript, $j=1\sim3$, refers to Reynolds averaged components in three directions respectively. Furthermore, momentum conservation can be described by the Reynolds averaged Navier-Stokes (RANS) equations which can be written as

$$U_j\frac{\partial U_i}{\partial x_j}=-\frac{1}{\rho}\frac{\partial P}{\partial x_i}+g_i+\frac{1}{\rho}\left(\frac{\partial \tau_{ij}}{\partial x_j}+\frac{\partial \tau'_{ij}}{\partial x_j}\right), \quad i,j=1\sim3, \tag{2}$$

where

$$\tau_{ij}=\mu\left(\frac{\partial U_i}{\partial x_j}+\frac{\partial U_j}{\partial x_i}\right) \tag{3}$$

and

$$\tau'_{ij}=-\rho\overline{u_iu_j}, \tag{4}$$

with τ_{ij} as the viscous shear stress of the mean flow and τ'_{ij} as the Reynolds stress due to velocity fluctuations. Because of the unknown Reynolds stress, more equations are required to close the RANS equations. Hence, a turbulence model is required to simulate the Reynolds stress in turbulent flows. The k-ε turbulence model (Launder [10]) is employed in this study. Coefficients appearing in the k-ε turbulence model are presented in Table 1.

Resultant governing equations are solved using a commercial CFD package, STAR-CD™. The finite volume method is the main approaches employed by STAR-CD™ to discretise the governing equations (1) and (2). In additions, the SIMPLE algorithm in STAR-CD™ was adopted to calculate the steady state solutions. The resultant systems of linear algebraic equations were solved by the algebraic multigrid (AMG) method. The fluid domain has to

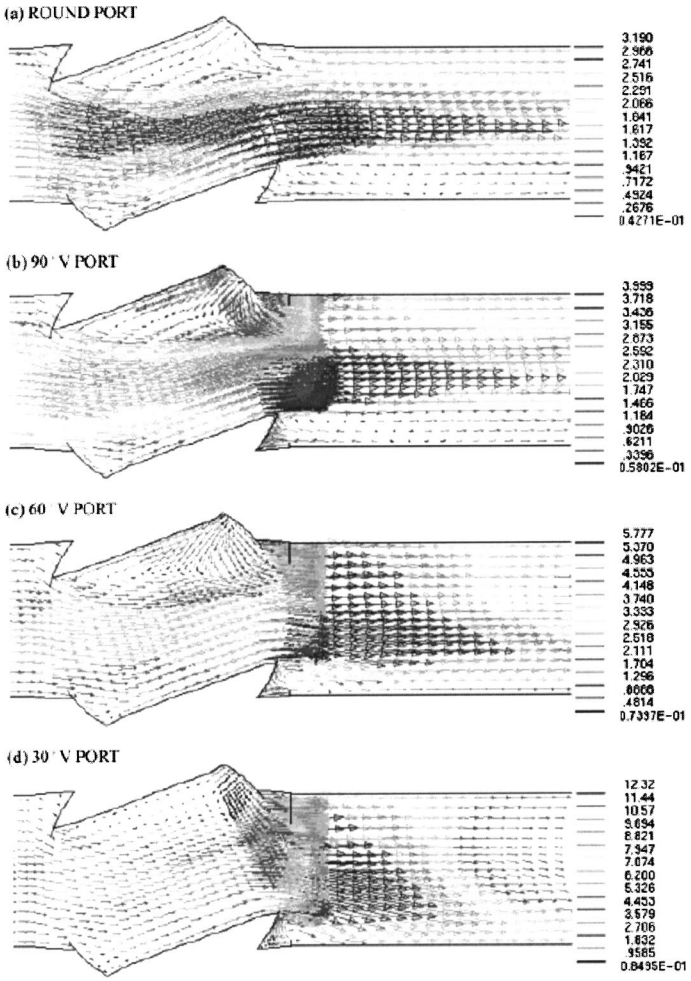

Fig. 7 Flow patterns of computational results at Re=0.64×10^5 and α=20 deg

be divided into control volumes before the numerical simulation. Figure 3 demonstrates the 3-D computational mesh utilized in the numerical simulation. The entrance length from the upstream boundary to the valve is 20D. The downstream length from the valve to the outlet boundary is 60D. Number of control volumes vary from 109770 to 101986 due to different V-ports and valve openings. Figures 4(*a*) and (*b*) show the grid size independency tests for various meshes. The original meshes have 109770, 103722 and 101986 computational cells for cases with 90 deg, 60 deg and 30 deg V-ports. In addition, the refined meshes have 203970, 197922 and 196186 cells for cases with 90 deg, 60 deg and 30 deg V-ports. The axial velocity component profiles along the *y*-direction 2D in front of the valve are given in Fig. 4(*a*). It is clear that results obtained by various meshes are close. Figure 4(*b*) demonstrates the axial velocity profiles along the *y*-direction 6D behind the valve. Results using various meshes are close also. Therefore, the grid size independency in the established numerical model can be approved.

A uniform velocity is imposed at the inlet boundary. Meanwhile, the floating boundary condition is utilized at the outlet boundary. To make sure that the mass conservation is satisfied at each cell, a mass residual requirement is set as 10^{-3}. Computations were executed at the National High Performance Center Taiwan. IBM SPP is the main workstation used to perform STAR-CD™. The CPU time for each case is about 6045 s.

4 Results and Discussion

4.1 Flow Conditions. Several inlet flows and valve openings have been tested. The values of inlet velocity for the numerical model and experiments are 2, 4, and 6 m/s, which correspond to Reynolds numbers, $\mathrm{Re}_D=\rho U_i D/\mu$, 0.64×10^5, 1.27×10^5 and 1.91×10^5, respectively. The valve openings, ϕ, under tests are 100%, 88.9%, 77.8%, 66.7%, 55.6% and 44.4%. These values correspond to the angles of the ball valve, $\alpha=0$, 10, 20, 30, 40 and 50 deg. Due to the limit of the pump and the increasing pressure drop, cases for openings less than 44.4% were not available in the established experimental system.

4.2 Flow Patterns. Since fluid flows studied are turbulent and at high Reynolds numbers, their characteristics are not affected by Reynolds number but the Reynolds stress (Tennekes & Lumely [11]). Chern & Wang [4] indicated that fluid flows through a ball valve at high Reynolds numbers have the same flow patterns under the same valve opening. Hence, the fluid flows at $\mathrm{Re}=0.64\times10^5$ are used to demonstrate variation in flows with respect to V-ports and the ball valve openings in this study.

4.2.1 Numerical Results. Figures 5(*a*)–5(*c*) show the 3-D numerical results at different view points. Figure 5(*b*) is the velocity field at the *z*-section plane. Figure 5(*c*) is the velocity field at the *x*-section plane. The last one is used in the following results.

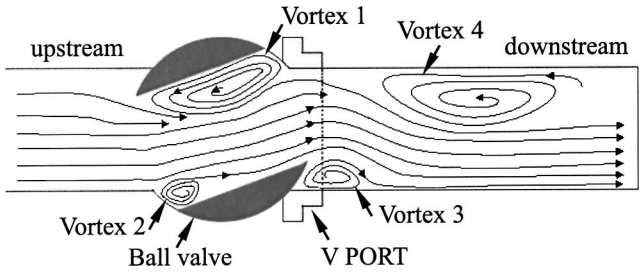

Fig. 8 Schematic flow pattern in the valve flow

Figure 6 shows the velocity field of the numerical results for the fully opened ball valves (α=0 deg) with various V-ports at a Reynolds number of 0.64×10^5. When the valve is fully open (α=0 deg), the velocity profile through the ball valve without a V-port is parabolic as shown in Fig. 6(*a*). The maximum velocity of 2.5 m/s appears at the center of the velocity profile. Figures 6(*b*)–(*d*) give the flow patterns when V-ports of angles 90 deg, 60 deg and 30 deg are installed. It is observed that the peak of the velocity profile moves down as a V-port is installed at the exit of a ball valve. The velocity profile is distorted to a triangular profile as the angle of the V-port decreases. Meanwhile, the maximum velocity of the profile increases as the angle of the V-port decreases. Maximum values of the velocity profile are 2.9, 4.1, and 8.7 m/s when 90 deg, 60 deg, and 30 deg V-ports are used respectively. Figure 6(*d*) reveals the velocity field in a ball valve with a 30 deg V-port. It is apparent that a recirculation region appears in the upper part of the downstream region even though the ball valve is fully opened. Also, most of the fluid flows though the lower part of a V-port due to its larger cross-section than the upper part. Figures 7 shows flow patterns of the ball-valve with α set at 20 deg. Three vortices are found in the ball valve without a V-port as shown in Fig. 7(*a*). These vortices grow as the valve angle, α, increases. When a V-port is installed, the vortex at the lower part of the downstream region decreases in size. This is shown schematically as vortex 3 in Fig. 8. The vortex 3 at the lower part behind the ball valve with a 30 deg V-port almost disappears due

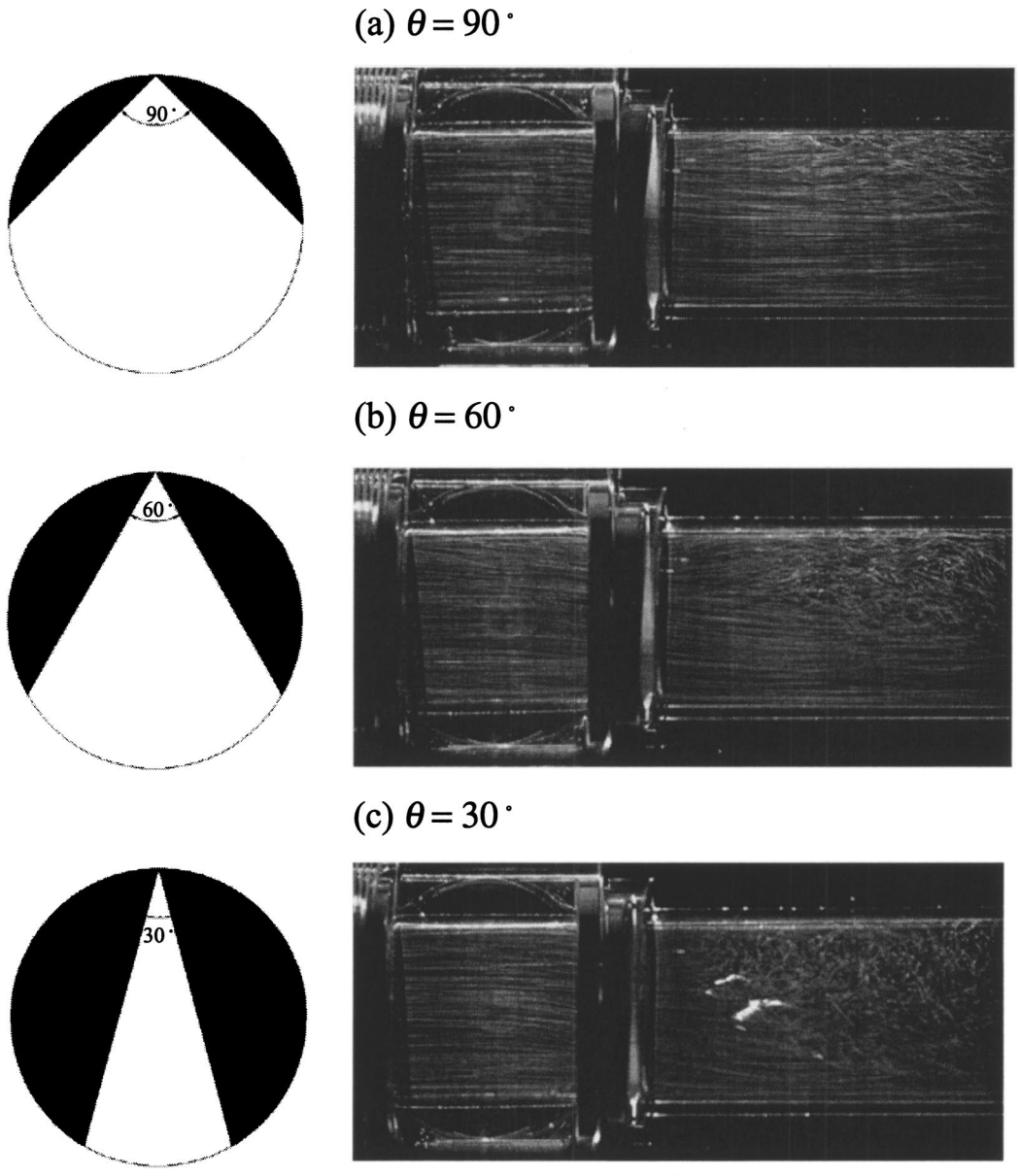

Fig. 9 Flow patterns at Re=0.64×10^5 and α=0 deg

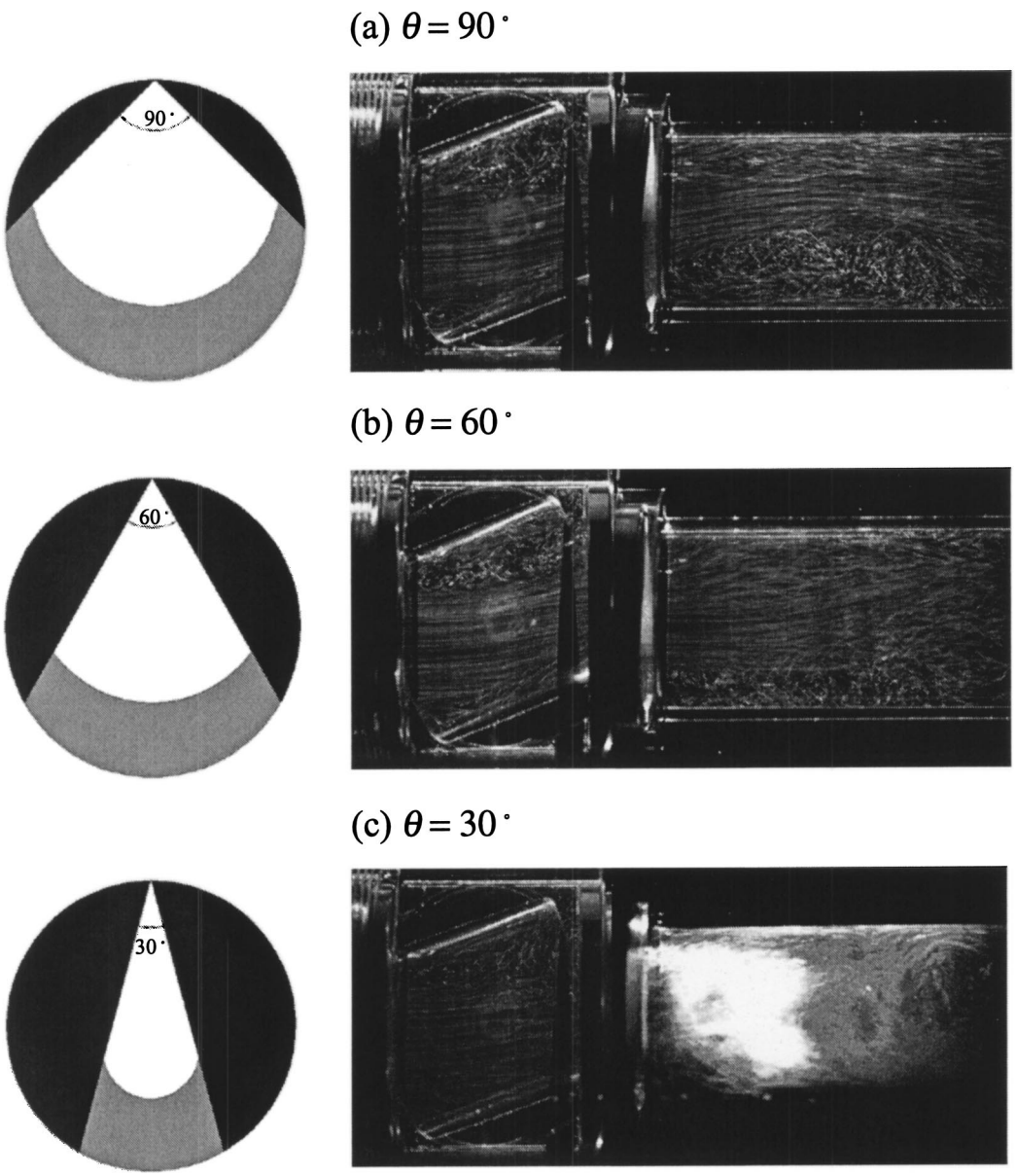

Fig. 10 Flow patterns at Re=0.64×10^5 and α=20 deg

to the vortex 4 shown in Fig. 8) at the upper part of the downstream region. Figure 8 shows a schematic flow pattern when a V-port is utilized. In general, there are two vortices (1 and 2 in Fig. 8) inside the ball valve. Two vortices (3 and 4 in Fig. 8) appear at the downstream region. The vortex 3 is observed at the lower region. The vortex 4, which is not found in the case without a V-port, appears at the upper part.

4.2.2 Results of PTFV. Flow patterns through the acrylic ball valve with various V-ports are visualized using the PTFV method. Figure 9 presents flow patterns when the ball valve with various V-ports are fully open. It is found that the vortex 4 appears at the downstream upper region when a V-port is installed. This agrees with the numerical results as shown in Fig. 6. Most of the fluid through the ball valve travels through the lower part of the V-ports because the upper open area of a V-port is smaller than that of the lower part. It should be noted that cavitation is observed at the downstream region when a 30 deg V-port is utilized as shown in Fig. 9(*c*). It is because that the 30 deg V-port causes the local pressure of the upper region to decrease to values lower than the vapor pressure. Therefore, the cavitation appears in the edge of the recirculation when the ball valve is fully open.

Figure 10 presents the flow patterns when the angle of the ball valve is 20 deg. (*a*), (*b*), and (*c*) refer to cases with V-ports of angles 30 deg, 60 deg, and 90 deg, respectively. The vortex 3 at the downstream lower region appears when the valve is not fully open. In general, vortices grow as the angle of the ball valve, α, increases. These flow patterns agree with numerical results (Fig. 7). The cavitation in the flow through the 30 deg V-port is worse than in previous cases as shown in Fig. 9(*c*).

4.3 Characteristic Coefficients. In general, a valve is evaluated using three coefficients: the loss coefficient, the flow coefficient and the cavitation index. Kirik & Driskell [12] provided formulas for these coefficients. The loss coefficient represents the energy loss due to a valve. It can be denoted as

$$K = \frac{\Delta P}{\frac{1}{2}\rho U_i^2}, \tag{5}$$

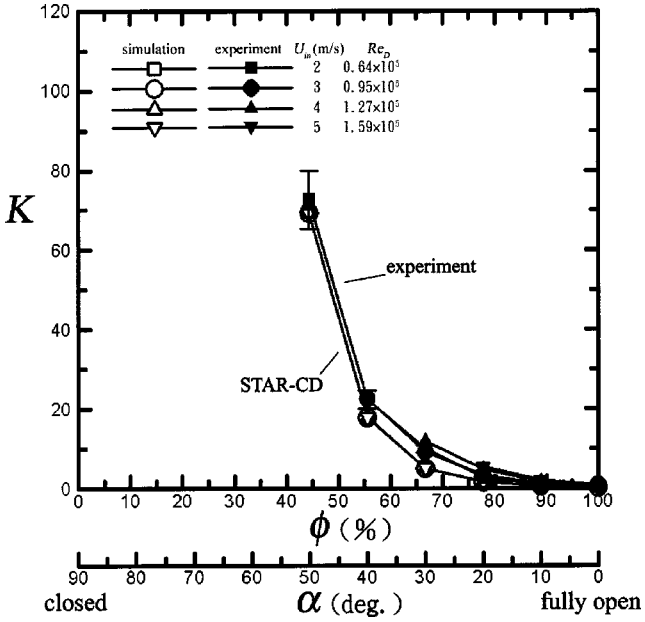

Fig. 11 Loss coefficient of 90 deg V-port

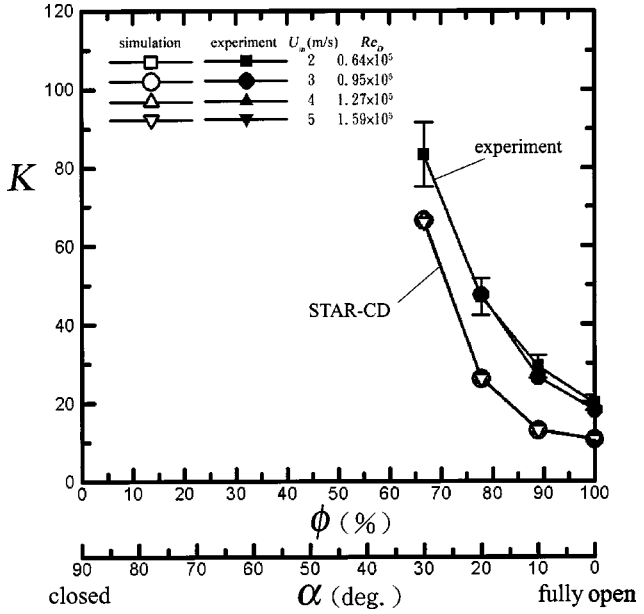

Fig. 13 Loss coefficient of 30 deg V-port

where U_i is the mean inlet velocity. ΔP is the pressure drop measured between 2D in front of the valve and 6D behind the valve. The flow coefficient refers to the capability of flow in a valve, defined as

$$C_V = \frac{q}{0.865 F_p}\sqrt{\frac{G}{\Delta P}}, \tag{6}$$

where q is the volume flow rate, G is the specific gravity relative to water at 4°C and F_p is the geometric factor. G and F_p are set to unity in this study. To predict the conditions where cavitation happens, the cavitation index is used and is denoted as

$$C_{cs} = \frac{\Delta P}{P_{\text{in}} - P_v}, \tag{7}$$

where P_v refers to the saturated vapor pressure (2.339 kPa at 20°C).

4.3.1 Loss Coefficient, K. Figure 11 provides the comparison result of the loss coefficient, K, between numerical and experimental results when the 90 deg V-port is installed. There is an agreement between numerical and experimental results. The variation of inlet velocity (or the corresponding Reynolds number) does not affect the loss coefficient in terms of Fig. 11. As the percent opening of the ball valve decreases, the loss coefficient increases. Subsequently, Figs. 12 and 13 demonstrates results of loss coefficient when the 60 and 30 deg V-ports are employed, respectively. In terms of Figs. 12 and 13, the loss coefficients

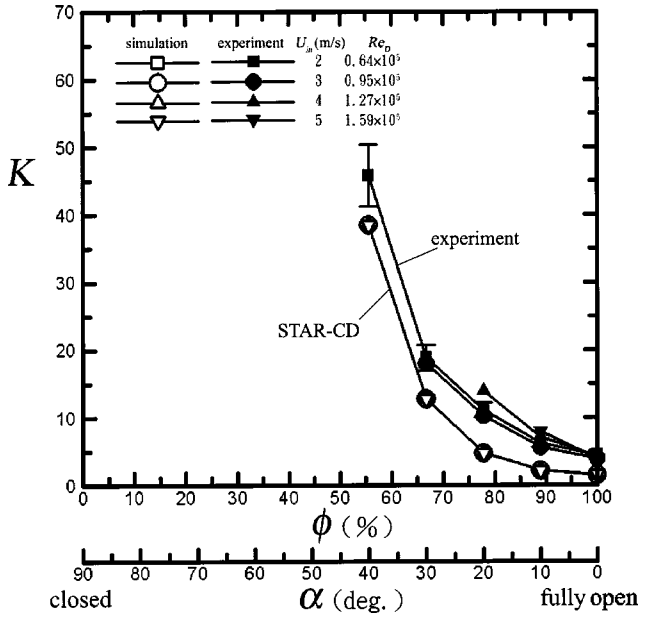

Fig. 12 Loss coefficient of 60 deg V-port

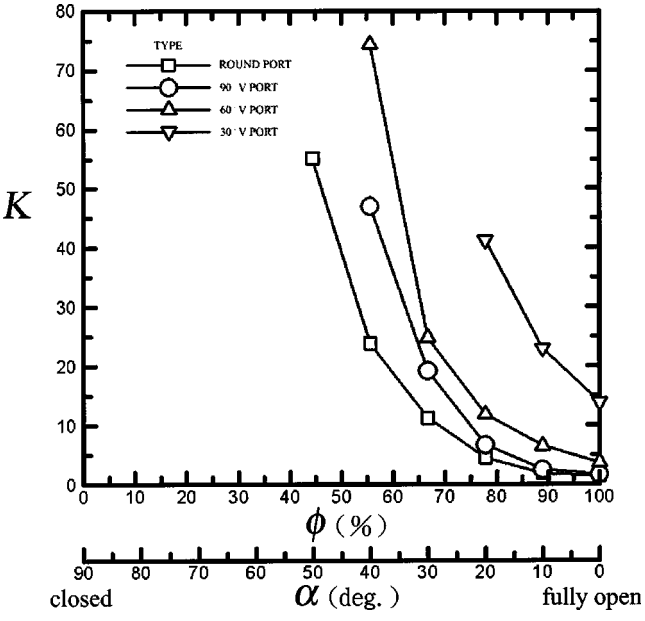

Fig. 14 Effect of various V-ports on loss coefficient. Results shown are obtained from experiments

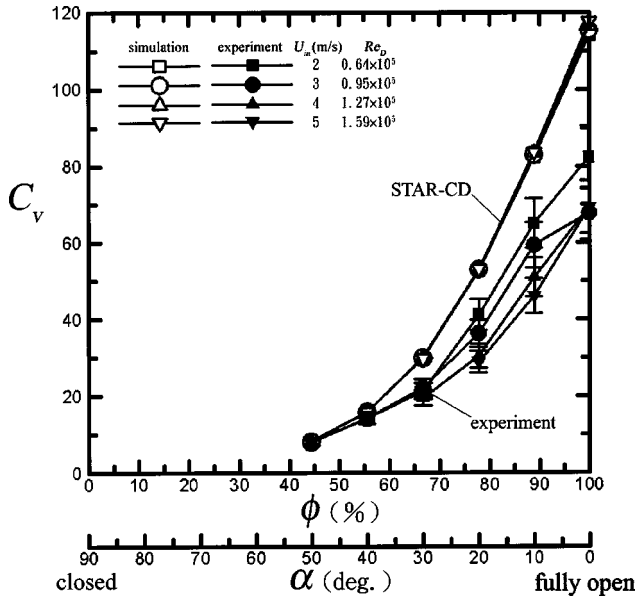

Fig. 15 Flow Coefficient of 90 deg V-port

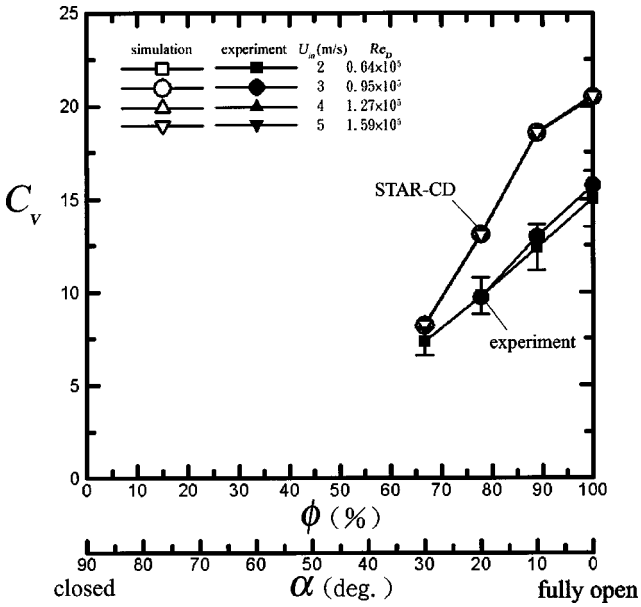

Fig. 17 Flow Coefficient of 30 deg V-port

estimated by the numerical model are less than the experimental results. This was also found in the fluid flow without V-ports (Chern & Wang [4]).

Figure 14 reveals experimental results of loss coefficient using various V-ports. It is clear that the loss coefficient increases when the angle of V-port decreases. V-ports with small angles cause more pressure loss than V-ports with large angles. As a result, using a V-port may control the volume flow rate in the pipe, but it also causes more energy loss.

4.3.2 Flow Coefficient, C_V. Effect of V-ports on the flow coefficient, C_V, can be found in Figures 15–17. Figure 15 shows the numerical and experimental results for the fluid flow through the 90 deg V-port. C_V increases as the valve open, ϕ, becomes large. However, the relationship between C_V and the valve open is not linear in terms of Fig. 15. Also, the numerical results are larger than the experimental results. Figure 16 reveals results for the fluid flow through the 60 deg V-port. It is found that C_V is proportional to the valve open in terms of numerical and experimental results for percent openings from 50% to 100%. Percent openings less than 50% were not investigated. In addition, when the 30 deg V-port is used, Fig. 17 presents that C_V is proportional to the valve opening. That means 60 and 30 deg V-ports can linearly control the volume flow rate in the piping system from 50 to 100 opening of the valve. Figure 18 indicates the comparison of C_V in fluid flows passing through various V-ports in terms of experimental results. It is found that C_V decreases as the angles of V-ports decreases. Although 60 and 30 deg V-ports can linearly control the volume flow rates, the volume flow rates in the piping system are less than the case without a V-port.

4.3.3 Cavitation Index, C_{cs}. Figure 19 demonstrates the variation of cavitation index, C_{cs}, with respect to the valve opening in the fluid flow passing through the 90 deg V-port. There is an

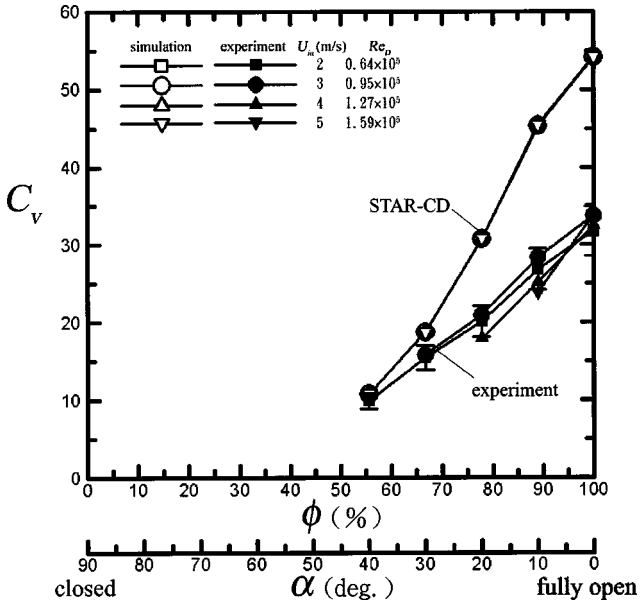

Fig. 16 Flow Coefficient of 60 deg V-port

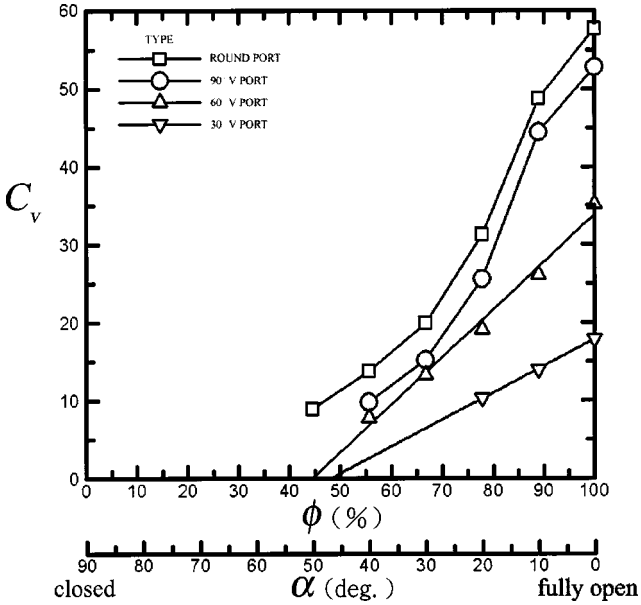

Fig. 18 Effect of various V-ports on flow coefficient

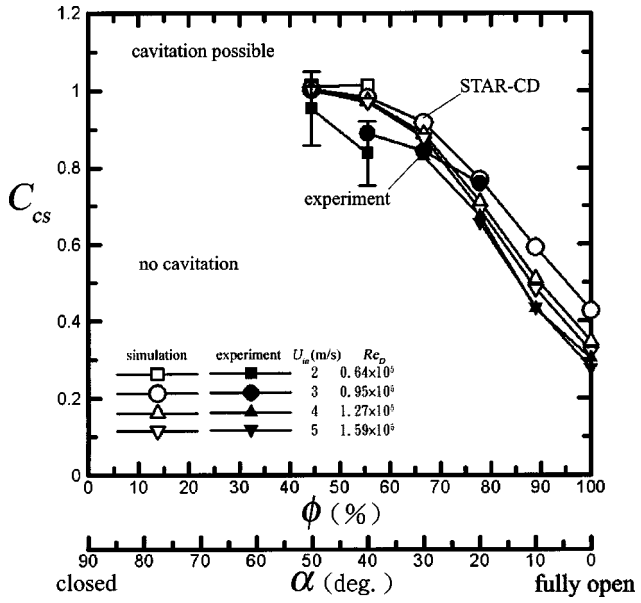

Fig. 19 Cavitation index of 90 deg V-port

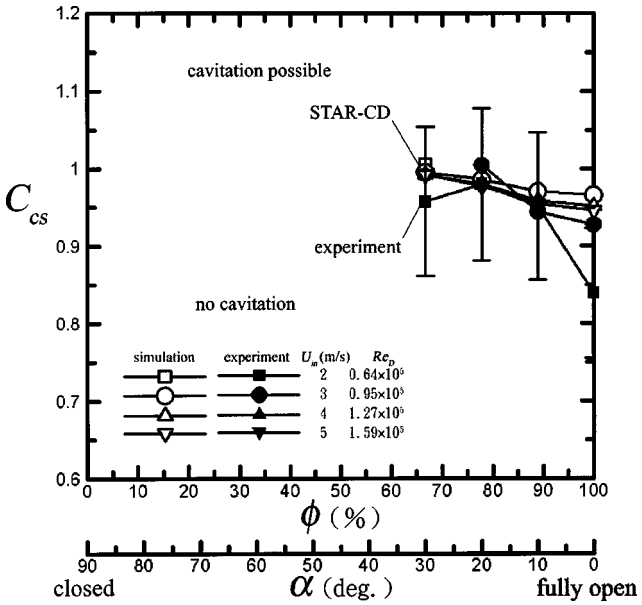

Fig. 21 Cavitation index of 30 deg V-port

agreement between numerical and experimental results in Fig. 19. Furthermore, Fig. 20 gives C_{cs} in the case with the 60 deg V-port. The cavitation index in Fig. 20 is higher than the one in Fig. 19. This implies that cavitation more possibly appears in the case with the 60 deg V-port. In addition, Fig. 21 shows C_{cs} in the fluid flow through the 30 deg V-port. The curve of C_{cs} is close to unity in all valve openings. This means cavitation appears in the flow with the 30 deg V-port even though the valve is fully opened. This agrees with the results of previous flow visualization (Figs. 9(*c*) and 10(*c*)). Although the 30 deg V-port can control the volume flow rate linearly, it also can induce cavitation in the flow even though the ball valve is fully open. Figure 22 demonstrates the comparison of cavitation indices for various V-ports in terms of experimental results, it is obvious that cavitation indices increase as the angle of V-port decreases.

Conclusions

Effect of V-ports on flows passing through a ball valve is investigated numerically and experimentally. Test cases were run for valves operating from 50% to 100% open. When a V-port is utilized, a new vortex (No. 4), which is not found in the case of ball valves-only, is observed at the downstream upper region. This study showed that V-ports can linearly control the volume flow rate from 50%–100% open. In our test cases, 60 and 30 deg V-ports both can attain this purpose. The 90 deg V-port, however, does not work well. The V-ports decrease the volume flow rate and increase the pressure loss. The smaller the angle of a V-port, the more the pressure loss. The cavitation should be considered when a V-port is used with a valve. The critical value of the valve open at which the cavitation appears increases when a V-port is employed. The cavitation is observed even when the valve with a

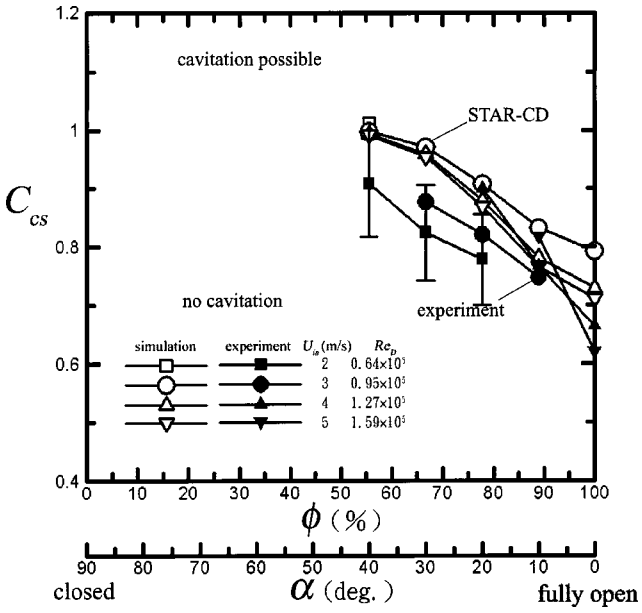

Fig. 20 Cavitation index of 60 deg V-port

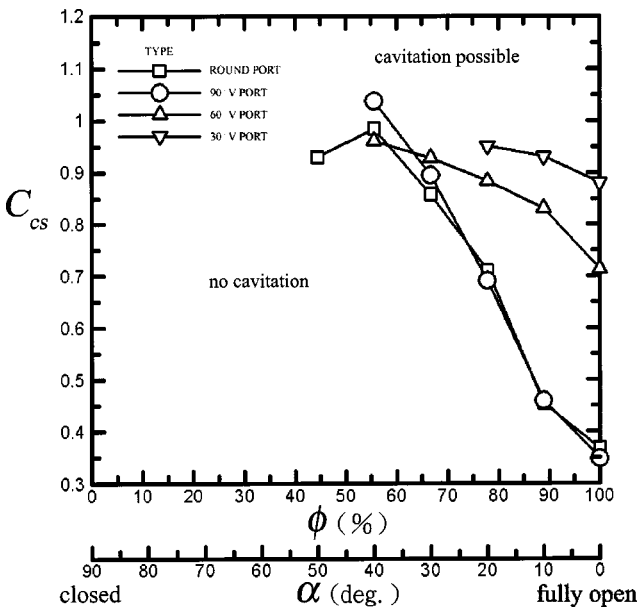

Fig. 22 Effect of various V-ports on cavitation index

30 deg V-port is fully open. According to all of the results, the 60 deg V-port seems to be the most appropriate one for the linear volume flow control.

Acknowledgments

We are truly grateful to MIRDC Taiwan for their support (Project No.:91AL237) and the National Centre for High Performance Computing, Taiwan for their computing resources. The project (NSC 91-2611-E-011-001) provided by the National Science Council Taiwan is also highly appreciated.

Nomenclatures

A = cross-section area of ball valve, m^2
A_V = cross-section area of V-port, m^2
C_{cs} = cavitation index
C_V = flow coefficient
D = diameter of straight pipe, m
g = gravitational acceleration, $m \cdot s^{-2}$
K = loss coefficient
k = turbulent kinetic energy, $m^2 \cdot s^{-2}$
P = pressure, Pa
P_v = saturated vapor pressure, Pa
q = volume flow rate, $m^3 \cdot s^{-1}$
Re_D = Reynolds number, $U_i D/\nu$
U_i = averaged velocity at the inlet boundary, $m \cdot s^{-1}$
$-\rho\overline{u_i u_j}$ = Reynolds stress, $kg \cdot m^{-1} \cdot s^{-2}$
α = angle of ball valve
θ = angle of V-port
ρ = density of water, $kg \cdot m^{-3}$
τ = viscous shear stress, $kg \cdot m^{-1} \cdot s^{-2}$
τ' = Reynolds stress, $kg \cdot m^{-1} \cdot s^{-2}$
ε = rate of dissipation, $m^2 \cdot s^{-3}$
ν = kinetic viscosity of water, $m^2 \cdot s^{-1}$
ϕ = open of ball valve

References

[1] Hutchison, J. W., 1976, *ISA Handbook of Control Valves*, Instrument Society of America, Pittsburgh, the 2nd Ed.
[2] Merati, P., Macelt, M. J., and Erickson, R. B., 2001, "Flow Investigation Around a V-Sector Ball Valve." J. Fluids Eng., **123**, pp. 662–671.
[3] Davis, J. A., Stewart, M., 2002, "Predicting Globe Control Valve Performance-Part II: Experimental Validation," J. Fluids Eng., **124**, pp. 778–783.
[4] Chern, M. J., and Wang, C. C., "Performance Test and Flow Visualization of Ball Valve." Submitted to Journal of Fluids Engineering.
[5] Kerh, T., Lee, J. J., and Wellford, L. C., 1997, "Transient Fluid-Structure Interaction in a Control Valve," Journal of Fluids Engineering, **119**, pp. 354–359.
[6] van Lookeren Campagne, C., Nicodemus, R., de Bruin, G. J., and Lohse, D., 2002, "A Method for Pressure Calculation in Ball Valves Containing Bubbles." Journal of Fluids Engineering, **124**, pp. 765–771.
[7] Davis, J. A., Stewart, M., 2002, "Predicting Globe Control Valve Performance-Part I: CFD Modeling," Journal of Fluids Engineering, **124**, pp. 772–777.
[8] Huang, C., and Kim, R. H., 1996, "Three-Dimensional Analysis of Partially Open Butterfly Valve Flows," Journal of Fluids Engineering, **118**, pp. 562–568.
[9] Richard, C. F. and John, H. S., 1988, *Fundamentals of Air Pollution Engineering*, Prentice Hall, New-Jersey, pp. 290–357.
[10] Launder, B. E., 1989, "Second-moment Closuer and Its Use in Modelling Turbulent Industrial Flows." Int. J. Numer. Methods Fluids, **9**, pp. 963–985.
[11] Tennekes, H. and Lumely, J. L., 1972, *A First Course in Turbulence*, MIT Press, Cambridge, pp. 59–65.
[12] Kirik, M. J. and Driskell, L. R., 1986, *Flow Manual for Quarter-Turn Valves*. Rockwell International Co.

Journal of Fluids Engineering

Technical Briefs

A Method for Analyzing the Performance of Centrifugal Oil Pumps

Wen-Guang Li
Department of Energy and Engineering for Power, Lanzhou University of Technology, 730050 Lanzhou, People's Republic of China
e-mail: Liwg38@yahoo.com.cn

[DOI: 10.1115/1.1760544]

Introduction

The hydraulic performance of centrifugal oil pumps can be illustrated by using three curves: head-flow rate, power-flow rate and efficiency-flow rate. Figure 1 shows the performance curves of the pumps. In general, the performance can be given exactly through experiment only. The attempt of this paper is to calculate the several parameters which describe the sub-macro-characteristics, such as the slip factor, hydraulic, volumetric and mechanical efficiencies, based on the performance and geometry of impeller at best efficiency point (BEP).

The hydraulic losses in centrifugal oil pumps include friction loss along flow channel wall, shock loss at leading edge of blade and local vortex loss at BEP. Friction loss due to high viscosity of liquid and shock loss have large percentage in the total, so the local vortex can be neglected. The energy conservation equation in centrifugal oil pumps can be written as

$$H = H_{th} - KQ^2 \tag{1}$$

where H stands for the known head of the pump at BEP, H_{th} presents the theoretical head, here H_{th}, K will be determined by the experimental data of performance and the geometry of impeller, Q denotes the known flow rate and K is hydraulic loss coefficient, which can be considered as a constant at BEP.

The head-flow rate curve has been worked out based on the experimental data of performance. The following equation can be obtained by differentiating equation (1) with respect to flow rate Q

$$\frac{dH}{dQ} = \frac{dH_{th}}{dQ} - 2KQ \tag{2}$$

where the slope dH/dQ of the head curve can be calculated via the head-flow rate curve.

Contributed by the Fluids Engineering Division for publication in the JOURNAL OF FLUIDS ENGINEERING. Manuscript received by the Fluids Engineering Division September 25, 2002; revised manuscript received January 20, 2004. Associate Editor V. Tsujimoto.

If the pre-circulation of flow in the inlet of impeller is ignored, the Euler's equation for centrifugal oil pumps will be written as

$$H_{th} = \frac{V_{u2} u_2}{g} \tag{3}$$

The circumferential component of the absolute liquid velocity at the discharge of impeller is

$$V_{u2} = \sigma u_2 - \frac{Q}{\eta_V A_2 \tan \beta_2} \tag{4}$$

where σ stands for the slip factor at BEP, σu_2 represents the impeller tip speed after considering the slip of flow at impeller discharge, η_V is volumetric efficiency of pump, A_2 the discharge area of impeller, β_2 blade discharge angle, and u_2 stands for the impeller tip speed. Here the slip factor σ is defined as

$$\sigma = 1 - \frac{\Delta V_{u2}}{u_2} \tag{5}$$

where ΔV_{u2} is the slip liquid velocity at impeller discharge in circumferential direction.

Then the theoretical head is written as

$$H_{th} = \frac{u_2}{g}\left(\sigma u_2 - \frac{Q}{\eta_V A_2 \tan \beta_2}\right) \tag{6}$$

H_{th} is differentiated with respect to Q, the following equation can be obtained

$$\frac{dH_{th}}{dQ} = -\frac{u_2}{g\,\eta_V A_2 \tan \beta_2} \tag{7}$$

The Eqs. (1), (2), (6) and (7) are solved simultaneously, and the slip factor can be calculated using the following equation

$$\sigma = \frac{g}{2u_2^2}\left[2H - Q\left(\frac{dH}{dQ} - \frac{u_2}{g\,\eta_V A_2 \tan \beta_2}\right)\right] \tag{8}$$

Hydraulic efficiency

$$\eta_h = \frac{H}{H_{th}} \tag{9}$$

where

$$H_{th} = H + KQ^2,$$

$$K = -0.5[dH/dQ + u_2/(g\,\eta_V A_2 \tan \beta_2)]/Q.$$

Mechanical efficiency

$$\eta_m = \frac{\eta}{\eta_V \eta_k} \tag{10}$$

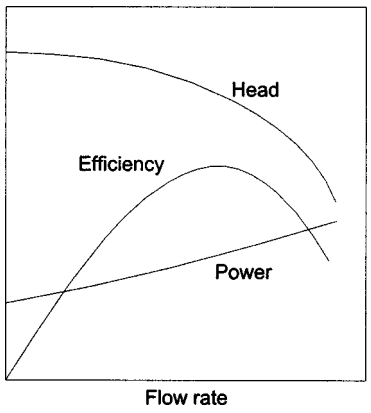

Fig. 1 Performance curves of centrifugal oil pumps

where η stands for the best efficiency of pump, which is known based on the performance test.

The method in [2] for estimating the flow rate of leakage from the clearance between the two concentric cylinders of the wear-ring mounted on impeller is adapted in this paper. Figure 2 illustrates the cross-section of test pump in present paper. There are two wear-rings in the impeller here, one is front wear-ring and the other is rear wear-ring. The front wear-ring and the rear one are installed on the shroud of impeller and the hub of impeller, respectively, to resist liquid flow from volute to impeller eye. Both wear-rings share the same geometry. There are five balance holes in the hub to balance the axial thrust on the impeller. The holes can allow less flow to pass the wear-ring due to their additional hydraulic resistance to flow. Therefore, the leakage through the rear clearance is less than that through the front one.

The flow rate of leakage through the front wear-ring can be written as

$$q_f=\frac{\pi d_m b_m}{\sqrt{0.02 l_m/b_m+1.5}}\sqrt{2g\Delta H_f} \tag{11}$$

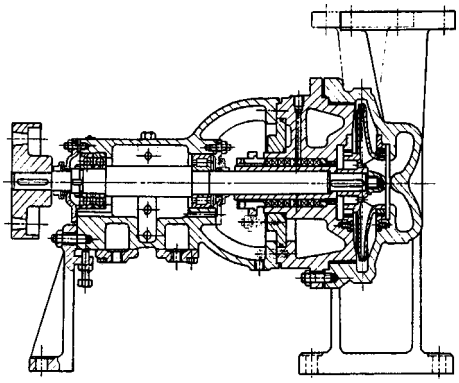

Fig. 2 The cross-section of test pump

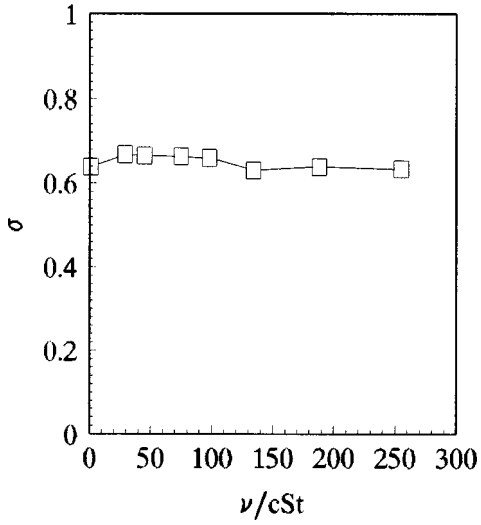

Fig. 3 Slip factor variation with viscosity

where d_m represents the diameter of the wear-ring, l_m is the length of the wear-ring, b_m is the radial clearance of the wear-ring and ΔH_f is the differential pressure across the wear-ring. Suppose that the fluid rotating angular velocity in the spaces between impeller shrouds and pump casing is half of the impeller rotating angular velocity, then ΔH_f can be written

$$\Delta H_f=H_p-\frac{1}{4}\left(\frac{u_2^2-u_m^2}{2g}\right) \tag{12}$$

where H_P is the static pressure in volute, and u_m denotes the rotating speed of the wear-ring. H_P can be gained by using the following equation

$$H_P=H-\frac{V_3^2}{2g} \tag{13}$$

where V_3 is mean liquid velocity in the volute, $V_3=Q/F_8$, F_8 is area of the volute throat.

The flow rate of leakage through the rear wear-ring can be written as

$$q_r=\frac{\pi d_m b_m}{\sqrt{0.02 l_m/b_m+1.5+(\pi d_m b_m/F_b)^2\xi_b}}\sqrt{2g\Delta H_r} \tag{14}$$

where F_b represents the total area of balance holes, $F_b=Z_b\pi d_b^2/4$, Z_b is number of balance holes, d_b diameter of the hole, ξ_b denotes local loss coefficient of a balance hole, in general, $\xi_b=2$. ΔH_r is the pressure difference across the rear wear-ring. It can be read as

$$\Delta H_r=H_p-\frac{1}{4}\left(\frac{u_2^2-u_b^2}{2g}\right) \tag{15}$$

Table 1 Geometries of impeller, volute, wear-ring and balance hole

Impeller and Volute		Wear-ring	
Impeller diameter, D_2	213 mm	Diameter, d_m	100 mm
Eye diameter, D_j	72 mm	Length, l_m	15 mm
Blade outlet width, b_2	7.5 mm	Clearance, b_m	0.25 mm
Blade outlet angle, β_2	30°	Balance hole	
Blade outlet thickness, S_{u2}	6.5 mm	Diameter, d_b	8 mm
Number of blades, Z	5	Number of holes, Z_b	5
Throat area, F_8	432 mm^2	Diameter of hole center, D_b	54 mm

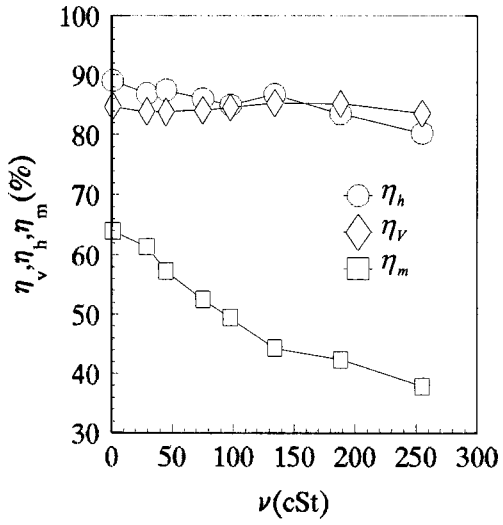

Fig. 4 Various efficiencies versus viscosity

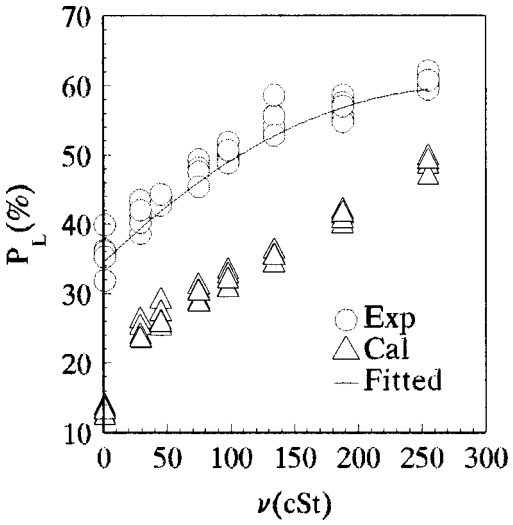

Fig. 5 Mechanical loss variation with viscosity

where u_b denotes the impeller rotating speed at the balance hole center.

After the flow rates of leakage being available, the volumetric efficiency can be evaluated by following formula

$$\eta_V = \frac{Q}{Q + q_f + q_r} \tag{16}$$

Obviously, if the performance curve and the geometry of impeller are available, the slip factor, hydraulic loss coefficient, hydraulic, volumetric and mechanical efficiency at BEP will be worked out immediately.

Results and Discussion

Test Pump. The test pump is a centrifugal oil pump of type 65Y60 (Fig. 2) based on API610 standard, which is commonly applied to transport hot oil with temperature less than 350°C. The parameters of the pump are: flow rate $Q=25\ \mathrm{m}^3/\mathrm{h}$, head $H=60$ m, rotating speed $n=2950$ r/min, and specific speed $n_s=3.65\,n\sqrt{Q}/H^{0.75}=41.6$ (r/min,m^3/s,m).

The test rig is composed of a tank, globe valve, suction and discharge pipes, turbine flow meter, gate valve, pressure sensor and torque detector. The sensor gives the difference of the liquid static pressure between the pump inlet and outlet and the detector indicates the torque input and the shaft speed. The total uncertainties of flow rate, head, input power and efficiency are 0.707%, 0.205%, 0.515% and 0.898%, respectively. The uncertainty of slip factor is 2.32%. The kinematical viscosity values in the performance test are: 1(water), 29cSt(oil), 45cSt(oil), 75cSt(oil), 98cSt(oil), 134cSt(oil), 188cSt(oil) and 255cSt(oil), respectively.

Data Input. A computer program has been written for performing the analysis in the method proposed above. The geometrical data input into the program has been shown in Table 1.

Slip Factor. Figure 3 illustrates the variations of the slip factor calculated with viscosity at BEP. The slip will grow as viscosity increase until 30cSt. As the viscosity greater than this value, the factor decreases gradually. However, the factor for pumping viscous oil is larger than for pumping water. It indicates that the thicker viscosity will help the impeller to produce a higher theoretical head. The liquid with higher viscosity would suppress the relative circulation in impeller channel [2] and reduce the flow slip at impeller discharge.

Hydraulic, Volumetric and Mechanical Efficiencies. Figure 4 demonstrates the variations of respective hydraulic, volumetric and mechanical efficiencies with various viscosities. The hydraulic efficiency decreases with viscosity increase due to larger friction loss on wall of flow channels in inlet casing, volute and impeller. This will result in a drop in head. This has been confirmed by performance test while pumping viscous oil. The volumetric efficiency has nothing to do with viscosity variation. The larger viscosity will suppress leakage through the clearances between wear-ring and casing of the pump. The mechanical efficiency drops dramatically with viscosity increase. When the viscosity is 250cSt, the efficiency is low as 40%. Therefore, the reason why the efficiency of the pump handling viscous oil drops quickly as oil's viscosity increases is the viscosity affects the mechanical efficiency heavily.

Figure 5 illustrates the both experimental mechanical loss and impeller disk friction loss calculated by using Pfleiderer's formula [2]. The large difference can be found between experimental data and results calculated. The formula was based on experimental data for rotating flat disk in cylindrical container with zero leakage. Actual geometry of impeller shrouds and flow pattern in varied clearance between shroud and casing wall in our test pump (Fig. 2) differ from those which the formula depends on. Therefore, the results of the formula shouldn't agree well with data based on our observations of this commercial centrifugal oil pump.

Because the mechanical efficiency of centrifugal oil pumps reduces very rapidly as the viscosity of liquid pumped increase, the efficiency of the pump will be controlled gradually by the mechanical efficiency. Therefore, how to improve the mechanical efficiency will be a critical problem in the improvement of the performance of centrifugal oil pumps when handling high viscosity oil. Nevertheless, how to reduce the disc friction loss is a key issue in this problem.

Conclusion

A method for determining some parameters, such as slip factor, hydraulic, mechanical and volumetric efficiencies based on the experimental performance of centrifugal oil pumps, is proposed. The follow conclusions can be made:

1. The slip factor grows and then drops while the viscosity increases, but it is larger for viscous oil than for water at the viscosity between 30 and 100cSt.

2. The hydraulic efficiency decreases while the viscosity gets higher due to larger friction loss over flow passage surfaces of impeller, inlet casing and volute.
3. The volumetric efficiency keeps constant or increases while the viscosity grows because of less leakage through the wearing-ring.
4. The mechanical efficiency reduces quickly as the viscosity grows. The reduction of the disc friction loss of impeller is a key issue to improve the performance of centrifugal oil pumps.

Acknowledgment

The author wishes to acknowledge the full support by the Key Research and Development Program for Outstanding Groups at Lanzhou University of Technology, People's Republic of China.

References

[1] Li, W.-G., Su, F.-Z., and Xiao, C., 2002, "Influence of the Number of Impeller Blades on the Performance of Centrifugal Oil Pumps," World Pumps, **427**, pp. 32–35.

[2] A. J. Stepanoff, 1957, Centrifugal and Axial Flow Pumps, New York: John Wiley & Sons, p. 46–47, 187.

Laminar Liquid Flow Through Silicon Microchannels

Gian Luca Morini

DIENCA-Università degli Studi di Bologna, Viale Risorgimento 2, 40136 Bologna, Italy Tel: +39 051 2093287, fax: +39 051 2093296

e-mail: gianluca.morini@mail.ing.unibo.it

The present work deals with the analysis of the fully developed laminar flow through silicon microchannels. The main integral flow parameters, such as the Poiseuille number (f Re), the momentum flux correction factor, the kinetic energy correction factor, the asymptotic incremental pressure drop number and the approximate value of the hydrodynamic entrance length are numerically evaluated for trapezoidal and double-trapezoidal cross sections of the silicon microchannels. The results are quoted in tabular and in graphic form as a function of the microchannel aspect ratio. Finally, very simple polynomial representations of the integral flow parameters are given. These numerical data are a useful tool for technicians and designers involved in microfluidic applications and it is demonstrated that these results can be used (instead of or before a CFD simulation approach) for a first evaluation of the pressure drop for liquid flows through smooth microchannels having a hydraulic diameter greater than 30 μm. [DOI: 10.1115/1.1760545]

Introduction

Micron size mechanical devices are today encountered both in commercial and in scientific applications. It is possible to assert that the manufacture of micro-pumps, micro-valves, micro-cold plates, micro-heat exchangers, and other micro-components and sensors used in chemical analysis, in biomedical diagnostics, in flow measurements or in electronic cooling, are today a consolidated reality. The research on MEMS (Micro-Electro-Mechanical Systems) is exploring different applications which intimately involve the dynamics of fluids, the single phase and two-phase forced convective heat transfer and new potential applications are continuously being proposed. The understanding of microscale transport phenomena is important for the design of a micro fluidic component. For this reason, many studies have been conducted in order to analyses the behavior of flows through microchannels. The literature is inconclusive with respect to the effect of miniaturisation on heat transfer and pressure drop; in fact, many experimental results obtained for laminar flow through microchannels present a significant deviation from the predictions of the conventional theory. Various motivations have been proposed to account for the deviations from the results of the conventional theory; the surface conditions (relative roughness) of the channel [1–5], the property variation effects [6,7], the electro-osmotic effects (EDL) [8,9] and the high experimental uncertainties (Palm [10]) have been invoked to explain the anomalous behavior of the transport mechanisms through microchannels.

Recently, Obot [11] presented critical reviews of the published results on the friction factor and convective heat transfer in microchannels. This work is particularly interesting because it represents a first attempt to compare critically, also from a quantitative point of view, the experimental results obtained for microchannels with the conventional theory validated for large sized channels. Obot demonstrated that the deviations from the conventional theory of the pressure drop and the convective heat transfer data are, in some cases, fictitious. He concluded that the predictions of the conventional theory hold for laminar liquid flow through microchannels having a hydraulic diameter greater than 40 μm. This fact has been confirmed by the succeeding experimental investigations [12,13].

Recently, Wu and Cheng [14] conducted an experimental investigation to measure the friction factor of the laminar flow of deionized water in silicon microchannels of trapezoidal cross-section. They demonstrated that the friction factor is greatly influenced by the cross-sectional aspect ratio. The authors compared their experimental friction factors by using the conventional results for pipes ($f\,\mathrm{Re}=16$) and with an approximate solution due to Ma and Peterson [15] because, for the typical cross-sections of the silicon microchannels, a complete series of data for fully developed laminar flow is not available in literature.

The aim of the present work is to fill this gap. A detailed analysis of the behavior of liquid laminar flow through silicon microchannels by using the conventional theory is developed. The main integral flow parameters are numerically evaluated for trapezoidal and double-trapezoidal cross sections of a silicon microchannel.

Analysis

Consider an integrated micro-fluidic system manufactured by etching on the back of a silicon wafer. When a photo-lithographic based process is employed, one can obtain microchannels having a cross-section fixed by the orientation of the silicon crystal planes; the microchannels etched in ⟨100⟩ or in ⟨110⟩ silicon using a KOH solution have a trapezoidal cross-section (with an apex angle of 54.74 deg imposed by the crystallographic morphology of the ⟨100⟩ silicon) or a rectangular cross-section, respectively. In the present paper, microchannels having a rectangular, trapezoidal and double-trapezoidal (obtained by gluing together two trapezoidal microchannels) cross-section will be considered (see Fig. 1). The fluid runs through the microchannels under an imposed pressure gradient. The microchannels have an axially unchanging and uniform cross-section with an area equal to Ω and the perimeter equal to Γ. The maximum width of the cross section is indicated with a, the minimum width with b and the height with h. A Cartesian system of coordinates ξ, η, ζ, is assumed, with its origin in the bottom left-hand corner of the inlet cross-section.

A 2-D analysis of the microchannel can be made under the following assumption:

Contributed by the Fluids Engineering Division for publication in the JOURNAL OF FLUIDS ENGINEERING. Manuscript received by the Fluids Engineering Division December 26, 2002; revised manuscript received November 8, 2003. Associate Editor: J. S. Marshall.

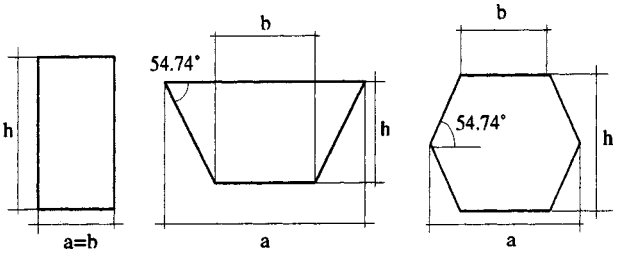

Fig. 1 Schematic representation of the microchannel cross-sections

1. the transport processes are considered to be steady-state and bi-dimensional;
2. the fluid is Newtonian, incompressible, isothermal and with a laminar fully developed velocity profile $u(\xi,\eta)$;
3. all the channel walls are rigid and nonporous;
4. the fluid physical properties are assumed as constant.

Consequently, the momentum equation for the fluid can be written as follows:

$$\nabla^2 u = -\frac{1}{\mu}\frac{dp}{d\zeta} \tag{1}$$

It is suitable to introduce the dimensionless quantities:

$$x=\frac{\xi}{D_h};\quad y=\frac{\eta}{D_h};\quad \Omega^*=\frac{\Omega}{D_h^2};$$

$$\Gamma^*=\frac{\Gamma}{D_h};\quad \nabla^*=D_h\nabla;\quad V(x,y)=\frac{u}{W};\quad p^*=-\frac{D_h^2}{\mu W}\frac{dp}{d\zeta}; \tag{2}$$

where W denotes the average velocity and D_h the hydraulic diameter of the microchannel. Consequently, the dimensionless momentum and energy balance equations are readily obtained in the following form:

$$\nabla^{*2}V + p^* = 0 \tag{3}$$

The momentum conservation equation is resolved by using the boundary condition of no-slip at the walls. For a liquid flow, this assumption is justified; by assuming the typical mean free path λ of molecules under ambient conditions equal to 0.1–1 nm indicatively, the Knudsen number ($\mathrm{Kn}=\lambda/D_h$) can assume values greater than 0.001 only if the hydraulic diameter of the microchannel is less than 1 μm.

From the velocity distribution $V(x,y)$ it is possible to derive the value assumed by the main flow parameters as a function of the microchannel aspect ratio ($\gamma=h/a$ or $\beta=h/b$). The flow parameters which can be useful during the design stage of a micromachined flow device are:

- the value of $V_{\max}$:

$$V_{\max}=\frac{u_{\max}}{W} \tag{4}$$

- the asymptotic value of the momentum flux correction factor K_d defined as:

$$K_d=\frac{1}{\Omega^*}\int_{\Omega^*} V^2(x,y)\,d\Omega^* \tag{5}$$

- the asymptotic kinetic energy correction factor K_e defined as:

$$K_e=\frac{1}{\Omega^*}\int_{\Omega^*} V^3(x,y)\,d\Omega^* \tag{6}$$

- the Poiseuille number defined as the product of the Fanning friction factor for fully developed flow (f) and the Reynolds number (Re):

$$(f\,\mathrm{Re})_{fd}=-\frac{1}{2\Omega^*}\int_{\Gamma^*}\left.\frac{\partial V}{\partial n^*}\right|_{\Gamma^*} d\Gamma^*=\frac{p^*}{2} \tag{7}$$

These flow parameters depend only on the geometry of the duct cross-section.

As is well known, the investigation of the velocity and the pressure distribution in the entrance flow field is possible by introducing the apparent Fanning friction factor. This parameter can be correlated, for a "long microchannel" ($L \gg D_h$), to the fully developed Poiseuille number $(f\,\mathrm{Re})_{fd}$ and to the asymptotic incremental pressure drop number $K_{\inf}$:

$$(f\,\mathrm{Re})_{app}=(f\,\mathrm{Re})_{fd}+\frac{K_{\inf}\,\mathrm{Re}\,D_h}{4L_{ch}} \tag{8}$$

where, in order to determine $K_{\inf}$, an approximate analytical method can be utilized [16]:

$$K_{\inf}=2(K_e-K_d) \tag{9}$$

As demonstrated by McComas [17], it is possible to determine an approximate value of the hydrodynamic entrance length by using the values of the flow parameters in the fully developed region:

$$L_{hy}^*=\frac{L_{hy}}{D_h\,\mathrm{Re}}=\frac{V_{\max}^2-1-2(K_e-K_d)}{4f\,\mathrm{Re}_{fd}} \tag{10}$$

The approximate values of L_{hy}^* computed by means of Eq. (10) are in general lower than those obtained from experiments.

The problem described by Eq. (3) with the boundary condition of no-slip at the walls has been solved numerically by means of a

Table 1 Benchmark of the numerical results for a rectangular cross section with the analytical results quoted by Shah and London [19]

	$V_{\max}$		K_d		K_e		$f\,\mathrm{Re}_{fd}$		L_{hy}^*
β or γ		[19]		[19]		[19]		[19]	
0	1.500	1.5000	1.200	1.2000	1.543	1.543	24.000	24.00000	0.00588
0.01	1.510	-	1.204	-	1.554	-	23.677	-	0.00613
0.05	1.549	1.5488	1.218	1.2183	1.599	1.5990	22.477	22.47701	0.00709
0.1	1.601	1.6009	1.237	1.2365	1.656	1.6560	21.169	21.16888	0.00856
0.2	1.715	-	1.271	-	1.770	-	19.071	19.07050	0.0124
0.3	1.829	-	1.303	-	1.878	-	17.512	17.51209	0.0171
0.4	1.924	1.9236	1.328	1.3283	1.969	1.9690	16.368	16.36810	0.0217
0.5	1.992	1.9918	1.347	1.3474	2.039	2.0389	15.548	15.54806	0.0255
0.6	2.038	-	1.361	-	2.088	-	14.980	14.97996	0.0284
0.7	2.067	-	1.370	-	2.121	-	14.605	14.60538	0.0303
0.8	2.085	-	1.375	-	2.141	-	14.378	14.37780	0.0316
0.9	2.094	-	1.378	-	2.151	-	14.261	14.26098	0.0322
1	2.096	2.0962	1.379	1.3785	2.154	2.1541	14.227	14.22708	0.0324

Table 2 Main flow parameters for trapezoidal ⟨100⟩ silicon microchannels

β	γ	$V_{\max}$	K_d	K_e	$f\,\mathrm{Re}_{fd}$	L^*_{hy}
0	0.000	1.5	1.2	1.543	24	0.0059
0.01	0.010	1.511	1.205	1.556	23.597	0.0062
0.0277	0.027	1.530	1.212	1.580	22.931	0.0066
0.05	0.047	1.555	1.222	1.610	22.174	0.0072
0.1	0.088	1.610	1.243	1.674	20.737	0.0088
0.2	0.156	1.719	1.279	1.793	18.650	0.0124
0.3	0.211	1.822	1.310	1.897	17.244	0.0166
0.4	0.255	1.908	1.334	1.984	16.263	0.0206
0.5	0.293	1.976	1.354	2.054	15.565	0.0242
0.6	0.325	2.027	1.368	2.108	15.060	0.0270
0.7	0.352	2.065	1.379	2.150	14.690	0.0293
0.8	0.375	2.094	1.388	2.182	14.417	0.0312
0.9	0.396	2.116	1.394	2.207	14.215	0.0326
1	0.414	2.132	1.399	2.225	14.063	0.0337
1/0.9	0.432	2.146	1.403	2.241	13.940	0.0346
1.25	0.452	2.158	1.407	2.254	13.832	0.0355
1/0.7	0.473	2.168	1.410	2.266	13.745	0.0362
1/0.6	0.497	2.177	1.412	2.275	13.685	0.0368
2	0.522	2.183	1.414	2.282	13.654	0.0372
2.5	0.551	2.189	1.415	2.287	13.654	0.0375
1/0.3	0.583	2.196	1.417	2.294	13.679	0.0378
5	0.620	2.206	1.420	2.307	13.694	0.0382
10	0.660	2.219	1.426	2.330	13.622	0.0388
∞	0.707	2.228	1.431	2.346	13.308	0.0401

code written using the software package FlexPDE™ [18]. This package is devoted to the solution of systems of partial differential equations through a Rayleigh-Ritz-Galerkin finite-element method. The numerical procedure implies an iterative refinement of the grid until the prescribed accuracy, correlated with the maximum local residual value R_k, is reached. The iterative procedure is stopped when the velocity field V satisfies the following condition:

$$\max(R_k(V,N)) < \varepsilon \quad \forall k \in [1,N] \tag{11}$$

where N denotes the number of triangular elements.

In order to determine the convergence error the numerical results obtained by varying ε have been compared with the analytical values of $V_{\max}, K_d, K_e, f\,\mathrm{Re}_{fd}$ quoted by Shah and London [19] for a rectangular channels. For ε equal to 10^{-7}, the following maximum relative differences between the numerical and the analytical values of $V_{\max}, K_d, K_e, f\,\mathrm{Re}_{fd}$ have been found:

$$\Delta_{V_{\max}} = 0.021\% \quad \Delta_{K_d} = 0.040\%$$
$$\Delta_{K_e} = 0.005\% \quad \Delta_{f\,\mathrm{Re}} = 0.003\% \tag{12}$$

The comparison between the numerical and the analytical results for rectangular channels is shown in Table 1. The estimates given for the convergence error on the main flow parameters for rectangular channels are considered reliable also for the numerical results obtained for the trapezoidal and the double-trapezoidal channels. By using the same value of ε (10^{-7}) for all the cross-sections considered, the required number of triangular elements (N) in order to satisfy the residual-based adaptive refinement criterion, ranges between a minimum value of 70,000 (for the square channel) and a maximum value of 350,000 (for the double-trapezoidal channel with $\gamma = 0.02$).

Table 3 Main flow parameters for double-trapezoidal ⟨100⟩ silicon microchannels

γ	$V_{\max}$	K_d	K_e	$f\,\mathrm{Re}_{fd}$	L^*_{hy}
0	1.500	1.200	1.543	24.000	0.00588
0.02	1.518	1.207	1.563	23.459	0.00631
0.1	1.598	1.233	1.648	21.507	0.00841
0.2	1.717	1.267	1.758	19.501	0.01239
0.4	1.931	1.321	1.950	16.746	0.02196
0.5	1.989	1.337	2.007	15.923	0.02537
0.6	2.019	1.346	2.039	15.403	0.02744
0.7	2.030	1.350	2.053	15.126	0.02834
0.8	2.033	1.351	2.057	15.027	0.02863
0.9	2.036	1.351	2.060	15.043	0.02871
1	2.044	1.353	2.068	15.111	0.02892
1.2	2.083	1.369	2.123	15.081	0.03035
1.3	2.106	1.381	2.164	14.785	0.03161
1.414	2.119	1.388	2.188	14.055	0.03362

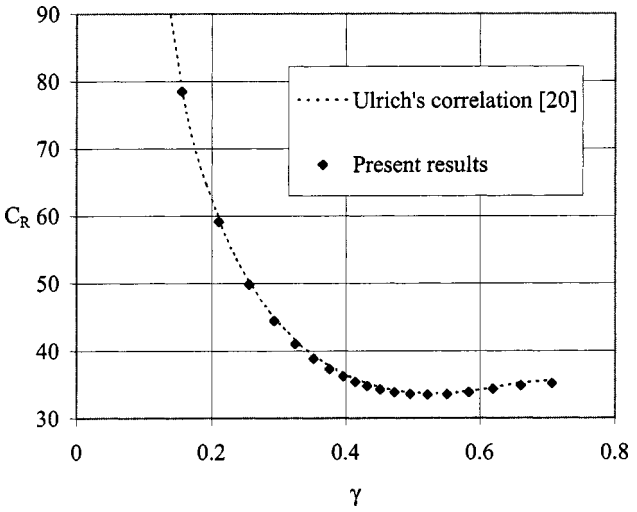

Fig. 2 Comparison between the present numerical results and Ulrich's correlation [20] for the geometry coefficient C_R of a ⟨100⟩ silicon trapezoidal microchannel

Results

In Tables 2 and 3, the numerical values obtained for the main flow parameters in the case of a trapezoidal and a double trapezoidal KOH-etched microchannel respectively are quoted as a function of the aspect ratio of the channel. Two different definitions of the aspect ratio are used in literature for trapezoidal channels ($\gamma = h/a$ or $\beta = h/b$ with reference to the symbols quoted in Fig. 1). In Table 2, both β and γ are quoted in order to simplify the use of the data. For a ⟨100⟩ silicon microchannels the aspect ratio γ

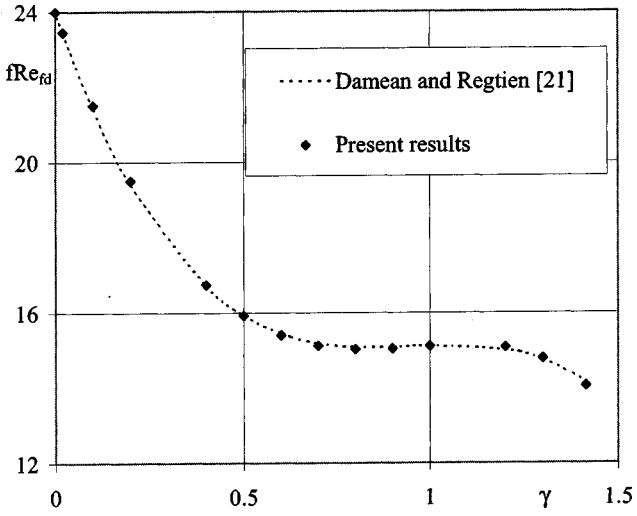

Fig. 3 Comparison with the correlation of Damean and Regtien [21] for a double-trapezoidal silicon microchannel having $\phi = 54.74$ deg

Table 4 Polynomial coefficients appearing in Eq. (13) for trapezoidal and double-trapezoidal ⟨100⟩ silicon microchannels

	Trapezoidal ⟨100⟩ silicon microchannel $0<\gamma<0.707$						
	g_0	g_1	g_2	g_3	g_4	g_5	Δ (%)
$f\,\mathrm{Re}_{fd}$	24	−42.267	64.272	−118.42	242.12	−178.79	−0.14
K_d	1.2	0.3962	0.9808	−1.4388	−2.5004	3.3655	−0.27
K_e	1.543	1.1296	3.7251	−2.6799	−14.585	15.496	−0.68
L^*_{hy}	0.0059	0.0165	0.1019	0.7176	−2.3256	1.6935	−3.9
	Double-trapezoidal ⟨100⟩ silicon microchannel $0<\gamma<1.414$						
	g_0	g_1	g_2	g_3	g_4	g_5	Δ (%)
$f\,\mathrm{Re}_{fd}$	24	−27.471	26.117	−6.6351	−0.2956	−0.5974	0.05
K_d	1.2	0.2833	0.5441	−1.7965	1.5499	−0.4277	−0.1
K_e	1.543	0.8343	2.3859	−6.9184	5.8104	−1.5876	−0.25
L^*_{hy}	0.059	0.0055	0.212	−0.4277	0.3091	−0.0762	3.5

cannot exceed the value of $tg(\phi)/2$ (equal to 0.707 for $\phi = 54.74$ deg) corresponding to the degeneration of the channel cross-section to the triangular geometry ($\beta=\infty$).

The aspect ratio γ of a double-trapezoidal channel is defined as the ratio between the height (h) and the maximum width (a); γ can assume all the values between 0, the parallel plates configuration, and 1.414, the rhombic configuration.

Richter et al. [20] gave a simple correlation, proposed by Ulrich, in order to calculate the value of the C_R (where $C_R = (f\,\mathrm{Re})_{fd}\Gamma^2/(8\Omega)$) for KOH-etched trapezoidal microchannel:

In Fig. 2, the results obtained in the present analysis are compared with the prediction of Ulrich's correlation. It is possible to underline the very good agreement of the present data with Ulrich's correlation; the maximum deviation of the present numerical data from Ulrich's correlation is equal to 1.5%.

More recently, Damean and Regtien [21] presented a correlation in order to calculate the fully developed Poiseuille number as a function of the aspect ratio for laminar flow through double-trapezoidal ducts etched in ⟨100⟩ silicon. In Fig. 3, the data quoted in Table 3 are compared with the prediction of the $(f\,\mathrm{Re})_{fd}$ obtained by using the Damean and Regtien correlation; the agreement with the polynomial approximation of Damean and Regtien [21] is good (maximum deviation equal to 0.83%).

No data are available in the open literature for $V_{\max}$, K_d, K_e and L_{hy} for the trapezoidal and double trapezoidal KOH-etched microchannels.

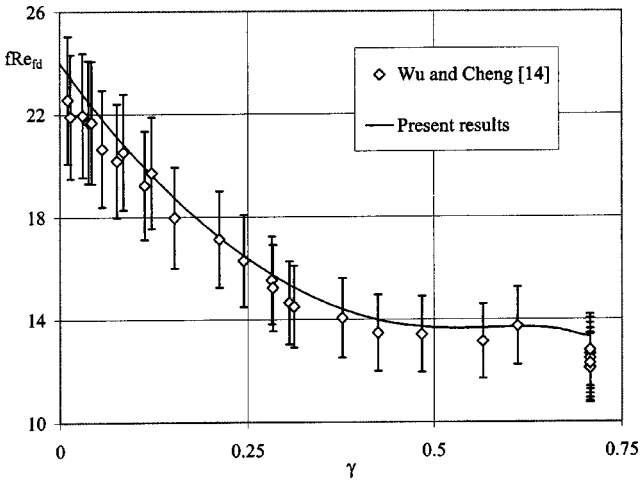

Fig. 4 Comparison between the present numerical results for ⟨100⟩ silicon microchannels and the experimental data of Wu and Cheng [14]

A fifth order polynomial approximation for calculating $(f\,\mathrm{Re})_{fd}, K_d, K_e, L_{hy}$ as a function of the channel aspect ratio (γ) is given with the aim of offering a very simple but accurate tool for technicians and designers involved in microfluidic applications:

$$f\,\mathrm{Re}_{fd} \;or\; K_d \;or\; K_e \;or\; L^*_{hy} = \sum_{n=0}^{5} g_i \gamma^n \qquad (13)$$

The values of the constants g_i are listed in Table 4 for microchannels having a trapezoidal and double-trapezoidal cross section; the maximum relative difference Δ quoted in Table 4 is positive when Eq. (13) gives values greater than the rigorous calculation.

In Fig. 4, the fully developed Poiseuille number quoted in Table 2 for trapezoidal microchannels is compared with those obtained by Wu and Cheng [14] testing 28 ⟨100⟩ silicon trapezoidal microchannels having different hydraulic diameters ($25.9<D_h<291$ μm) and aspect ratios ($0.01<\gamma<0.707$). In Fig. 4, the experimental average values of $f\,\mathrm{Re}_{fd}$ for each microchannel are quoted. By using the standard error analysis, the authors predicted the maximum uncertainty in determining the Poiseuille number equal to 11%. It can be highlighted that the agreement between the experimental data and the present results obtained the conventional theory is very good. This fact indirectly confirms that the Navier-Stokes equations are still valid for the liquid laminar flow in smooth silicon microchannels having a hydraulic diameter as small as 25.9 μm.

Conclusions

If one excludes the rectangular geometry, for the typical cross-sections of the KOH-etched silicon microchannels, a complete series of data for fully developed laminar flow is not available in literature. In this paper the main integral flow parameter, like the Poiseuille number ($f\,\mathrm{Re}$), the momentum flux correction factor (K_d), the kinetic energy correction factor (K_e), the asymptotic incremental pressure drop number (K_{inf}) and the approximate value of the hydrodynamic entrance length (L_{hy}) are numerically evaluated by means of a numerical code written with FLEXPDE™ for ⟨100⟩ trapezoidal and double trapezoidal microchannels. The comparison of the present results with the recent experimental data on the friction factors of pressure driven laminar liquid flow through ⟨100⟩ silicon microchannels [14] confirmed that the Navier-Stokes equations have to be considered valid for microchannels having a hydraulic diameter greater than 30 μm.

Acknowledgments

This work was financially supported by grants from the MIUR-URST (Ministero dell'Istruzione, dell'Università e della Ricerca).

Nomenclature

a = maximum width of the cross-section [m]
b = minimum width of the cross-section [m]
C_R = geometry coefficient
D_h = hydraulic diameter ($=4\Omega/\Gamma$) [m]
f = Fanning friction factor
h = height of the cross-section [m]
K_d = momentum flux correction factor
K_e = kinetic energy correction factor
K_{inf} = incremental pressure drop number
Kn = Knudsen number ($=\lambda/D_h$)
L_{hy} = hydrodynamic entry length [m]
p = pressure [Pa]
Re = Reynolds number ($=\rho W D_h/\mu$)
$u(.)$ = fluid axial velocity [m/s]
$V(.)$ = dimensionless axial fluid velocity
W = average velocity [m/s]
x, y = dimensionless rectangular coordinates

Greek symbols

β = aspect ratio ($=h/b$)
γ = aspect ratio ($=h/a$)
Γ = cross section perimeter [m]
μ = dynamic viscosity [kg/ms]
Ω = cross section area [m^2]
ρ = density [kg/m^3]
ξ, η, ζ = Cartesian coordinates [m]

Subscripts

fd = fully developed
app = apparent

References

[1] Pfund, D. A., Shekarriz, A., Popescu, A., and Welty, J. R., 1998, "Pressure Drops Measurements in Microchannels," MEMS, ASME-DSC, 66, pp. 193–198.
[2] Qu, W., Mala, M., and Li, D., 2000, "Pressure-driven Water Flows in Trapezoidal Silicon Microchannels," Int. J. Heat Mass Transfer **43**, pp. 353–364.
[3] Celata, G. P., Cumo, M., Guglielmi, M., and Zummo, G., 2000, "Experimental Investigation of Hydraulic and Single Phase Heat Transfer in 0.130 mm Capillary Tube," Proc. International Conference On Heat Transfer and Transport Phenomena in Microscale, G. P. Celata et al. eds., Begell House, New York, pp. 108–113.
[4] Jiang, P. X., Fan, M. H., Si, G. S., and Ren, Z. P., 2001, "Thermal-Hydraulic Performance of Small Scale Micro-channel and Porous-Media Heat-Exchangers," Int. J. Heat Mass Transfer **44**, pp. 1039–1051.
[5] Kandlikar, S. G., Joshi, S., and Tian, S., 2001, "Effect of Channel Roughness on Heat Transfer and Fluid Flow Characteristics at Low Reynolds Numbers in Small Diameter Tubes," Proc. of 35th National Heat Transfer Conference, paper 12134, June 10–12, Anaheim CA.
[6] Pfalher, J., Harley, J., Bau, H. H., and Zemel, J. N., 1990, "Liquid Transport in Micron and Submicron Channels," Sens. Actuators, A, **21–23**, pp. 431–434.
[7] Toh, K. C., Chen, X. Y., and Chai, J. C., 2002, "Numerical Computation of Fluid flow and Heat Transfer in Microchannels," Int. J. Heat Mass Transfer **45**, pp. 5133–5141.
[8] Yang, C., Li, D., and Masliyah, J. H., 1998, "Modeling Forced Liquid Convection in Rectangular Microchannels with Electrokinetic Effects," Int. J. Heat Mass Transfer **41**, pp. 4229–4249.
[9] Ren, L., Qu, W., and Li, D., 2001, "Interfacial Electrokinetic Effects on Liquid Flow in Microchannels," Int. J. Heat Mass Transfer **44**, pp. 3125–3134.
[10] Palm, B., 2001, "Heat Transfer in Microchannels," Microscale Thermophys. Eng., **5**(3), pp. 155–175.
[11] Obot, N. T., 2000, "Toward a Better Understanding of Friction and Heat/Mass Transfer in Microchannels—A Literature Review," Proc. International Conference On Heat Transfer and Transport Phenomena in Microscale, G. P. Celata et al., eds., Begell House, New York, 1, pp. 72–79.
[12] Xu, B., Ooi, K. T., Wong, N. T., and Choi, W. K., 2000, "Experimental Investigation of Flow Friction for Liquid Flow in Microchannels," Int. Commun. Heat Mass Transfer, **27**, pp. 1165–1176.
[13] Judy, J., Maynes, D., and Webb, B. W., 2002, "Characterization of Frictional Pressure Drop for Liquid Flows Through Microchannels," Int. J. Heat Mass Transfer **45**, pp. 3477–3489.
[14] Wu, H. Y., and Cheng, P., 2003, "Friction Factors in Smooth Trapezoidal Silicon Microchannels with Different Aspect Ratios," Int. J. Heat Mass Transfer **46**, pp. 2519–2525.
[15] Ma, H. B., and Peterson, G. P., 1997, "Laminar Friction Factor in Microscale Ducts of Irregular Cross-Section," Microscale Thermophys. Eng., **1**, pp. 253–265.
[16] Lundgren, T. S., Sparrow, E. M., and Starr, J. B., 1964, "Pressure Drop Due to the Entrance Region in Ducts of Arbitrary Cross Section," J. Basic Eng., **86**, pp. 620–626.
[17] Mc Comas, S. T., 1967, "Hydrodynamic Entrance Lengths for Ducts of Arbitrary Cross Section," J. Basic Eng., **89**, pp. 847–850.
[18] FLEXPDE™, Finite element Software, PDE Solution Inc., 1999.
[19] Shah, R. K., and London, A., 1978, "Laminar Flow Forced Convection in Ducts," Adv. Heat Transfer, **14**, pp. 196–220.
[20] Richter, M., Woias, P., and Weißb, D., 1997, "Microchannels for Applications in Liquid Dosing and Flow-Rate Measurements," Sens. Actuators, A, **62**, pp. 480–483.
[21] Damean, N., and Regtien, P. P. L., 2001, "Poiseuille Number for the Fully Developed Laminar Flow Through Hexagonal Ducts Etched in ⟨100⟩ Silicon, Sensors and Actuators A," Sens. Actuators, A, **90**, pp. 96–101.

Hydrodynamic Model for Microscale Flows in a Channel With Two 90 deg Bends[§]

Reni Raju and Subrata Roy
Computational Plasma Dynamics Laboratory, Department of Mechanical Engineering, Kettering University
Flint, MI 48504, USA
e-mail: sroy@kettering.edu

[DOI: 10.1115/1.1760547]

Introduction

Over the past decade *micro-machining* technology has shown rapid development enabling manufacture of complex microelectromechanical systems (MEMS). Microscale pumps, turbines, thrusters, sensors and actuators are a few examples of these small-scale devices. The reduction in scale increases the complexity of these systems. Physical laws governing these devices vary greatly from macro scale systems, especially from the fluidics perspective.

As the mean free path of the gas becomes comparable to the length scale of the system, the fluid behavior tends to become rarefied (molecular) and the gas layer adjacent to walls move. The no-slip continuum model no longer can predict the flow without accommodating other factors like rarefaction, compressibility, viscous dissipation and thermal creep effects [1] at these scales for gaseous flows. The Knudsen number (Kn) is a measure of the degree of rarefaction of gases encountered in small flows through narrow channels. It is defined as the ratio of the fluid mean free path, λ and the length scale of the physical system, Λ as Kn $=\lambda/\Lambda$. As Kn$\rightarrow$0 the flow can be assumed sufficiently continuous while for Kn$>$10 it becomes a free-molecule flow [2]. However for $0.001<\text{Kn}<10$ the flow is neither sufficiently continuum nor completely molecular, hence has been further divided into two subcategories; slip-flow regime for $0.001<\text{Kn}<0.1$ and transition regime for $0.1<\text{Kn}<10$.

Researchers have applied various numerical techniques for validating the computational models with the experimental data in slip and transition regimes of low speed flows. Liu et al. [3,4] have conducted both experiments and modeling of pressure distribution in microchannels. Chen et al. [5] have studied the experimental results of Pong et al. [6] and Arkilic et al. [7] using the finite difference method with first-order slip boundary conditions.

[§]Also published in the Proceedings of FEDSM'03, 4th ASME/JSME Joint Fluids Engineering Conference, Paper no. FEDSM2003-45535

Contributed by the Fluids Engineering Division for publication in the JOURNAL OF FLUIDS ENGINEERING. Manuscript received by the Fluids Engineering Division April 10, 2003; revised manuscript received November 24, 2003; Associate Editor: J. Celik

Karniadakis and Beskok [8] have carried out both analytical and numerical study of flow in several micro geometries using direct simulation Monte Carlo (DSMC) and spectral element method. Available DSMC, molecular dynamics and Burnett equation methods and their limitations are listed elsewhere [9].

This paper aims to apply a computationally efficient hydrodynamic algorithm developed at the Computational Plasma Dynamics Laboratory by Roy et al. [9] for complex micro-geometries. While the study in [9] benchmarked microchannel solution with reported numerical results [5] and experimental data [6], present study focuses on flow through a wide micro-column with two sharp 90 deg bends, which is a geometric modification of the straight microchannel studied by Poiseuille flow [5,6]. The subject geometry has applications in many practical microfluidic devices that require serpentine channels to allow longer contact length within a compact area. Following sections cover the model description, governing hydrodynamic equations and discussion of numerical results. The solution obtained for the bends are also compared to the reported numerical results for the straight microchannel [9]. To the best of our knowledge, no other published report has addressed microflow in this particular geometry.

Model Description

The two-dimensional micro-column geometry under consideration is shown in Fig. 1. The overall dimensions of the microchannel with two 90 deg bends are based on the first generation straight microchannel system [6] numerical flow prediction through which was documented earlier [9]. The present focus is isolated on the serpentine channel (Fig. 1) for which the centerline length L, height H and width W remain the same as in Ref. [6]. The working fluid is Nitrogen and its properties along with other flow parameters are listed in Table 1. Since the $H/W \ll 1$, the three-dimensional effects in this case is assumed non-dominant and only two-dimensional modeling is pursued. For two-dimensional analysis the end effects across the width W (normal to the xy-plane) have been ignored. The aspect ratio of the channel is 2500 with a centerline length of 3000 μm and the Knudsen number at the outlet is 0.0585 for the given conditions.

The compressible two-dimensional Navier-Stokes equations with constant viscosity and Stoke's hypothesis are used to model the system. For the no-slip wall condition in continuum description, all components of the velocity vanish at the solid wall. As the system length scale becomes comparable to the mean free path of the working fluid, the streaming velocity at the wall becomes important. The boundary condition in this case can be interpreted as the flux or Neumann condition from the macroscopic point of view. We shall implement first order slip boundary conditions [10,11] in the momentum and energy equations. Using the

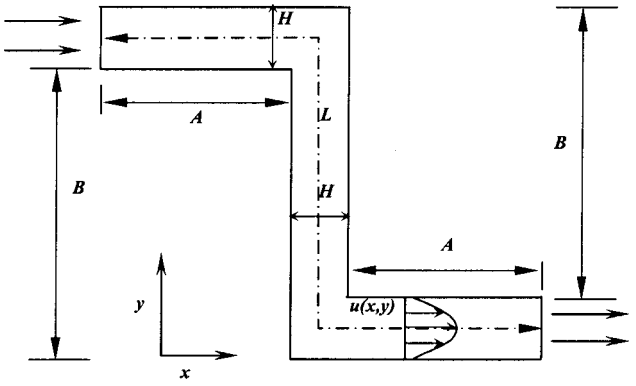

Fig. 1 Two dimensional geometry schematic used for microflow analysis

Table 1 Model dimensions and gas properties

Parameters	Value
Centerline length, L	3000 μm
Length, A	999.4 μm
Length, B	1000 μm
Width, W	40 μm
Height, H	1.2 μm
Pressure Ratio, P_{in}/P_{out}	1.34, 1.68, 2.02, 2.36, 2.70
Outlet Pressure, O_{out}	100.8 kPa
Temperature at the Inlet, T_i	314 K
Wall Temperature, T_w	314 K
Exit Knudsen Number, **Kn**	0.0585
Dynamic viscosity, μ	1.85×10^{-5} Ns/m^2
Specific gas constant, R	296.8 J/kg K
Ratio of specific heats, γ	1.4

Chapman-Enskog relation for hard spherical molecules of ideal gas at temperature T, the wall-slip boundary condition and temperature jump relations are given as,

$$u_{gas}-u_{wall}=\frac{16\mu}{5\rho\sqrt{2\pi RT}}\frac{2-\sigma_V}{\sigma_V}\left(\frac{\partial u}{\partial y}\right)_{wall}+\frac{3}{4}\frac{\mu}{\rho T_{gas}}\left(\frac{\partial T}{\partial x}\right)_{wall} \quad (1a)$$

$$T_{gas}-T_{wall}=\frac{2-\sigma_T}{\sigma_T}\left[\frac{2\gamma}{\gamma+1}\right]\frac{16k}{5\rho\sqrt{2\pi RT}}\left(\frac{\partial T}{\partial y}\right)_{wall} \quad (1b)$$

Above, $0\leqslant\sigma_v\leqslant1$ is the tangential-momentum accommodation coefficient and $0\leqslant\sigma_T\leqslant1$ is the thermal accommodation coefficient. These depend on the different parameters like the surface finish, the fluid, temperature and local pressure. Karniadakis and Beskok [8] have presented a second-order accurate slip boundary condition for predicting higher Knudsen number ($Kn>0.1$) flows. Studies by Sreekanth [12] suggest Maxwell's first-order boundary condition breaks down near $Kn=0.15$. However contrary to the common practice, Roy et al. [9] have successfully applied the first-order boundary condition for higher Knudsen number (up to 7.36). The present problem has an outlet Knudsen number of 0.0585.

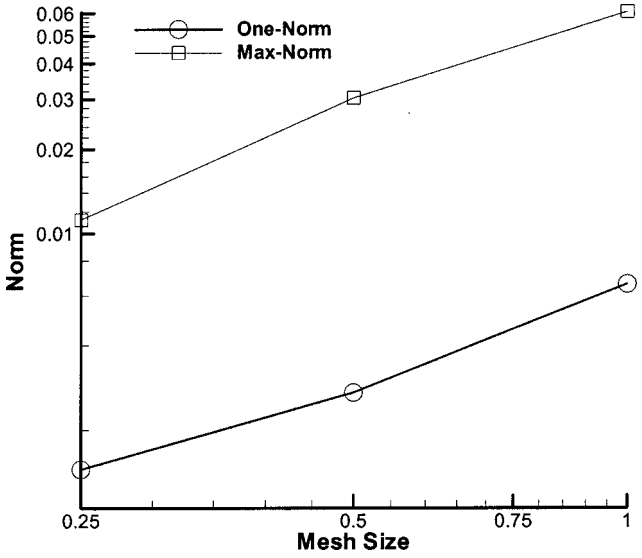

Fig. 2 Richardson extrapolation plotted on a log-log scale documents the mesh convergence in L_1 (one-) and L_∞ (max-) norm

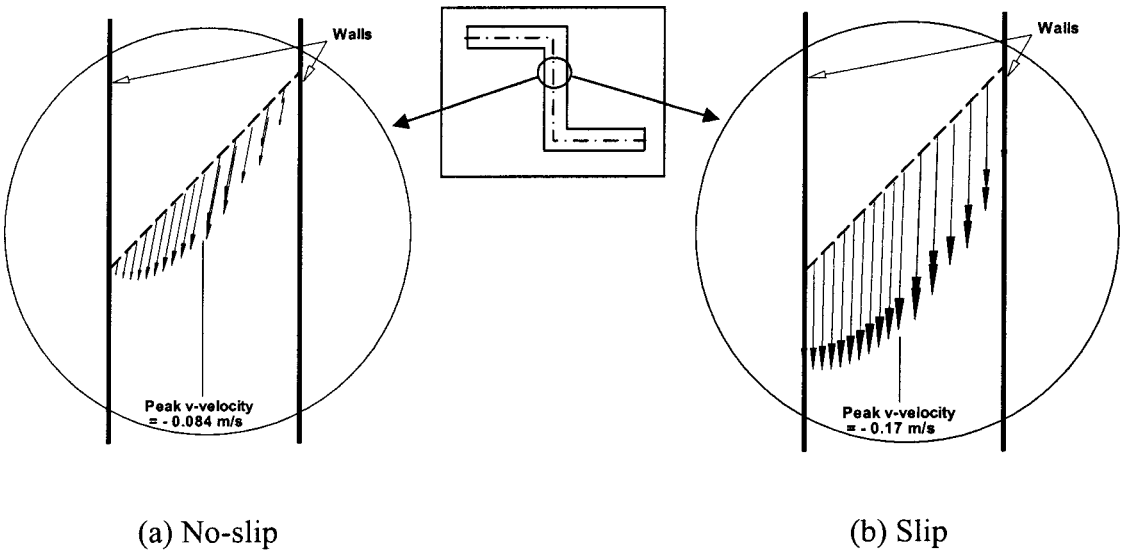

Fig. 3 Velocity vectors in the micro-column for $P_{in}/P_{out}=2.701$. The peak *v*-velocities are shown at the centerline distance of 1200 μm from the inlet in the vertical section.

Results and Discussions

Nitrogen gas flow through the channel has been analyzed for both slip and no-slip boundary conditions. The hydrodynamic model is based on the finite element algorithm developed in Ref. [9]. The computational domain is discretized using 560 (28 along L, 20 along H in Fig. 1) two-dimensional biquadratic finite elements that consist of 2337 nodes. Except for solving the continuity (pressure) and the equation of state (density) where four corner nodes are used, all variables are integrated on all nine nodes of the biquadratic element. The solution is declared convergent when the maximum residual for each of the state variables becomes smaller than a chosen convergence criterion of $\epsilon=10^{-4}$. The gas temperature T_i at the inlet and a uniform wall temperature T_w are specified as 314 K. The velocity flux $\partial u/\partial x=0$ and the y-component of the velocity $v=0$ is specified at the inlet. For no-slip conditions $u=0$ and $v=0$ is used on the walls, while Eqs. (1*a*-1*b*) are used for the slip boundary conditions. For slip boundary since the roughness of the channel is not known, we assume $\sigma_V=\sigma_T \approx 1.0$, implying that the channel surface is rough [5,9]. The pressure at the outlet, P_0 is maintained at 100.8 kPa while the inlet pressure, P_i is specified based on the pressure ratio.

Richardson's extrapolation has been utilized to determine the mesh independence of the solution on this mesh. Using a second order accurate interpolation, Fig. 2 plots the solution L_1 (one-) and L_∞ (max-) norms. For a 90 deg bend the flow undergoes skewing due to the change in streamwise direction in comparison to the flow through a straight duct. In Fig. 3(*a*), the no-slip condition the flow shows a skewed parabolic profile with a zero velocity on the walls, while for the slip boundary condition there is an increase in the curvature showing relatively higher velocities at the walls and the center, Fig. 3(*b*).

For five selected pressure ratios, comparison of the numerical centerline slip results of the straight and 90 deg bend in Fig. 4 shows a marked difference in the pressure distribution. This is due to the higher shear stress caused by the sharp change in momentum at the bends. The difference becomes larger as the pressure ratio increases. The distribution for the bend shows a maximum difference of $\sim+4\%$ at the upstream bend and $\sim-20\%$ along the downstream bend. Fig. 5 shows increasing divergence for increasing pressure ratios between the no-slip and the slip wall solutions with a maximum difference of $\sim-6\%$ at the first bend and $\sim+10\%$ at the downstream bend.

For the micro-column the *u*-velocity rises till the first transition point and then encounters a sudden drop (to nearly zero) due to change in direction of the flow, Fig. 6. The *u*-velocity again picks up at the second transition point (bend). The increase in velocity is proportional to the pressure ratio for a fixed outlet pressure. For the peak outlet velocity, the maximum Reynolds number is 0.04. The slip condition indicates that lesser frictional force has to be overcome on the walls generating a higher velocity as compared to the no-slip condition. Thus the slip flow shows nearly 55% more velocity at the peak point than the no-slip condition for $P_{in}/P_{out}=2.701$. The negative values of *u*-velocity indicate small recirculation downstream of both bends as flow turns sharply. Similar effect is observed in Fig. 7 for *v*-velocity at transition points where positive values point toward existence of small local vortices.

Fig. 8 compares the mass flow rate against the pressure ratios for slip and no-slip conditions. Up to 2.4 times more mass flow rate is observed for slip flows than for the no-slip flows due to lower shear stress on the walls resulting in less momentum exchange. As compared to the straight microchannel the gas flow

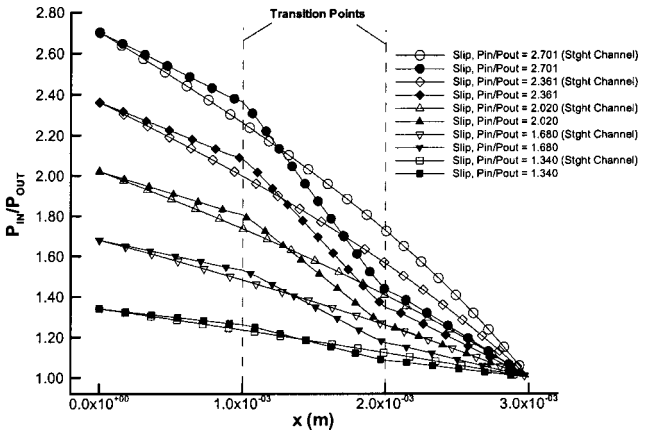

Fig. 4 Pressure distribution comparison of numerical results for the micro-column with 90 deg bend and a straight microchannel [6,9] with slip flow along the centerline

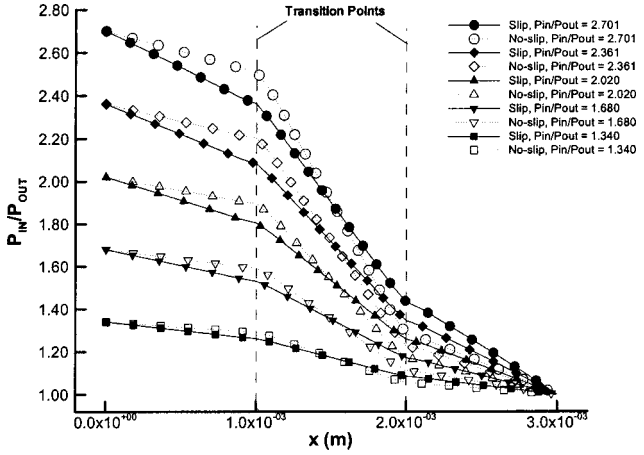

Fig. 5 Pressure distribution comparison of slip and no-slip boundary condition along the centerline of the micro-column with 90 deg bend

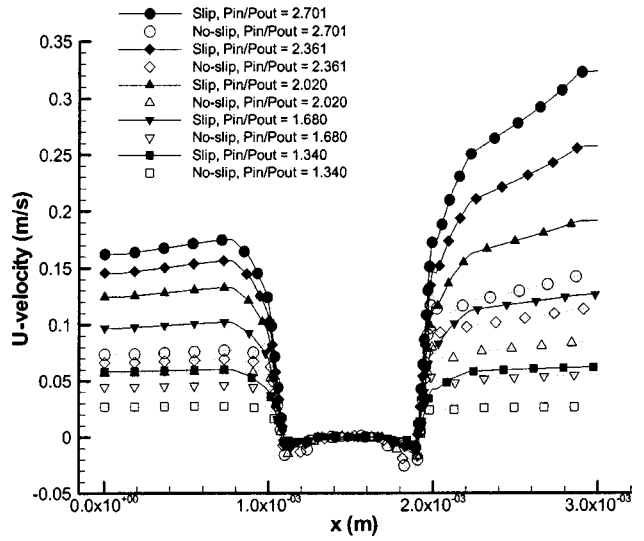

Fig. 6 *U* velocity distribution comparison of slip and no-slip boundary condition along the centerline of the micro-column with 90 deg bends

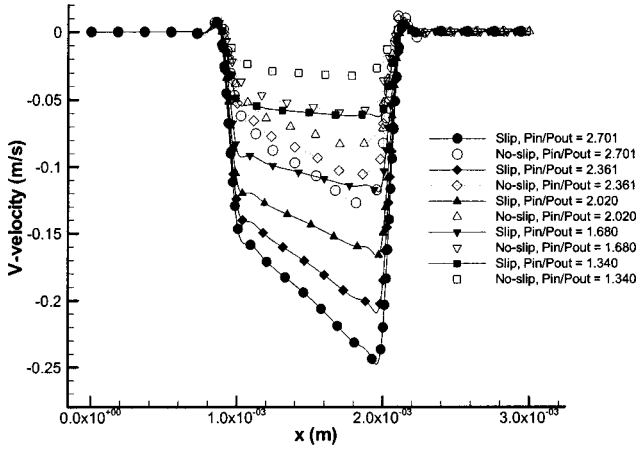

Fig. 7 *V*-velocity distribution comparison of slip and no-slip boundary condition along the centerline of the micro-column with 90 deg bends

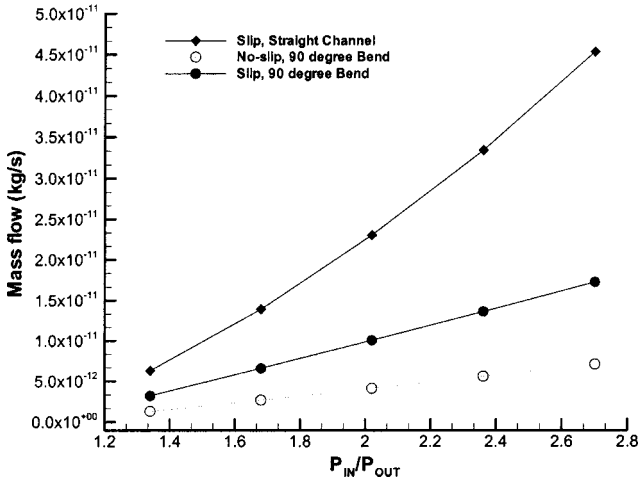

Fig. 8 Numerical mass flow comparison for the five pressure ratios for slip and no-slip flow for the micro-column with 90 deg bends and corresponding mass flow for a straight microchannel

inside the micro-column with two 90 deg bends has to overcome relatively higher shear stress reducing the overall mass flow rate by approximately 0.4 times.

Conclusion

A finite element based hydrodynamic model has been applied to simulate low speed Nitrogen gas flow through a micro-column with two 90 deg bends for an outlet Knudsen number of 0.0585 and a maximum Reynolds number of 0.04. The gaseous flow has been modeled using both no-slip and first-order slip boundary conditions. The twisted geometry of the present study reduces the mass flow rate by ~160% than that for a straight microchannel with the same overall dimensions. Velocity solutions predict small re-circulations at bends indicating three-dimensional nature of the flow that should be addressed in the future.

References

[1] Beskok, A., Karniadakis, G. E., and Trimmer, W., 1996, ''Rarefaction and Compressibility effects in Gas micro flows,'' J. Fluids Eng., **118**, pp. 448–456.

[2] Gad-el-hak, M., 1999, ''The Fluid mechanics of Microdevices—The Freeman scholar lecture,'' J. Fluids Eng., **121**, pp. 5–33.

[3] Liu, J., Tai, Y. C., Pong, K., and Ho, C. M., 1993, ''Micromachined channel/pressure sensor systems for micro flow studies,'' *The 7th International Conference on Solid-state Sensors and Actuators, Transducers'93*, pp. 995–998.

[4] Liu, J., Tai, Y. C., and Ho, C. M., 1995, ''MEMS for pressure distribution studies of Gaseous flows in microchannels,'' *Proceedings, IEEE Micro Electro Mechanical Systems Workshop, Amsterdam*, pp. 209–215.

[5] Chen, C. S., Lee, S. M., and Sheu, J. D., 1998, ''Numerical analysis of gas flow in microchannels,'' Numer. Heat Transfer, Part A, **33**, pp. 749–762.

[6] Pong, K. C., Ho, C., Liu, J., and Tai, Y. C., 1994, ''Non-linear pressure distribution in uniform microchannels,'' *Application of Microfabrication to Fluid Mechanics*, FED—**197**, pp. 51–6.

[7] Arkilic, E. B., Schmidt, M. A., and Breuer, K. B., 1997, ''Gaseous slip flow in long microchannels,'' J. Microelectromech. Syst., **6**(2), pp. 167–178.

[8] Karniadakis, G. E., and Beskok, A., 2002, *Micro Flows-Fundamentals and Simulation*, Springer-Verlag, New York.

[9] Roy, S., Raju, R., Chuang, H., Kruden, B., and Meyyappan, M., 2003, ''Modeling gas flow through microchannels and nanopores,'' J. Appl. Phys., **93**(8), pp. 4870–4879.

[10] Maxwell, J. C., 1879, ''On stresses in rarefied gases arising from inequalities of temperature,'' Philosophical Transactions of the Royal Society Part 1, **170**, pp. 231–256.

[11] von Smoluchowski, M., 1898, ''Ueber wärmeleitung in verdünnten gasen,'' Annalen der Physik und Chemi, **64**, pp. 101–30.

[12] Sreekanth, A. K., 1969, ''Slip Flow through Long Circular Tubes,'' *Rarefied Gas Dynamics, eds. Trilling, L. and Wachman, H. Y., Academic Press, New York*, **1**, pp. 667–680.

Hydrodynamics of the Water and Gas Jet That Initiated the Lake Nyos Catastrophe

Rudolf X. Meyer
University of California, Los Angeles

[DOI: 10.1115/1.1760543]

On August 21, 1986, a large quantity of water and gas, mainly CO_2, was released from Lake Nyos in Cameroon, leading to the deaths by asphyxiation of more than 1700 people, Freeth and Kay [1]. Based in part on eyewitness reports made to an international team of volcanologists and biologists that visited the site, the event was initiated by a very large column of water and gas that suddenly erupted from a point in the lake. The gas desorbed from the water filled the lake basin to a great height and then flowed into the populated valleys below. The earliest reports by the volcanologists are collected in [2]. More recent papers by Evans et al. [3,4] and Simkin and Siebert [5] have described changes in the lake since the event and efforts towards early warning against a new outbreak and towards degassing the lake. The most recent data on current efforts by volcanologists and others are available on Web Sites [6]. The exact trigger mechanism is still controversial, but the majority of the volcanologists have assumed that the event most likely started on the magma surface [2]. In the analysis below, the start of the column on the magma surface is represented as a simple singularity, acting as a sink for the surrounding lake water. Entrainment of lake water by the upper portions of the column is neglected. The present Brief Note is restricted to an analysis of the water and gas column. It points out that the jet velocity at the lake surface must have been the sonic velocity for the water/gas mixture. This simple result agrees closely with the conclusion drawn by the international team from eyewitness accounts of the observed height of the resulting geyser.

Water/Carbon Dioxide Equilibrium as a Function of Pressure

As a preliminary, the solution equilibrium is considered of the heterogeneous mixture of water and carbon dioxide, the latter partly absorbed and partly in the gas phase as bubbles. For the present purposes it is convenient to use the mass ratio m_{ga}/m_{lq} as a function of pressure (and of temperature, but insignificant in the present case) hence of depth in the lake, where m_{ga} and m_{lq} are the mass of the *absorbed* gas and of the saturated liquid, respectively, in a unit volume. This mass ratio is nearly proportional to the pressure, a fact known as Henry's law. Although this law becomes inaccurate at very high pressure, it is in error by only about 8% [7], even at the high lake pressure at the lake bottom (the magma surface). The proportionality factor will be designated by μ. For CO_2 absorbed in water, at the lake temperature of about 23°C at the time of the event, $\mu = 13.7\ 10^{-9}\ (\mathrm{Pa})^{-1}$.

Density of the Water/Carbon Dioxide Mixture

The properties of the liquid when saturated with the gas, *without* gas bubbles, will be designated by the subscript $(\ )_0$. Because it is assumed that at the lake bottom the gas is fully absorbed, the same subscript will also be applied to the pressure p_0, temperature T_0, density ρ_0, and speed of sound c_0 at the lake bottom. As the mixture moves upwards into lower pressure, some of the absorbed gas will desorb in the form of bubbles. Quantities referring to the desorbed gas will be designated by $(\ )_{gd}$; quantities without subscript will refer to the mixture. Taking a constant mass m_{lq} (the mass difference of pure liquid and of saturated liquid can be neglected), one obtains $\rho = m_{lq}(m_{lq}/\rho_{lq} + m_{gd}/\rho_{gd})^{-1}$. From the mass conservation of the gas, $m_{ga} + m_{gd} = m_{ga0}$. Because from Henry's law $m_{ga0} = \mu p_0 m_{lq}$ and $m_{ga} = \mu p m_{lq}$ it follows that $m_{gd} = m_{lq}\mu(p_0 - p)$. If the gas bubbles expand with decreasing pressure in the lake *isothermally* at the (constant) lake temperature, as would be the case with small bubbles with rapid heat transfer, then $\rho_{gd} = p/(R_g T_0)$ where $R_g = 188.9\ \mathrm{J\,kg^{-1}\,K^{-1}}$ is the gas constant for CO_2 and T_0 the lake temperature. Therefore

$$\rho/\rho_{lq} = (1 + \mu\rho_{lq} R_g T_0 (p_0/p - 1))^{-1} \quad \text{isothermal} \qquad (1a)$$

The pressure $p(z)$ in the column is closely approximated by the pressure of the lake water that surrounds the column, hence is the sum of the hydrostatic and of the atmospheric pressure p_{atm}, so that $p = g\rho_{lq}(h - z) + p_{\mathrm{atm}}$ where z is the vertical coordinate with $z = 0$ at the magma surface, and $h = 210$ m the depth of the lake from the magma surface. The calculation for the *isentropic* case, which is for large bubbles with negligible heat transfer from the water, is similar, except that now the depth in the lake at which a particular bubble originates by desorption needs to be taken into account. Let dm_{gd} the mass of desorbed gas generated at the depth interval with pressures p_1 and $p_1 - dp_1$. Then $dm_{gd} = m_{lq}\mu dp_1$. Moving from a depth with pressure p_1 to one with pressure $p < p_1$, the volume of dm_{gd} becomes $\rho_{gd,1}^{-1}(p_1/p)^{1/\gamma} dm_{gd}$, where $\gamma = 1.30$ is the ratio of the specific heats for CO_2. The density $\rho_{gd,1} = p_1/(R_g T_0)$ is the density of the gas bubbles where they originate. Hence the volume of dm_{gd} at

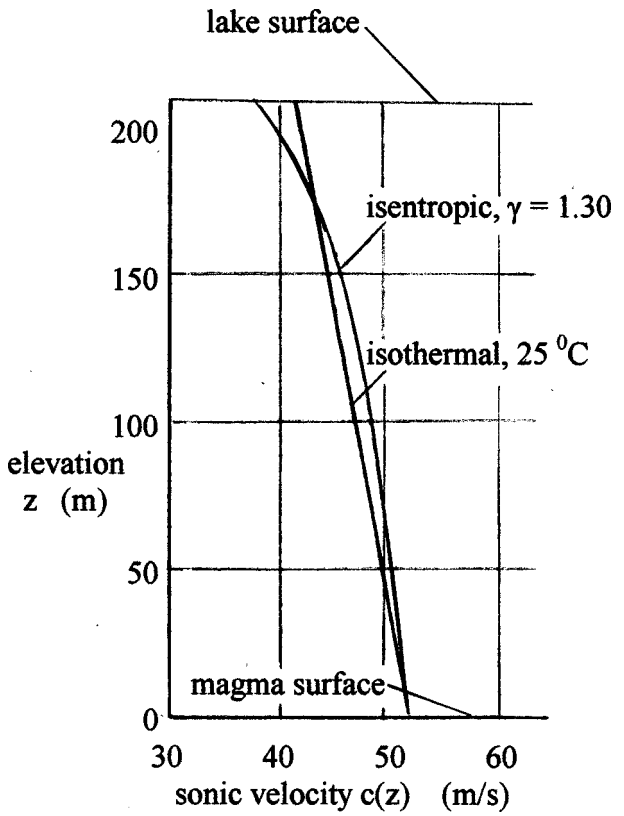

Fig. 1 Upwelling from the bottom of Lake Nyos. Sonic velocity of the liquid/gas mixture of the underwater column, as a function of the depth in the lake. From Eqs. (2*a*) and (2*b*).

Contributed by the Fluids Engineering Division for publication in the JOURNAL OF FLUIDS ENGINEERING. Manuscript received by the Fluids Engineering Division January 16, 2002; revised manuscript received November 13, 2003. Associate Editor: M. W. Plesnial.

$p = p_1 - dp$ becomes $(m_{lq}\mu R_g T_0/p_1)(p_1/p)^{1/\gamma} dp_1$. Since the origin of the rising column is at $z=0$ with $p=p_0$ and where at the start of the event, by assumption, the water is saturated, the density ρ of the mixture is now given by

$$\rho/\rho_{lq} = \{1 + \mu\rho_{lq}\gamma R_g T_0((p_0/p)^{1/\gamma} - 1)\}^{-1} \quad \text{isentropic} \tag{1b}$$

Speed of Sound of the Mixture and Height of the Jet: In the *isothermal* case, from differentiation of (1*a*), with the square of the speed of sound $c^2 = \delta p/\delta\rho$,

$$c^2 = \{1/\rho_{lq} + \mu(p_0/p - 1)R_g T_0\}^2\{\mu p_0 R_g T_0/p^2\}^{-1} \quad \text{isothermal} \tag{2a}$$

Similarly, by differentiation of (1*b*), in the *isentropic* case,

$$c^2 = \{1/\rho_{lq} + \mu\gamma R_g T_0((p_0/p)^{1/\gamma} - 1)\}^2\{(\mu R_g T_0/p) \times (p_0/p)^{1/\gamma}\}^{-1} \quad \text{isentropic} \tag{2b}$$

The Runge-Kutta method with a step size in p of $h = p_0/200$ was used in the calculations. The maximum error in the sonic velocity occurs at the lake surface in the isentropic case. It is approximately $(c(p) - c(p+2h))/(2^5 - 1) \sim 0.015$ m/s.

The numerical results for Lake Nyos, Fig. 1 show that the two sonic speeds differ relatively little from each other. At the lake bottom, where the liquid is assumed to contain as yet no gas bubbles, the two sound speeds are equal; at intermediate depths the isentropic sound speed is higher, but lower at low depth. As a result, the sonic speeds of the mixture at the lake surface are approximately equal, with $c = 40$ m/s. This low sonic velocity of course is caused by the combination of the large inertia of the water and the great compressibility of the desorbed gas in the mixture. The pressure ratio (determined by the hydrostatic plus atmospheric pressure difference between lake bottom and surface) was far greater than the critical pressure ratio that would be needed for supersonic flow. In the absence of a throat, the velocity at which the under-water column emerged at the lake surface must therefore have been just sonic, at a velocity of 40 m/s. The calculated height $H = 1/2\, c^2/g$ of the resulting geyser becomes 82 m. This is very close to the height of 80 m inferred from eyewitness reports [2] that were based on the line of sight from the location of the witnesses to the hills behind the lake, particularly to a 75 m high promontory.

Acknowledgment

The author would like to thank Mr. Justin F. Works for his work in computer programming.

References

[1] Freeth, S. J., and Kay, R. L. F., 1987, "The Lake Nyos Gas Disaster," Nature (London), **325**, pp. 104–105.

[2] Collection of papers on Lake Nyos in the Journal of Volcanology and Geothermal Research, 39, 1989.

[3] Evans, W. C. et al., 1993, "Gas Buildup in Lake Nyos, Cameroon: The Recharge Process and its Consequences," Appl. Geochem., **8**, pp. 207–221.

[4] Evans, W. C. et al., 1994, "Six Years of Change at Lake Nyos, Cameroon, Yield Clues to the Past and Cautions for the Future," Geochemistry, **28**, pp. 139–162.

[5] Kling, G. W. et al., 1994, "Degassing of Lake Nyos," Nature (London), **368**, pp. 405–406.

[6] http://volcano.und.nodak.edu/vwdocs/volc_images/africa/nyos.html, and http://www.biology.lsa.umich.edu/~gwk/research/nyos.html

[7] Landolt-Börnstein, 1962, Chpt. on Solution Equilibria, **II2b**, pp. 1–28, Springer Verlag, Heidelberg.

Pump Power Gain for Heated Porous Medium Channel Flows

Arunn Narasimhan
Department of Mechanical Engineering, Indian Institute of Technology Madras, Chennai, TN 600036, India

José L. Lage*
Laboratory for Porous Materials Applications, Mechanical Engineering Department, Southern Methodist University, Dallas, TX-75275-0337

[DOI: 10.1115/1.1760546]

Introduction

For sustaining a desired flow rate in a thermo-hydraulic engineering system (channels, ducts etc.), the required pressure-drop is achieved by means of a pump. Reduction in the power required by this pump, without adversely affecting the pressure-drop value, is obviously an important issue, which is given careful thought by the design engineer. Heating a channel for liquid flows reduces the viscosity and by consequence the resulting pressure-drop [1–2]. Obviously, one might then consider the benefit of heating the liquid as a means to reduce the viscosity and the pumping power, while maintaining the same pressure-drop [3].

However, as the reduction in the liquid viscosity diminishes for increased temperature (heating), so does the degree of reduction in pump power. Therefore, the study of the overall energy efficiency of the system (heat power spent versus pump power gained) is of fundamental importance.

Compared to clear (of porous medium) channel flows, the liquid pressure-drop across a porous medium (for the same flow rate) is always higher than the pressure-drop across a clear channel, immaterial of the hydraulic characteristics of the medium (vis-à-vis porosity, permeability and form coefficient). Therefore, the alternative of heating a liquid to reduce the pump power necessary to make it flow is even more relevant when the liquid flows through a porous medium.

Our interest in addressing this issue emerged from a practical application of foam metals in cooling electronics. Using porous medium in forced convection has become an accepted heat transfer enhancement option ([4–6]). Considering that heating (or cooling) always takes place in forced convection, it is then surprising to verify the dearth of work in this area, revealed by our own bibliographic searches and by consulting recent authoritative published reviews on the subject of convection through porous media ([5–8]).

The practical project from which this work emanates involves the design of a compressed porous medium enhanced cold plate for cooling airborne military phased-array radars (details are available in [9] and [10]). The F-22 aircraft, for which the radar is designed, has an environmental control unit providing a limited pressure-drop across the cold plate. This limit is well above what is usually achieved with a clear (with no enhancement) cold plate, but it gets surpassed quite rapidly when compressed metal foam is used as enhancement [9]. In this case, the question is then to the

*Corresponding author: Phone: (214)768-2361; Fax: (214)768-1473; e-mail: JLL@engr.smu.edu.

Contributed by the Fluids Engineering Division for publication in the JOURNAL OF FLUIDS ENGINEERING. Manuscript received by the Fluids Engineering Division February 6, 2003; revised manuscript received January 13, 2004. Associate Editor: Y. Tsujimoto and J. Katz.

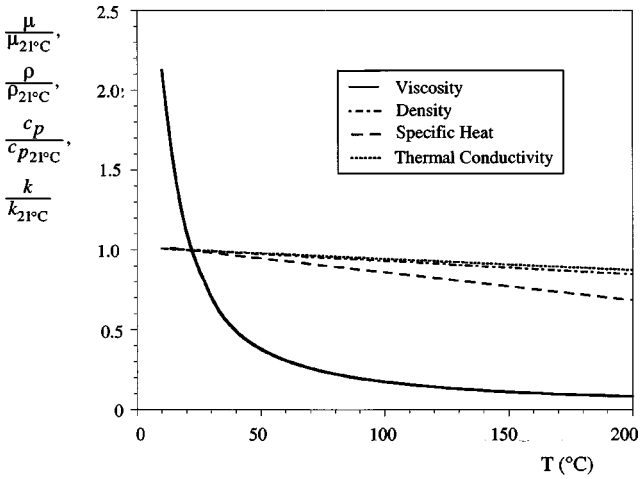

Fig. 1 Properties of PAO with temperature (from [16]) normalized by values at 21°C

impact of heating the liquid (already taking place) on the pump power necessary to make it flow through the cold plate.

Consistent to our original practical interest, we decided to use configuration (e.g., channel geometry) and liquid property values similar to the designed cold plate. Nevertheless, the fundamental ideas presented in this study (e.g., Eq. (5)) are independent of the configuration, or the specific liquid and porous medium characteristics considered here. They are also independent of the liquid flowing through a convective system, considering that heating (or cooling) can be added to the system.

System Configuration and Numerical Scheme

Numerical simulations are performed for a liquid with temperature-dependent viscosity flowing through an isoflux, parallel-plates porous medium configuration. Using the pressure-drop versus fluid speed data for three different inlet temperatures over a range of heat fluxes, the overall energy efficiency of the flow system is studied.

Transport equations and their respective boundary conditions, used to model the momentum and energy transport through a parallel-plate porous medium channel with uniformly heated surfaces, and all of the simulation details (including mesh geometry, grid independence tests, convergence criteria used, second-order accuracy of the numerical results and validation against published experimental and analytical results) remain identical to those reported in [11] and [12]. As found in those literatures, adopting a control volume formulation, the transport equations are discretized by a fully implicit scheme and solved through a line-by-line relaxation method (Thomas algorithm) for a channel geometry with aspect ratio $L/(2H)=10$. The porous matrix used for the simulations has characteristics of compressed aluminum foam, with $k_s=170$ W/m°C, $\phi=0.58$, $K=4.4\times10^{-10}$ m^2 and $C=1.2\times10^5$ m^{-1} (as reported in [13] and [14]). The results were primarily obtained for poly-alpha-olefin (PAO), the base-stock for motor oils and lubricants and the cold-plate coolant of preference in airborne military avionics. The strong temperature-dependent dynamic viscosity of PAO, based on the data gathered by [10], can be modeled as

$$\mu(T)=0.1628T^{-1.0868},\quad 5°\mathrm{C}\leqslant T\leqslant 170°\mathrm{C} \tag{1}$$

Equation (5), when the values of temperature T are given in °C, predicts the viscosity in Nsm^{-2} within 3 percent accuracy [10]. Variations of the dynamic viscosity and other thermo-physical properties of PAO with temperature are shown in Fig. 1, with their respective values at the normalizing temperature of 21°C being: $\mu_0=5.95\times10^{-3}$ kg/ms, $\rho=768.5$ kg/m^3, $c_p=1971.35$ J/kg°C, and $k_f=0.1424$ W/m°C. From the figure, it can be seen that, within the temperature range prescribed in Eq. (1), the variations of density, specific heat and thermal conductivity of PAO are negligible.

Pump Power: Overall Energy Gain

A good way to establish the energy efficiency of the heated pumping system is by using a figure of merit R, defined as

$$R=\frac{\dot{W}_{\mu_0}-\dot{W}_h}{\dot{Q}} \tag{2}$$

where $\dot{W}_{\mu_0}$ is the power necessary to pump the liquid without heating (i.e. isothermal flow, for any inlet temperature), and $\dot{W}_h$ is the power necessary to pump the liquid when heating it with a certain amount of heat power $\dot{Q}=q''A_W$.

The pump power, $\dot{W}$, necessary to flow a liquid at a certain volumetric flow rate, $\dot{V}=UA$ (where U is the average fluid speed across a surface area A_c), through a channel imposing a certain pressure-drop, ΔP, can be calculated as $\dot{W}=\Delta P(UA_c)$. A way for reducing the pump power is by heating the liquid as it flows through the channel. Hence, the liquid viscosity decreases, decreasing by consequence the pressure-drop. Pressure-drop and fluid speed results, for computing R, were obtained via numerical simulations.

The pressure-drop for an isothermal flow through a porous medium, used to find $\dot{W}_{\mu_0}$, can be predicted by the Hazen-Dupuit-Darcy (HDD) model (popularly known as the Darcy-Forchheimer model, [15])

$$\frac{\Delta P|_{\mu_0}}{L}=\left(\frac{\mu_0}{K_0}\right)U+(\rho C_0)U^2=D_{\mu_0}+D_{C_0} \tag{3}$$

where D_{μ_0} and D_{C_0} represent the global viscous and form drags, respectively.

However, the accuracy of this model in predicting the pressure-drop across porous medium channels under non-isothermal flow configuration with strong viscosity variation was proven to be poor by Narasimhan and Lage [11] and Narasimhan et al. [13].

It has been shown in [11] that the HDD model does not capture important thermo-hydraulic interactions occurring in the flow, due to the fluid viscosity varying locally with temperature (thus influencing the global viscous as well as the global form drag terms), when the channel is heated/cooled. This recent understanding led to the development of the Modified HDD (M-HDD) model, as proposed in [11], incorporating the temperature-dependent viscosity effects in the prediction of global pressure-drop

$$\frac{\Delta P|_h}{L}=\zeta_\mu\left(\frac{\mu_0}{K_0}\right)U+\zeta_C(\rho C_0)U^2=\zeta_\mu D_{\mu_0}+\zeta_C D_{C_0} \tag{4}$$

with the coefficients ζ_μ and ζ_C representing the lumped local effect of temperature dependent viscosity and the effect of viscosity on the fluid velocity profile [11].

Combining Eqs. (2), (3), (4), one obtains

$$R=\Phi D_{\mu_0}[(1-\zeta_\mu)+(1-\zeta_C)\lambda] \tag{5}$$

where Φ represents $(H/L)(U/q'')$, and λ is D_{C_0}/D_{μ_0}.

Equation (5) is instructive for revealing the functional between R and other porous medium characteristics through Φ and λ. It also provides means for determining the asymptotic behavior of R. For instance, when the heat flux tends to infinity, for a finite value of fluid speed, ζ_μ and ζ_c tend to zero and unity [11,16], respectively, so R will tend to zero. Recall from [11] that with continuously increasing heat flux, eventually the *inviscid form-drag limit* is reached because the viscosity value asymptotically goes to zero and, by consequence, the viscous effects becomes negligible confirming the asymptotic result derived from Eq. (5).

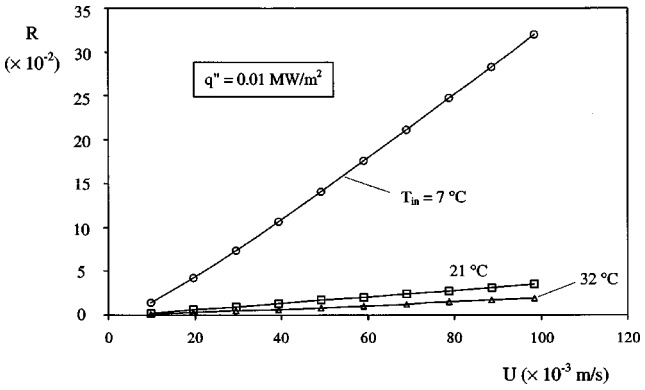

Fig. 2 Overall system energy efficiency *R* versus fluid speed, for $q''=0.01$ MW/m^2 and several fluid inlet temperatures

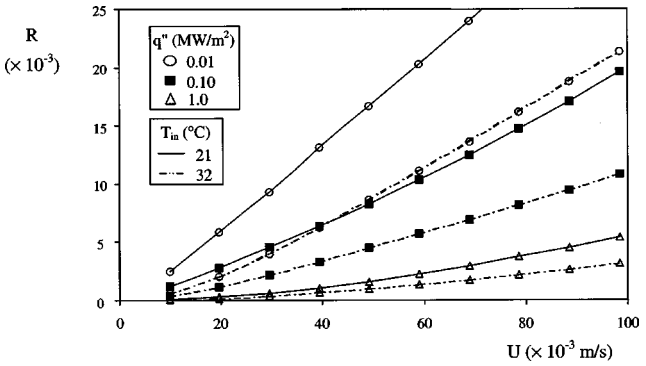

Fig. 4 Comparison of heat flux and inlet temperature effects on overall system energy efficiency

Results and Analysis

Figure 2 shows the variation of R with increasing fluid speed, for three inlet fluid temperatures, when the channel is heated with $q''=0.01$ MW/m^2. A very pronounced variation is observed when the inlet temperature goes from 7 to 32°C, with low inlet fluid temperature yielding more energy efficient process. The increase in the inlet fluid temperature reduces the energy efficiency of the process for the same fluid speed value, because a higher inlet fluid temperature yields a low fluid viscosity making the flow pump power less sensitive to heating (or, equivalently, to an increase in temperature). Noticeable is the temperature-dependent viscosity effect even for relatively high inlet temperatures, such as 32°C, when the fluid speed increases.

The effect of increasing the heat flux is shown by the graph of Fig. 3, where curves for inlet fluid temperature fixed at 7°C and increasing heat flux are presented. Notice the relatively stronger effect of changing the heat flux while the heat flux increases from 0.01 MW/m^2 to 0.1 MW/m^2, as compared to the effect when the heat flux grows from 0.1 MW/m^2 to 1.0 MW/m^2. Again, this trend confirms relatively smaller temperature-dependent viscosity effect when the heat flux is very high because the fluid becomes hot enough soon after entering the channel, weakening the viscous drag effect.

Finally, Fig. 4 presents a comparison of the inlet temperature and heat flux effects all together, for inlet temperature 21°C (continuous lines) and 32°C (dashed lines). Somewhat unexpected is the crossing of the curve for heat flux 0.10 MW/m^2 and inlet temperature 21°C (continuous line with black-square symbol) with the curve for heat flux 0.01 MW/m^2 and inlet temperature 32°C (dashed line with hollow-circle symbol), occurring at fluid speed 42×10^{-3} m/s. This crossing highlights the different sensibility of the temperature-dependent viscosity effect to inlet temperature and heat flux as it indicates that beyond fluid speed 42 $\times10^{-3}$ m/s, heating a higher inlet temperature fluid with a lower heat flux is more energy efficient.

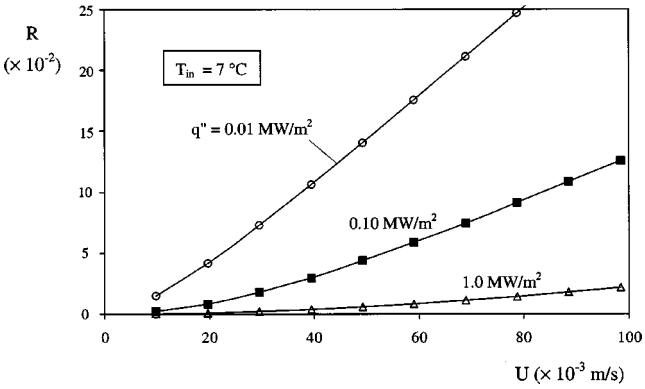

Fig. 3 Overall system energy efficiency *R* versus fluid speed, for $T_{in}=7°C$ and several heat fluxes

Summary and Conclusion

Pump power reduction is a practical engineering incentive in heating the flow of a variable (with temperature) viscosity liquid. However, the overall system energy gain (pump power gained versus heat power spent) is a realistic design constraint. The role played by the heat flux and the inlet liquid temperature on the pump-power reduction and the overall energy efficiency R, as defined in Eq. (2), is studied here for parallel-plate porous medium channel flows, considering the design of a cold plate for cooling phased-array radars. Pressure-drop versus fluid speed results obtained through numerical simulations of a strong temperature dependent viscosity poly-alpha-olefin oil flow, along with the recently proposed Modified Hazen-Dupuit-Darcy (M-HDD) model, incorporating temperature-dependent viscosity effects, is used in the analysis.

For a fixed heat flux (thus, heat power), the increase in the inlet temperature reduces the energy efficiency of the process at a fluid speed value. In addition, for high heat flux, as the fluid gets hotter earlier while it flows along the channel, the overall energy gain R progressively decreases because the viscosity decreases more rapidly.

Moreover, the pumping power reduction by heating the fluid and the overall energy efficiency of the system is shown to respond differently to changes in inlet temperature and heat flux respectively, making analytical estimates very difficult to accomplish.

The porous medium configuration considered here, has been demonstrated to operate with 30 percent maximum overall energy efficiency when the heat flux is minimum (0.01 MW/m^2), the fluid speed is maximum ($U=10^{-3}$ m/s), and the fluid inlet temperature is the lowest ($T_{in}=7°C$). For the same heat flux and fluid speed the energy efficiency reduces to less than 3 percent for the highest inlet temperature tested ($T_{in}=32°C$). Therefore, the strategy of heating the temperature-dependent viscosity liquid to reduce pump power presents itself as an effective practical engineering tool for porous medium flows. As a final note, the heat transfer implications of heating the liquid as it flows through the cold plate is considered in [11], [12], [13] and [16].

Nomenclature

A = area, m^2
C = form coefficient, m^{-1}
D = specific drag, Pa m^{-1}
H = half-channel spacing, m

k = thermal conductivity, $\mathrm{W\,m^{-1}\,K^{-1}}$
K = permeability, $\mathrm{m^2}$
L = channel length, heated section, m
P = global (cross-section averaged) pressure, Pa
q'' = channel surface heat flux, $\mathrm{W\,m^{-2}}$
$\dot{Q}$ = overall heating power, W
R = overall energy gain, Eq. (2)
T = temperature, °C
U = global (cross-section averaged) longitudinal velocity, $\mathrm{m\,s^{-1}}$
$\dot{W}$ = pump power, W

Greek Symbols

ϕ = porosity
λ = ratio of global form to viscous drag
μ = dynamic viscosity, $\mathrm{kg\,m^{-1}\,s^{-1}}$
ρ = density, $\mathrm{kg\,m^{-3}}$
ζ = correction coefficients for the M-HDD model

Subscripts

c = cross-section
C = form
f = fluid
in = inlet
s = solid
w = surface, wall
0 = isothermal condition
μ = viscous

References

[1] Oskay, R., and Kakaç, S., 1973, ''Effect of Viscosity Variations on Forced Convection Heat Transfer in Pipe Flow,'' METU J. Pure Appl. Sci., **6**, 211–230.

[2] Shin, S., Cho, Y. I., Gringrich, W. K., and Shyy, W., 1993, ''Numerical Study of Laminar Heat Transfer with Temperature Dependent Fluid Viscosity in a 2:1 Rectangular Duct,'' Int. J. Heat Mass Transfer, **36**, 4365–4373.

[3] Xie, C., and Hartnett, J. P., 1992, ''Influence of Variable Viscosity of Mineral Oil on Laminar Heat Transfer in a 2:1 Rectangular Duct,'' Int. J. Heat Mass Transfer, **35**, 641–648.

[4] Boomsma, K., and Poulikakos, D., 2002, ''The Effects of Compression and Pore Size Variations on the Liquid Flow Characteristics in Metal Foams,'' ASME J. Fluids Eng., **124**, 263–272.

[5] Lauriat, G. and Vafai, K., 1991, ''Forced Convective Flow and Heat Transfer through a Porous Medium Exposed to a Flat Plate or a Channel,'' *Convective Heat and Mass Transfer in Porous Media*, S. Kakaç et al., eds., Kluwer, Dordrecht, 289–327.

[6] Lage, J. L. and Narasimhan, A., 2000, ''Porous Media Enhanced Forced Convection: Fundamentals and Applications,'' In *Handbook of Porous Media* (Edited by K. Vafai), 357–394. Marcel-Dekker, New York.

[7] Nield, D. A., and Bejan, A., 1999, *Convection in Porous Media*, 2nd Ed, Springer Verlag.

[8] Ingham, D. B., and Pop, I., 2002, *Transport Phenomena in Porous Media II*, Pergamon, Oxford.

[9] Lage, J. L., Weinert, A. K., Price, D. C., and Weber, R. M., 1996, ''Numerical Study of a Low Permeability Microporous Heat Sink for Cooling Phased-Array Radar Systems,'' Int. J. Heat Mass Transfer, **39**, 3633–3647.

[10] Porneala, D. C., 1998, *Experimental Tests of Microsporous Enhanced Cold Plates for Cooling High Frequency Microwave Antennas*, Ph.D. Dissertation, Southern Methodist University, Dallas, Texas.

[11] Narasimhan, A., and Lage, J. L., 2001, ''Modified Hazen-Dupuit-Darcy Model for Forced Convection of a Fluid with Temperature Dependent Viscosity,'' J. Heat Transfer, **123**, 31–38.

[12] Narasimhan, A., and Lage, J. L., 2001, ''Forced Convection of a Fluid with Temperature-Dependent Viscosity through a Porous Medium Channel,'' Numer. Heat Transfer **40**(8), 801–820.

[13] Narasimhan, A., Lage, J. L., Nield, D. A., and Porneala, D. C., 2001, ''Experimental Verification of Two New Theories for Predicting the Temperature-Dependent Viscosity Effects on the Forced Convection through a Porous Media Channel,'' ASME J. Fluids Eng., **123**, 948–951.

[14] Lage, J. L., Antohe, B. V., and Nield, D. A., 1997, ''Two types of Nonlinear Pressure-Drop versus Flow-Rate relation Observed for Saturated Porous Media,'' Ann. Chim. (Rome), **119**, 700–706.

[15] Lage, J. L., 1998, ''The Fundamental Theory of Flow through Permeable Media from Darcy to Turbulence,'' in Transport Phenomena in Porous Media (Eds. D. B. Ingham and I. Pop), Pergamon, Oxford, 1–30.

[16] Narasimhan, A., 2002, *Unraveling, Modeling and Validating the Temperature Dependent Viscosity Effects in Flow through Porous Media*, Ph.D. Dissertation, Southern Methodist University, Dallas, Texas.

Journal of Fluids Engineering

Discussion

Transition to Meandering Rivulet Flow in Vertical Parallel-Plate Channels

Glenn E. McCreery and Donald M. McEligot
Idaho National Engineering and Environmental Laboratory (INEEL), Idaho Falls, Idaho 83415-3885

While there have been many studies of gravity-driven rivulet flow over an external surface, treatment of internal rivulets has been sparse. A notable exception is the analytical and experimental study by Anand and Bejan [1]; they derived an approximate solution for a laminar rivulet developing between two parallel vertical planes and employed it to examine the transition to a meandering flow.

For rivulets flowing between closely spaced plates, the velocity becomes "slow" (i.e., "low" Reynolds number) and an approximately fully-developed flow at its terminal velocity can be reached in a short distance. Conceptually, this value can be derived from the analysis of Anand and Bejan. However, for cases where the inlet volumetric flow rate Q is sufficiently high that the rivulet becomes wide relative to the plate spacing, a simple treatment can describe the resulting flow.

For this treatment, we orient the coordinates as x = vertical, y = spanwise and z = normal to the vertical plates and assume:

- an incompressible fluid with constant properties
- steady, laminar flow (except at the leading edge outside the region of interest)
- fluid density much greater than density of its surroundings (so $p_s\{x\} \approx$ constant)
- negligible interface shear with surroundings at edges ($\rightarrow \partial u/\partial y \approx 0$)
- fully-developed flow away from the inlet
- rivulet width in spanwise direction (W) considerably larger than edge region formed by curvature of free surfaces at the edges

Under these assumptions and approximations, the one-dimensional governing equations reduce to:

$$\text{continuity:} \quad \dot{m} = \rho Q \approx \rho V_b (Ws) = \text{constant}$$

$$x\text{-momentum:} \quad \rho g s = 2 g_c \tau_W$$

when applied to a horizontal element. If one starts with a wide rivulet at a velocity lower than terminal as Anand and Bejan did, the frictional force is less than the body force so the flow accelerates under gravity, making the cross sectional area less until the balance of these two terms suppresses the advective term (not shown). For steady laminar flow between parallel plates [2], the development length is of the order of $(x_L/s) \approx 0.02\,\mathrm{Re}$ so the lower the Reynolds number Re is, the shorter the distance required for the following treatment to become reasonable.

For a fully developed laminar flow between parallel plates, the wall shear stress may be non-dimensionalized as $f = 24/\mathrm{Re}$ with the Reynolds number based on the hydraulic diameter of twice the plate spacing (e.g., as by Schade and McEligot [2], Kays and Crawford [3] and many others). Substitution and rearrangements lead to:

$$\text{bulk velocity,} \quad V_b \approx g s^2/(12\nu)$$

and

$$\text{Reynolds number,} \quad \mathrm{Re} = (\rho V_b D_h/\mu) \approx g s^3/(6\nu^2)$$

depending on the plate spacing and fluid properties and independent of the total flow rate. The rivulet width then is determined by the volumetric flow rate provided at the inlet as

$$W \approx 12 Q \nu/(g s^3) \quad \text{or} \quad (W g s^3/(Q\nu)) \approx 12$$

Provided that the assumptions and approximations above are approached so that this treatment is valid, the results offer the possibilities of employing this configuration as a viscometer or flowmeter by measuring the appropriate quantities. For such applications the sensitivity to plate spacing makes its accurate measurement important. Alternatively, the measurement of the rivulet width, flow rate and viscosity can be used to estimate the plate spacing and, as a first approximation, its variation or the degree to which the plates are parallel.

Acknowledgments

The study reported was partly supported by the Environmental Management Science program through DoE Idaho Operations Office contract DE-AC07-99ID13727. The encouragement and advice of Dr. Paul Meakin, the Principal Investigator of the project, is appreciated.

Nomenclature

D_h = hydraulic diameter, $2s$
f = Fanning friction factor, $2 g_c \tau_W/(\rho V_b^2)$
g = acceleration of gravity
g_c = units conversion factor, e.g., 1 kg m/(N s^2)
$\dot{m}$ = mass flow rate
p_s = static pressure of surroundings (typically air)
Q = volumetric flow rate
Re = Reynolds number, $\rho V_b D_h/\mu$
s = spacing between plates
u = vertical velocity component
V_b = bulk or mixed mean vertical velocity
W = rivulet width
x = vertical coordinate
y = spanwise coordinate
z = normal coordinate
μ = absolute viscosity
ν = kinematic viscosity, μ/ρ
ρ = fluid density
τ_W = wall shear stress

References

[1] Anand, A., and Bejan, A., 1986, ''Transition to Meandering Rivulet Flow in Vertical Parallel-Plate Channels,'' ASME J. Fluids Eng., **108**, pp. 269–272.

[2] Schade, K. W., and McEligot, D. M., 1971, ''Cartesian Graetz Problems with Air Property Variation,'' Int. J. Heat Mass Transfer, **14**, pp. 653–666.

[3] Kays, W. M., and Crawford, M. E., 1980, *Convective heat and mass transfer, 2nd edition*, McGraw-Hill, New York.

Journal of Fluids Engineering

Erratum

Erratum: "On Preferred Perturbations Selected by Centrifugal Instability" [Journal of Fluids Engineering, 2001, 123, pp. 702–705]

O. A. Likahachev

1. The fourth equation in the system (2) was printed incorrectly. The correct system is:

$$\begin{gathered}\gamma U u + Go^2 U' v - B f u' = u'' - \beta^2 u \\ \gamma U v + V' v - B f v' + 2Uu + q' = v'' - \beta^2 v \\ \gamma U w - B f w' - \beta q = w'' - \beta^2 w \\ \gamma u + Go^2 (v' + \beta w) = B \eta u'\end{gathered} \tag{2}$$

2. The functions G_1 and G_6 in the Appendix were printed incorrectly. The correct functions are:

$$G_1 = v + \beta \eta w$$

$$G_6 = \beta^2 \eta w + (1 - B \eta V) Dw + \beta \eta q$$

